Mathematical Modelling of Airflow in Shipping Systems: Model Development and Testing

A thesis presented in partial fulfilment of the requirements for the degree of Doctor of Philosophy in Food Technology at Massey University, Palmerston North, New Zealand.

Nicholas John Smale
B.Tech. (Hons) (Food Technology)

2004

Abstract

Horticultural exports are of economic significance to New Zealand. Only through providing consistently high quality products to distant markets can New Zealand hope to command a premium price. New Zealand's two major horticultural exports, apples and kiwifruit, are transported to foreign markets by sea; either in refrigerated holds on-board cargo vessels or in refrigerated containers. Long transit times mean that conditions in these systems must be carefully controlled to ensure high quality product arrives at market. Effective distribution of air is a key consideration in transport systems.

A mathematical model to describe the flow of air in marine transport systems was developed. The model was based on a resistance network framework, relying on simplification of the complex geometry within the refrigerated space to a discrete number of flow paths and points of convergence and divergence. Correlations quantifying the flow resistance of each channel were required. Some of these correlations were already available, and some were developed specifically for this purpose. A general method for predicting the flow resistance of enclosed conduits based on the Darcy-Weisbach, laminar and Colebrook equations was found to be sufficiently accurate for use. The flow resistance of horizontally vented horticultural packages was quantified and the cause of the flow resistance investigated. Entrance and exit effects were found to be significant, and a relationship between vent size and flow resistance was developed.

Air interchange between a vented carton and the general refrigerated space was shown to be a significant mode of heat transfer. The effect of vent design on the rate of air interchange was found to be complex. Quantitative relationships between vent characteristics and rates of air interchange could not be developed; however, some general observations were made. Vent size, aspect ratio and alignment were all found to affect the rate of interchange.

An existing method for determining in-package fluid velocities was refined to improve the accuracy of data and reduce the measurement time. A low-cost method for measuring airflows in transport systems was also developed utilising thermistors. These thermistor anemometers were used to monitor velocities in four shipments of fresh produce from New Zealand. Three of the four vessels monitored showed large variation in the circulation rate in the period between evaporator defrosts due to frosting. In some cases, frosting was severe enough to cause loss of delivery air temperature control. Management of defrosts was identified as an area of improvement in refrigerated hold management.

Validation of the model developed was performed using four systems: a laboratory scale test-rig, a 40' container and two of the surveyed refrigerated holds. Airflow predictions were used with a heat transfer model to predict in-package temperatures. Comparison of measured and predicted flows and in-package temperatures showed good agreement given uncertainty of geometry and input data.

The implications of altering a number of operational and design variables in both containers and refrigerated holds were investigated using the developed models. Increased circulation rates were found to increase cooling rates and reduce temperature variability in both types of systems; however, the magnitude of the benefit decreased with increasing circulation rate. Removal of the floor gratings and the use of pallet bases as an air distribution channel was found to increase temperature variability in both types of systems. The magnitude of the increase was small in a 40' container but substantial in a refrigerated hold.

The correlations and models developed in this thesis provide useful tools to analyse and optimise the design and operation of refrigerated marine transport systems.

Acknowledgements

Firstly, I'd like to acknowledge the support and guidance of my supervisors: David Tanner, Nevin Amos and Don Cleland. Their knowledge and advice was shared without reservation and was invaluable throughout the PhD experience. The supervisor-student relationship was relaxed and open; it would be difficult to find a better group of guys to work with.

I would also like to acknowledge the help of the scientific and technical staff of Fresh Technologies within the Institute of Food Nutrition and Human Health at Massey University and the Supply Chain Innovation team at Food Science Australia. A wealth of knowledge and abilities were made available to me through the staff of these two organisations and I am grateful for that.

Also, a big thanks to the companies involved: ENZAFRUIT NZ Ltd, Zespri International Ltd, Seatrade NZ Ltd, LauritzenCool NZ Ltd and Maersk Sealand. Their support, both financially and logistically, contributed to the successful collection of datasets which, without their input, would have been impossible to gather.

Finally, a big thank you to Keryn, for everything.

If you go on hammering away at a problem, it seems to get tired,
lies down and lets you catch it.

W.L. Bragg
(Nobel Prize laureate - 1915)

Table of Contents

Nomenclature

a	=	Ramsin equation coefficient	$(kg.s^{(b-2)}.m^{-(b+2)})$
a	=	Thermistor property	
A	=	Area	(m^2)
b	=	Ramsin equation exponent	
b	=	Thermistor property	(K^{-1})
c	=	Vent resistance coefficient	$(kg.s^{(b-2)}.m^{-(b+2)})$
c	=	Thermistor calibration coefficient	$(J.s^{n-1}.m^{-n}.K^{-1})$
C	=	Constant	
CC	=	Configuration coefficient	
C_g	=	Geometric constant	
col	=	Jacobian matrix column index	
C_p	=	Specific heat capacity	$(W.kg^{-1}.K^{-1})$
d	=	Vent resistance exponent	
D	=	Dimension	(m)
D_h	=	Channel hydraulic diameter	(m)
D_{short}	=	Rectangular channel short dimension	(m)
E	=	Criteria employed for 'backtracking' procedure	
f	=	Friction factor	
$F(a)$	=	Function of a	
$\mathbf{F(\psi)}$	=	Vector of function values	$(kg.s^{-1})$
Fr	=	Energy lost through friction effects	$(J.m^{-3})$
$FUTC$	=	Fraction unaccomplished temperature change	
g	=	Acceleration due to gravity	$(m.s^{-2})$
g_i	=	External force per unit mass of fluid in the i_{th} direction	$(N.kg^{-1})$
h	=	Height relative to arbitrary datum	(m)
h_s	=	Surface heat transfer coefficient	$(W.m^{-2}K^{-1})$
H	=	Number of horizontal zones	
I	=	Current	(A)
i,j,k	=	Cartesian co-ordinates	
$\mathbf{J}$	=	Jacobian matrix	$(kg.s^{-1}.Pa^{-1})$
k	=	Laminar friction geometric parameter	
k	=	Turbulent kinetic energy	$(m^2.s^{-2})$
K_1	=	Ergun equation constant	
K_2	=	Ergun equation constant	
K_{add}	=	Additional frictional losses stated as number of velocity heads	
L	=	Distance	(m)
M'_{H2O}	=	Effective permeance of the fruit surface to movement of water vapour under prevailing conditions	$(mol.s^{-1}.m^{-2}.Pa^{-1})$
m_t	=	Thermistor thermal mass	$(J.K^{-1})$
$\dot{m}$	=	Mass flow rate	$(kg.s^{-1})$
n	=	Index	
n	=	Thermistor calibration exponent	
Nu	=	Nusselt number	
O	=	Ratio of vent area to face area	
Δp_{H2O}	=	Partial pressure driving force	(Pa)
P	=	Fluid pressure	(Pa)
Pm	=	Perimeter of conduit	(m)
Pr	=	Prandtl number	

Q	=	Fluid volumetric flow	($m^3.s^{-1}$)
r'_{H2O}	=	Rate of water loss from product	($mol.s^{-1}$)
R	=	Channel aspect ratio	
Re	=	Reynolds number	
row	=	Jacobian matrix row index	
SCP	=	Scale parameter	
SHP	=	Shape parameter	
t	=	Time	(s)
T	=	Temperature	(°C)
u	=	Superficial velocity	($m.s^{-1}$)
v	=	Fluid velocity	($m.s^{-1}$)
v'	=	Turbulent velocity component	($m.s^{-1}$)
V	=	Number of vertical zones	
V	=	Voltage	(V)
$VRC_{i,j}$	=	Velocity relativity coefficient	
W	=	Weibull distribution	
x,y,z	=	Co-ordinates	(m)
α	=	Calculated proportion of correction to add to solution vector	
β	=	Flow resistance	
γ	=	Expansion factor	
$\boldsymbol{\delta\psi}$	=	Vector of corrections of total pressure	(Pa)
ε	=	Absolute roughness	(m)
ε	=	Bed porosity	
$\varepsilon_{\varphi t}$	=	Viscous dissipation function	($m^2.s^{-3}$)
λ	=	Thermal conductivity	($W.m^{-1}.K^{-1}$)
μ	=	Fluid viscosity	(Pa.s)
ρ	=	Fluid density	($kg.m^{-3}$)
υ	=	Kinematic viscosity	($m^2.s^{-1}$)
υ_τ	=	Turbulent eddy viscosity	($m^2.s^{-1}$)
ϕ	=	Rate of heat transfer	(W)
χ	=	Dissipation factor	($W.K^{-1}$)
ψ	=	Total pressure	(Pa)
$\boldsymbol{\psi}$	=	Vector of total pressures	(Pa)
Ω	=	Electrical resistance	(Ω)

1 Introduction

Exporting fruit is big business. The volume of marine refrigerated cargoes totalled 61.9 million tonnes in 2001 and is growing at approximately 5% per annum (Heap, 2003). Bananas contributed approximately 33% of this volume in 2001, while deciduous products contributed around 10% and citrus 15% in 1998 (Stera, 1999, Heap, 2003).

New Zealand relies heavily on primary produce for export earnings and fruit exports are a major contributor to this export income. Goods valued at $24.5 billion were exported from New Zealand in 2000, with the meat and dairy sectors accounting for 30% of this value and 'fruit and nuts' accounting for a further 4% (Statistics NZ, 2003). Apples and kiwifruit make up most of the 'fruit and nuts' classification.

By virtue of the fact that fruit is a biological organism, variability in the quality of fresh fruit at the point of sale is unavoidable. Fruit competes with processed food for its place in consumers' diets, and consumers' previous experiences will influence the likelihood of repeat purchases. Negative experiences as a result of fruit that the consumer considers below acceptable standards will reduce consumption. By reducing the level of quality variability of produce at the point of sale, the frequency of negative experiences will diminish, thereby increasing demand. Associating a brand with a product of consistent high quality also provides competitive advantage and possibly a price premium.

Variability in product quality can be introduced at any stage through the supply chain; whilst reduction of variability is generally only achieved through sorting and grading processes, which are expensive and become more difficult logistically closer to market. Quality maintenance is achieved by reducing the temperature of the product, which reduces the rate of the biological reactions that cause product quality loss. Refrigeration systems generally aim to maintain chilled products at temperatures as low as possible without freezing or causing chilling injury. Alongside this, the refrigeration system will aim to avoid excessive dehydration of the product, which can cause significant quality loss as well as loss of saleable weight of product. Therefore, heat and mass transfer are the key processes in storage and transport.

New Zealand is geographically distant from many of its export markets, with transport a major component of the supply chain in terms of both time and investment. Apples and kiwifruit are transported by sea, either in refrigerated holds on-board cargo vessels or in refrigerated containers. With transit times to European markets of approximately four to six weeks, there is adequate opportunity for introduction of substantial quality variability as well as significant product deterioration if conditions in-transit are not carefully controlled.

Refrigerated containers and holds rely on the flow of cool air around horticultural produce to complete cooling and remove respiratory heat during transport. Influences such as diurnal ambient temperature cycles, evaporator frosting, and palletisation cause inevitable temperature variability within the system both spatially and temporally. As the product temperature influences the rate of quality deterioration, this temperature variability will cause increased quality variability. Design of transport systems and operating procedures should aim to reduce this variability.

Minimisation of temperature variability is not a simple problem. For example, increased air velocities will generally reduce temperature variability; however, they may also accelerate quality deterioration through excessive water loss. Greater fan power also introduces more heat to the system and increases power consumption. In essence, there are several motivations to be considered when determining an appropriate rate of air circulation, and a single design is unlikely to provide the optimum solution for all cargoes.

Unfortunately, physically testing numerous alternative designs or operating practices is impractical due to the large scale of marine transport systems and the high value of the product. Mathematically modelling airflow in refrigerated containers and holds offers an alternative method to estimate the airflow patterns for alternative systems, without requiring the researcher to physically build and test the configuration. This allows rapid assessment of changes and presents the opportunity to assess numerous configurations.

Development of mathematical models to predict airflow is not a novel concept, and has been previously applied to refrigerated spaces. Models have been developed employing a number of mathematical techniques with varying complexity and degrees of success.

This project aimed to develop a mathematical model of airflow within refrigerated marine transport systems. The model was designed to compliment existing heat and mass transfer models for packaged horticultural produce. The purpose of the model was to provide greater insight into the effect of altered operational and design parameters on the performance of refrigerated marine transport systems.

Figure 1-1 shows a conceptual diagram of the important factors in a refrigerated marine transport system affecting the rate of product quality loss of horticultural products. Items highlighted in red in Figure 1-1 have been addressed in this work.

Figure 1-1 – Conceptual diagram showing the major factors determining the rate of product quality loss of a horticultural product. Arrows show dependencies and areas covered in this thesis are highlighted in red

The thesis is structured in five parts. Part I summarises the available literature and states the objectives of the work. Part II describes the development of two flow measurement techniques. The first measurement technique (Section 5) was designed to measure the external air velocity, highlighted in Figure 1-1. The second measurement method (Section 6) was an improvement of an existing method designed to estimate in-package air velocities in ventilated packages. The method was developed in anticipation that in-package air velocity estimation would be important for predicting product temperatures during validation of the airflow model; however, the technique was ultimately not required as product temperatures were only recorded during shipments of products packaged in unvented cartons. The technique remains an important tool for translating average flows through vented packages (as predicted by the airflow model) into the specific in-package velocities required for heat and mass transfer prediction.

Part III describes the mathematical basis of the model and the method of solution (Section 7), as well as presenting the required flow resistance correlations (Section 8). The model was designed to predict the external and average in-package velocities highlighted in Figure 1-1. Section 8 also reports on investigations of the relationships between packaging vent design and in-package velocity (Section 8.3.1) and rates of air displacement (Section 8.4).

Part IV presents implementation and validation of the model in four test systems. The predicted effects of altered operational and design factors are also reported. Part V concludes the thesis by summarising the main findings of the work and highlights those areas where improvements of marine transport systems are possible.

Part I
Background

This part contains general information pertinent to the project. Section 2 provides information gathered from the published literature on marine transport systems, airflow measurement methods and relevant mathematical models which have been developed previously. Mathematical modelling frameworks are summarised and discussed in Section 3 and the specific objectives of the work are outlined in Section 4.

2 Literature Review

The following literature review provides background information regarding marine transport of horticultural produce from New Zealand. Methods of airflow measurement and mathematical modelling methods previously employed by researchers are discussed. Whilst a complete model of the refrigerated transport system would include all sources of variation within the system, focus was made on the measurement and modelling of airflow. Modelling of refrigeration systems is covered elsewhere (Cleland, 1990, Lovatt, 1992), while models specifically applied to reefer containers are also available (e.g. Jolly *et al.*, 2000).

2.1 Shipping systems and the transport environment

Three basic configurations for refrigerated marine transport are in use today:

- Conventional reefer vessels carry their cargo in large refrigerated holds
- Integral refrigerated containers are supplied with power but are equipped with their own refrigeration plant
- Porthole containers are supplied with refrigerated air by a central refrigeration plant or a clip-on refrigeration unit. Porthole containers are now not commonly used both worldwide, and for cargos exported from New Zealand

The direction of airflow in reefer vessel holds and integrated containers is generally vertically upward through the cargo. Refrigerated air is delivered via floor gratings and returns to the refrigeration plant via the headspace above the cargo. There are four options for floor design, each with different advantages and limitations (Figure 2-1).

- Perforated floors have traditionally been used in refrigerated ships and have been modified for use in containers. They give less obstruction to airflow and better distribution in containers than castellated floors, but they are difficult to clean unless they are removable
- Castellated floors cause greater obstruction to airflow but are very strong and easy to clean
- T-bar floors cause minimum obstruction to airflow but can be damaged by forklifts and are difficult to keep clean
- Pallet bases may be used to provide an air duct with a flat floor, which is easily cleaned

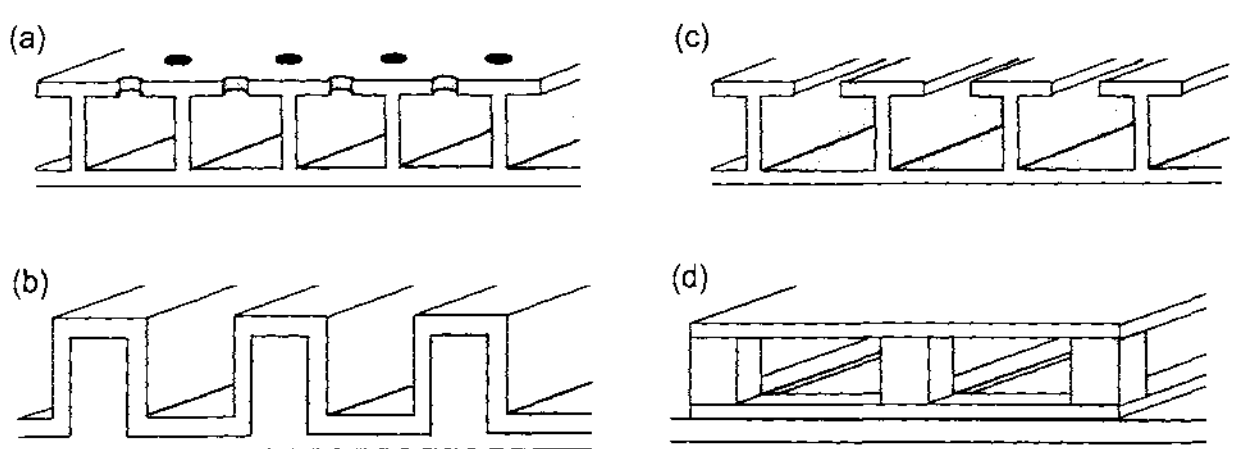

Figure 2-1 – Four alternative floor designs for air distribution in refrigerated marine transport: (a) perforated, (b) castellated, (c) T-bar and (d) a flat floor with pallet bases acting as air ducts (adapted from Frith, 1991)

High rates of air circulation are used for both containers and vessels to initially complete cooling of the produce to the desired transport temperature and to ensure refrigerated air is distributed throughout the cargo space. The rate of circulation is often expressed as the air circulation rate, which is the volume of air circulated in the enclosed space per hour divided by the volume of the empty enclosed space. Air circulation rates vary widely but typically range from 60-120 air changes per hour during initial cooling and, in systems where the circulation rate can be reduced, 30-60 air changes per hour once the desired product temperature is achieved (storage mode) (IIF/IIR, 1995). Reduced air circulation rates are used once cooling is achieved to reduce refrigeration load and power consumption.

2.1.1 Refrigerated containers

Specialised container ships have holds designed with vertical guides to hold containers in stacks of around 6 to 9 containers below deck. Containers carried on the decks of ships are lashed to hatch covers and decks, stacked 3 to 4 high. The capacity of container vessels is measured in TEU's or FEU's (twenty-foot or forty-foot equivalent units), indicating the number of 20' of 40' containers the vessel can carry. Vessel capacities are generally 1,000 - 5,000 TEU's, although modern vessels can be as large as 6,600 TEU's. Figure 2-2 shows a fully laden container ship with stacks of containers above deck clearly visible.

Figure 2-2 – The container vessel LAURA MAERSK (3,700 TEU capacity) at sea (Maersk Sealand, 2003)

Two configurations are used in containerised transport, varying in the use of a central refrigeration plant versus individually equipped containers. In the former configuration, porthole containers are used with two sealable portholes on the front bulkhead, through which refrigerated air is circulated. If these containers are to be left on shore, clip-on refrigeration units are available to ensure a break in the cold chain does not occur. This configuration is generally used on 'liner' trades, in which large and regular quantities of perishable goods are shipped between regular ports of call (IIF/IIR, 1995). Their use is becoming less frequent, with clip-on refrigeration units no longer available at many ports in New Zealand and Australia.

Integral containers are equipped with a refrigeration plant and need merely to be supplied with electricity (3-phase, 380 V / 50 Hz or 440 V / 60 Hz) to maintain their internal environment. This configuration is

more widely used. Integral containers are generally carried on deck; however, modern ships include space below deck for these containers with additional air renewal to remove heat from the containers' condensers. Some ships are also fitted with water-cooling facilities for containers with water-cooled condensers, although not all heat is removed and ventilation is still necessary. Those carried on deck may be protected from the sun with an upper layer of non-refrigerated containers (IIF/IIR, 1995).

Marine reefer containers are suitable for multimodal transport; allowing cargo to be loaded away from the port and transported by land to the port. Containers usually come in standard sizes in accordance with ISO standards to allow for interchange of containers between shipping companies, although these standards are not always observed. There are two general size classes, 20' and 40', with a number of specifications within each class. Exact specifications are given in ISO standard 668 (ISO, 1995). Air circulation in these containers is generally vertical, with air delivered into the floor channels and returning to the refrigeration plant through a grill near the ceiling as shown in Figure 2-3. Aluminium T-bar floors running the length of the container are most commonly used. There are usually 36 floor channels, and sometimes holes in the T-bars to allow air to flow between channels near the walls are incorporated (Figure 2-4).

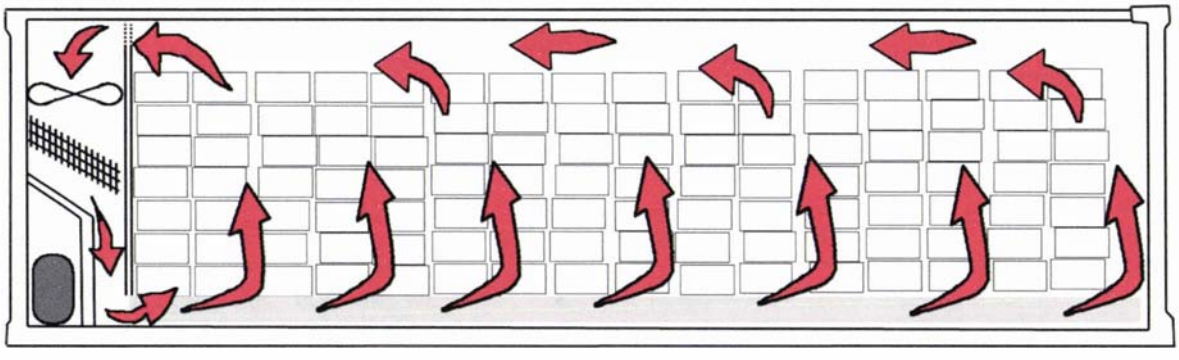

Figure 2-3 - Typical airflow configuration in an integral refrigerated container

Figure 2-4 – Photographs showing aluminium T-bar floors without (left) and with (right) holes to allow flow between floor channels

Some reefer containers are equipped with fully variable-capacity units with which both refrigeration capacity and air circulation rate may be adjusted during successive stages of handling (IIF/IIR, 1995). For sensitive chilled goods, temperature is controlled at the air delivery and the refrigeration capacity is modulated for control. For frozen goods, temperature is generally regulated at the air return.

Ambient temperature, insulation quality, respiration rate of the cargo, initial temperature of the cargo, the rate of fresh air exchange and leakage all affect the refrigeration capacity required of a container. Ambient temperatures experienced by containers on deck may be as high as 50°C in tropical parking areas with additional radiant heat from the sun. The quality of insulation in the container decreases with age, with typical values of 22 $W.K^{-1}$ for newer 20' containers and 30 $W.K^{-1}$ for older 20' containers (Heap, 1989, Boldrin *et al.*, 1993). Values for 40' containers are approximately double these figures.

Controlled atmosphere (CA) containers are capable of altering the gas atmosphere inside the container to reduce the rate of quality loss of the produce. These containers are generally equipped with N_2 generators, O_2 controllers and CO_2 scrubbers, and rely on the respiration of the cargo to provide CO_2 to raise its concentration to the required set point.

Products of respiration and ethylene may need to be removed from the internal atmosphere of the container when transporting fruit and vegetable products in conventional (non-CA) containers. A fresh air exchange vent that utilises the fan generated pressure gradients inside the container is used to achieve exchange of air between the cargo space and the surrounding environment. Suggested fresh air exchange rates vary widely depending on the source of the information. For example, suggested rates for apples in a 40' container ranged from 264 $m^3.h^{-1}$ (Frith, 1991) to just 10 $m^3.h^{-1}$ (Irving, 1997). Excessive fresh air exchange increases the heat and moisture load on the container unnecessarily. Air leakage of containers without fresh air exchange will have the same effect and may also negatively impact on the efficacy of CA systems. Methods for measurement of air leakage rates are discussed in Section 2.2.5.

Thermo King, a manufacturer of container refrigeration systems, have recently developed an 'Advanced Fresh Air Management' system which delays the opening of the fresh air exchange vent for a given period of time (AFAM) or until gas levels reach a set-point (AFAM+) (Anon, 2001a). These systems reduce the heat load during product cool-down and AFAM+ also ensures fresh air is not admitted unnecessarily during the remainder of the voyage. Another innovation is the use of variable frequency fan drives (VFD) depending on temperature difference between delivery and return air (Anon, 2001a). The frequency of the power source to the fans is varied to maintain a minimum difference between delivery and return air temperatures. Reported benefits are reduction in the both the heat input through fan power and power consumption of the container. Possible negative effects include increased temperature variability within the container, caused by the reduction in air circulation rate and poorer air distribution.

2.1.2 Refrigerated vessels

A typical modern middle size reefer ship will have a capacity of approximately 12,000 m^3, divided into around 4 holds, 8 temperature zones and 12 to 16 cargo chambers (Stera, 1999). All vessels built after 1987 are designed for palletised product (but not high-cube). Figure 2-5 shows the typical layout of a refrigerated vessel.

Vessels are usually equipped with their own cranes for loading cargo; alternatively, the port may supply land-based cranes. Pallets are loaded using cages and then arranged within the deck using pallet trolleys or forklifts. When there is no longer enough space for the pallet trolleys or forklifts to be effective, the final pallets are strapped into harnesses and lowered into place directly using the crane. Once a deck has been filled, the retracted floor of the layer above is extended into place. Loading of a full size deck in New Zealand (approximately 360 ISO pallets - 1.2 × 1.0 m) generally takes 5 to 7 hours.

There are two common systems of air distribution in reefer holds. Most commonly, air is delivered in the longitudinal direction from the coolers, or less commonly, air is delivered in a transverse direction, generally referred to as the Robson System (Stera, 1993).

In both systems, air is cooled by passing vertically down through the coolers. With a longitudinal air delivery system, the refrigerated air is introduced directly from the cooler to the under-floor air delivery system. The air then passes vertically through the produce and back to the coolers along the ceiling. By contrast, in the Robson system the refrigerated air travels to the side-walls of the hold, where it runs down ducts separating the flow into individual streams. This ducted air is introduced to the floor at different sections along the length of the hold. The air flows through the floor gratings, vertically through the cargo and back to the coolers along the ceiling.

As is the case with containers, renewal of refrigerated air within holds is necessary to avoid the build-up of respiratory products. Most ships are equipped with gas monitoring instruments and the ventilation is varied to maintain gas levels below specified thresholds. Some ships are equipped with recovery heat exchangers to reduce the heat input from air exchange (IIF/IIR, 1995).

In contrast to containers, reefer holds have a smaller surface area relative to volumetric capacity so that the proportion of heat load from infiltration through the walls is lower. Space for refrigeration equipment is also not at such a premium on board refrigerated vessels as compared to containers, allowing larger evaporator areas. Larger evaporators allow higher evaporator temperatures to be used to provide the same quantity of cooling and therefore the rate of evaporator frosting is reduced.

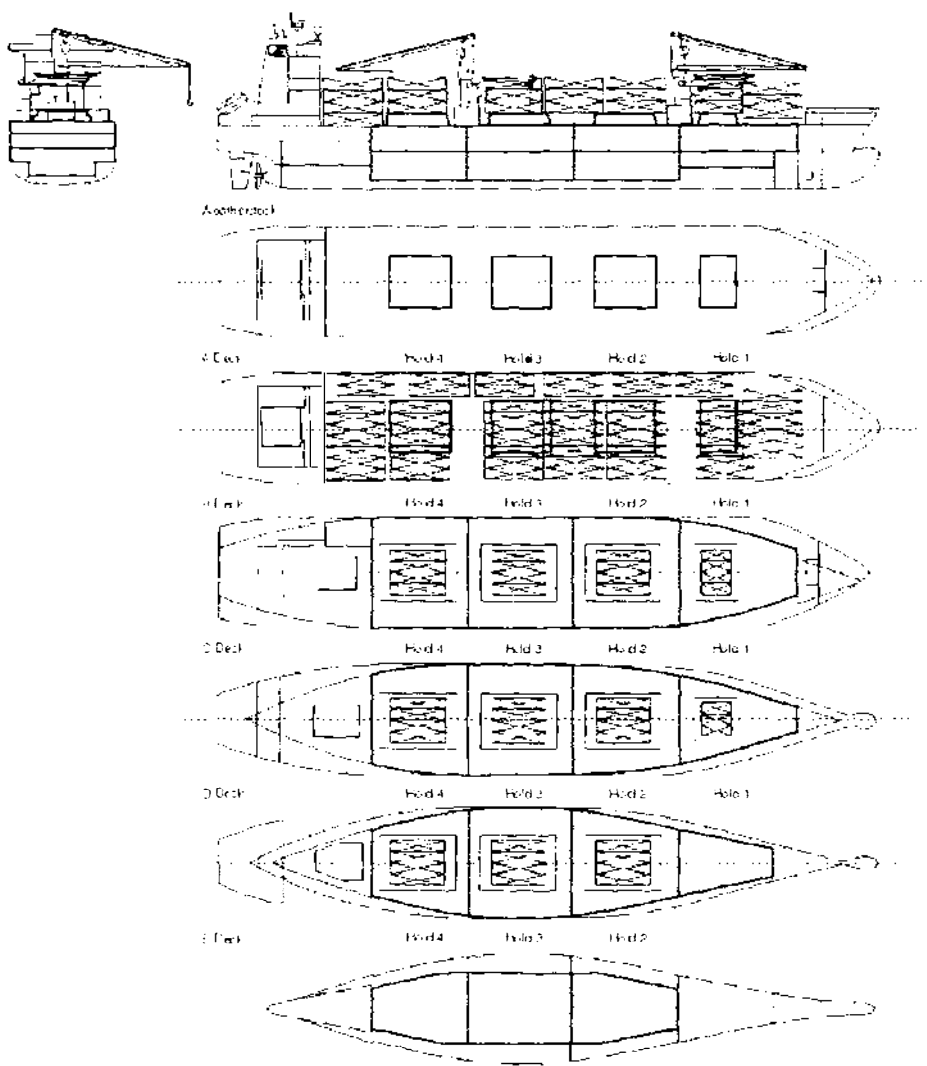

Figure 2-5 - Typical layout of a refrigerated vessel showing the placement of four decks and holds to give 16 cargo chambers (Seatrade Reefer Chartering, 2001)

2.2 Measurement methods

As is the case with all endeavours in the art of prediction, measurement is of vital importance. One must know accurately what has occurred, before it is possible to predict what is going to occur. To investigate the airflow in any system, whether the aim is to discover problems in existing systems or to validate models, accurate measurement is crucial. Unfortunately, measurement of airflow is problematic because a non-uniform flow profile exists in laminar flow, and airflow becomes turbulent at low velocities. Turbulent flow is characterised by unstable flow patterns caused by three-dimensional irregular eddies within the fluid and consequently velocities normal to the overall flow direction. The size of turbulent eddies range from those the size of the flow passage, down to eddies whose Reynolds numbers based on the eddy diameter are in the order of unity (Miller, 1990). Turbulent fluctuations make accurate measurement difficult. The principles of available measurement methods, their strengths, weaknesses and previous uses are described in the following sections.

2.2.1 Flow visualisation

Since the time of Leonardo da Vinci, visualising the flow of fluids has been an important part of fluid dynamics research. Most methods are purely qualitative, used to validate patterns predicted by researchers, however some semi-quantitative methods have been developed. There are a number of different visualisation methods available to the researcher wishing to visualise airflow.

Santanam & Tietbohl (1983) outline a method of photographing or videotaping small (1/8" diameter) helium filled soap bubbles. Lighting of the bubbles to ensure visibility is a major consideration in this method, and is most suitable for use with scale models constructed of clear plastic. If photographed with a known shutter speed, this method can be used to estimate the air velocity (Grace, 1985). Worley & Manbeck (1995) used this method for validation of an airflow model of a ceiling ventilated livestock facility. A $1/5^{th}$-scale model was used and bubble paths captured using a 35mm camera.

Wall tracing methods, including the spreading of a thin film of liquid over a surface, or the use of tufts attached to the wall can also be used to visualise airflow patterns (Tanner, 1998). Lomax *et al.* (1995) developed a low cost method of investigating the flow in mushroom houses based on these methods. Small strips of plastic film were attached to vertical pins to form flags, which were inserted into a mushroom bed and the deflection of the flag used as a measure of the air velocity. A quantitative relationship between the level of deflection and velocity was described and reported to be accurate in the range of 0.05 to 0.4 $m.s^{-1}$. The accuracy of the measurement is questionable however, as the effect on air movement patterns of the interference caused by the person standing next to the bed taking the measurement was not investigated. Despite this reservation, the method remains a useful, low-cost technique.

The use of smoke as a visible tracer to visualise airflow is a relatively popular method, and the most widely used visualisation method encountered in relevant literature (van Gerwen & van Oort, 1989; Van Pee *et al.*, 1994; Amos, 1995; Tanner, 1998). Smoke is produced through various methods including the use of a heated wire coated with organic oil to produce a two-dimensional smoke plane. Another method employs $TiCl_4$, which reacts with moisture in the air to produce a white smoke of TiO_2. This method suffers the severe limitation that $TiCl_4$ is toxic and not readily available. Van Pee *et al.* (1994) discuss the use of a saturated water vapour as a tracer, with the advantage of allowing recirculation of the air after removal of the saturated vapour. The method is not appropriate when studying the thermodynamic state of the air. Commercially available fog generators are also available which vaporise a water/glycol solution to form fog. They provide a non-toxic, dry fog from a small, convenient and reasonably inexpensive piece of equipment.

A fog generator was used to collect qualitative information about airflow patterns in a commercial apple coolstore to complement velocities measured using a uni-directional hot wire anemometer (Amos, 1995). The test was conducted with the coolstore empty, doors shut and fans on low speed. Results showed three major pathways with some cross mixing. Although the coolstore was empty, the author believed general trends of flow direction were shown.

In an attempt to glean quantitative data from a smoke tracer experiment, Van Pee *et al.* (1994) used a computer based image analysis technique. A 'plexiglass' room was built and studied, and the flow of the smoke through the room recorded using a video camera. These images were then transferred to a computer and analysed using an image analysis algorithm. A very simple geometry was used with the room designed to ensure stable airflow patterns. The method depended on an untested assumption that the particle density was linearly related to the reflected light intensity.

Lovatt *et al.* (1993) built a scale model of a section of a beef chiller to visualise flows for various configuration options. The model was filled with water and an electrode used to produce small hydrogen bubbles. The bubbles were clearly visible and their movement captured using videotape. The model was used to highlight major flow trends and illustrate the effect of turning vanes, rather than to model any particular chiller. The system was only useful for investigation of forced convection as the hydrogen bubbles slowly rose to the surface. No validation was performed.

2.2.2 Direct airflow measurement

Several types of anemometer are available for measurement of air velocity or flow rate.

2.2.2.1 Laser doppler anemometry

Laser Doppler Anemometry (LDA) is a non-invasive technique for measuring fluid velocity. It works on the principle that two intersecting laser beams create an interference fringe pattern consisting of alternate bright and dark areas. This region of interference is the measurement volume, the size of which depends on the focal length, angle of intersection and the beam diameters but is of the order of $0.1 \times 0.1 \times 0.9$ mm for a lens with a focal length of 120 mm (Chandrasekaran *et al.*, 1997). When a particle such as dust or an air bubble passes through the measurement volume, it scatters the incident light in all directions. This scattered light can be measured, and the particle velocity calculated from the frequency of the light to dark oscillations created as the particle moves through the interference pattern. The LDA system is capable of measuring velocities from a few $mm.s^{-1}$ to hundreds of $m.s^{-1}$ very accurately. One, two and three-dimensional systems are available. Limitations of the method include that the fluid to be measured must be optically transparent, only a single point is sampled and a transparent window to the laser light must be provided for the measuring equipment. The equipment is bulky and very expensive, especially so for three-dimensional measurement.

Moureh *et al.* (2002) used a one-dimensional LDA to measure air velocities within a 1:3.3 scale model of a refrigerated truck. The model was constructed with a glass front wall in order to allow optical access to the inside of the trailer. Closed glass boxes were used in the model to simulate pallets. LDA has also been used to improve understanding of food processing equipment such as mixers, extruders, fermenters and hot-air jet impingement ovens (Chandrasekaran *et al.*, 1997).

2.2.2.2 Particle image velocimetry

The particle image velocimetry (PIV) system can be thought of as a quantitative flow visualisation device (Cheng *et al.*, 1997). PIV is an extension of LDA with similar advantages and disadvantages when compared to other methods. A sheet of laser light is produced by expanding a laser beam with cylindrical and spherical lenses. Sufficiently small and non-buoyant seeding particles are dispersed in the fluid and their motion is captured using a recording device such as a digital camera. The laser sheet pulses twice

each time the camera shutter opens, so that a pair of images of the particles is captured. The separation distance of the particles is used to calculate a velocity field using Fourier transforms.

The advantage of the PIV method over LDA is that instead of measuring one point, large numbers of points in a plane are measured, allowing a length scale of turbulence to be determined. Disadvantages include a further increase in cost and the geometric considerations, with a need for transparent windows to allow optical access to the sample plane.

Cheng *et al.* (1997) used PIV to investigate turbulence structures in a mixing jar. Excellent turbulence data was generated by the technique, although observation of temporal change was limited due to the speed and data storage capacity of the camera. The frequency of measurement and number of total measurements was limited to three frames per second, and storage constraints allowed only 23 consecutive frames. These constraints should be overcome with improvements in digital camera technology.

Whale *et al.* (1996) used PIV to measure the wake structure of a wind turbine for use in wind-farm design. PIV was used in the laboratory with scale models, utilising water as the flow medium to facilitate seeding and illumination. Comparison of PIV results with measurements of full-scale turbines made with hot-wire anemometers was not favourable. The authors argued that inconsistencies were due to the difference in Reynolds number between model and full scale.

PIV is best suited to systems where there are sufficiently large open spaces to allow optical access. Models may be used where optical access is impractical in the real system. No examples of the use of PIV in horticultural or refrigeration applications were found.

2.2.2.3 Hot wire/hot film anemometry

Hot wire/film anemometers measure air velocity using the principle that convective heat losses from a surface are related to the air velocity. The surface used is a small film or a wire, where the wire is typically 1-3 mm long and 5-25 μm in diameter (Grace, 1985). There are two types of hot wire anemometer: constant temperature, where the wire's resistance is constant and the required voltage measured; and constant current, where the applied current is constant and the resulting resistance measured. Advantages of such instruments are that they are very small, resulting in little interference in flow patterns, reasonably inexpensive, and they work over a wide range of fluid velocities with a very low threshold velocity. Hot wire and hot film anemometers are readily available commercially at reasonable cost. This method is limited in that sensors are generally non-directional and reported velocities may be affected by impurities in the fluid as they adhere to the wire and affect heat transfer. Specialised multi-sensor probes are available, capable of measuring flow magnitude and direction.

Hot wire anemometers have been used extensively by researchers in the horticultural and refrigeration sectors to measure air velocities in previous studies (Wang, 1990; Worley & Manbeck, 1995; Harral & Boon, 1997; Alvarez & Flick, 1999).

Hot film anemometers operate in the same fashion as hot wire anemometers but offer the advantage of greater mechanical strength. Typically the hot film anemometer is constructed of platinum or nickel deposited on Pyrex glass. Due to appreciable conduction of heat from the glass to the air, the hot film probe is less well suited to turbulent flows than the hot wire alternative. Hot film anemometers have been commonly used in relevant applications (Mirade & Daudin, 1998; Verboven *et al.*, 1998; Hoang *et al.*, 2000).

Thermistor anemometers are a variation on a hot wire/film anemometer where a thermistor is used instead of the wire/film. Thermistors are semi-conducting materials, the resistance of which varies with

temperature. They have been used in the same fashion as both constant current and constant temperature hot wire anemometers (Irving & Sharp, 1975).

In the only example of their use in relevant application, Irving & Sharp (1976) used thermistor anemometers to measure the air distribution in a porthole container. Forty thermistors were placed inside the container in the floor channels, dunnage gaps and wall gaps. Velocity profile ratios were presented which relate the maximum velocity with the average velocity for the different flow channel types. Calculated average flow rates for the various types of channels were reported.

2.2.2.4 Sonic anemometry

A sonic anemometer works on the basic principle that the speed of sound is affected by the velocity of the medium in which the sound is travelling, i.e. sound travels faster down-wind. The anemometer is a pair of transducers that measure the time of flight of an ultrasound pulse (Wang *et al.*, 1999). The transducers act alternately as transmitters and receivers and the difference in time of flight is used to calculate the velocity of the fluid. Consequently, the velocity measured is the average of the velocity over the sampling area between the transducers. Three-dimensional sonic anemometers are available commercially but are expensive and bulky.

Wang *et al.* (1999) developed an inexpensive two-dimensional network of sonic anemometers for characterising the airflow in a greenhouse. The system was used to measure airflow in a horizontal plane of the greenhouse. Results compared well to those obtained using more expensive, commercially available three-dimensional sonic anemometers, however no comparison was made with other methods of measurement.

Harral & Boon (1997) used both hot-wire and sonic anemometers to validate their model of airflow in a mechanically ventilated livestock building. A one-dimensional sonic anemometer was used at a sampling frequency of 28 Hz to measure three orthogonal velocity components, with the variance of readings used as a measure of turbulence. The sonic path length was 150 mm. As the two anemometers were used in different regions of the facility no comparison between methods was made.

Advantages of the sonic anemometer include the accuracy of the instrument over a wide range of velocities and a high sampling frequency. The limitations of the instrument are that it is reasonably expensive, especially for three dimensional measurement, bulky and readings are averaged over the sonic path length.

2.2.2.5 Vane anemometry

The vane (or propeller) anemometer is essentially a windmill, made of flat metallic vanes with a means of measuring rotation (Ower & Pankhurst, 1966). The anemometer is one-dimensional but 3-propeller models capable of measuring three-dimensional flows are available. Limitations of the vane anemometer are the high threshold velocity, lack of responsiveness and the relatively bulky size of the probe in relation to the hot wire anemometer. Vane anemometers were used infrequently in horticultural and refrigeration research, the only relevant examples of use were estimation of air circulation rates in containers (Irving & Shepherd, 1982) and measurement of air velocities between pallets in a test rig (Lindqvist, 2000).

2.2.2.6 Pressure methods

Measurement of pressure losses through obstructions of known dimensions or comparison of pressure constituents can be used to calculate fluid flow rates or velocities. Methods of pressure measurement are discussed in Section 2.2.4.

The Pitot tube is an example of an instrument utilising pressure measurement to calculate fluid velocity. The tube measures both the static pressure and the dynamic pressure, with the differential related to fluid velocity by Equation 2-1 (Grace, 1985).

$$\Delta P = P_d - P_s = \frac{1}{2}\rho v^2 \qquad \textit{Equation 2-1}$$

Where:

v	=	Fluid velocity	($m.s^{-1}$)
ρ	=	Fluid density	($kg.m^{-3}$)
ΔP	=	Pressure difference	(Pa)
P_s	=	Static pressure	(Pa)
P_d	=	Dynamic pressure	(Pa)

The advantages of the Pitot tube are that it is inexpensive and easy to use. The foremost disadvantages are the sensitivity to flow direction and that at low air speeds the response (ΔP) is difficult to measure (due to the low density of air and poorly understood viscous effects that begin to influence ΔP at speeds lower than 1 $m.s^{-1}$).

Van Nieuwenhuizen (1974) used a Prandtl tube, employing the same principle as a Pitot tube, to measure the flow in a monorail-model of a T-bar floor and an actual container floor. The measured flow rates were used to compare different stacking patterns and the uniformity of air distribution. Yekutieli (1974) used a Pitot tube to measure the air distribution in a container loaded with paprika cartons in a break-bulk configuration.

Talbot (1988) used a Pitot tube along with hot-wire anemometers to determine the airflow rate through fibreboard orange containers. An electronic differential pressure manometer was used to measure the static and velocity pressure. A Pitot tube was also used by Emond *et al.* (1996) to measure the flow rate of air through strawberry packaging.

The pressure drop over an orifice plate can also be used to measure the fluid flow rate. The pressure loss is related to the volumetric flow by Equation 2-2.

$$Q = C\sqrt{\frac{\Delta P}{\rho}} \qquad \textit{Equation 2-2}$$

Where:

Q	=	Fluid volumetric flow	($m^3.s^{-1}$)
ΔP	=	Pressure loss across orifice	(Pa)
C	=	Coefficient specific to orifice geometry	(m^{-2})

Irving & Shepherd (1982) used such a method to characterise the air circulation rate of containers under different load conditions. A plenum and an orifice plate were constructed to fit neatly over the air grill near the ceiling, allowing both measurement of flow rate and adjustment of load. Both top-delivery and top-return containers were tested, and results compared to values estimated with both vane and hot wire anemometers. Results using the various methods were presented for both container types; the anemometers overestimated flow rates by 5 to 55%.

2.2.3 Tracer methods

Tracer methods can be thought of as an extension of flow visualisation, where movement of a tracer gas is monitored using instruments rather than by visual observation. Tracer methods generally involve injecting a tracer gas into a flow path and monitoring concentration changes at numerous sample points. Analysis can involve either calculation of a 'time to arrival' for each of the sample points or the concentrations at the sample points can be used to determine the level of mixing.

Barber & Ogilvie (1984) used a tracer technique to measure the degree of divergence from perfect mixing in a ventilated livestock facility. A 1:5 scale model was used and a mix of CO_2 and CH_4 was injected near the air inlet. The density of the tracer was described as ranging between 0.5% heavier and 0.4% lighter than air. The proportion of CO_2 at each sample point was measured and compared to the expected values for a perfectly mixed enclosure.

Tanner (1998) developed a tracer method utilising air as the flow medium and CO_2 as the tracer to characterise a two-dimensional flow profile through vented apple packaging in forced air cooling applications. CO_2 was used as the tracer because instrumentation to measure real-time concentration changes was available in the horticulture industry, making the technique inexpensive. The 'time to arrival' following injection of a CO_2 pulse was measured for each of 12 sample points within a carton, and a relative flow profile calculated assuming flow was dominant in one direction. Good agreement was found with a qualitative validation using a smoke tracer in a carton with a transparent wall.

Tumambing *et al.* (2001) used a carbon monoxide tracer to measure the airflow patterns and velocities in a commercial apple cold store. Ninety-five sensors were placed throughout the store; CO was injected at numerous locations and concentrations were recorded. Velocities were also measured using a hot wire anemometer for comparison. The authors found that the technique could successfully determine the airflow path and air velocities with reasonable accuracy.

Tracer gases have also been used to measure the exchange of air between an enclosure and its surroundings (Section 2.2.5).

2.2.4 Pressure measurement

Pressure loss is closely related to fluid velocity and can be used as an indirect means of measuring airflow. Pressure is defined as force per unit area and thus measurement of pressure is closely related to the measurement of force. Pressure is generally measured by the distortion of a sensing element, which is usually a membrane, plate or cavity.

Lindqvist (2000) used a digital micro-manometer to measure the pressure distribution in a full-scale model of a section of a reefer hold. Thirteen test conditions were investigated, with measurements made over a range of flow rates. Forty-three measurement points were monitored; each measured manually. The pressure difference between the bottom of a pallet and the ceiling above a pallet was then used to calculate a "flow factor", which was described as a measure of local cooling capacity. The assumption that the resistance to flow between channels was identical for all channels was made when relating the pressure difference to the "flow factor"; however, the author commented that this assumption was dubious, with the non-uniformity of the packages influencing the reliability of the "flow factor". Pressure data from the trials was reported in full (Lindqvist, 2000).

2.2.4.1 Packaging flow resistance

Packaging is a major factor in determining the rate of heat and mass transfer during refrigerated storage and transport of horticultural products. Respiratory heat generation can pose problems, causing the cartons in the centre of a pallet to be significantly warmer than those on the outside of the pallet (Tanner & Amos, 2003). Such temperature variability can lead to variable quality at out-turn, which in turn can lead to marketing problems. Packaging design provides a relatively simple means by which these processes can be controlled. The traditional approach to this problem has been to design cartons with open vents; however the vents are usually designed to facilitate horizontal airflow despite vertical airflow being the standard configuration in transport systems.

A number of researchers have characterised the airflow properties of horticultural packaging. Resistances to flow have generally been reported as forms of the Ergun equation (Equation 2-3), which is a special case of the Darcy-Forcheimer-Brinkman equation for flow through porous media, or the Ramsin Equation (Equation 2-4) which is purely empirical.

$$\frac{\Delta P}{L} = K_1 \frac{(1-\varepsilon)}{\varepsilon^3} \frac{\mu u}{D^2} + K_2 \frac{(1-\varepsilon)}{\varepsilon^3} \frac{\rho u^2}{D} \qquad \textit{Equation 2-3}$$

$$\frac{\Delta P}{L} = a u^b \qquad \textit{Equation 2-4}$$

Where:

ΔP	=	Pressure loss	(Pa)
L	=	Distance	(m)
u	=	Superficial velocity	($m.s^{-1}$)
ε	=	Bed porosity	
μ	=	Fluid viscosity	(Pa.s)
D	=	Fruit diameter	(m)
K_1	=	Ergun equation constant	
K_2	=	Ergun equation constant	
a	=	Ramsin equation coefficient	($kg.s^{(b-2)}.m^{-(b+2)}$)
b	=	Ramsin equation exponent	

Haas *et al.* (1976) studied the flow through stacks of oranges in a test chamber with vent area ranging from 9 to 27% of the cross-sectional area. The shape of the vents was found to have no effect on the pressure loss, and a relationship between the vent area and Ramsin coefficient was presented (Equation 2-5). Summation of pressure losses across empty cartons and bulk fruit was reported to give accurate values for losses across full cartons.

$$a = e^{2.97-10.72O} \qquad \textit{Equation 2-5}$$

Where:

O	=	Ratio of vent area to face area

Chau *et al.* (1985) investigated flow through bulks of oranges of four sizes, simulated cartons and vent holes. The Ergun equation was found to fit the data for bulk oranges, although the values for K_1 and K_2 varied with fruit size and stacking arrangement. Flow through vent holes of different shapes gave slightly different losses. The pressure-flow relationships for oranges in cartons of a single vent area were presented. Summation of losses for empty cartons and bulk fruit was found to significantly under-estimate the total losses across a packed carton.

Haas & Felsenstein (1987) investigated vertical flow through full and empty avocado cartons with vent areas ranging from 3.5 to 10.2% of the cross-sectional area. Relationships between flows and pressure losses were presented graphically for the full and empty cartons; however, no coefficients were reported. The relationship between the Ramsin coefficient and the vent area was unclear.

Talbot (1988) developed a finite element model to predict airflow in orange cartons. Comparison of predictions to published data was reported to give good agreement, although specific comparisons were not reported. No specific pressure-flow relationships were reported.

van der Sman (2002) modelled the airflow through vented cartons using the Darcy-Forchheimer equation. Both bulk stacks of potatoes and oranges were simulated as well as packaged tomatoes and mandarins. The Ergun equation was found to accurately predict losses in the bulk products, where the product diameter was sufficiently small in comparison to the cross-sectional flow area. For the packaged products, the Darcy-Forchheimer equation was found to accurately predict the pressure-flow relationship. Both numerical and experimental data indicated that the Ramsin coefficient was related to the vent area by a power law (Equation 2-6) with an exponent equal to -1.5.

$$a = cO^{d} \qquad \textit{Equation 2-6}$$

Where:

c	=	Vent resistance coefficient	$(kg.s^{(b-2)}.m^{-(b+2)})$
d	=	Vent area exponent	

Haas *et al.* (1976), Chau *et al.* (1985) and van der Sman (2002) reported the exponent (b) of Equation 2-4 to be approximately 2 for flow through vented packages. This is unlikely to be true in other geometries such as narrow gaps between cartons, where laminar flow is likely and pressure loss will be proportional to velocity.

2.2.5 Container fresh air exchange & gas tightness measurement

Fresh air exchange and leakage can contribute significant heat and moisture to refrigerated containers. For low temperature cargoes, moisture is deposited as frost on the evaporator coil, which may cause a reduction in air circulation and loss of temperature control. For chilled cargo, Tanner & Amos (2003) found delivery air temperatures varied across the width of a container severely enough to result in air temperatures capable of freezing the cargo. The authors attributed the problem to uneven frosting associated with positioning of the fresh air exchange vent and poor mixing of the fresh air across the container width.

Gas tightness of containers is of greatest importance in applications where fresh air exchange does not occur, contributing unnecessary heat and moisture load and negatively impacting on the efficacy of CA equipment. The widely accepted method of testing the gas tightness of a container is a steady-state pressure test; a method measuring the rate at which air is supplied to a container to maintain a given pressure difference between the container's interior and surrounding pressures. Another method is the pressure decay test where the time taken for the pressure difference to decay to a certain level is measured and used as an indicator of gas tightness (Sharp, 1982a). A theoretical relationship between the steady-state and decay methods has been reported (Sharp, 1982b), and comparison to experimental results gave an excellent fit.

Sharp *et al.* (1976) surveyed the leakage rate of eight 20' containers measured over a range of pressure values. The tests showed large variation between containers ranging from $0.18 \times 10^{-3} m^3.s^{-1}$ to

18.3×10^{-3} $m^3.s^{-1}$ at 250 Pa. Sharp *et al.* (1976) also used a gas tracer technique to measure the leakage rate of the containers, concluding that there was a correlation between the tracer gas method and the steady-state pressure test, although the nature of the correlation and its reliability were not reported. In another survey of 143 containers of various constructions, no relationship was found between the age of a container and its gas tightness (Sharp *et al.*, 1986).

Smale *et al.* (2003a) used a gas tracer technique to measure rates of leakage and deliberate fresh air exchange in refrigerated containers. The measured fresh air exchange rates did not correlate well with the nominal vent settings.

2.3 Modelling techniques

There are two approaches available to those looking to develop a model of physical phenomenon: mechanistic and empirical. Mechanistic models are deduced from the underlying scientific principles and fundamental laws governing the phenomenon being modelled. In contrast, empirical models involve fitting output data as an arbitrary function of input data. Mechanistic models offer a significant advantage over empirical models, as they are applicable to a wider range of systems using different inputs and internal parameters. Empirical models may only be applicable to the system with which the model was generated, as any changes to the system could change underlying mechanisms thus invalidating the model. Mechanistic models allow the boundaries of their applicability to be estimated à priori.

In practice there is a continuous spectrum of approaches from mechanistic through to empirical, with modellers generally attempting to use a mechanistic approach where possible and empirical correlations where a theory-based approach is not feasible.

Similarly, the complexity of the model must be balanced between the competing motivations of improved accuracy and reduced implementation cost. The intended purpose of the model and the required accuracy should be considered when choices are made regarding model complexity. Incorporation of all physical effects may be prohibitively complicated and make implementation of the model impossible. At the same time, all sources of significant variation must be included for the model to be capable of useful prediction. The most appropriate model is the simplest one that provides a sufficiently accurate description of the system.

Heat and mass transfer are the processes of primary importance in quality maintenance in storage and transport, and models of these processes between product and air masses are well established. However, successful prediction of heat and mass transfer relies on air temperature, velocity and humidity data. Accurate prediction of these particular quantities is a more difficult task. The following sections provide a background to heat and mass transfer models and describe relevant airflow models previously developed.

2.3.1 Heat transfer models

Heat transfer occurs by three mechanisms: conduction, convection and radiation. All three modes may occur simultaneously to varying degrees in any given system and all should be considered even if one or two are eventually disregarded.

There are numerous models of heat transfer available, each tailored to different conditions. Models are available for both steady and unsteady state conditions and for single or combined modes of transfer (e.g. steady-state heat transfer by conduction and convection only). Heat transfer from unpacked or packaged produce, using air as the flow medium, occurs primarily by convection. Steady-state convection-only heat transfer is described by Equation 2-7.

$$\phi = h_s A(T_1 - T_2)$$ *Equation 2-7*

Where:

A	=	Area for heat transfer	(m^2)
(T_1-T_2)	=	Temperature difference	(K)
ϕ	=	Rate of heat transfer	(W)
h_s	=	Surface heat transfer coefficient	($W.m^{-2}K^{-1}$)

The significance of the surface heat transfer coefficient and means of calculation are discussed in Section 2.3.1.1.

Amos (1995) developed a model of heat and mass transfer processes for a vented apple carton. The domain was divided into a moderate number of cuboidal zones (150). Each zone contained a mass of product, packaging material, and fluid. Heat and mass transfer coefficients were calculated between each of the zone constituents and between adjacent zones. ODE's were formulated for each of the zone constituents and the temperature and mass profiles calculated using the Runge-Kutta-Fehlberg method.

Tanner (1998) developed a model using a similar zoning approach to predict the heat transfer and mass transfer in generic horticultural packages. The model was designed for a non-specific system to allow a wide range of application. For ventilated packages, the overall airflow rate through the system and a profile of relative velocities inside the package were required to be input by the user. The model consisted of two distinct parts: pre-cooling where heat transfer was important and mass transfer was ignored, and static storage where constant temperature was assumed and mass transfer modelled. Validation showed good agreement between predicted and measured results.

2.3.1.1 Surface heat transfer coefficients

The surface heat transfer coefficient is a measure of the ease of heat transfer from a surface to a cooling medium and can be represented by Equation 2-8.

$$h_s = \frac{1}{\text{resistance between surface and cooling medium}}$$ *Equation 2-8*

Surface heat transfer coefficients can be predicted from empirical relationships reported by experimenters for a given application. Natural convection occurs where the fluid movement is due to thermal gradients in the fluid, whereas in forced convection the fluid movement is generated externally. Correlations for forced convection usually come in the form of dimensionless relations, usually involving the Reynolds, Prandtl and Nusselt numbers.

$$Re = \frac{\rho v D}{\mu}$$ *Equation 2-9*

$$Pr = \frac{C_p \mu}{\lambda}$$ *Equation 2-10*

$$Nu = \frac{h_s D}{\lambda}$$ *Equation 2-11*

Where:

Re	=	Reynolds number	
Pr	=	Prandtl number	
Nu	=	Nusselt number	
D	=	Characteristic dimension	(m)
λ	=	Thermal conductivity	($W.m^{-1}.K^{-1}$)
C_p	=	Specific heat capacity	($W.kg^{-1}.K^{-1}$)

Other dimensionless groups such as the ratio of length to diameter and the ratio of wall to bulk viscosity are often used as modifications, and other variations such as the use of the Stanton number in place of the Nusselt number are also common. Dimensional equations may also be reported; which are expansions of the dimensionless relations, grouping together all the fluid properties into a single constant.

Calculations of surface heat transfer coefficient have been reported extensively by Cleland & Cleland (1992) and Lin *et al.* (1994). The best possible accuracy is likely to be ± 10%. Equation 2-12 is an example of a correlation for airflow over large flat surfaces such as in the chilling of large cartons (most accurate for 1 to 5 $m.s^{-1}$) (Cleland & Cleland, 1992).

$$h_s = 7.3v^{0.8} \qquad \textit{Equation 2-12}$$

2.3.2 Mass transfer models

The mass transfer phenomenon of primary importance in horticultural applications is the loss of saleable weight of the product. Weight loss occurs via two pathways, carbon loss through respiration, and moisture loss due to transpiration (evaporation). Moisture loss is generally the dominant component of total product weight loss and carbon loss is usually insignificant, except when moisture loss rates are very low (Gaffney *et al.*, 1985).

The relative importance of respiration changes with the humidity of the environment. With increased humidity, the rate of water loss by evaporation decreases and as a result the importance of respiration increases. For a 'Royal Gala' apple at 90% RH, 5% of the total mass loss will be through respiration, but at 99% RH the figure increases to 30% (Maguire, 1998).

Water loss from horticultural products via transpiration can be modelled by the diffusion of water vapour from the fruit into the surrounding environment. This process can be described mathematically by the steady state solution of Fick's first law of diffusion (Equation 2-13) (Nobel, 1991).

$$r'_{H_2O} = M'_{H_2O}.A.\left(p'_{H_2O} - p^e{}_{H_2O}\right) \qquad \textit{Equation 2-13}$$

Where:

r'_{H2O}	=	Rate of water loss from product	($mol.s^{-1}$)
p'_{H2O}	=	Partial pressure of water at apple surface	(Pa)
$p^e{}_{H2O}$	=	Partial pressure of water in the environment	(Pa)
A	=	Fruit surface area	(m^2)
M'_{H2O}	=	Effective permeance of the fruit surface to movement of water vapour under prevailing conditions	($mol.s^{-1}.m^{-2}.Pa^{-1}$)

Maguire (1998) provides a review of the environmental and product specific factors affecting the mass loss of apples during storage. The following diagram summarises the many diverse factors affecting mass loss in apples and their inter-relationships. Airflow is included in the 'coolstore design and management' factor in Figure 2-6. Increased airflow rates will tend to reduce the build up of humidity in the immediate

environment of the produce and increase mass transfer coefficients which may increase rates of mass loss. However, increased airflow rates may also improve product temperature control thereby reducing rates of mass loss.

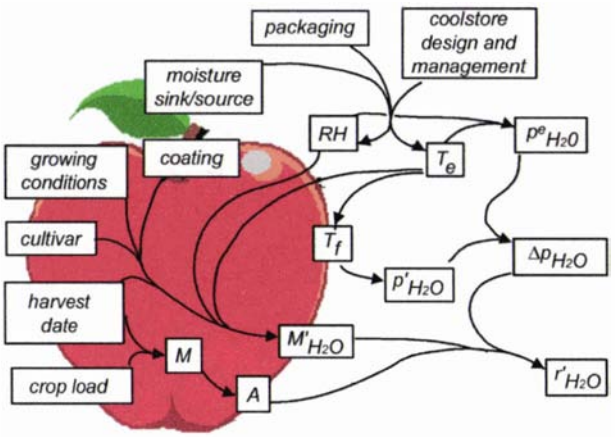

Figure 2-6 - Factors affecting mass loss in apples, from Maguire (1998) where M = mass of apple (kg), T_e = environment temperature (°C) and T_f = fruit temperature (°C)

2.3.3 Airflow models

Three fundamental principles govern the physical aspects of any fluid flow: conservation of mass, Newton's second law, and conservation of energy. The mathematical expression of the conservation of mass and momentum for a Newtonian fluid are shown in Equation 2-14 to Equation 2-17.

Conservation of Mass – Continuity Equation

$$\frac{\partial \rho}{\partial t}+\frac{\partial}{\partial x}\left(\rho v_x\right)+\frac{\partial}{\partial y}\left(\rho v_y\right)+\frac{\partial}{\partial z}\left(\rho v_z\right)=0 \qquad \textit{Equation 2-14}$$

Conservation of Momentum (Navier-Stokes equations)

$$\rho\left(\frac{\partial v_x}{\partial t}+v_x\frac{\partial v_x}{\partial x}+v_y\frac{\partial v_x}{\partial y}+v_z\frac{\partial v_x}{\partial z}\right)=\mu\left[\frac{\partial^2}{\partial x^2}v_x+\frac{\partial^2}{\partial y^2}v_x+\frac{\partial^2}{\partial z^2}v_x\right]-\frac{\partial P}{\partial x}+\rho g_x \qquad \textit{Equation 2-15}$$

$$\rho\left(\frac{\partial v_y}{\partial t}+v_x\frac{\partial v_y}{\partial x}+v_y\frac{\partial v_y}{\partial y}+v_z\frac{\partial v_y}{\partial z}\right)=\mu\left[\frac{\partial^2}{\partial x^2}v_y+\frac{\partial^2}{\partial y^2}v_y+\frac{\partial^2}{\partial z^2}v_y\right]-\frac{\partial P}{\partial y}+\rho g_y \qquad \textit{Equation 2-16}$$

$$\rho\left(\frac{\partial v_z}{\partial t}+v_x\frac{\partial v_z}{\partial x}+v_y\frac{\partial v_z}{\partial y}+v_z\frac{\partial v_z}{\partial z}\right)=\mu\left[\frac{\partial^2}{\partial x^2}v_z+\frac{\partial^2}{\partial y^2}v_z+\frac{\partial^2}{\partial z^2}v_z\right]-\frac{\partial P}{\partial z}+\rho g_z \qquad \textit{Equation 2-17}$$

(I) *(II)* *(III)* *(IV)*

Where:

t	=	Time	(s)
v_i	=	Fluid velocity in the i_{th} direction	($m.s^{-1}$)
x,y,z	=	Orthogonal direction co-ordinates	(m)
P	=	Fluid pressure	(Pa)
g_i	=	External force per unit mass of fluid in the i_{th} direction	($N.kg^{-1}$)
(I)	=	Convective transport term	
(II)	=	Diffusion transport term	
(III)	=	Pressure gradient term	
(IV)	=	External force term	

Wang & Touber (1988) describe three possible methods of simplifying the Navier-Stokes equations. Firstly, there is numerical approximation in which time and space are discretised and software used to calculate results. Computational fluid dynamics (Section 2.3.3.2) is a method of this nature, that solves the Navier-Stokes equations in full for discrete sections of the modelled domain, and incorporates a turbulence model to account for flow structures smaller than the discrete sections. The authors stated its disadvantages as complexity and costliness with advantages being completeness, accuracy and reliability. Prediction of flow from experimental measurement of temperature was the second option discussed. This method was described as limited due to the need for measurable temperature gradients throughout the refrigerated space and the large numbers of temperature measurements required. The final approach discussed was a resistance network model in which the Navier-Stokes equations are simplified to include only pressure gradient and diffusion friction effects (terms *(II)* and *(III)* in Equation 2-15 to Equation 2-17). This method was described as flexible, simple and economical.

2.3.3.1 Resistance network models

Resistance network models have been used in the design of water distribution systems by civil engineers for many years. Pipe network analysis is conducted using one of several methods, with the original Hardy-Cross method dating back as far as 1936 (Cross, 1936). Improved algorithms have been developed as computers have increased in availability and power.

Wood & Rayes (1981) summarised the algorithms available at the time and discussed their merits. There are two basic approaches, both of which solve mass and energy balances throughout the system. The first approach treats the pressures at convergent/divergent points as unknowns, and solves the mass balances at each of these points. This is known as solving the node equations. The other approach treats the flow-rates as the unknowns in energy balance equations around primary loops, and again solves mass balances at convergent/divergent points. This method is known as solving the loop equations. Wood & Rayes (1981) tested five methods of solution, three solving loop equations and two solving node equations, with the finding that loop equations were more likely to converge. Problems with the node equations arose in systems with low resistance pipes, where small errors in pressure led to large errors in flow rates. It was noted that when node equations successfully converged, the solution was highly accurate and found relatively quickly.

Figure 2-7 shows a graphical representation of a node within a resistance network model. Equation 2-18 describes the mass and energy balance for the node (Wang & Touber, 1988). Use of this equation for a full network results in a set of non-linear equations, the solution of which is a three-dimensional flow pattern corresponding to the given boundary conditions.

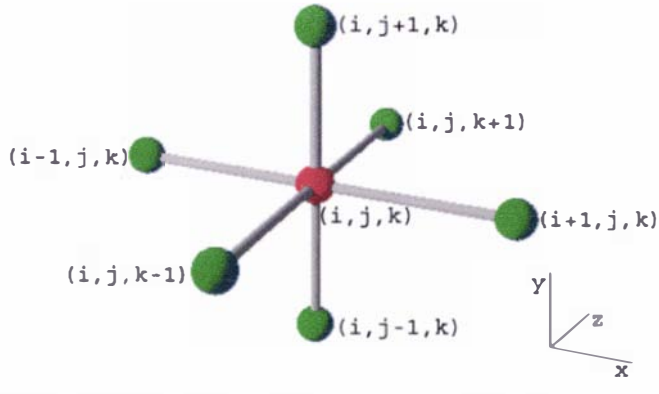

Figure 2-7 – Graphical representation of nodes within a resistance network model. The red sphere represents the node for which the mass balance is conducted, with green spheres representing adjacent nodes

$$\sum_{\substack{ii=i-1 \\ jj=j-1 \\ kk=k-1}}^{\substack{ii=i+1 \\ jj=j+1 \\ kk=k+1}} \left(P_{ii,jj,kk} - P_{i,j,k}\right) \sqrt{\left(\frac{D_h}{\rho f L}\right)_{ii,jj,kk} \frac{2}{\left|P_{ii,jj,kk} - P_{i,j,k}\right|}} = 0 \qquad \text{Equation 2-18}$$

Where:

i,j,k	=	Indices in the co-ordinate axes (x,y,z)	
D_h	=	Channel hydraulic diameter	(m)
f	=	Friction factor	
L	=	Channel length	(m)

van der Ree *et al.* (1974) developed a very simple channel network model. The model was based on the velocity of air calculated from the vertical channel size, air circulation rate and calculated friction factor. The model also included temperature prediction. The model was solved using a finite element program called BERTEM, and results were used for qualitative observations. No validation was performed.

Meffert & van Beek (1983) developed a resistance network model for airflow in a cargo space. An electrical circuit analogy was used for laminar flow (Equation 2-19).

$$\Delta P = Q\beta_{lam} \qquad \text{Equation 2-19}$$

Where:

Q	=	Fluid volumetric flow	($m^3.s^{-1}$)
β_{lam}	=	Laminar resistance	($Pa.s.m^{-3}$)

A more complex model was required for turbulent flow to meet the second power law, where the flow resistance is itself a function of fluid flow rate. A graphical method was used for this case in which the flow rate - pressure loss relationships for the channels needed to be known. The model described was then extended to calculate the qualitative effects of various factors on the temperature distribution within a loaded container (Meffert & van Beek, 1988). The model was kept simple, with heat generation and density the only properties of the product considered.

Wang & Touber (1988) used a resistance network model to predict heat and mass transfer in a simple refrigerated room. Comparison of experimental results with temperatures calculated from predicted flow patterns showed reasonable agreement, however significant errors were apparent.

Lindqvist (2000) attempted to use a proprietary channel network model to simulate the air distribution in reefer holds. The model connected all of the air gaps forming channels in the hold into a network and associated a flow resistance coefficient with each. The model considered the effect of heat loss from the pallets, but did not include buoyancy effects, heat transfer from walls, packaging, ceiling or floor. By inputting inlet air pressure and temperature to the model, it was reported that pressure, temperature and mass flow rate through the model could be predicted. Lindqvist (2000) was unable to successfully implement the model, citing the complex geometry and lack of a graphical user interface as the key difficulties.

Zertal-Menia *et al.* (2002) developed a resistance network model to predict the airflows within a 1:3.3 scale model of a refrigerated road vehicle trailer. Two loading patterns were simulated and the results compared to simulations performed using the CFD code FLUENT® (Section 2.3.3.2) and flows observed experimentally. The model assumed flow was either in the laminar or turbulent regime depending on the channel type and the flow predictions made using CFD. The vehicle was configured with the air delivery

near the ceiling, and an increase in pressure due to the abrupt expansion of the delivery air jets was included in the model. The model divided the vehicle into four quarters and the resistances in each section were combined to formulate a set of 10 equations for solution using the Hardy-Cross method. Comparison of the flows calculated by the two simulation methods gave good agreement, and the resistance network model's results also compared well with the experimental observations. The authors postulated that disagreement between the two models was caused by the assumption of flow regime, the assumption of vertical flow in channels adjacent to the walls (where flow may have been diagonal) and the effects of combining flow and recirculation of air in the ceiling headspace which were not included in the resistance network model.

Rizzi (2003) developed a model of airflow within a sausage-ripening chamber. Channel dimensions and flow resistances were calculated from the geometry of the chamber and the placement of the sausages. The network equations were resolved using the Hardy-Cross method. Flow resistances in key positions inside the chamber were adjusted to simulate the effects of momentum. Comparison of velocity predictions with values measured with a hot-wire anemometer at nine positions amongst the sausages showed excellent agreement.

2.3.3.2 Computational fluid dynamics (CFD)

Computational fluid dynamics is a numerical technique for the solution of the equations governing the flow of fluids inside a defined flow geometry (Scott & Richardson, 1997). It comprises the Navier-Stokes transport equations, which describe the conservation of mass, momentum and energy. These equations are then discretised and solved for the input flow geometry and boundary conditions using the finite volume, finite difference or finite element methods depending on the software package used. Due to the relatively large size of the spatial discretisation turbulence is missed, therefore inclusion of a turbulence model is needed for airflow problems. The most commonly used are the fully turbulent k-ε model and the low Reynolds number k-ε model.

There are several commercial CFD software packages available including "Kameleon FireEx 98", FLUENT®, FLOW 3-D®, PHOENICS® and CFX®.

CFD has been previously used with varying degrees of success in the horticulture sector for predicting airflow patterns in a model section of a reefer hold (Lindqvist, 2000), a refrigerated road vehicle (Moureh *et al.*, 2002, Zertal-Menia *et al.*, 2002), coolstores (van Gerwen & van Oort, 1989; Wang, 1990; van Gerwen *et al.*, 1991; Mariotti *et al.*, 1995; Tassou & Xiang, 1998; Verboven *et al.*, 1998; Hoang *et al.*, 2000) and horticultural packages (Zou, 1998; Yongfu-Xu & Burfoot, 1999). Other relevant previous applications include modelling flow inside livestock facilities (Hoff *et al.*, 1992; Worley & Manbeck, 1995; Harral & Boon, 1997) and refrigerated display cabinets (Hu *et al.*, 1993).

Previous models have often assumed forced convection to be predominant and natural (free) convection has been ignored (Wang, 1990; van Gerwen *et al.*, 1991). This acts to decouple the airflow calculation from the heat and mass transfer calculations allowing steady state airflow patterns to be determined and used as an input to heat and mass transfer calculations. Consequently, computation time is greatly reduced, as the airflow calculation needs to be performed just once, rather than at each iteration. This assumption is only valid however if the forced convection is dominant throughout the calculation domain. Tassou & Xiang (1998) found that buoyancy was significant in a vegetable store in areas of low air velocity. This result suggests that this assumption must be made with care.

Wang (1990) modelled a refrigerated room coupled with the refrigeration system. The commercial CFD package PHOENICS® was used to model the steady state flow of air inside the refrigerated room, using the assumption of forced convection predominance discussed above. The author gave a criterion for the validity of the assumption as follows:

$\frac{Gr}{Re^2} >> 1$ free convection dominant

$\frac{Gr}{Re^2} \cong 1$ free and forced convection of comparable magnitude

$\frac{Gr}{Re^2} << 1$ forced convection dominant

Where:

Gr	=	Grashof number = $\frac{g\omega D^3 \Delta T}{v^2}$	
g	=	Acceleration due to gravity	($m.s^{-2}$)
ω	=	Fluid volumetric coefficient of thermal expansion	(K^{-1})
D	=	Characteristic dimension	(m)
ΔT	=	Temperature difference	(K)

The predicted airflow patterns were used to calculate heat and mass transfer rates in the room. Validation of the airflow model was performed in an empty coolstore to facilitate the positioning of the anemometer. Fifty-nine measurements of air velocity were taken using a hot wire anemometer in a two-dimensional cross-section in the middle of the refrigerated room and compared with values predicted by the PHOENICS® model. There was significant divergence between measured and predicted velocities which the author argued were caused by: inaccurate boundary conditions, non-identical geometry between model and reality, k-ε model reliability and small eddies affecting the anemometer reading.

Using a similar model, van Gerwen & van Oort (1989) used the PHOENICS® package to predict airflow in a cold store. The authors made use of planes of symmetry to reduce the calculation volume; however, comment was made that flows were not symmetrical and this was a major cause of error in predictions. Using the forced convection predominance assumption, the authors addressed the problem in two stages: first calculating airflow and then using those values to predict heat transfer. The airflow model was validated qualitatively, comparing predicted flow patterns with observed smoke patterns. Good agreement between calculated and actual flow patterns was reported. There was no reported comparison of measured and predicted velocity, although measurements of air velocity were made. The authors made use of the model to predict the effect of varying cool store design to optimise energy use and control airflow patterns.

Many CFD models have been validated indirectly via the measurement of temperature as opposed to air velocity or flow rate. Validation by temperature measurement has shown reasonable agreement in some studies. Tassou & Xiang (1998) found that beetroot temperatures predicted using a 2-dimensional CFD model were within 0.5°C of measured values throughout a 15-hour cooling period. This means of validation is questionable however, as measured temperatures can be affected by numerous factors other than air velocity (e.g. product mass, product respiration rate, surface heat transfer coefficient), and the sensitivity of product temperatures to changes in air velocity is often low.

Models validated directly through the measurement of air velocity have produced less convincing results. For example, Harral & Boon (1997) used sonic and hot wire anemometers to measure velocity and turbulence in a livestock facility and found excellent agreement with predicted values in most areas (<5% difference), however differences in some areas were much larger (>20%).

Lindqvist (2000) used the "Kameleon FireEx 98" CFD code to simulate flows through wooden pallet bases and in a full-scale model of a section of a reefer hold. Results were compared to experimental

observations of pressure at 43 points and velocity at 2 points. Prediction of pressure drop across four pallet bases was excellent for a wide range of volumetric flows. Prediction of pressure distribution in the model hold was not as accurate, with similar trends but absolute values were significantly under-predicted. This systematic error was attributed to the assumption of zero pressure at the outlet, which was eventually considered unrealistic by the author. Comparison of "flow factors" (discussed in Section 2.2.4) showed reasonable agreement between measured and calculated values. The author reported that agreement between velocity measurements and predictions was poor.

Moureh *et al.* (2002) used FLUENT® to model a 1:3.3 scale model of a refrigerated road vehicle in both loaded and unloaded configurations. The vehicle was configured to deliver air near the ceiling. A novel approach was used to characterise the gaps between pallets, which were treated as a fictitious but aerodynamically equivalent porous media. The assumption underlying the analogy was that the flow was laminar in the gaps. This was likely to be valid in the scale model but may not be the case at full scale. Two turbulence models were implemented (RSM and k-ε, Section 2.3.3.2.1) and the results of simulations compared with velocities measured using a Laser-Doppler anemometer. Results compared reasonably well for simulations using the RSM model, but less well with the k-ε model.

CFD simulations are generally steady-state solutions, however the actual flow may not be steady. Zhang *et al.* (2000) investigated airflow in a test room, and found the major flow path changed from one side of the room to the other without any obvious disturbance in the room. The test room investigated was to be used to validate CFD results calculated in a 2-dimensional plane. They suggested the use of vertical guiding plates to create a more uniform 2-dimensional flow.

Research comparing heat transfer coefficients calculated through CFD and those measured experimentally showed that the calculated results do not compare well with experimental values (Kondjoyan & Boisson, 1997; Verboven *et al.*, 1997). Discrepancies were attributed to the turbulence models and the wall function employed.

2.3.3.2.1 TURBULENCE MODELS

Modelling turbulence is critical to computational fluid dynamics becoming more efficient, accurate and useful (Hefner, 1999). Lack of turbulence data has been a problem for the developers of turbulence models. The focus of past research has been on modelling the effects of turbulence on mean flows rather than turbulence physics itself, hence data collected tends to be of mean flows (Hefner, 1999). For some turbulence quantities, measurement is difficult, for others it is impossible. Possibly the most important defect of current models, is that the boundaries of their range of usefulness cannot be estimated à priori (Bradshaw, 1999). Therefore, the suitability of a model for a given system cannot be determined by any method other than through experience.

The following sections present the various approaches available for modelling turbulence.

DIRECT NUMERICAL SIMULATION (DNS)

The Navier-Stokes equations are almost universally accepted as an accurate description of turbulence in simple fluids. The DNS method involves solving these equations to obtain converged statistics. The time and length scales employed must therefore be small enough to resolve turbulent fluctuation and tiny near-wall eddies. This method of solution requires computer power proportional to the cube of the Reynolds number; so there is a limit to the attainable Reynolds number, at present around the order of small-scale laboratory experiments (Bradshaw, 1999). DNS can be used to help develop new models, or improve existing turbulence models for use in practical applications, but not solve practical problems. It has not been used, nor is it likely to be used to solve problems in the horticultural industry in the foreseeable future.

REYNOLDS AVERAGED NAVIER-STOKES MODELS (RANS)

According to Bradshaw (1999), Reynolds averaging is a brutal simplification, involving throwing away nearly all the information in the instantaneous Navier-Stokes equations and replacing it with empirical correlations. However, Bradshaw (1999) also states that the best turbulence models for engineers right now are the Reynolds-averaged models.

Eddy viscosity modelling

Eddy viscosity modelling (EVM) requires the calculation of one or more turbulence quantities, which are then combined and directly related to the turbulent eddy viscosity. Various models have been developed although the 2-equation k-ε model and its derivatives are the most widely used. Prandtl's mixing length theory utilises no partial differential equations (PDE's) and one algebraic equation to calculate an eddy length scale which is related to the eddy viscosity. The k-ε model uses two PDE's to describe the turbulent kinetic energy and the dissipation function, which is related to the eddy viscosity. Equation 2-20 to Equation 2-22 are the relevant functions (Kleinstreuer, 1997).

$$\upsilon_t = C\left(\frac{k^2}{\varepsilon_{ij}}\right) \qquad \textit{Equation 2-20}$$

$$k = 1/2\overline{(v_i')^2} \qquad \textit{Equation 2-21}$$

$$\varepsilon_{ij} = 2\upsilon\overline{\left(\frac{\partial v_i'}{\partial x_k}\right)\left(\frac{\partial v_j'}{\partial x_k}\right)} \qquad \textit{Equation 2-22}$$

Where:

υ_t	=	Turbulent eddy viscosity	($m^2.s^{-1}$)
C	=	Constant	
k	=	Turbulent kinetic energy	($m^2.s^{-2}$)
v_i'	=	Turbulent velocity component in the i^{th} direction	($m.s^{-1}$)
v_j'	=	Turbulent velocity component in the j^{th} direction	($m.s^{-1}$)
ε_{ij}	=	Viscous dissipation function	($m^2.s^{-3}$)
υ	=	Kinematic viscosity	($m^2.s^{-1}$)
x_k	=	Coordinate on the k-axis	(m)

Several variations of the k-ε model have been developed and each provides a possible improvement over the basic k-ε model for the conditions for which it was developed.

The k-ε model was used by Wang (1990), who gave the unreliability of the model as a reason for discrepancies between measured and predicted velocities. Hoang *et al.* (2000) also used the standard k-ε model along with the RNG (renormalisation group) variant to model airflow inside a coolstore. The authors found an error of 26% in predicted velocities, and concluded that an enhanced turbulence model was needed to improve prediction accuracy. Others to use a k-ε model variant to model airflow in agricultural applications include van Gerwen & van Oort (1989), Hoff (1995), Mariotti *et al.* (1995), Worley & Manbeck (1995), Harral & Boon (1997) and Verboven *et al.* (1998).

Reynolds stress modelling

Reynolds stress modelling (RSM) involves solving partial differential equations for each of the important components of the turbulence stress tensor, plus the turbulence energy. Numerous empirical coefficients have to be tuned to match system-specific turbulent flow patterns (Kleinstreuer, 1997). Bradshaw (1999) states that despite being more realistic in principle than the eddy-viscosity approach, only modest

improvements in performance are gained. Considered alongside the increased numerical difficulties of the technique (complexity of programming, expense of calculation, occasional instability) most engineers have decided changing to RSM from eddy viscosity modelling is unwarranted.

Moureh *et al.* (2002) used both RSM and a k-ε model, to model airflow in a scale model of a refrigerated road vehicle. Comparison between predicted and measured velocities was more favourable for the RSM model than the k-ε model.

LARGE EDDY SIMULATION (LES)

LES is a less severe simplification than RANS, however only a tiny fraction of the full DNS information remains. LES thus resides in the middle ground between RANS and DNS. Conceptually, a local spatial filter is applied to the equations and large eddies are simulated with the full Navier-Stokes equations (DNS) but the smaller eddies are considered only in a turbulence closure model using the eddy-viscosity concept (Mason, 1998). In wall-bounded flow, the scale of the dominant eddies decreases to that below the filter scale, and thus serious errors at the wall occur as with RANS models. Due to its computational demands and the near-wall problems, LES has not yet been used in horticultural applications.

2.3.3.3 Other models

A numerical model was developed by Kang (1996) to predict airflow in a cold storage room. The model used heavily simplified Navier-Stokes equations to derive an equation based on the Poisson equation; with two-dimensional, steady, isothermal and inviscid flow assumed. The model developed used just two variables for prediction: the stream function and the vorticity. The results of the model were compared to the results of other recent airflow models and the agreement of overall predicted airflow patterns was investigated. Comparison was made with models of slot ventilated enclosures with inlet and return air slots both on opposite walls and the same wall, as well as with/without obstacles. The models agreed well in terms of general airflow patterns, although no comparison of absolute velocity values was reported.

2.3.4 Overall modelling techniques

Several other model frameworks have been used previously by researchers to predict heat and mass transfer in transport systems. They range widely in complexity, from simple empirical correlations to complex mathematical schemes capable of fundamental heat, mass, and momentum transfer calculations.

2.3.4.1 Lattice methods

Lattice schemes model physical phenomena with quasi-particles. These particles represent discrete packets of matter or fluid and move and collide on a regular lattice obeying the laws of conservation of momentum, mass and energy (van der Sman, 1999). The modelling method provides a number of advantages over the finite element and finite difference methods of discretisation: boundary conditions are easily implemented, a variety of physical processes can be modelled within a single framework, complex phenomena such as convection-diffusion can be modelled by straightforward application of Lattice-Boltzmann algorithms and due to their simplicity, the schemes are easy to implement.

Chen & Doolen (1998) provide a recent review of the Lattice-Boltzmann method (LBM). The reviewers show evidence that there has been good quantitative agreement between the LBM and both other numerical methods and experimental results. The authors applaud the simplicity of the method and its ability to incorporate new physics.

van der Sman (1999) provides three examples of Lattice-Boltzmann based models describing the convection-diffusion processes in vented transport packaging for fresh agricultural produce. The first system was the cooling of cut flowers, simulated using a one-dimensional model. The model was

validated using cooling curves with good agreement found. The second model was of heat transfer in a 1000 kg corrugated board container for seed potatoes. Again the model was validated against measured cooling curves with excellent agreement, and pressure distributions were also predicted favourably. The final model extended the second model to include mass transfer, with the aim of designing a vent hole configuration to avoid condensation. Again, experimental results compared well with the numerical simulations.

2.3.4.2 Scale modelling

Scale modelling can be an effective technique in the investigation of airflow. Researchers have used scale models to measure airflow or validate models under a number of conditions and then extended these results to full-scale applications. In order for the scale model to represent results relevant to the full-scale, a similarity criterion is usually employed.

Hoff *et al.* (1992) used a 1:5 scale model of a swine growing/finishing facility. Worley & Manbeck (1995) used a 1:5 scale model of a poultry facility to help develop a model of airflow and particle transport. The scale models were used to validate the numerical models developed by the authors. No similarity criteria were given.

Lovatt *et al.* (1993) used a scale model of a beef chiller to highlight major airflow trends and illustrate the effect of turning vanes. The model was filled with water and an electrode used to produce small hydrogen bubbles allowing visualisation of flow. The Reynolds number was used as the similarity criterion. The model was intended as a qualitative tool and consequently no validation was performed.

Yu & Hoff (1999) investigated similarity criteria used for ceiling slot ventilated agricultural enclosures. Two models, 1:6 and 1:3 scale, were used in the study and Reynolds number (Re) and inlet jet momentum ratio (Rm) were investigated as possible similarity criteria. Results of the study showed that Rm was the best similarity criterion for ceiling slot-ventilated enclosures with intermediate airflow.

Moureh et al. (2002) used a 1:3.3 scale model of a refrigerated truck to develop and validate a numerical model. The model was constructed with a glass front wall in order to allow optical access to the inside of the trailer for velocity measurement with a laser doppler anemometer. Air was used as the fluid and closed glass boxes were used to simulate pallets. No similarity criteria were given.

2.3.4.3 Other methods

Meffert (1993) provides a semi-empirical model for predicting the difference between maximum cargo temperature and air delivery temperature. The temperature difference was related to the internal and external heat loads of the refrigerated system, as well as two coefficients A' and B' which measure the efficiency of the system. The values for A' and B' are specific to a particular cargo, refrigerated space and stowage pattern, and depend strongly on the air distribution in the space. The model was described as useful for selection of suitable equipment, with A' and B' evaluated at standard conditions.

Further to this line of work, a configuration coefficient (CC) to be used for analysing stowage and equipment used in refrigerated containers was defined (Meffert, 1998). The CC was defined by Equation 2-23.

$$CC = \frac{\Delta T_p}{\Delta T_a + \Delta T_{pl}} \qquad \textit{Equation 2-23}$$

Where:

CC = Configuration coefficient

ΔT_p	=	Maximum temperature difference within products	(K)
ΔT_a	=	Maximum temperature difference within the circulating air	(K)
ΔT_{pP}	=	Over-temperature in heat generating bodies	(K)

Meffert (1998) states that the over-temperature of product was often not separately measured and therefore included in the product temperature range. As a result, the configuration coefficient was the ratio of measured product temperature range over the return-delivery air temperature difference. The CC's for several 20' ISO reefer containers were analysed using 54 published data sets, giving CC's of 2.45 ± 0.82. The author argued the large uncertainty was due to unspecified air distribution and thermal stacking properties. Another source of uncertainty may be the inaccurate assumption that the measured return air temperature was the maximum air temperature, as cool air that short-circuited through channels near the refrigeration unit would have cooled the return air below its maximum temperature.

In complimentary work, Meffert (1993) attempted to fit temperature distribution data for a product in a refrigerated space using a Weibull distribution. This distribution was applicable only if the air supply was under continuous temperature control. Given the limited data available, very good agreement was found. The distribution was described mathematically using Equation 2-24.

$$W = 1 - e^{\left[-\left(\frac{T-T_0}{SCP}\right)^{SHP}\right]} \qquad \textit{Equation 2-24}$$

Where:

W	=	Temperature distribution	
T	=	Temperature	(°C)
T_0	=	Minimum (foot) temperature	(°C)
SCP	=	Scale parameter	
SHP	=	Shape parameter	

Meffert (1993) used the air delivery temperature for T_0, which should be a good indication of the minimum product temperature if evaporative cooling did not significantly affect product temperature, and there was not significant variation in air delivery temperature. Relationships between Weibull model parameters and operating conditions were investigated with a correlation found between SCP and return-delivery air temperature difference for a given vehicle-cargo configuration.

In further work, Meffert (1995) used the Weibull distribution to model data presented by Irving & Sharp (1993). Inconclusive relations between model parameters and operational factors were achieved although the model was shown to fit the distribution of temperature data well. Meffert (1998) presents the following values for the Weibull parameters calculated from 36 experimental data sets with an $R^2 = 0.99$.

$$SCP / \Delta T_a = 0.79 \pm 0.27 \qquad \textit{Equation 2-25}$$

$$SHP = 1.76 \pm 0.64 \qquad \textit{Equation 2-26}$$

3 Summary of Literature

Refrigerated marine transport is an important link in the supply chain, especially for remote countries such as New Zealand and Australia. Improving carriage conditions, to give product of consistent quality, offers the exporter a significant advantage in a competitive market. The use of mathematical models is one option for developing improved operating procedures and equipment. Heat and mass transfer are the processes of primary importance in quality maintenance in storage and transport, and excellent models of these processes have been developed. However, successful prediction of heat and mass transfer relies on air temperature, velocity and humidity data. Accurate prediction of these quantities is a more difficult task.

Several models of airflow within refrigerated spaces have been developed previously. Recent models have used CFD almost exclusively as the method of calculation, with results that are often described as successfully describing trends qualitatively. Unfortunately, results of CFD model validation continue to show significant discrepancies between predicted and measured flows, most notably in areas of turbulence. The turbulence model employed has almost always been cited as a cause of divergence. Turbulence models are highly empirical and their application problematic; the boundaries of their usefulness can only be found through experience. It is highly likely that turbulence models capable of accurate prediction in transport systems exist, but without knowledge of the boundaries of the model's usefulness it is difficult to develop confidence in predictions. Given these limitations and the high implementation costs, it was considered that until more is known about the applicability of current turbulence models or improved turbulence models are developed, CFD was not considered sufficiently reliable in this application.

Other model frameworks employed recently include a two-dimensional Poisson model, which was not considered capable of predictions in complex three-dimensional geometries. Lattice-Boltzmann schemes appear promising; however, the technique is in its infancy and implementation in a large complex geometry may be premature. Resistance network models have shown promise, with general agreement shown between predictions and measured data in validation of both simple early models and more complex, recent models. There is currently a paucity of flow resistance correlations for the geometries found in refrigerated transport systems.

Resistance network models are an alternative framework that offers the distinct advantage that the models' boundaries of applicability are more clearly defined. There was sufficient evidence to suggest that a network resistance model, appropriately combined with empirical flow correlations, would be capable of successful prediction of airflow in marine transport systems.

4 Objectives

The goal of this project was to develop a mathematical model capable of predicting air distribution in refrigerated containers and holds. The aim was that the model would give results accurate enough to calculate mass and heat transfer quantities with reasonable confidence and provide greater understanding of the effect of operating procedures and system design variables on these processes.

It was ascertained from relevant literature that a resistance network model, together with the improved computing power of the present day, was most likely to meet the requirements of the application. Consequently, the specific objectives of the work were to:

1. Assess existing, published flow resistance correlations for relevant geometries and materials, and where necessary develop new correlations.

2. Using the correlations tested or developed in (1), develop a computer-based, three-dimensional model capable of predicting average air velocities in shipping systems.

3. Validate the model with existing literature data and velocity measurements made in fully loaded refrigerated containers and refrigerated vessel holds.

4. Test the suitability of the model for use alongside existing heat and mass transfer models through prediction of temperatures within marine transport systems.

5. Investigate the effect of various cargo arrangements, air circulation rates and loading practices on air distribution profiles to ascertain the effect of these parameters and make recommendations for improvement of operating practices and equipment design.

Part II
Measurement Method Development

As discussed in Section 2.2, measurement is vitally important in the development and testing of a model. This part describes the development of two measurement techniques used to characterise airflows in refrigerated transport applications.

5 Development of a Thermistor Anemometry System

5.1 Introduction

Measuring air velocity in a crowded environment such as a refrigerated container or hold is difficult, with the instrument itself and/or operator likely to influence the measured flow field and affect the validity of readings. Coupled with this, access for an operator to a loaded container or hold is difficult, so remote reading or data-logging instruments positioned prior to loading are the only realistic possibilities. In addition, to characterise the flows within large systems requires numerous sensors.

Ideally, a measurement method would be non-invasive, accurate, inexpensive and automatic. Unfortunately, such a measurement technique is not currently available, with instruments fulfilling the physical requirements prohibitively expensive. Given the nature of marine transport systems, sensor damage or loss is likely to occur, further contributing for the need for inexpensive sensors.

In order to validate the airflow model, an affordable method of airflow measurement in marine transport systems was required. As discussed in Section 2.2.2.3, thermistors have previously been used as an alternative air velocity measurement method (Irving & Sharp, 1975, Irving & Sharp, 1976). This chapter describes the development of a thermistor anemometry system to measure air velocities within refrigerated transport systems as a low-cost alternative to commercial sensors.

5.2 Sensor design

5.2.1 Thermistor basics

A thermistor is a thermally sensitive resistor, with a resistance that varies rapidly and predictably as a function of temperature. Thermistors are available in both NTC (negative temperature coefficient) and PTC (positive temperature coefficient) varieties. The temperature dependence of resistance for NTC thermistors can be characterised by an almost linear relationship between the logarithm of the resistance and the reciprocal of absolute temperature (Equation 5-1).

$$\Omega_t = e^{\left(\frac{a}{T_t+273.15}-b\right)} \qquad \textit{Equation 5-1}$$

Where:

a	=	Thermistor property	
b	=	Thermistor property	(K^{-1})
Ω_t	=	Resistance of thermistor	(Ω)
T_t	=	Thermistor temperature	(°C)

Alternatively, PTC thermistors can either exhibit a large increase in resistance at a 'switch' or 'Curie' temperature, or a fairly constant increase in resistance with temperature over the operating range (approximately 0.7 $\%.K^{-1}$).

A thermistor anemometer operates using the same principle as a hot-wire anemometer, where the rate of heat transfer from a heated sensing element is related to the fluid velocity (Section 2.2.2.3). As is the case for hot-wire/film anemometers, the instrument may be configured to operate in a number of ways.

- Constant temperature. Sensor operates at a fixed temperature and the power dissipation is measured.
- Constant current. Current supplied to the sensor is fixed and the resulting resistance of the sensor is measured.
- Constant voltage. Voltage supplied to the sensor (in series with a resistor) is fixed and the resulting resistance of the sensor is measured.

Constant temperature anemometers offer the ability to take readings at high frequency, as the sensor is not limited by the thermal inertia of the sensor element. This configuration is the standard for commercial devices and the electronics are relatively complex. Constant current was the configuration of choice for hot-wire anemometers prior to the introduction of constant temperature devices, and requires less complex electronics. Constant voltage performs similarly to constant current, but requires only rudimentary electronics. As all the configurations rely on a correlation between heat dissipation and fluid velocity, inherent differences in measurement accuracy are unlikely to be a limiting factor. However, the needs of a specific application, e.g. high frequency readings or large measurement range, need to be considered when choosing a configuration.

5.2.2 Sensor model

Although it is often cited as an application for thermistors, there is sparse information available concerning thermistor anemometry in the public domain (Siemens, 1986, RS Components, 1999, Thermometrics Inc., 2002). To accelerate the design process, a thermistor and a resistor in series were described mathematically to investigate the effect of thermistor properties and aid component selection. The thermistor and resistor system were described by Equation 5-2 to Equation 5-6.

Rate of Energy Accumulation = Heat production through resistive heating − Heat transfer from thermistor *Equation 5-2*

$$m_t \frac{dT_t}{dt} = \phi_p - \phi_h \qquad \textit{Equation 5-3}$$

$$\phi_h = \chi\left(T_t - T_{amb}\right) \qquad \textit{Equation 5-4}$$

$$\phi_p = I^2 \Omega_t \qquad \textit{Equation 5-5}$$

$$I = V_s / \left(\Omega_r + \Omega_t\right) \qquad \textit{Equation 5-6}$$

Where:

m_t	=	Thermistor thermal mass	($J.K^{-1}$)
t	=	Time	(s)
I	=	Current	(A)
ϕ_p	=	Heat production through resistive power dissipation in the thermistor	(W)
V_s	=	Voltage input	(V)
ϕ_h	=	Rate of heat transfer from the thermistor	(W)
χ	=	Dissipation factor	($W.K^{-1}$)
T_{amb}	=	Ambient temperature	(°C)
Ω_r	=	Resistance of resistor	(Ω)

There are large numbers of thermistors available, varying in a number of key attributes. Those considered of primary importance in this application were: maximum power dissipation, maximum temperature, resistance – temperature (Ω-T) relationship and dissipation factor. Circuit design variables were the resistor size and the supply voltage.

The dissipation factor was defined as the power required to raise the thermistor temperature 1 K above ambient temperature. The dissipation factor is dependent on the environmental conditions, and is usually quoted in thermistor specifications for still air and/or stirred oil. In this application, the dissipation factor was used as a measure of the fluid velocity, having calibrated the sensor over the range of expected velocities. To calculate the dissipation factor for a thermistor with a known Ω-T relationship, the required measured quantities were the power dissipation, thermistor and fluid temperatures (Equation 5-4).

At equilibrium, resistive heating is balanced with heat transfer and the temperature of the thermistor is constant. Plots of the predicted thermistor heating through resistive power dissipation against thermistor temperature were used to elucidate the effect of both thermistor and circuit design variables. The ambient temperature expected in the application of the thermistors was 0°C.

Figure 5-1 shows the calculated shapes of the resistive heating curves for several alternative circuit designs based on typical properties of readily available thermistors. A small number of initial tests were performed to determine approximate values of the dissipation factor in static air and air at velocities up to 10 $m.s^{-1}$. The intersection between the heat transfer curve and the resistive heating curve is the predicted equilibrium condition. A constant temperature circuit was considered unsuitable, as the temperature chosen would need to be low to avoid exceeding the maximum power dissipation at high velocity. With low temperature differences, uncertainties expected in measuring fluid temperature create significant uncertainties in the calculated dissipation factor. NTC thermistors in a constant current configuration suffered from a similar problem as the constant temperature configuration, where the steep resistive heating curve limited the temperature difference to a relatively low value. PTC thermistors in both a constant voltage and constant current configuration, along with NTC thermistors with constant voltage, gave suitable resistive heating curve characteristics.

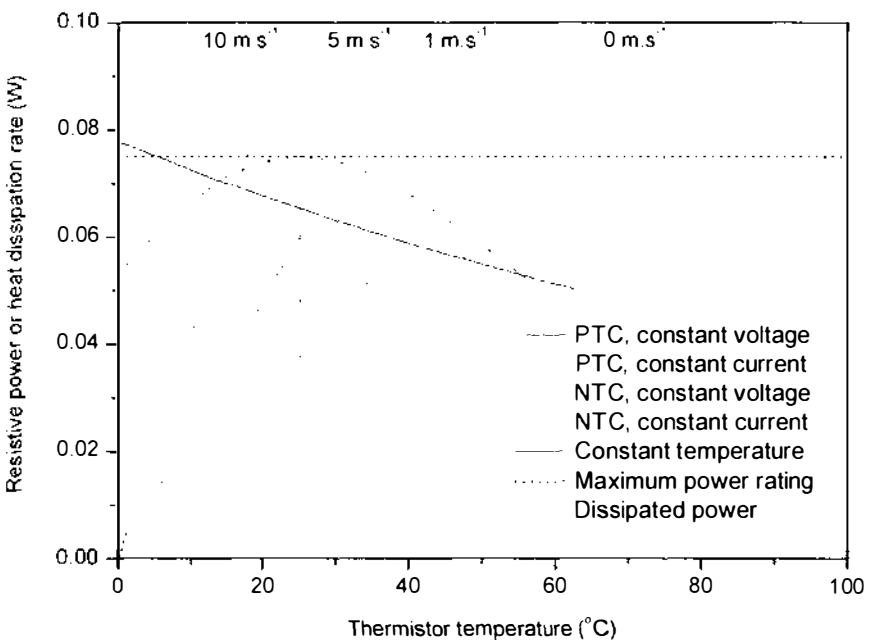

Figure 5-1 – Predicted resistive heating and heat transfer(dissipation) from five alternative thermistor configurations in air at 0°C

PTC thermistors with suitably low dissipation factors were not readily available. The NTC thermistor with a constant voltage circuit was chosen due to the availability of an 'off the shelf', low cost model with a sufficiently low dissipation factor. Four models of NTC thermistors from a single product range were chosen for testing. The properties of the thermistors were as shown in Table 5-1.

Table 5-1 – NTC thermistor properties

Thermistor attribute	Thermistor 1	Thermistor 2	Thermistor 3	Thermistor 4
Dissipation constant (in still air)	1 mW.K^{-1}	1 mW.K^{-1}	1 mW.K^{-1}	1 mW.K^{-1}
Maximum power	0.075 W	0.075 W	0.075 W	0.075 W
Maximum temperature	105°C	105°C	105°C	105°C
a	3935.47	3935.47	3935.47	4203.43
b	5.21 K^{-1}	4.70 K^{-1}	4.00 K^{-1}	2.61 K^{-1}
Resistance (@ 25°C)	3000 Ω	5000 Ω	10000 Ω	100000 Ω

Figure 5-2 to Figure 5-4 show the predicted resistive heating curves for a thermistor in series with a resistor (constant voltage configuration), along with the rate of heat transfer (dissipation) from the thermistor for air velocities ranging from 0 to 10 m.s^{-1}. Figure 5-2 shows the resistor limiting the resistive heating of the thermistor. It was necessary to match the resistor size to a thermistor and supply voltage to ensure the maximum power rating of the thermistor was not exceeded, for example Figure 5-2 suggests a resistor of greater than 1250 Ω was required.

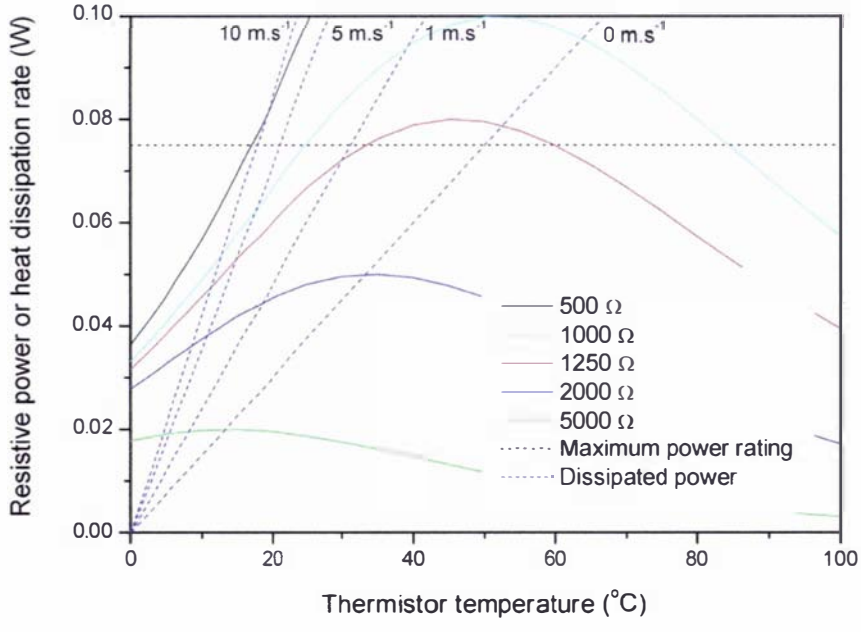

Figure 5-2 – Predicted resistive heating and heat transfer (dissipation) from a single NTC thermistor in series with a resistor ranging in resistance from 500 to 10000 Ω in air at 0°C (constant voltage circuit). The thermistor had a resistance of 3000 Ω at 25°C and the supply voltage was 20 V

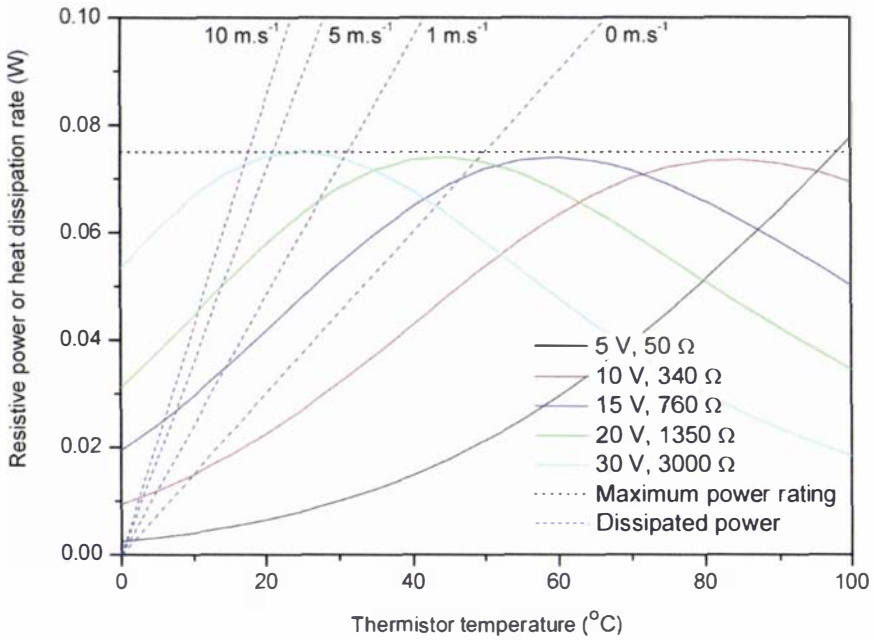

Figure 5-3 – Predicted resistive heating and heat transfer (dissipation) from a single thermistor in series with a resistor ranging in resistance from 50 to 3000 Ω, and a supply voltage of 5 to 30 V in air at 0°C (constant voltage circuit). The thermistor had a resistance of 3000 Ω at 25°C

Figure 5-3 shows the calculated curves for supply voltages ranging from 5 to 30 V and resistors matched to avoid exceeding the thermistors maximum power dissipation. Ideally, the intersection of the curves would be approximately perpendicular, as this reduces the effect of measurement uncertainty, and near the maximum power dissipation of the thermistor to increase the signal size. It can be shown that for a given configuration, the maximum resistive power dissipation occurs at the temperature where the resistance of the resistor exactly matches the resistance of the thermistor. The resistive dissipation at this point is described by Equation 5-7.

$$\phi_{max} = V_s^2 / 4\Omega_r = V_s^2 / 4\Omega_t \qquad \textit{Equation 5-7}$$

Where:

ϕ_{max} = Maximum heat production through resistive power (W) dissipation in the thermistor

Inspection of Figure 5-3 shows that the point of maximum dissipation should be slightly higher than the ambient air temperature expected to get near perpendicular intersections of the heating and dissipation curves. Given values for the maximum power dissipation of the thermistor and the thermistor resistance at the expected air temperature, the required supply voltage can be calculated using Equation 5-7. Effectively, increasing the supply voltage and the resistor size shifts the resistive dissipation curve horizontally to the left along the temperature axis. Figure 5-3 shows the supply voltage must be at least 30 V for the curve to intersect the heat transfer curves in an appropriate range for thermistor 1.

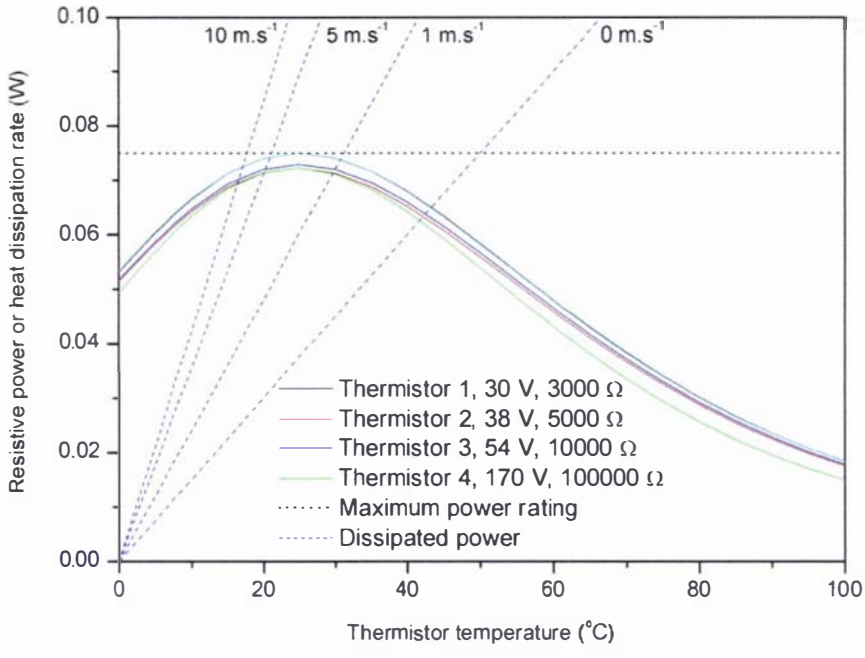

Figure 5-4 – Predicted resistive heating and heat transfer (dissipation) from four different thermistors with resistances of 3000 to 100000 Ω at 25 °C in series with a resistor ranging in resistance from 3000 to 100000 Ω, and a supply voltage of 30 to 170 V in air at 0°C (constant voltage circuit)

Figure 5-4 shows the calculated resistive dissipation curves for the four thermistors investigated along with the optimised supply voltage and resistor size. Resistors were matched to the thermistor resistance at 25°C, and the required supply voltage relates to the thermistor resistance by the square root law given in Equation 5-7.

5.3 Sensor implementation

The sensors were designed to function with Eltek Squirrel data-loggers (1000 series, Eltek Ltd. Cambridge, England). Therefore, factors such as the Squirrel measurement range and precision needed to be considered during sensor circuit design. For the thermistor to function as an anemometer, the output of the sensor needed to be calibrated against air velocity. Essentially this means the relationship between the dissipation factor and the air velocity was measured and a suitable calibration function chosen. Finally, the significance of sensor orientation relative to airflow direction was investigated, as irregularities in the physical shape of the thermistors were considered likely to affect the measured dissipation factor/velocity relationship.

Remote measurement and signal size

Sensors were designed to function automatically with 16 and 32 channel Eltek Squirrel data-loggers. Consequently, the sensor circuitry was designed to accommodate 15 sensors, as the output of 15 sensors and a common supply voltage could be recorded using a single 16-channel Squirrel data-logger. Figure 5-5 shows the circuit diagram incorporating a 16-channel Eltek Squirrel data-logger.

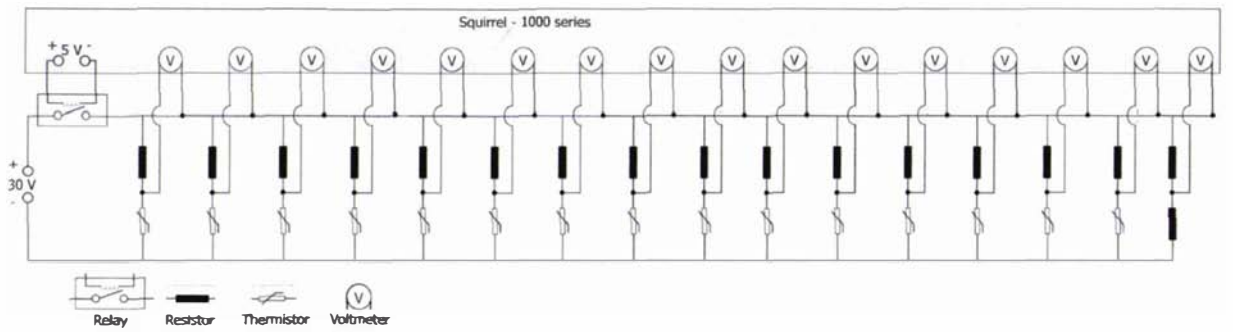

Figure 5-5 – Circuit diagram showing the circuit design used to measure the dissipation factor for fifteen thermistor anemometer sensors

The squirrel had a maximum measurement range of 0 to 20 V, with a resolution of 0.005 V. As the supply voltage was greater than the measurement range of the Squirrel, the signal size was halved by measuring the voltage across one of two matched resistors (right-most voltage measurement in Figure 5-5). Calculations as described in Section 5.2.2 showed use of thermistor 1 from Table 7-2, along with a voltage supply of approximately 30 V and an appropriate current limiting resistor (2000 Ω), gave an output signal of approximately 10 to 20 V over the velocity range of 1 to 12 $m.s^{-1}$.

The squirrel allowed an excitation voltage to be applied for up to 1 minute prior to measurement. Whilst the excitation voltage was not suitable for supplying the sensor with power, it was used along with a relay to switch on and off an external power supply. The equilibration time of several sensors was measured. The time (and therefore thermal mass) was found to vary significantly between sensors; however, 1-minute was found to be adequate for all sensors to equilibrate under all flow conditions (Figure 5-6).

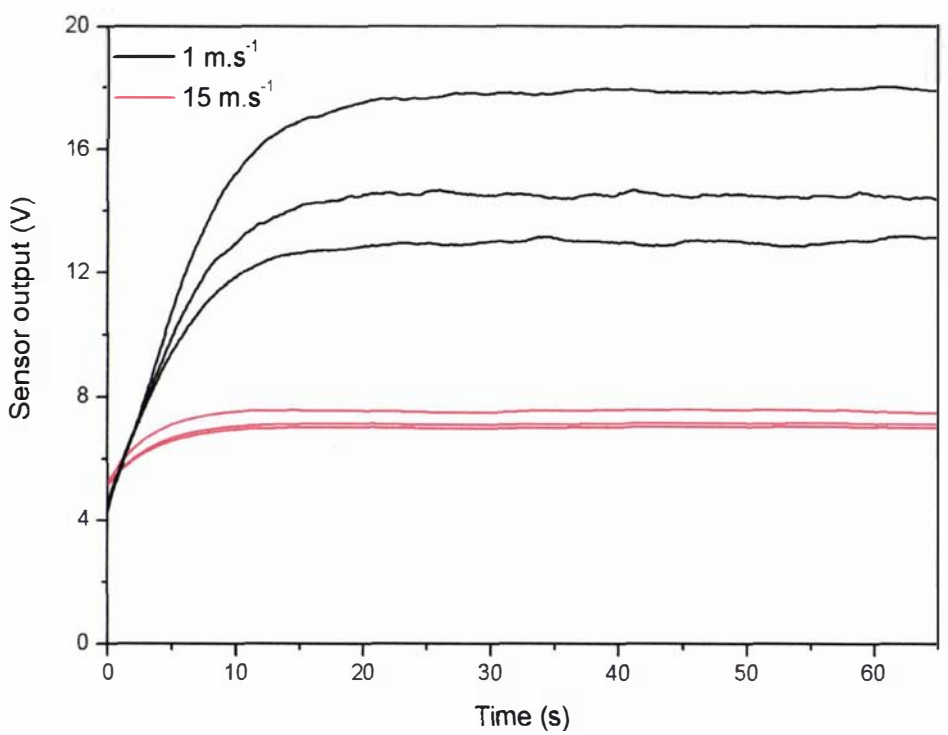

Figure 5-6 – Dynamic response of three thermistor anemometer sensors during equilibration with air velocities of 1 and 15 $m.s^{-1}$

Over the 1-minute equilibration time, power consumption was calculated to be approximately 0.1 mA.h per sensor. To supply 15 sensors sufficient power for a 45-day voyage with a measurement interval of 10-minutes required 10 A.h of power at 0°C. This quantity of power was supplied using alkaline batteries.

SENSOR CALIBRATION

The dissipation factor of seven thermistors was measured over a range of fluid velocities at approximately 0°C, and the relationship between dissipation and air velocity determined. The dissipation factor was calculated from the voltage drop across the resistor, the supply voltage and the air temperature (Equation 5-8 to Equation 5-11).

$$\chi = \frac{I^2 \Omega_t}{(T_t - T_{amb})} \qquad \textit{Equation 5-8}$$

$$I = \frac{V_r}{\Omega_r} \qquad \textit{Equation 5-9}$$

$$\Omega_t = \frac{V_s - V_r}{I} \qquad \textit{Equation 5-10}$$

$$T_t = \frac{a}{ln(\Omega_t) + b} - 273.15 \qquad \textit{Equation 5-11}$$

Where:

V_r	=	Voltage across resistor	(V)

Sensors and a hot-wire anemometer (TSI VelociCalc, model 8355-M-GB) were carefully positioned in the centre of a 5.5 m long tube (150 mm diameter) at 0.4 m intervals. A fan was used to draw air through the tube, with various perforated plates placed at the entrance of the tube used to vary the velocity between 1 and 15 $m.s^{-1}$.

Figure 5-7 shows the measured dissipation factor for seven sensors plotted against measured velocity using a logarithmic scale. The data behaved according to a power-law relationship (Equation 5-12). Calibration of numerous sensors showed that the power law relationship held for all sensors with air velocities between 1 and 12 $m.s^{-1}$ with R^2 values typically between 0.96 and 0.99. Below 1 $m.s^{-1}$ and above 12 $m.s^{-1}$, linearity was lost in a number of sensors, with the dissipation factor typically levelling out beyond these limits. Typical values for the calibration coefficient and exponent were 0.002 and 0.28 respectively.

$$\chi = cv^n \qquad \textit{Equation 5-12}$$

Where:

v	=	Fluid velocity	($m.s^{-1}$)
c	=	Thermistor calibration coefficient	($J.s^{n-1}.m^{-n}.K^{-1}$)
n	=	Thermistor calibration exponent	

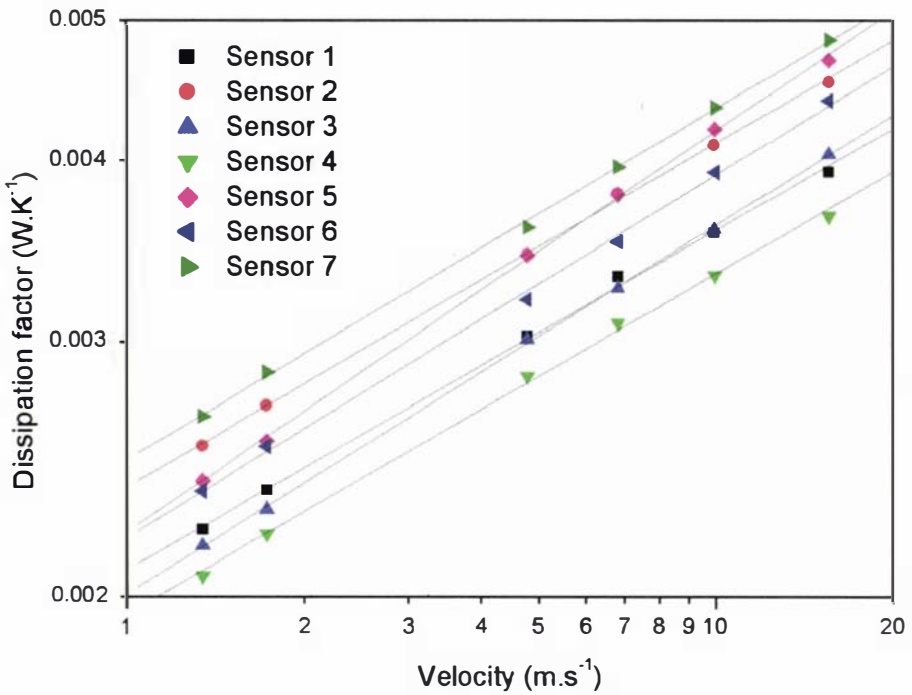

Figure 5-7 – Measured dissipation factor vs. fluid velocity for seven thermistor sensors at 0°C

The reliability of the calibration over a range of air temperatures was investigated by recording the output of three sensors with a varying incident air temperature profile. The effect of rapid temperature variation on the data-logger was also investigated, which may be experienced in practice during evaporator defrost. The three thermistor anemometers were placed in a forced air current, down-stream of an electric heater. The measured velocities were between 4 and 7 $m.s^{-1}$. A second electric heater was placed adjacent to the data-logger. Type-T thermocouples along with an Eltek Squirrel data-logger were used to record the surface temperature of the data-logger and the incident air temperature. Figure 5-8 and Figure 5-9 show the recorded temperatures along with the velocity readings of the three thermistor sensors normalised to the average velocity reading during steady temperature conditions.

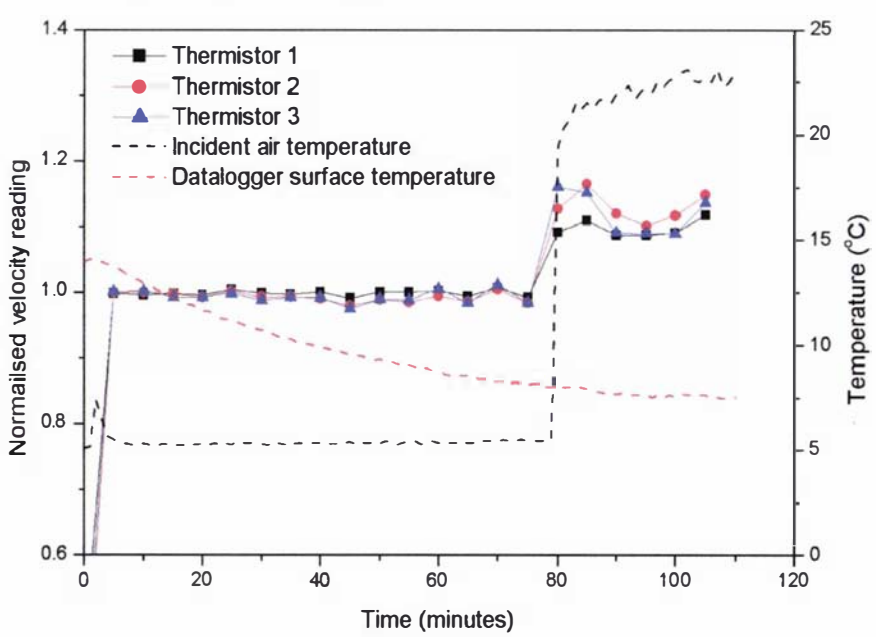

Figure 5-8 – Normalised thermistor anemometer output during a variable incident temperature profile and constant air velocity

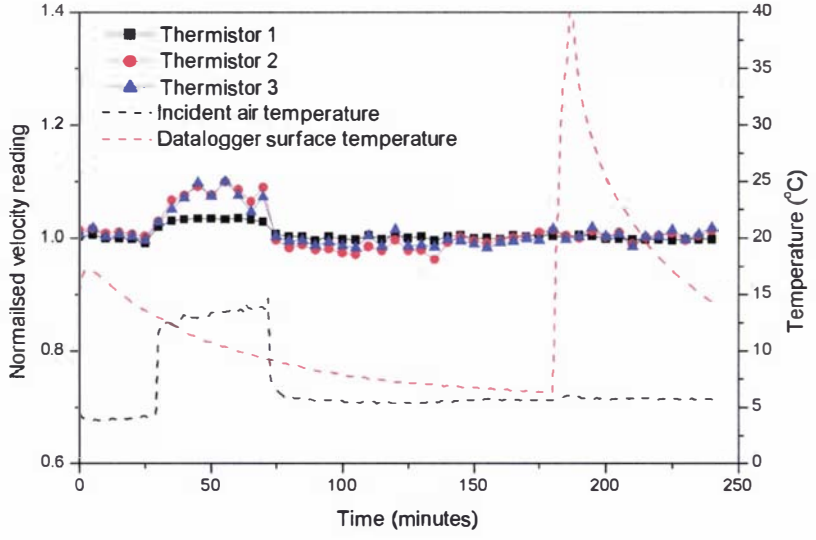

Figure 5-9 – Normalised thermistor anemometer output during a variable incident temperature profile, a rapid change in data-logger temperature and constant air velocity

Figure 5-8 and Figure 5-9 show the sensor reading was affected by the incident air temperature, although the magnitude of the effect was small. Incident air temperature shifts of approximately 20°C and 10°C respectively caused maximum changes in sensor outputs of 16% and 10%. Figure 5-9 shows that a sharp temperature change of the data-logger had no effect on the recorded sensor response. The magnitude of uncertainty caused by the temperature dependency of the readings was considered acceptable given the narrow range of temperatures likely to be experienced within refrigerated shipping systems. However, it is advisable to calibrate the sensors at the air temperature close to that they are in which likely to operate.

Sensor orientation

Tests were also conducted to assess the effect of sensor orientation. The thermistors were irregular in size and shape, so orientation relative to flow direction was considered likely to affect the relationship between fluid velocity and dissipation factor. Figure 5-10 to Figure 5-12 show the measured relationships for 3 thermistors in various orientations. Differences between orientations were found to be small over the range of measured air velocities (5-10% typical, 20% maximum). To reduce this effect, sensors were produced with markings to indicate the sensor orientation during calibration (Figure 5-13).

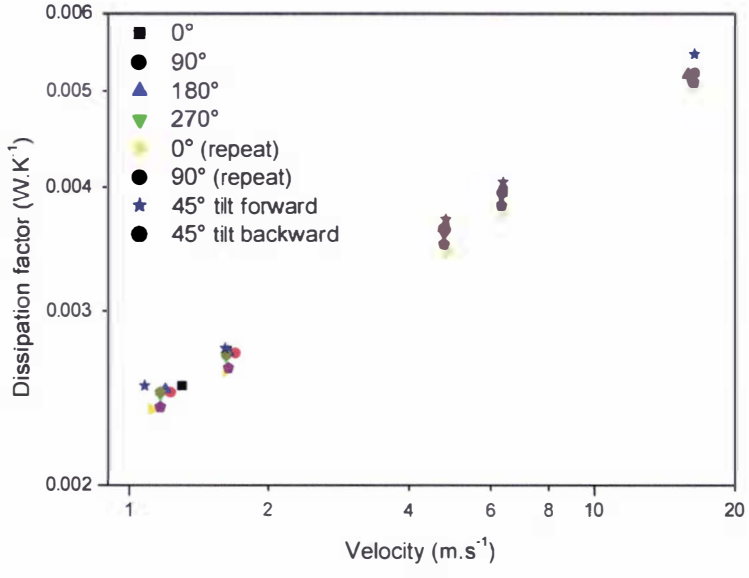

Figure 5-10 – Measured dissipation factor vs. fluid velocity for a thermistor sensor in various orientations

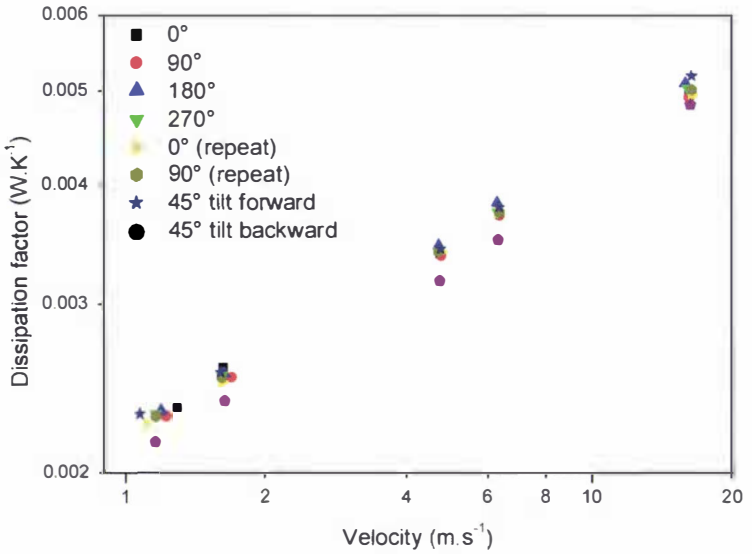

Figure 5-11 – Measured dissipation factor vs. fluid velocity for a thermistor sensor in various orientations

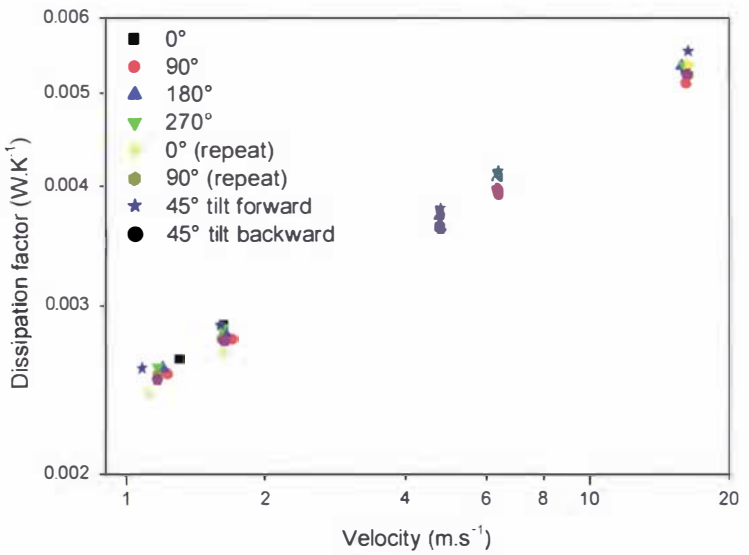

Figure 5-12 – Measured dissipation factor vs. fluid velocity for a thermistor sensor in various orientations

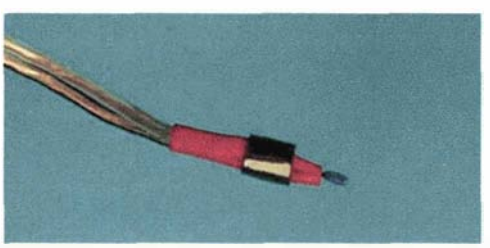

Figure 5-13 – Thermistor sensor showing marking for calibration orientation (white stripe)

Due to the relatively crude method of calibration, the accuracy of the sensors was estimated to be ±20%. This was considered to be an acceptable level of error in this application, where channel sizes were often ill-defined and accurate positioning of the sensors was difficult. As the error in the velocity measurement was mainly due to sensor positioning and calibration issues, changes in readings from a single sensor were considered an accurate indication of velocity changes.

5.4 Shipping trials

Thermistor anemometers were used to monitor airflow during four shipments of NZ kiwifruit and apples. Results from the final two shipments were used to validate the airflow model and observations are discussed in Section 11 and Section 12. The first two shipments were part of a commercial temperature monitoring program which provided an opportunity for testing the sensors during development. The following sections present the observations made during the first two monitored shipments.

5.4.1 Vessel 1

The first monitored shipment carried kiwifruit from Tauranga, NZ to Zeebrugge, Belgium via the Panama Canal in September/October. The duration of the shipment was approximately 26 days.

5.4.1.1 Experimental method

Fourteen thermistor anemometers were used to measure air delivery velocity in a single deck. Thirty-two type-T thermocouples were used to measure the delivery air temperature. Both sets of sensors were placed in the under-floor channels approximately 0.15 m from the refrigeration end wall. Sensors were spaced evenly across the width of the deck. Sensor output was recorded using 16 and 32-channel Eltek Squirrel data-loggers (1000 series, Eltek Ltd. Cambridge, England). Velocity readings were taken at 4-hour intervals and temperatures at 10-minute intervals. Thermistor sensors were calibrated prior to the trial. The deck measured approximately 22 m wide and 23 m long and narrowed in width with distance from the refrigeration end (Figure 5-14). The air delivery set-point was -0.8°C.

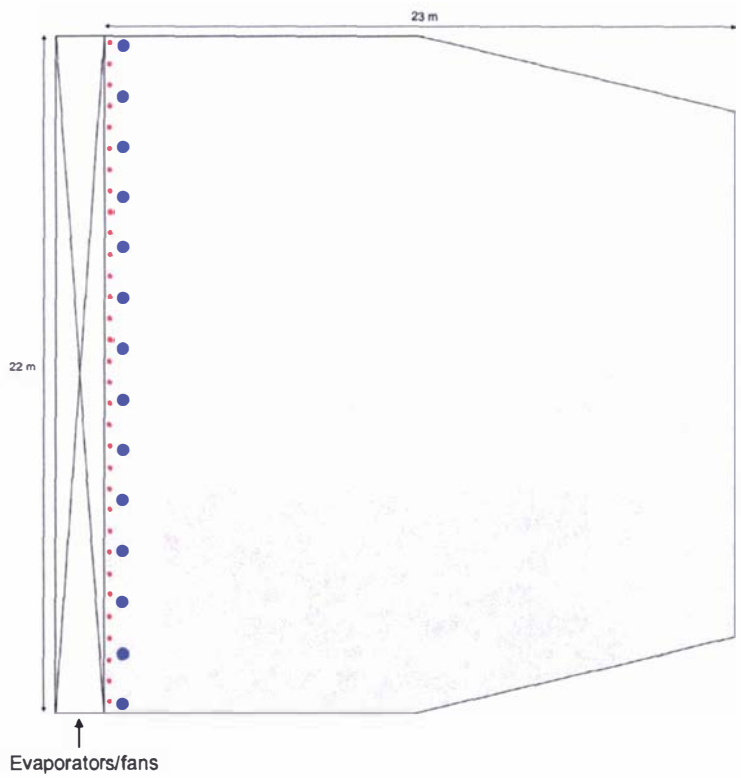

Figure 5-14 – Plan view of the deck showing the position of thermistor anemometers (•) and thermocouples (•)

5.4.1.2 Results

Failure of one data-logger meant velocity data was only successfully recorded from the seven sensors on the starboard side of the hold. Figure 5-15 shows the average measured delivery air temperature and velocity over the duration of the shipment. Spikes in temperature and velocity indicate defrosting of the

evaporator. Velocities were stable both throughout the shipment and the defrost cycle. Defrosts were performed approximately every two days during the first 13 and final 5 days of the voyage. During the other period, the interval was approximately 1-day. The increased defrost frequency was likely to have been due to increased ambient temperatures and humidity while travelling through the tropics.

Figure 5-16 shows the average delivery air temperature and velocity across the width of the deck. Unfortunately, the data-logger failure gave an incomplete picture of velocity variability across the width and no trends of significance were seen apart from a lower velocity near the starboard wall. Temperature variability across the width of the deck was substantial, with averages ranging from -0.9°C to 0.2°C. The cause of the variability was not obvious, although there was a higher average temperature near the starboard wall corresponding to the lower air velocity.

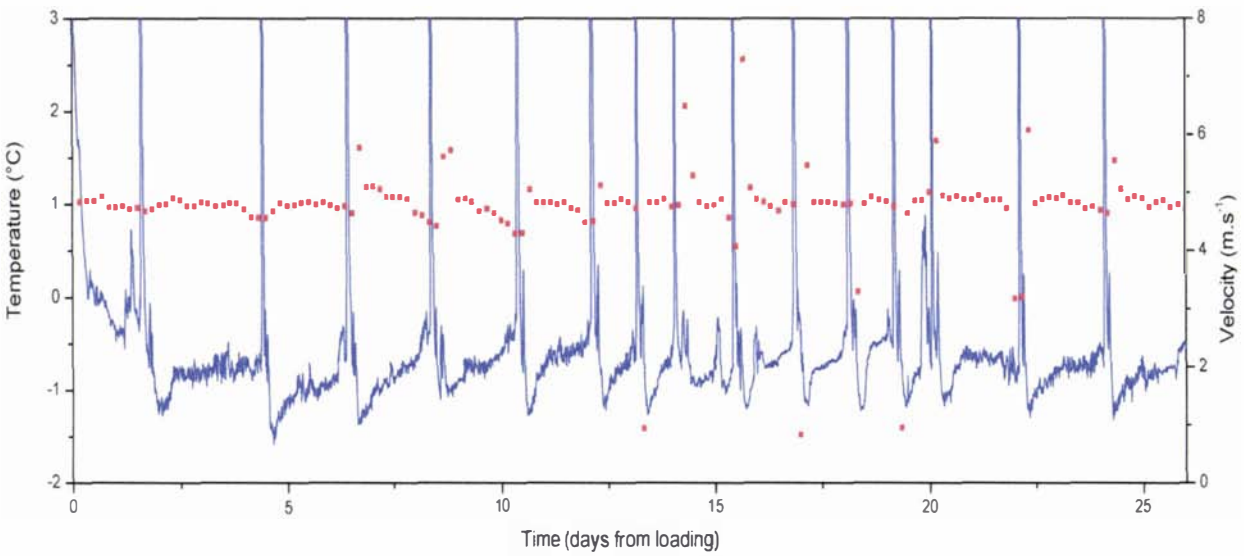

Figure 5-15 – Spatially-averaged measured delivery temperature (-) and velocity (■) across the width of the deck throughout the voyage

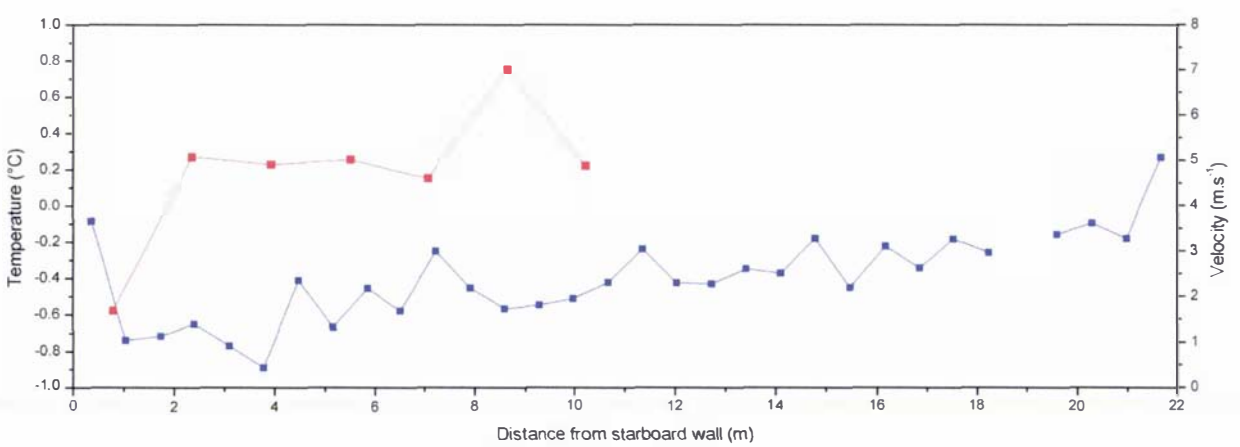

Figure 5-16 – Time-averaged delivery temperature (■) and velocity (■) over the duration of the journey for each measured position across the width of the deck

5.4.2 Vessel 2

The second monitored shipment carried kiwifruit from Tauranga, NZ to Tokyo, Japan in November/December. The duration of the shipment was approximately 19 days.

5.4.2.1 Experimental method

Twenty-eight thermistor anemometers were used to measure air delivery and air return velocities across the width of a single deck. Sixty-four type-T thermocouples were used to measure the delivery and return air temperatures. Sensors were placed in the under-floor channels approximately 0.15 m from the refrigeration end wall or attached to the return air grill. Sensors were spaced evenly across the width of the deck. Sensor output was recorded using 16 and 32-channel Eltek Squirrel data-loggers (1000 series, Eltek Ltd. Cambridge, England). Velocity readings were taken at 20-minute intervals and temperatures at 10-minute intervals. Thermistor sensors were calibrated prior to the trial and thermocouples calibrated both prior to and following the trial. The deck measured approximately 16 m wide and 23 m long, and the air delivery set-point was -0.8°C.

5.4.2.2 Results

Figure 5-17 and Figure 5-18 show the average measured delivery air temperature and velocity and return air temperature and velocity across the width of the deck over the duration of the shipment respectively. A cyclic pattern of velocity occurred throughout the shipment. Between defrosts, velocities fell steadily; reducing to approximately 50% of the initial velocity just prior to defrost. Defrosts were performed approximately every two days during the first 5 days of the voyage, and once a day, or even more during the remainder of the voyage. As was the case with vessel 1, the increased defrost frequency was likely to be associated with increased ambient temperatures and humidity while travelling through the tropics.

Figure 5-19 and Figure 5-20 show the delivery and return air temperature and velocity trends between defrosts in greater detail. The average delivery air temperature was pulled down rapidly immediately following defrost, and then continued to decline slightly during the following period. Once the evaporator became significantly frosted the average delivery air temperature began to rise, presumably due to reduced evaporator heat-transfer performance. The magnitude of this cycle was approximately 0.4°C. The rate of velocity decline was influenced by the stage of the journey. It was greater when fruit temperatures and/or increased ambient temperatures provided an increased heat-load on the evaporator and therefore increased rates of evaporator frosting.

Figure 5-21 and Figure 5-22 show the average delivery and return air temperature and velocity profiles over the duration of the voyage across the width of the deck. No trends of significance were observed in the velocity profiles, with the level of variation shown likely to be a function of the sensor positioning within the flow channel and the variable channel properties. Temperature variability across the width of the deck was substantial, with average delivery temperatures ranging from –1.4°C to -0.4°C. The central region of the hold was coolest with the extremities warmer; likely due to heat loads from heat conduction through the hold's walls. The return air temperature profile showed similar trends; however, the magnitude of variation was reduced. This indicates there was significant mixing of air across the width of the hold.

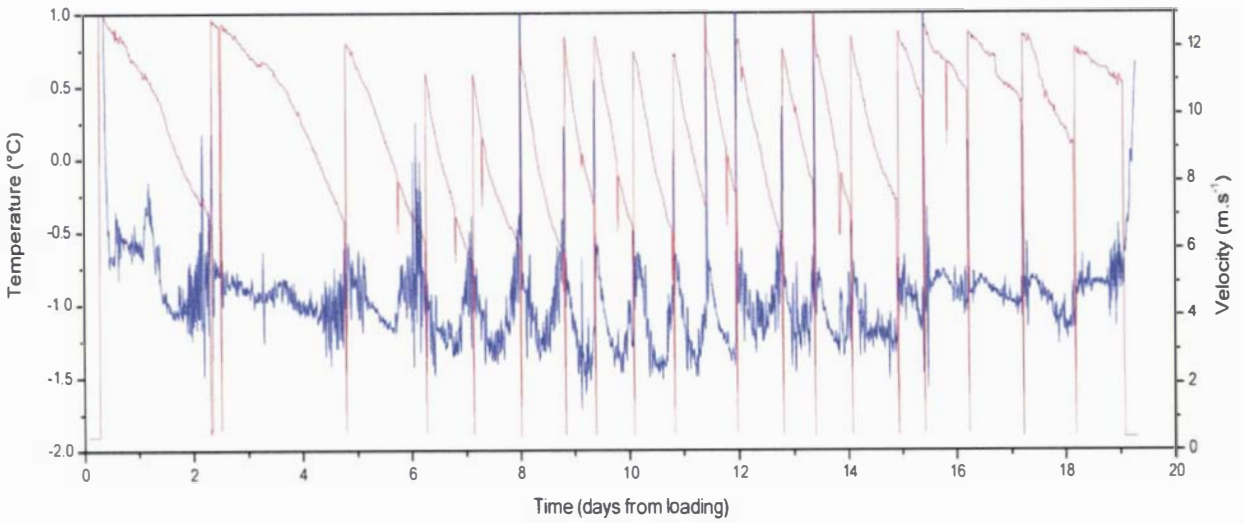

Figure 5-17 – Spatially-averaged measured delivery temperature (-) and velocity (-) across the width of the deck throughout the voyage

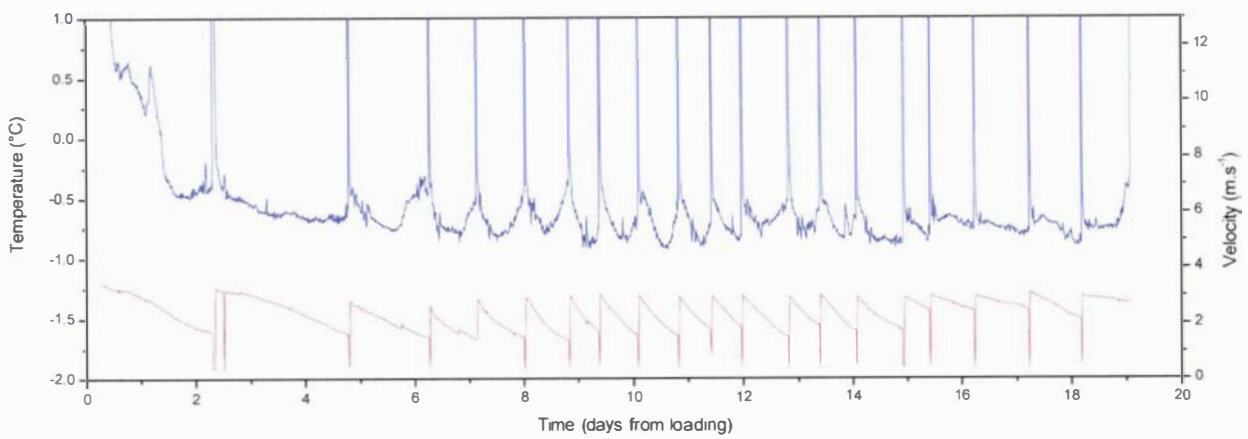

Figure 5-18 – Spatially-averaged measured return temperature (-) and velocity (-) across the width of the deck throughout the voyage

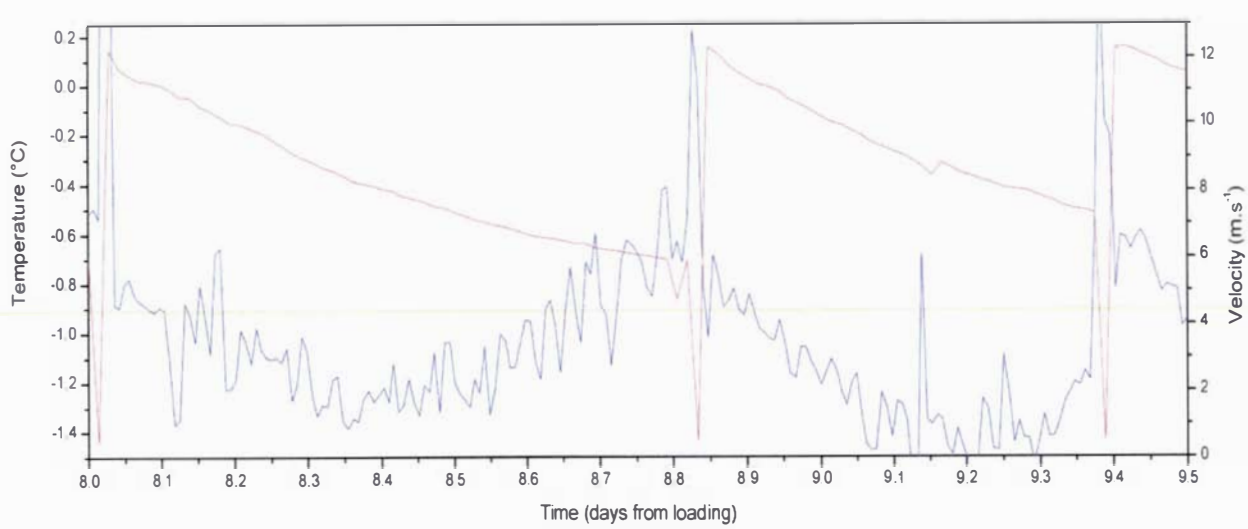

Figure 5-19 – Spatially-averaged measured delivery temperature (-) and velocity (-) across the width of the deck over the duration of two defrost cycles

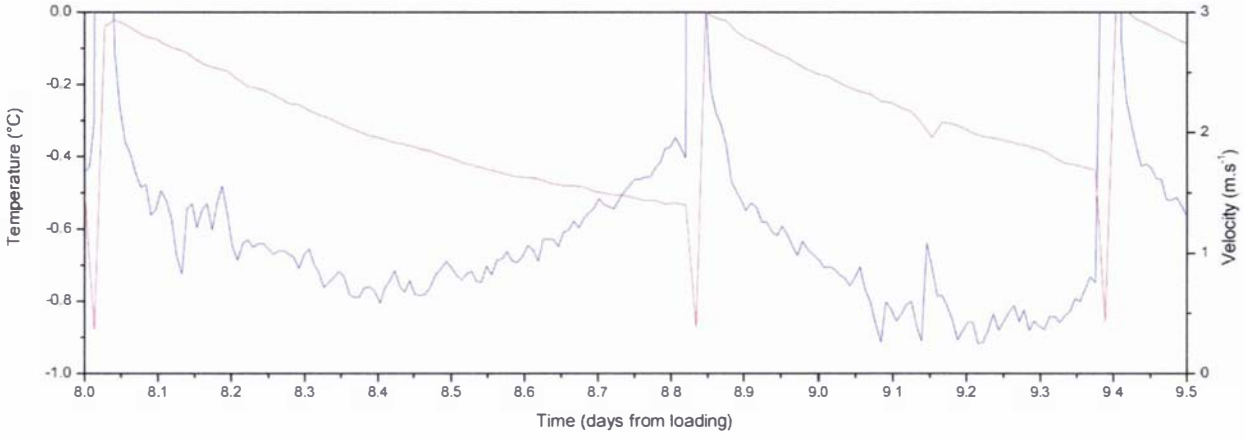

Figure 5-20 – Spatially-averaged measured return temperature (-) and velocity (-) across the width of the deck over the duration of two defrost cycles

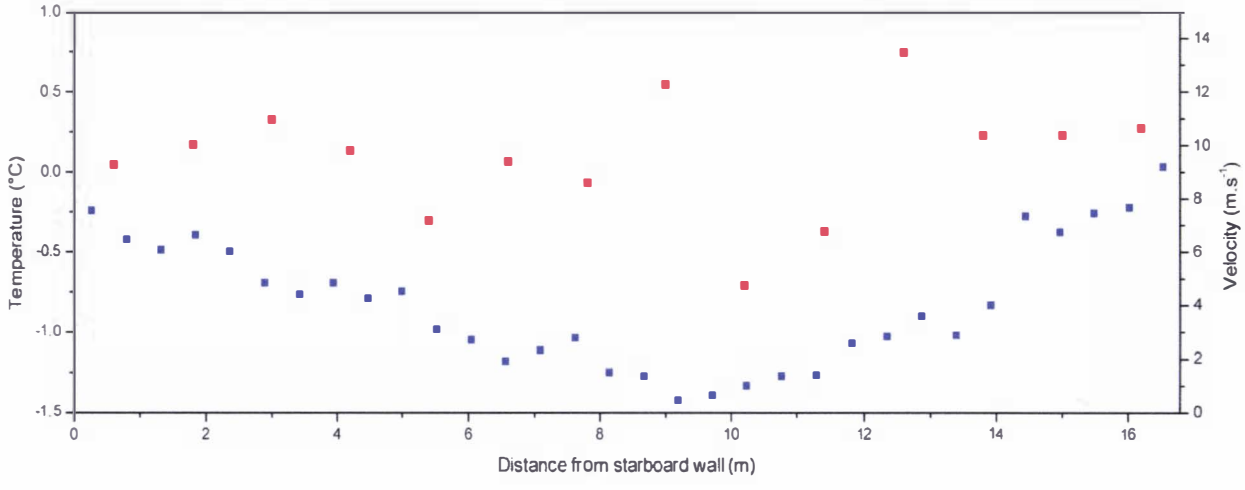

Figure 5-21 – Time-averaged delivery temperature (■) and velocity (■) over the duration of the journey for each measured position across the width of the deck

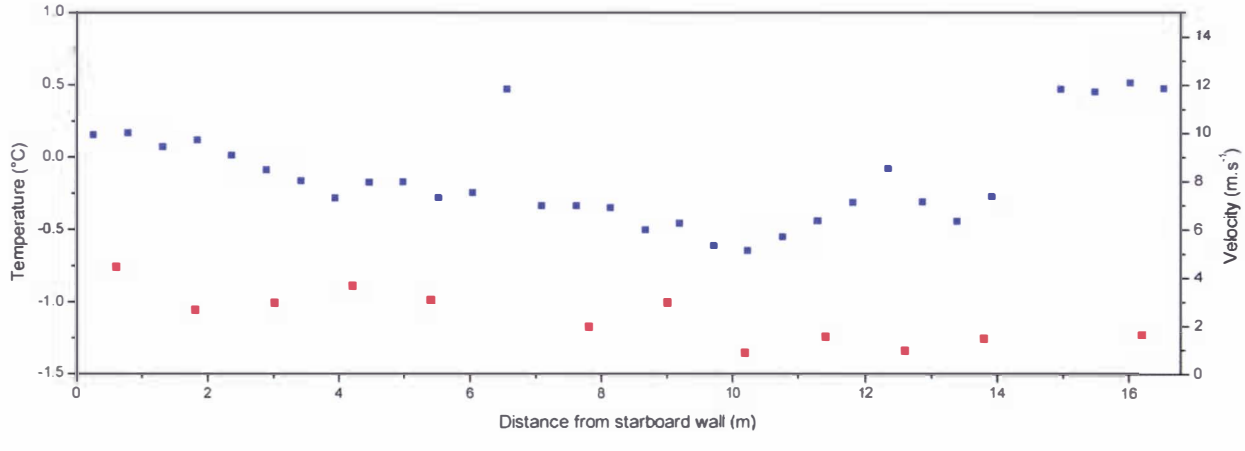

Figure 5-22 – Time-averaged return temperature (■) and velocity (■) over the duration of the journey for each measured position across the width of the deck

5.5 Conclusions

A low-cost thermistor anemometry system for use in refrigerated marine transport systems was successfully developed and tested. Although the system developed had many limitations, it provided a viable method to collect useful information in these systems that would have been prohibitively expensive to collect by other means. When coupled with an appropriate data-logger and power supply, the system could measure and record velocities throughout the duration of a shipment, thereby providing important data for validation of the airflow model. Sensors were observed to be insensitive to the direction of flow, and were inexpensive and expendable (<$5 NZ each).

The sensors were limited to velocity ranges of approximately 1 to 12 $m.s^{-1}$, with velocities outside these ranges best interpreted as < 1 $m.s^{-1}$ or > 12 $m.s^{-1}$. Whilst a complete investigation of the sources of error such as air temperature effects or sensor orientation has not been conducted, the repeatability of calibrations indicates accuracy of the sensors can be considered ±20% at best. The sensors consume significant quantities of power, so battery life is an important consideration in determining measurement frequency.

Improved accuracy and measurement range could be achieved through the sourcing of better suited thermistors and improvement of the calibration method; however, the increased cost in terms of calibration times and likely component costs must be weighed up against the benefits considering the likely attrition rate during use.

The thermistor anemometers were tested in two shipments of kiwifruit exported from New Zealand. In the first shipment, air delivery velocities were consistent throughout the voyage; however, in the second trial, a recurring pattern of delivery air velocity decline and variable delivery air temperature was observed. Increased rates of velocity decline were observed during initial cooling of the cargo and transit through the tropics. In both shipments there was substantial temperature variability across the width of the deck.

6 Further Development of an In-Package Velocity Profile Determination Technique

6.1 Introduction

In vented horticultural packaging systems, it is unlikely that air flowing through the package will be evenly distributed throughout the package. The uneven velocity profile leads to different rates of heat and mass transfer at different positions within the package. Prediction of these heat and mass transfer rates requires an estimate of the various flow rates throughout the package.

The airflow model developed in this work treated packaged products as a single or small number of flow paths (Part III). In the case of vented packages, these flow paths represent an agglomeration of the many channels through the packages. Therefore, prediction of flow through the modelled flow path (representing the vented packages) would provide the average flow rate through the packages rather than the specific in-package velocities required for heat and mass transfer prediction. Heat and mass transfer prediction in vented packages therefore requires a method to transform the average flow rate into the required in-package velocities.

Tanner (1998) used a zoned-model approach to predict heat and mass transfer processes in horticultural packages. The total flow through the system was apportioned to several pre-defined flow paths according to a relative velocity profile. It was assumed that the flow profile was uniform for each cross-section down the length of the package (i.e. the profile was 2-dimensional). To estimate this profile, a simple tracer technique was developed utilising air as the carrier gas for a CO_2 tracer. The CO_2 concentration was monitored using a constant flow CO_2 analyser and the time between an injection of CO_2 into the supply air and a measurable rise in concentration at the sample point was measured. Figure 6-1 shows a typical measured concentration profile. By assuming a 2-dimensional flow pattern, a velocity relativity coefficient (VRC) for each of the predefined zones was calculated using Equation 6-1. For further details of the analysis, the reader is referred to Tanner (1998) and Tanner *et al.* (2000).

$$VRC_{i,j} = \frac{L_{i,j} / \Delta t_{i,j}}{\sum_{h=1}^{H} \sum_{v=1}^{V} L_{h,v} / \Delta t_{h,v}} \qquad \textit{Equation 6-1}$$

Where:

$VRC_{i,j}$	=	Velocity relativity coefficient	
$L_{i,j}$	=	Length of shortest flow path to measurement position	(m)
$\Delta t_{i,j}$	=	Time between injection of tracer and rise in concentration	(s)
i,j	=	Horizontal and vertical axes	
H	=	Number of horizontal zones	
V	=	Number of vertical zones	

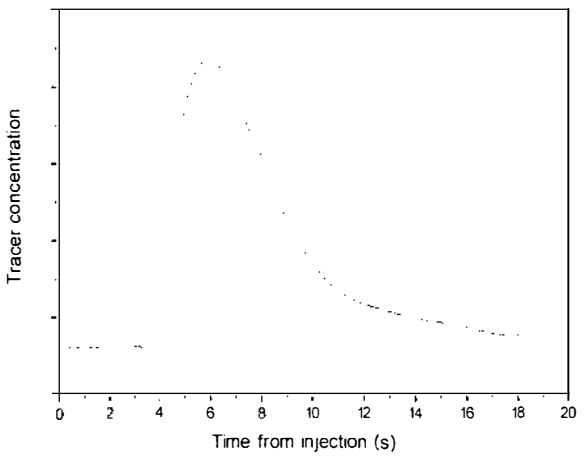

Figure 6-1 –Typical sensor output following an injection of tracer gas into a ventilated package

Although a CO_2 tracer was used previously, the experimental method and analysis can be applied to any measurable gaseous tracer. Density differences between the tracer gas and air were not considered important due to the high flow rates investigated.

The tracer method was designed to be a quick and relatively simple alternative to more advanced techniques such as computational fluid dynamics (Section 2.3.3.2). It provided data necessary for apportioning flow between sections of a package for prediction of heat and mass transfer rates. The method was not designed to give detailed descriptions of flow properties. Highly accurate flow determination within packages was not considered worthwhile due to other sources of variation affecting heat and mass transfer such as fruit size, orientation, respiration rate and skin permeability.

The CO_2 tracer technique for measuring a flow profile in horticultural packages was useful, but did require the user to have access to a constant flow CO_2 analyser and was tedious in complex packages as only one point could be sampled with each injection. Furthermore, the slow response of the CO_2 analyser may have adversely affected the accuracy of results. To address these issues an alternative tracer was sought. It was considered important that the tracer concentration could be easily measured with inexpensive sensors; the sensors could respond quickly to a change in concentration; and the tracer was inexpensive and readily available. This chapter describes the development of a multi-sensor method for characterising the flow profile of a package using a propylene glycol fog as a tracer, which greatly reduced the measurement time and required little specialised equipment.

It was envisaged that this technique would provide important information for modelling heat transfer during validation of the airflow model; however, ultimately the technique was not used as temperature information was not collected in any shipments with vented packaging.

6.2 Equipment development

Several alternative tracers were considered. The primary requirements were the availability of sensors of a sufficiently small size, fast response time and low cost, and that the tracer was safe and readily available. Several gases were considered including carbon monoxide, carbon dioxide and sulphur hexafluoride. Carbon monoxide sensors were available at a reasonable price, however their response was not sufficiently rapid and the electronics required to operate the sensors were complex. Sulphur hexafluoride has been used in air exchange measurement (Chen *et al.*, 1999), but suitably fast and cheap sensors were not available. Carbon dioxide was also excluded due to a lack of fast, inexpensive sensors.

Two alternatives to gas tracers were considered: a thermal tracer and a fog tracer. A thermal tracer would operate by sensing a change in air temperature due to a sudden alteration of the incident air temperature. Such a change may be measured with sufficient speed using fine thermocouples. A fog tracer operates by measuring the change in the optical properties of the air associated with the presence of fog. Although a fine thermocouple would create less obstruction to flow, practical difficulties associated with achieving a sudden change in incident air temperature and the faster response time of a fog sensor favoured the implementation of a fog tracer in this work. The thermal tracer presents an alternative technique that warrants further investigation.

Fog generating machines are available from electronics retailers at a reasonable price (<$100 AUS). Fog generators use a non-toxic 'fog' solution (generally propylene glycol and water) to produce large quantities of fog from relatively small amounts of solution. Propylene glycol has been classified as GRAS (generally regarded as safe) by the FDA (U.S. Department of Health and Human Services, 1997).

Fog generators operate by pumping the 'fog' solution through a heat exchanger and a fine nozzle. The fluid is heated under pressure in the heat exchanger, which flashes off after it exits the nozzle, forming small droplets that appear optically as a fog.

In this work, by pairing a light source and a light sensor, the arrival of fog was measured as a reduction in the intensity of light incident on the sensor. A light emitting diode (LED) and a phototransistor were chosen as the most suitable light source and sensor respectively. A phototransistor is an inexpensive semiconductor that limits current depending upon the intensity of incident light. The response time of the phototransistor was 3 μs (Sharp Corp., 2003); effectively instantaneous in this application. The sensors were designed to minimise obstruction to flow (Figure 6-2 & Figure 6-3).

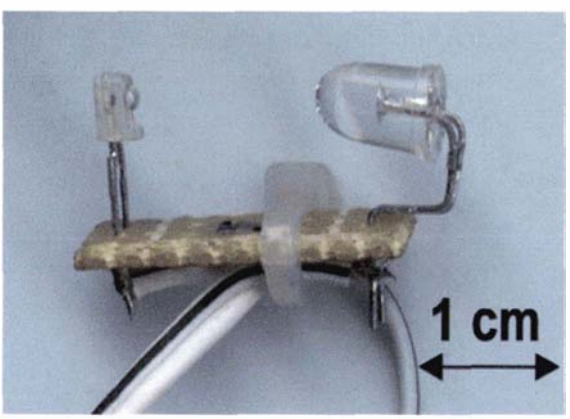

Figure 6-2 – A single fog sensor

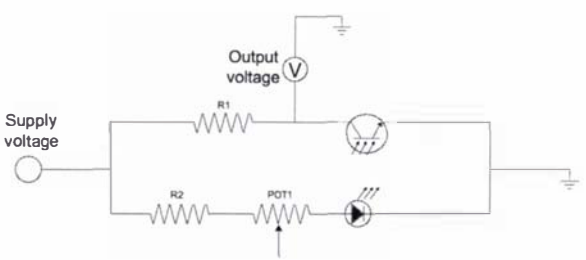

Figure 6-3 –Fog sensor circuit diagram

Initial experiments were conducted to establish the sensitivity of the sensors. Phototransistors were extremely sensitive to changes in light intensity over a narrow range, above which the transistor became saturated and current was not affected by changes in light intensity. Individual sensors were easily adjusted with a variable resistor to provide a light intensity in the appropriate range.

A number of phototransistors and LED's were tested in combination, to find the pair that gave the strongest response to fog arrival. The particle size of the fog was reportedly similar to the wavelength of light; approximately 0.3 μm (Corona Integrated Technologies Inc., 2002). Mie scattering, which affects different wavelengths of light approximately equally, is the predominant mode of scattering in this case and experimental evidence confirmed the colour of the LED had minimal effect on the sensor's response. Less sensitive phototransistors in combination with bright LED's were found to give the strongest response to fog arrival.

As the sensors were available at low cost, the number of sensors used was limited only by data logging capacity. Data analysis required a minimum sampling frequency of approximately 20 Hz per channel for in-package testing.

6.3 Experimental method

Part of an experiment performed by Tanner (1998) was replicated to compare results of the CO_2 and fog tracer techniques. The relative velocity profile of a standard Z-Pack as used by ENZAFRUIT International Ltd. (Figure 6-4) was measured using both the CO_2 and fog tracer techniques. The flow profiles within two prototype carton designs were also investigated to test the utility of the fog tracer technique in more complex flow geometries.

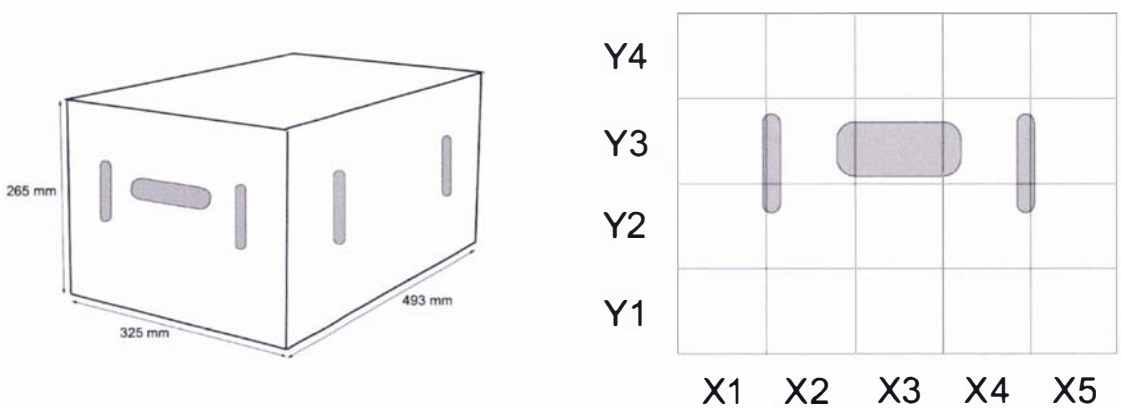

Figure 6-4 –A standard apple Z-Pack showing package dimensions, approximate vent positions and pre-defined zones

A variable speed fan and duct system was used to force air through a single carton with fruit (var. Royal Gala, count 100) positioned in four layers using moulded-pulp cardboard trays (Figure 6-5). Time to tracer arrival was measured at 12 to 24 sample points within the carton.

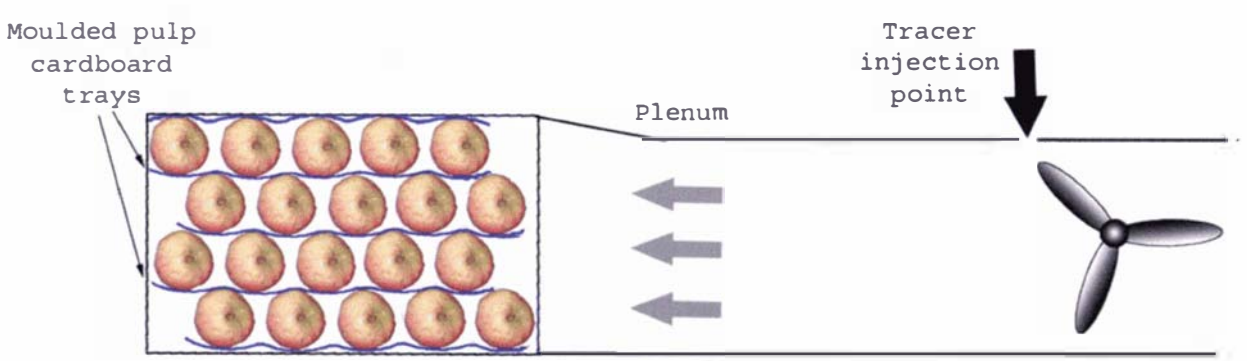

Figure 6-5 – Experimental set-up used to measure the flow profile through an apple carton

For the CO_2 tracer, 6.5 mm (3.8 mm ID) flexible rubber tubing was positioned at the sample point and attached to a LI-6262 constant flow gas analyser (LI-COR Inc. Lincoln, Nebraska, USA). The analogue output of the LI-6262 was recorded at 100 Hz using a DAQCard 1200 data acquisition card (National Instruments, Austin, Texas, USA). A burst of CO_2 was injected upstream of the carton using a switch with a voltage source incorporated to allow electronic monitoring of the time of injection.

For the fog tracer, the response of up to seven fog sensors was logged at 50 Hz using the DAQCard 1200. One or two sensors placed over the package vents were used as 'trigger' sensors, with the time of arrival

at the vent used as the 'time of injection' for calculation of VRC's. Five or six fog sensors inside the package were monitored at once.

The shortest path length between the entry vent and each of the sample points was measured by threading a length of string between the vent and the sample point. The tracer was injected a minimum of five times for each measurement.

6.3.1 Z-Pack

Tracer concentration profiles were measured at three points on each layer, each corresponding to a single zone, with a plane of symmetry assumed to run down the length of the box (Figure 6-4& Figure 6-6). The side vents of the cartons were covered to simulate the flow experienced in an end-on cooling operation.

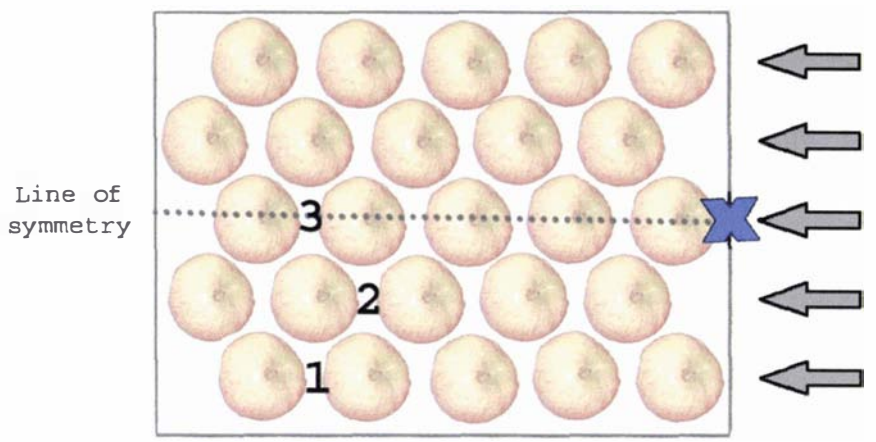

Figure 6-6 – Sensor placement within a single layer of a Z-Pack, showing a line of symmetry through the package. Black numbers represent the sensor positions while the blue × represents the 'trigger' sensor position

To measure the response time of the CO_2 sensor, the sample point was placed as close as possible to the CO_2 injection point and the resulting tracer concentration profile measured. The CO_2 concentration profile at the inlet vent was also measured. A sensor response lag was simulated with the fog tracer method by positioning a 'trigger' sensor approximately 1 m upstream of the package inlet. The velocity profile was characterised at two flow rates to verify that the relative velocity profile was independent of total flow rate as reported by Tanner (1998). Measured pressure losses across the carton and velocities exiting the vent were 10 Pa and 2.0 $m.s^{-1}$ for the high flow condition and 4.3 Pa and 1.3 $m.s^{-1}$ for the low flow condition respectively.

6.3.2 Alternative vent designs

Two cartons with alternative vent designs were constructed (Figure 6-7) and characterised using the fog tracer method. The cartons were designed to provide a more complex flow profile to test the suitability of the tracer method in this situation. Cartons were not designed to offer feasible alternatives to current designs for practical application and consequently no regard was given to manufacturing issues or carton strength.

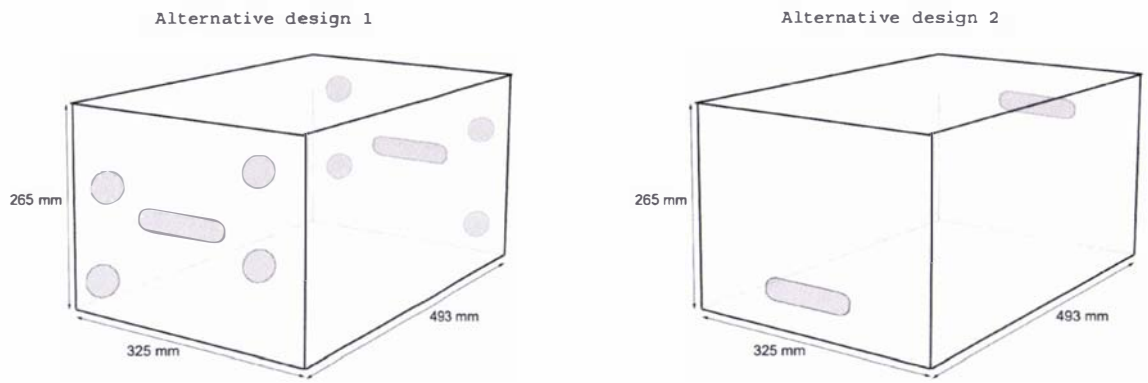

Figure 6-7 – Two alternative vent designs for a Z-pack used to test the efficacy of a fog tracer technique for measuring flow profiles

Dimensions of both the prototype cartons were identical to the Z-Pack. Rectangular hand holes, used to improve the ease of handling, were included in both designs. For both the alternative vent designs the pattern was mirrored at opposing ends of the carton: in design 1 circular holes promoted diagonal flow within each layer of the carton and in design 2 air entered the carton in layer Y1 and exited from layer Y4.

For design 1, sensors were placed at six positions on each layer (Figure 6-8). For design 2, five sensors were positioned on each layer with a line of symmetry assumed along the centre of the carton (Figure 6-9). Tracer concentration was measured at all positions on a single layer simultaneously. For design 1, the circular inlet vent on the layer being characterised was used as the 'trigger' point. For design 2, the air flowed into the lower level vent and this point was used as the 'trigger'. Pressure losses across the carton and velocities exiting the vent were 5.2 Pa and 1.8 $m.s^{-1}$ for design 1 and 7.2 Pa and 1.9 $m.s^{-1}$ for design 2 respectively.

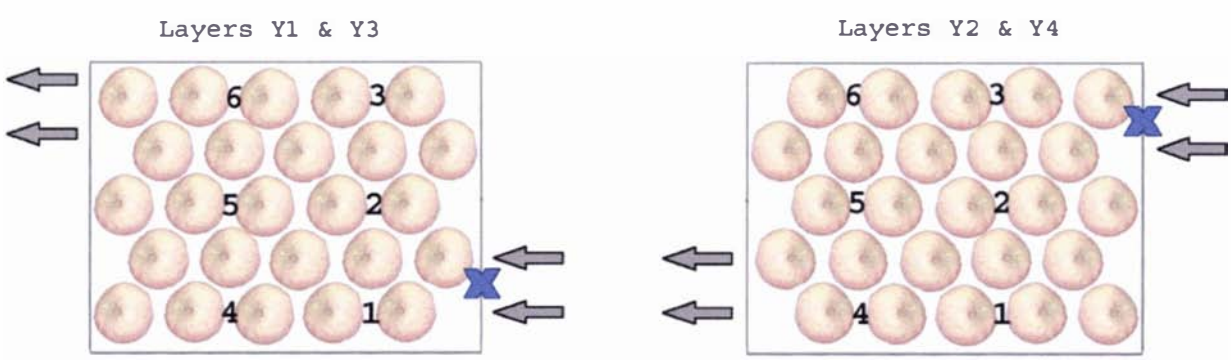

Figure 6-8 – Plan view of fog sensor placement in a carton with alternative vent design 1. Black numbers represent the sensor positions while the blue × represents the 'trigger' sensor position

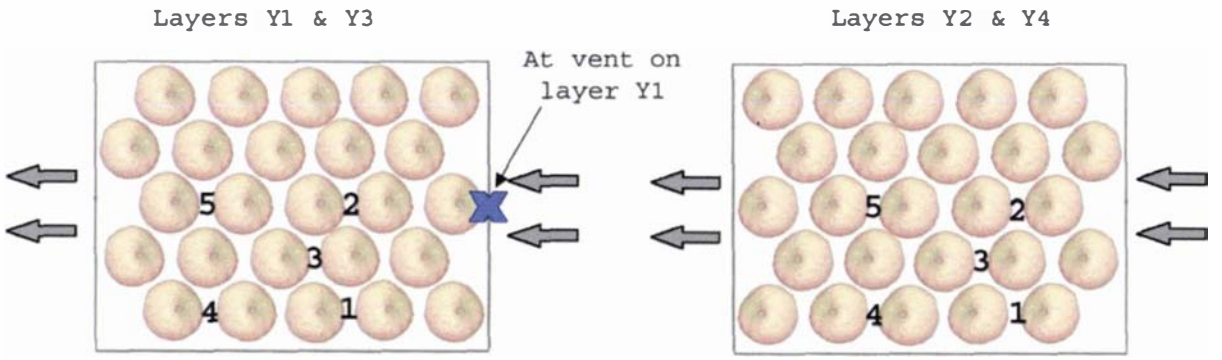

Figure 6-9 – Plan view of fog sensor placement in a carton with alternative vent design 2. Black numbers represent the sensor positions while the blue × represents the 'trigger' sensor position

6.4 Results and discussion

Typical output from both the CO_2 and fog tracer techniques are shown in Figure 6-10 and Figure 6-11. Measurement of the response time of the CO_2 analyser was replicated 5 times, with an average response time of 2.9 s and standard deviation of 0.15 s. The measured time to arrival of CO_2 at the package inlet was also 2.9 s indicating that the time to arrival at the package inlet was negligible. Therefore, times to arrival for the CO_2 method were adjusted by subtracting 2.9 s. The three options considered for analysing the concentration profiles are depicted graphically in Figure 6-12 – time of first arrival, time of bulk front arrival and time to peak concentration.

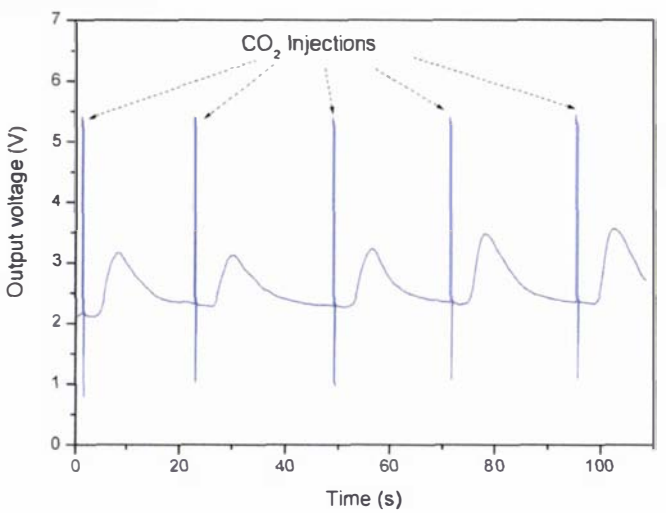

Figure 6-10 – Typical measured response of CO_2 sensor following injection of CO_2 to the incident airflow. Five injections of CO_2 are shown

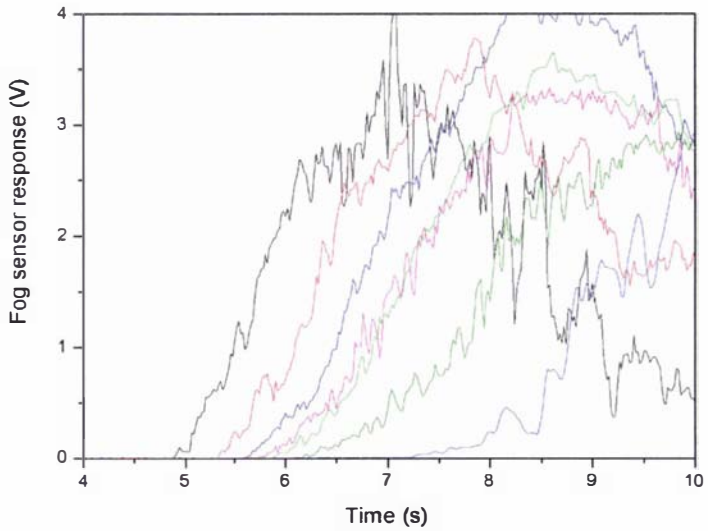

Figure 6-11 – Typical measured response of seven fog sensors following a single injection of fog to the incident airflow

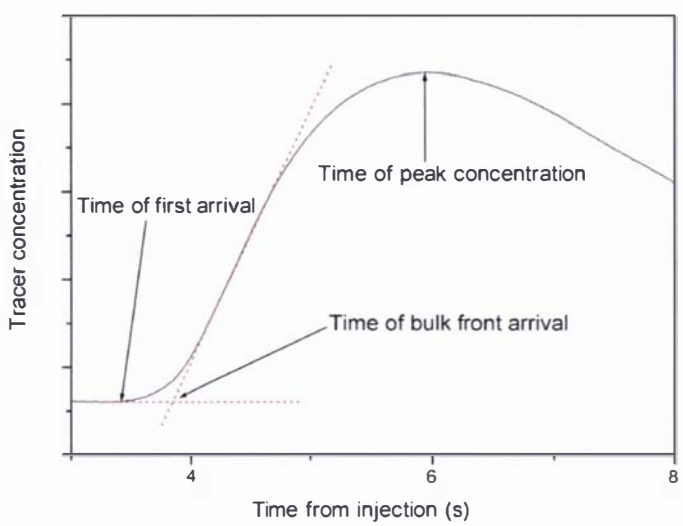

Figure 6-12 – Concentration profile analysis alternatives

The CO_2 tracer data for the Z-Pack was analysed by all three methods. Comparison of the variation of times measured for the five CO_2 injections showed little difference between the three methods, with average standard deviations of 0.28 s for the first arrival method, 0.24 s for the bulk front method and 0.33 s for the peak concentration method. VRC's were calculated using all three sets of time data (adjusting for the response time of the CO_2 analyser) and comparison showed that differences between the results of the three methods were insignificant (Figure 6-13 and Figure 6-14).

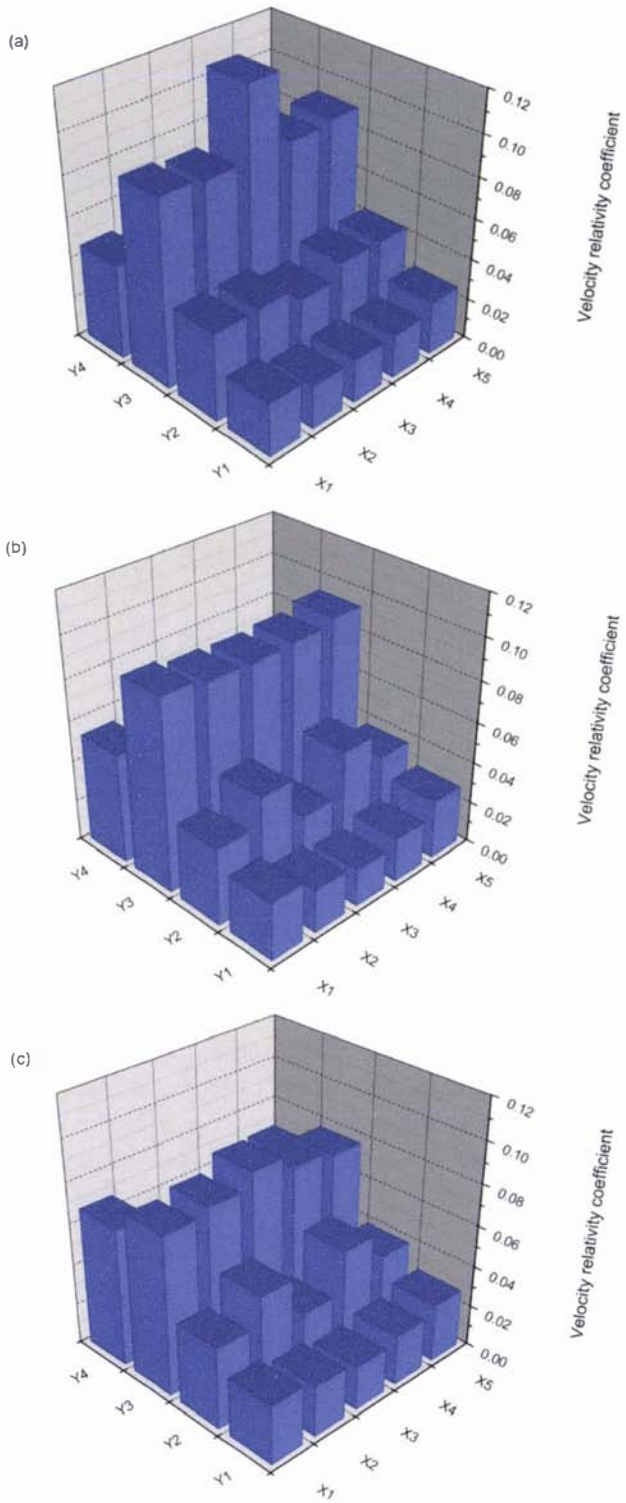

Figure 6-13 – Velocity relativity coefficient for each zone in the cross-section for flow through a standard Z-pack measured using a CO_2 tracer and analysed using (a) time to first arrival, (b) time to bulk front arrival and (c) time to peak concentration

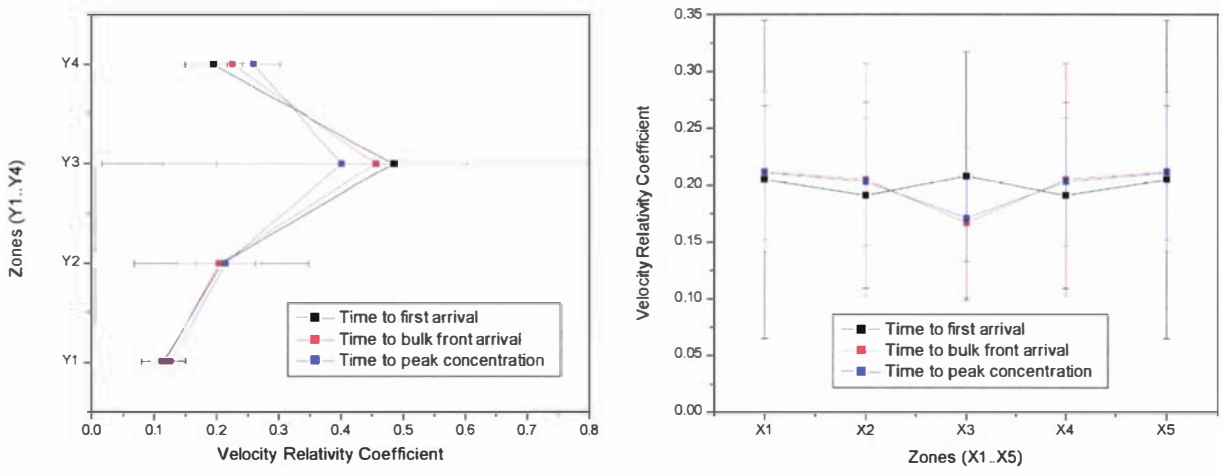

Figure 6-14 – Average velocity relativity coefficient and 95% confidence intervals for each vertical and horizontal slice in a standard Z-pack measured using a CO_2 tracer and analysed using time to first arrival, time to bulk front arrival and time to peak concentration

Time to peak concentration was the fastest and easiest method of analysis; however, the tracer was injected manually and differences in tracer injection length may affect the accuracy of this method. The noisy output of the fog sensors (Figure 6-11) was not well suited to analysis by the bulk front method, which was the most time-consuming analysis method. Time to first arrival was considered the most appropriate method of analysis. All tracer data were analysed using this method by manual inspection for the moment at which the response began to rise.

6.4.1 Z-Pack

6.4.1.1 Velocity profiles

Average times to arrival are shown in Figure 6-15 for the fog tracer and Figure 6-16 and Figure 6-17 for the CO_2 tracer (adjusted and unadjusted average times to arrival respectively). Trends were similar with both methods; however some disagreement was evident. Times to arrival of the CO_2 tracer were longer than those of the fog tracer on layers Y1 and Y4 and similar or shorter on layers Y2 and Y3. The variance of replicated measurements for the CO_2 tracer was greater than that of the fog tracer.

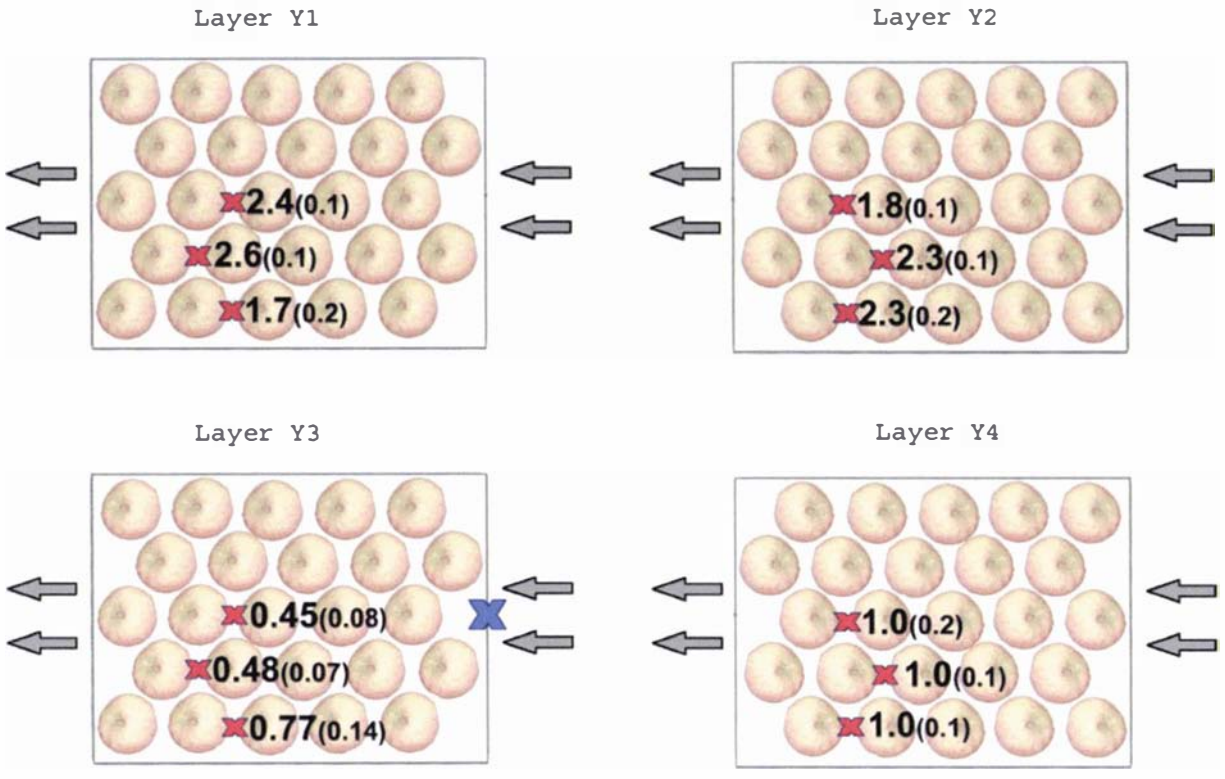

Figure 6-15 - Time to fog arrival in a standard Z-Pack. Average times (s) are shown with standard deviations in parentheses. Red × 's represent the sensor placement while the blue × represents the 'trigger' sensor position

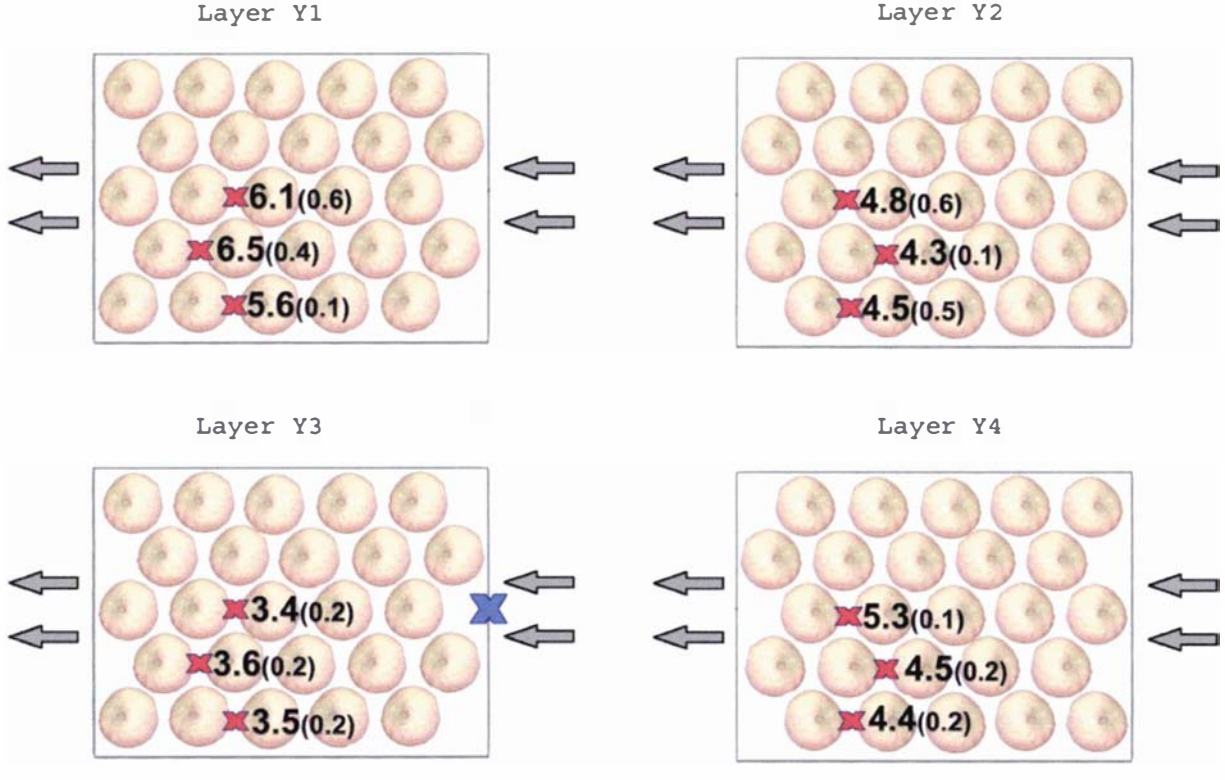

Figure 6-16 – Unadjusted time to CO_2 arrival in a standard Z-Pack. Average times (s) are shown with standard deviations in parentheses. Red × 's represent the sensor placement while the blue × represents the 'trigger' sensor position

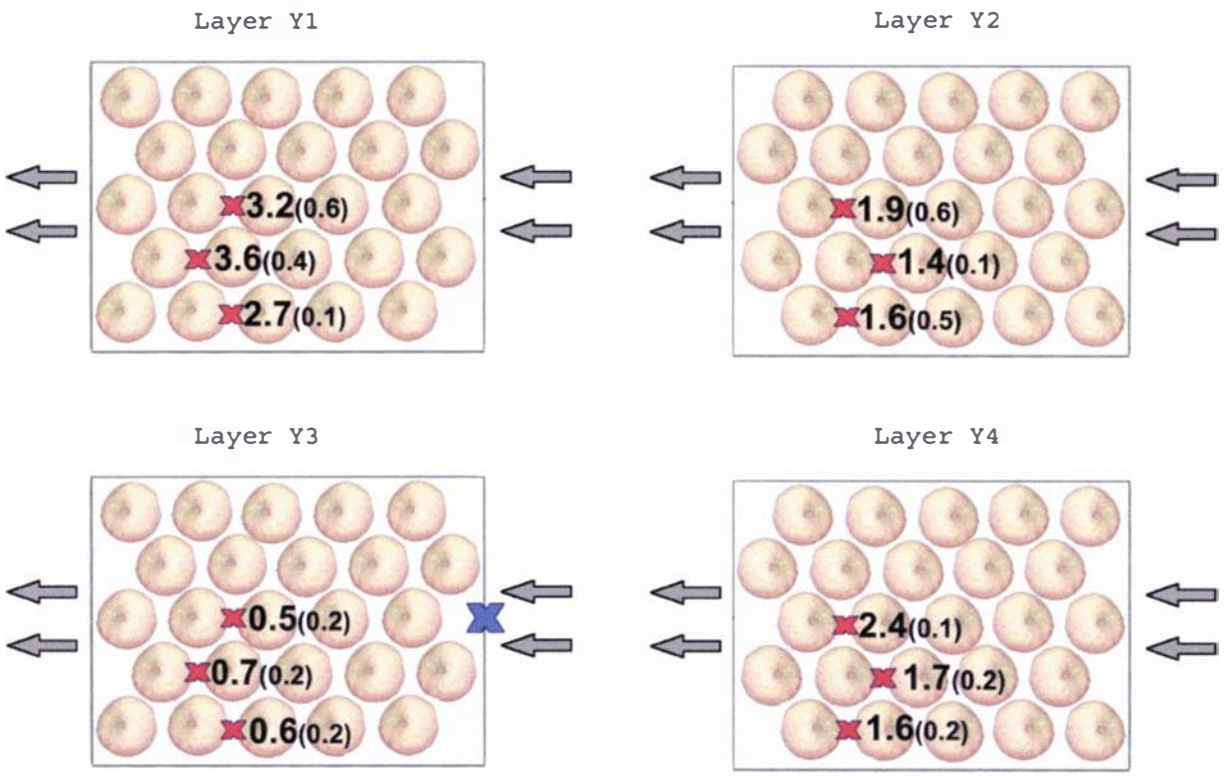

Figure 6-17 - Adjusted time to CO_2 arrival in a standard Z-Pack. Times were adjusted by subtracting the measured response time of the CO_2 analyser. Average times (s) are shown with standard deviations in parentheses. Red × 's represent the sensor placement while the blue × represents the 'trigger' sensor position

The disagreement between tracer methods may have been due to the higher density of CO_2 relative to air causing the CO_2 tracer to preferentially fall to layer Y2 rather than rise to layer Y4. However, longer times to arrival on layer Y1 with the CO_2 tracer contradict this hypothesis, so it was considered unlikely that buoyancy effects had a significant effect in the forced flow conditions. It was possible that dimensional variation introduced by carton disassembly and assembly required to position the CO_2 tube was a significant cause of disagreement.

VRC values were calculated using Equation 6-1 for both the fog and CO_2 tracers and are shown in Figure 6-18 and Figure 6-19. Despite the differences between measured times to arrival; the adjusted CO_2 tracer method and the fog tracer method gave similar VRC profiles.

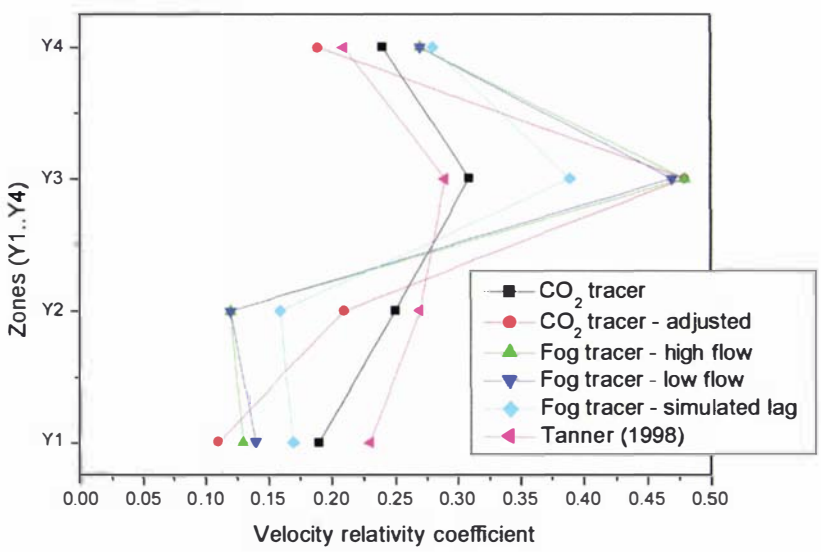

Figure 6-18 - Average VRC for each vertical zone in a standard Z-Pack

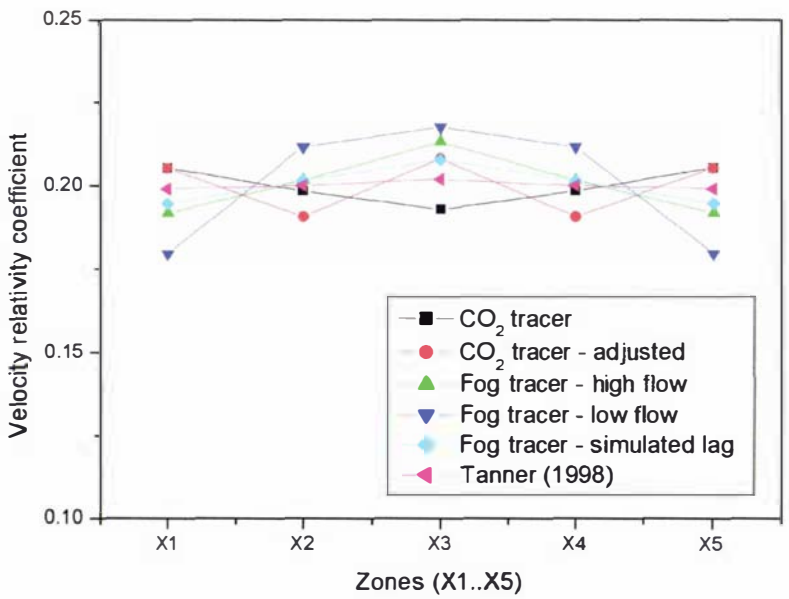

Figure 6-19 - Average VRC for each horizontal zone in a standard Z-Pack

Comparison of the flow profiles calculated from adjusted and unadjusted CO_2 tracer times showed that failing to adjust for the response lag effectively flattened the profile (Figure 6-18). The same effect was created with the fog tracer technique by a simulated lag (achieved with a 'trigger' sensor positioned upstream of the carton), which effectively increased all times to arrival by 0.5 s. All methods agreed and showed that the profile across the width of the carton was even (Figure 6-19). The flattening effect of response time was not evident in the horizontal distribution profile. There was fair agreement between profiles measured using the two tracers after adjustment of the CO_2 data for the response time. There were no substantial differences between profiles at two airflow rates, confirming the observation of Tanner (1998).

Figure 6-20 shows the VRC for each zone calculated from the fog tracer technique using average values from the two fan speeds, and the profile reported by Tanner (1998). Figure 6-20 shows the flow rate was greatest through the central three zones of the Y3 layer, corresponding to the position of the hand-hole. The flow profile measured was highly non-uniform, with almost 50% of the total flow travelling through

the Y3 layer. The profile measured by Tanner (1998) shows a substantially more uniform flow distribution, with slightly more flow through layers Y2 and Y3 than layers Y1 and Y4.

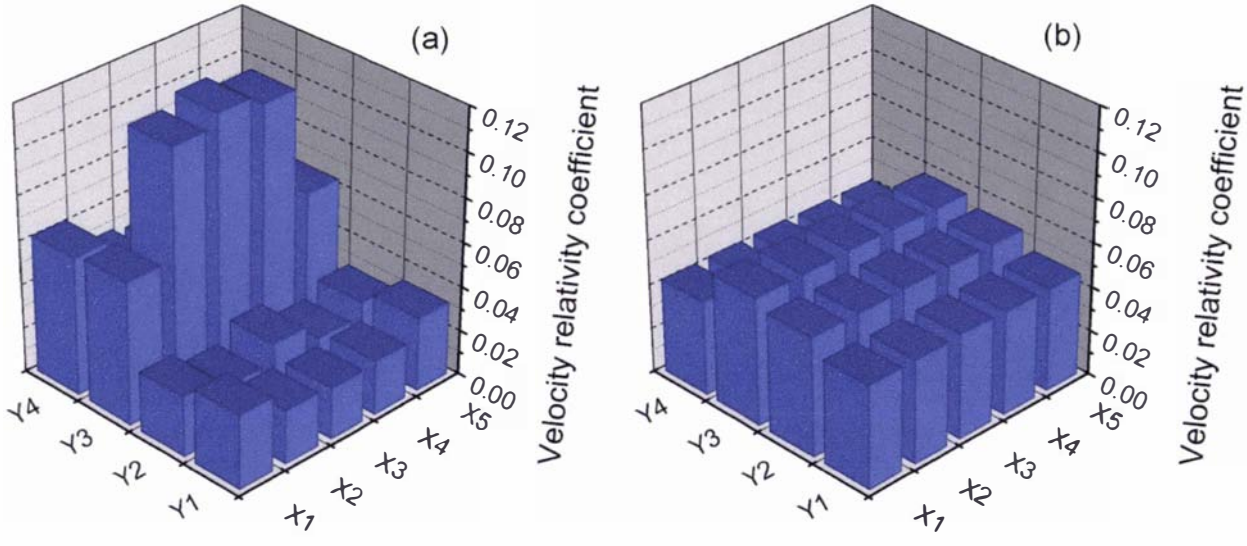

Figure 6-20 – Velocity distribution for flow through a standard Z-pack (a) measured using a fog-tracer technique and (b) reported by Tanner (1998)

Reasonable agreement was found between the unadjusted CO_2 profile and the profile reported by Tanner (1998). Tanner's data showed a relatively high volume of flow in layer Y1 despite the lack of vents on this layer. Such quantities of flow in a section of the package where there was no direct ventilation was considered unlikely, and indicates a possible failure to adjust results for the analyser response time or an error in the measurement of the response time. The different observations of flow on layer Y2 (where Tanner found relatively high flow, whereas in this work relatively low flow was observed) were attributed to differences between packaging used in the two trials. Changes in the vent position on the face of the carton, and rigidity of the moulded-pulp cardboard trays may have led to different positioning of the trays relative to the vents. The vents were aligned with layer Y3 in this trial, but may have been aligned between layer Y2 and Y3 during collection of Tanner's data.

6.4.1.2 Temperature prediction

The flow velocity profile measured using the fog tracer was used as data input to the dynamic heat transfer model developed by Tanner (1998) for testing against forced-air cooling data collected by Falconer (1995) for apple cartons. Details of other input data are given by Tanner (1998). Measured and predicted temperature profiles are presented in Figure 6-21. Temperature profiles predicted using the velocity profile measured by Tanner (1998) are also presented. Simulations using the fog tracer data over-predicted cooling rates on layer Y3 and under-predicted rates on layer Y2. These discrepancies were attributed to differences in vent alignment as discussed earlier (Section 6.4.1). Cooling rates on layer Y1 were over-predicted using Tanner's data, supporting the suggestion that flow on this layer was substantially over-estimated by Tanner. Layer Y1 temperatures predicted using the fog tracer data showed good agreement with experimental data.

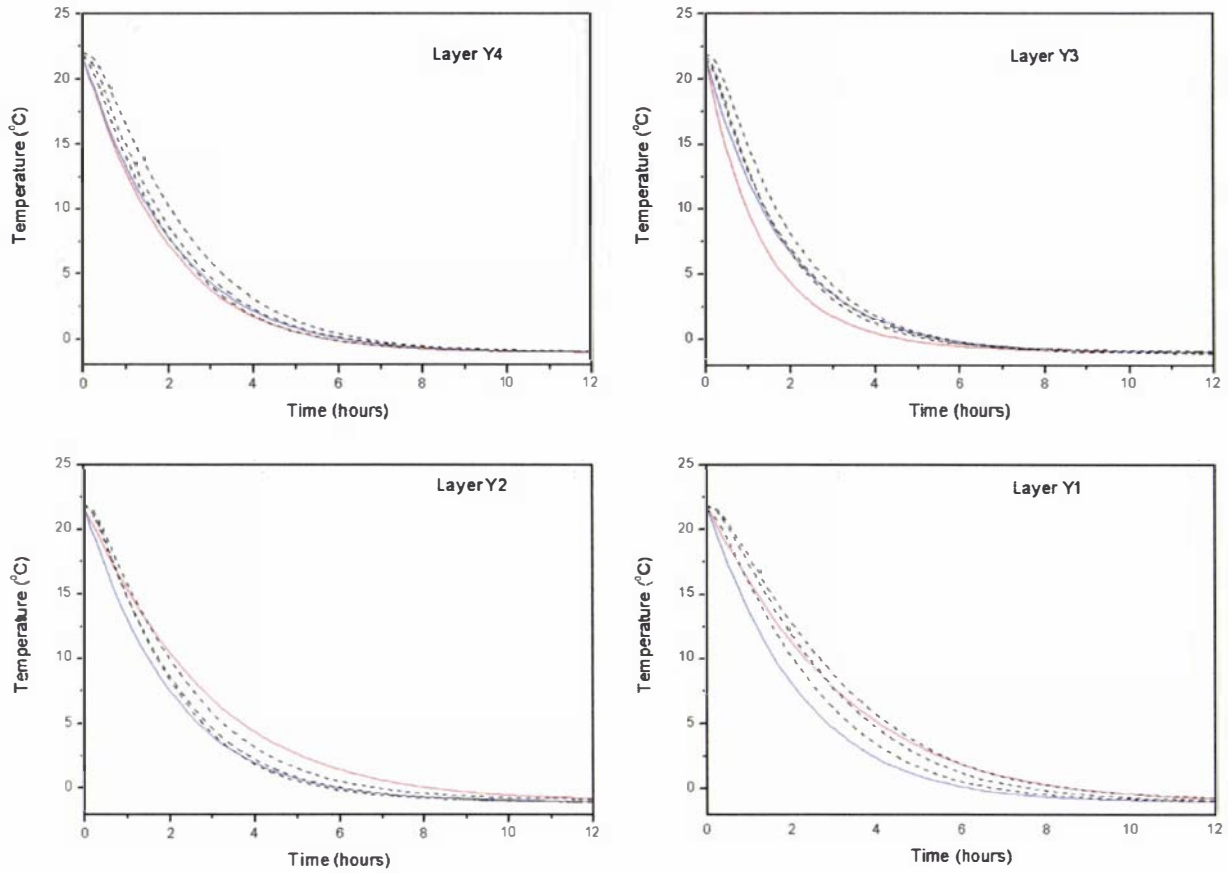

Figure 6-21 – Predicted (— fog tracer profile, — CO_2 tracer profile from Tanner (1998)) and measured (--- Falconer (1995)) fruit temperatures (3 replicates) located at the centre of layers Y1-Y4 of a Z-Pack of apples during forced-air cooling

6.4.2 Alternative vent designs

6.4.2.1 Alternative design 1

Figure 6-22 shows the average time to fog arrival for each of the sample positions. It should be noted that although the trigger sensor was placed over the circular vents, there was also a rectangular vent aligned between layers Y2 and Y3.

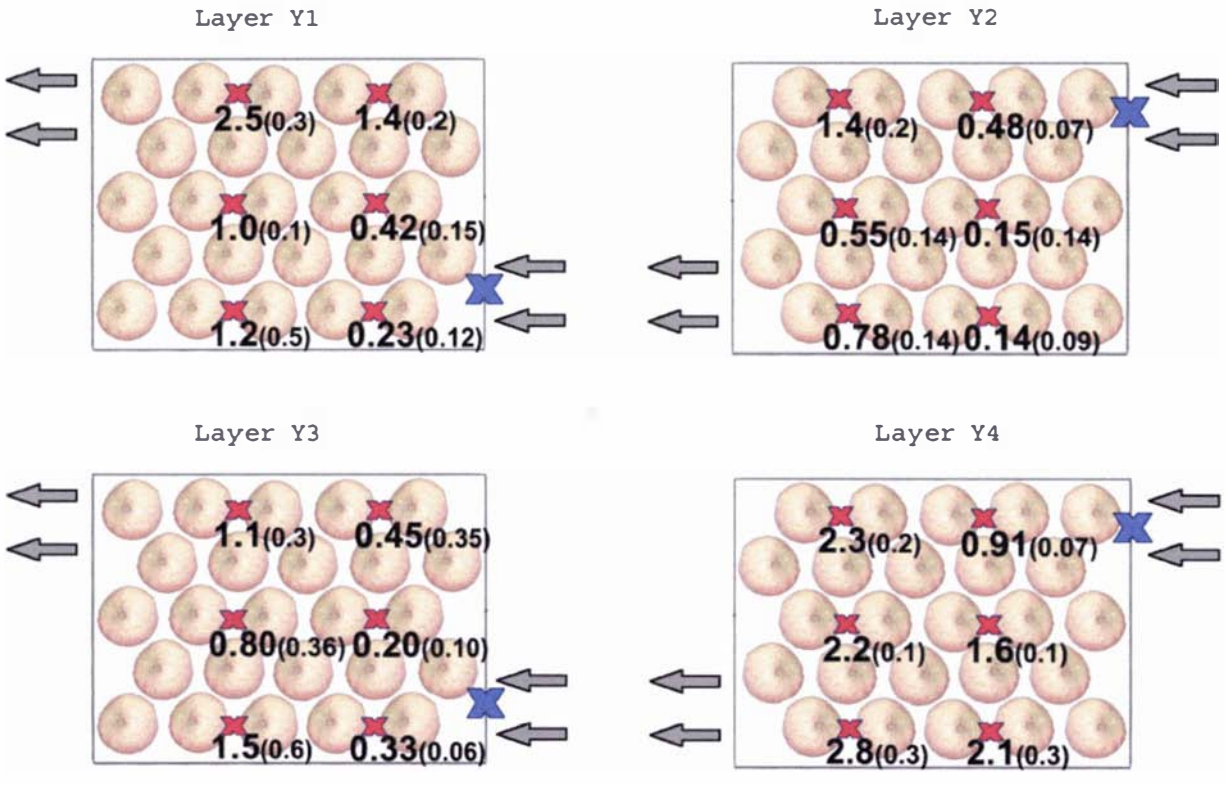

Figure 6-22 - Time to fog arrival for alternative vent design 1. Average times (s) are given with standard deviations in parentheses. Red × 's represent the sensor placement while blue × 's represent the 'trigger' sensor position

The flow pattern within the carton could not be established by inspection but was unlikely to be simply along the length of the carton due to the different vent positions at each end of the carton. This meant a 2-dimensional flow pattern could not be assumed and therefore calculation of VRC's was not possible. Due to the small number of sensors on each layer, the tracer method did not render the flow pattern obvious; however, a number of useful observations were still made.

Sensors were positioned and cardboard trays oriented identically in layers Y1 and Y3; except that layer Y3 was ventilated by a rectangular hand hole. The same situation existed if layers Y4 and Y2 are compared. Table 6-1 shows the ratio of time to arrival for each sensor position on these pairs of layers. The ratios are highly variable but with a mean of 3.9, indicate that flow rates were greater on layers Y2 & Y3 than layers Y1 and Y4. The variability of the ratios suggests the inclusion of the hand hole substantially influenced the flow patterns within the layer.

Table 6-1 - Alternative Design 1 – ratios of time to arrival data for layers not aligned/aligned with a hand hole

Layer	Ratio of times to tracer arrival					
	Sensor 1	Sensor 2	Sensor 3	Sensor 4	Sensor 5	Sensor 6
Y1/Y3	0.7	2.1	3.1	0.8	1.3	2.3
Y4/Y2	15.0	10.7	1.9	3.6	4.0	1.6

Table 6-2 shows the estimated velocity to sensors 4, 5 & 6 on each layer, calculated using the shortest path length between the vent and sensor position. As the flow pattern within the carton was not clear, the shortest paths were not likely to represent the actual flow paths and as such, these values were not intended to give actual in-package velocities, but serve as a means of comparison. Comparison with the equivalent values for the standard Z-Pack showed both designs gave a similar range of velocities (0.2 to 0.7 $m.s^{-1}$).

Table 6-2 - Alternative Design 1 – estimates of average velocities

Layer	Average velocity estimate ($m.s^{-1}$)				
	Alternative design 1			Standard Z-Pack	
	Sensor 4	Sensor 5	Sensor 6	Sensor 1 (equiv. Sensor 4)	Sensor 3 (equiv. Sensor 5)
Y4	0.2	0.2	0.2	0.4	0.4
Y3	0.2	0.4	0.3	0.4	0.7
Y2	0.5	0.7	0.3	0.2	0.2
Y1	0.3	0.3	0.2	0.2	0.2

The quality of the data and resulting understanding of the flow could be improved by increasing the number of sensors on each layer. Increasing sensor numbers requires greater data-logging capacity and increases the analysis time. With increased sensor numbers, interpretation of the tracer times in terms of quantitative flow information may become possible (i.e. a 3-dimensional profile could be determined).

6.4.2.2 Alternative design 2

Measured times to arrival are shown in Figure 6-23. As with the first alternative design, the flow pattern within the carton could not be established by inspection, and calculation of VRC's was not possible as it was not uniform for each cross-section down the length of the carton. Again, due to the small number of sensors on each layer, the tracer method did not make the full 3-dimensional flow pattern obvious.

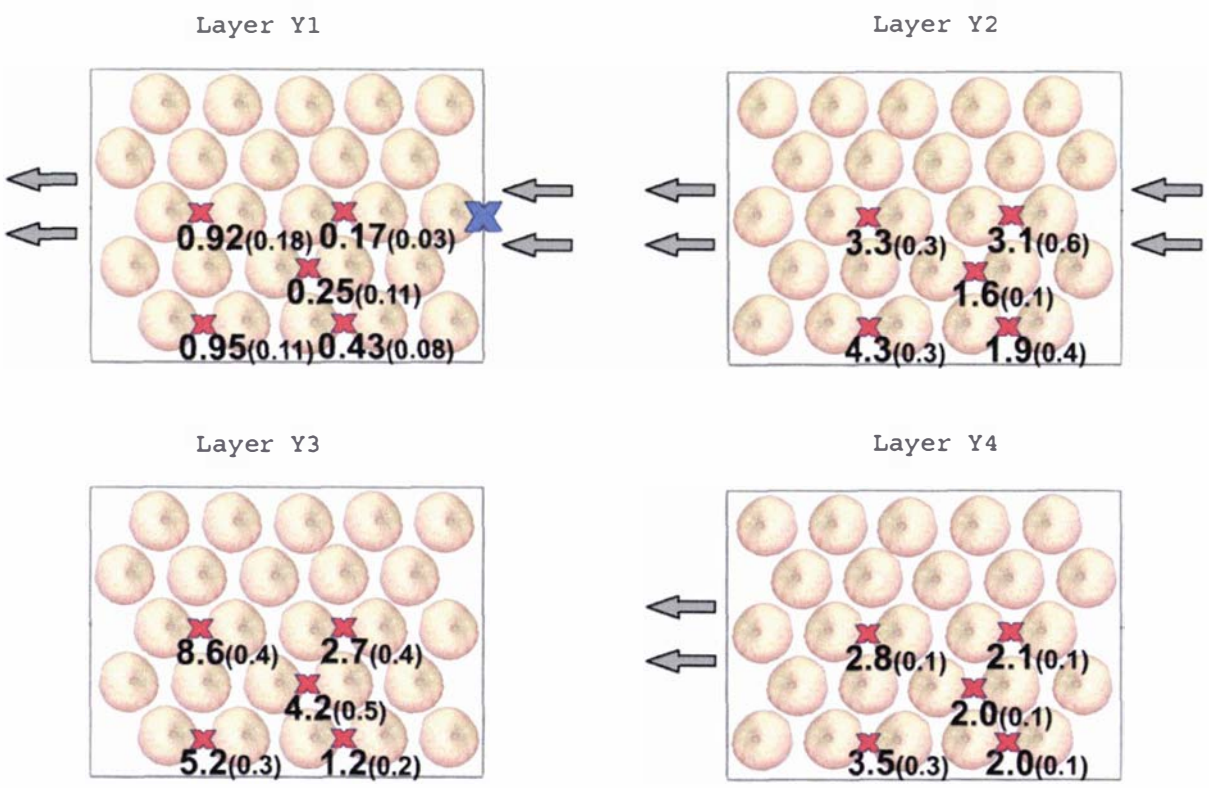

Figure 6-23 – Time to fog arrival for alternative vent design 2. Average times (s) are given with standard deviations in parentheses. Red × 's represent the sensor placement while the blue × represents the 'trigger' sensor position

The difference between the maximum and minimum times to arrival on each layer gives an indication of the rate of flow and velocity along each layer (Table 6-3). These values suggest the greatest flow was along layer Y1, followed by layer Y4, with less flow along Y2, and very little flow on layer Y3. The variance between replicated readings shows higher levels of variation on layers Y2 and Y3, further

suggesting flow on those layers was weaker than layers Y1 and Y4. Hence the flow was probably dominated by flow either along the bottom layer and up the gap between the tray and the end wall or up the gap at the front of the carton and along the top layer to the exit vent.

Table 6-3 - Alternative Design 2 – difference between maximum and minimum time to arrival data for each layer

Layer	Difference between maximum and minimum time to tracer arrival
Y1	0.8 s
Y2	2.7 s
Y3	7.4 s
Y4	1.5 s

As with alternative design 1, increasing the number of sensors on each layer would improve understanding of the flow pattern within the carton and possibly allow quantitative 3-dimensional flow information to be calculated.

6.5 Conclusions

The fog tracer technique offers several advantages over the CO_2 tracer technique. Neither method was designed to give detailed or highly accurate flow information, but both provide a relatively quick and low-cost method of determining the relative flow distribution for use in heat and mass transfer prediction systems. In doing so, they provide a method for transforming the average flow rate data provided by the airflow model into the in-package velocity data required for heat and mass transfer prediction. The fog tracer offers advantages in terms of costs, ease of measurement and ease of analysis.

The response time of the sensor significantly affected the accuracy of results of the CO_2 tracer method and needs to be considered when using this technique. Fair agreement was found between profiles measured using the two tracer techniques when the response time of the CO_2 sensor was considered. No substantial difference was evident between profiles measured using the fog tracer at two flow rates, confirming the flow profile was independent of flow rate over the range of flows investigated. The flow profile measured for a Z-Pack was highly non-uniform. Comparison of cooling rates predicted using the measured flow profile with experimental data showed reasonable agreement.

The fog tracer technique provided limited information on the flow profile inside both alternative carton designs particularly because the flow profiles were not uniform down the length of the carton. Quantitative data (such as VRC's) could not be calculated for either of the alternative carton designs. Increased sensor numbers would provide greater understanding of the flow profiles within the carton and may allow for the calculation of quantitative flow information in a 3-dimensional rather than a 2-dimensional grid.

The tracer technique was found to be suitable for measuring quantitative relative flow information in systems where flow patterns can be clearly defined. The tracer technique was less suitable for quantitative measurement in systems where the flow pattern could not be established à priori.

Part III
Model Development

This part outlines the development of a mathematical model to predict airflow inside refrigerated marine transport systems. The underlying mathematics and method of solution are presented in Section 7 whilst Section 8 discusses the flow resistance correlations. Validation of the model and simulation results can be found in Part IV.

7 Model Formulation and Solution Method

7.1 Introduction

A flow resistance network was chosen as the underlying framework, having considered the published results of previously developed models and the accuracy required. Discussion of the alternative frameworks and previously developed models can be found in Section 2.3. The required outputs were velocities and flow rates throughout the system being modelled, which were to be used as input data to existing heat and mass transfer prediction systems for packaged horticultural products.

7.2 Flow channel definition

The basis of a resistance network model is that the system can be broken down into a number of flow paths, to which a flow resistance can be attributed. The flow resistance is a function of the geometry of the flow path and the flow rate. Pressure differences between nodes provide the driving force for flow, and natural convection is ignored. In this work, heat transfer was decoupled from the mass transfer calculations with fluid temperature and density assumed constant throughout the domain. Whilst it was acknowledged that buoyancy effects may have a significant effect on the fluid flows and rates of heat transfer in areas of low velocity, these areas were considered to be in the minority given the high rates of air circulation used in marine transport systems. As such, buoyancy effects were considered unlikely to significantly affect the major flow patterns and the increased complexity required to incorporate these effects was not considered worthwhile.

Figure 7-1 shows a graphical representation of a resistance network that might be used for a refrigerated container. Figure 7-2 depicts a single node within a network connected to 6 adjacent nodes; however, in the model developed there was no limit to the number of flow paths connected to a single node or the direction of fluid flow along any channel.

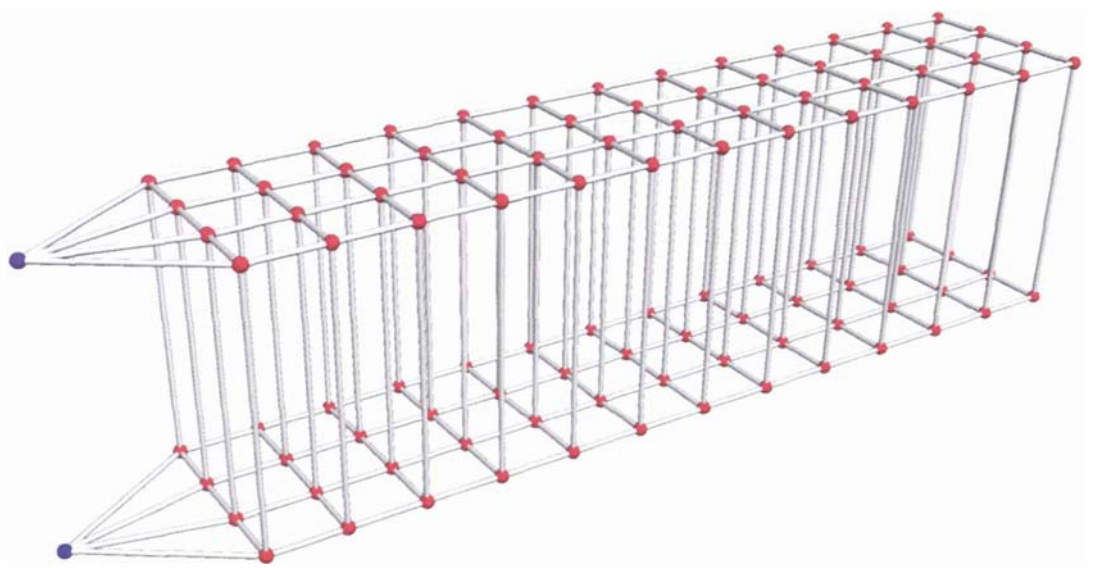

Figure 7-1 – Graphical representation of a resistance network. The red spheres represent nodes, blue spheres represent inlet/outlet nodes and grey cylinders represent flow channels

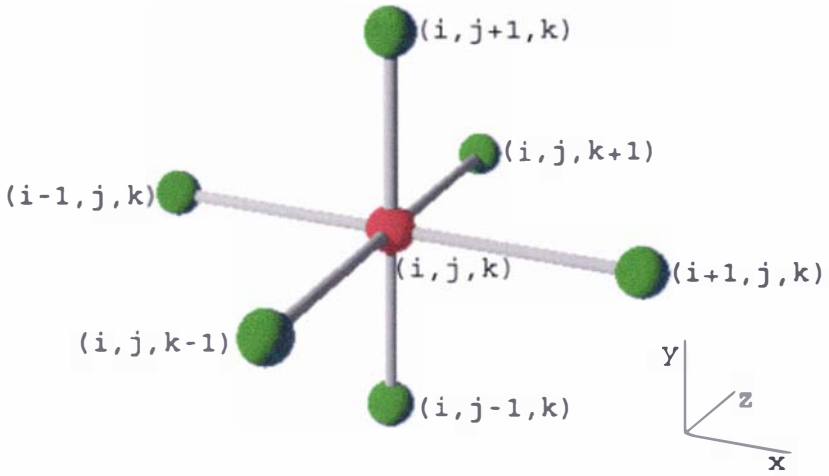

Figure 7-2 - Graphical representation of a node within a resistance network model. The red sphere represents the node of interest and green spheres represent adjacent nodes

In general, the definition of flow networks for marine transport systems requires the flow paths of significance to be predetermined. Channels can be defined for each significant flow path, mindful of quantifying the resistance and the required output information. Nodes were positioned at points of convergence/divergence. Information quantifying the resistance of the channel was required for each channel, and the elevation of each node relative to an arbitrary datum. The solution then provided the pressure at each node and the flow rate in each channel. To illustrate definition of flow resistance networks, networks for three hypothetical systems are presented in the following sections.

The model developed in this work did not attempt to describe the refrigeration system. Input and outlet nodes were instead positioned at the points of air delivery and return, and a fixed pressure difference assumed. As such, the flow networks were non-circular; however, the method does not preclude inclusion of a sub-model describing the refrigeration system within a circular network.

7.2.1 Example 1 – 20' container with spaced bulk cargo

The first example system is a 20' refrigerated shipping container, bulk loaded with packaged produce (non-palletised). Air was delivered from the refrigeration system to the floor channels and returned near the ceiling. The cartons were stacked using spacers to create gaps between cartons to improve cooling throughout the load. Figure 7-3 shows the 20' container and the position of the cartons inside.

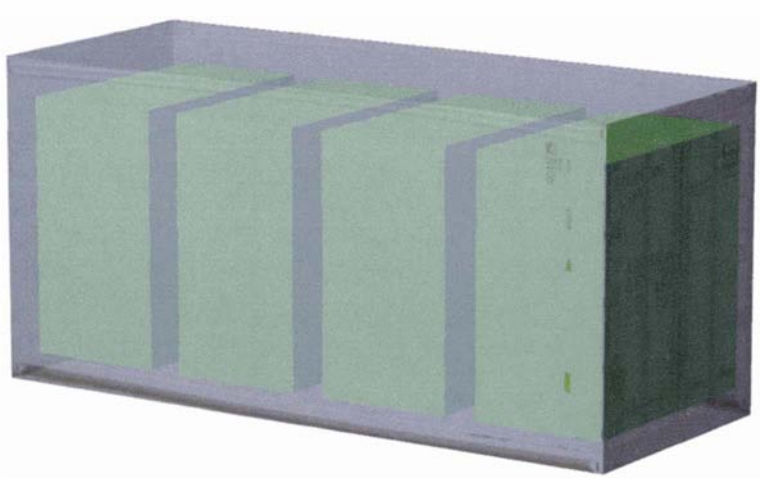

Figure 7-3 – Three-dimensional depiction of a 20' container showing a hypothetical loading pattern utilising spacers for non-palletised packaged products

Each of the vertical flow channels within the container was classified into one of three categories: (1) between the product and the container wall, (2) between two stacks of product and (3) vertically through a stack of product.

The horizontal flow paths were classified into one of several categories. In the T-bar floor layer, flow paths along the length of the container represent flow within the T-bar floor channels, whilst paths across the width of the container represent flow between T-bar channels. Flow across channels may be possible via holes in the T-bars, which are often found near the walls of the container depending on the container design. Horizontal flow paths in the middle layer of product are represented as one of three categories of flow channel: (a) between the cargo and the container walls, (b) between two stacks of product and (c) horizontally through a stack. Horizontal flow paths on the uppermost layer represent the gap formed between the ceiling of the container and the top of the cargo.

Nodes within this system were positioned in a rectangular grid (Figure 7-4 and Figure 7-5). Nodes were positioned on three layers vertically: below the cargo in the T-bar floor channels ($y = 1$), at half the height of the cargo ($y = 2$) and in the headspace above the cargo ($y = 3$). Along the length of the container there were 9 slices ($x = 1$ to 9), corresponding with the gaps between product stacks and the centre of each stack. There were seven slices across the width of the container ($z = 1$ to 7). A slice was positioned near each side-wall of the container, so flow channels along the wall could be effectively described. The width of the container was cut into 5 slices, and the 5 remaining nodes each positioned in the centre of a slice. Multiple slices were used to allow for variation across the width of the container; however, the exact number of slices was arbitrarily chosen. Air delivery and return were described using 7 fixed pressure nodes, allowing flexibility to define a non-uniform delivery or return pressure profile.

The overall network consisted of 189 unknown pressure nodes, 14 fixed pressure nodes and 470 flow channels. Figure 7-6 shows a 3-dimensional illustration of the flow network.

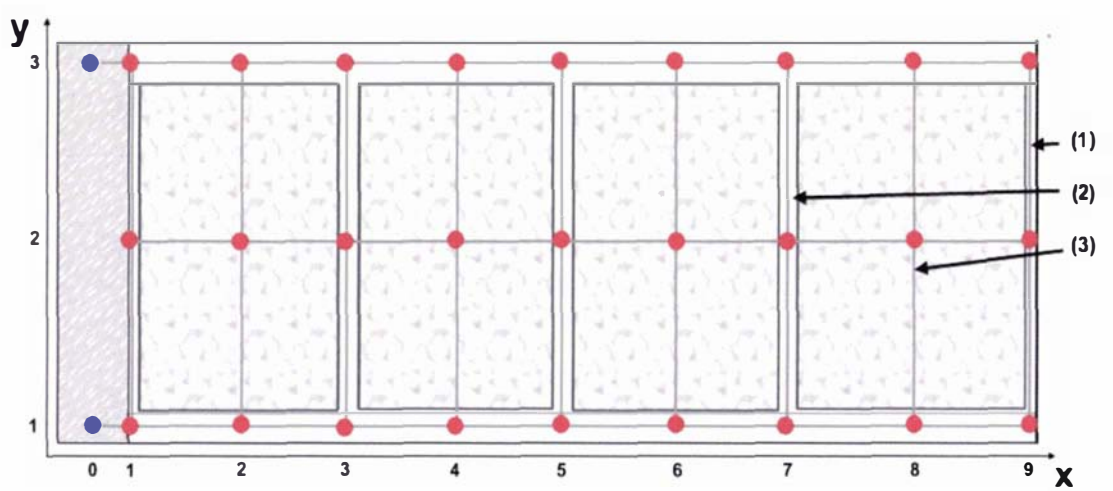

Figure 7-4 - Elevation view of the flow resistance network for a 20' container loaded with non-palletised product and spacers. Blue circles represent fixed pressure nodes, red circles represent unknown pressure nodes, and grey cylinders represent flow channels. Examples of each type of vertical flow channel are indicated

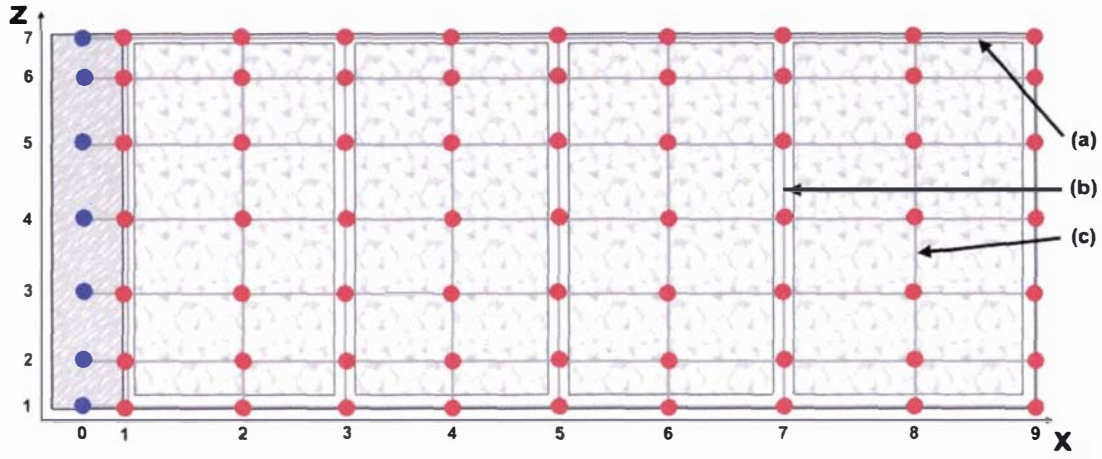

Figure 7-5 - Plan view of the flow resistance network for a 20' container loaded with non-palletised product and spacers. Blue circles represent fixed pressure nodes, red circles represent unknown pressure nodes, and grey cylinders represent flow channels. Examples of each type of horizontal flow channel are indicated

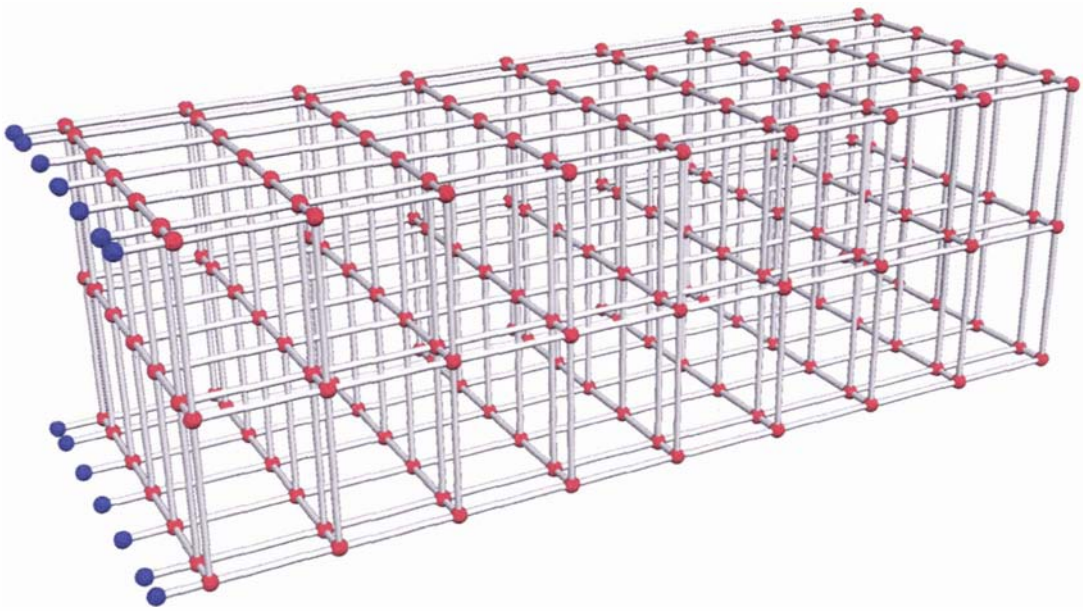

Figure 7-6 - Three-dimensional representation of the flow resistance network for a 20' container loaded with non-palletised product and spacers. Blue circles represent fixed pressure nodes, red circles represent unknown pressure nodes, and grey cylinders represent flow channels

7.2.2 Example 2 – 20' container with bulk cargo

The second example system was the same 20' refrigerated shipping container, again bulk loaded (non-palletised) with packaged produce but without spacers. Figure 7-7 shows the 20' container and the position of the cartons inside.

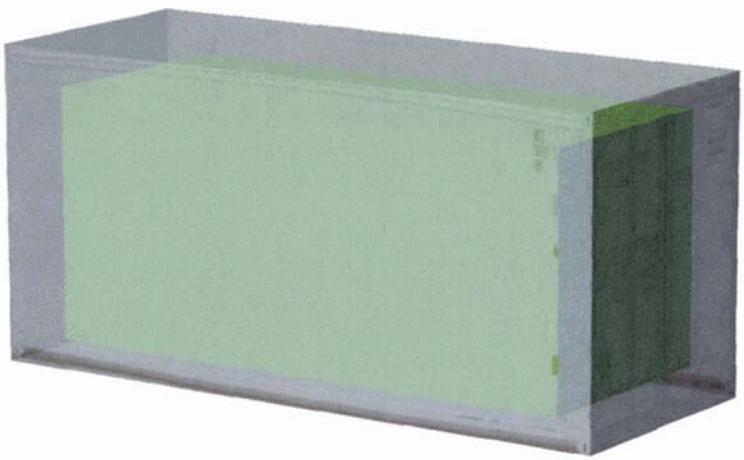

Figure 7-7 - Three-dimensional depiction of a 20' container showing a hypothetical loading pattern for non-palletised packaged products

With this stacking pattern, the vertical flow channels within the container could be categorised as one of just two types: between the cargo and the container wall or vertically through the stacked product. The horizontal flow paths in the T-bar floor layer and the uppermost layer would be the same as the first example. Horizontal flow channels in the middle layer ($y = 2$) represent one of two types: between the cargo and the container walls and horizontally through the stacked product.

Hence, the network used to define this geometry was almost identical to the first example, with only minor alterations required. Again, the nodes were positioned in a rectangular grid (Figure 7-8 and Figure 7-9). The difference between the two stacking patterns was manifest in the positioning of the 9 slices along the length of the container and the channel properties.

In the first example, a single flow channel was used to represent a slice of the stack between two spacers. In this example, there are no spacers and the cargo stack must be divided into arbitrary sections along the length of the container; 9 nodes were used for consistency with the previous geometry. As for the first example, a slice was positioned at both end-walls so flow channels along the wall could be effectively described. The length of the container was cut into 7 slices, and the 7 remaining nodes each positioned in the centre of a slice. Again, seven fixed pressure nodes were positioned across the width of the container at both the air delivery duct and air return slot.

The overall network consisted of 189 unknown pressure nodes, 14 fixed pressure nodes and 470 flow channels. Figure 7-10 shows a 3-dimensional illustration of the flow network.

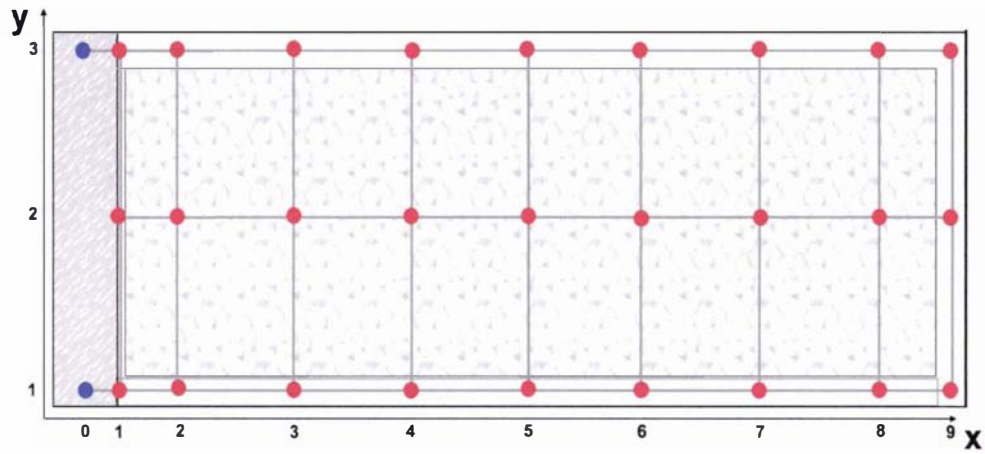

Figure 7-8 - Elevation view of the flow resistance network for a 20' container loaded with non-palletised product. Blue circles represent fixed pressure nodes, red circles represent unknown pressure nodes, and grey cylinders represent flow channels

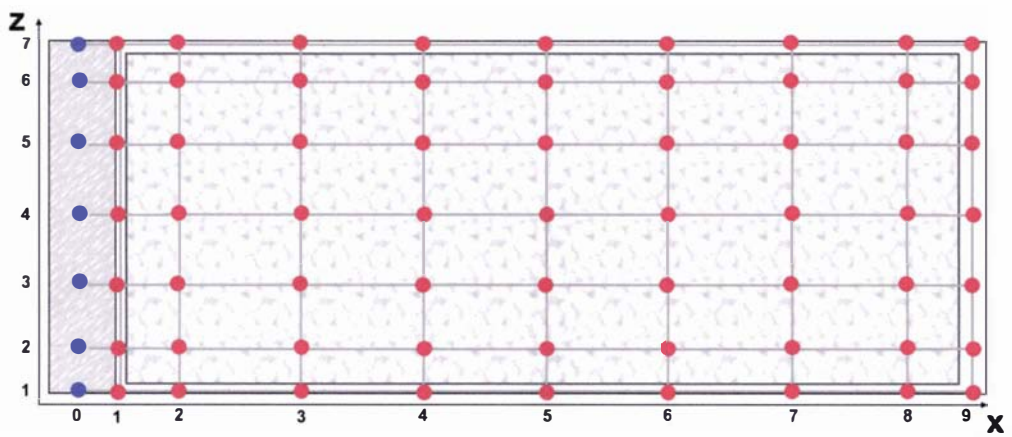

Figure 7-9 - Plan view of the flow resistance network for a 20' container loaded with non-palletised product. Blue circles represent fixed pressure nodes, red circles represent unknown pressure nodes, and grey cylinders represent flow channels

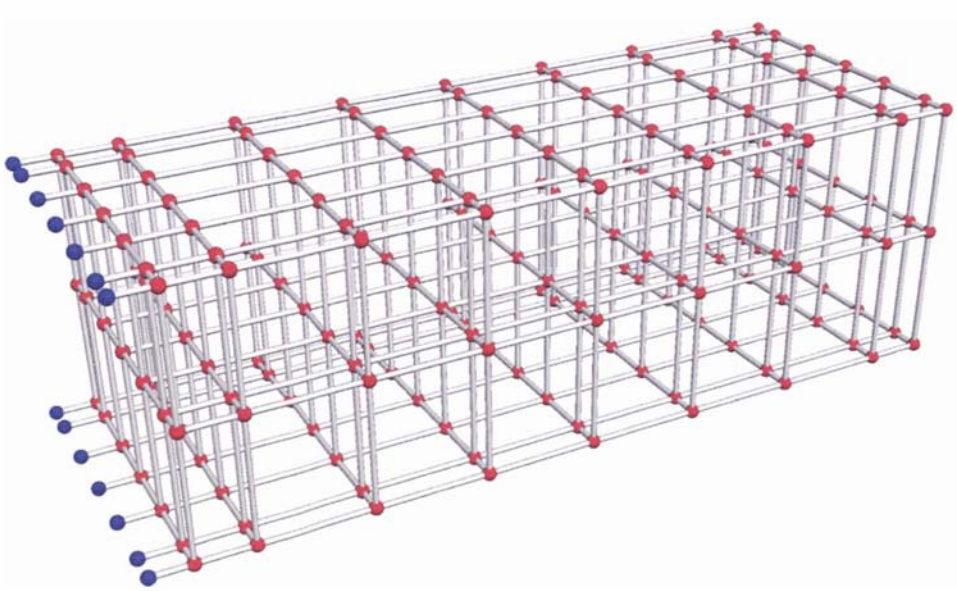

Figure 7-10 - Three-dimensional representation of the flow resistance network for a 20' container loaded with non-palletised product. Blue circles represent fixed pressure nodes, red circles represent unknown pressure nodes, and grey cylinders represent flow channels

7.2.3 Example 3 - Forced draft pre-cooler

The final example system was a hypothetical forced-draft pre-cooler for packaged horticultural products. Figure 7-11 shows the arrangement of the pallets.

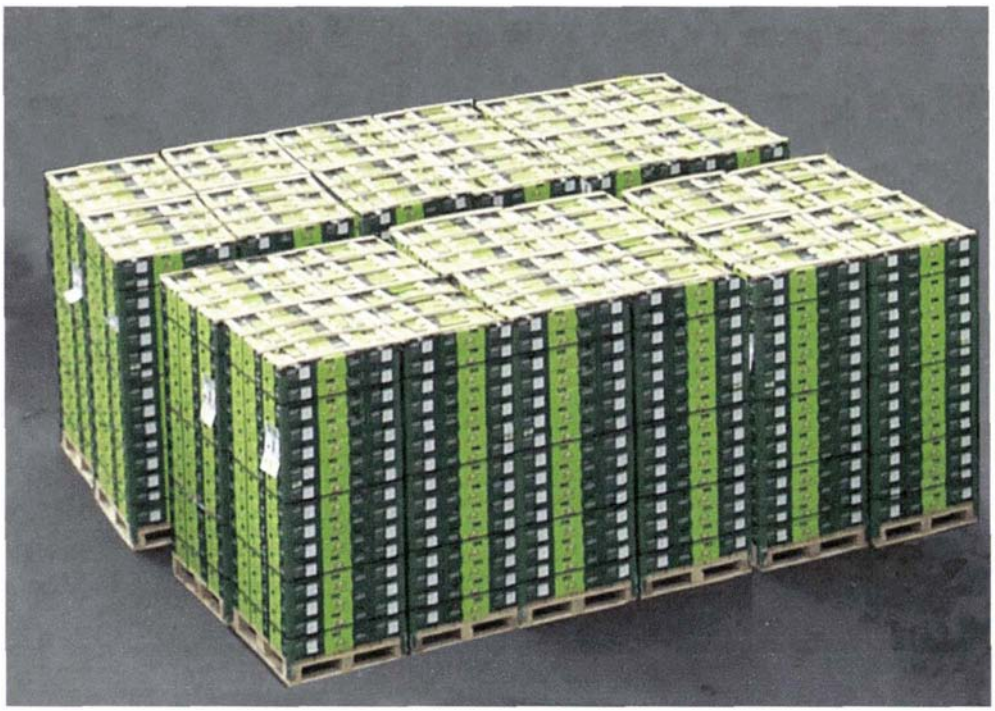

Figure 7-11 - Pallet arrangement for a hypothetical forced draft pre-cooler

Refrigerated air was drawn through the pallets arranged two-deep around a central channel. A non-porous sheet was placed across the top of the pallets and along the non-fan end of the arrangement to ensure air flowed through the pallets as shown in Figure 7-12.

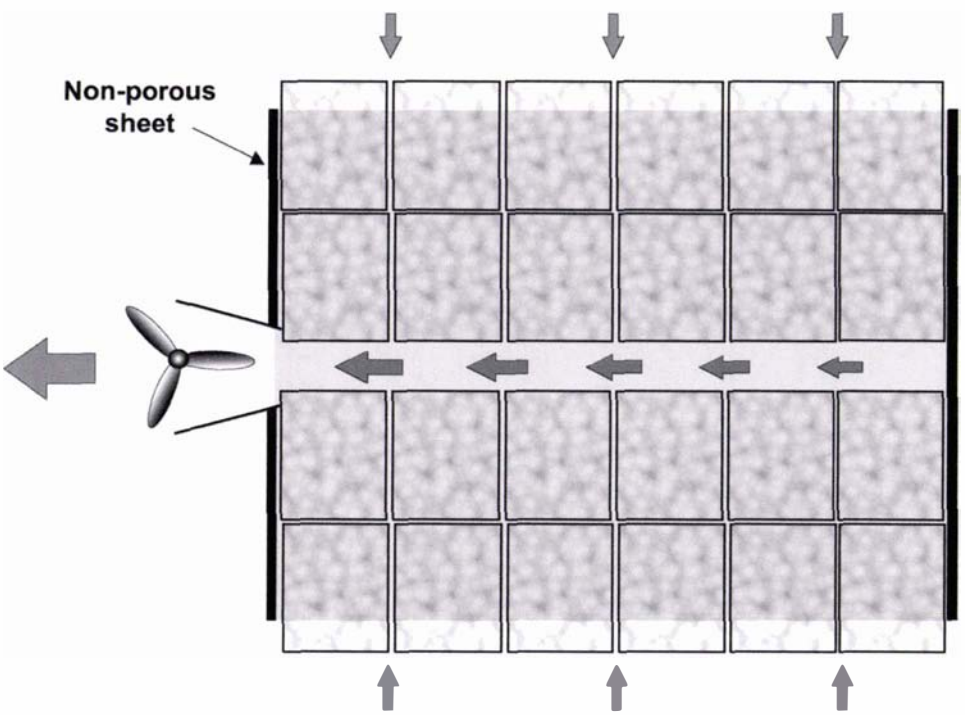

Figure 7-12 - Plan view of a hypothetical forced draft pre-cooler showing the non porous sheet and predominant airflow direction

Several different categories of horizontal flow channels were defined. Below the product, horizontal flow paths represent flow through the pallet bases or in the gaps between pallet bases. Horizontal flow paths at the height of the product represent flow in channels formed between pallets or horizontal flow through pallets. Horizontal flow paths above the product represent the flow between the non-porous sheet and the top of the pallets. The vertical flow paths represented one of three possible flows: in gaps between pallets, vertically through pallets or between a pallet and the non-porous sheet.

Nodes within this system were positioned in a rectangular grid (Figure 7-13 and Figure 7-14). The system was symmetrical meaning the domain could be divided along the symmetry plane to reduce the computation time; however, some flexibility in defining flow path properties would be lost. Nodes were positioned on four layers vertically: at the level of the pallet bases ($y = 1$), at one-quarter the height of the pallet ($y = 2$), at three-quarters the height of the pallet ($y = 3$) and above the pallet ($y = 4$). Along the length of the pre-cooler, there were 13 slices ($x = 1$ to 13) corresponding with the gaps between pallets and the centre of each pallet. There were nine slices across the width of the pre-cooler ($z = 0$ to 8) corresponding with the gaps between the pallets, pallet centres and the spaces around pallets. Two fixed pressure nodes were positioned outside the pre-cooler and a single node within the pre-cooler. By defining a single fixed pressure node inside the central channel of the pre-cooler, it was assumed that the channel was wide enough that pressure losses along its length were insignificant.

A fan was used to maintain a pressure difference between the central internal space and external space to create a driving force for flow. The network as described consisted of 312 unknown pressure nodes, 3 fixed pressure nodes and 938 flow channels. Figure 7-15 shows a 3-dimensional illustration of the flow network.

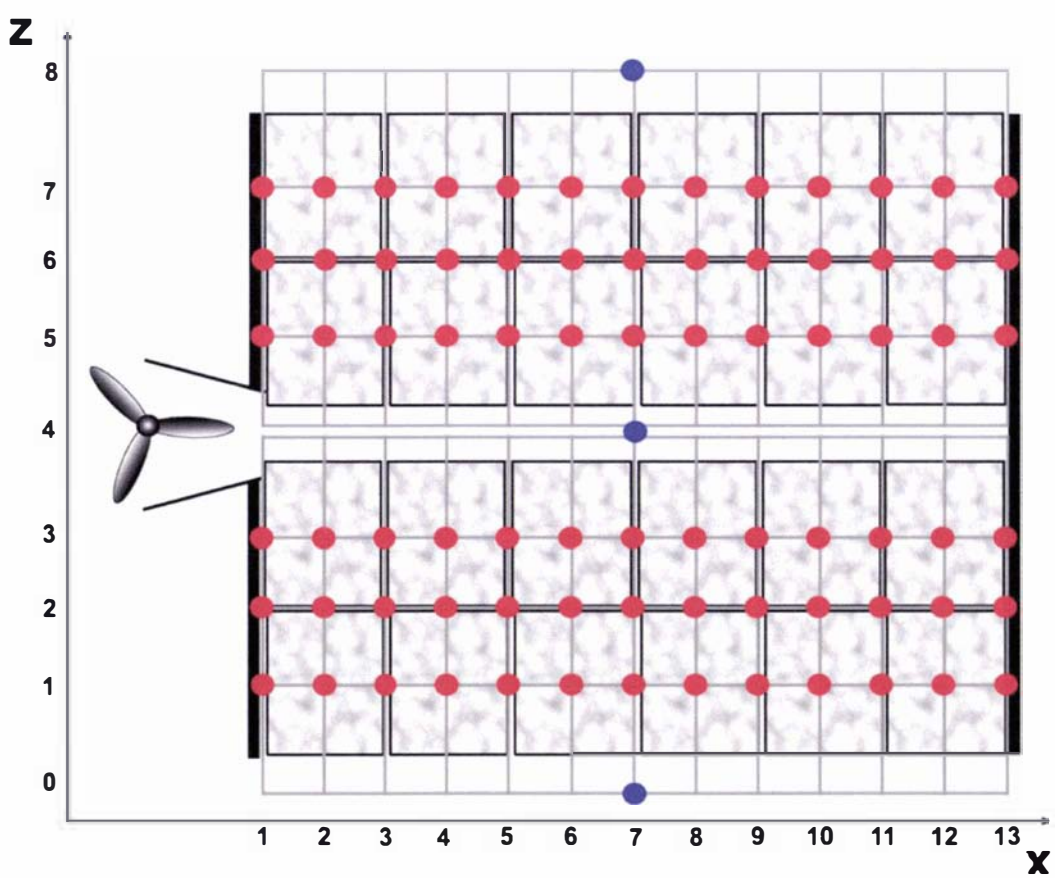

Figure 7-13 - Plan view of a hypothetical forced draft pre-cooler. Blue circles represent fixed pressure nodes, red circles represent unknown pressure nodes, and grey cylinders represent flow channels

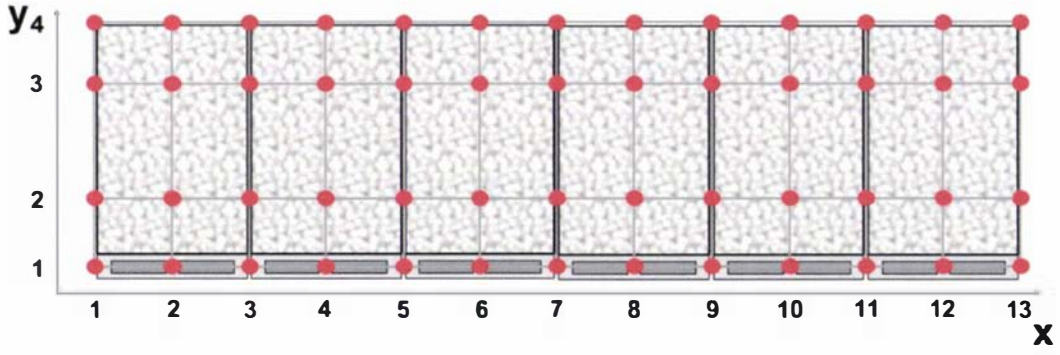

Figure 7-14 - Elevation view of a hypothetical forced draft pre-cooler. Red circles represent unknown pressure nodes, and grey cylinders represent flow channels

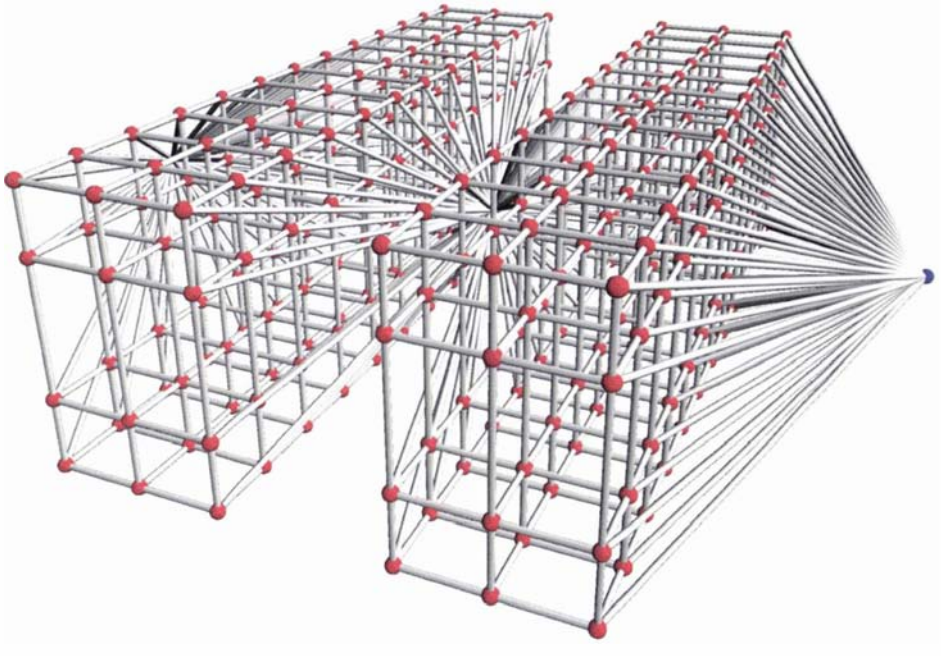

Figure 7-15 - Three-dimensional representation of the flow network approximation of a hypothetical forced draft pre-cooler. Blue circles represent fixed pressure nodes, red circles represent unknown pressure nodes, and grey cylinders represent flow channels

7.3 Mathematical basis

There are two basic approaches to the solution of steady-state pressure and flow in a network of flow channels. Both methods require the solution of non-linear algebraic equations; written in the first method in terms of unknown pressures at points of convergence/divergence (node equations) and in the second method in terms of unknown flow rates in the channels (loop equations).

Figure 7-16 shows a simple example of a network of flow channels (labelled 1 to 13), where the nodes labelled A, E, J and K represent fixed pressure nodes.

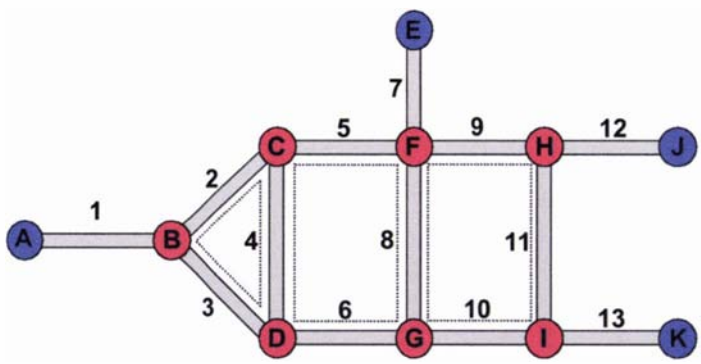

Figure 7-16 - Example of a simple network of flow channels. Blue circles represent nodes of fixed pressure, red circles represent nodes of unknown pressure and grey cylinders represent flow channels. Broken black lines indicate the primary loops

7.3.1 Loop equations

To determine the flows using the loop equations, a continuity balance would be written for each of the nodes of unknown pressure (e.g. Equation 7-1 for node B).

$$Q_1 + Q_2 + Q_3 = 0 \qquad \textit{Equation 7-1}$$

Where:

Q_i = Volumetric flow rate in channel *i* ($m^3.s^{-1}$)

As pressure losses are additive, pressure balances can be written for each of the three primary loops marked on Figure 7-16; defined as closed flow circuits that have no additional closed flow circuits within them (e.g. Equation 7-2).

$$\Delta P_8 + \Delta P_9 + \Delta P_{10} + \Delta P_{11} = 0 \qquad \textit{Equation 7-2}$$

Where:

ΔP_i = Pressure loss along channel *i* (Pa)

Independent pressure equations can be written for one less than the total number of fixed pressure nodes using the paths between fixed pressure nodes (e.g. Equation 7-3 for node A→E).

$$\Delta P_1 + \Delta P_2 + \Delta P_5 + \Delta P_7 = P_A - P_E \qquad \textit{Equation 7-3}$$

Where:

P_j = Pressure at node *j* (Pa)

Assuming that the pressure loss in each of the flow channels can be quantified by some function of the flow rate (Equation 7-4), the pressure equations can be rewritten in terms of the unknown flow rates (Equation 7-5 and Equation 7-6).

$$\Delta P_i = F(Q_i) \qquad \textit{Equation 7-4}$$

$$F(Q_8) + F(Q_9) + F(Q_{10}) + F(Q_{11}) = 0 \qquad \textit{Equation 7-5}$$

$$F(Q_1) + F(Q_2) + F(Q_5) + F(Q_7) = P_A - P_E \qquad \textit{Equation 7-6}$$

Where:

$F(a)$ = Function of a

Sign conventions for flow direction must be implemented; i.e. flows into and out of a node are given opposite signs and flows in a clockwise direction and an anticlockwise direction are given opposite signs. Seven equations of the form of Equation 7-1, three equations of the form of Equation 7-5 and three equations of the form of Equation 7-6 form a set of 13 equations in 13 unknown flow rates that when solved simultaneously yield the equilibrium flow rate in each of the channels.

7.3.2 Node equations

To determine the flows using the node equations, a continuity balance would be written for each of the nodes of unknown pressure (e.g. Equation 7-1 for node B). Functions relating the flow rate and pressure loss for each channel (Equation 7-7) are substituted into Equation 7-1, yielding an equation of the form of Equation 7-8.

$$Q_i = F(\Delta P_i) \qquad \textit{Equation 7-7}$$

$$F(\Delta P_1) + F(\Delta P_2) + F(\Delta P_5) = 0 \qquad \textit{Equation 7-8}$$

A sign convention where flows into and out of a node are given opposite signs must be implemented. Seven equations of the form of Equation 7-8 can be written in terms of the seven unknown pressures, which when solved yield the equilibrium pressure at each of the unknown pressure nodes. Flow rates in each of the channels can then be calculated using the functions of the form of Equation 7-7.

Wood and Rayes (1981) compared five alternative solution algorithms for flow networks and concluded the loop equations were more likely to converge. The authors noted when the node equations converged successfully, they did so quickly and accurately. Convergence problems with the node equations were associated with low resistance flow paths, where small errors in pressure values led to large errors in flow rates and consequent continuity imbalances. In this case, large differences in flow resistances produce a set of ill-conditioned equations. Low resistance channels were considered unlikely to cause problems in this application.

Formulation of the loop equations requires identification of the primary loops and independent paths between fixed pressure nodes. For large irregular networks, automatic identification of the primary loops and independent paths is difficult. Maintaining the sign conventions for flow direction within loops also poses problems for irregular 3-dimensional models.

It was considered vitally important in this model that the software derive the model equations automatically from the input geometry. Therefore, the node equations were chosen to form the basis of the model to give greater flexibility in defining the network whilst maintaining automatic derivation of the governing equations.

7.3.3 Mass and energy balances

This section describes the derivation of the specific mass and energy balances used for flow prediction, having defined a geometry that approximates the real system and chosen the node equations as the basis of calculation.

A mass balance for each divergent or convergent point with N attached flow paths assuming no accumulation or loss of fluid from the system can be written as Equation 7-9.

$$\sum_{n=1}^{N} \dot{m}_n = 0 \qquad \textit{Equation 7-9}$$

Where:

N	=	Number of channels attached to the node	
n	=	Channel index	
$\dot{m}$	=	Fluid mass flow rate into node	($kg.s^{-1}$)

Assuming the fluid is incompressible and ensuring definitions of velocity and area are consistent, the mass balance may also be stated as Equation 7-10.

$$\sum_{n=1}^{N} \rho v_n A_n = 0 \qquad \textit{Equation 7-10}$$

Where:

v_n	=	Fluid velocity in channel n toward node	($m.s^{-1}$)
ρ	=	Fluid density	($kg.m^{-3}$)
A_n	=	Cross sectional area of channel n	(m^2)

The assumption of fluid incompressibility was considered valid due to the small changes in temperature and static pressure relative to atmospheric pressure expected in marine transport systems. For example, a change in static pressure of 100 Pa results in only a 0.1% change in density.

The mass balance must be satisfied for all nodes at all times. There are infinite combinations of flows that satisfy the mass balance (e.g. no flow); however, consideration of thermodynamics results in a unique solution describing the steady-state condition.

At any point (node), the total pressure(ψ) is given by Equation 7-11. The three terms represent the pressure head, static head and velocity head of the fluid respectively, expressed in pressure units (Pa). The velocity head term applies only for a uniform velocity across a given cross section; where there is a distribution of fluid velocities, the appropriate average velocity value considering the fluid velocity profile should be used. This was not considered an issue of major importance in this application however; as it is the total pressure that provides the driving force for flow. As such, an error in the estimation of the velocity head would result in an error in the calculated static pressure but not in the calculated flow rate.

$$\psi = P + \rho g h + \frac{1}{2}\rho v^2 \qquad \text{Equation 7-11}$$

Where:

ψ	=	Total pressure	(Pa)
P	=	Fluid static pressure	(Pa)
g	=	Acceleration due to gravity	($m.s^{-2}$)
h	=	Height relative to arbitrary datum	(m)

A mechanical energy balance on a fluid between two nodes within a flow system, assuming the system is isothermal, the fluid is incompressible, there is no accumulation or depletion of fluid, energy losses are due to friction only and ignoring work input by fans can be written as Equation 7-12.

$$\left(P_i + \rho g h_i + \frac{1}{2}\rho v_i^2\right) - \left(P_{i+1} + \rho g h_{i+1} + \frac{1}{2}\rho v_{i+1}^2\right) = -Fr \qquad \text{Equation 7-12}$$

$$\Delta\psi_n = Fr \qquad \text{Equation 7-13}$$

Where:

Fr	=	Energy lost through friction effects	($J.m^{-3}$)
$\Delta\psi_n$	=	Pressure loss in channel n (between node i and i+1)	(Pa)
i	=	Node index	

The frictional loss (Fr) is the result of the flow resistance of the channel, and is a function of the channel properties and flow rate within the channel. Fr was arbitrarily defined by Equation 7-14, with which reflects the form of many important flow resistance correlations.

$$Fr = \frac{1}{2}\rho v_n^2 . \beta_n = \Delta\psi_n \qquad \text{Equation 7-14}$$

Where:

β_n	=	Flow resistance of channel n	

Correlations between flow rate and the flow resistance (β_n) were required for all the channels in the modelled domain. Rearranging Equation 7-14 to solve for velocity gives Equation 7-15. To maintain the sign convention for flow direction and avoid computation of a negative root, the relationship given in Equation 7-16 was used. Combining these with Equation 7-10 yields Equation 7-17.

$$v_n = \sqrt{\Delta\psi_n . \frac{2}{\beta_n \rho}} \qquad \text{Equation 7-15}$$

$$\sqrt{\Delta\psi_n} = \frac{\Delta\psi_n}{\sqrt{|\Delta\psi_n|}} \qquad \text{Equation 7-16}$$

$$\sum_{n=1}^{N} \frac{\Delta\psi_n}{\sqrt{|\Delta\psi_n|}} \sqrt{\frac{2\rho}{\beta_n}} A_n = 0 \qquad \text{Equation 7-17}$$

Equation 7-17 forms the mathematical basis of the model. For each node in the modelled space, an equation of this form can be written. The equations are non-linear, and the flow resistance (β_n) may be a function of velocity. Simultaneous solution of these equations yields the total pressure at each of the nodes, from which the mass flow and velocity in each flow channel can be calculated.

7.3.3.1 Example 1 cont. – 20' container with spaced bulk cargo

To illustrate the formulation of equations for a defined geometry, an example mass/energy balance equation for one node from Example 1 (Section 7.2.1) was derived. As the nodal grid was rectangular in this case, nodes are identified using Cartesian co-ordinates. The node of interest was positioned at x = 5, y = 2, z = 7; approximately halfway down the length of the container, halfway up the height and against a side-wall. This node was directly connected to 5 other nodes as shown in Figure 7-17. The mass/energy balance formulated for this node was Equation 7-18.

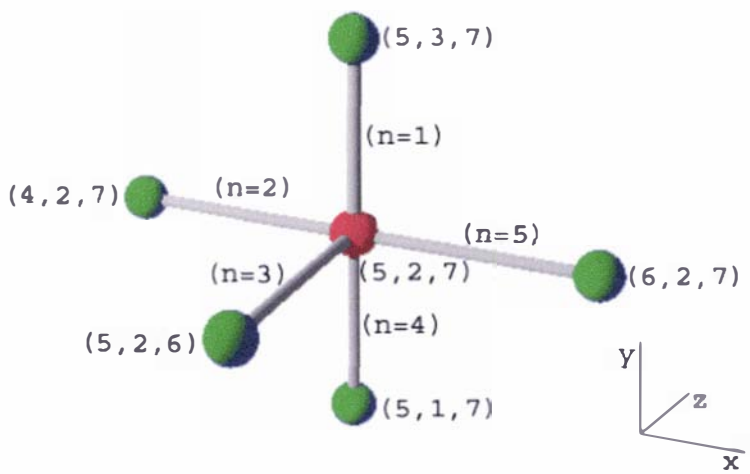

Figure 7-17 - Graphical representation of the node positioned at (x,y,z) = (5,2,7) within the resistance network for a 20' container. The red sphere represents the node of interest and green spheres represent adjacent nodes. Nodes are labelled with co-ordinates and channels labelled with indices

$$\frac{\psi_{4,2,7}-\psi_{5,2,7}}{\sqrt{|\psi_{4,2,7}-\psi_{5,2,7}|}}\sqrt{\frac{2}{\beta_2\rho}}A_2 + \frac{\psi_{6,2,7}-\psi_{5,2,7}}{\sqrt{|\psi_{6,2,7}-\psi_{5,2,7}|}}\sqrt{\frac{2}{\beta_5\rho}}A_5 + \frac{\psi_{5,1,7}-\psi_{5,2,7}}{\sqrt{|\psi_{5,1,7}-\psi_{5,2,7}|}}\sqrt{\frac{2}{\beta_4\rho}}A_4 + \frac{\psi_{5,3,7}-\psi_{5,2,7}}{\sqrt{|\psi_{5,3,7}-\psi_{5,2,7}|}}\sqrt{\frac{2}{\beta_1\rho}}A_1 + \frac{\psi_{5,2,6}-\psi_{5,2,7}}{\sqrt{|\psi_{5,2,6}-\psi_{5,2,7}|}}\sqrt{\frac{2}{\beta_3\rho}}A_3 = 0$$

Equation 7-18

Where:

$\psi_{i,j,k}$	=	Total pressure at node positioned at *(x,y,z) = (i,j,k)*	(Pa)
β_n	=	Flow resistance of channel *n*	

For each term in Equation 7-18, the only variable determining sign is the total pressure difference, meaning a higher total pressure at the satellite node will give the term a positive sign (flow into the node); and lower total pressure at the adjacent node will give the term a negative sign (flow out of the node). A total of 189 equations similar to Equation 7-18 make up the set of simultaneous equations describing the flow patterns in Example 1.

7.3.4 Flow resistance correlations

Correlations used for calculation of flow resistances were split into two categories. Type I flow channels were those characterised as an enclosed conduit, and the flow resistance was calculated using the laminar, Colebrook and Darcy-Weisbach equations. Type II flow channels were those unable to be characterised as enclosed conduits so the resistance was calculated from specific correlations for each geometry. The following sections describe the form of the correlations and their integration into the model. Development and testing of specific correlations is presented in Section 8.

7.3.4.1 Type I flow channels

The method for determining the relationship between frictional losses and flow rate is well established for conventional hydraulic systems, where a fluid flows in enclosed conduits. The method defines a friction factor relating the total pressure loss to a characteristic dimension of the conduit and a characteristic measure of the velocity of the fluid. The quantities generally used are the wetted surface area of the conduit and the kinetic energy of the fluid, which for circular conduits yields Equation 7-19, known as the Darcy-Weisbach equation (Bird *et al.*, 1960).

$$\Delta\psi_n = 4f.\frac{L}{D}.\frac{1}{2}\rho v_n^2 \qquad \textit{Equation 7-19}$$

Where:

f	=	Friction factor	
D	=	Channel diameter	(m)
L	=	Channel length	(m)

Comparison of Equation 7-19 with Equation 7-14 yields the definition of resistance for Type I channels as shown in Equation 7-20.

$$\beta_n = 4f\frac{L}{D} \qquad \textit{Equation 7-20}$$

For fully developed laminar flow, the friction factor (f) is dependent only on the Reynolds number (Equation 7-21) and in turbulent conditions it depends on the Reynolds number and relative roughness of the conduit (Bird *et al.*, 1960). The relative roughness is defined as the ratio of absolute roughness to conduit diameter, where absolute roughness is a measure of the surface coarseness of the conduit material.

$$Re = \frac{Dv\rho}{\mu} \qquad \textit{Equation 7-21}$$

Where:

μ	=	Fluid viscosity	(Pa.s)

The Colebrook equation (Equation 7-22) is the generally accepted method of calculating the friction factor in turbulent flow (Perry & Green, 1997).

$$\frac{1}{\sqrt{f_{turb}}} = -2\log_{10}\left(\frac{\varepsilon}{3.7D} + \frac{2.51}{Re\sqrt{f_{turb}}}\right) \qquad \textit{Equation 7-22}$$

Where:

f_{turb}	=	Friction factor for turbulent flow	
ε	=	Absolute roughness	(m)

The Colebrook equation requires iterative solution, so an explicit approximation (Equation 7-23) was used to simplify calculation (Miller, 1990).

$$f_{turb} = \frac{0.25}{\left(\log_{10}\left(\frac{\varepsilon}{3.7D} + \frac{5.74}{Re^{0.9}}\right)\right)^2} \qquad \textit{Equation 7-23}$$

For turbulent flow in non-circular conduits, the same correlations have been found to be valid using the hydraulic diameter as defined in Equation 7-24 (Miller, 1990).

$$D = D_h = 4A / Pm \qquad \textit{Equation 7-24}$$

Where:

D_h	=	Channel hydraulic diameter	(m)
A	=	Cross-sectional area for flow in conduit	(m^2)
Pm	=	Perimeter of conduit	(m)

For laminar flow of incompressible fluids, Perry & Green (1997) summarise relationships between fluid mass flow rate and total pressure loss for a number of conduit geometries. The correlations can be generalised using Equation 7-25, with k representing a factor dependent on the conduit geometry.

$$f_{lam} = \frac{k}{Re} \qquad \textit{Equation 7-25}$$

Where:

f_{lam}	=	Friction factor for laminar flow	
k	=	Laminar friction geometric parameter	

Perry & Green (1997) give the theoretical relationships for a number of conduit shapes including circular conduits of diameter D (Equation 7-26) and rectangular channels of dimensions D_{long} *and* D_{short} (Equation 7-27).

$$f_{lam} = \frac{16}{Re} \qquad \textit{Equation 7-26}$$

$$f_{lam} = \frac{C_g}{Re}\frac{2R^2}{(R+1)^2} \qquad \textit{Equation 7-27}$$

Where:

R	=	Channel aspect ratio = D_{long}/D_{short}	
D_{short}	=	Rectangular channel short dimension	(m)
D_{long}	=	Rectangular channel long dimension	(m)
C_g	=	Geometric constant	

The value of C_g is a function of the aspect ratio and was given in tabular form (Table 7-1). By transforming and regressing the data, a relationship was developed to estimate the C_g value from the aspect ratio (Equation 7-28).

Table 7-1 - Values of C_g for rectangular channels of dimensions D_{long} and D_{short} (Perry & Green, 1997)

R	1	3/2	2	3	4	5	10	∝
C_g	28.45	20.43	17.49	15.19	14.24	13.73	12.81	12

$$1 < R \le 10 \quad C_g = -0.04(\log R)^2 + 0.0822(\log R) + 0.0355$$
$$R > 10 \quad C_g = 12$$

Equation 7-28

Flow was assumed to be laminar for a Reynolds number of 1500 or less and turbulent at Reynolds numbers greater than 3000. Between these values, a weighted average of the laminar and turbulent friction factors was used (Equation 7-29). The friction factor was assumed to remain constant above a Reynolds number of 10^8, with a value equal to the friction factor at that point. Figure 7-18 shows the relationship between friction factor and Reynolds number for channels of several geometries and relative roughness.

$$f = \frac{(Re - 1500)}{1500} f_{turb} + \frac{(3000 - Re)}{1500} f_{lam}$$

Equation 7-29

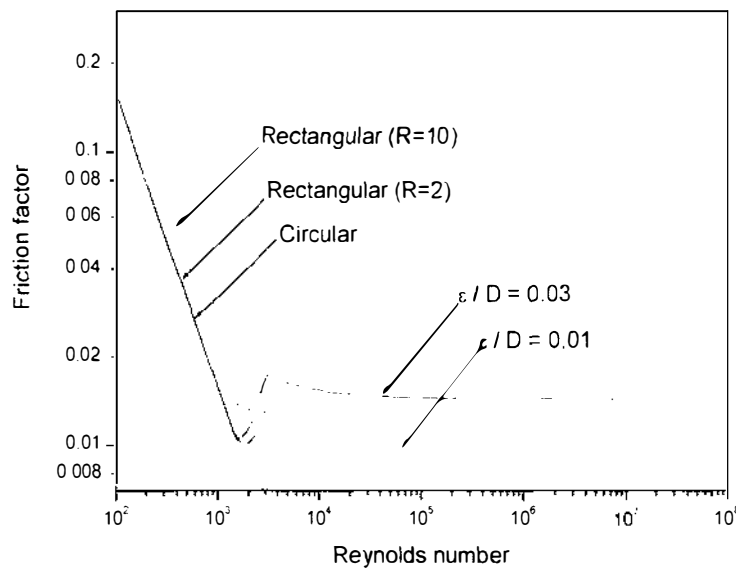

Figure 7-18 – Effect of channel shape, aspect ratio and roughness on friction factor

In addition to calculation of frictional losses in lengths of straight conduits, large volumes of information were available quantifying the effect of other friction causing elements within flow channels. Elements such as junctions, divergent points, bends, contractions, expansions and other miscellaneous elements making up the flow channel cause additional frictional losses. There are two methods in common use for including the effect of these elements: the equivalent length and the velocity head methods. In the first method, the length of conduit that would cause an equivalent pressure drop is reported, and added to the length of the flow path. In the second method, losses are reported as a number of 'velocity heads', which can be added to the mechanical energy balance to allow for the extra resistance to flow (Equation 7-30).

$$\beta_n = 4f\frac{L}{D} + K_{add} \qquad \textit{Equation 7-30}$$

Where:

K_{add} = Additional frictional losses stated as number of velocity heads

Perry & Green (1997) state the second method is preferable, as equivalent length measures are less accurate over a range of diameters. Miller (1990) provides a large number of correlations for additional friction causing elements.

Equation 7-30 gives the resistance equation for Type I channels as used in the model. As f is dependent on the Reynolds number and hence the velocity of the flow, β is also dependent on fluid velocity. However, f and β become independent of fluid velocity at Reynolds numbers exceeding 10^8.

7.3.4.2 Type II flow channels

For flow channels where approximation to an enclosed conduit cannot be made, such as flow through a perforated plate or a fruit carton, more specific relationships were used. Reported relationships generally related the volumetric flow or superficial velocity to the total pressure loss via a power law (Haas *et al.*, 1976; Chau *et al.*, 1985; van der Sman. 2002) so this approach was universally adopted (Equation 7-31). Superficial velocity was defined as the ratio of volumetric flow rate to the cross-sectional area for flow if no obstruction was present (empty-bed velocity). Relationships reported in other forms were converted to equations of the form of Equation 7-31.

$$\frac{\Delta\psi_n}{L} = au_n^{\,b} \qquad \textit{Equation 7-31}$$

Where:

a	=	Resistance coefficient	$(kg.s^{(b-2)}.m^{-(b+2)})$
b	=	Resistance exponent	
u	=	Superficial velocity	$(m.s^{-1})$

Comparison of Equation 7-14 and Equation 7-31 yields the definition of the flow resistance of Type II channels as stated in Equation 7-32. Inspection of Equation 7-32 indicates that β_n for Type II channels is dependent on fluid velocity unless $b = 2$.

$$\beta_n = \frac{2L}{\rho}au_n^{\,b-2} \qquad \textit{Equation 7-32}$$

7.4 Solution method

Manual solution of a large set of non-linear equations is not easily achieved, however solution is not only possible, but can be achieved quickly with the use of a modern PC and a suitable algorithm. Press *et al.* (1992) present a discussion of solution methods for sets of non-linear equations. The Newton-Raphson method including 'backtracking' to improve convergence as presented by Press *et al.* (1992) was chosen and adapted for this application.

For a system with i nodes, a set of i equations of the form of Equation 7-33 can be written where N is the number of channels attached to node i.

$$F(\psi_i) = \sum_{n=1}^{N} \frac{(\psi_j - \psi_i)}{\sqrt{|\psi_j - \psi_i|}} \sqrt{\frac{2\rho}{\beta_n}} A_n = 0 \qquad \textit{Equation 7-33}$$

Where:

i	=	Node of interest index	
j	=	Node at opposite end of channel n	

These equations can be written in matrix notation as shown in Equation 7-34.

$$\mathbf{F}(\boldsymbol{\psi}) = 0 \qquad \textit{Equation 7-34}$$

Where:

$\mathbf{F}(\boldsymbol{\psi})$	=	Vector of function values (mass imbalances)	($kg.s^{-1}$)

The Newton-Raphson method applied to non-linear sets of equations calculates a set of corrections ($\boldsymbol{\delta\psi}$) to be applied to the initial guess of the solution vector ($\boldsymbol{\psi}$); in this case calculated using Equation 7-35 (Press *et al.*, 1992).

$$\boldsymbol{\delta\psi} = -\mathbf{J}^{-1} \cdot \mathbf{F}(\boldsymbol{\psi}) \qquad \textit{Equation 7-35}$$

Where:

$\mathbf{J}$	=	Jacobian matrix	($kg.s^{-1}.Pa^{-1}$)
$\boldsymbol{\delta\psi}$	=	Vector of corrections of total pressure	(Pa)
$\boldsymbol{\psi}$	=	Vector of total pressures	(Pa)

'Backtracking' was incorporated into the method, where the correction was checked to ensure it reduced the overall mass imbalance. The criterion employed to determine if the correction was acceptable was that it must reduce E, as defined in Equation 7-36.

$$E = \mathbf{F}(\boldsymbol{\psi}) \cdot \mathbf{F}(\boldsymbol{\psi}) \qquad \textit{Equation 7-36}$$

Where:

E	=	Criterion employed for 'backtracking' procedure

If the full correction failed to reduce E, a proportion of the correction to implement was calculated (α). Corrections were added to the solution vector and the process iterated to convergence (Equation 7-37).

$$\Psi_{new} = \Psi_{old} + \alpha\delta\Psi \qquad \textit{Equation 7-37}$$

Where:

α = Calculated proportion of correction to add to solution vector

The Jacobian matrix required in Equation 7-35 is defined in Equation 7-38.

$$\mathbf{J} = \begin{bmatrix} \frac{\partial F(\psi)_1}{\partial \psi_1} & \frac{\partial F(\psi)_1}{\partial \psi_2} & \frac{\partial F(\psi)_1}{\partial \psi_3} & \cdots & \frac{\partial F(\psi)_1}{\partial \psi_{N-1}} & \frac{\partial F(\psi)_1}{\partial \psi_N} \\ \frac{\partial F(\psi)_2}{\partial \psi_1} & \frac{\partial F(\psi)_2}{\partial \psi_2} & \frac{\partial F(\psi)_2}{\partial \psi_3} & \cdots & \frac{\partial F(\psi)_2}{\partial \psi_{N-1}} & \frac{\partial F(\psi)_2}{\partial \psi_N} \\ \frac{\partial F(\psi)_3}{\partial \psi_1} & \frac{\partial F(\psi)_3}{\partial \psi_2} & \frac{\partial F(\psi)_3}{\partial \psi_3} & \cdots & \frac{\partial F(\psi)_3}{\partial \psi_{N-1}} & \frac{\partial F(\psi)_3}{\partial \psi_N} \\ \cdots & \cdots & \cdots & \cdots & \cdots & \cdots \\ \frac{\partial F(\psi)_{N-1}}{\partial \psi_1} & \frac{\partial F(\psi)_{N-1}}{\partial \psi_2} & \frac{\partial F(\psi)_{N-1}}{\partial \psi_3} & \cdots & \frac{\partial F(\psi)_{N-1}}{\partial \psi_{N-1}} & \frac{\partial F(\psi)_{N-1}}{\partial \psi_N} \\ \frac{\partial F(\psi)_N}{\partial \psi_1} & \frac{\partial F(\psi)_N}{\partial \psi_2} & \frac{\partial F(\psi)_N}{\partial \psi_3} & \cdots & \frac{\partial F(\psi)_N}{\partial \psi_{N-1}} & \frac{\partial F(\psi)_N}{\partial \psi_N} \end{bmatrix} \qquad \textit{Equation 7-38}$$

Along the matrix's diagonal, partial differentials were calculated analytically using Equation 7-39.

$$\frac{\partial F(\psi)_{row}}{\partial \psi_{col}} = \sum_{n=1}^{N} -\sqrt{\frac{\rho}{\beta_n}} A_n \sqrt{|\psi_n - \psi_{row}|} \qquad row = col \qquad \textit{Equation 7-39}$$

Where:

row = Jacobian matrix row index
col = Jacobian matrix column index

For the remainder of the matrix, partial differentials were equated to zero for nodes where there was no direct connection or calculated using Equation 7-40 where a flow channel connected the nodes.

$$\frac{\partial F(\psi)_{row}}{\partial \psi_{col}} = \sqrt{\frac{\rho}{\beta_n}} A_n \sqrt{|\psi_{col} - \psi_{row}|} \qquad row \neq col \qquad \textit{Equation 7-40}$$

As shown in Equation 7-40, equating the partial differential to zero is equivalent to attributing the channel an infinitely large resistance.

Solution in this fashion assumes that the resistance of the channels is constant. As discussed in Section 7.3.4 this is true only in Type I channels with highly turbulent flow ($Re > 10^8$) or Type II channels with a resistance exponent of 2. For all other channels, the resistance is dependent on the flow rate of the fluid. Solution required an additional calculation, correcting the channel resistances to reflect the calculated flow rates. A simple iterative technique was employed: resistances were recalculated using the latest guess of the solution vector and the steady-state flow profile calculated iteratively.

7.5 Implementation

7.5.1 Calculation algorithm

Figure 7-19 shows the execution procedure of the solution algorithm. The Newton-Raphson method as described above was employed to solve Equation 7-34. To improve convergence, a moving average of the 5 most recently calculated resistances was used. In the initial stages of calculation, four iterations of the Newton-Raphson algorithm were performed and the resistance estimates recalculated to improve the initial resistance estimates.

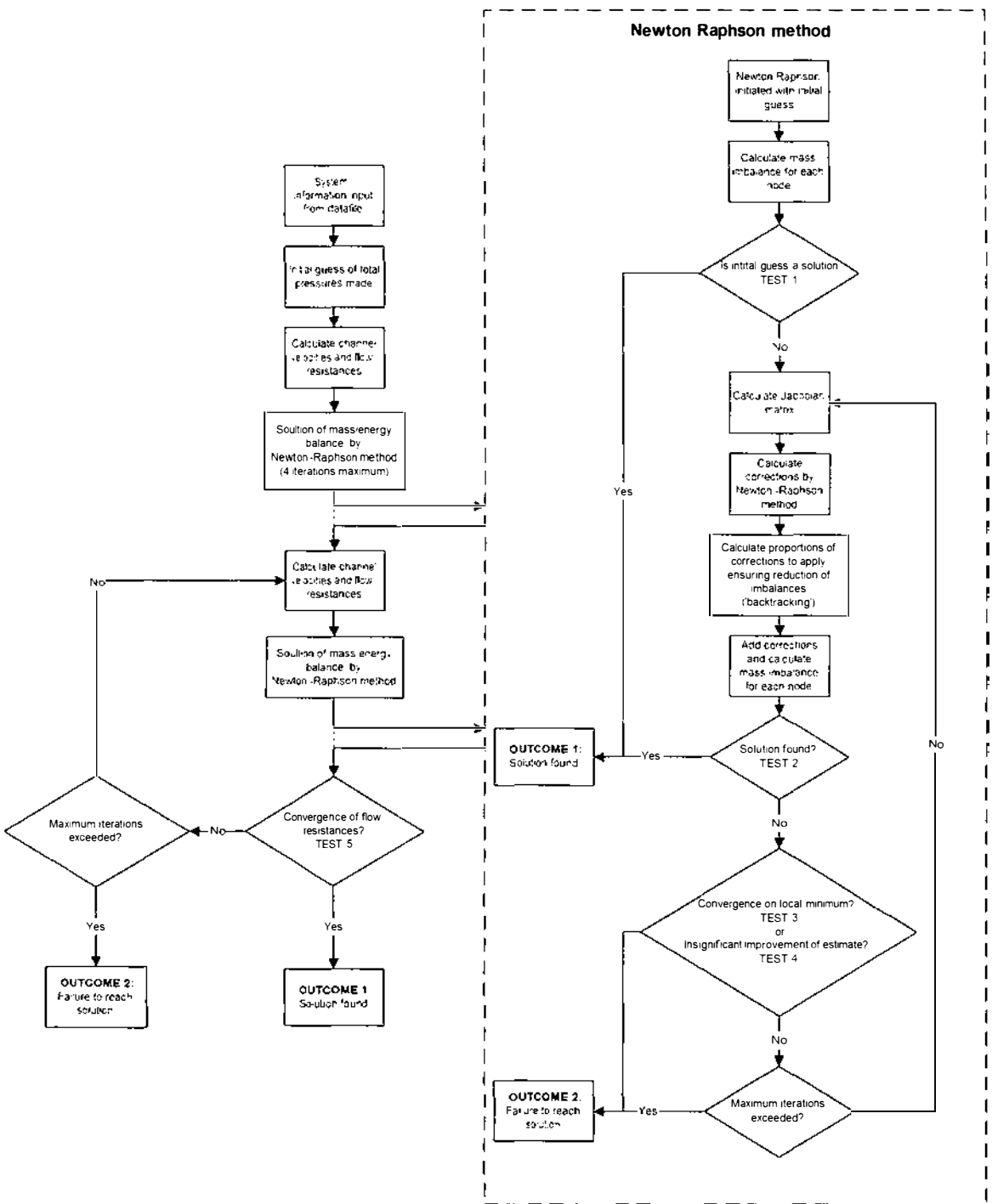

Figure 7-19 – Flow diagram showing the execution procedure of the solution algorithm

The algorithm included a number of tests of convergence. The criteria and tolerances used by each of the tests are given in Table 7-2.

Table 7-2 - Tests for convergence and tolerances used within solution algorithm

Test # (Figure 7-19)	Testing for:	Test criteria	Tolerance
1	Solution of Equation 7-34 by initial guess	Maximum imbalance at a single node	1×10^{-10}
2	Solution of Equation 7-34	Maximum imbalance at a single node	1×10^{-8}
3	Minimum of E found without solution of Equation 7-34	Minimum rate of change of E	1×10^{-6}
4	Convergence of ψ without solution of Equation 7-34	Minimum fractional change of ψ	1×10^{-12}
5	Convergence of resistances	Maximum change of resistance of a single channel	0.1%

The model required the following information:

1. System information
   - Fluid properties (viscosity, density)
   - Maximum number of iterations for both the Newton-Raphson and resistance loops
   - Convergence tolerances
2. Node information
   - Height relative to datum
   - Total pressure at fixed pressure nodes
3. Channel information
   - Resistance variables:
     i. Type I channel - area, perimeter, length, K_{add}, absolute roughness, aspect ratio
     ii. Type II channel - area, length, resistance coefficient, resistance exponent
   - Terminal nodes

The air viscosity and density were calculated from the temperature input by the user assuming a relative humidity of 90% and was assumed to be constant throughout the domain. Unique initial guesses of ψ were required to avoid a zero denominator in Equation 7-33, so nodes were numbered arbitrarily and assigned a total pressure using Equation 7-41. The model calculated and reported the total pressure and static pressure for each node and the velocity and volumetric flow for each flow channel.

$$\psi_n = \psi_{min} + \frac{(\psi_{max} - \psi_{min})}{N+1} \times n \qquad \textit{Equation 7-41}$$

Where:

ψ_{min}	=	Minimum outlet total pressure	(Pa)
ψ_{max}	=	Maximum inlet total pressure	(Pa)
N	=	Total number of nodes	
n	=	Node index	

7.5.2 Software implementation

The solution algorithm was implemented to develop software titled "Airflow Simulation for Transport Applications" (or FlowSim) using the C++ programming language. Borland C++ Builder version 5 (Inprise Corporation, USA) and its rapid application development environment were used to develop the application for the 32-bit Microsoft Windows platform (Microsoft Corporation, USA).

The user interface of FlowSim was kept as simple as possible (Figure 7-20). The user was required to input the location of an input data file and a filename for output of results in a configuration dialogue. Data input and results analysis were kept separate to the calculation software.

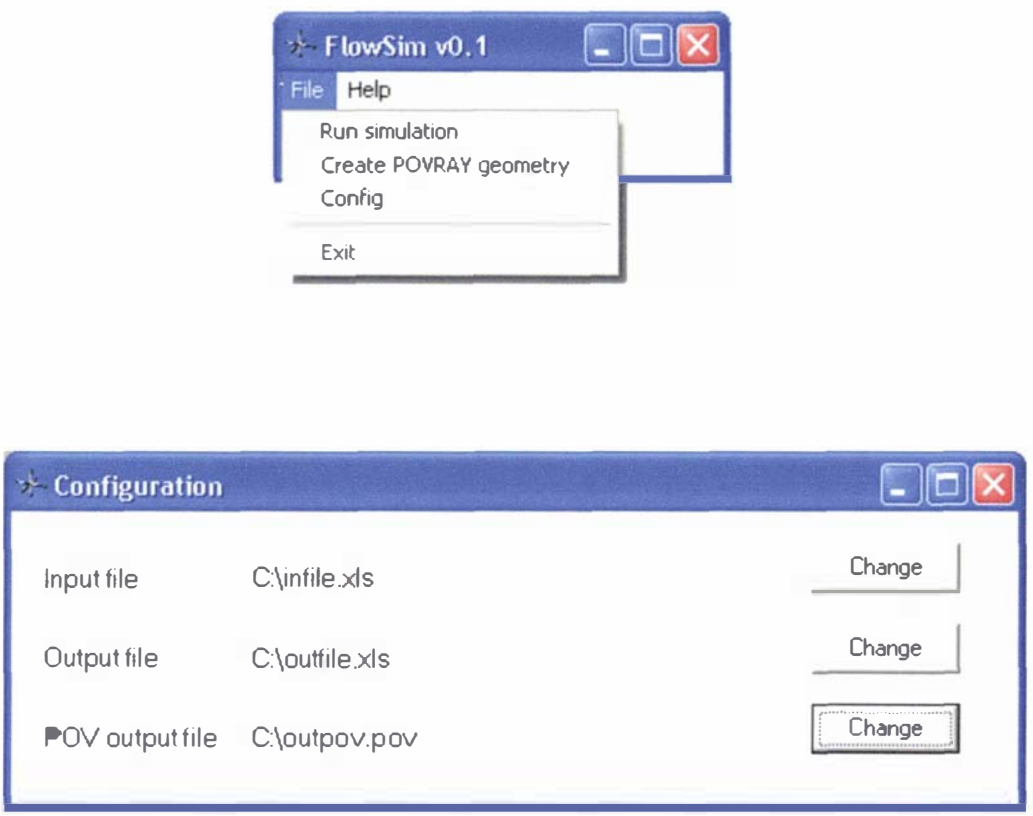

Figure 7-20 – Screenshots of the FlowSim user interface

The system geometry was input using the Microsoft Excel Workbook format (Microsoft Corporation, USA); with general network information in one worksheet, information required for calculation of channel resistances in another worksheet and required node information in a third worksheet. The general network information worksheet contained the fluid temperature, calculation tolerances and maximum number of iteration data; as well as summary information about the network (Figure 7-21). Cells within the input worksheets with red text were calculated automatically by the worksheet, while cells in black required user input.

The flow channel information sheet contained the bulk of the required data (Figure 7-22). For each channel, the channel type and data necessary to calculate the flow resistance was required, as well as the index of the two terminating nodes.

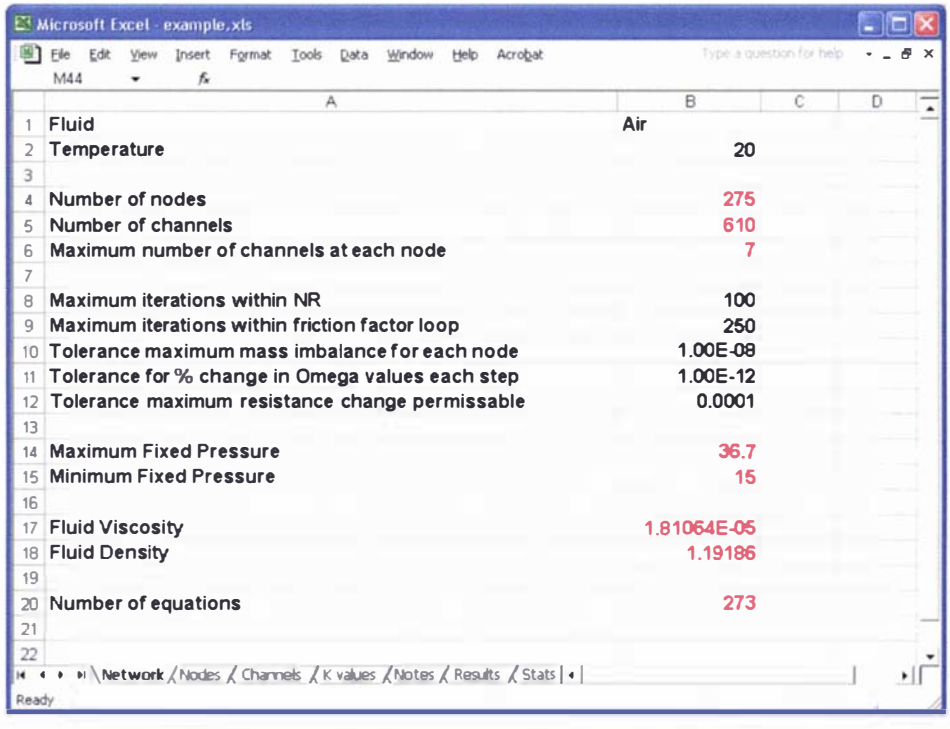

	A	B
1	Fluid	Air
2	Temperature	20
3		
4	Number of nodes	275
5	Number of channels	610
6	Maximum number of channels at each node	7
7		
8	Maximum iterations within NR	100
9	Maximum iterations within friction factor loop	250
10	Tolerance maximum mass imbalance for each node	1.00E-08
11	Tolerance for % change in Omega values each step	1.00E-12
12	Tolerance maximum resistance change permissable	0.0001
13		
14	Maximum Fixed Pressure	36.7
15	Minimum Fixed Pressure	15
16		
17	Fluid Viscosity	1.81064E-05
18	Fluid Density	1.19186
19		
20	Number of equations	273
21		
22		

Figure 7-21 – Screenshot of general network information input worksheet

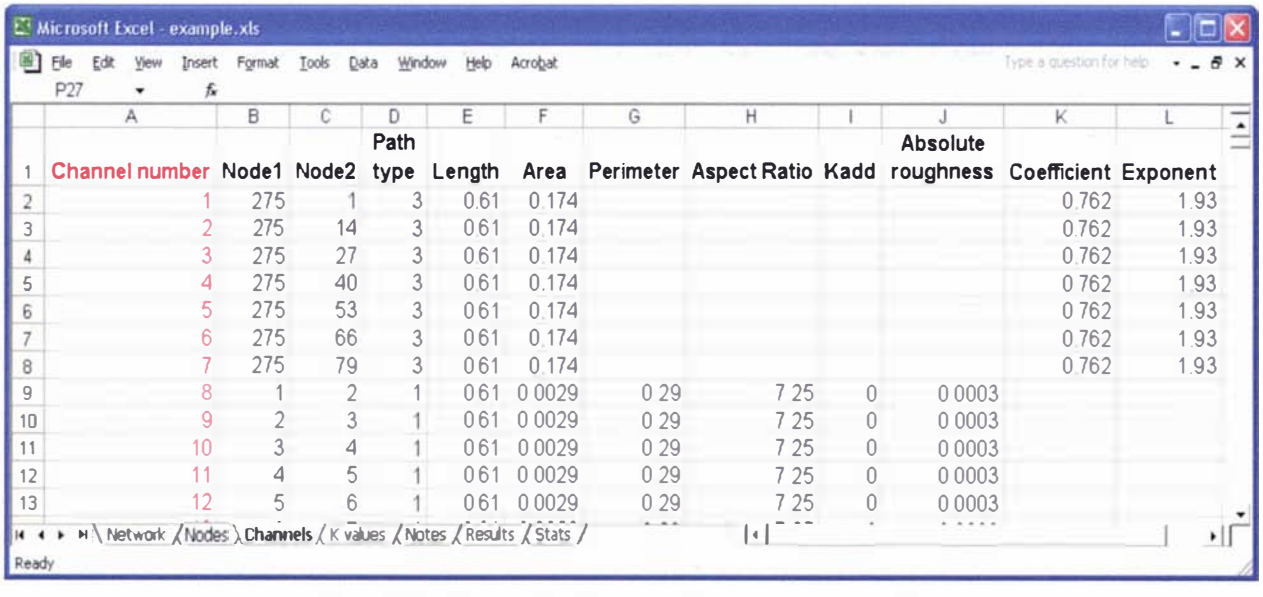

	A	B	C	D	E	F	G	H	I	J	K	L
1	Channel number	Node1	Node2	Path type	Length	Area	Perimeter	Aspect Ratio	Kadd	Absolute roughness	Coefficient	Exponent
2	1	275	1	3	0.61	0.174					0.762	1.93
3	2	275	14	3	0.61	0.174					0.762	1.93
4	3	275	27	3	0.61	0.174					0.762	1.93
5	4	275	40	3	0.61	0.174					0.762	1.93
6	5	275	53	3	0.61	0.174					0.762	1.93
7	6	275	66	3	0.61	0.174					0.762	1.93
8	7	275	79	3	0.61	0.174					0.762	1.93
9	8	1	2	1	0.61	0.0029	0.29	7.25	0	0.0003		
10	9	2	3	1	0.61	0.0029	0.29	7.25	0	0.0003		
11	10	3	4	1	0.61	0.0029	0.29	7.25	0	0.0003		
12	11	4	5	1	0.61	0.0029	0.29	7.25	0	0.0003		
13	12	5	6	1	0.61	0.0029	0.29	7.25	0	0.0003		

Figure 7-22 – Screenshot of channel information input worksheet

The node information sheet contained the node elevations (y-values) and total pressure values for the fixed pressure nodes (Figure 7-23). The node information sheet also contained a list of attached channels for each node, which was calculated automatically from the information given in the channel information sheet.

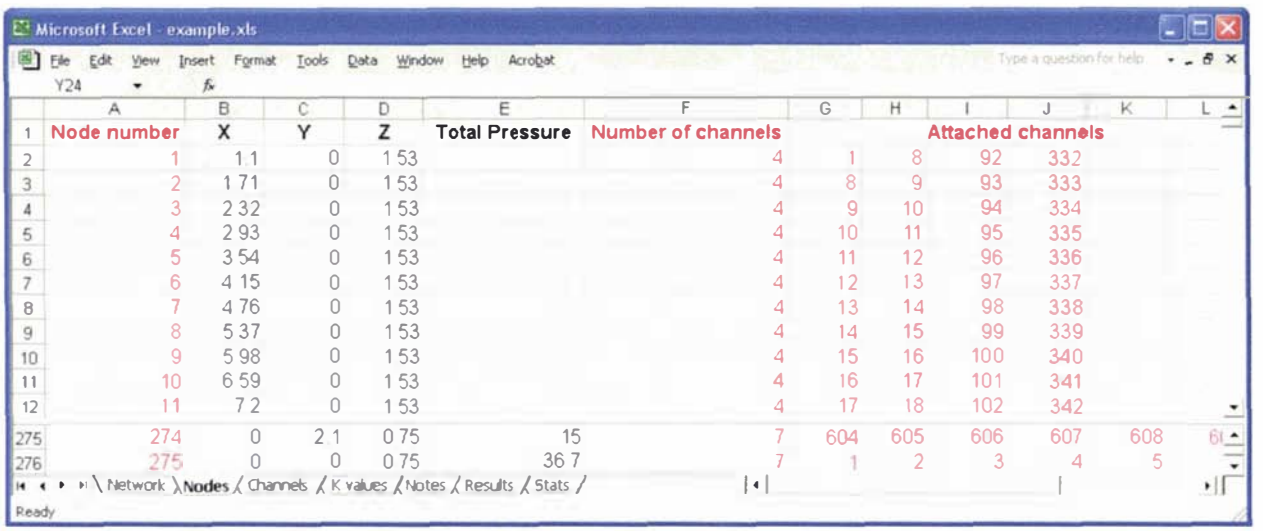
Microsoft Excel - example.xls

File Edit View Insert Format Tools Data Window Help Acrobat

Y24

	A	B	C	D	E	F	G	H	I	J	K	L
1	Node number	X	Y	Z	Total Pressure	Number of channels	Attached channels					
2	1	1.1	0	1.53		4	1	8	92	332		
3	2	1.71	0	1.53		4	8	9	93	333		
4	3	2.32	0	1.53		4	9	10	94	334		
5	4	2.93	0	1.53		4	10	11	95	335		
6	5	3.54	0	1.53		4	11	12	96	336		
7	6	4.15	0	1.53		4	12	13	97	337		
8	7	4.76	0	1.53		4	13	14	98	338		
9	8	5.37	0	1.53		4	14	15	99	339		
10	9	5.98	0	1.53		4	15	16	100	340		
11	10	6.59	0	1.53		4	16	17	101	341		
12	11	7.2	0	1.53		4	17	18	102	342		
275	274	0	2.1	0.75	15	7	604	605	606	607	608	6
276	275	0	0	0.75	36.7	7	1	2	3	4	5	

Network Nodes Channels K values Notes Results Stats

Ready

Figure 7-23 – Screenshot of node information input worksheet

In addition to the information required for flow calculation, it was possible to input (though not required) Cartesian co-ordinates of the nodes. FlowSim was equipped with a function to take this co-ordinate data and produce a 'Persistence of Vision Ray-Tracer' (POV-Ray) data file describing the geometry (Persistence of Vision development team, http://www.povray.org/). POV-Ray is a freely available software package that creates three-dimensional images from a text file describing the objects, lighting and viewpoint. Processing the data file produced a graphical representation of the input geometry and served as a useful means of verifying that the geometry input was correct (e.g. Figure 7-6).

On completion of calculations, the simulation results and the input data were saved in the Microsoft Excel Workbook format using the specified output file name. In this fashion, a record of both the input data and calculated outputs were stored in a single file. The information output included the static and total pressure at each node, and the volumetric flow and superficial velocity in each channel (Figure 7-24). The sheet also stated whether the calculation had successfully converged and the time required for convergence. Figure 7-25 shows a second results sheet that contains information regarding the calculation process. For every iteration of the resistance loop, the number of iterations required for convergence of the Newton-Raphson algorithm, any indication of convergence problems and the maximum fractional change of a resistance were given. This information was included to aid troubleshooting of any convergence problems.

The FlowSim software along with a blank input workbook can be found in the CD-ROM Appendix.

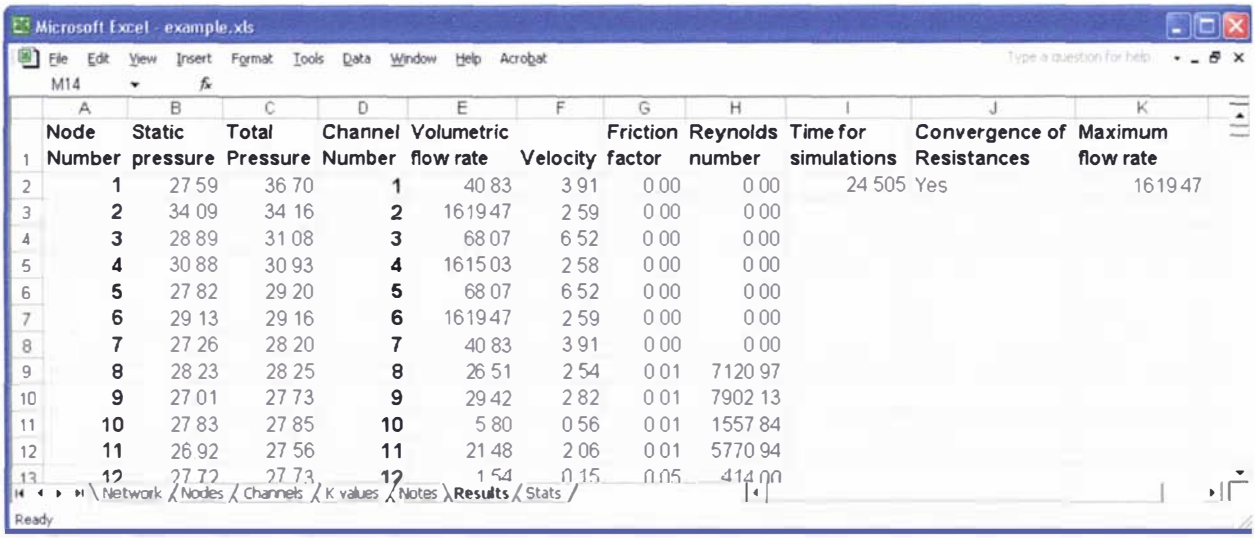

Microsoft Excel - example.xls

File Edit View Insert Format Tools Data Window Help Acrobat

M14

	A	B	C	D	E	F	G	H	I	J	K
1	Node Number	Static pressure	Total Pressure	Channel Number	Volumetric flow rate	Velocity	Friction factor	Reynolds number	Time for simulations	Convergence of Resistances	Maximum flow rate
2	1	27 59	36 70	1	40 83	3 91	0 00	0 00	24 505	Yes	161947
3	2	34 09	34 16	2	161947	2 59	0 00	0 00			
4	3	28 89	31 08	3	68 07	6 52	0 00	0 00			
5	4	30 88	30 93	4	161503	2 58	0 00	0 00			
6	5	27 82	29 20	5	68 07	6 52	0 00	0 00			
7	6	29 13	29 16	6	161947	2 59	0 00	0 00			
8	7	27 26	28 20	7	40 83	3 91	0 00	0 00			
9	8	28 23	28 25	8	26 51	2 54	0 01	7120 97			
10	9	27 01	27 73	9	29 42	2 82	0 01	7902 13			
11	10	27 83	27 85	10	5 80	0 56	0 01	1557 84			
12	11	26 92	27 56	11	21 48	2 06	0 01	5770 94			
13	12	27 72	27 73	12	1 54	0 15	0 05	414 00			

Network / Nodes / Channels / K values / Notes / Results / Stats /

Ready

Figure 7-24 – Screenshot of node and channel information output worksheet

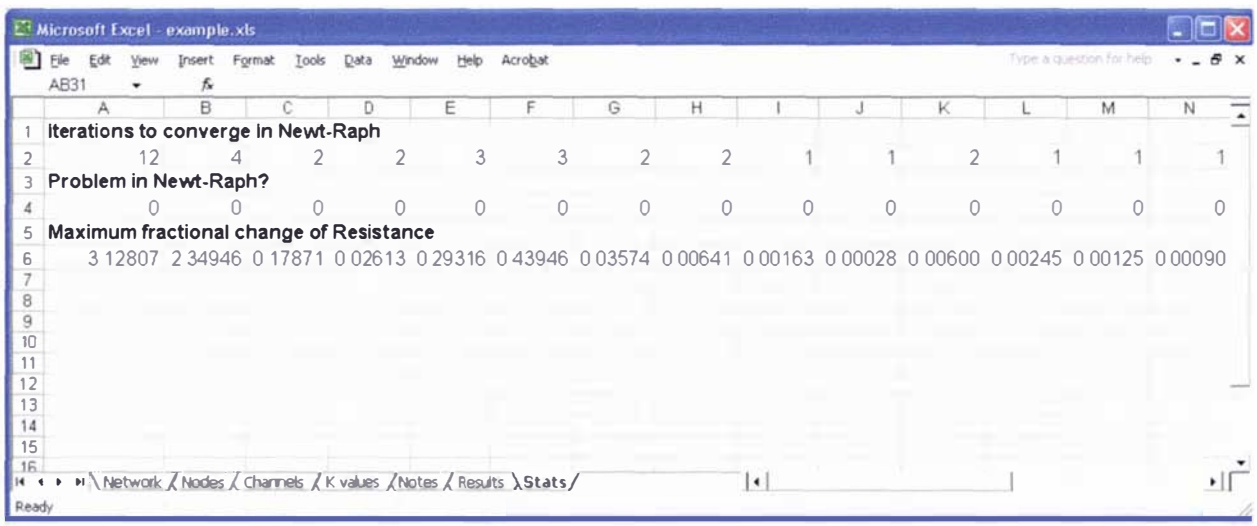

Microsoft Excel - example.xls

File Edit View Insert Format Tools Data Window Help Acrobat

AB31

	A	B	C	D	E	F	G	H	I	J	K	L	M	N
1	Iterations to converge in Newt-Raph													
2	12	4	2	2	3	3	2	2	1	1	2	1	1	1
3	Problem in Newt-Raph?													
4	0	0	0	0	0	0	0	0	0	0	0	0	0	0
5	Maximum fractional change of Resistance													
6	3 12807	2 34946	0 17871	0 02613	0 29316	0 43946	0 03574	0 00641	0 00163	0 00028	0 00600	0 00245	0 00125	0 00090

Network / Nodes / Channels / K values / Notes / Results / Stats /

Ready

Figure 7-25 – Screenshot of calculation information output worksheet

7.6 Conclusions

The underlying framework and method of solution of the airflow model along with an overview of the implementation in software has been presented. The flow paths of significance were required to be predetermined and a corresponding flow network could then be defined. Equations were formulated in terms of unknown pressures at points of convergence/divergence and solution of the equations was achieved using a Newton-Raphson algorithm implemented in C++.

8 Flow Resistance Correlations

8.1 Introduction

The preceding chapter presented the theoretical basis of the model and described the method of solution. A flow resistance (β_n) was defined that quantified the frictional energy loss associated with fluid flow through a particular channel. The resistance of a channel may be dependent on the rate of fluid flow. For each channel within the modelled domain, the relationship between the flow resistance and the rate of flow was required.

A great deal of pressure loss data was available for piping and ducting applications (e.g. Miller, 1990; Perry & Green, 1997). Section 8.2 presents testing of the generally accepted methods for determining pressure loss within enclosed conduits for their accuracy in estimating losses in flow channels found in marine transport systems.

For geometries where the use of these methods was inappropriate, specific correlations were sought, and where unavailable, were developed. A case of particular significance was the pressure loss resulting from flow through vented packages. Section 8.3.1 presents an experimental investigation of this geometry. The relative importance of the vent and the carton contents was ascertained, and the relationship between vent size and flow resistance was investigated. The possibility of extrapolating measured carton characteristics to the characteristic of a pallet stack was also investigated.

Finally, Section 8.4 presents an investigation of the effect of airflow past open vents. Shipping systems often create conditions where significant flows through horizontally vented packages are unlikely; however, there may be substantial airflows past open vents. Air flowing past the vent will entrain air from inside the carton, causing a cooling effect as the entrained air is replenished with external air. This air interchange may contribute significantly to heat transfer. The relative importance of air interchange as a mode of heat transfer and the effect on the air interchange rate of flow conditions past the vent, vent size, shape and location were investigated.

8.2 Type I channels

The previous chapter described Type I channels as those where the flow resistance could be determined using the method employed for conventional hydraulic systems. It was postulated that the geometry of many channels within shipping systems could be represented by an equivalent hydraulic channel. For example, gaps between pallets, or between a pallet and the container wall form elongated rectangular channels. The Darcy-Weisbach (Equation 8-1), laminar (Equation 8-2) and Colebrook (Equation 8-3) equations have commonly been used to quantify the resistance to flow of enclosed conduits (Miller, 1990).

$$\Delta P = 4 f \frac{L}{D_h} \frac{1}{2} \rho v^2 \qquad \textit{Equation 8-1}$$

$$f_{lam} = \frac{k}{Re} \qquad \textit{Equation 8-2}$$

$$\frac{1}{\sqrt{f_{turb}}} = -2\log_{10}\left(\frac{\varepsilon}{3.7D_h} + \frac{2.51}{Re\sqrt{f_{turb}}}\right) \qquad \textit{Equation 8-3}$$

Where:

ΔP	=	Pressure loss	(Pa)
f	=	Friction factor	
f_{lam}	=	Laminar friction factor	
f_{turb}	=	Turbulent friction factor	
L	=	Flow channel length	(m)
D_h	=	Channel hydraulic diameter	(m)
ρ	=	Fluid density	($kg.m^{-3}$)
v	=	Fluid velocity	($m.s^{-1}$)
k	=	Laminar friction geometric parameter	
ε	=	Absolute roughness	(m)
Re	=	Reynolds number = $\frac{\rho v D_h}{\mu}$	
μ	=	Fluid viscosity	(Pa.s)

Equation 8-4 is a commonly used explicit approximation of Equation 8-3 (Miller, 1990).

$$f_{turb} = \frac{0.25}{\left(\log_{10}\left(\frac{\varepsilon}{3.7D_h} + \frac{5.74}{Re^{0.9}}\right)\right)^2} \qquad \textit{Equation 8-4}$$

The applicability of these equations to the channels formed by palletised packages has not been assessed.

This section describes testing of the suitability of the Darcy-Weisbach, laminar and Colebrook equations for predicting rates of flow and pressure losses through channels formed by cardboard packaging and estimation of the effective absolute roughness parameter for use in the Colebrook equation. Part A used single manufactured cardboard channels to test the method and estimate the effective absolute roughness parameter and its dependence on the channel characteristics. Part B tested the roughness parameter found in Part A and further validated the method using flows measured in a real packaging system.

8.2.1 Experimental method

8.2.1.1 Part A – Single channels

To assess the Darcy-Weisbach, laminar and Colebrook equations for predicting pressure loss in flow channels formed by cardboard cartons, 5 conduits of various dimensions were produced. Cartons with dimensions 0.70 × 0.31 × 0.30 m or 0.50 × 0.30 × 0.20 m (L×W×H) were glued together as shown in Figure 8-1 to form a rectangular conduit of 2.3 m minimum length. Care was taken to ensure the conduit was as airtight as possible. The conduit was attached to a rotameter (GEC-Elliot Process Instruments Ltd England, models Metric 10G, Metric 24XG & Metric 35E) and a fan (Figure 8-2). Pressure taps were installed at points approximately 2 m apart, 0.4 m from the air entrance and 0.15 m from the air exit (Figure 8-3) and attached to a pressure sensor using 6 mm OD pressure tubing and T-junctions as described in BS 848 (British Standards Institute, 1980). Four pressure taps were used where the four faces of the conduit were large enough to permit installation, and two used where the short dimension of the conduit was not of sufficient size for installation. Air velocity at the conduit inlet was measured using

a hot wire anemometer (TSI model 8355-M-GB). Pressure loss was measured using a MKS 698A pressure transducer (MKS Instruments Inc. Andover MA, USA) for each conduit over a range of flow rates from 1.7×10^{-4} to 8×10^{-3} $m^3.s^{-1}$. Pressure readings were recorded every second for 1 to 2 minutes and the average value used for analysis. To achieve higher flow rates, the rotameter was removed from the system and the anemometer reading used alone to predict the flow rate.

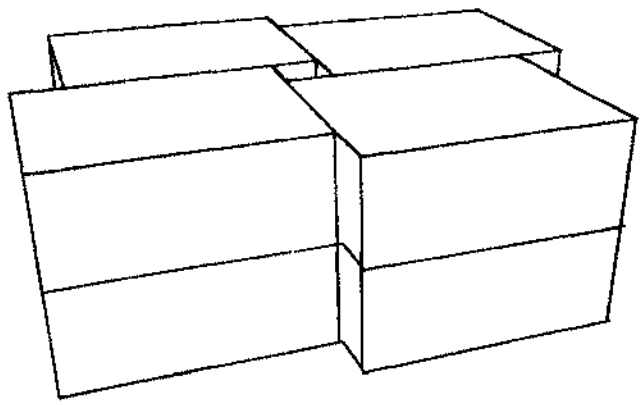

Figure 8-1 -- The construction pattern used to create enclosed conduits of various dimensions constructed from cardboard cartons

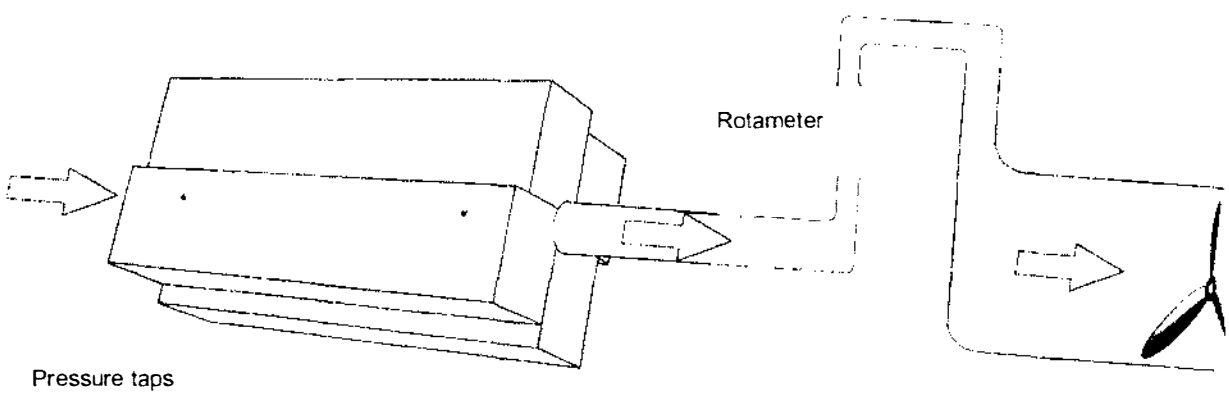

Figure 8-2 –Experimental set-up to measure pressure loss in channels formed between cardboard packages

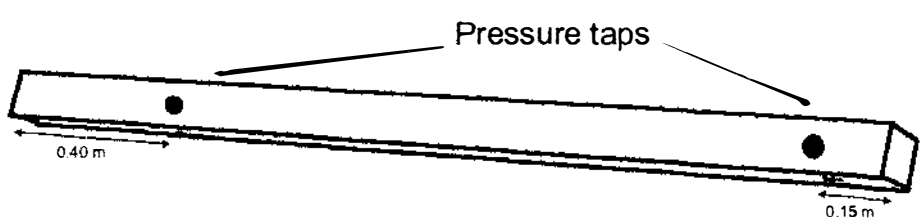

Figure 8-3 –Close-up of manufactured channel between cardboard packages showing placement of pressure taps

In these conduits, the joints between cartons effectively ribbed the walls of the conduit. Cartons of different heights created conduits with different frequencies of 'ribs'. To study the effect of this, one conduit was constructed using an alternative carton of a different height (0.20 m). Similarly, one conduit was constructed using vented cartons to investigate the effect of open vents within the conduit. The seams and vents not on the face forming the conduit were sealed to ensure flow was along the length of the conduit and not through the vented cartons. Table 8-1 describes the five conduits studied. Experiments were conducted at 2°C.

Table 8-1 – Conduit dimension and values used for flow prediction in manufactured conduits

Conduit #	Conduit dimensions (m)	Hydraulic diameter (m)	ε (m)	Notes
1	0.02 x 0.06	0.03	0.0003	
2	0.04 x 0.04	0.04	0.0003	
3	0.02 x 0.20	0.036	0.0003	
4	0.04 x 0.12	0.06	0.0003	Constructed with 0.20 m tall cartons
5	0.023 x 0.31	0.043	0.0003	Constructed with vented cartons

The stated accuracy of the hot wire anemometer was ±2.5% of the reading. The pressure transducer had a resolution of 0.0001 Pa and was calibrated prior to use. Measured pressure fluctuations and sensor drift were in the order of 0.1 Pa; however, the systematic error associated with imperfect positioning of the pressure taps was likely to be larger than these errors. Overall uncertainties in the pressure measurements were estimated to be ±10%. The level of the rotameter was manually inspected and the flow rate determined from calibration charts. Measurement uncertainties for the volumetric flows were in the order of ±15%.

8.2.1.2 Part B – Palletised packaging system

Further validation of the method was performed using a prototype packaging system for kiwifruit. A purpose-built rig designed to accommodate a pallet of cartons was used to investigate the packaging system under vertical flow conditions (Figure 8-4). The rig consisted of an insulated cupboard measuring 1.2 m × 1.2 m × 2.47 m (W×D×H) with a variable speed fan to draw air up through the cupboard. Incoming air flowed below the walls and upward through the cupboard. The floor of the cupboard was constructed with 30 mm wide wooden slats spaced every 90 mm to allow the passage of air. Pressure taps were placed in the centre of the 4 walls near both the top and the bottom of the rig. The outlet of the fan was ducted to an orifice plate used to measure the volumetric flow. Three orifice plates were used depending on the flow range: 50 mm, 120 mm and 186 mm. A secondary fan was placed downstream of the orifice plate to achieve higher flow rates.

The prototype packaging system made use of vertical channels within the pallet stack; allowing refrigerated air better access to the central columns of the stack. A graphical depiction of the concept is shown in Figure 8-5. Exact dimensions of the prototype package could not be described, as they were commercially sensitive; however, the information required for flow resistance prediction is given in Table 8-2. The vertical channels were formed between cartons and ran the full height of the pallet. Channels formed in the stack were either full or half width depending on their position within the stack.

In this system, the measured flow was considered to be made up of three parts: flow through the defined vertical channels, diffusive flow through the stack between cartons and flow in channels formed between the stack and the walls of the rig. The existing kiwifruit 'modular-bulk' packaging system as used by Zespri International Ltd was used to quantify the proportion of each type of flow. Modular-bulk cartons measure approximately 0.40 × 0.30 × 0.19 m (L×W×H) and are stacked ten layers high with ten cartons on each layer to form a pallet. For the standard packaging system, the only significant vertical channels were between the walls of the rig and the stack of cartons.

Table 8-2 - Geometry of prototype kiwifruit carton stack

Geometric Property	Value
Total cross-sectional area of full-width channels	0.0077 m^2
Total cross-sectional area of half-width channels	0.01 m^2
Total stack base area	1.2 m^2
Total channel cross-sectional area for flow	0.01785 m^2
Channel area fraction	1.5%
Average width of full-width channel (24 measurements)	0.0085 m
Stack height	1.755 m

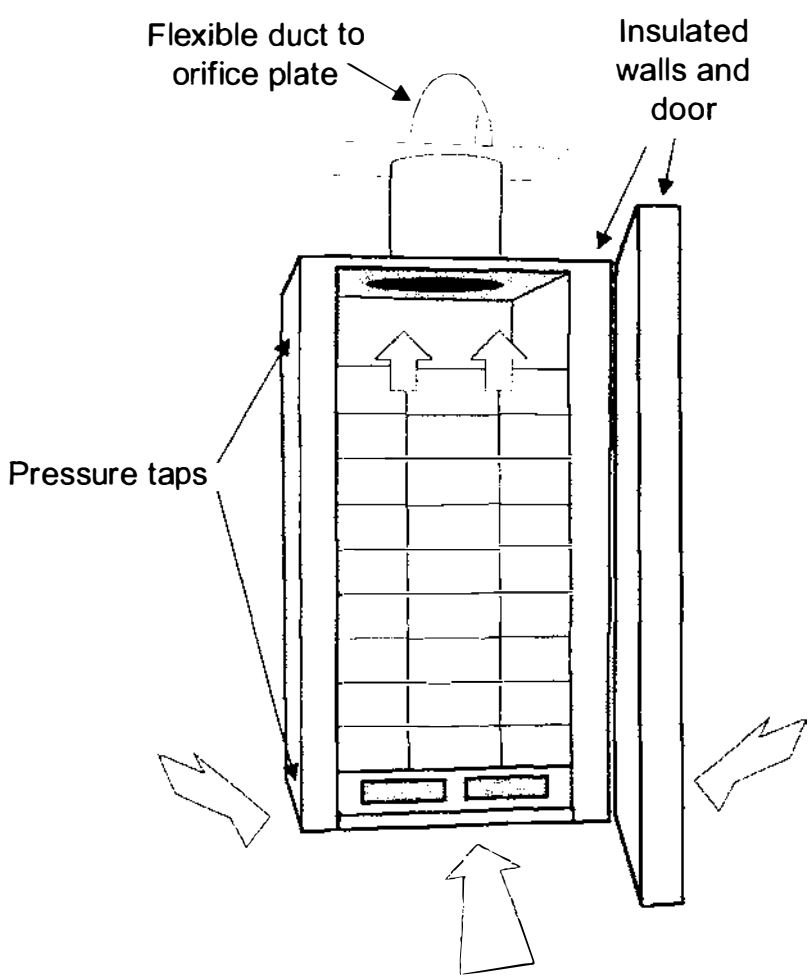

Figure 8-4 - The insulated vertical airflow rig used to investigate the flow of air vertically upward through pallets of packaged produce

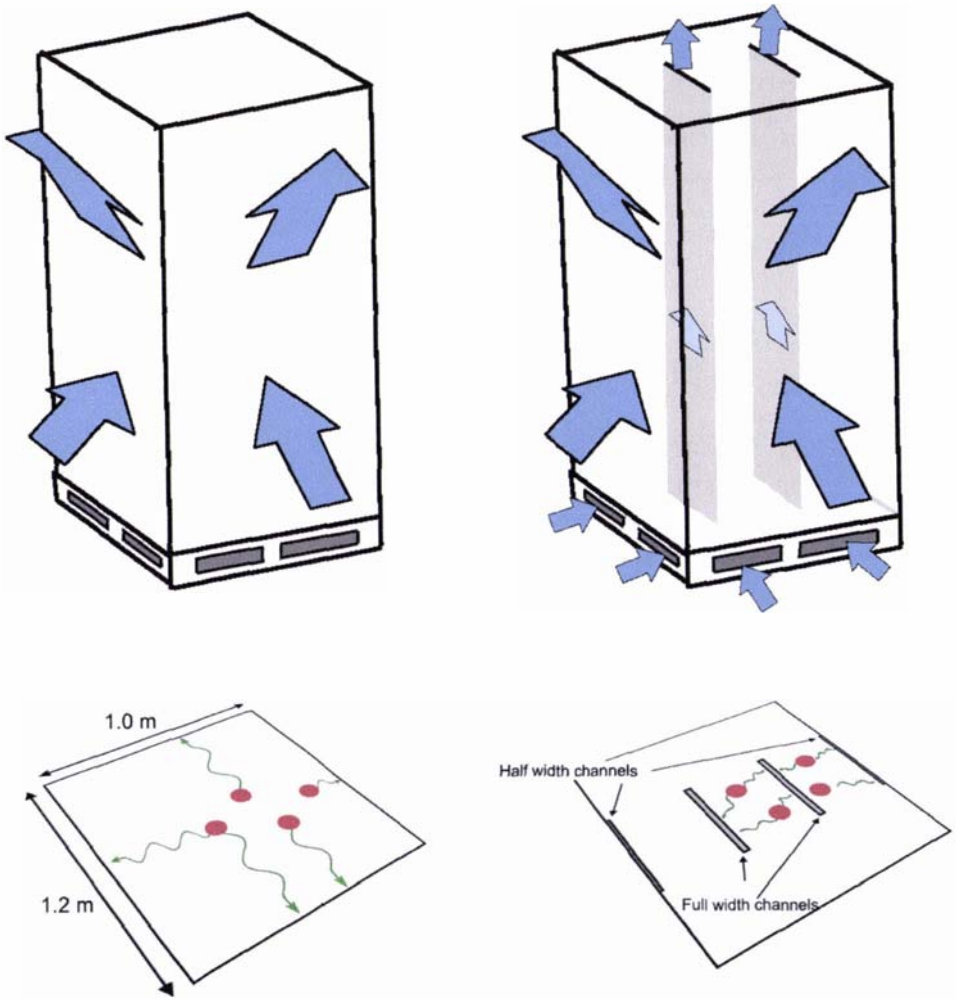

Figure 8-5 –Concept diagram showing the use of vertical channels to reduce the temperature variability within a stack of cartons. The red circles represent fruit; blue arrows airflow and green arrows heat transfer

The relationship between the static pressure loss over the height of the stack, and the volumetric flow rate was measured for both packaging systems. To quantify the relative flows of air between the walls/cartons and diffusively through the stack itself, the standard carton was also tested with two plastic sheets placed between each layer of cartons. The sheets prevented flow between cartons thereby allowing estimation of the flow between the stack and walls.

A 200 mm thick polystyrene sheet was used to reduce the dimensions of the cupboard to 1 m x 1.2 m to match the dimensions of the pallet. To simulate more closely the flow conditions experienced in actual transport systems, pallet bases were placed in the rig and the pallet stack built on top of them. Pallets were built to a height of nine layers using full cartons. Full height pallets (10 layers) were not used so as to accommodate the pallet bases. The resistance to flow of each of the pallets was tested with all four walls nominally flush with the pallet.

The pressure taps at the top and bottom of the rig as well as on either side of the orifice plate were attached to pressure sensors using pressure tubing (6 mm OD) and T-junctions as described in BS 848 (British Standards Institute, 1980). The upper pressure taps were in the headspace above the pallet and the lower pressure taps were in the middle of the pallet base. Pressure was measured using pressure transducers (Setra, model 2604, Setra Systems Inc, MA, USA) and an inclined manometer.

8.2.2 Results

8.2.2.1 Part A – Single channels

The average measured pressure loss over each conduit was calculated for each flow rate. These values were then compared to predicted values using the Darcy-Weisbach equation, the laminar equation and an explicit approximation of the Colebrook equation (Miller, 1990) (Equation 8-1, Equation 8-2 & Equation 8-4). The coefficients used for prediction are given in Table 8-1, and calculations were performed as outlined in Section 7.3.4.1. Comparison showed good agreement between the predicted and measured pressure losses for all 5 conduits over the range of flow rates tested (Figure 8-6 to Figure 8-10).

Under the flow conditions investigated, predictions were insensitive to the absolute roughness value used. Even at high Reynolds number, a 100% difference in roughness caused only a 10% difference in friction factor and thus a 5% difference in flow rates predicted from a measured pressure loss. In contrast, the method was sensitive to the dimensions of the conduit, which was variable due to the method of construction. If an accuracy of ±10% was considered reasonable for measurement of the width of the conduit, the error caused in volumetric flow prediction would be ±15%. The broken lines in Figure 8-6 to Figure 8-10 show these bounds. Agreement was sufficiently good to confirm that the equations used were suitable for this application; that is the differences could be explained by uncertainty in data such as the hydraulic diameter rather than the prediction method uncertainty.

Prediction of flow within the conduit constructed with an alternative carton height was equally accurate using the roughness parameter employed for the original package suggesting the frequency of ribs had negligible effect on pressure loss (Figure 8-9). The incorporation of vents in the conduit also had no substantial effect (Figure 8-10). Use of an absolute roughness of 0.0003 m was found to be suitable for both package designs tested and whether vents were present in the conduit or not.

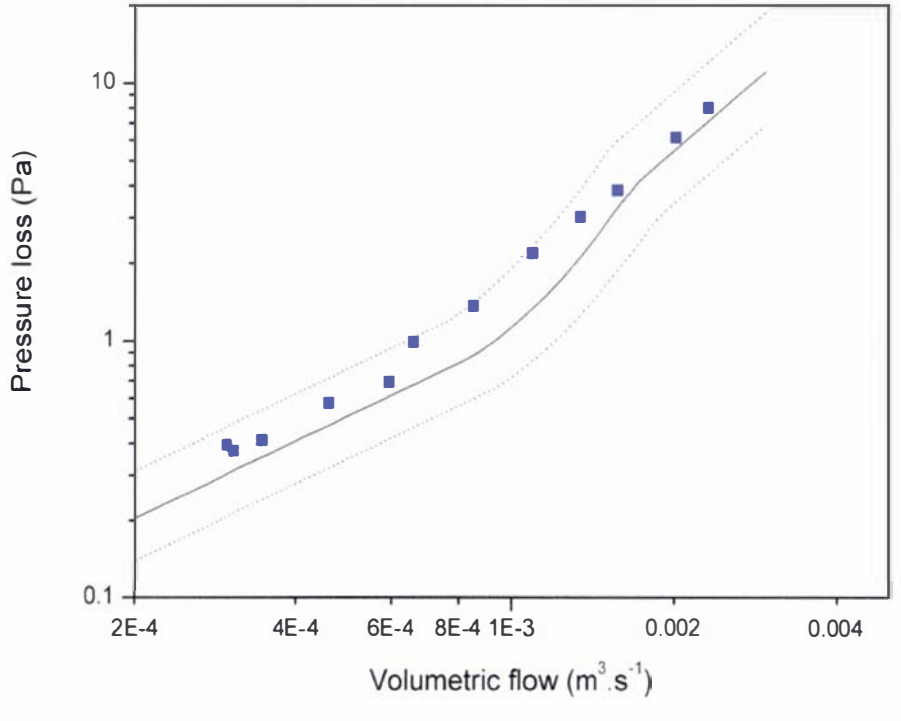

Figure 8-6 – Comparison of the measured pressure loss for a 0.02×0.06 m cardboard conduit and that predicted using the laminar, Colebrook & Darcy-Weisbach equations. The solid line represents the predicted pressure loss using the measured dimensions and dotted lines represent the predicted pressure loss using the measured dimensions ±10%

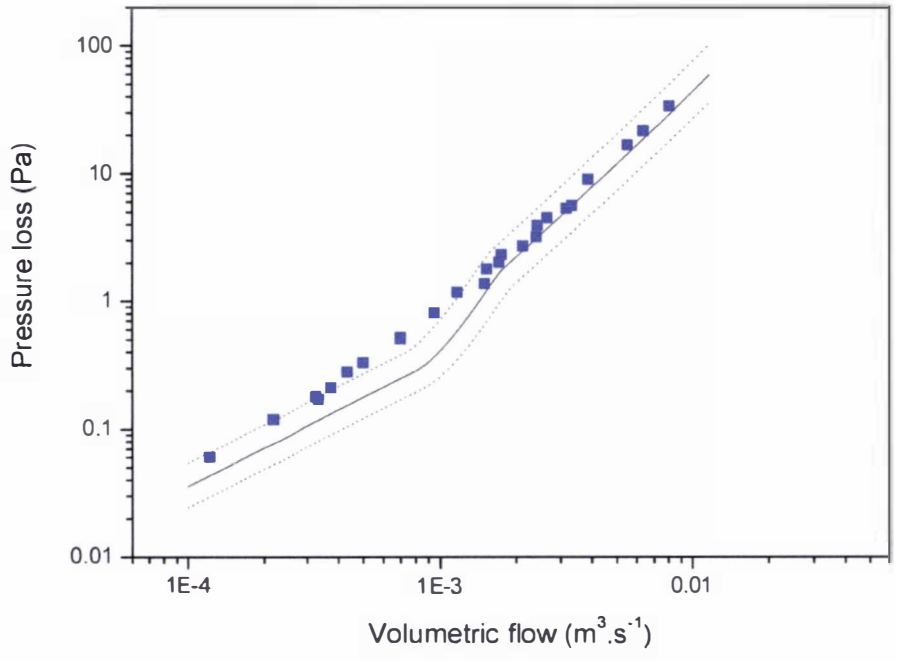

Figure 8-7 – Comparison of the measured pressure loss for a 0.04×0.04 m cardboard conduit and that predicted using the laminar, Colebrook & Darcy-Weisbach equations. The solid line represents the predicted pressure loss using the measured dimensions and dotted lines represent the predicted pressure loss using the measured dimensions ±10%

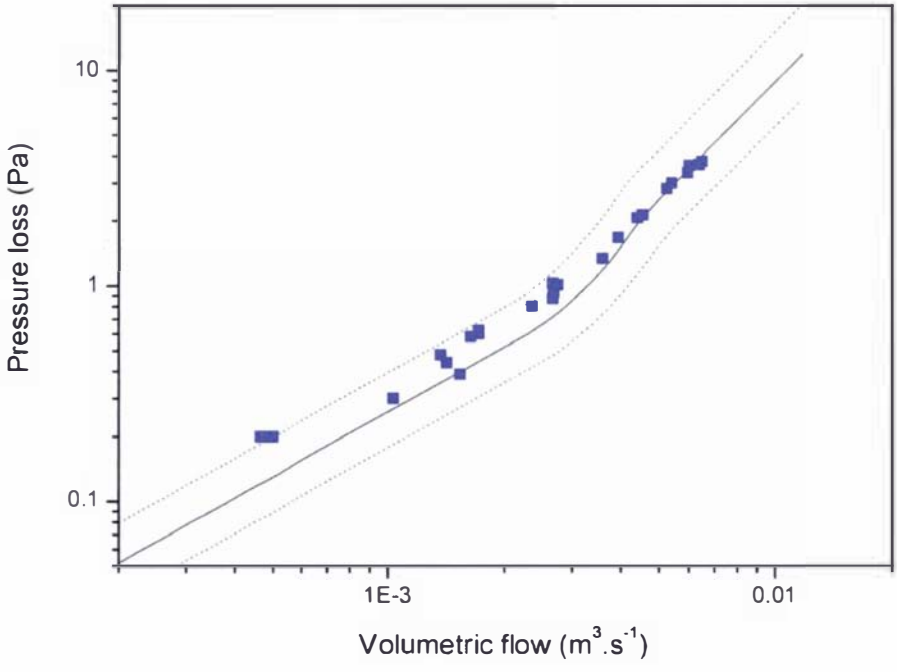

Figure 8-8 - Comparison of the measured pressure loss for a 0.02×0.20 m cardboard conduit and that predicted using the laminar, Colebrook & Darcy-Weisbach equations. The solid line represents the predicted pressure loss using the measured dimensions and dotted lines represent the predicted pressure loss using the measured dimensions ±10%

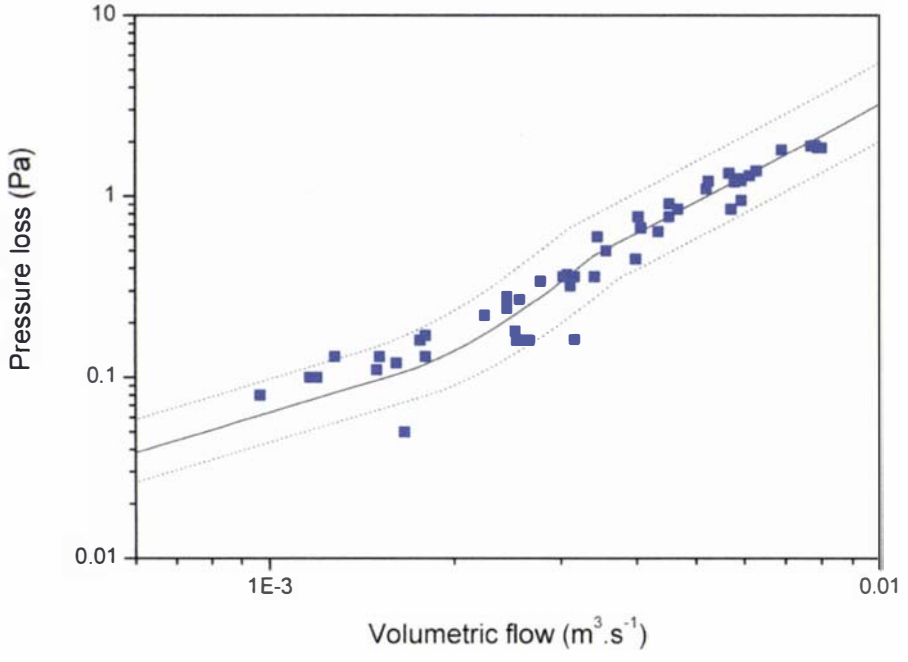

Figure 8-9 - Comparison of the measured pressure loss for a 0.04×0.12 m cardboard conduit constructed using an alternative carton of different height and that predicted using the laminar, Colebrook & Darcy-Weisbach equations. The solid line represents the predicted pressure loss using the measured dimensions and dotted lines represent the predicted pressure loss using the measured dimensions ±10%

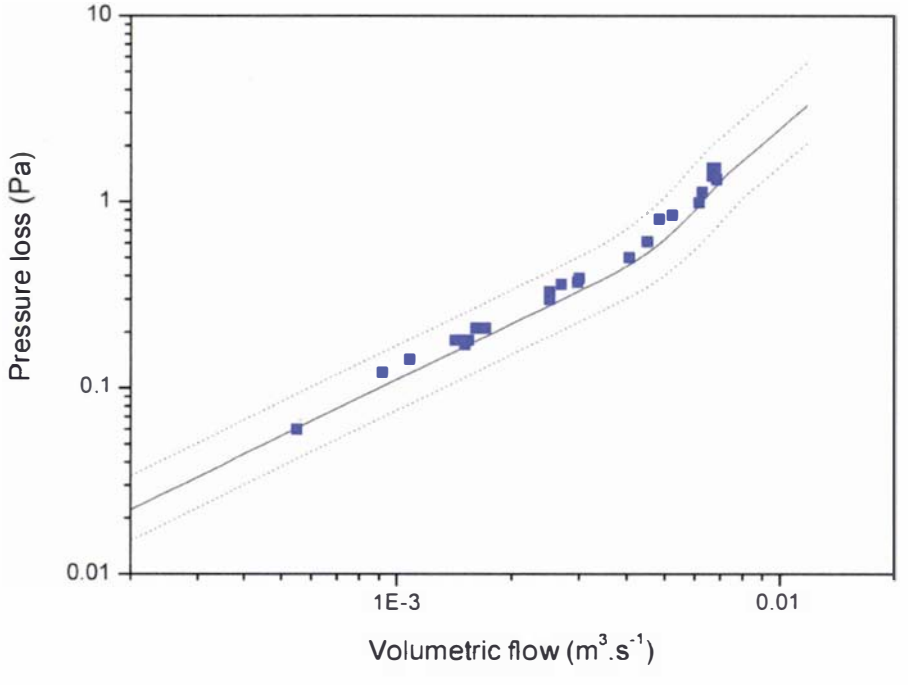

Figure 8-10 - Comparison of the measured pressure loss for a 0.023×0.31 m cardboard conduit constructed with vented cartons and that predicted using the laminar, Colebrook & Darcy-Weisbach equations. The solid line represents the predicted pressure loss using the measured dimensions and dotted lines represent the predicted pressure loss using the measured dimensions ±10%

8.2.2.2 Part B – Palletised packaging system

Figure 8-11 shows the relationship between pressure drop and the superficial velocity through the stacks as measured in the vertical flow rig. All data could be accurately represented by the power-law relationship given in Equation 8-5; regression results are given in Table 8-3. Flows are presented as superficial velocities which were defined as the ratio of fluid volumetric flow rate to the cross-sectional area for flow had there been no obstructions, i.e. an empty rig. For example, the pallet base area was 1.2 m^2 so for a volumetric flow of 0.024 $m^3.s^{-1}$ the superficial velocity would be 0.02 $m.s^{-1}$. Taking the blockage due to packaging to be 98.5% into account the actual fluid velocity in the channels could be estimated to have been approximately 1.6 $m.s^{-1}$.

$$\frac{\Delta P}{L} = au^b \qquad \textit{Equation 8-5}$$

Where:

a	=	Ramsin equation coefficient	$(kg.s^{(b-2)}.m^{-(b+2)})$
u	=	Superficial velocity	$(m.s^{-1})$
b	=	Ramsin equation exponent	

Table 8-3 - Results of fitting flow resistance data for kiwifruit packages to the equation $\Delta P.L^{-1} = au^b$

Carton Design	a	std error in a	b	std error in b	R^2
Standard	6470	180	1.61	0.01	>0.99
Prototype	1640	83	1.61	0.02	>0.99
Standard with plastic sheet	5480	350	1.58	0.03	>0.99

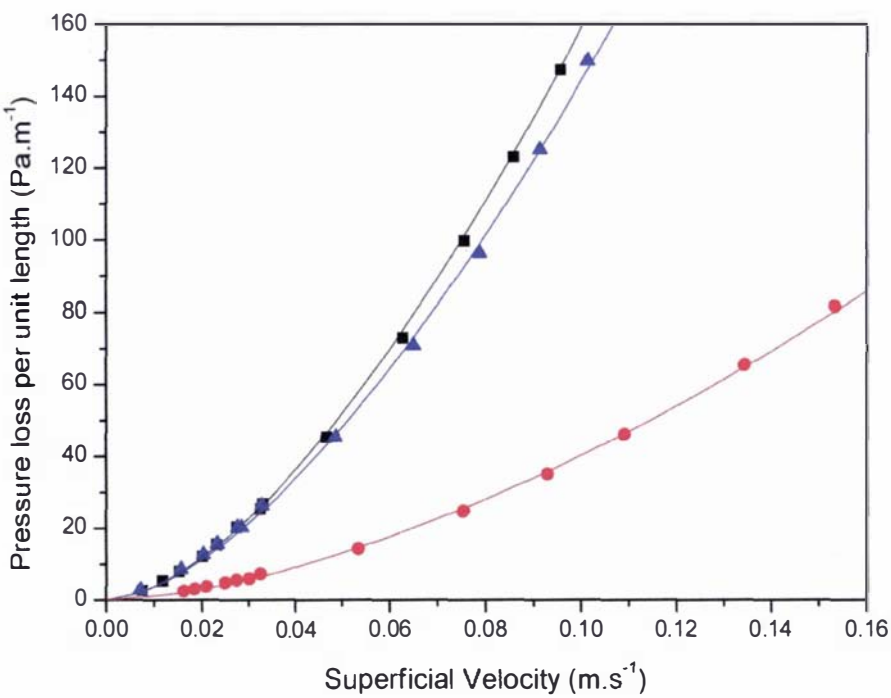

Figure 8-11 - The relationship between pressure loss and volumetric flow for a stack of standard kiwifruit cartons (■), of alternative prototype cartons (●) and a stack of standard kiwifruit cartons with two plastic sheets placed between layers (▲). The lines depict curves fitted assuming the relationship can be described by the function $\Delta P.L^{-1} = au^b$

The prototype kiwifruit carton showed a substantially lower flow resistance than the standard carton. For the prototype packaging system, the measured flow was the sum of the flow through the vertical channels, diffusive flow through the stack and flow between the stack and the walls of the rig. For the standard carton, the measured flow was the sum of the diffusive flow through the stack and the flow between the stack and the walls of the rig. Figure 8-11 also shows a comparison of the flow resistance curve measured for the standard carton with and without two plastic sheets placed between layers. Flows measured with the plastic sheets in place were considered to be due to flow between the cartons and the walls of the rig, or leakage within the system. The flow resistance was reduced slightly with the inclusion of the plastic sheets, although the difference was not significant, indicating flow was predominantly between the stack and the walls of the rig and there was minimal diffusive flow through the pallet stack with this packaging system. Flow through the vertical channels alone in the prototype packaging was estimated by subtracting the flow through the standard packaging system from the flow through the prototype packaging system.

Flows through the vertical channels within the prototype carton stack were predicted using the methodology outlined in Section 7.3.4.1, the geometry given in Table 8-2 and an absolute roughness value of 0.0003 m. Additional frictional losses were included to account for the sudden contraction and expansion at the channel entrance and expansion at the channel exit. These additional loss values were estimated from the contraction and expansion correlations of Perry & Green (1997), which gave K_{add} values of 0.7 at the channel entrance and 1.0 at the channel exit. Figure 8-12 shows the predicted flows using channel widths of 7.5 mm, 8.5 mm and 9.5 mm. Figure 8-12 also shows the flow through the channels in the prototype carton stack calculated from the measured data.

Comparison of the measured and predicted flows for the average measured hydraulic diameter of 8.5 mm showed good agreement. There was some disagreement at the higher flow rates, which is consistent with over-estimation of the K_{add} value. Over the range of pressure losses/velocities likely to be experienced in practice (<70 Pa), the predictions were insensitive to the K_{add} value as the resistance associated with the narrow channel was large in comparison to the resistance associated with the contractions/expansions.

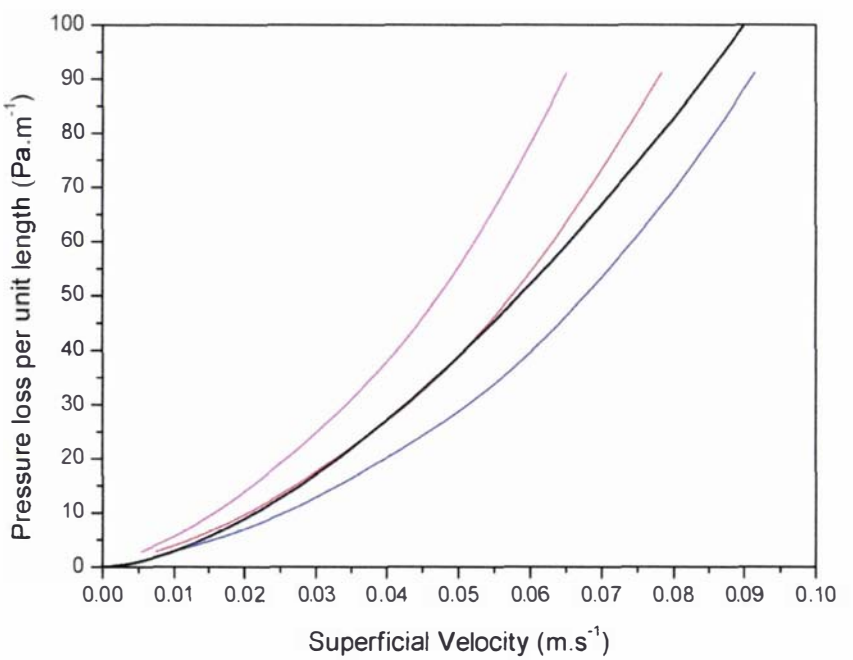

Figure 8-12 - The relationship between pressure loss and superficial velocity predicted for a stack of prototype kiwifruit cartons, using the laminar, Colebrook and Darcy-Weisbach equations and a channel width of 7.5 mm (-), 8.5 mm (-) and 9.5 mm (-). The black line depicts the flow in the channels calculated as the difference between the measured flow through a stack of standard cartons and a stack of prototype cartons

8.2.3 Conclusions

The laminar, Colebrook & Darcy-Weisbach equations were found to be suitable for predicting flow in distinct channels formed between palletised packages. An absolute roughness of 0.0003 m gave good predictions for all the manufactured conduits tested irrespective of the presence of vents in the conduit or the height of the carton. Further validation in a prototype packaging system incorporating vertical channels confirmed the suitability of the method. Flow in packaging systems where the channels could not be clearly defined were described accurately by a power-law relationship between pressure loss and fluid superficial velocity.

8.3 Type II channels

Many flow channels within marine transport systems cannot be approximated effectively by an equivalent hydraulic conduit. For example, defining a cross-sectional area, hydraulic diameter, roughness and length for flow through a stack of vented cartons would be a difficult task. For such less well defined flow channels, the methods used for Type I channels are inappropriate. In this situation, a specific correlation quantifying the flow resistance was required.

Flow resistance has typically been reported as a relationship between pressure loss and volumetric flow or superficial velocity, where superficial velocity is defined as the ratio of volumetric flow to the cross-sectional flow area if no obstruction was present (Section 8.2.2.2). Such relationships are referred to as pressure-flow relationships and can be written as the Ramsin equation (Equation 8-5). For geometries where the length parameter is not appropriate, such as flow through an orifice, the length was arbitrarily defined as one.

Section 7.3.4.2 discussed the integration of Type II channels into the model and calculation of the flow resistance from the pressure-flow relationship parameters. The following sections outline an experimental investigation of pressure losses caused by flow through vented horticultural packaging and report several specific pressure-flow correlations.

8.3.1 Horizontally vented packages

Several investigations of the pressure-flow relationships of horticultural products and packages have been performed and were discussed in Section 2.2.4.1. Most investigations offer specific relationships and some insight into trends; however, more recent studies have offered some generalised relationships based on Equation 8-5. The value of the Ramsin exponent for produce in vented cartons has been widely reported to be approximately 2. van der Sman (2002) reported that the relationship between the Ramsin coefficient and vent area (expressed as a fraction of the carton face area) could be characterised by a power law with an exponent of -1.5 (Equation 8-6). Generalising this equation for an unknown exponent and substitution into the Ramsin equation gives Equation 8-7.

$$a = cO^{-1.5} \qquad \textit{Equation 8-6}$$

$$\frac{\Delta P}{L} = cO^{d}u^{b} \qquad \textit{Equation 8-7}$$

Where:

c	=	Vent resistance coefficient	$(kg.s^{(b-2)}.m^{-(b+2)})$
d	=	Vent resistance exponent	
O	=	Ratio of vent area to face area	

This section reports on an experimental investigation that aimed to increase the understanding of pressure losses across stacks of vented horticultural packaging. Specifically the investigation aimed to determine the relative influence of fruit, vents and entrance and exit effects on the pressure flow relationship for palletised cartons. It also aimed to investigate the possibility of extrapolating a single carton's pressure-flow characteristics to predict the characteristics of a complete pallet stack. Apple cartons used for exports of 'Pink Lady' apples from Australia were used as the example packaging system.

8.3.1.1 Experimental method

Five full apple cartons in a horizontal line were used to investigate the effect of vent design on flow resistance and the relative importance of vent, internal space, entrance and exit losses. Four pressure taps were installed at the midpoint of the carton walls at each of 9 positions along the length of the line (Figure 8-13) as well as outside the end cartons to measure the total pressure loss. As illustrated in Figure 8-13, the line of 5 cartons gave a total of 4 vents internal to the stack (internal vents), 5 fruit spaces, and a single entry and exit vent. To ensure air flowed through the entire length of the set-up, care was taken to ensure vents were aligned and cling-film was wrapped around the line of cartons. The volumetric flow rate through the cartons was measured using rotameters (GEC-Elliot Process Instruments Ltd England, model Metric 10G and metric 24XG).

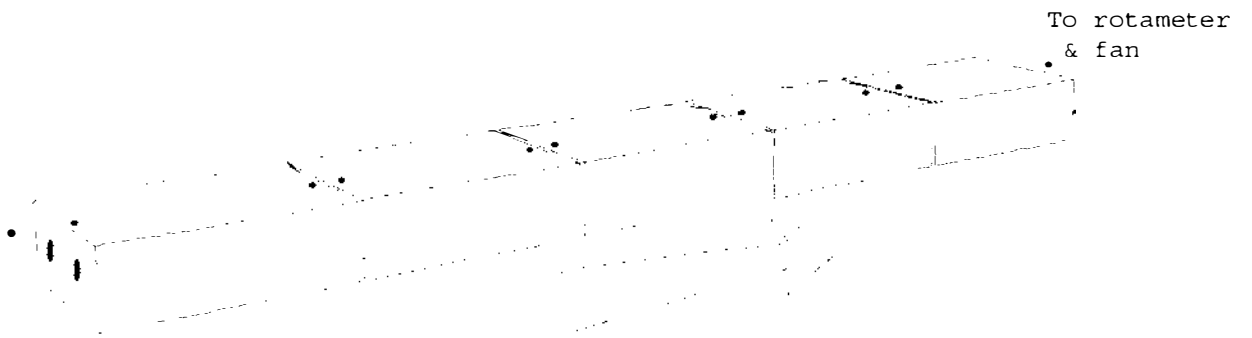

Figure 8-13 - Experimental set-up for measurement of pressure loss over a line of five apple cartons showing positioning of pressure taps (•)

Pressures were measured using a MKS 698A pressure transducer at each of the 10 positions relative to the atmospheric pressure upstream of the line of cartons for between three and eight airflow rates once steady state conditions had been established. Trials were conducted with five vent designs, with vent areas ranging from 0.8% to 6.7%. All trials were conducted at 2°C.

Figure 8-14 shows the carton dimensions and the vent positions used during the investigation. Three vent designs used one or two circular vents of 20 or 42 mm diameter to give 0.8%, 1.7% or 3.4% vent area, one had a rounded rectangular hand-hole (3.3% vent area) and one design used a combination of both circular and rectangular vents (6.7% vent area). The cartons were filled with apples (var Golden Delicious, count 98) arranged in two layers using moulded-pulp cardboard trays.

The horizontal flow resistance of ten full apple cartons stacked using the pattern shown in Figure 8-15 to form two layers of a pallet stack was also measured. The cartons were placed in a tunnel designed to tightly fit the stack and attached to a fan and orifice plate system to draw through a known volume of air. Pressures upstream and downstream of the stack were measured using the MKS transducer described above, at a minimum of 20 flow rates between 0.008 and 0.17 $m^3.s^{-1}$. Four carton designs were tested - one unvented and three vented, with vent areas of 1.7%, 3.4% and 6.7%.

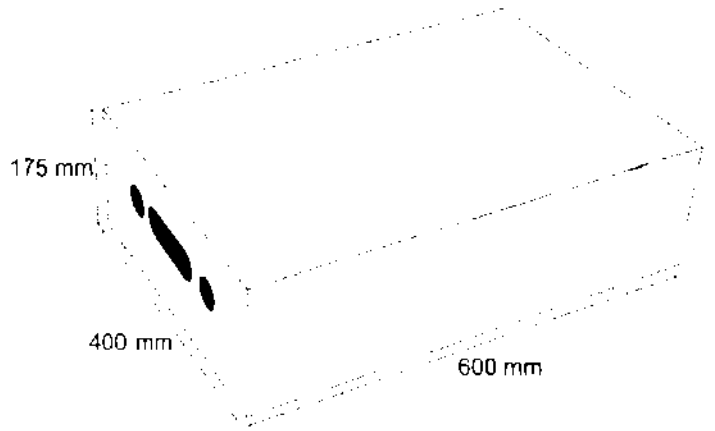

Figure 8-14 - Carton dimensions and vent positions used during the investigation of pressure losses across a line of cartons

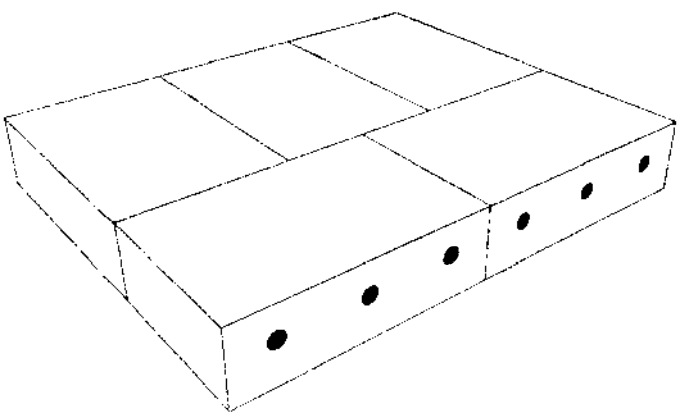

Figure 8-15 - Stacking arrangement of a layer in the double pallet layer of apple cartons used to test horizontal flow resistance

8.3.1.2 Results

For each vent design and flow rate, the pressure loss across each of the four internal vents, five fruit spaces, entry vent and exit vent were calculated from the 10 pressure measurements. Variation of pressure losses between each of the 4 internal vents and 5 fruit spaces were small, so average values were used for analysis.

Figure 8-16 shows the average measured pressure loss across internal vents and fruit spaces for each of the vent designs. Measured pressure losses over internal vents were much larger than across fruit spaces (e.g. fruit space pressure loss was approximately 30% of that for a vent with 6.7% open area, and 10% of that for a vent with 3.3% open area). The vent area was the primary factor affecting the loss profile; however, other effects such as placement of the vent relative to fruit position were also important as indicated by the relatively large difference between the profiles for 3.3% and 3.4% vent area designs. Figure 8-17 shows the measured pressure losses over the entry and exit vents.

Vent pressure loss data were fitted to Equation 8-7; regression results are given in Table 8-4. An excellent fit of the internal vent data was achieved. The quality of fit of the loss data for entry and exit vents was not as good, but gave significantly different vent resistance exponent values (d) indicating quite different flow characteristics. None of the data gave a vent resistance exponent of -1.5 as reported by van der Sman (2002), although the internal vent exponent was similar.

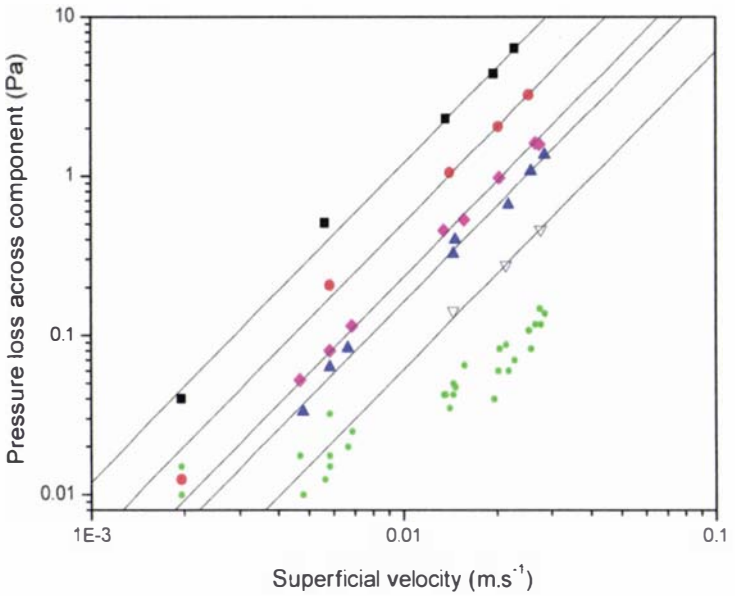

Figure 8-16 – The relationship between pressure loss and superficial velocity for horizontal flow through carton vents internal to the stack with 0.8% (■), 1.7% (●), 3.3% (◆), 3.4% (▲), 6.7% (▽) vent open area and fruit spaces (•). The lines depict fitted curves assuming the relationships can be described by the function $\Delta P = au^b$

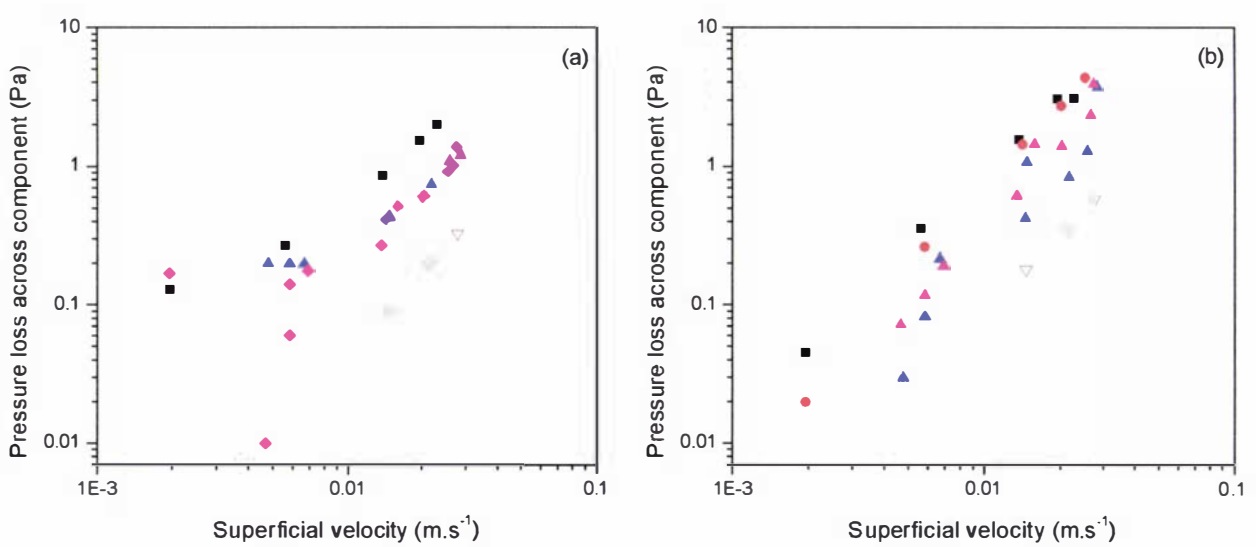

Figure 8-17 – The relationship between pressure loss and superficial velocity for horizontal flow through carton vents (a) at the stack entry and (b) at the stack exit with 0.8% (■), 1.7% (●), 3.3% (◆), 3.4% (▲), 6.7% (▽) vent open area

Table 8-4 - Flow resistance coefficients for carton vents based on the equation $\Delta P = cO^d u^b$

Vent Position	c	std error	d	std error	b	std error	R^2
Internal	8500	2800	-1.26	0.03	1.98	0.09	0.99
Entry	750	460	-0.66	0.05	1.6	0.16	0.94
Exit	13150	21200	-0.58	0.11	2.17	0.43	0.80

The pressure losses across double pallet layers of cartons with vent areas ranging from 1.7% to 6.7% were predicted and compared to experimental values (Figure 8-18). Predictions were made using Equation 8-7, Equation 8-8 and the curve-fitted coefficients.

$$\Delta P_{pallet} = \Delta P_{entry} + \Delta P_{vent} + 1.67\Delta P_{fruit} + \Delta P_{exit} \qquad \textit{Equation 8-8}$$

Where:

ΔP_{pallet}	=	Pressure loss across a pallet stack	(Pa)
ΔP_{entry}	=	Pressure loss across an entry vent	(Pa)
ΔP_{exit}	=	Pressure loss across an exit vent	(Pa)
ΔP_{vent}	=	Pressure loss across an internal vent	(Pa)
ΔP_{fruit}	=	Pressure loss across an internal fruit space	(Pa)

The coefficient of 1.67 in Equation 8-8 reflects that the cumulative fruit space across a pallet was 1.67 times the length of a single carton. Measured flow rates for unvented cartons (due to diffusive flow between cartons and between the cartons and the walls of the rig) were subtracted from the total flow rates to give an estimate of the flow through the vents only.

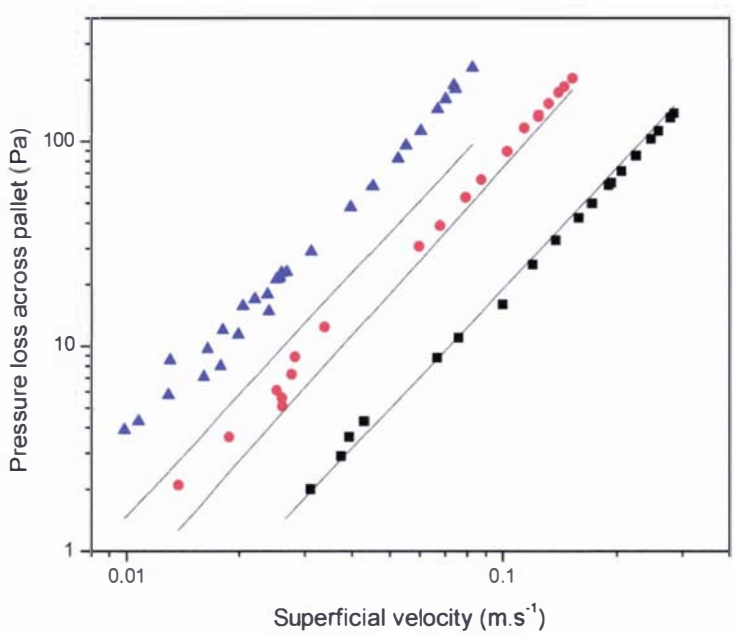

Figure 8-18 – The predicted (—) and measured relationships between pressure loss and superficial velocity for horizontal flow through a double layer of a pallet stack of apple cartons with 1.7% (▲), 3.4% (●) and 6.7% (■) vent open areas

Excellent agreement was found for the largest vent design, but the quality of fit deteriorated with decreasing vent size. The flow resistance was substantially underestimated for the smaller vent sizes, which was attributed to two factors. Firstly, misalignment of the vents. Accurate vent alignment became more difficult with decreasing vent size. Slight misalignment of the small vents caused a sharp reduction in the effective vent area leading to the increased flow resistance observed. The size of this effect diminishes with increasing vent size, consistent with the observed results.

The second cause of disagreement was poor estimation of the diffusive flow bypassing the vents along the walls or between cartons. For the 1.7% vent area cartons, just over 50% of the measured flow was estimated to flow through the carton vents, with the remainder assumed to be due to air flowing between the cartons and along the walls of the rig. The quantity of flow bypassing the vents may have been different for each vent design, as the rig required partial disassembly to change cartons. Predictions for cartons with a smaller vent area would be most affected by this uncertainty. The estimated flow through

the vents made up over 80% of the total flow for the 6.7% vent area cartons, so uncertainty in the diffusive flow would be less influential. In hindsight, blocking the vents and measuring the bypassing flow for each vent design would have led to an improved estimate of the flow through the cartons.

Figure 8-19 shows the calculated relative contributions of fruit spaces, internal vents, entry vents and exit vents to the total pressure loss across the double pallet layer for a carton with 3.4% vent area. Entrance and exit vents contributed approximately 60% of the total flow resistance.

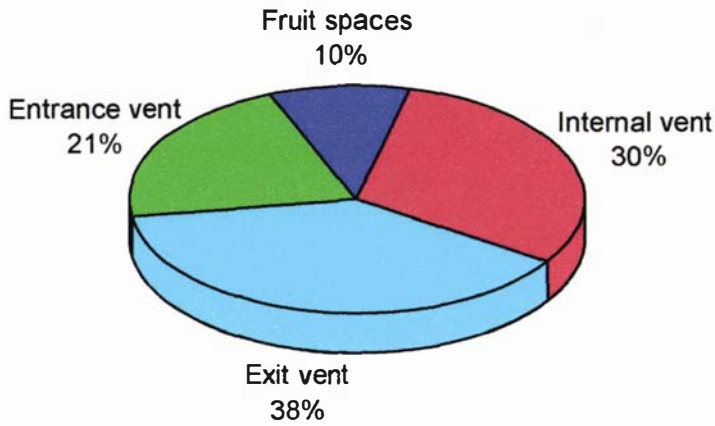

Figure 8-19 – Relative contributions of package components to total pressure loss across a stack of vented apple cartons with 3.4% vent open area

8.3.1.3 Conclusions

Pressure losses across vents in horizontal flow were much larger than losses within the internal fruit space in an apple carton for the range of vent sizes investigated. This is likely to be true in other horticultural applications as the vents reduce the cross-sectional flow area more than the fruit within the carton (that is, carton porosity is generally much higher than vent area). Losses over entry and exit vents were significantly different to internal vents, and contributed significantly to the total pressure loss across a pallet. The loss across the exit vent was greater than the entry vent, which is consistent with well known correlations for sudden flow contractions and expansions (Perry & Green, 1997).

The Ramsin coefficient was found to relate to the vent area by a power law, although the coefficient was significantly different to a previously reported value of -1.5 (van der Sman, 2002). The Ramsin coefficient for entry and exit vents had quite a different relationship to that for internal vents.

Measured flow resistances were found to be additive with losses over a pallet stack predictable from the pressure-flow characteristics of the individual carton, although these characteristics need to be measured for a specific carton design. Imprecise carton alignment could also add significant additional flow resistance for cartons with small vents.

8.3.2 Vertically vented packages

Despite vertical airflow being the standard configuration in transport systems, horizontal vent alignment has been the norm for horticultural packaging. Pressure flow relationships for flow through horticultural packages with vents designed for vertical flow are relatively sparse. Haas & Felsenstein (1987) graphically presented pressure-flow relationships for full and empty avocado cartons with vents designed for vertical flow. Vent areas ranged from 3.5 to 10.2% of the cross-sectional flow area. Smale *et al.* (2003b) measured pressure-flow relationships for a pallet of apple cartons with vents designed for vertical flow. Relationships were reported in the form of Ramsin equation coefficients. The effect of vent size,

stacking pattern and use of vented fruit trays were investigated. Smale *et al.* (2003b) also presented pressure-flow relationships for potatoes in bulk-stacked polypropylene and jute bags under vertical flow conditions.

8.3.3 Bulk products

Horticultural products may be stored in bulk bins for transport. In such systems the product essentially acts as a porous media. Chau *et al.* (1985) attempted to use the Ergun equation (Equation 8-9) to quantify pressure-flow relationships for bulk oranges of various sizes in a number of stacking arrangements. The Ergun equation assumes near spherical products and a large cross-sectional bed area in proportion to the product size.

$$\frac{\Delta P}{L} = K_1 \frac{(1-\varepsilon)}{\varepsilon^3} \frac{\mu u}{D^2} + K_2 \frac{(1-\varepsilon)}{\varepsilon^3} \frac{\rho u^2}{D} \qquad \textit{Equation 8-9}$$

Where:

ε	=	Bed porosity	
D	=	Fruit diameter	(m)
K_1	=	Ergun equation constant	
K_2	=	Ergun equation constant	

The equation constants were found to vary with fruit size and stacking arrangement. van der Sman (2002) predicted the airflow through bulk potatoes and oranges using the Ergun equation with standard values of the constants ($K_1 = 180$, $K_2 = 1.8$). The Ergun equation was found to accurately predict losses in the bulk products where the product diameter was sufficiently small in comparison to the cross-sectional flow area. Smale *et al.* (2003b) used the Ergun equation with the standard value of the constants to predict the bulk porosity of apples of two sizes and potatoes from the measured pressure-flow relationship. Comparison of calculated porosities to bulk porosities reported by Chau *et al.* (1985) showed good agreement.

From the evidence previously published, the Ergun equation with standard constants was considered sufficiently accurate to predict the pressure-flow relationship for beds of bulk products.

8.3.4 Miscellaneous geometries

Several other geometries were of particular importance to shipping systems. Correlations for flow through pallet bases and through perforated floors as used in most refrigerated vessels were required. Contractions, expansions, bends and T-junctions were also of interest.

Lindqvist (2000) investigated the pressure-flow relationships of wooden pallet bases both experimentally and numerically. Experimental results were reported in full. The reported experimental data was used to develop a relationship in the form of the Ramsin equation for flow through wooden pallet bases (Equation 8-10). The specific design of the pallet base may affect the pressure flow relationship; however, the relationship was considered sufficiently accurate given the simulated pallet base was of a design commonly used worldwide.

$$\frac{\Delta P}{L} = 0.762\, u^{1.93} \qquad \textit{Equation 8-10}$$

Several correlations for perforated screens of various designs were presented by Miller (1990); however, the correlations did not extend to the low flow areas expected for perforated floors (approximately 1 to

3% of the floor area). Perry and Green (1997) reported a relationship for perforated plates with square edged holes in an equilateral triangle spacing (Equation 8-11).

$$\dot{m} = CA_f\gamma\sqrt{\frac{2\rho\Delta P}{1-\left(\frac{A_f}{A_p}\right)^2}} \qquad \textit{Equation 8-11}$$

Where:

$\dot{m}$	=	Mass flow rate of fluid	($kg.s^{-1}$)
C	=	Orifice coefficient	
A_f	=	Total free area of holes	(m^2)
A_p	=	Total area of perforated plate	(m^2)
γ	=	Expansion factor	

The relationship was valid for a Reynolds number range of 400 to 20,000 (based on the properties of the holes) and pitch/diameter ratios from 2 to 5. As the fluid was considered incompressible, the expansion factor was unity. Using these values, the equation can be rearranged to the form of the Ramsin equation (Equation 8-12).

$$\Delta P = \frac{\rho\left(1-O^2\right)}{2C^2O^2}u^2 \qquad \textit{Equation 8-12}$$

Where:

O	=	Ratio of total hole area to total plate area

The orifice coefficient was presented graphically for a range of Reynolds numbers, pitch/diameter ratios and plate thickness/diameter ratios. For the pitch/diameter and plate thickness/diameter ratios expected for perforated floors, the orifice coefficient varied from 1.0 to 1.1; hence a value of 1.05 was considered sufficiently accurate. Whilst this relationship was not specifically developed for transport applications, it was considered sufficiently relevant to use unchanged.

Miller (1990) graphically presented a large number of correlations for contractions, expansions, bends and T-junctions of various geometries. Losses were presented as K_{add} values that generally varied with various flow ratios. To account for the additional frictional pressure losses due to expansions, contractions and turning flow geometries, analogies were drawn between the geometries within the transport system and the geometries presented by Miller (1990). For example, flow diverging from floor channels up through gaps between pallets of produce was assumed to behave similarly to a T-junction (Figure 8-20). Where necessary, the K_{add} values were determined using an assumed flow ratio, which could then be verified using the results of the simulation. For the example shown in Figure 8-20, the Q_3/Q_1 ratio would be estimated using the judgement of the operator and the validity of the estimates checked using the Q_3/Q_1 ratio predicted. If the estimate was in error, the predicted ratio would then be used as an improved estimate. Perry and Green (1997) also report K_{add} values for various geometries; however, often a solitary value or range of values are given for each geometry making value selection less precise.

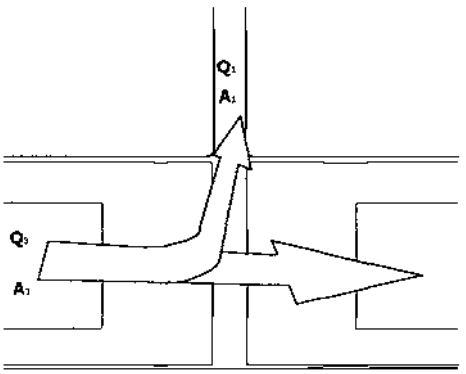

Figure 8-20 – An example of a turning flow geometry in a marine transport system. Q_i and A_i represent the channel flow rate and area respectively

Overall, for the range of miscellaneous geometries likely to be experienced in transport systems, flow resistance relationships available in the literature were considered adequate and no measurement or development of specific new relationships was undertaken.

8.4 Air interchange

Air flowing in transport or storage systems may remove heat from vented horticultural cartons by two major mechanisms: displacement of warm in-package air with cool external air and/or convective/conductive heat transfer through the package wall. Displacement of warm air may be caused by air flowing through the carton (ventilation) or by interchange of package and external air through the vents on a single face of the carton (interchange). Air flowing past open vents may entrain air from inside the package, accelerating the rate of interchange. These modes are depicted graphically in Figure 8-21. Analogously, moisture transfer via diffusion through the packaging material, air ventilation and air interchange affects the humidity within the package.

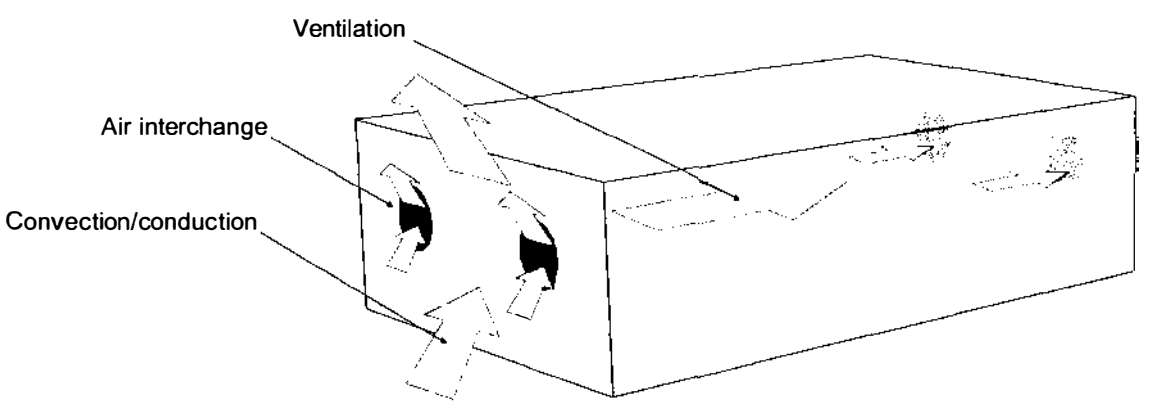

Figure 8-21 – Modes of heat transfer between a vented package and surrounding air during storage/transport

An airflow model designed with prediction of heat and mass transfer rates in mind, should estimate the flow quantities required to predict heat and mass transfer caused by each of these modes. Methods to predict flow rates and velocities were considered sufficient for the first two modes; however, the final mode required the rate of interchange to be established. This section outlines an investigation of the relative importance of air interchange as a mode of heat transfer and the effect of flow conditions past the vent, vent size, shape and location on the air interchange rate.

8.4.1 Experimental method

A novel technique was employed to measure the rate of gas interchange between a package and its environment. The gas composition inside a package was altered by flushing with nitrogen and the subsequent return of oxygen concentration to ambient conditions was monitored. The interchange rate was calculated from the rate of change of oxygen concentration (ASTM, 2000).

GS Oxygen sensors (GS Oxygen Sensor KE-25, Japan Storage Battery Co. Ltd. Kyoto, Japan) and a Eltek Squirrel data-logger (1000 series, Eltek Ltd. Cambridge, England) were used to measure O_2 concentration at 1-second intervals at three points within the package. Sensors were calibrated at 0% and ambient oxygen conditions, and adjusted in-situ using the equilibrium response at the ambient condition.

Vents on all but one face of the package were taped closed and the package walls were coated in plastic tape to ensure no ventilation occurred and to reduce the diffusion of oxygen through the package walls. The moulded-pulp cardboard trays used for arranging fruit in layers were replaced with a wire mesh to improve mixing of gas within the package. Replacement of the trays may have affected the rate of interchange but was considered necessary as good mixing inside the package was the basis for calculation of the rate of interchange. The package was placed at the top of a channel, which was varied in width from 0.018 to 0.075 m. A fan was placed above the channel and air drawn up past the open vent (Figure 8-22).

The air velocity past the vent was varied from 0 to 7 $m.s^{-1}$ and measured using a hot wire anemometer (TSI model 8355-M-GB). The number of vent holes (1 to 6), open area (0.9 to 6.8 %) and the vent aspect ratio (0.3 to 3.2) were all varied. The package was filled with fruit (var. Granny Smith, count 60) arranged in three layers and the carton dimensions were 0.31 × 0.20 × 0.40 m (W×H×L). The experiment was conducted at ambient temperature.

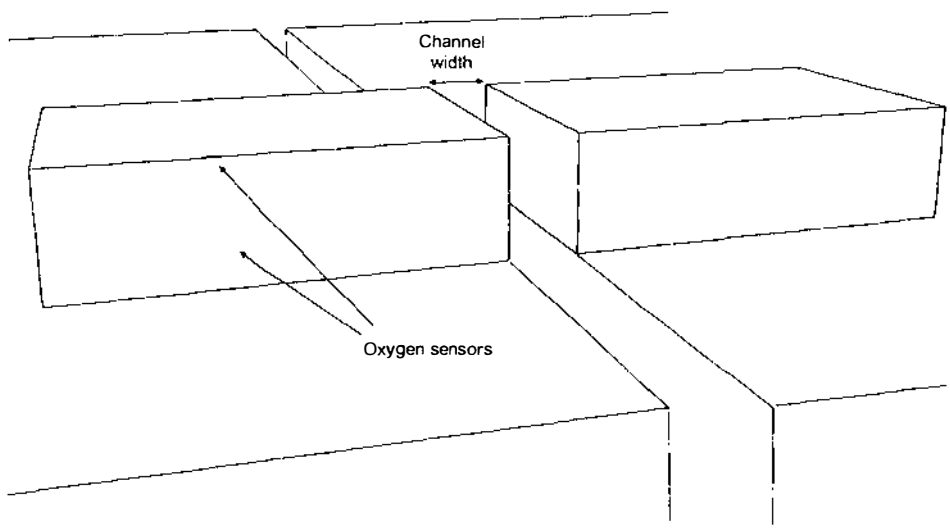

Figure 8-22 - Experimental set-up to measure air interchange through vents

8.4.2 Results

The response of each sensor was converted to a concentration driving force, log transformed, plotted against time to assess the linearity, and the gradient used to determine the interchange rate (ASTM, 2000). There were some runs for which all of the sensors did not agree or results were not linear (13 of 101 total). These were not included in further analyses. Examples of a linear and non-linear decay curve are given in Figure 8-23. Sensor disagreement or non-linearity was thought to be caused by the establishment

of a stable airflow pattern within the carton, which in turn led to violation of the assumption of perfect mixing inside the carton.

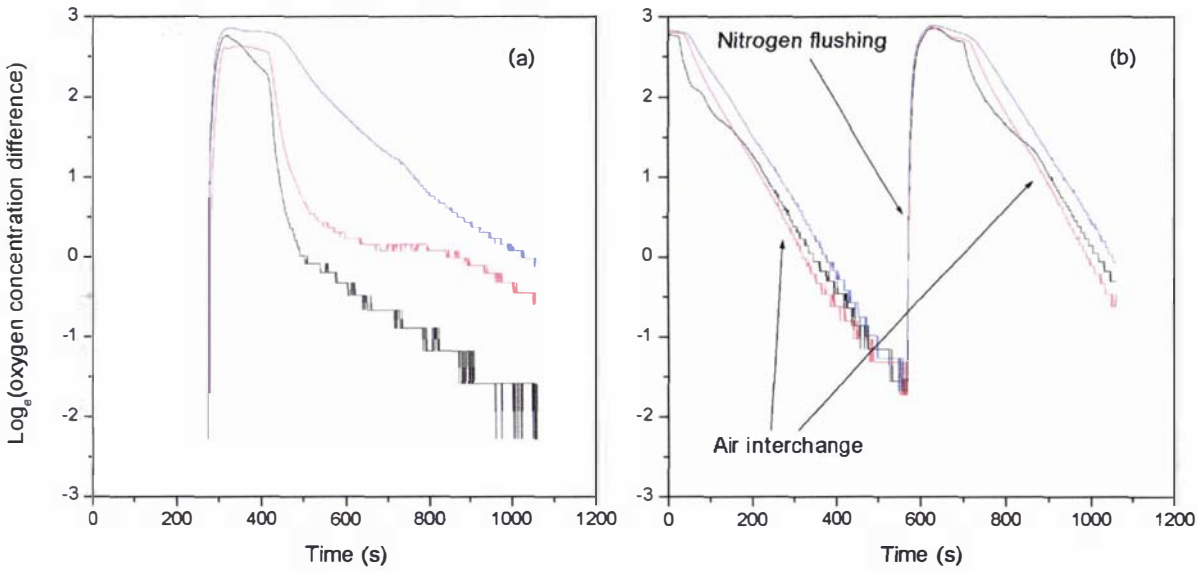

Figure 8-23 – Examples of (a) non-linear and (b) linear oxygen concentration difference decay due to air interchange through vents as measured using three oxygen sensors

A run with all vents taped closed was performed to determine the level of O_2 diffusion through the package wall and from within the fruit. The measured interchange rate was 1.1×10^{-7} $m^3.s^{-1}$, which was insignificant in comparison to the interchange rates measured for vented packages.

Both velocity and Reynolds number of the flow past the vent(s) were investigated as possible predictors of interchange rate. Reynolds number was calculated using the velocity of the flow past the vent and the channel width as indicated in Figure 8-22. Regression results indicated velocity was a superior predictor of the interchange rate ($R^2 = 0.97$) than Reynolds number ($R^2 = 0.81$) (Figure 8-24)

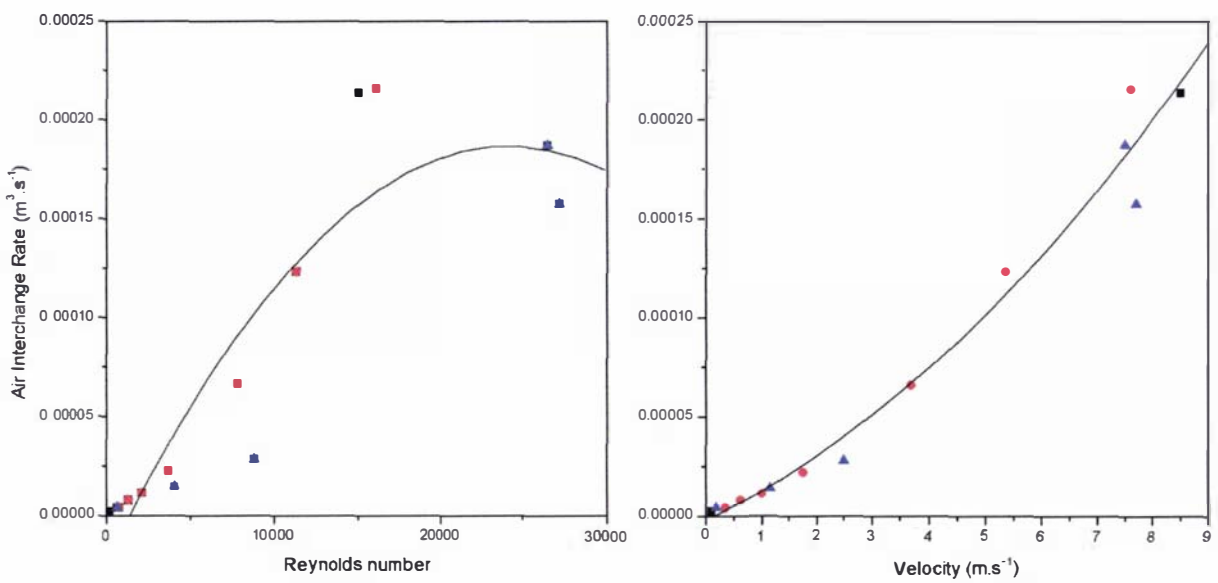

Figure 8-24 - Measured air interchange rate for a carton with a 0.9% open vent area and channel widths of 25 mm (■), 30 mm (●) and 50 mm (▲) using (a) Reynolds number and (b) velocity as the predictor

To assess the contribution of air interchange to the overall cooling of a package, the energy removed by air interchange was calculated and compared to the energy removed by convection and conduction in series through the cardboard wall. Results were based on a 2°C temperature difference between package and external air; however, as both modes of heat transfer are proportional to temperature difference, the relative contributions are constant regardless of temperature difference. The parameters used for calculation of the convection/conduction heat transfer rate are given in Table 8-5, and the heat transfer correlation for the external convective heat transfer coefficient used was Equation 8-13 (Geankoplis, 1993).

$$Nu = 0.0366\, Re^{0.8}\, Pr^{1/3} \qquad \textit{Equation 8-13}$$

$$Nu = \frac{h_s D}{\lambda} \qquad \textit{Equation 8-14}$$

$$Pr = \frac{C_p \mu}{\lambda} \qquad \textit{Equation 8-15}$$

Where:

Nu	=	Nusselt number	
Pr	=	Prandtl number	
h_s	=	Surface heat transfer coefficient	($W.m^{-2}.K^{-1}$)
D	=	Characteristic dimension	(m)
λ	=	Thermal conductivity	($W.m^{-1}.K^{-1}$)
C_p	=	Specific heat capacity	($W.kg^{-1}.K^{-1}$)

Table 8-5 - Parameters used for prediction of conductive/convective heat transfer through a carton face

Parameter	Value
Face area	0.06 m^2
Cardboard thermal conductivity	0.065 $W.m^{-1}.K^{-1}$
Cardboard thickness	0.006 m
Natural convection heat transfer coefficient (inside the carton)	6 $W.m^{-2}.K^{-1}$

Figure 8-25 compares the two mechanisms of heat transfer for a package with 3.6% open area, and illustrates the importance of air interchange at velocities expected during refrigerated transport (generally >0.5 $m.s^{-1}$). The proportion of total heat transferred by air interchange increases with increasing velocity, as the heat transferred by conduction/convection is limited by natural convection inside the package and conduction through the cardboard. As expected, a larger open area caused an increase in the interchange rate (Figure 8-26).

Where there were multiple or non-circular vents, vent alignment affected the interchange rate. The interchange rate was greater for multiple vents aligned vertically rather than horizontally (Figure 8-27). This increase could be due to a pressure difference between the lower and higher vents causing a net flow in the lower and out the higher vent. Similarly, the interchange rate was higher when the vent's longest axis was parallel to the external flow direction (Figure 8-28).

Where the vents were circular and arranged horizontally, there was no evidence that the number of vents affected the interchange rate (Figure 8-29).

As the interchange rate was found to vary depending on a large number of variables including the vent size, position and shape; generalising the data to give a relationship between interchange rate, vent characteristics and air velocity was not possible with the data available. Much more detailed experimental studies, or possibly CFD simulations are required before quantitative relationships between interchange rate and vent design can be formulated.

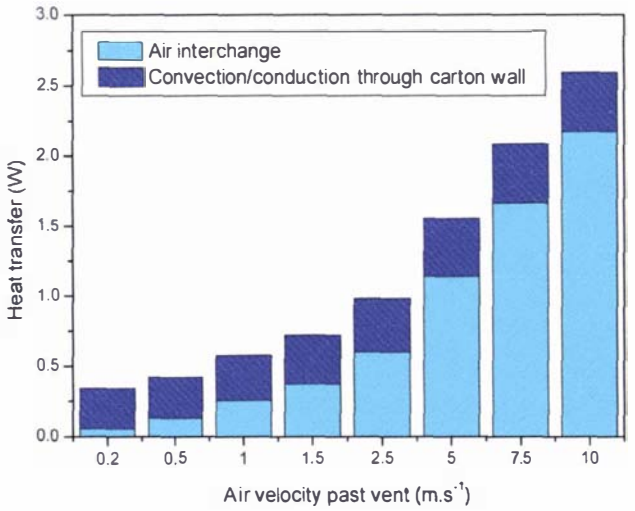

Figure 8-25 – Heat transfer rate by air interchange & convection/conduction through the face of a vented package (3.6% open vent area, 2°C air temperature difference)

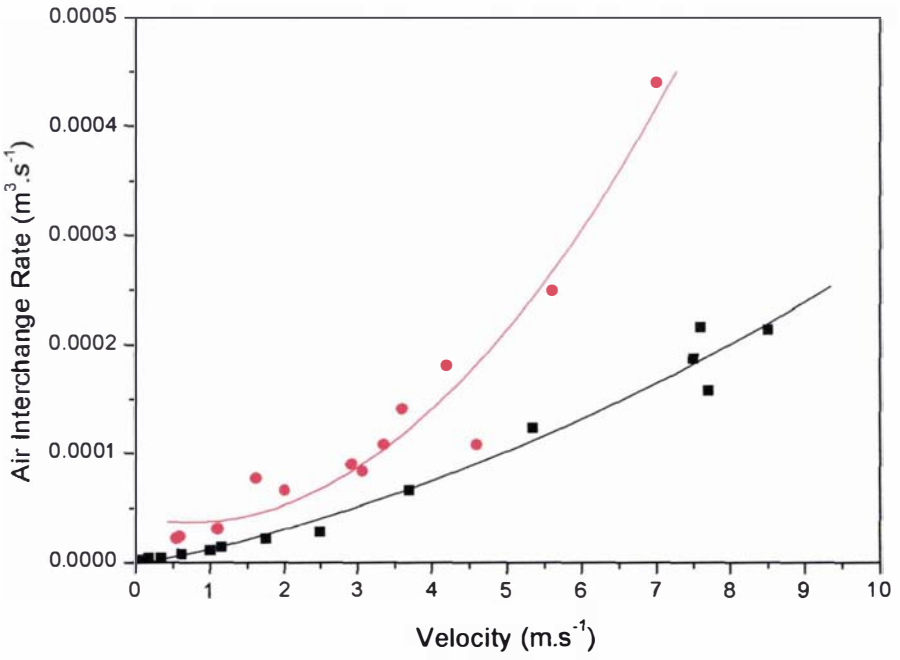

Figure 8-26 – Measured air interchange rate for a carton with a single vent making up an open vent area of 0.9% (■) or 3.1% (●)

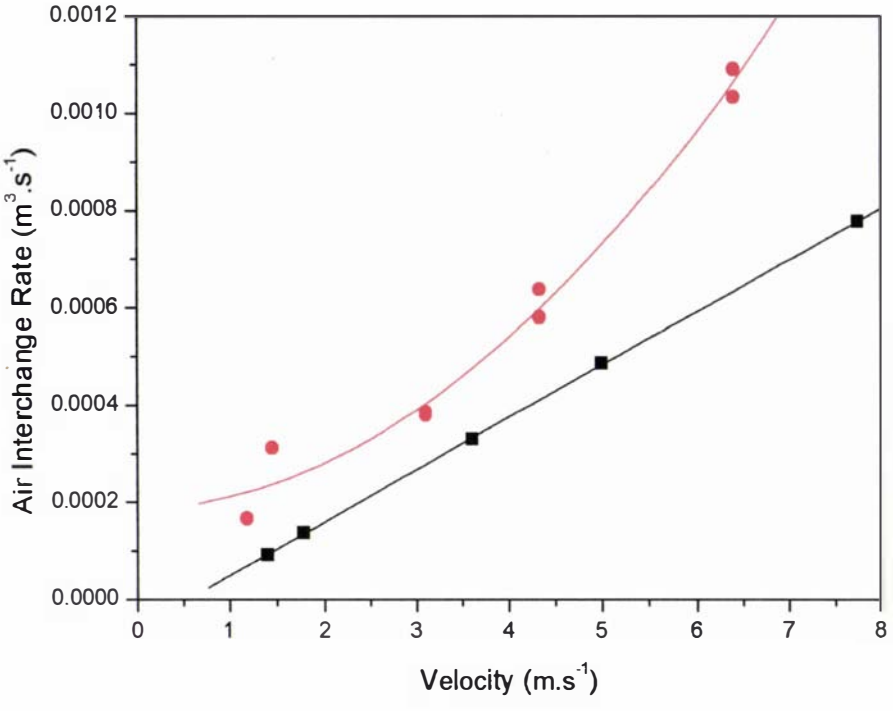

Figure 8-27 – Measured air interchange rate for a carton with 2.3 % open vent area made up of two horizontally aligned vents (■) or two vertically aligned vents (●)

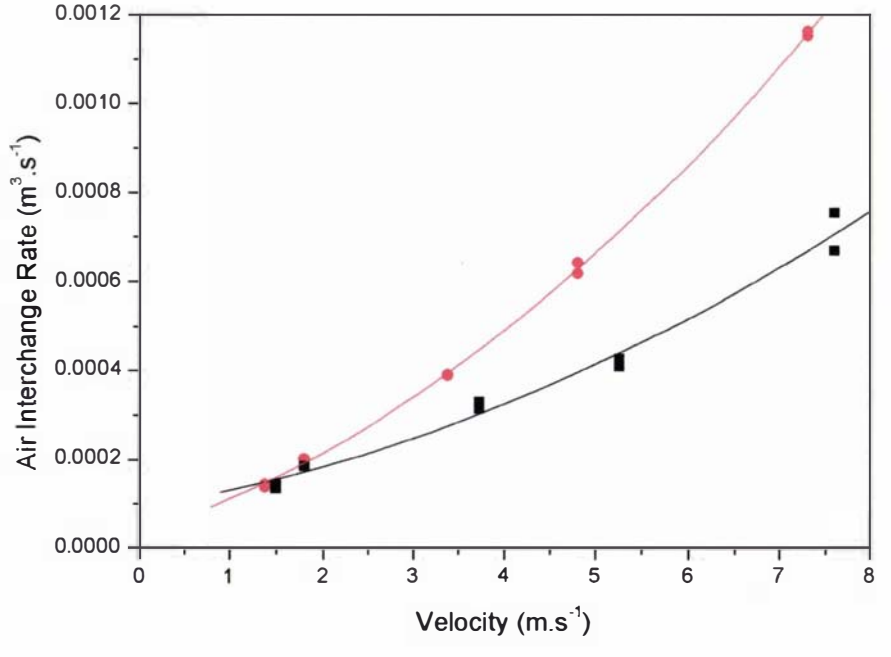

Figure 8-28 – Measured air interchange rate for a carton with 3.6 % open vent area made up of one rectangular vent with its long axis perpendicular (■) or parallel (●) to the flow direction

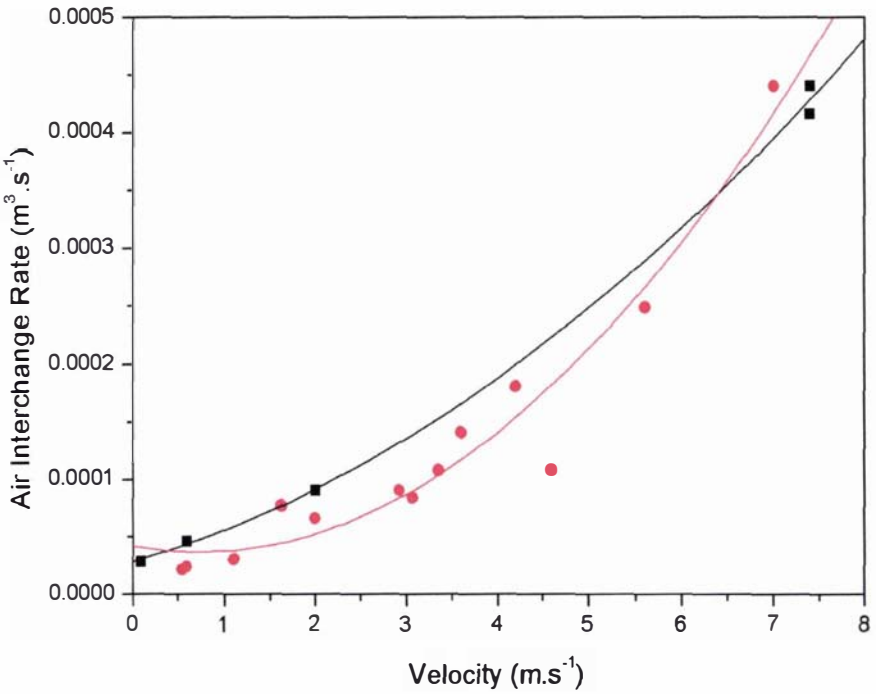

Figure 8-29 – Measured air interchange rate for a carton with three small horizontally aligned vents (■) or one large vent (●) making up 3.4% and 3.1% open vent areas respectively

8.4.3 Conclusions

The measurement technique employed to measure air interchange between a vented horticultural package and its environment appeared to give valid results. The measured rates of air interchange indicate that it can be an important mode of heat transfer in marine transport systems. A large number of variables were found to affect the air interchange rate including the vent open area, their placement on the package face and their aspect ratio. Results indicated that velocity was a superior predictor of interchange rate than Reynolds number. As the interchange rate was affected by a large number of variables, it was difficult to develop a relationship to predict air interchange rate. Further, more detailed investigations of air interchange are required to develop a better understanding of the phenomenon.

8.5 Conclusions

Section 7 presented the mathematical basis of a resistance network model, which required a relationship between the flow resistance and flow rate for each flow channel. Sufficient flow resistance data has been presented in this section to enable the use of the airflow model. The well-known Darcy-Weisbach, laminar, and Colebrook equations provide a method for estimating flow resistance of many of the flow channels in transport systems. The method was tested and found to be suitable for predicting the flow resistance of rectangular conduits formed by cardboard packaging. The uncertainty in channel dimensions outweighed all other sources of variability.

An experimental investigation of the flow resistance of horizontally vented cartons showed pressure losses across vents were much larger than losses within the carton over the range of vent sizes investigated. Losses over entry and exit vents were significantly different to vent internal to the stack. The loss at the exit vent was greater than the entry vent, which was consistent with well known correlations for sudden flow contractions and expansions. The Ramsin coefficient was found to relate to the vent area by a power law, although the calculated coefficient was significantly different to a

previously reported value. The Ramsin coefficient for entry and exit vents had quite a different relationship to that for internal vents.

The measured flow resistances of vented packages were found to be additive with losses over a pallet stack predictable from the pressure flow characteristics of the individual carton, although these characteristics need to be measured for a specific carton design. Imprecise carton alignment could also add significant additional flow resistance for cartons with small vents.

Air interchange between a vented horticultural package and its environment was investigated experimentally. A measurement technique was successfully developed to measure the rate of air interchange, with measured rates indicating that it can be an important mode of heat transfer in marine transport systems. A large number of variables were found to affect the air interchange rate, therefore a relationship to predict air interchange rate could not be developed.

Part IV
Model Validation and Scenario Testing

A mathematical model is worthless unless there is confidence that the model accurately predicts the behaviour of the real system. Confidence in a model is generally built through validation, by comparison of predicted quantities to quantities considered accurate; be they measured experimentally or calculated analytically.

In the next 4 chapters, specific model implementation and validation is presented for a number of test cases. Airflows were predicted and compared to data measured in a 40' refrigerated container, two differently configured refrigerated holds and data measured by Lindqvist (2000) in a laboratory test rig designed to simulate a refrigerated hold. Comparison of predicted pressures, velocities and temperatures with measured values are presented.

In addition, a number of scenarios were investigated. In these scenarios, model inputs were altered and the resulting predicted flows analysed. The purpose of these scenarios was twofold: to investigate the sensitivity of the model to uncertainties in input data and to assess the implications of altering key operational and design variables.

All simulations were carried out on a desktop PC: Pentium III 1000 MHz, 256 MB RAM, Microsoft Windows 2000.

9 NTNU Laboratory Model

9.1 Introduction

All of the descriptions of the experimental work and the experimental data given in this section are taken from Lindqvist (2000).

Lindqvist (2000) made use of a full-scale laboratory test rig located at the Norwegian University of Science and Technology (NTNU) to investigate airflow within refrigerated holds (Sections 2.2.4 and 2.3.3.2). Measured static pressure data from the test rig were reported in tabular form. Through comparison of predicted and published static pressure data for a number of experimental runs, the accuracy of the airflow model was tested. As these sets of data were collected under controlled conditions, they were not subject to many of the sources of variability found in real systems. As such, they provided an excellent test of the airflow model. Alongside this, the sensitivity of predictions to the K_{add} value used for turning flows as well as the flow resistance of the perforated floor were also investigated.

9.2 System description

The rig was described as containing 18 pallets, arranged in three columns, six rows deep with a standard spacing of 0.02 m between each pallet (Figure 9-1 and Figure 9-2). Pressure taps were installed throughout the test rig, and static pressures measured throughout a series of 13 tests.

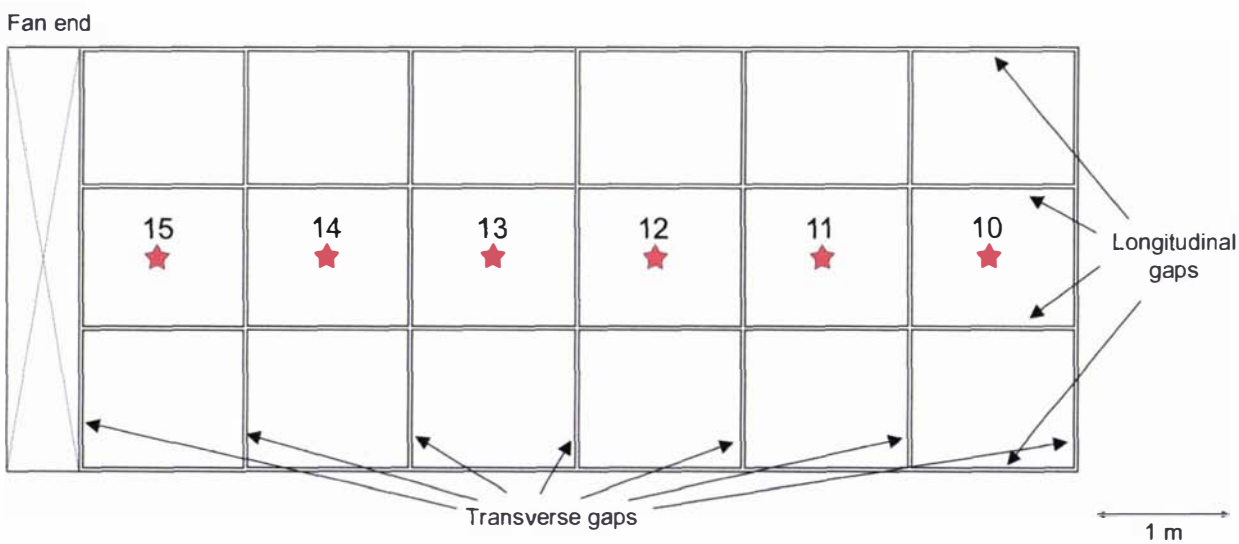

Figure 9-1 - Plan view of the laboratory test rig used by Lindqvist (2000) showing pallet arrangement and location (and original numbering) of the pressure taps in the ceiling of the rig (★). Pallets and gaps are drawn to scale; pallets measured 1.0 × 1.2 m and were spaced with 0.02 m gaps

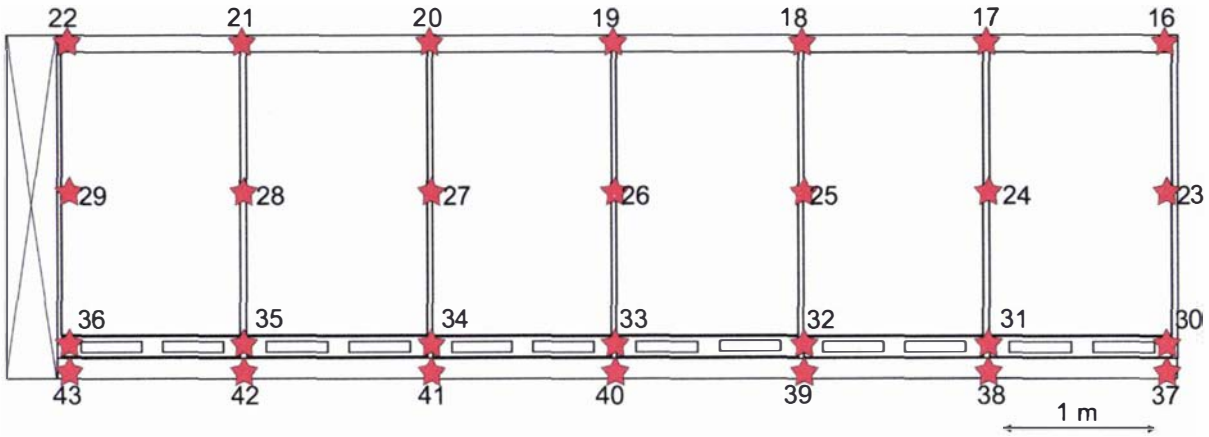

Figure 9-2 - Elevation view of the laboratory test rig used by Lindqvist (2000) showing pallet arrangement and location (and original numbering) of the pressure taps in the side wall of the rig (★). Pallets and gaps are drawn to scale; pallets measured 1.0 x 1.2 m, were spaced with 0.02 m gaps and the pallet bases were 0.145 m high

Pallets within the rig were constructed from used, empty banana cartons. Vents on the cartons were taped closed to simulate more closely the conditions experienced in practice, where a plastic liner effectively blocks the vents. In addition, cardboard sheets were placed between layers of cartons to eliminate any vertical flow through the pallets, which was considered to have only a minor influence on the overall airflow pattern.

The configuration of the rig was altered for each test series to investigate the effect on airflow distribution. Some tests were conducted with the air introduced below a perforated floor, whilst in others a slot above a flat floor was used - making use of the pallet bases as a plenum. Lindqvist (2000) investigated two pallet orientations (short end facing the fan end and long end facing the fan end) as well as two interventions: a perforated board to cover the pallet gaps near the fan end and solid boards and foam rubber to cover the longitudinal pallet gaps. In this work, three test series as presented by Lindqvist (2000) were used as test cases for the FlowSim model: series 8 (flat floor), series 5 (perforated floor) and series 9 (flat floor plus boards blocking the longitudinal gaps). All three series used the same pallet orientation. For each of the three series, measured static pressures were reported for three air circulation rates (2500, 3500 and 4400 $m^3.h^{-1}$). The following sections present the model implementation and simulation results for each of the cases including comparison with measured results.

9.3 Flat floor – test series 8

This test series was conducted with a flat floor, making use of the pallet bases as an air duct to distribute air under the simulated cargo. The under-floor air delivery duct was sealed and air was delivered through an opening above the floor. Wooden sheets were used to cover the perforated floor. The pallets were oriented with their longest dimension parallel to the main flow direction and there were no interventions (Figure 9-1 and Figure 9-2).

9.3.1 Flow channel definition

The vertical flow channels within the container were classified into one of three categories: between a pallet and the wall of the rig, between two or more pallets or vertically through a pallet. Channels formed between the wall of the rig and a pallet, and between two pallets were both treated as Type I channels with an absolute roughness of 0.0003 m. This roughness value was considered sufficiently accurate for the wooden walls of the rig given the relative insensitivity of the method to the roughness value (Section 8.2). A uniform spacing between pallets and between pallets/walls of 0.02 m was assumed. Flow

vertically through the pallets was assigned an arbitrarily high flow resistance due to the cardboard sheets placed between layers (Equation 9-1).

$$\beta_n = 1.67 \times 10^{12}$$

$$\Delta P = \beta_n \frac{1}{2} \rho u^2 \approx 1 \times 10^{12} u^2 \qquad \textit{Equation 9-1}$$

Where:

β_n	=	Flow resistance of channel n	
ρ	=	Fluid density	($kg.m^{-3}$)
ΔP	=	Pressure loss	(Pa)
u	=	Superficial velocity	($m.s^{-1}$)

The channels adjacent to the corners of pallets were defined as Type I channels with dimensions as shown in Figure 9-3. Hence, the dimensions of the cross-section of a vertical channel between pallets were either 0.02 m × 0.8 m (1.0 m face) or 0.02 m × 1.0 m (1.2 m face).

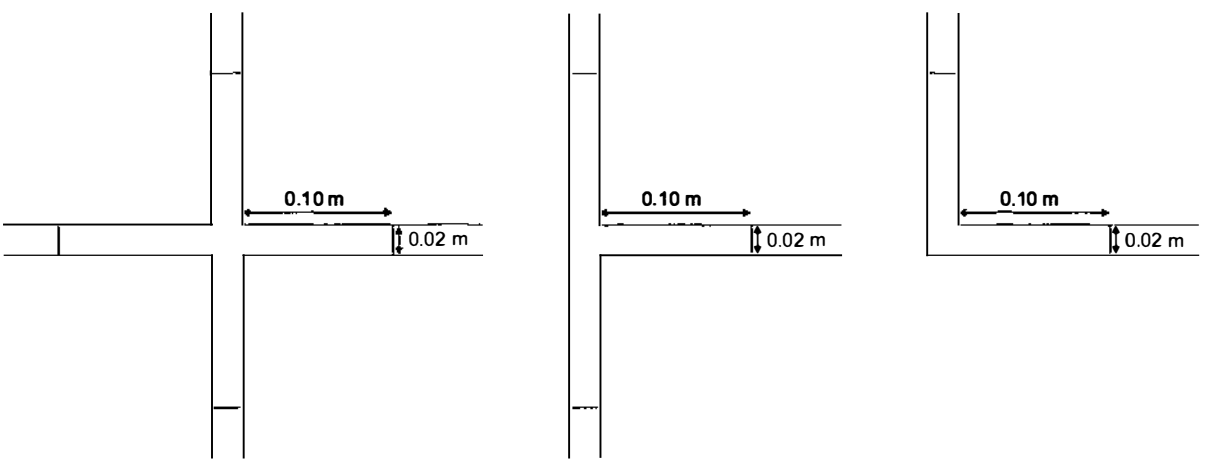

Figure 9-3 – Plan views of the boundaries of the three Type I vertical channels defined at the corners of pallets within the laboratory test rig (a) 'X' corners, (b) 'T' corners and (c) 'L' corners

The horizontal flow paths near the floor were classified into one of two categories: through a pallet base, or between a pair of pallet bases. Channels between pallet bases were modelled as Type I channels (0.02 m × 0.145 m), with an absolute roughness value of 0.0003 m. Flow through the pallet bases was modelled using the correlation presented in Section 8.3.4 (Equation 8-10).

Horizontal flow paths near the middle of the pallet height were classified in of one of two categories: through a pallet, or between a pair of pallets. Flow channels between pallets were modelled as Type I channels (0.02 m × 1.8 m), with an absolute roughness value of 0.0003 m. Horizontal flow channels through the pallets were assigned an arbitrarily high flow resistance (Equation 9-1) as there were no open horizontal vents in the cartons.

The uppermost horizontal flow channel was formed between the ceiling of the container and the top of the cargo. The clearance between pallets and rig ceiling was calculated from the dimensions given to be 0.12 m. These flow channels were treated as Type I channels with an absolute roughness of 0.0003 m.

Nodes were positioned in a rectangular grid at points of channel intersection: three cross-sections vertically, thirteen columns down the length and seven rows across the width of the rig (Figure 9-4 and Figure 9-5). The nodes adjacent to the inlet were connected to a single inlet fixed pressure node and the nodes adjacent to the outlet connected to a single outlet fixed pressure node. Singular inlet and outlet

fixed pressure nodes were used as velocities across the width of the air supply were found to be relatively uniform by Lindqvist (2000). Figure 9-6 shows a 3-dimensional illustration of the flow network.

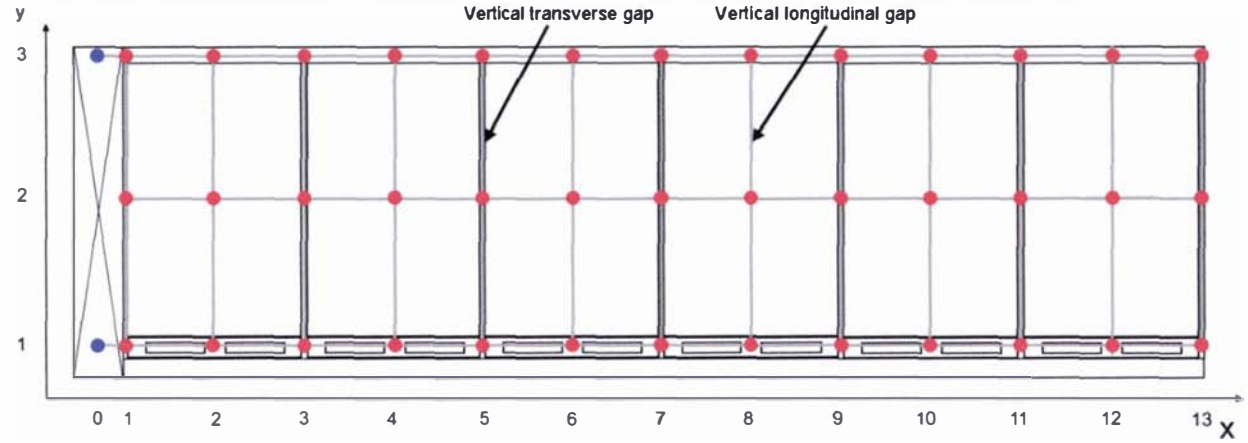

Figure 9-4 - Elevation view of the test rig loaded with 18 pallets showing a horizontal cross-section of the flow resistance network. Blue circles represent fixed pressure nodes, red circles represent unknown pressure nodes, and grey cylinders represent flow channels

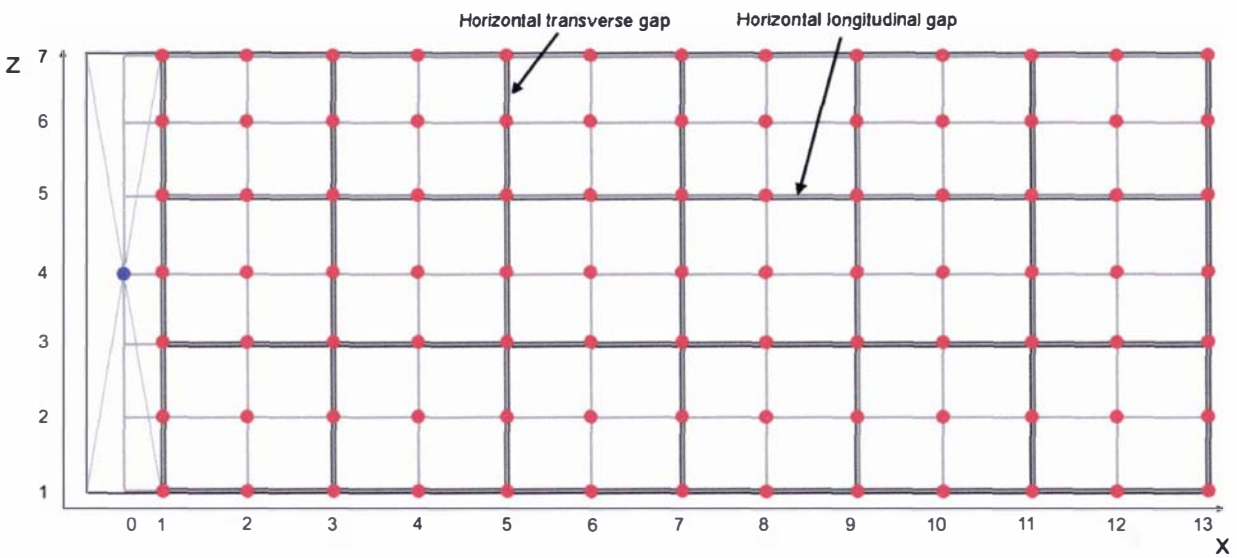

Figure 9-5 - Plan view of the test rig loaded with 18 pallets showing a vertical cross-section of the flow resistance network. Blue circles represent fixed pressure nodes, red circles represent unknown pressure nodes, and grey cylinders represent flow channels

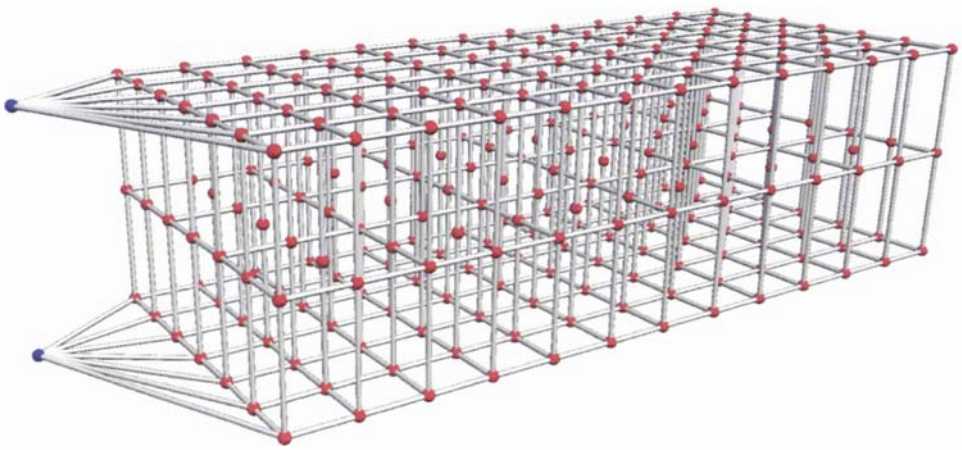

Figure 9-6 - Three-dimensional representation of the flow resistance network approximation of the test rig loaded with 18 pallets. Blue circles represent fixed pressure nodes, red circles represent unknown pressure nodes, and grey cylinders represent flow channels

As the air inlet and outlet of the rig were horizontal; vertical flows inside the rig required the air to turn corners. To include the frictional effect of turning flow, four turning geometries were considered. Each geometry was modelled as a standard fitting and assigned a K_{add} value from Miller (1990) or Perry & Green (1997). Area ratios were calculated using the square of the hydraulic diameters and flow ratios were estimated from expected flow patterns and checked using simulation results. Sharp bends with dividing flow (Figure 9-7a) as experienced by flows transitioning from horizontal channels in the pallet base level to vertical transverse channels were modelled as T-junctions (90° dividing T-junction, $A_1/A_3 = 0.1$, $Q_1/Q_3 = 0.2$, $K_{add} = 2.5$ - Miller). Where flows were able to make a less sharp turn (Figure 9-7b), such as in the elongated longitudinal gaps running the length of the rig, the losses were modelled as a rounded bend (Standard 'L' bend, $K_{add} = 0.8$ - Perry). Flows turning a sharp bend without dividing or combining flows (Figure 9-7c), such as at the end of the rig opposite the fan end, were modelled as an elbow and a contraction (90° square bend and a contraction $A_2/A_1 = 0.1$, $K_{add} = 2$ - Perry). Flows entering the ceiling headspace from the vertical channels combined with the horizontal flows in the channel and experienced a moderately sharp bend and expansion (Figure 9-7d). These effects were modelled as a T-junction (90° combining T-junction, $Q_1/Q_3 = 0.2$, $K_{add} = 0.3$ - Miller) and an expansion (infinite expansion, $K_{add} = 1.0$ - Perry).

The network as described consisted of 2 fixed pressure nodes, 273 unknown pressure nodes and 610 flow channels.

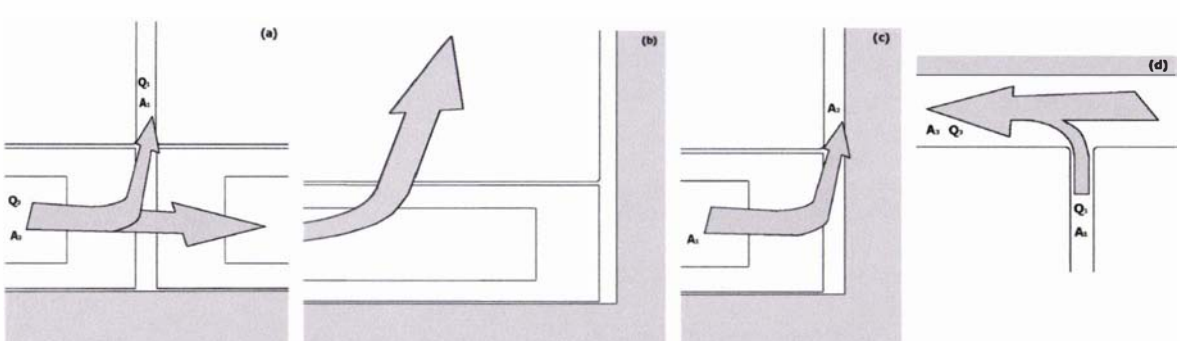

Figure 9-7 – Turning flow geometries modelled as (a) a diverging T-junction, (b) a standard 'L' bend (c) a 90° square bend and a contraction and (d) a converging T-junction

9.3.2 Simulation results

Simulation took approximately 40 seconds and there were no convergence problems. The decision was made to set the total pressure at the inlet and outlet nodes to match the measured static pressure profiles as opposed to the reported circulation rate. Static pressures were measured using a digital manometer while reported rates of circulation were measured using a digital manometer and a 0.20 m orifice plate. As there was a larger quantity of measured static pressure data and the circulation rate data was reliant on a correlation between measured pressure and volumetric flow, the static pressure data was considered more reliable.

The total pressures set at the inlet/outlet and the resulting total predicted flow rates through the rig were 12 Pa/4.75 Pa and 3000 $m^3.h^{-1}$, 22 Pa/10 Pa and 3900 $m^3.h^{-1}$ and 35 Pa/15 Pa and 5100 $m^3.h^{-1}$. These values represent a 12 to 16% over-estimation of the reported total circulation rate through the rig. The discrepancy may have been due to inaccuracies in the model predictions but may also have been due to inaccuracies in the reported circulation rates.

Figure 9-8 to Figure 9-10 show the measured and predicted pressures at each of the measurement points shown in Figure 9-1 and Figure 9-2 for each of the three flow rates. The figures show good agreement was achieved.

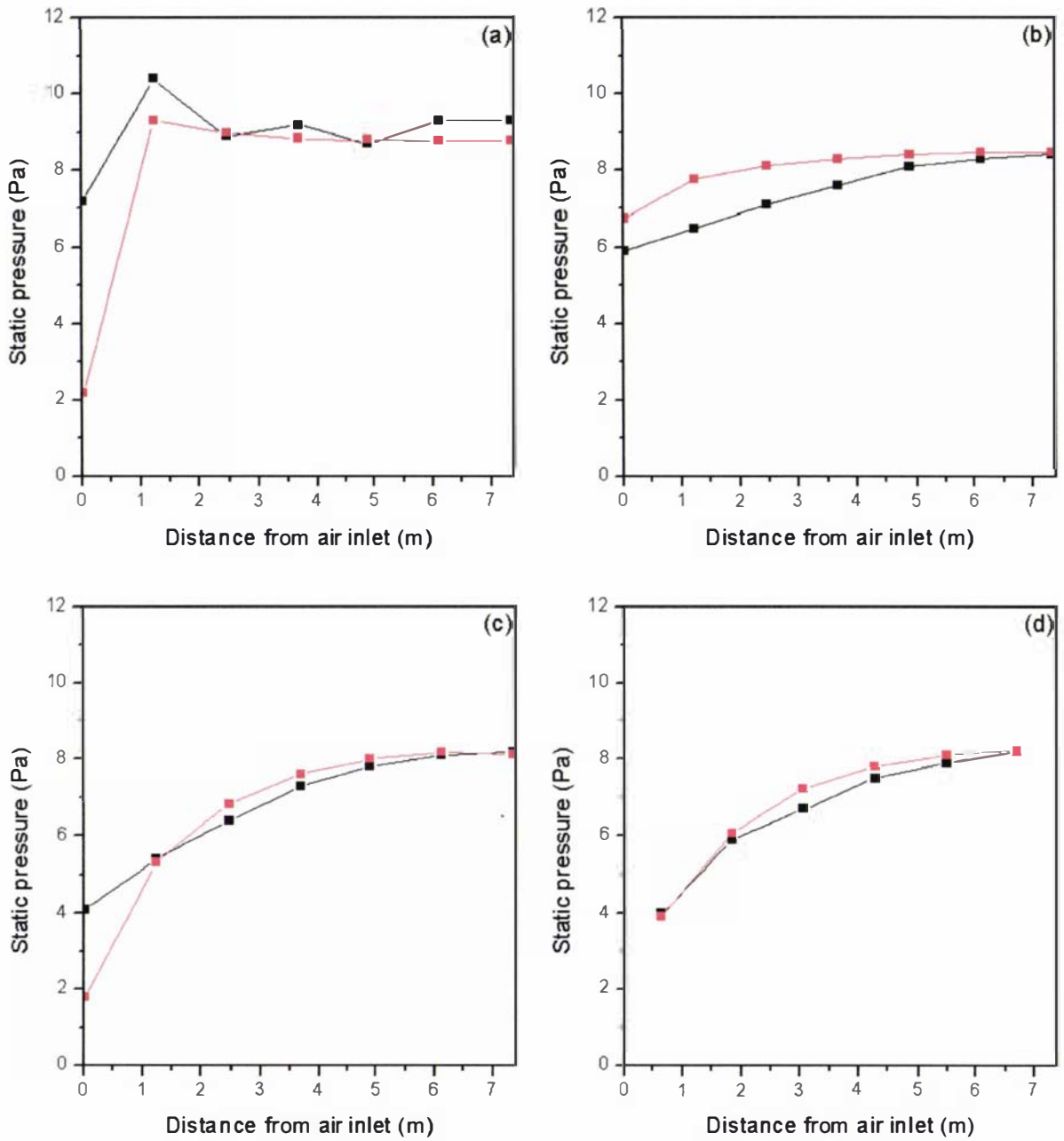

Figure 9-8 - Measured (■) and predicted (■) static pressures in the full-scale laboratory test rig with a flat floor and total flow rate of 2500 $m^3.h^{-1}$. (a) Measurement points at the level of the pallet bases on the side-wall (pressure taps 30 to 36). (b) Measurement points at the level halfway up the height of the pallet on the side-wall (pressure taps 23 to 29). (c) Measurement points in the headspace above the pallets on the side-wall (pressure taps 16 to 22). (d) Measurement points in the headspace above the pallets, in the centre of the ceiling (pressure taps 10 to 15)

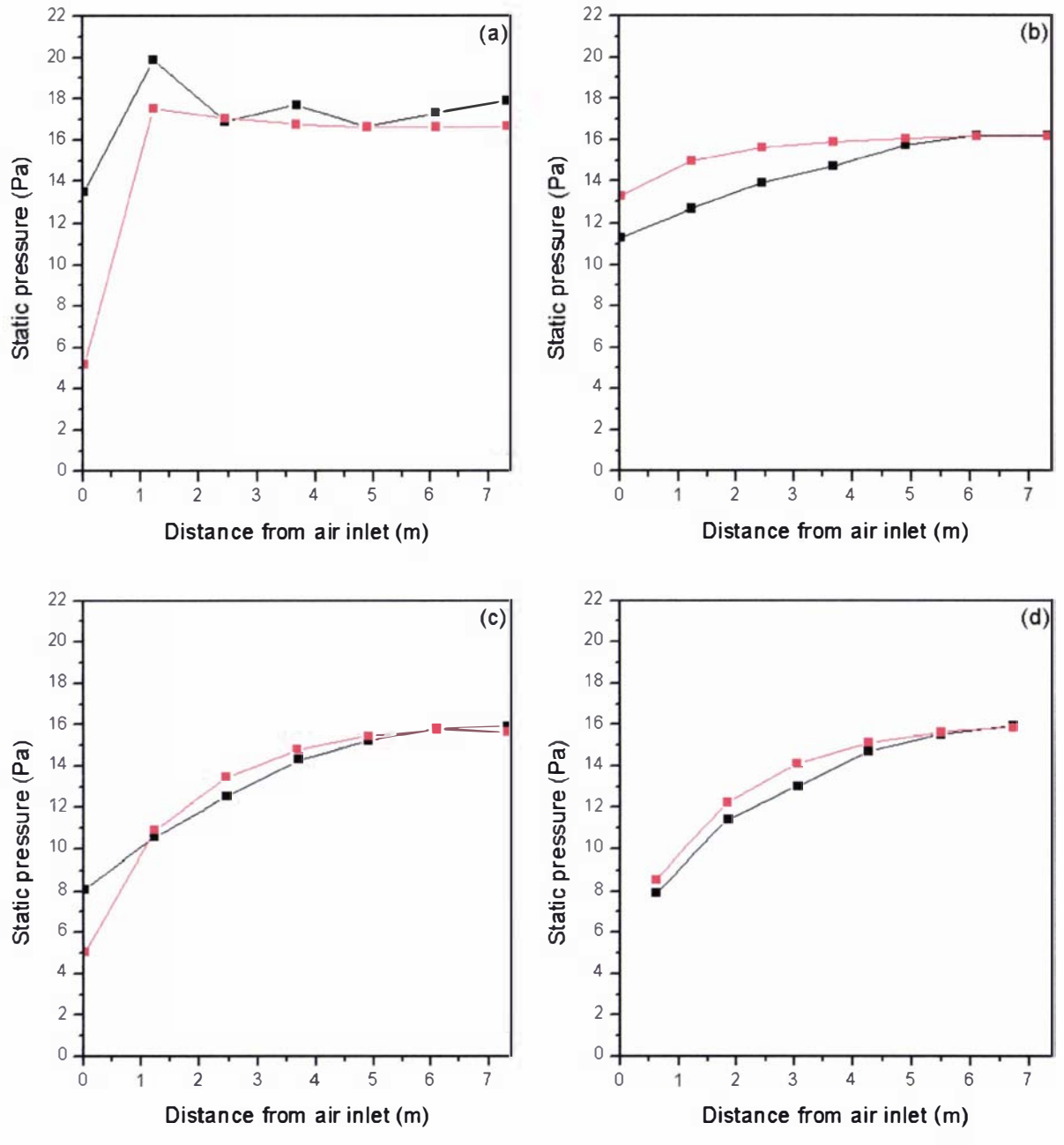

Figure 9-9 - Measured (■) and predicted (■) static pressures in the full-scale laboratory test rig with a flat floor and total flow rate of 3500 $m^3.h^{-1}$. (a) Measurement points at the level of the pallet bases on the side-wall (pressure taps 30 to 36). (b) Measurement points at the level halfway up the height of the pallet on the side-wall (pressure taps 23 to 29). (c) Measurement points in the headspace above the pallets on the side-wall (pressure taps 16 to 22). (d) Measurement points in the headspace above the pallets, in the centre of the ceiling (pressure taps 10 to 15)

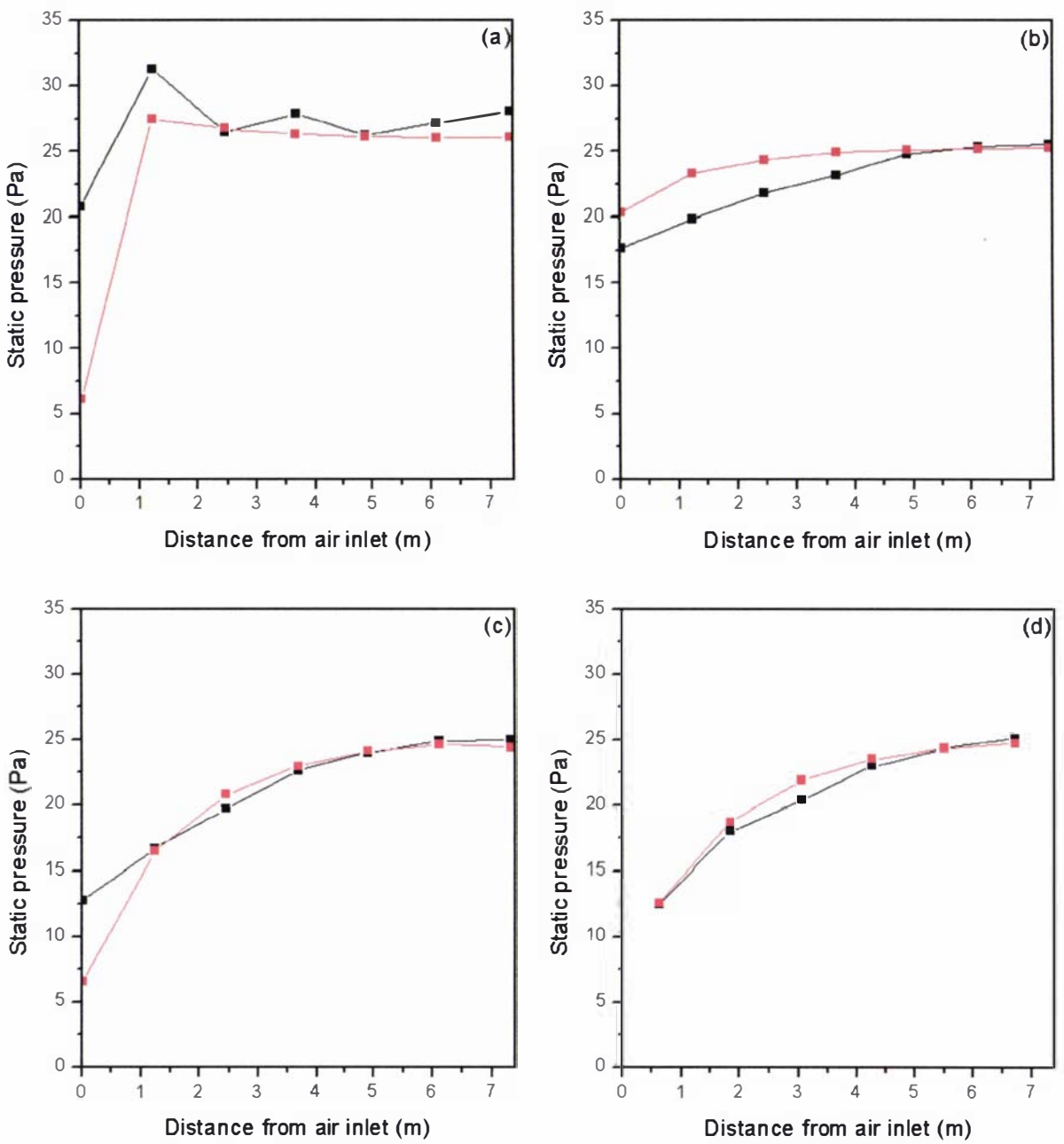

Figure 9-10 - Measured (■) and predicted (■) static pressures in the full-scale laboratory test rig with a flat floor and total flow rate of 4400 $m^3.h^{-1}$. (a) Measurement points at the level of the pallet bases on the side-wall (pressure taps 30 to 36). (b) Measurement points at the level halfway up the height of the pallet on the side-wall (pressure taps 23 to 29). (c) Measurement points in the headspace above the pallets on the side-wall (pressure taps 16 to 22). (d) Measurement points in the headspace above the pallets, in the centre of the ceiling (pressure taps 10 to 15)

Trends in predicted static pressure along the length of the rig were consistent with measured values for each of the flow rates. Discrepancies between measured and predicted results were greatest near the air inlet, which corresponds to the positions of highest velocity. At these points, a significant proportion of the mechanical energy of the fluid was in the form of kinetic energy, causing the flow profile to significantly affect the measured static pressure. Predicted static pressures at each node were calculated by subtracting the kinetic energy of the fluid in the attached channel with the greatest volumetric flow. Discrepancies between estimated and actual kinetic energy do not affect the predicted flow rates, but do affect the calculated static pressure. As such, discrepancies between measured and predicted static pressures were more likely to occur in areas of high velocity; however, as flow rates were not affected by this discrepancy, improved methods of kinetic energy estimation were not considered critical.

Figure 9-11 to Figure 9-13 depict the velocity in each of the vertical channels around the pallets. As there were two channels for each position (from below the pallet to halfway up the pallet and from halfway up the pallet to the ceiling headspace), the average velocity was calculated. Differences between velocities in the two channels were generally small and the averages served as a fair indication of the air distribution. Figure 9-11 to Figure 9-13 show the vertical velocity decreasing with distance from the fan end of the rig. Predicted velocities were symmetric and reasonably uniform across the half-width of the rig. The spatial velocity trends were uniform for each of the three flow rates, with flows almost exactly proportional to the total flow rate for the range of flow rates investigated. Fluid velocities in the channels near the fan end of the rig were approximately three times greater than those in channels at the opposite end of the rig. There was no measured data for comparison with predictions.

Figure 9-14 to Figure 9-16 depict the predicted temperature rise in each of the vertical channels, if the rig was likened to a refrigerated container. Values were calculated assuming the cargo was at constant temperature, with the circulating air removing all respiratory heat and heat infiltrating the walls. It was assumed each pallet contained 1000 kg of apples producing 0.035 $W.kg^{-1}$ of heat. Infiltrative heat was based on a wall K-value of 0.6 $W.m^{-2}.K^{-1}$ and an internal/external temperature difference of 32°C. It was also assumed that respiratory heat was removed evenly from all the vertical faces of the pallet, but not from the top or bottom faces. Whilst it was acknowledged that conditions were not representative of the laboratory rig, nor was the rig a model of a container, the figures were considered a useful way to assess the temperature implications of the predicted airflows.

Figure 9-14 to Figure 9-16 show relatively large temperature rises associated with the channels adjacent to external walls in comparison to those channels formed between pallets. The fruit at carriage temperatures produced small quantities of respiratory heat relative to wall heat infiltration under the conditions specified above, although it was sufficient to cause an air temperature rise of 1.3°C at the far end of the rig with a total flow rate of 2500 $m^3.h^{-1}$. With a flow rate of 4400 $m^3.h^{-1}$ the temperature rise in the same channel was 0.75°C. Channels adjacent to external walls at the end furthest from the fan gave the largest temperature rises; 2.4°C with a total flow of 4400 $m^3.h^{-1}$ and 4.1°C with a total flow of 2500 $m^3.h^{-1}$. Clearly, getting enough air flowing to the far end of the rig is critical if significant increases in air and therefore cargo temperatures are to be prevented.

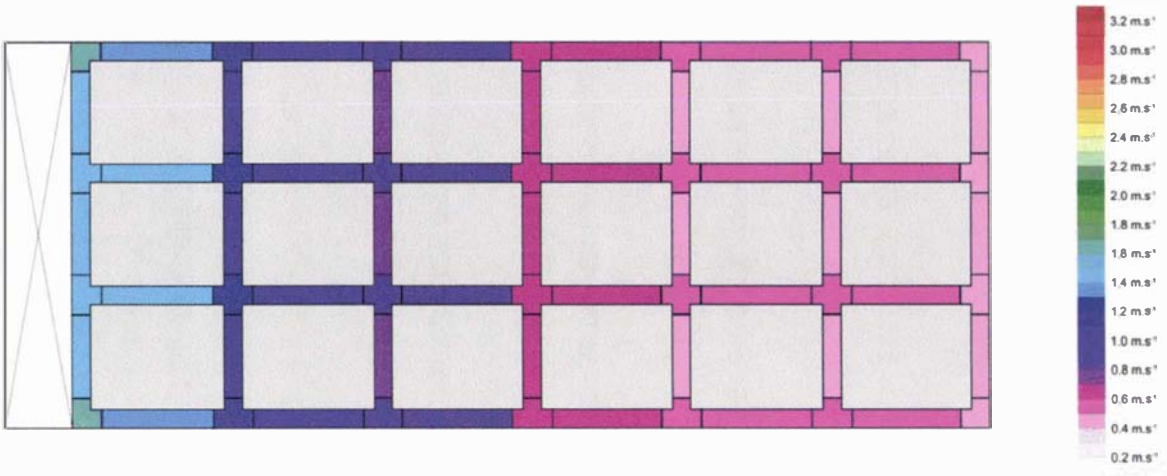

Figure 9-11 - Predicted velocity in each of the vertical flow channels within the laboratory test rig with a flat floor and total flow rate of 2500 $m^3.h^{-1}$ (gap dimensions not to scale)

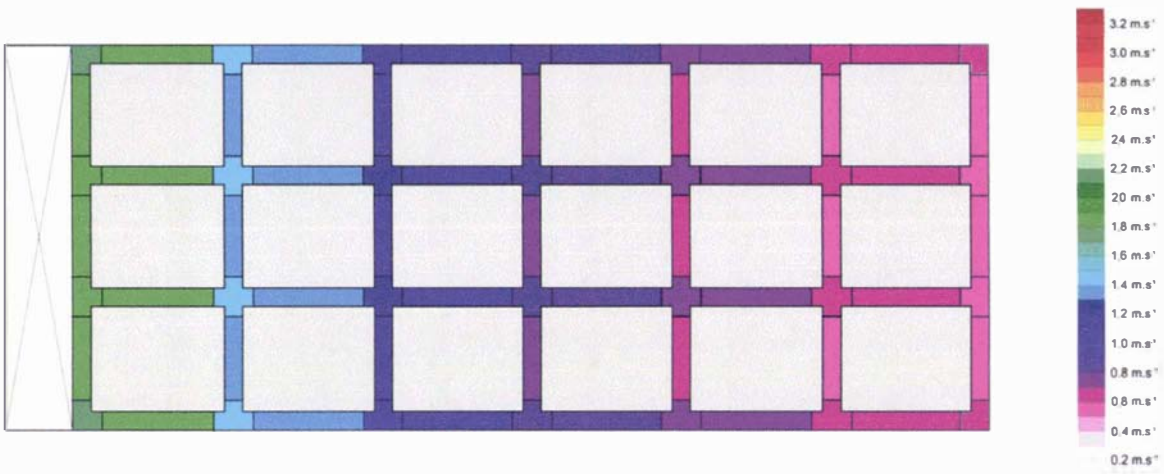

Figure 9-12 - Predicted velocity in each of the vertical flow channels within the laboratory test rig with a flat floor and total flow rate of 3500 $m^3.h^{-1}$ (gap dimensions not to scale)

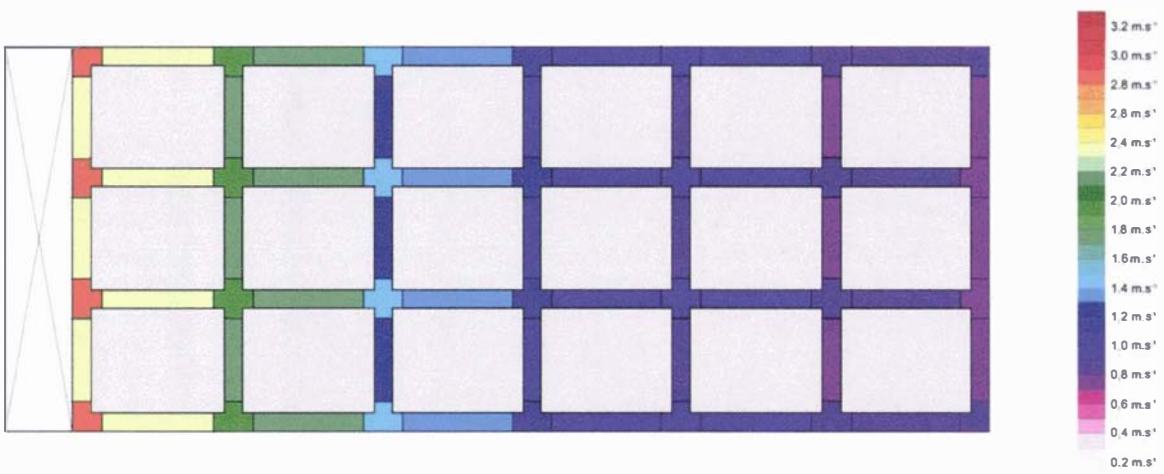

Figure 9-13 - Predicted velocity in each of the vertical flow channels within the laboratory test rig with a flat floor and total flow rate of 4400 $m^3.h^{-1}$ (gap dimensions not to scale)

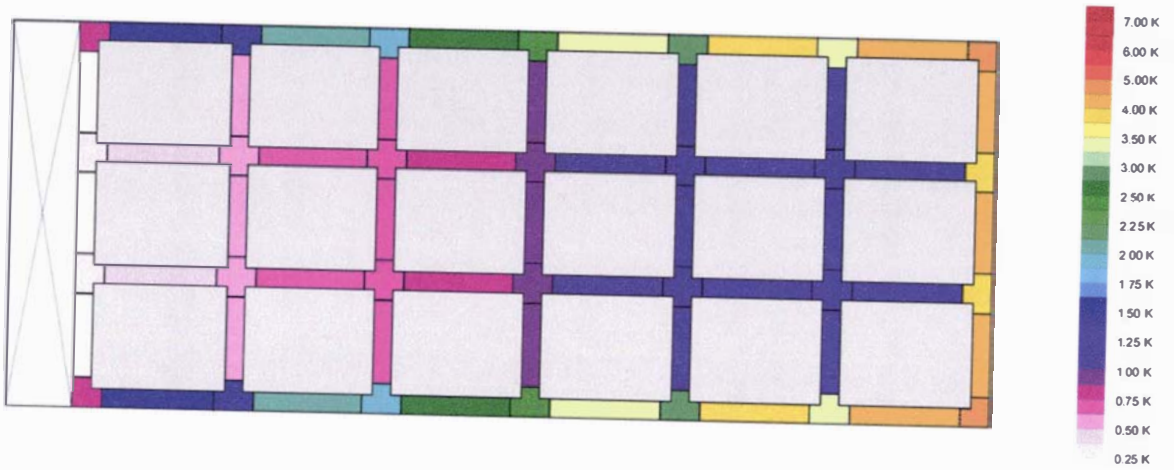

Figure 9-14 - Predicted temperature rise in each of the vertical flow channels within the laboratory test rig with a flat floor and total flow rate of 2500 $m^3.h^{-1}$ (gap dimensions not to scale)

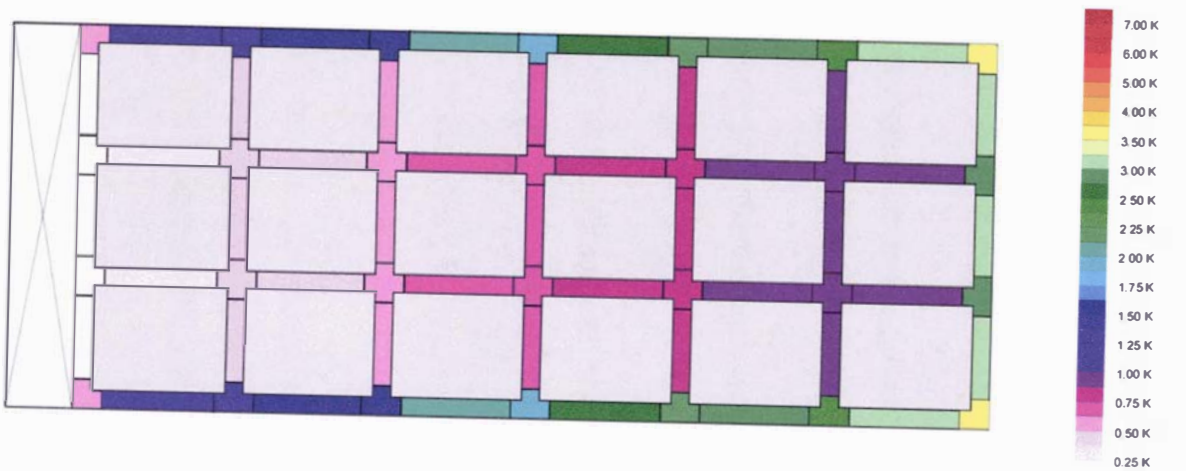

Figure 9-15 - Predicted temperature rise in each of the vertical flow channels within the laboratory test rig with a flat floor and total flow rate of 3500 $m^3.h^{-1}$ (gap dimensions not to scale)

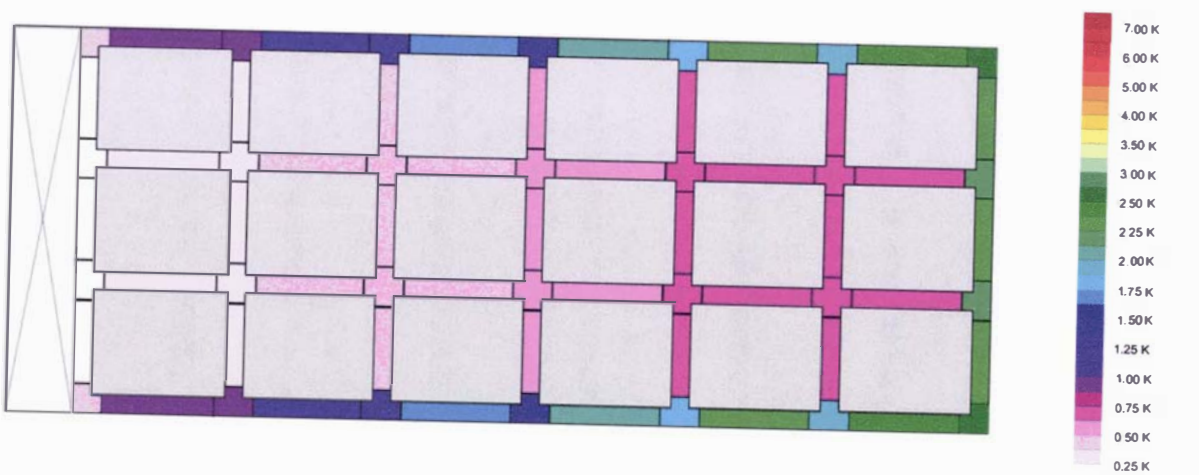

Figure 9-16 - Predicted temperature rise in each of the vertical flow channels within the laboratory test rig with a flat floor and total flow rate of 4400 $m^3.h^{-1}$ (gap dimensions not to scale)

9.4 Perforated floor – test series 5

This test series was conducted under the same conditions as test series 8, except air was delivered into channels below a perforated floor, with the slot above the floor sealed. The floor of the rig had 2300 holes of 12 mm diameter evenly distributed to give a free flow area equal to 1.2% of the floor area.

9.4.1 Flow channel definition

Flow channels within the rig were identical to those defined in Section 9.3.1, with an additional layer of nodes defined below the perforated floor. Channels below the floor were modelled as Type I channels with an absolute roughness of 0.00005 m (wood stove – Perry & Green, 1997). Channels connecting the nodes below the perforated floor with the nodes in the pallet base level were modelled as a perforated plate and the flow resistance was calculated using the correlation presented in Section 8.3.4 (Equation 8-10). The flow resistance caused by directional changes in the under-floor channels was assumed to be negligible in comparison to the flow resistance of the perforated floor. Figure 9-17 and Figure 9-18 show the positions of the nodes and Figure 9-19 shows a 3-dimensional illustration of the flow network.

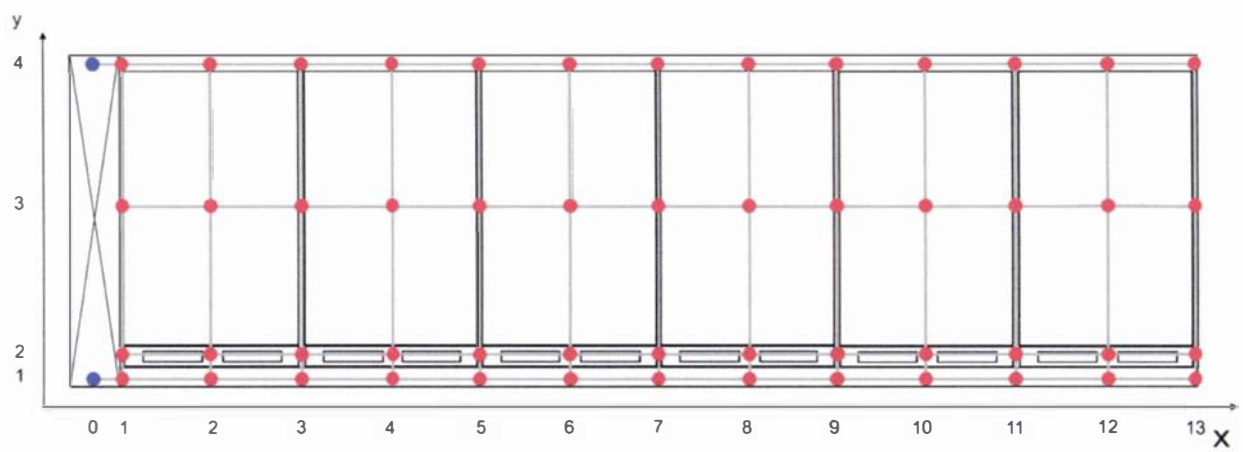

Figure 9-17 - Elevation view of the test rig loaded with 18 pallets showing a vertical cross-section of the flow resistance network. Blue circles represent fixed pressure nodes, red circles represent unknown pressure nodes, and grey cylinders represent flow channels

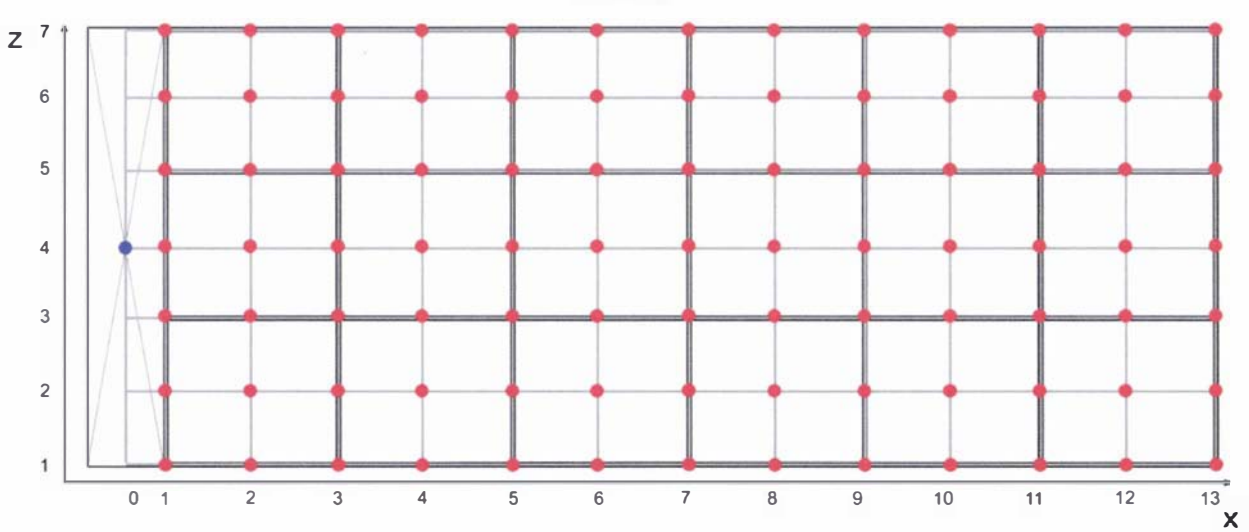

Figure 9-18 - Plan view of the test rig loaded with 18 pallets showing a horizontal cross-section of the flow resistance network. Blue circles represent fixed pressure nodes, red circles represent unknown pressure nodes, and grey cylinders represent flow channels

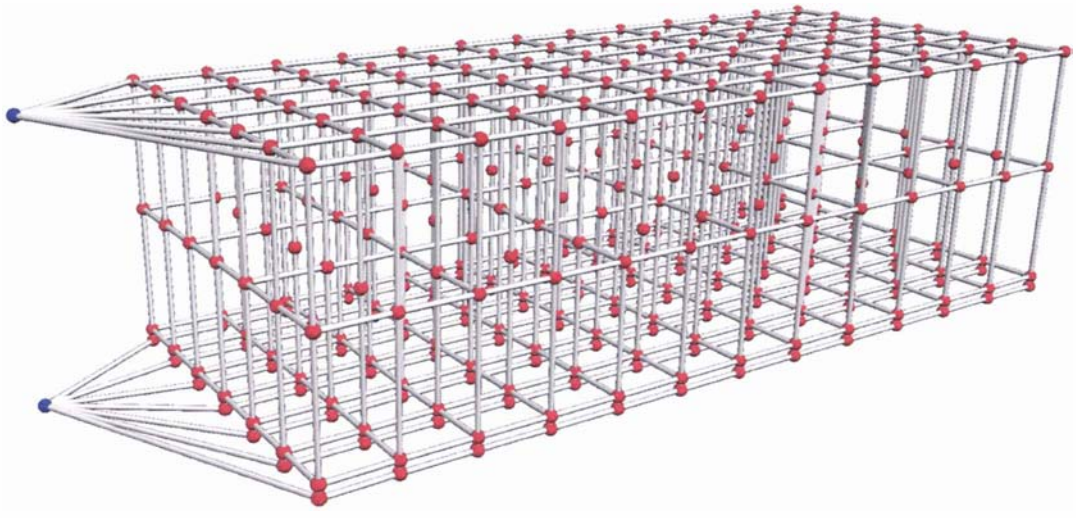

Figure 9-19 - Three-dimensional representation of the flow resistance network approximation of the test rig loaded with 18 pallets. Blue circles represent fixed pressure nodes, red circles represent unknown pressure nodes, and grey cylinders represent flow channels

9.4.2 Simulation results

Simulation took approximately 75 seconds and there were no convergence problems. As for the series 8 predictions, the total pressure at the inlet and outlet nodes was set to give predicted static pressures that matched the measured values. The inlet and outlet pressures and resulting total predicted flow rates through the rig were 21 Pa/5 Pa and 3000 $m^3.h^{-1}$, 36 Pa/10 Pa and 3800 $m^3.h^{-1}$ and 55 Pa/16 Pa and 4700 $m^3.h^{-1}$. Total circulation rates were over-estimated by 6 to 18%, consistent with earlier predictions (Section 9.3.2). Figure 9-20 to Figure 9-22 show the measured and predicted pressures at each of the measurement points shown in Figure 9-1 and Figure 9-2.

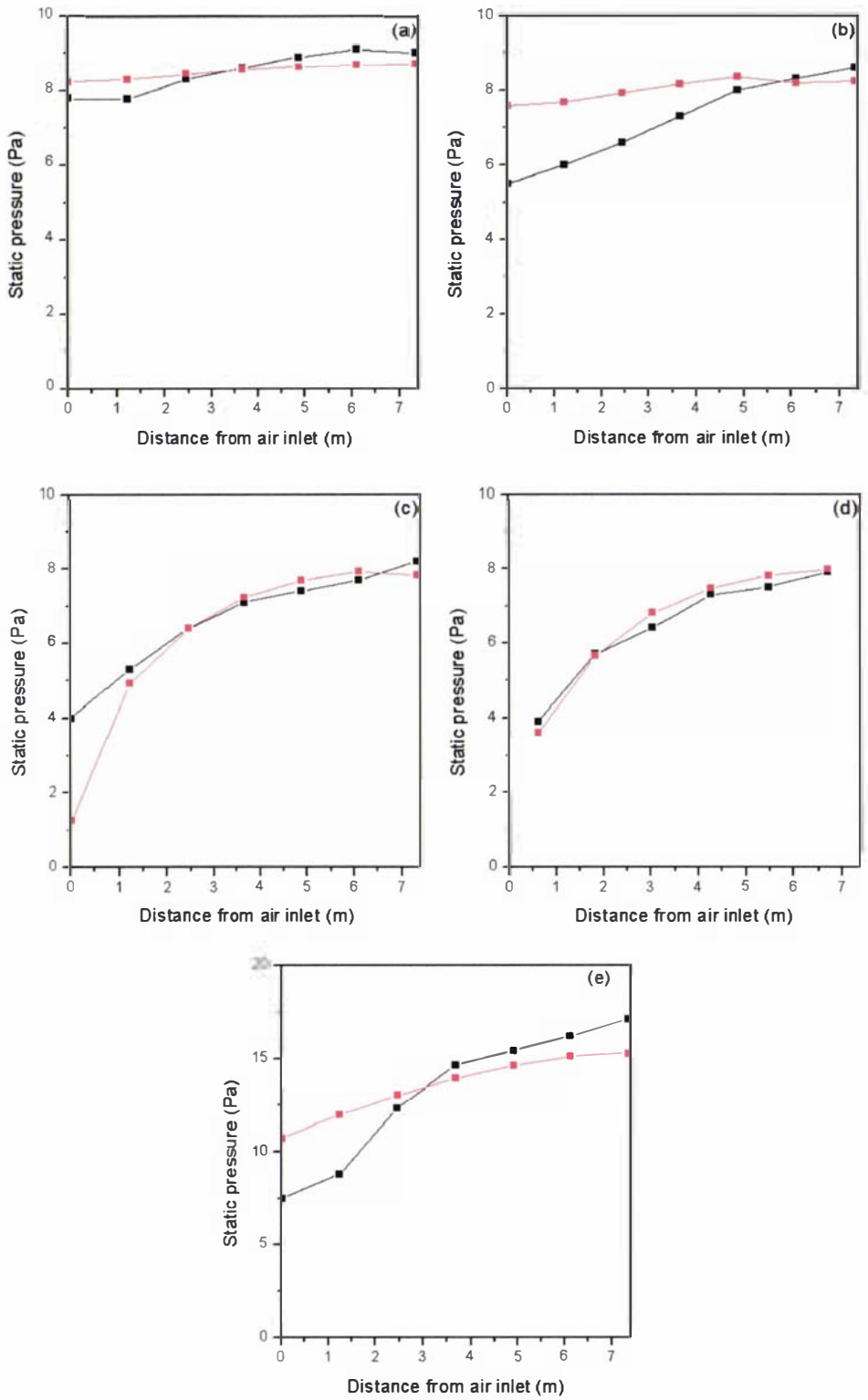

Figure 9-20 - Measured (■) and predicted (■) static pressures in the full-scale laboratory test rig with a perforated floor and total flow rate of 2500 $m^3.h^{-1}$. (a) Measurement points at the level of the pallet bases on the side-wall (pressure taps 30 to 36). (b) Measurement points at the level halfway up the height of the pallet on the side-wall (pressure taps 23 to 29). (c) Measurement points in the headspace above the pallets on the side-wall (pressure taps 16 to 22) (d) Measurement points in the headspace above the pallets, in the centre of the ceiling (pressure taps 10 to 15) (e) Measurement points below the gratings (pressure taps 37 to 43)

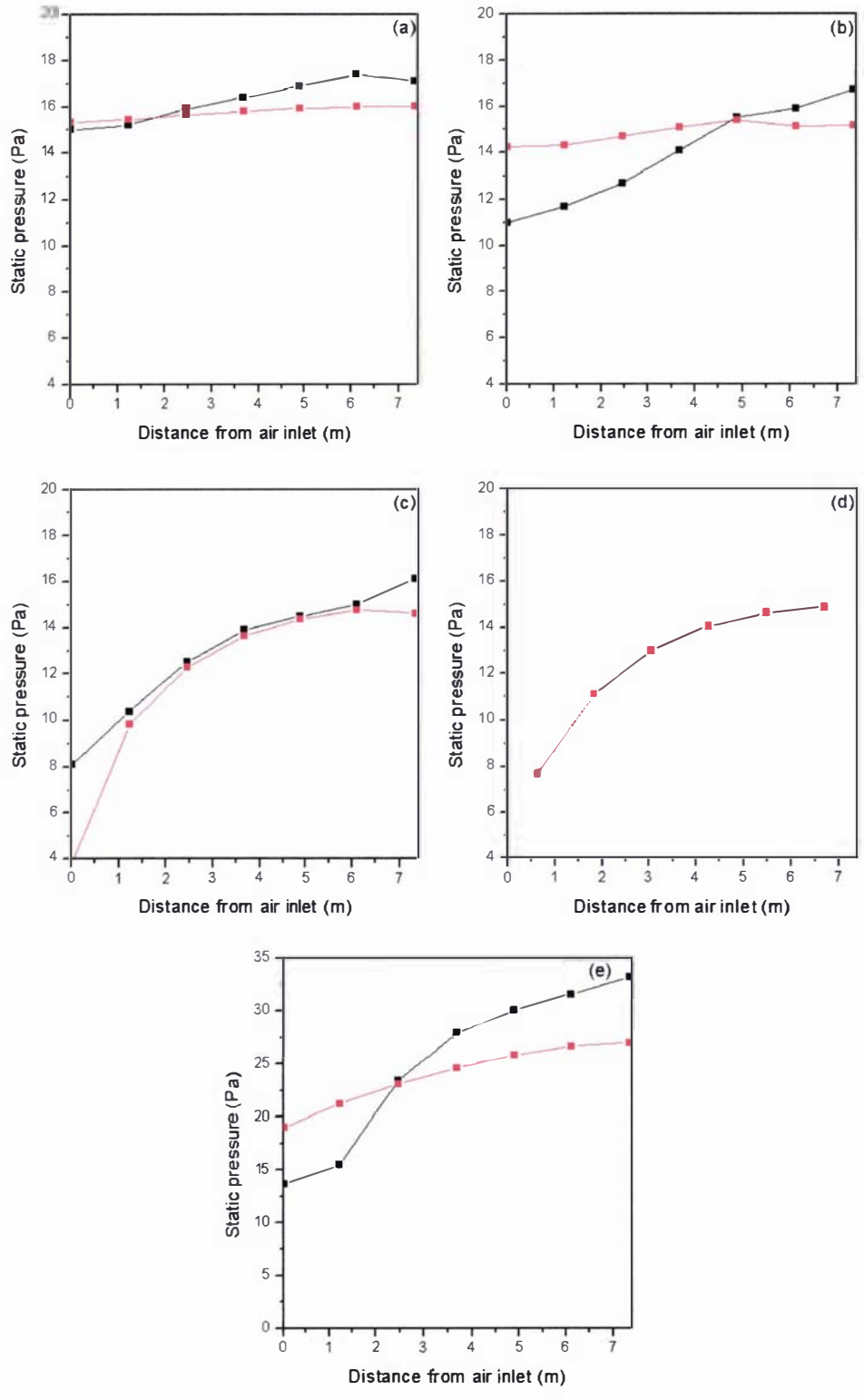

Figure 9-21 - Measured (■) and predicted (■) static pressures in the full-scale laboratory test rig with a perforated floor and total flow rate of 3500 $m^3.h^{-1}$. (a) Measurement points at the level of the pallet bases on the side-wall (pressure taps 30 to 36). (b) Measurement points at the level halfway up the height of the pallet on the side-wall (pressure taps 23 to 29). (c) Measurement points in the headspace above the pallets on the side-wall (pressure taps 16 to 22) (d) Measurement points in the headspace above the pallets, in the centre of the ceiling (pressure taps 10 to 15) (e) Measurement points below the gratings (pressure taps 37 to 43)

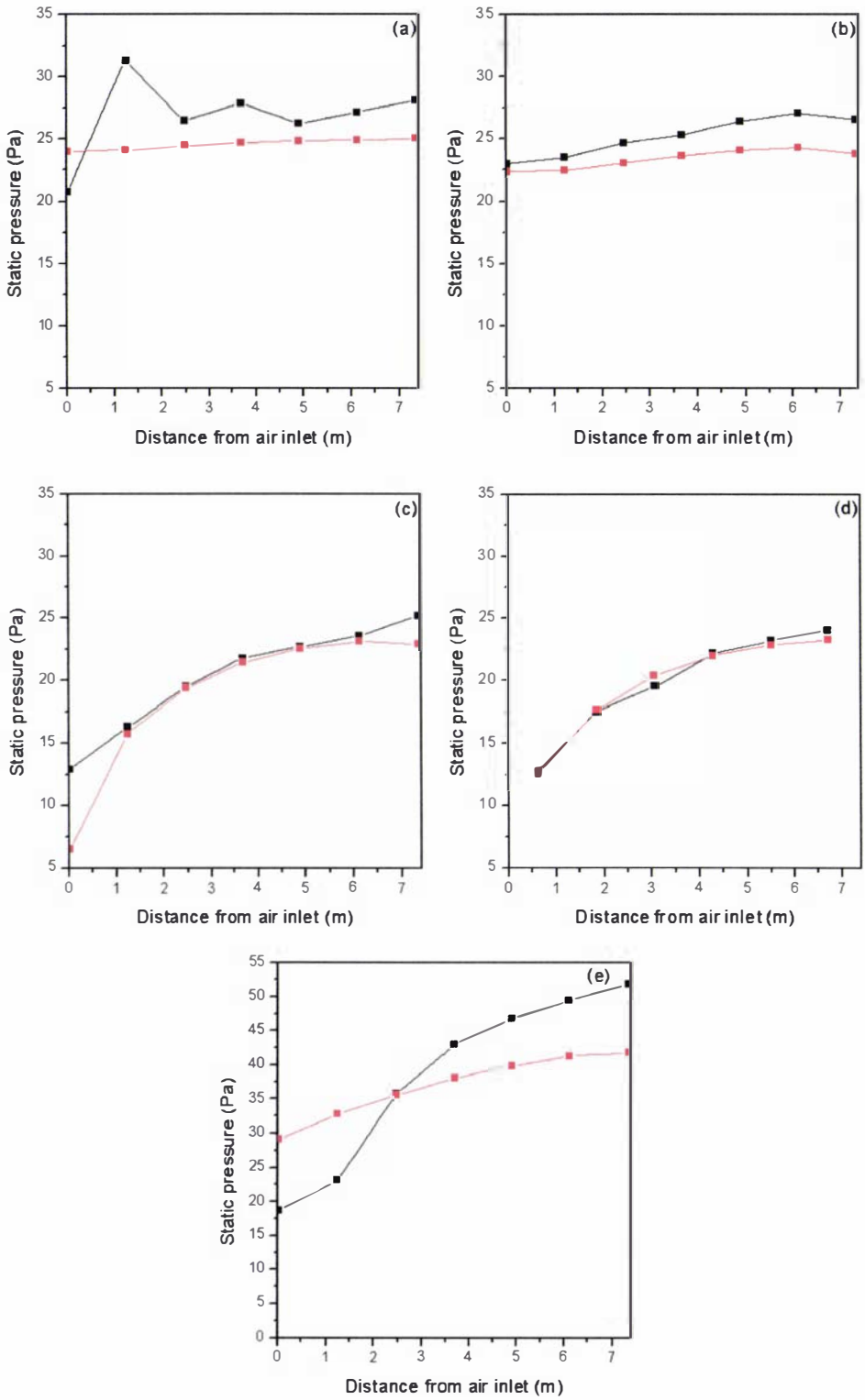

Figure 9-22 - Measured (■) and predicted (■) static pressures in the full-scale laboratory test rig with a perforated floor and total flow rate of 4400 $m^3.h^{-1}$. (a) Measurement points at the level of the pallet bases on the side-wall (pressure taps 30 to 36). (b) Measurement points at the level halfway up the height of the pallet on the side-wall (pressure taps 23 to 29). (c) Measurement points in the headspace above the pallets on the side-wall (pressure taps 16 to 22) (d) Measurement points in the headspace above the pallets, in the centre of the ceiling (pressure taps 10 to 15) (e) Measurement points below the gratings (pressure taps 37 to 43)

Comparisons of predicted and measured static pressures above the perforated floor showed good agreement and were similar to those for test series 8. Measured static pressures in the layer below the perforated floor were predicted less well; with measured pressure differences along the length of the rig much larger than those predicted. This discrepancy was thought to be caused by measurement errors due to turbulent eddies in the under-floor region as a consequence of the relatively high energy of the air and also poor estimation of kinetic energy as discussed in Section 9.3.2.

The measured static pressure at the point nearest the inlet in the under-floor region did not conform to the measured trend along the length of the rig. This may have been due to air recirculation, so the static pressure was increased as a consequence of the reduced velocity.

Figure 9-23 to Figure 9-25 show the predicted velocities in each of the vertical channels around the pallets. As for test series 8, the vertical velocity decreased with distance from the fan end of the rig. Velocities were uniform across the width of the rig, and trends were consistent for each of the flow rates. Incorporation of the perforated floor reduced the variation in vertical velocity along the length of the rig; with velocities in the channels near the fan end of the rig approximately double those in channels at the opposite end of the rig, compared with a threefold increase without the perforated floor shown in Figure 9-11 to Figure 9-13. Again, the spatial vertical velocity trends were uniform for each of the three flow rates, with flows almost exactly proportional to the total flow rate for the range of flow rates investigated.

Figure 9-26 to Figure 9-28 depict the calculated temperature rise in each of the vertical channels. These values were calculated in the same fashion as for test series 8. Patterns were similar as for test series 8; however, the more even flow distribution achieved with the perforated floor reduced the predicted temperature rise at the far end of the hold by up to 0.8°C for a circulation rate of 2500 $m^3.h^{-1}$. Increases in the predicted temperature rise of a similar magnitude were evident in channels near the fan end.

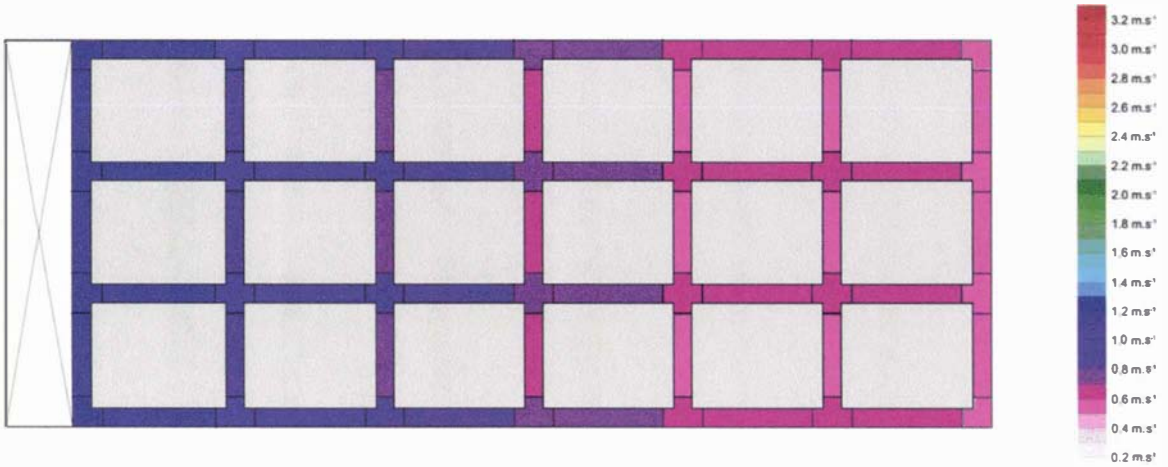

Figure 9-23 - Predicted velocity in each of the vertical flow channels within the laboratory test rig with a perforated floor and total flow rate of 2500 $m^3.h^{-1}$ (gap dimensions not to scale)

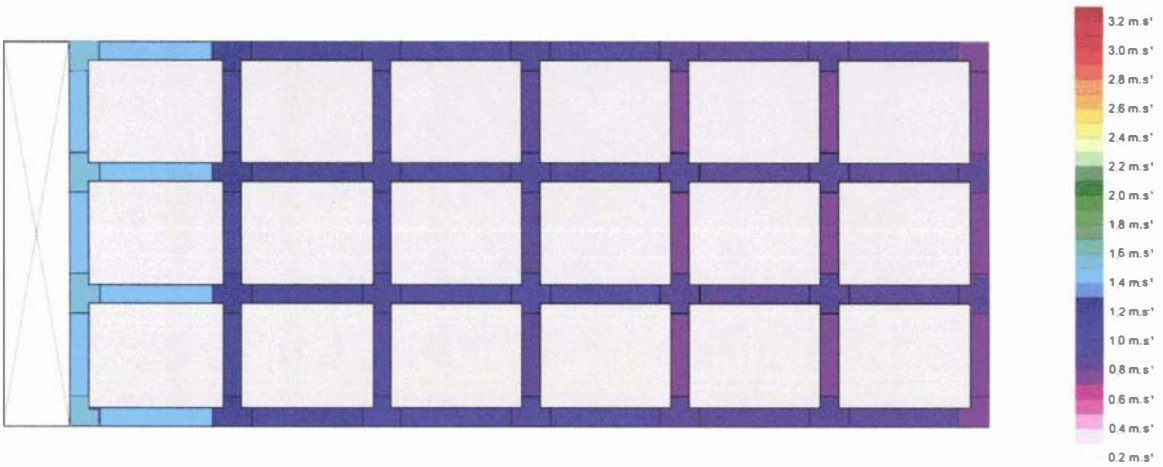

Figure 9-24 - Predicted velocity in each of the vertical flow channels within the laboratory test rig with a perforated floor and total flow rate of 3500 $m^3.h^{-1}$ (gap dimensions not to scale)

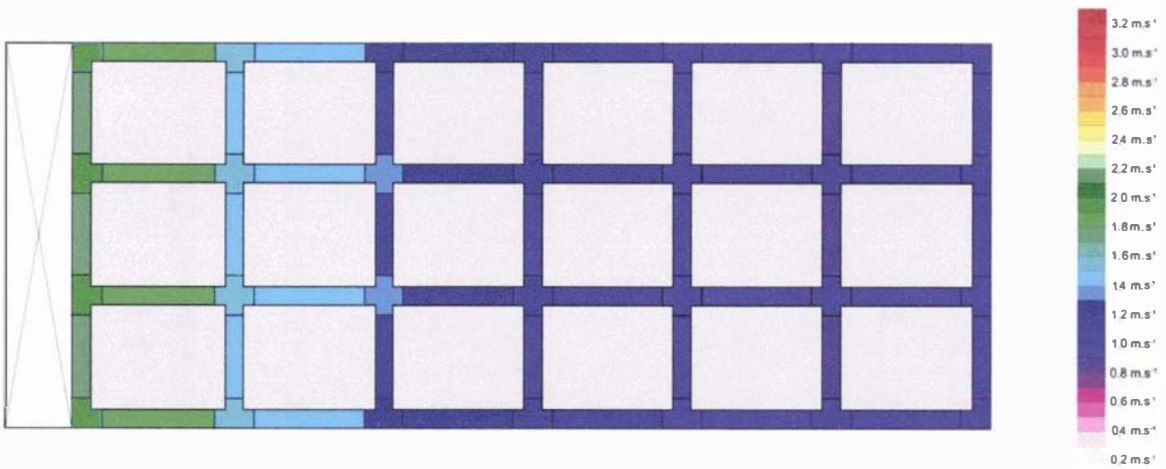

Figure 9-25 - Predicted velocity in each of the vertical flow channels within the laboratory test rig with a perforated floor and total flow rate of 4400 $m^3.h^{-1}$ (gap dimensions not to scale)

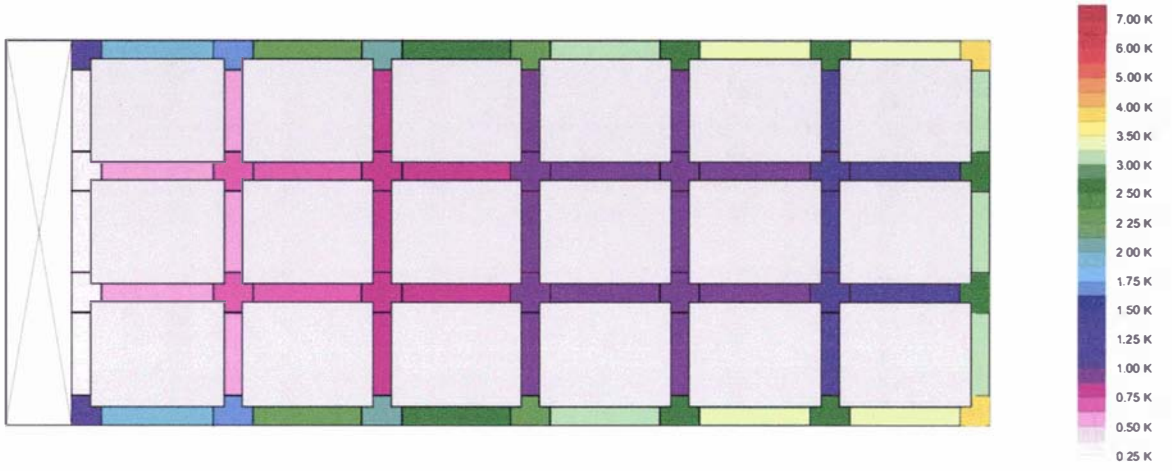

Figure 9-26 - Predicted temperature rise in each of the vertical flow channels within the laboratory test rig with a perforated floor and total flow rate of 2500 $m^3.h^{-1}$ (gap dimensions not to scale)

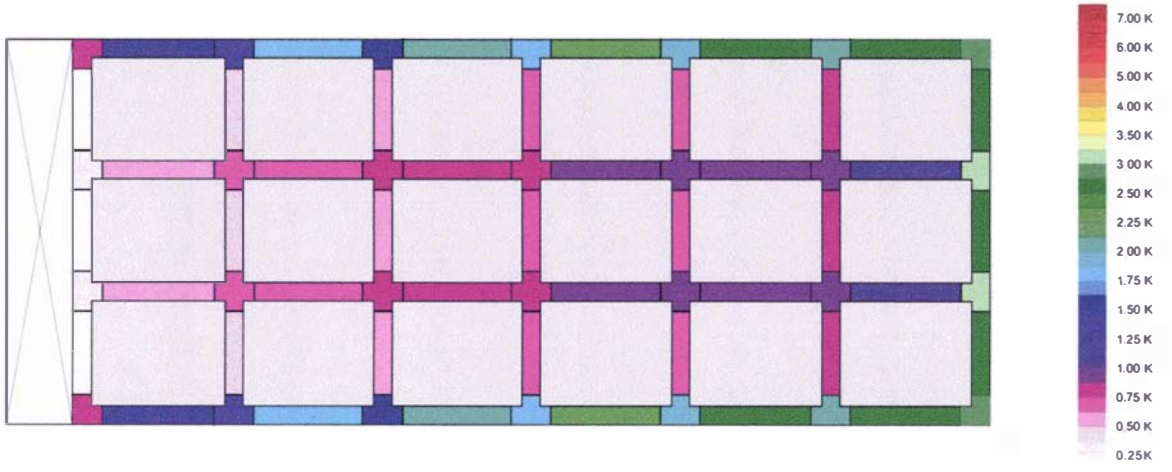

Figure 9-27 - Predicted temperature rise in each of the vertical flow channels within the laboratory test rig with a perforated floor and total flow rate of 3500 $m^3.h^{-1}$ (gap dimensions not to scale)

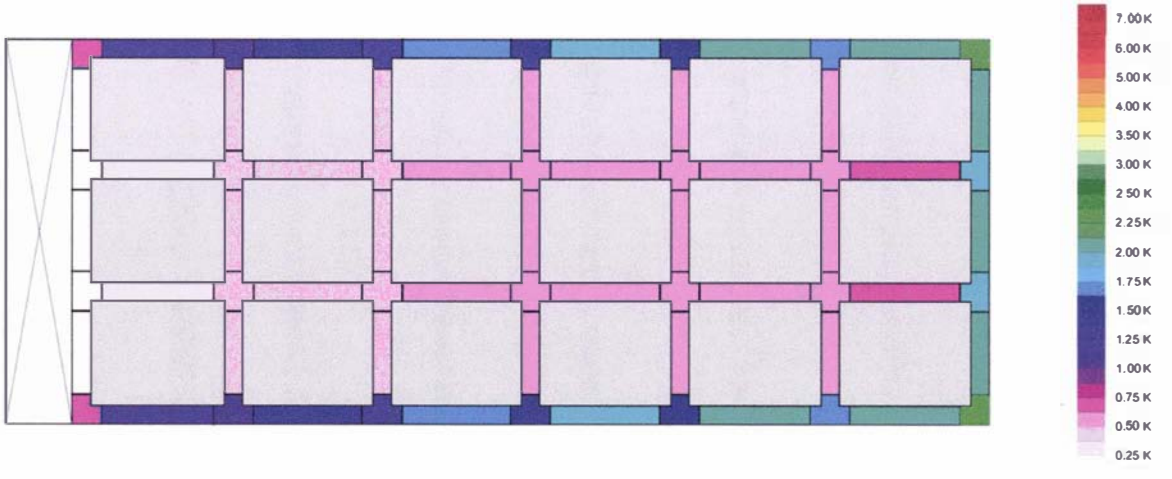

Figure 9-28 - Predicted temperature rise in each of the vertical flow channels within the laboratory test rig with a perforated floor and total flow rate of 4400 $m^3.h^{-1}$ (gap dimensions not to scale)

9.5 Flat floor plus intervention – test series 9

This test series was conducted with the test rig in the same configuration as test series 8; a flat floor making use of the pallet bases as an air duct to distribute air throughout the rig. However, in this test series wooden boards and foam rubber were used to block the longitudinal gaps between pallets (Figure 9-1), which Lindqvist (2000) considered unlikely to be present in real refrigerated holds.

9.5.1 Flow channel definition

Flow channels were the same as those defined for test series 8, with the only exception an arbitrarily high resistance assigned to the channels affected by the boards: $K_{add} = 1 \times 10^5$. The value was chosen to provide sufficient resistance to reduce the flow rate to insignificant levels without using a value so high as to create an ill-conditioned set of equations.

9.5.2 Simulation results

Simulation took approximately 35 seconds and there were no convergence problems. The total pressure at the inlet and outlet nodes was set to give predicted static pressures that matched the measured values. The inlet and outlet pressures and resulting total predicted flow rates through the rig were 13 Pa/5 Pa and 2900 $m^3.h^{-1}$, 24 Pa/10 Pa and 3900 $m^3.h^{-1}$ and 37 Pa/16 Pa and 4800 $m^3.h^{-1}$. Total circulation rates were over-estimated by 9 to 17%, consistent with earlier predictions (Sections 9.3.2 and 9.4.2). Figure 9-29 to Figure 9-31 show the measured and predicted pressures at each of the measurement points shown in Figure 9-1 and Figure 9-2 for each of the flow rates.

There was good agreement between predicted and measured static pressures. Trends were again consistent for all flow rates tested, and measured pressures were not substantially different to those measured and simulated for test series 8, suggesting the intervention had little impact.

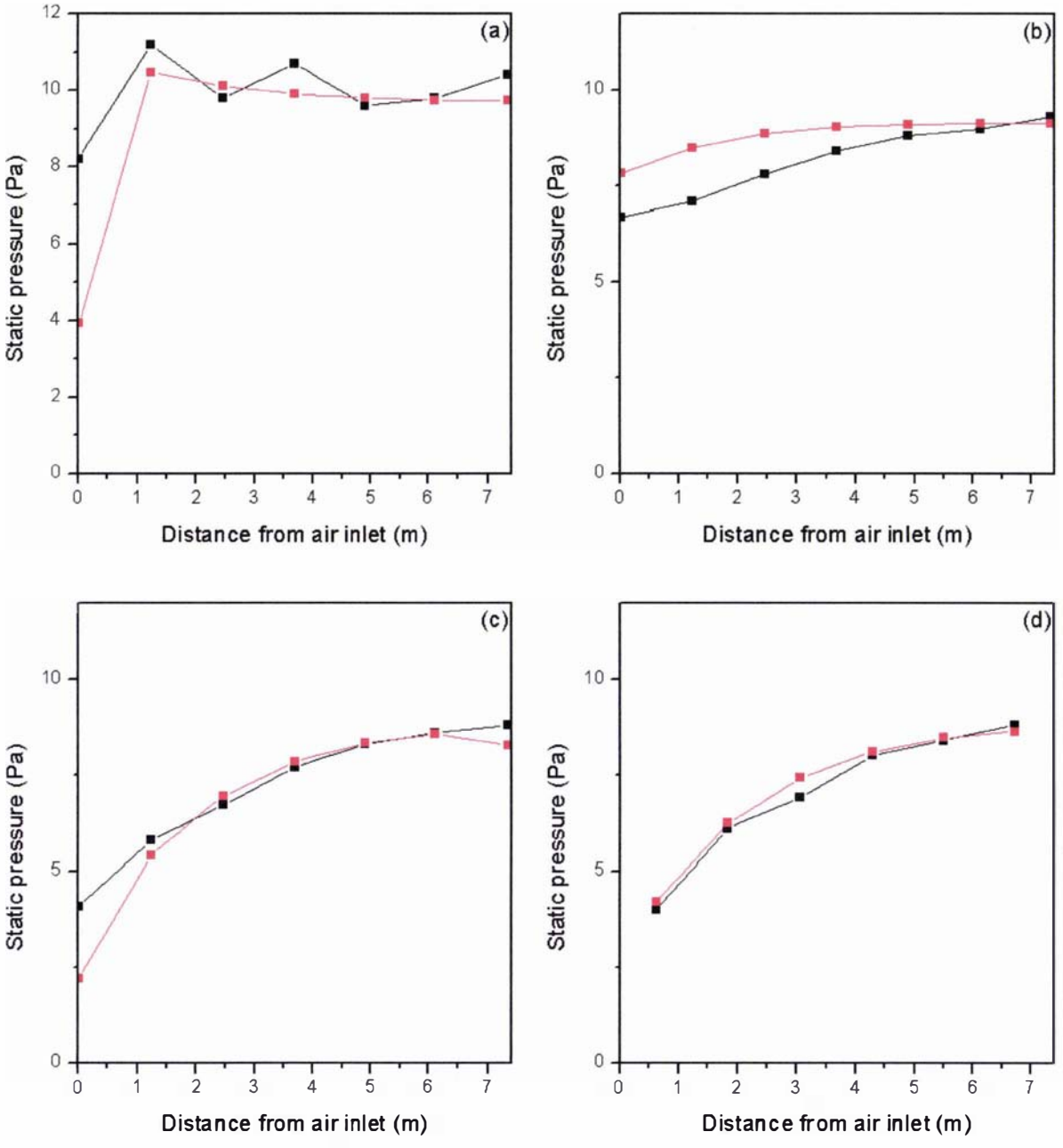

Figure 9-29 - Measured (■) and predicted (■) static pressures in the full-scale laboratory test rig with a flat floor, plates reducing flow through longitudinal gaps and total flow rate of 2500 $m^3.h^{-1}$. (a) Measurement points at the level of the pallet bases on the side-wall (pressure taps 30 to 36). (b) Measurement points at the level halfway up the height of the pallet on the side-wall (pressure taps 23 to 29). (c) Measurement points in the headspace above the pallets on the side-wall (pressure taps 16 to 22). (d) Measurement points in the headspace above the pallets, in the centre of the ceiling (pressure taps 10 to 15)

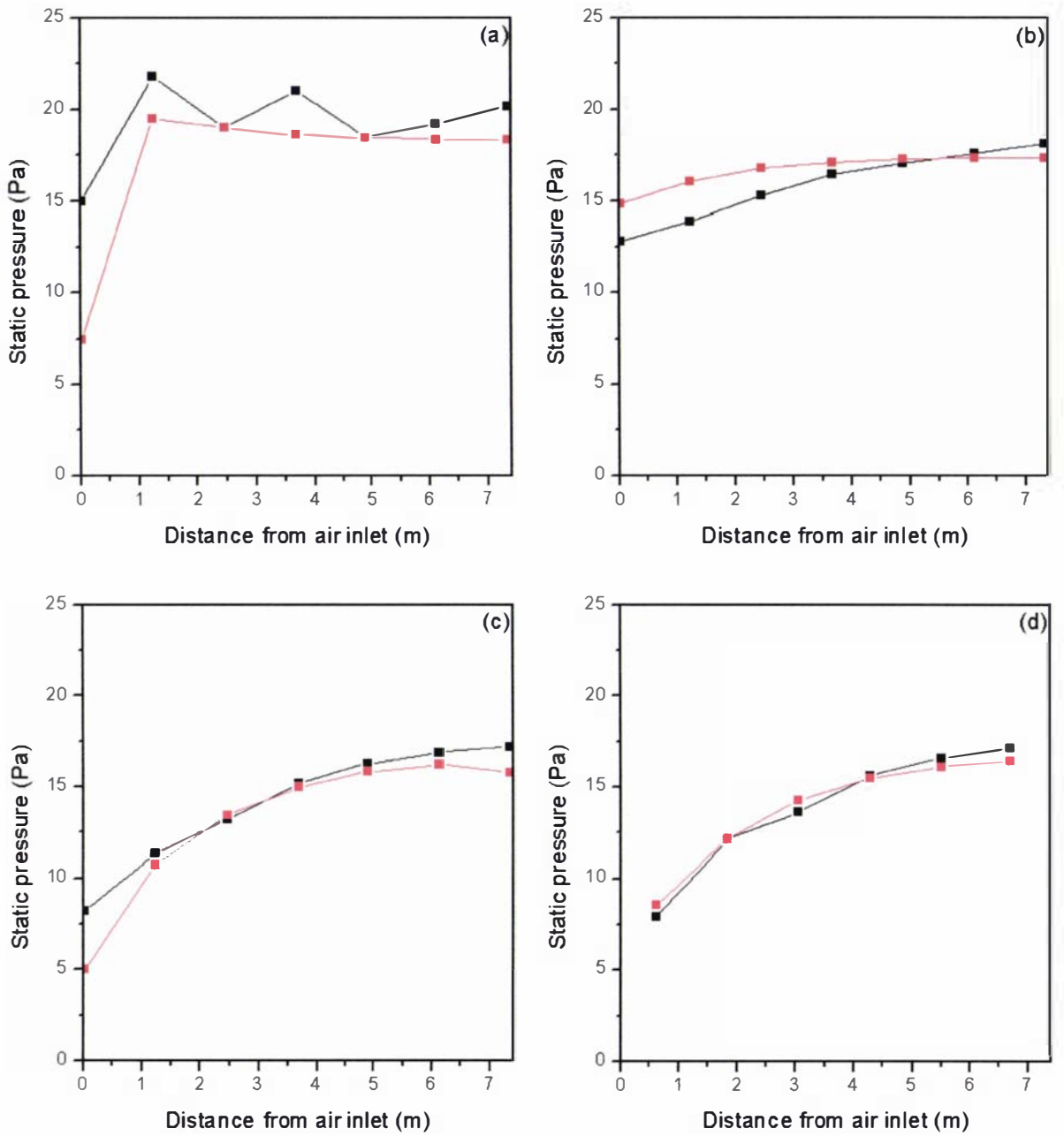

Figure 9-30 - Measured (■) and predicted (■) static pressures in the full-scale laboratory test rig with a flat floor, plates reducing flow through longitudinal gaps and total flow rate of 3500 $m^3.h^{-1}$. (a) Measurement points at the level of the pallet bases on the side-wall (pressure taps 30 to 36). (b) Measurement points at the level halfway up the height of the pallet on the side-wall (pressure taps 23 to 29). (c) Measurement points in the headspace above the pallets on the side-wall (pressure taps 16 to 22). (d) Measurement points in the headspace above the pallets, in the centre of the ceiling (pressure taps 10 to 15)

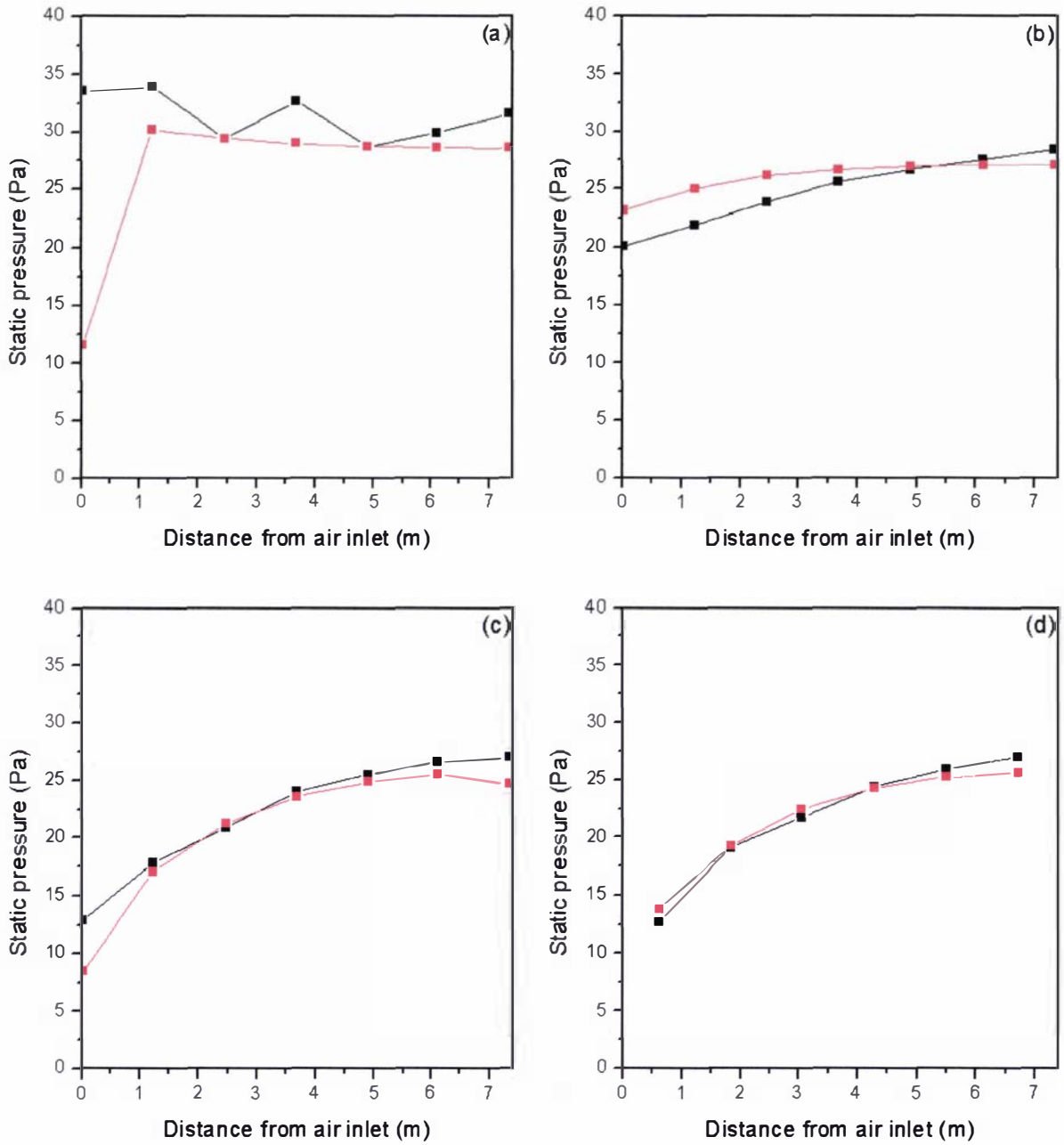

Figure 9-31 - Measured (■) and predicted (■) static pressures in the full-scale laboratory test rig with a flat floor, plates reducing flow through longitudinal gaps and total flow rate of 4400 $m^3.h^{-1}$. (a) Measurement points at the level of the pallet bases on the side-wall (pressure taps 30 to 36). (b) Measurement points at the level halfway up the height of the pallet on the side-wall (pressure taps 23 to 29). (c) Measurement points in the headspace above the pallets on the side-wall (pressure taps 16 to 22). (d) Measurement points in the headspace above the pallets, in the centre of the ceiling (pressure taps 10 to 15)

9.6 Scenario testing

Flows were predicted using altered input data for test series 5 and 8. In particular, the aspects investigated were the additional frictional loss values (K_{add}) for turning flow and the flow resistance caused by the perforated floor. Inlet and outlet pressures were set to give a total circulation rate consistent with earlier simulations.

9.6.1 Perforated floor

Simulations were performed using the geometry described for test series 5 (Section 9.4.1), with increased open areas of the perforated floor (3% and 20%). Whilst in this scenario the correlation employed remained the same whilst the open area was altered, a similar result would be obtained by using an alternative correlation and maintaining a constant open area. Therefore, results provided an insight into both the sensitivity of the model to the correlation employed for the perforated floor and the effect of altering the floor design. The total pressure at the inlet/outlet was 37.5 Pa/16 Pa for the 3% open floor and 31 Pa/16 Pa for the 20% open floor (previously 55 Pa/16 Pa for the 1.2% open floor) to give a circulation rate of 4700 $m^3.h^{-1}$.

Figure 9-32 shows the predicted static pressures at each of the locations shown in Figure 9-1 and Figure 9-2 for perforation areas of 1.2%, 3% and 20%. The static pressures for the three perforation levels were almost identical except for positions below the level of the perforated floor. Figure 9-33 shows the predicted change in velocity in each of the vertical channels caused by a change in the open area of the perforated floor from 1.2% to 20%. The reduced resistance of the floor increased the velocity in the channels near the fan end of the rig by approximately 7% and subsequently reduced the velocities in the opposite end of the rig by a similar amount. No discernable differences in velocities were evident between the 1.2% and 3% open perforated floors.

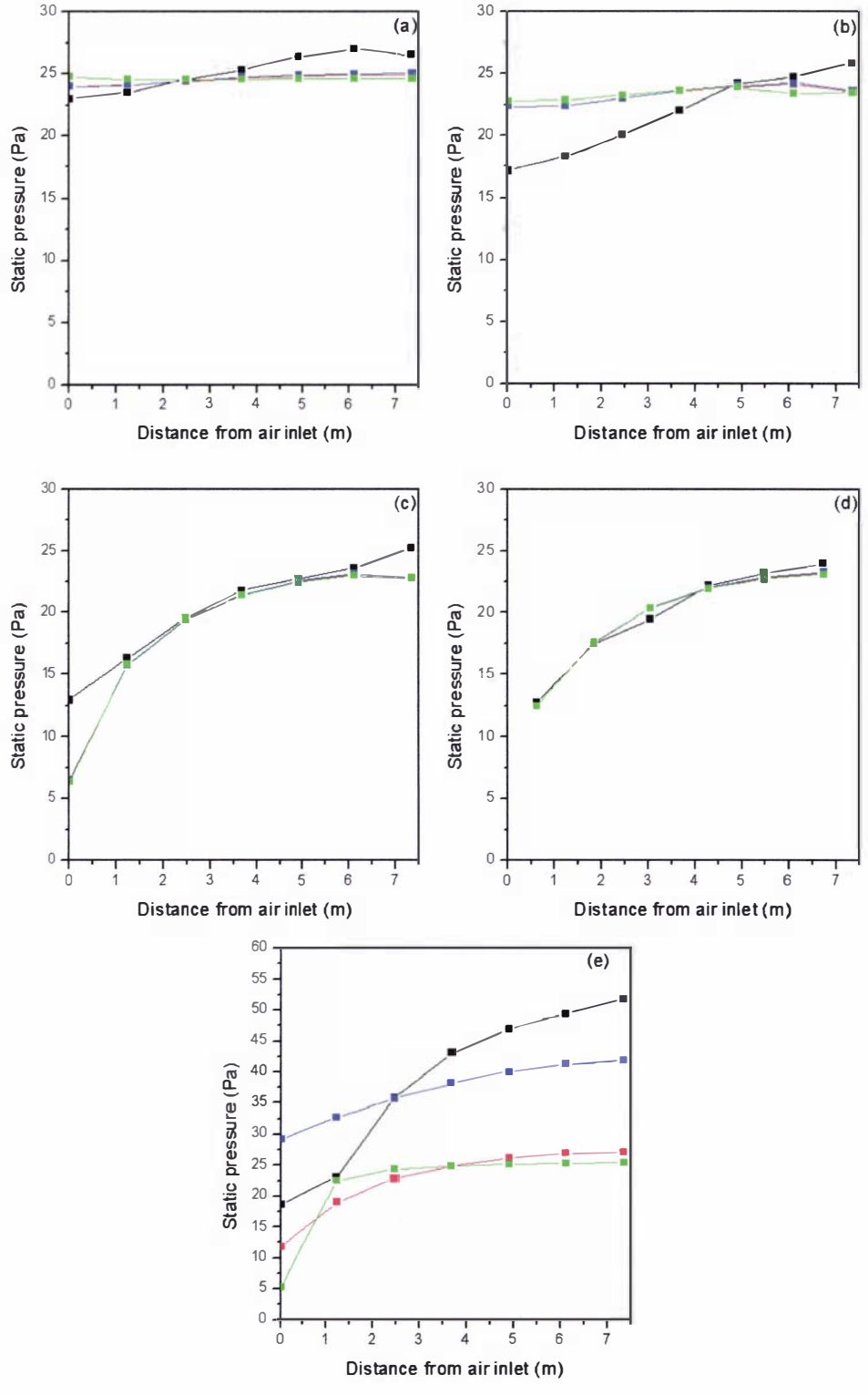

Figure 9-32 - Static pressures measured (■) and predicted using a floor perforation of 1.2% (■), 3% (■) and 20% (■) in the full-scale laboratory test rig with a total flow rate of 4400 $m^3.h^{-1}$. (a) Measurement points at the level of the pallet bases on the side-wall (pressure taps 30 to 36). (b) Measurement points at the level halfway up the height of the pallet on the side-wall (pressure taps 23 to 29). (c) Measurement points in the headspace above the pallets on the side-wall (pressure taps 16 to 22). (d) Measurement points in the headspace above the pallets, in the centre of the ceiling (pressure taps 10 to 15). (e) Measurement points below the gratings (pressure taps 37 to 43)

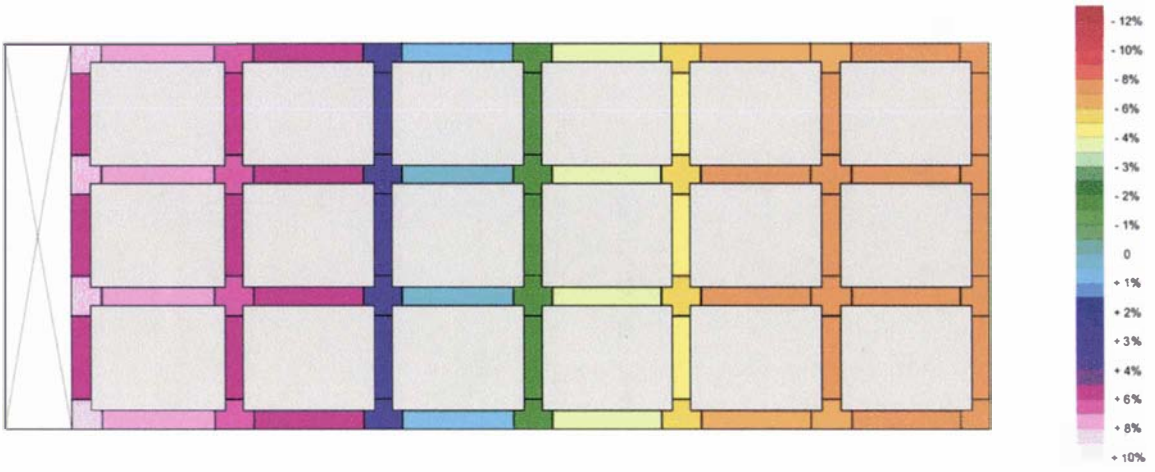

Figure 9-33 – Percentage changes in predicted velocity for each of the vertical channels within the laboratory test rig caused by changing from a perforated floor with a 1.2% open area to 20% open area (gap dimensions not to scale)

Results showed the predicted static pressures above the perforated floor were not substantially affected by the flow resistance caused by the perforated floor. Furthermore, changes in the perforated floor did not reduce the discrepancies between predicted and measured static pressures below the perforated floor.

The reduced flow resistance of the system due to the increased perforation area was not considered in these simulations as the inlet and outlet pressures were set to give a total flow rate of 4700 $m^3.h^{-1}$. In practice, the increased resistance of the system associated with a lower perforation area requires greater fan power, which increases the energy consumption of both the refrigeration and fan systems. Optimisation of the system would require analysis of the trade-off between improved air distribution and increased installation and running costs associated with a lower perforation area. Analysis of this nature was considered outside the scope of this work.

9.6.2 Turning flow additional losses

Increased frictional losses caused by turning flow is an important consideration in prediction of airflow within shipping systems. Whilst the additional loss correlations used to quantify these losses in this work were similar to those for which the correlations were intended for use, they may not reflect exactly the flow patterns experienced in the modelled system. Given the large volume of possible geometries experienced in marine transport systems and inherent measurement difficulties, developing specific correlations for these flow elements within the cargo area is a considerable task and as such the published correlations currently provide the best available source of information. The sensitivity of the predictions to the K_{add} values used was investigated to ascertain the importance of the accuracy of these correlations.

Simulations were performed using the geometry described for test series 8 (Section 9.3.1), but increasing the K_{add} values for all turning flow geometries to twice the original value. The total pressure at the inlet/outlet was set at 36.7 Pa/15 Pa (previously 35 Pa/15 Pa) to give a circulation rate of 5100 $m^3.h^{-1}$. Figure 9-32 shows the measured and predicted static pressures at each of the locations shown in Figure 9-1 and Figure 9-2 using both sets of K_{add} values. There were only small differences between the static pressures predicted using the two sets of K_{add} values, with a consistent (but small) increase in the static pressure predicted at the measurement points near the floor.

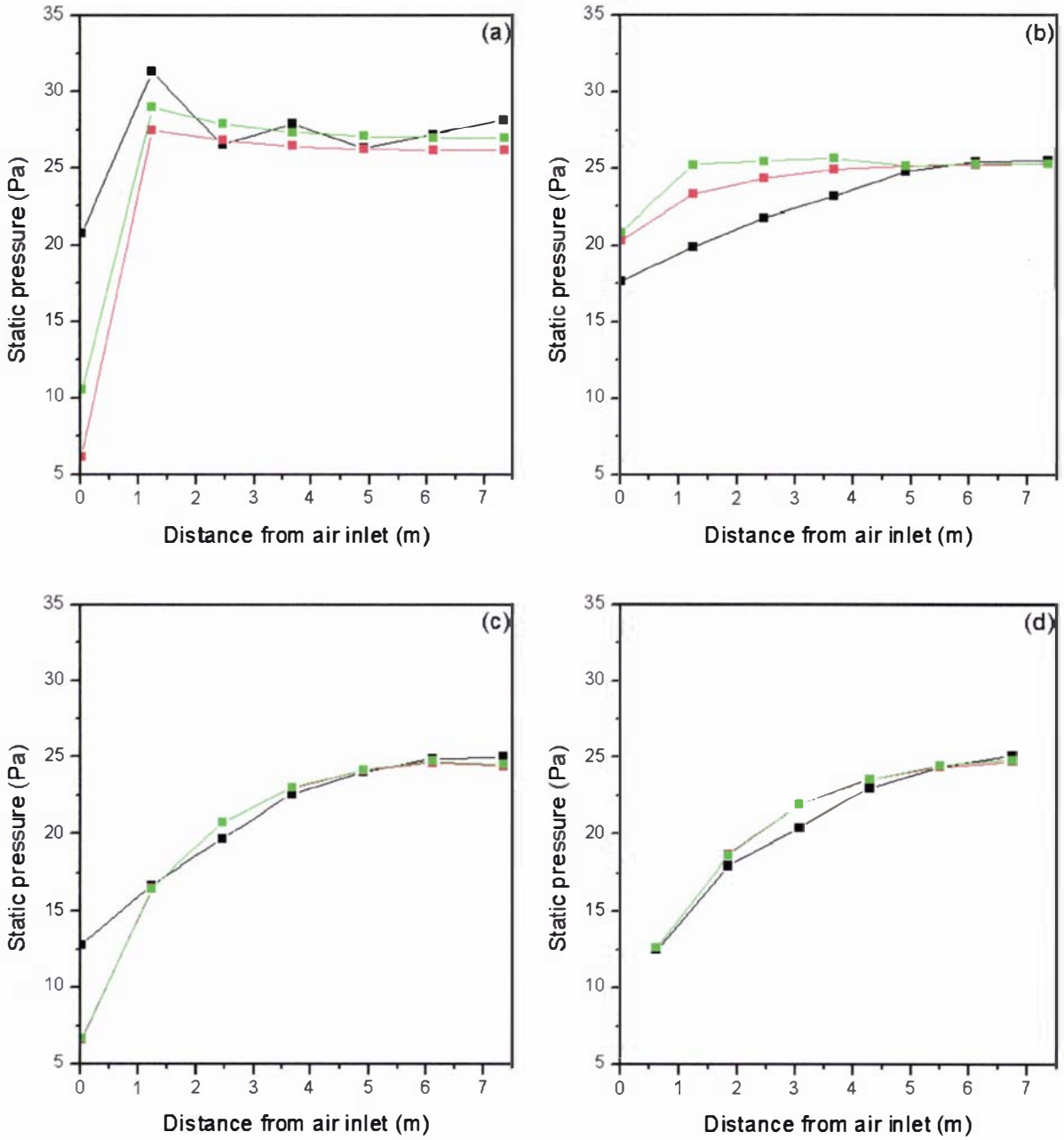

Figure 9-34 - Static pressures in the full-scale laboratory test rig measured (■), predicted using standard turning flow losses (■) and predicted using doubled turning flow losses (■). The test rig had a flat floor and a total flow rate of 4400 $m^3.h^{-1}$. (a) Measurement points at the level of the pallet bases on the side-wall (pressure taps 30 to 36). (b) Measurement points at the level halfway up the height of the pallet on the side-wall (pressure taps 23 to 29). (c) Measurement points in the headspace above the pallets on the side-wall (pressure taps 16 to 22). (d) Measurement points in the headspace above the pallets, in the centre of the ceiling (pressure taps 10 to 15)

Figure 9-35 shows the change in predicted velocity within each vertical channel in the rig. The increased resistance associated with turning flow caused a reduction in velocities of approximately 7% at the end of the rig nearest the fan end and a similar rise in velocity at the end opposite the fan. As flow rate is related approximately to pressure loss by a square law, the increased pressure near the floor caused by the doubled K_{add} values increased the flow in the vertical channels with the least flow.

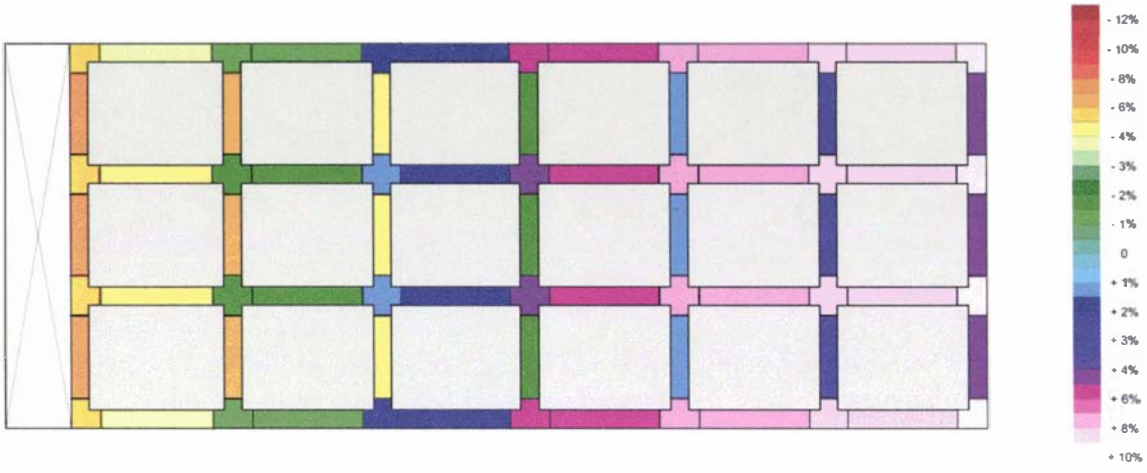

Figure 9-35 - Changes in predicted velocity for each of the vertical channels within the laboratory test rig caused by doubling the turning flow additional frictional loss values (gap dimensions not to scale)

Overall, the results showed the predicted static pressures were insensitive to the loss values used for turning flow. Air velocities in the vertical channels were affected by the change in additional loss values; however, these were also relatively insensitive to the values used, with an approximate 7% change in velocity predicted for a 100% change in the K_{add} values.

9.7 Conclusions

Comparison of predicted and published static pressure data showed excellent agreement in all treatments for all positions except those under the perforated floor. Discrepancies in the under-floor region were attributed to poor estimation of kinetic energy along with measurement difficulties due to turbulent eddies. Circulation rates in the rig were over-estimated by 6 to 18%.

Predicted pressures and airflows were insensitive to the flow resistance of the perforated floor, with no significant differences in air distribution predicted between systems with floor open areas of 1.2% and 3%. Predictions were also insensitive to the additional loss value attributed to turning geometries; doubling the additional loss values caused only relatively moderate changes in the predicted air distribution (7% maximum change in vertical velocity).

10 Integrated 40' Container

10.1 Introduction

Monitoring of in-package temperatures and airflow parameters within a 40' container during a simulated shipment was conducted in conjunction with commercial testing of prototype packaging systems for kiwifruit. Through comparison of predicted and measured velocity data for two experimental runs, the accuracy of the airflow model was tested. Through comparison of predicted and measured in-package temperature data, the accuracy of the airflow model used alongside a heat transfer model was assessed. The sensitivity of predictions to an alternative flow network definition was also tested, as well as a small number of operational and design parameters.

10.2 System description

Twenty pallets of kiwifruit were used to compare the performance of two packaging systems during transport in an integrated 40' refrigerated container. The standard 'modular-bulk' packaging system and a prototype packaging system incorporating vertical channels as described earlier (Section 8.2.1.2) were tested. Figure 10-1 shows the modular-bulk packaging system incorporating a plastic liner to reduce product moisture loss. Pallets were constructed from 100 cartons in a 10-layer configuration.

Figure 10-1 - Photographs depicting the modular-bulk packaging system used by Zespri International Ltd showing placement of a single thermocouple

Temperatures were monitored intensively with 32 type-T thermocouples positioned per pallet along with 18 thermocouples positioned across the width of the air delivery duct and 6 thermocouples across the width of the air return grill of the container. Eight thermocouples were positioned within packages on each of 4 layers (bottom layer, 4th layer up, 7th layer up and top layer) for each of the 20 pallets. The accuracy of the thermocouples was checked using an ice-water slurry (using flake ice and distilled water) prior to commencement of the trial. All temperatures were recorded at 10-minute intervals using Eltek Squirrel data-loggers (1000 series, Eltek Ltd. Cambridge, England). Figure 10-2 shows the position of thermocouples on a single layer.

Thermistor anemometers (Section 5) were used to measure velocities at numerous positions within the container. Twenty-four thermistor sensors were positioned in the floor channels and fifteen in the headspace in three cross-sections along the length of the container as shown in Figure 10-3. A further 21 thermistor sensors were positioned in channels formed between pallets, or within vertical channels within

pallets (if present) during loading. Sensors were calibrated prior to the trial using at least six velocities between 1 and 15 $m.s^{-1}$. Voltages were recorded at 10-minute intervals using 16-channel voltage loggers (1000 series, Eltek Ltd. Cambridge, England).

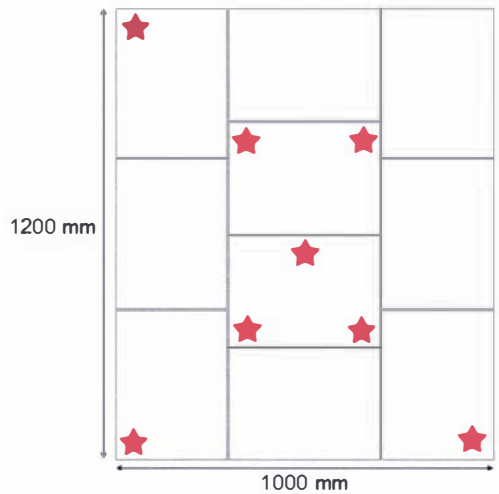

Figure 10-2 - Plan view of a single pallet layer of kiwifruit showing the 8 locations (★) of the type-T thermocouples used to monitor in-package air temperature

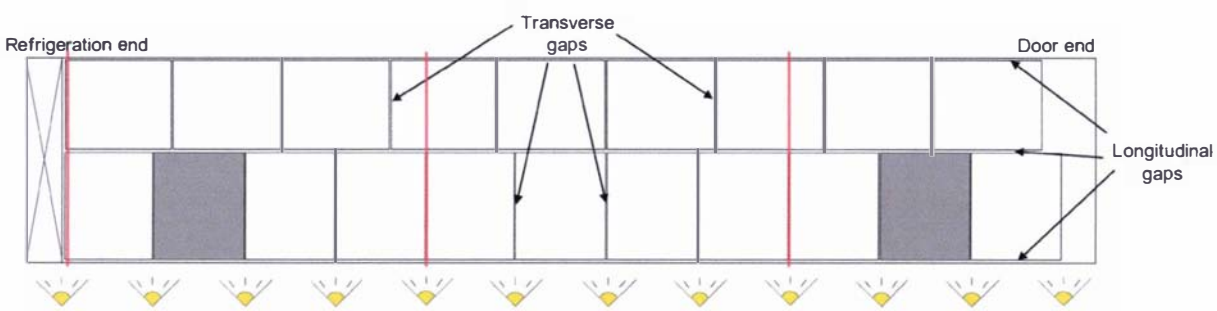

Figure 10-3 - Plan view of the loading configuration used to accommodate 20 pallets of kiwifruit measuring 1.2 × 1.0 m. Red lines indicate the approximate position of thermistor anemometers in the ceiling and floor of the container. Temperatures within shaded pallets were predicted and compared to experimental results

Following instrumentation, the pallets were placed in cool-storage at approximately 5°C. The pallets were left to warm for several hours prior to loading. The loading arrangement shown in Figure 10-3 was used.

The container was positioned within a controlled temperature and humidity chamber specifically designed for testing of refrigerated transport equipment. Conditions within the chamber were varied according to the following schedule over a 5.75-day test cycle:

- 48 hrs at 20°C and 60% RH
- 1 hour ramp to 35°C and 80% RH
- 35°C and 80% RH for 71 hours
- 2 hour ramp to 20°C and 60% RH
- 20°C and 60% RH for 16 hours

In addition, a bank of halogen lights was used to simulate a radiant heat load upon a single side-wall of the container as shown in Figure 10-3. The lights were operated with a 15 hr on, 9 hr off cycle. The container set-point was -0.6°C, and the fresh air exchange vent was set to a nominal 15 $m^3.h^{-1}$. However, the actual rate of fresh air exchange was measured to be approximately 3 $m^3.h^{-1}$ using a gas decay method as outlined by Smale *et al.* (2003a). The defrost interval was 6 hours.

10.3 Flow channel definition

Each of the vertical flow channels within the container was classified into one of four categories: from the T-bar floor channel level to the pallet base level, between a pallet and the wall of the container, between two pallets or vertically through a pallet. Flow channels between the T-bar floor channels and the pallet base level were short but included a contraction and expansion in the cross-sectional flow area and were therefore modelled as a Type I channel, with an additional friction element comprising of a thin orifice with a free area of 65%, giving an additional loss coefficient of 1.0 (Miller, 1990). Channels formed between the wall of the container and a pallet, and between two pallets were both treated as Type I channels with an absolute roughness of 0.0003 m. No specific channels were defined at the corners of pallets, so the vertical channels measured the full dimension of the pallet (e.g. cross-sectional area of a channel between the long face of a pallet and the wall = 1.2 m × 0.025 m). The roughness value was considered appropriate despite the smooth metal walls of the container, as the roughness of the packaging was expected to dominate the flow characteristics.

Pressure-flow relationships were measured for both the packaging systems using a rig specifically designed to simulate refrigerated transport systems (Section 8.2.1.2). Flow vertically through the packaging systems was described using the Ramsin equation coefficients calculated from experimental data (Table 8-3). Insignificant flow was observed through the standard modular-bulk packaging system and so within pallet channels were assigned an arbitrarily high flow resistance (Equation 9-1).

Gaps between pallets were considered unavoidable, as evidenced by the significant quantity of airflow measured through the vertical flow rig stacked with unvented cartons and plastic sheets (Section 8.2.2.2). A minimum spacing of 0.005 m between pallets was used to account for flows between pallets that appeared flush, which gave flows consistent with those measured through unvented pallets in the vertical flow rig. Gaps running down the length of the container (longitudinal gaps) between pallets and between pallets and walls were assumed to be uniform with a width of 0.025 m. Gaps running across the width of the container (transverse gaps) were assumed to be flush. Transverse gaps between the doors and the two nearest pallets, as shown in Figure 10-3, were measured to be 0.55 m or 0.27 m wide.

The horizontal flow channels on the T-bar layer were modelled as Type I channels, with an absolute roughness for aluminium quoted by Perry & Green (1997) of 0.00026 m. The width of the container was broken into nine flow channels, each representing four T-bar channels. There were no holes in the T-bars to allow flow in the transverse direction and therefore no transverse flow channels were defined on this layer. Horizontal flow channels on the pallet base layer were described using the correlation presented in Section 8.3.4. No transverse flow channels between pallet bases were defined as flows in this direction were assumed to be small and insignificant in comparison with the flows in the same direction through the channels through the pallet bases themselves.

Horizontal flow channels at half the height of the pallets were classified into one of two categories: horizontally through a pallet, or between a pair of pallets. Flow channels between pallets were modelled as Type I channels, with an absolute roughness value of 0.0003 m. As the packaging systems were not vented horizontally, horizontal flow channels through the pallets were assigned an arbitrarily high flow resistance (Equation 9-1). Transverse horizontal channels between pallets were not defined as significant horizontal airflows were not expected between pallets.

The horizontal flow channels formed between the ceiling of the container and the top of the cargo were treated as Type I channels with an absolute roughness of 0.0003 m. The clearance between the pallets and ceiling was measured to be approximately 0.30 m.

Nodes were positioned in an irregular grid, made up of four cross-sections through the height of the container: within the T-bar floor channels, at the level of pallet bases, halfway up the height of the pallet and within the headspace (Figure 10-4). Figure 10-5 shows the position of nodes within the floor channels and Figure 10-6 shows the positions on the remaining three levels. Nodes adjacent to the air delivery duct were connected to nine fixed pressure nodes (inlets) and nodes adjacent to the return air grill connected to two fixed pressure nodes (outlets). Multiple inlet and outlet nodes were used to facilitate simulation of a non-uniform pressure profile across the width of the refrigeration unit. Figure 10-7 shows the 3-dimensional illustration of the flow network generated.

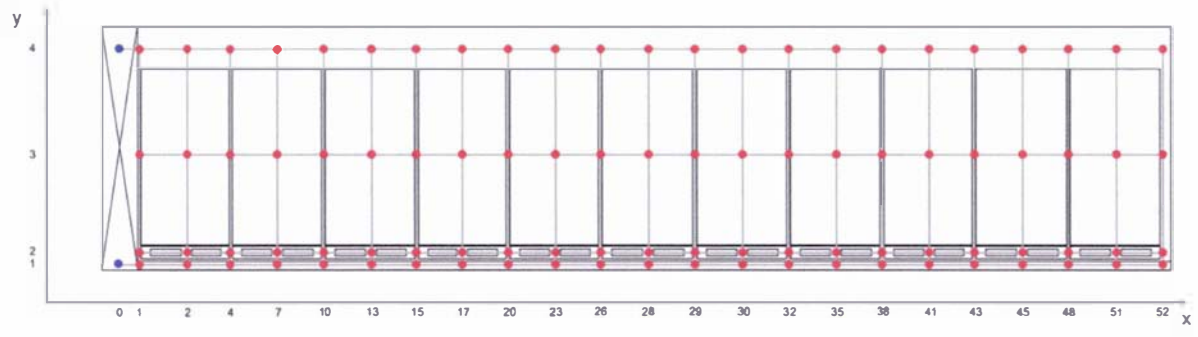

Figure 10-4 - Elevation view of the 40' container loaded with 20 pallets showing the flow resistance network defined for the Z = 3 plane. Blue circles represent fixed pressure nodes, red circles represent unknown pressure nodes, and grey cylinders represent flow channels

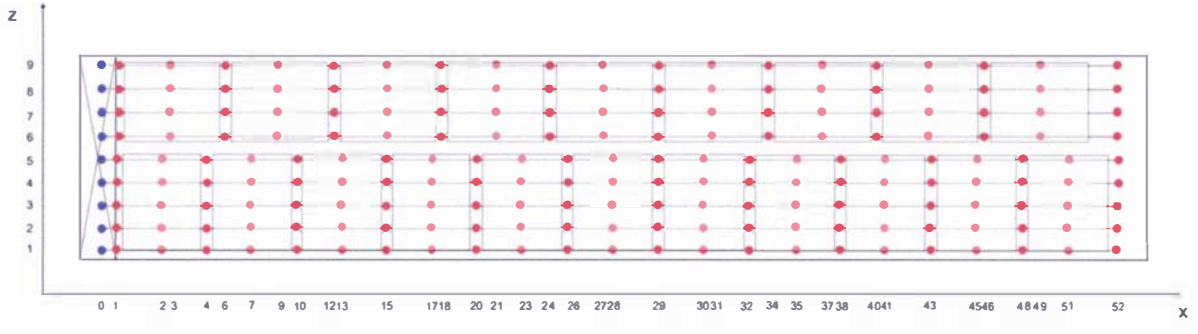

Figure 10-5 - Plan view of the 40' container loaded with 20 pallet showing the flow resistance network defined on the floor grating layer (Y = 1). Blue circles represent fixed pressure nodes, red circles represent unknown pressure nodes, and grey cylinders represent flow channels

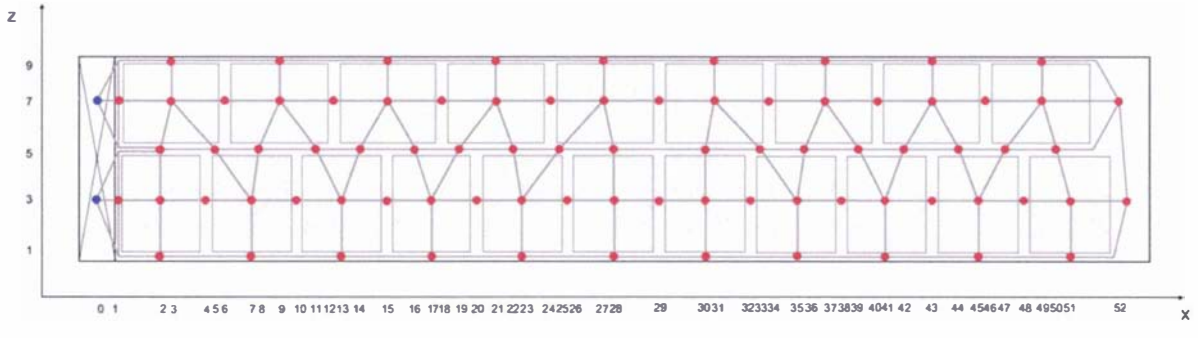

Figure 10-6 - Plan view of the 40' container loaded with 20 pallet showing the flow resistance network defined on the layers above the floor grating layer (Y > 1). Blue circles represent fixed pressure nodes (on Y = 4 layer only), red circles represent unknown pressure nodes, and grey cylinders represent flow channels

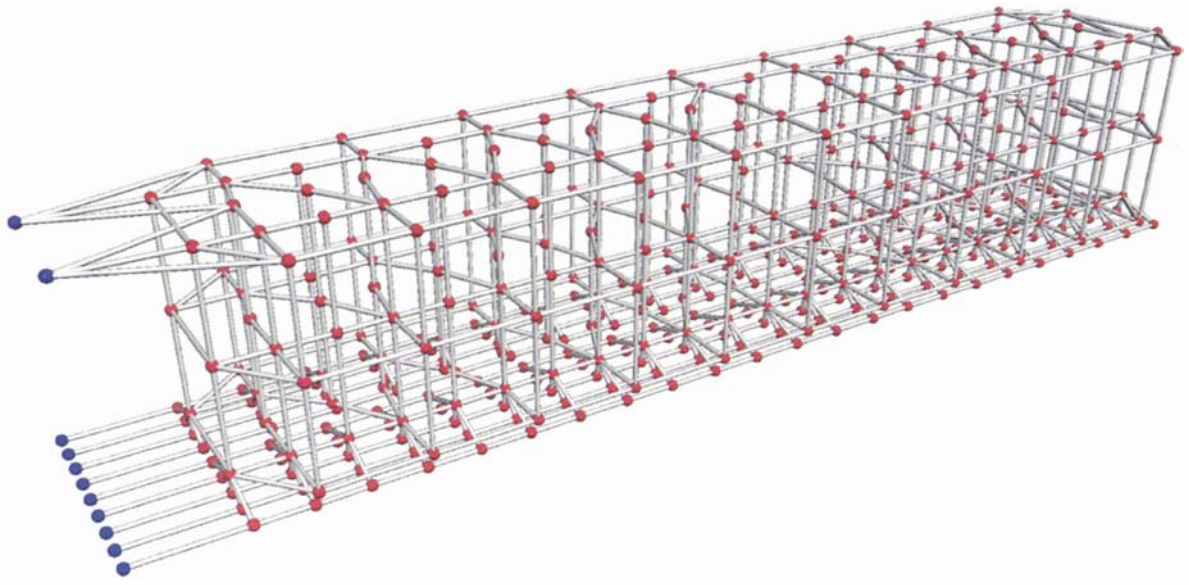

Figure 10-7 - Three-dimensional representation of the flow network approximation of the 40' container loaded with 20 pallets of kiwifruit. Blue circles represent fixed pressure nodes, red circles represent unknown pressure nodes, and grey cylinders represent flow channels

Miscellaneous friction causing elements were also included in the model. Flow exiting the top of the pallets experienced an infinite expansion (K_{add} = 1.0). The geometry of flow entering the vertical channels formed by gaps around pallets was modelled as a contraction and a square bend (Perry & Green, 1997, square 90° bend (1.3) and contraction (0.3); K_{add} = 1.6). Due to the large size of the channel above the cargo and subsequent low horizontal velocity, fluid entering these channels combining with the horizontal flow was unlikely to cause increased frictional losses.

The overall network consisted of 11 fixed pressure nodes, 431 unknown pressure nodes and 911 flow channels. A non-uniform pressure profile was assumed across the nine inlet fixed pressure nodes, as shown in Figure 10-8, while outlet fixed pressure nodes were assigned total pressures of zero. The non uniform pressure profile was used due to the 2-fan design of the refrigeration unit and was scaled to give a total flow rate of approximately 75 air changes per hour.

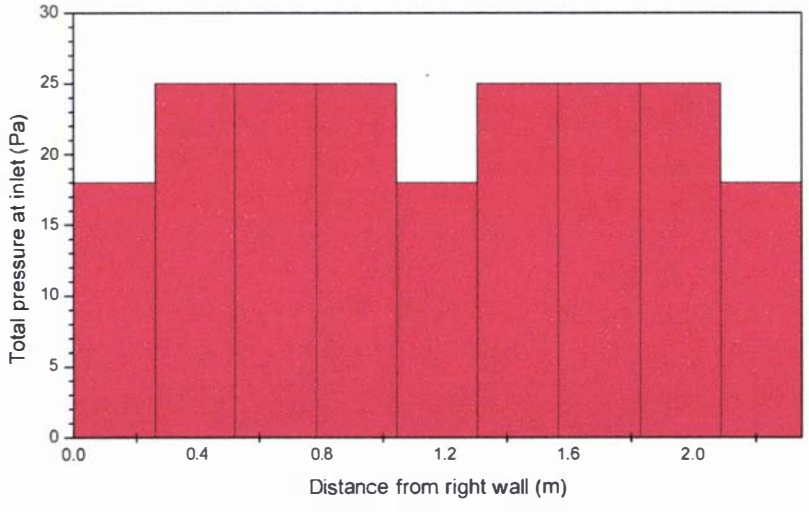

Figure 10-8 - Assumed inlet pressure conditions across the air delivery duct of the 40' container

10.4 Simulation results

Simulations took approximately 100 seconds and there were no convergence problems. The predicted circulation rate was 4900 $m^3.h^{-1}$ (73 air changes per hour) for the standard packaging system and 5000 $m^3.h^{-1}$ (75 air changes per hour) for the prototype packaging system.

10.4.1 Standard packaging system

Measured velocities and air temperatures were reasonably consistent over both the frosting/defrost cycle and the 5.75 day test cycle (Figure 10-9). The average delivery velocity across the width of the container fell only slightly between defrosts; however, the low rate of fresh air exchange (3 $m^3.h^{-1}$) compared with the nominal vent setting (15 $m^3.h^{-1}$) will have reduced the quantity of moisture deposited as frost on the evaporator.

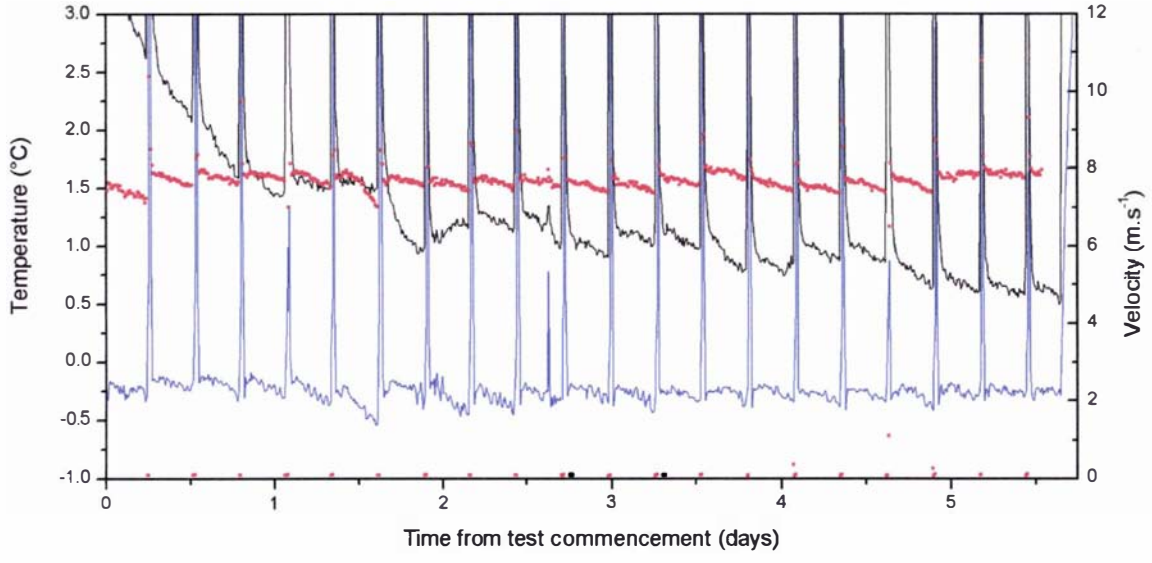

Figure 10-9 – Spatially-averaged measured delivery temperature (-), return temperature (-) and velocity (•) over the duration of the simulated shipment with standard packaging

Figure 10-10 shows the predicted and measured air velocities in the floor channels and Figure 10-11 shows the predicted and measured air velocities in the headspace above the cargo. Measured velocities varied widely across the width of the container, which was attributed to sensor movement during loading affecting positioning within the flow channels and possibly subsequent damage to the sensors. Predicted velocities were relatively uniform across the width of the container, with slightly lower velocities predicted on the right side of the container (facing the refrigeration unit from the door end) where the pallets had their short end facing the primary airflow direction and gap adjacent to the door was larger. Almost all thermistor anemometers placed between pallets gave velocity readings lower than 1 $m.s^{-1}$. As the accuracy of the thermistor anemometers was poor at these low flows, little detailed information could be inferred from this data.

Figure 10-12 shows the average measured and predicted velocity at each measurement position along the length of the container. Agreement between the predicted and measured velocities in the floor at different positions down the length of the container was good if the variation with width across the container was ignored. Predicted velocities in the ceiling headspace were significantly higher than those measured. The disagreement was thought to be due to positioning of the thermistor anemometers in the upper part of the ceiling headspace to facilitate loading, rather than the centre of the channel.

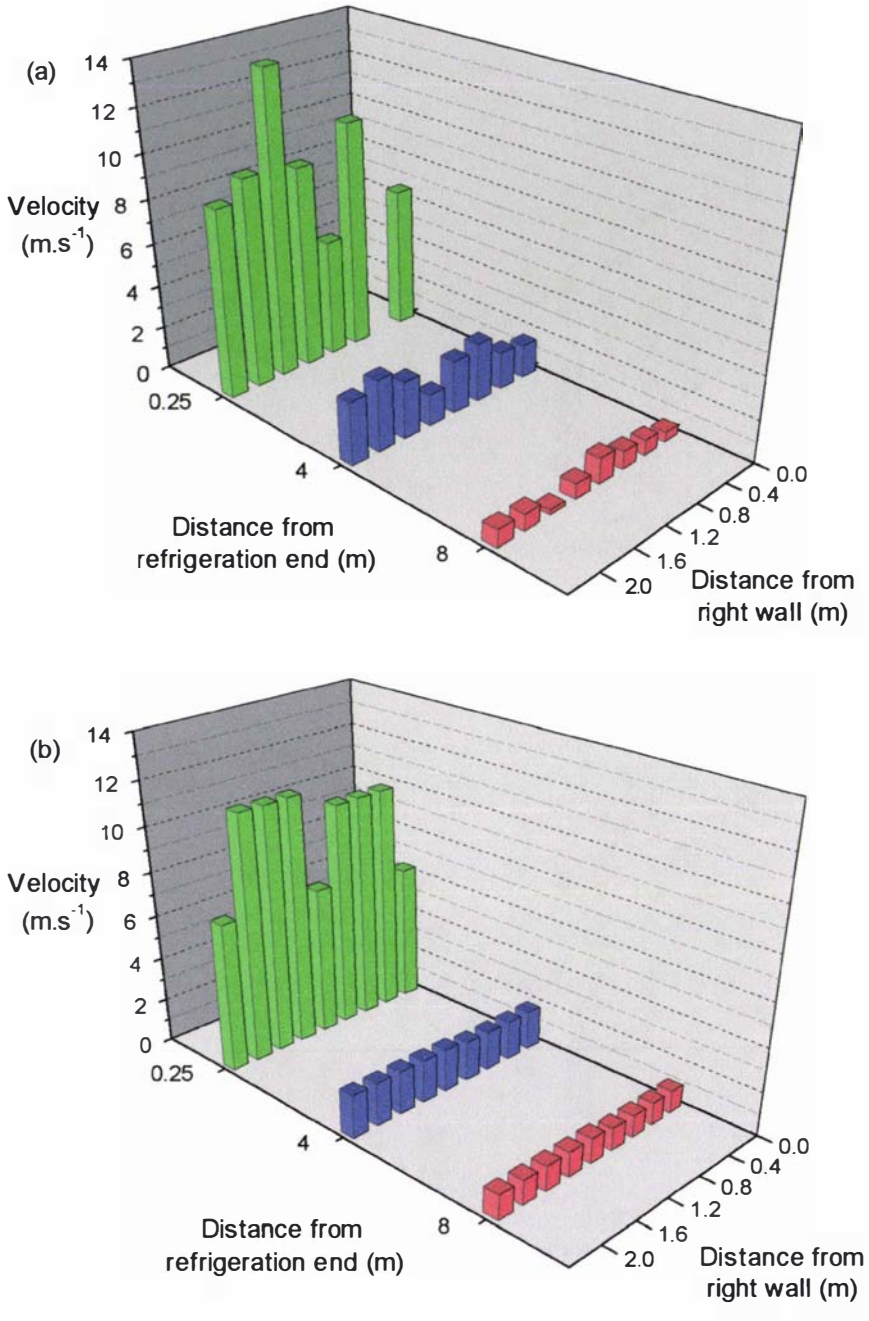

Figure 10-10 - (a) Measured and (b) predicted horizontal velocities in the T-bar floor channels of the 40' container loaded with kiwifruit packaged in the standard packaging system

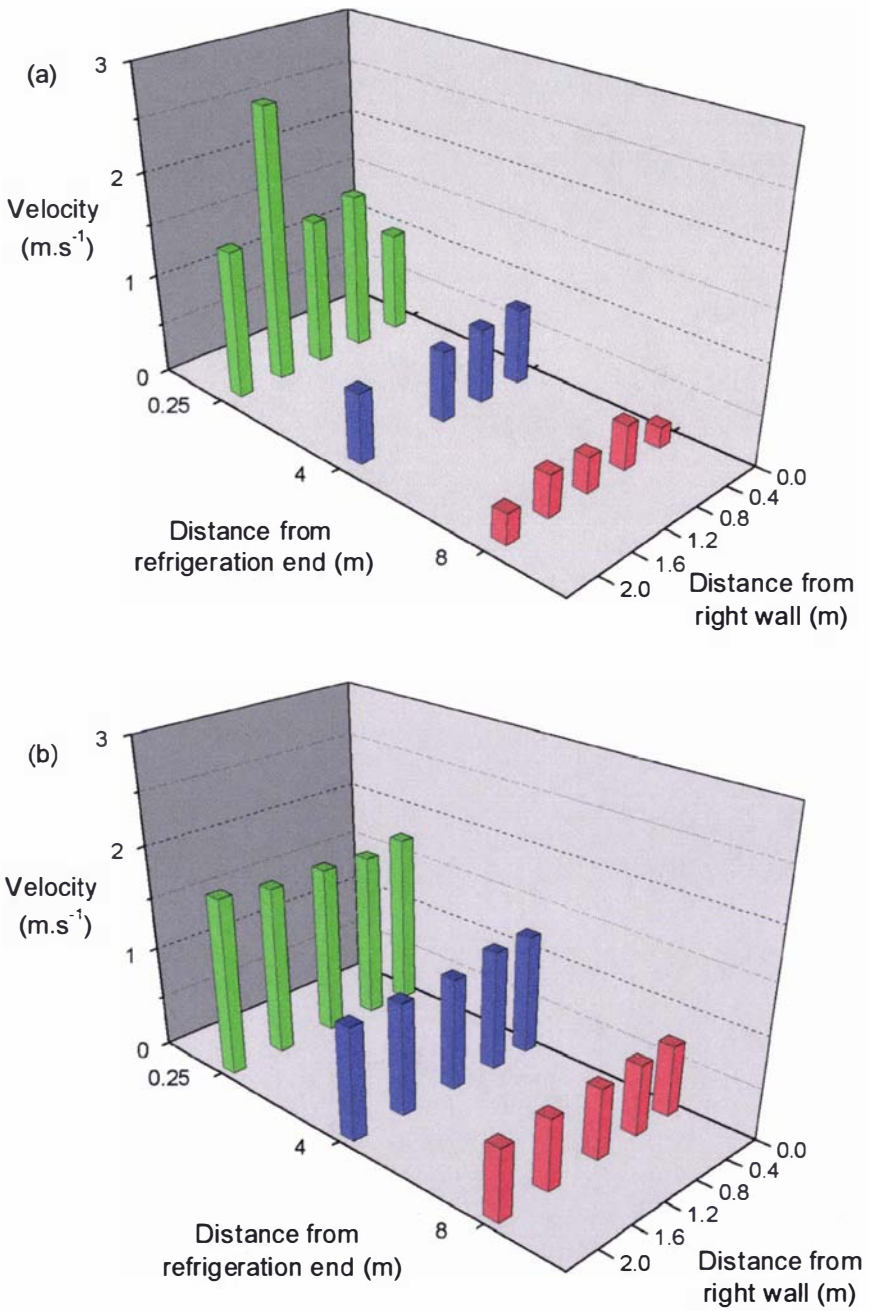

Figure 10-11 - (a) Measured and (b) predicted horizontal velocities in the ceiling headspace of the 40' container loaded with kiwifruit packaged in the standard packaging system

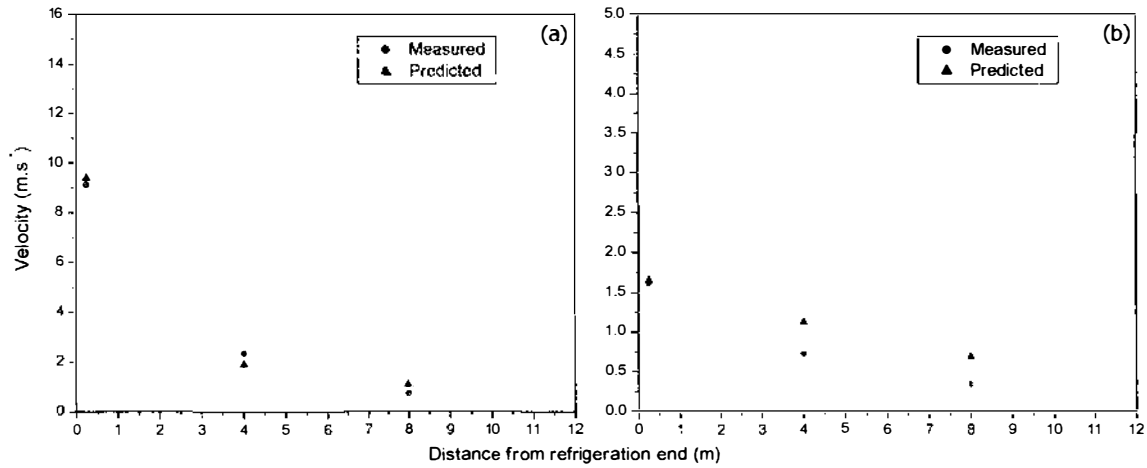

Figure 10-12 - Measured and predicted horizontal velocities (a) in the floor and (b) ceiling headspace of the 40' container loaded with kiwifruit packaged in the standard packaging system (error bars show the estimated 95% confidence interval for each measurement position along the length of the container)

Figure 10-13 shows the predicted velocities in each of the vertical channels surrounding the pallets. The channel sizes have been exaggerated in this diagram to aid visualization of the data. Velocities in the transverse channels were low due to their small width and associated high flow resistance. Velocities in the longitudinal gaps were higher, ranging from around 2 $m.s^{-1}$ near the refrigeration end, to 0.4 $m.s^{-1}$ near the door end. The vertical velocity decreased with distance from the fan end of the rig; however, the low velocities in the very large spaces formed near the doors were still associated with movement of significant flow rates of air. Velocity trends down the length of the container were uniform across the width for both the longitudinal and transverse vertical channels. Fluid velocities in vertical channels near the refrigeration end of the container were 5 to 8 times greater than those in similar channels near the door end.

Anemometers placed in vertical channels near the refrigeration unit gave readings <1 $m.s^{-1}$; however, predictions were for velocities as large as 2 $m.s^{-1}$. The discrepancy was attributed to sensor positioning and non-standard gap widths in the real system plus variation in the widths of individual channels. Whilst a single channel width value was recorded where sensors were placed, the large level of variation in gap width through the height of the pallets rendered the data unreliable. Placement of the thermistor anemometers in the centre of the very narrow channels was difficult, so it was probable that many sensors were positioned near the walls of the channel rather than in the centre. The boundary layer effects near the channel walls may explain the lower measured velocities than predicted.

Figure 10-14 shows the predicted temperature rise in each of the vertical channels, calculated in the same fashion as described in Section 9.3.2. Predicted temperature rise in the transverse channels was high, due to their narrowness and consequently low volumetric flow rates. In contrast, low temperature rises were predicted for the channels near the door due to their large width and high volumetric flow rates. The predicted temperature rise in the longitudinal channels increased with distance from the refrigeration end and channels adjacent to the wall gave substantially higher temperature rises than those in the central channel. Temperature rises in the central channels ranged from 0.25°C to 1.5°C, whilst those against the walls ranged from 0.8°C to 4.4°C.

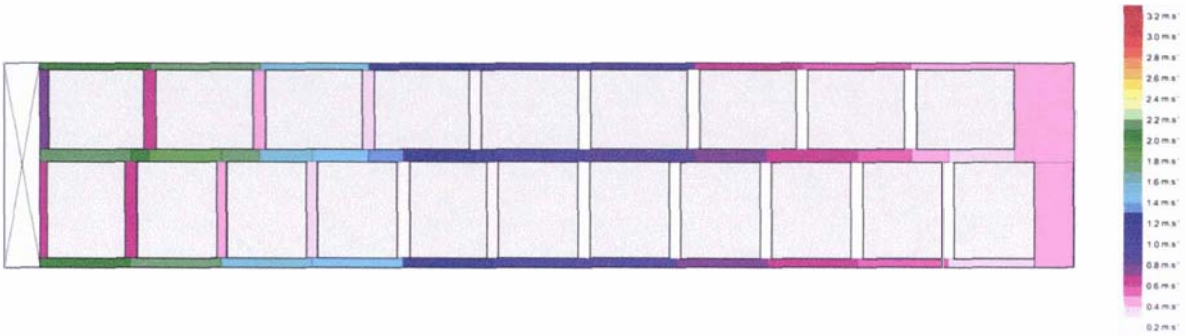

Figure 10-13 - Predicted velocity in each of the vertical channels formed by gaps around pallets within the 40' container loaded with kiwifruit packaged in the standard packaging system (gap dimensions not to scale)

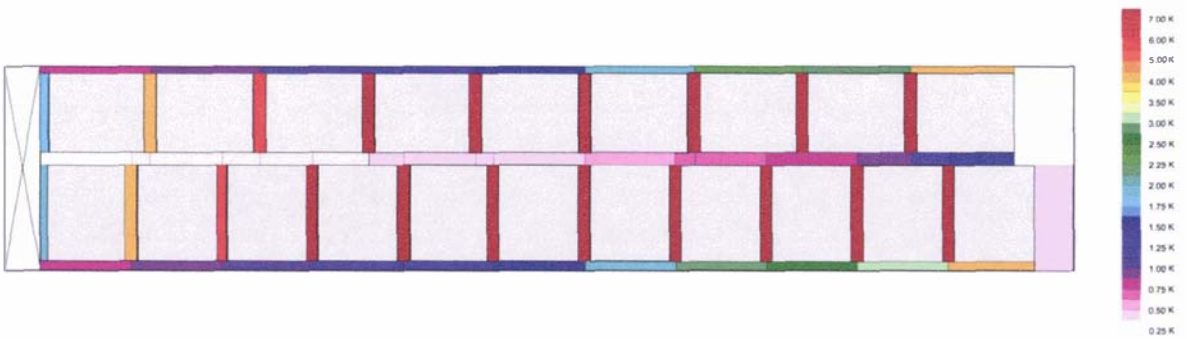

Figure 10-14 - Predicted temperature rise in each of the vertical channels formed by gaps around pallets within the 40' container loaded with kiwifruit packaged in the standard packaging system (gap dimensions not to scale)

10.4.2 Prototype packaging system

Figure 10-15 shows the predicted and measured air velocities in the floor channels and Figure 10-16 shows the predicted and measured horizontal air velocities in the headspace above the cargo. Measured velocities varied more widely across the width of the container than for the standard carton, which was attributed to further sensor movement and damage associated with loading/unloading of pallets; which occurred three times between the two trials. Figure 10-17 shows the average measured and predicted velocity at each measurement position along the length of the container. Good agreement was again found between measured and predicted velocities when measured variability across the width of the container was ignored.

As shown by comparison of Figure 10-12 with Figure 10-17, differences between measured velocities for the two packaging systems were not significant. Predicted horizontal velocities were similar to the standard packaging system, with velocities slightly higher near the delivery duct (3.5%), and lower in the two slices further along the length of the container (5% and 12% respectively). Again, almost all thermistor anemometers placed between pallets gave velocity readings lower than 1 $m.s^{-1}$, meaning little detailed information could be interpreted from this data.

Measured velocities in the floor channels and ceiling headspace showed no significant change caused by the change in packaging flow resistance. The differences predicted by the model were also very small. A key observation was that the reduced packaging vertical flow resistance was predicted to have little effect on the overall flow patterns, in agreement with the measured velocities.

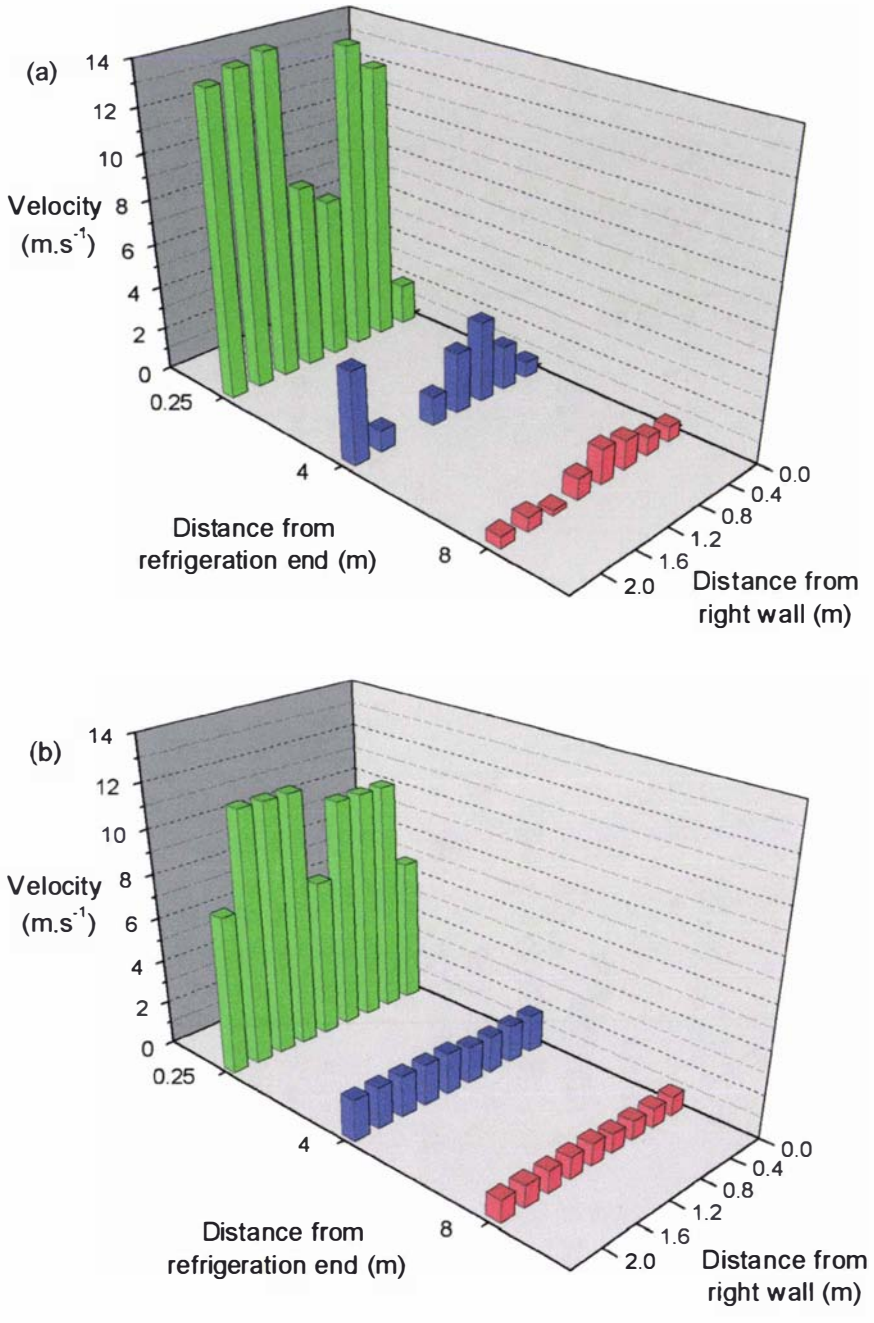

Figure 10-15 - (a) Measured and (b) predicted horizontal velocities in the T-bar floor channels of the 40' container loaded with kiwifruit packaged in the prototype packaging system

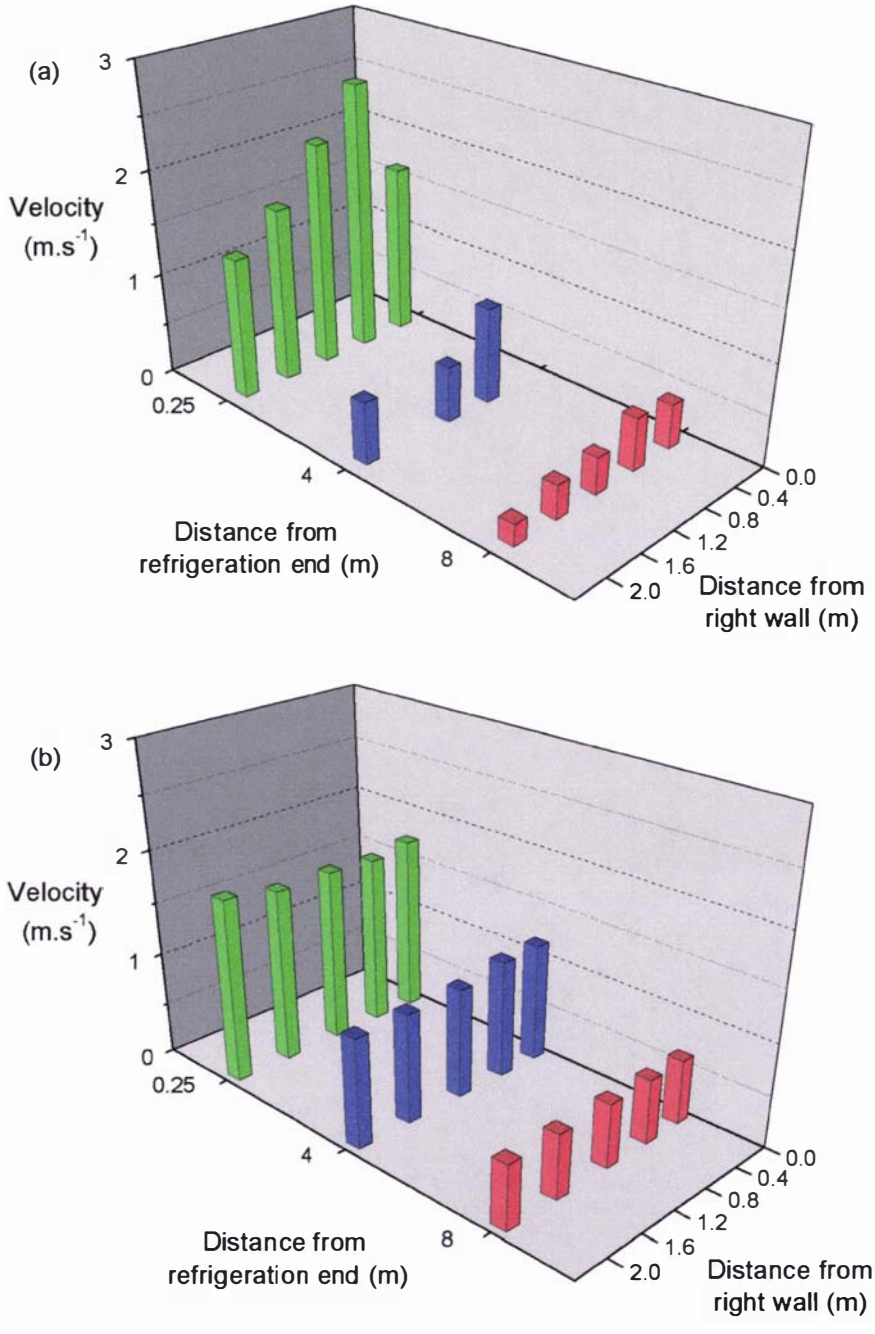

Figure 10-16 - (a) Measured and (b) predicted horizontal velocities in the ceiling headspace of the 40' container loaded with kiwifruit packaged in the prototype packaging system

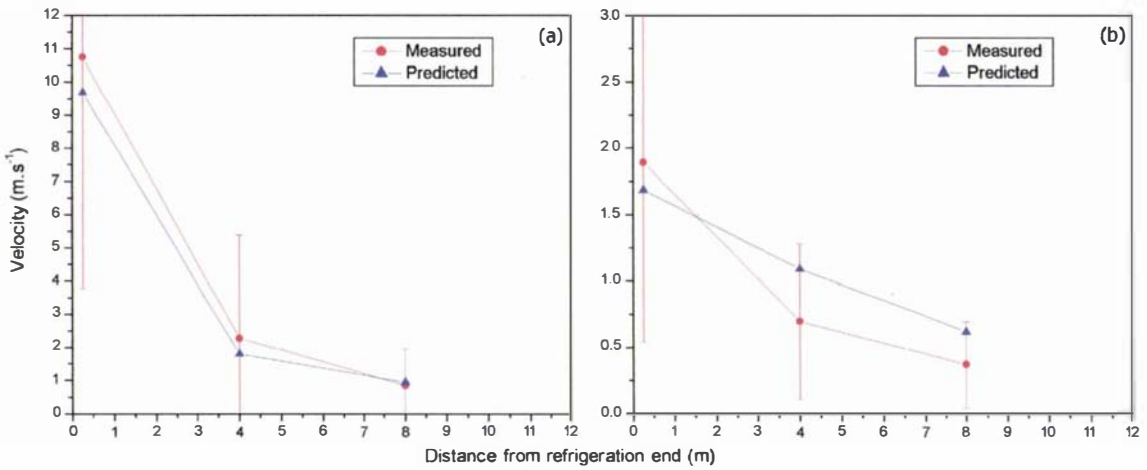

Figure 10-17 - Measured and predicted horizontal velocities (a) in the floor and (b) ceiling headspace of the 40' container loaded with kiwifruit packaged in the prototype packaging system (error bars show the estimated 95% confidence interval for each measurement position along the length of the container)

Figure 10-18 shows the predicted velocities in each of the vertical channels surrounding the pallets and through the channels within the pallets. Velocities in the transverse channels were again low due to their small width and associated high flow resistance. Velocities in the channels within the pallet ranged from 2.5 $m.s^{-1}$ near the refrigeration end to 0.3 $m.s^{-1}$ near the door end. The predicted velocities in the channels around the pallets were lower for the prototype packaging system than the standard system. Channel velocities were reduced proportionally more in the channels near the door end (15%) than the refrigeration end (3%). As shown in Figure 10-19, the reduction in flow caused an increased predicted temperature rise in longitudinal channels near the walls and a slight reduction in temperature rise in the central channels. Near the door end, the predicted temperature rise in channels near the walls was 0.6°C higher, whilst in the central channel the predicted temperature rise was 0.2°C lower.

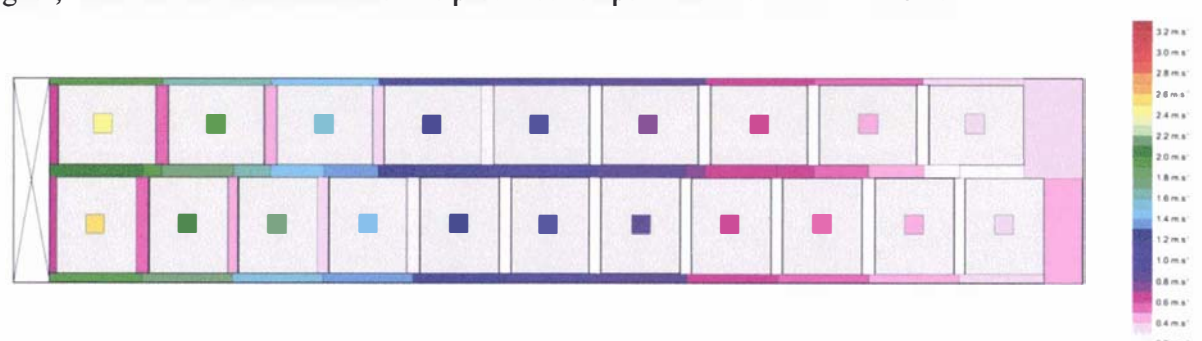

Figure 10-18 - Predicted velocity in each of the vertical channels formed by gaps around pallets and channels formed within pallets in the 40' container loaded with kiwifruit packaged in the prototype packaging system (gap and in-pallet channel dimensions not to scale)

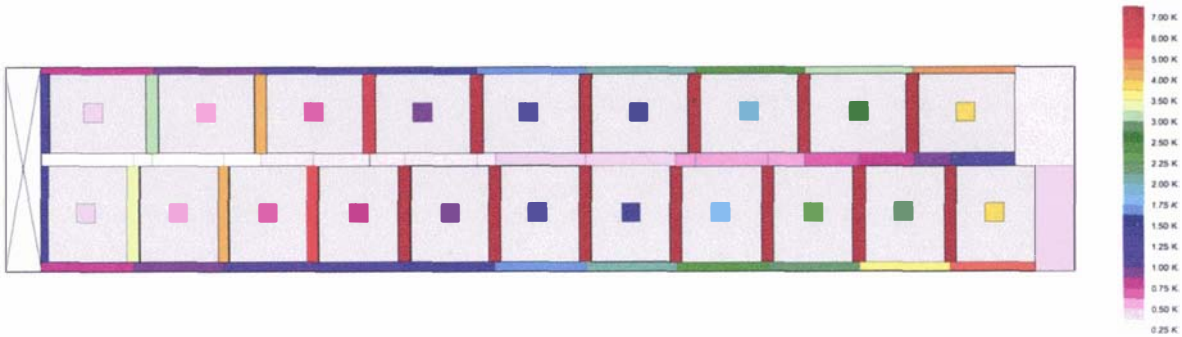

Figure 10-19 - Predicted temperature rise in each of the vertical channels formed by gaps around pallets and channels formed within pallets in the 40' container loaded with kiwifruit packaged in the prototype packaging system (gap and in-pallet channel dimensions not to scale)

The prototype packaging system allowed a greater quantity of air to flow through the pallet stacks themselves; but in doing so, reduced the quantity of air flowing around the pallets. Decreasing the flow resistance within pallets at the refrigeration end slightly decreased the quantity of air that flowed to the door end of the container. The magnitude of the flow reduction at the door end and the quantity of flow though each of the pallets will affect the overall cooling effectiveness of the system. These factors have contrary effects and assessment of the system requires quantitative analysis of these factors.

10.4.3 In-package temperatures

To further investigate the influence of the confounding effects of the prototype packaging system, heat transfer predictions were performed for both packaging systems. A heat transfer model, "PackSim" (Tanner, 1998) was used to predict the cooling of one pallet positioned near the refrigeration end and one pallet positioned near the door end of the container (Figure 10-3).

Table 10-1 gives the input data used in the model and Figure 10-20 shows the bounds of each of the zones on a single layer of cartons. A line of symmetry was used to reduce the domain and decrease the simulation time.

Table 10-1 - Data used in the simulation of cooling in a pallet of kiwifruit. Data values were sourced from physical measurement of the cartons and Tanner (1998)

Variable	Value	Units
Physical System Data		
Width of system (x)	0.503	m
Height of system (y)	1.9	m
Length of system (z)	1.36	m
Package properties		
Zones in x - direction	4	
Zones in y – direction	10	
Zones in z – direction	11	
Number of V boundaries	484	
Number of H boundaries	550	
Number of P boundaries	480	
Total internal zones	440	
Total external zones	4	
Number of pack materials	6	
Number of active surfaces	6	
Product data		
Specific heat capacity	3650	$J.kg^{-1}.K^{-1}$
Thermal conductivity	0.427	$W.m^{-1}.K^{-1}$
Total mass of product	500	kg
Radius of each product item	0.02	m
Number of products in pack	5000	
Is respiration considered?	Yes	
Respiration coefficient a	8.97×10^{-5}	
Respiration coefficient b	1.74	
Fluid data		
Specific heat capacity	1005	$J.kg^{-1}.K^{-1}$
Thermal conductivity	0.026	$W.m^{-1}.K^{-1}$
Density	1.28	$kg.m^{-3}$
Convection factor	1	
External environment data		
Delivery temperature	-0.4	°C
Delivery temperature (against wall)	0	°C
Return temperature	0.75	°C
External temperature	50	°C
Packaging material data		
Package wall (1, 2, 3, 4, 6 thicknesses)		
Specific heat capacity	1700	$J.kg^{-1}.K^{-1}$
Thermal conductivity	0.065	$W.m^{-1}.K^{-1}$
Density	250	$kg.m^{-3}$
Single thickness	0.004	m
Container wall		
Specific heat capacity	1210	$J.kg^{-1}.K^{-1}$
Thermal conductivity	0.06	$W.m^{-1}.K^{-1}$
Density	250	$kg.m^{-3}$
Thickness	0.1	m

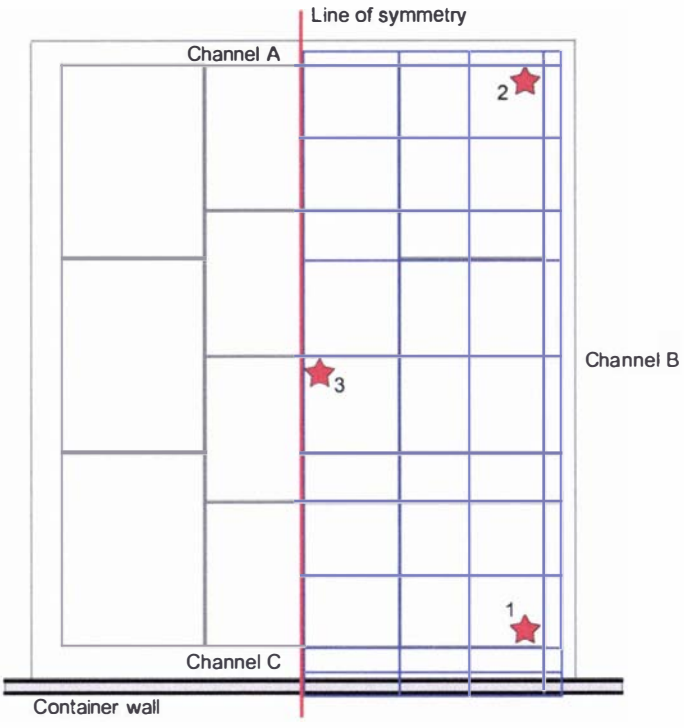

Figure 10-20 - Plan view of a single pallet layer of kiwifruit showing the defined zone boundaries on each layer of cartons and the three locations (★) used for comparison of simulated temperatures

The average air delivery temperature over the length of the test was used as the incident air temperature for the majority of the system. A second air temperature was used for the channel between the pallet and the wall (channel C), because air delivery measurements indicated that air temperatures adjacent to the wall were elevated above those across the remainder of the container width (Figure 10-21, Table 10-1). Variation in delivery air temperatures over the length of the test was not considered a significant source of error (Figure 10-9). The container wall was treated as a layer of packaging, with a thermal resistance of 0.6 $W.m^{-2}.K^{-1}$ and a constant external temperature of 50°C. The container's external wall temperature was measured to be approximately 70°C when under solar load and either 25°C or 35°C when not under solar load depending on the stage of the simulated voyage. For simplicity, the mid-point of 50°C was used.

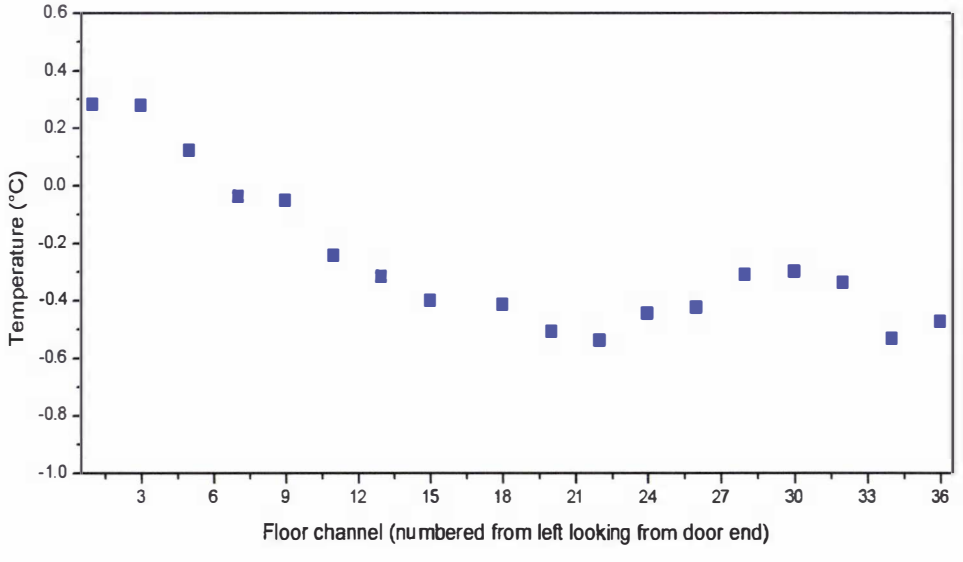

Figure 10-21 – Time averaged air delivery temperature (•) across the width of the container

The system was assumed to be at a uniform initial temperature equal to the average measured fruit temperature following loading of the container. Initial temperature variability within a pallet was significant; however, insufficient data was available to accurately describe the variability.

The heat transfer model allowed the external boundaries of the domain to be either null (no heat transfer) or assigned a fixed external temperature and heat transfer coefficient. As the gaps between the pallet of interest and other pallets remove heat from both pallets, the gaps were modelled as half their actual width with no heat transfer across the external boundary. In this fashion it was assumed the adjacent pallet was at the same temperature as the pallet of interest. The top and bottom faces of the pallet were modelled as external boundaries over which heat transfer may occur with the fluid above and below the pallet assumed to be at a constant temperature and velocity. The average delivery and return air temperatures were used as the external fluid temperatures for these boundaries.

As the incident air temperatures and velocities were assumed to be constant, defrosting of the evaporator was ignored.

10.4.3.1 Standard packaging system

Figure 10-22 to Figure 10-24 show the predicted and measured cooling curves for pallets near the refrigeration end and the door end of the container. Presented temperatures correspond to the positions depicted in Figure 10-20. Positions 1 and 2 in the corner of the pallet were the positions most sensitive to the predicted fluid velocity in the channels, while position 3 near the centre of the pallets was less sensitive to the predicted velocities.

Agreement between predicted and measured cooling was good for positions 1 and 2 given the widely variable initial temperatures within the pallet (1.5°C to 6.1°C). Agreement in position 3 was poorer, which was thought to be due to a small quantity of diffusive flow through the pallet stack, not accounted for in the model. As mentioned above, there was no obvious pattern in the initial temperature distribution and consequently the influence of the temperature of adjacent cartons was significant but not able to be accurately reflected in the model initial conditions. Also, initial temperatures were not significantly greater than the delivery air temperature, which made cooling rates difficult to characterise and subject to substantial uncertainty. The variable initial temperatures and only moderately elevated initial temperature were shortcomings of the experiment.

Predicted cooling rates were lower near the wall due to the higher delivery air temperatures and heat load infiltrating the container wall. The predicted temperature rise in channels A, B & C surrounding the pallets (Figure 10-20) was approximately 0.2°C, 1.7°C, 0.9°C respectively near the refrigeration end and 0.7°C, 3.4°C, 2.7°C near the door end. No corresponding air temperatures were measured for comparison.

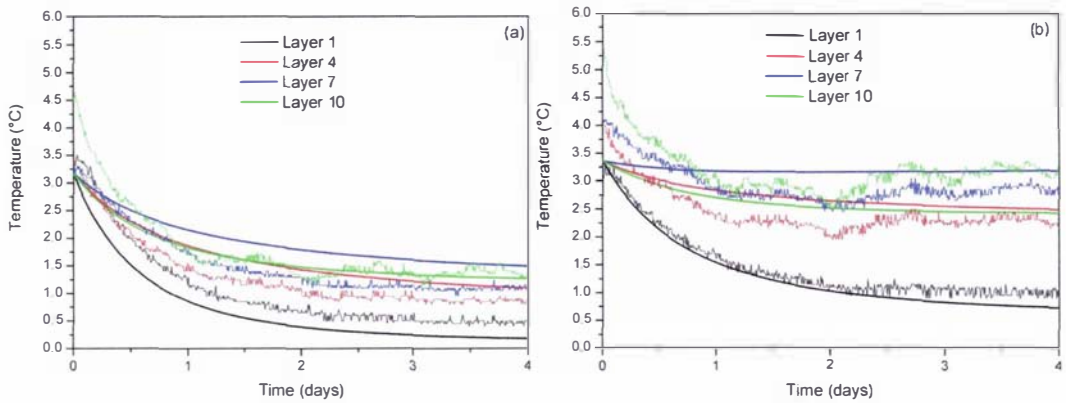

Figure 10-22 - Predicted (smooth lines) and measured (noisy lines) cooling curves for position 1 on four layers within a pallet constructed with standard cartons (a) near the refrigeration end of the container and (b) near the door end of the container

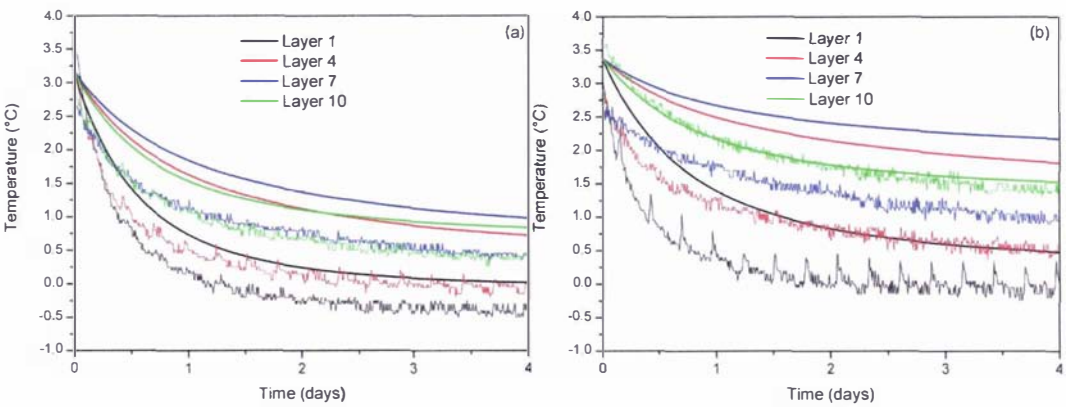

Figure 10-23 - Predicted (smooth lines) and measured (noisy lines) cooling curves for position 2 on four layers within a pallet constructed with standard cartons (a) near the refrigeration end of the container and (b) near the door end of the container

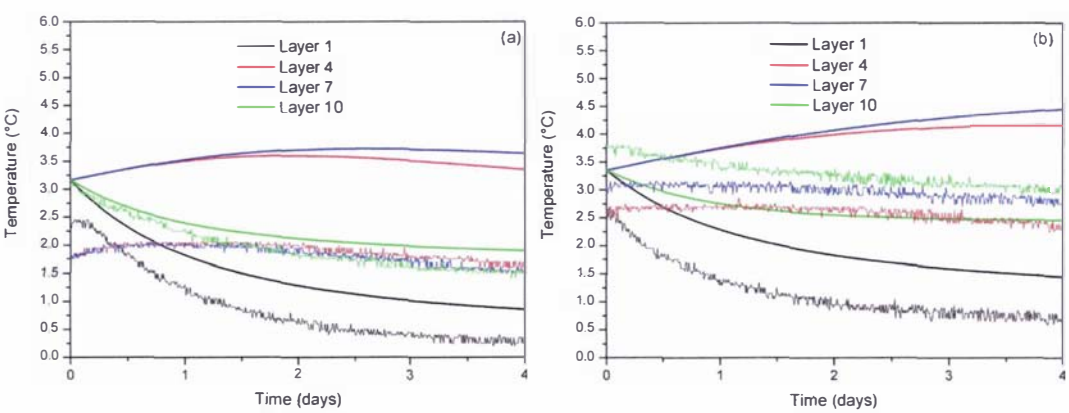

Figure 10-24 - Predicted (smooth lines) and measured (noisy lines) cooling curves for position 3 on four layers within a pallet constructed with standard cartons (a) near the refrigeration end of the container and (b) near the door end of the container

10.4.3.2 Prototype packaging system

Figure 10-25 to Figure 10-27 show the predicted and measured cooling curves for pallets using the prototype packaging system near the refrigeration end and the door end of the container. Again, initial temperatures varied widely within the pallets (1.9°C to 7.8°C) but were not able to be accurately reflected in the model initial conditions. Initial temperatures were elevated above the delivery air temperature to a greater extent than for the standard packaging system.

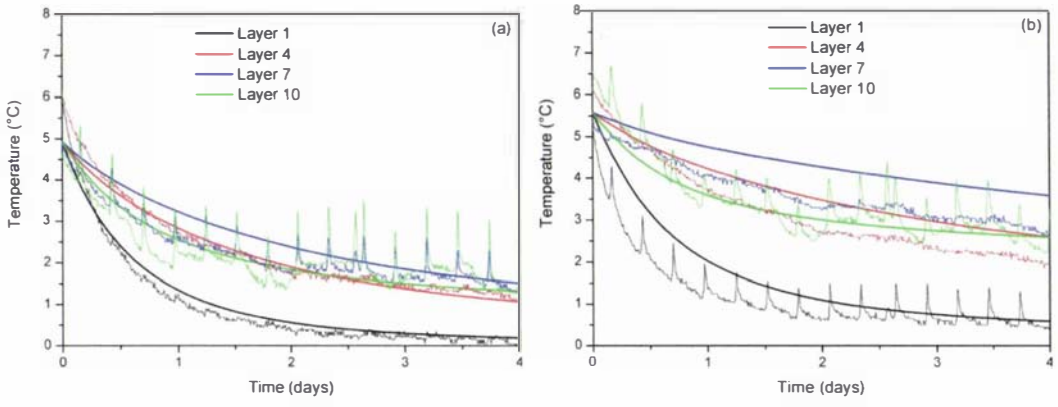

Figure 10-25 - Predicted (smooth lines) and measured (noisy lines) cooling curves for position 1 on four layers within a pallet constructed with prototype cartons (a) near the refrigeration end of the container and (b) near the door end of the container

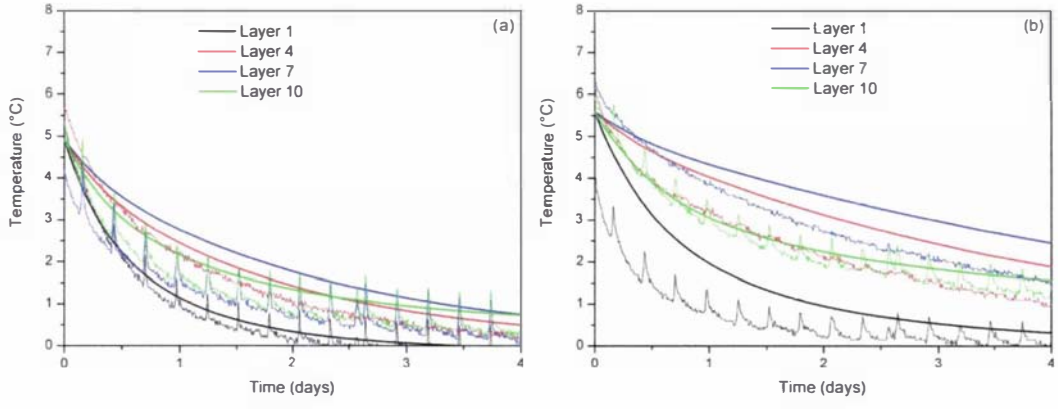

Figure 10-26 - Predicted (smooth lines) and measured (noisy lines) cooling curves for position 2 on four layers within a pallet constructed with prototype cartons (a) near the refrigeration end of the container and (b) near the door end of the container

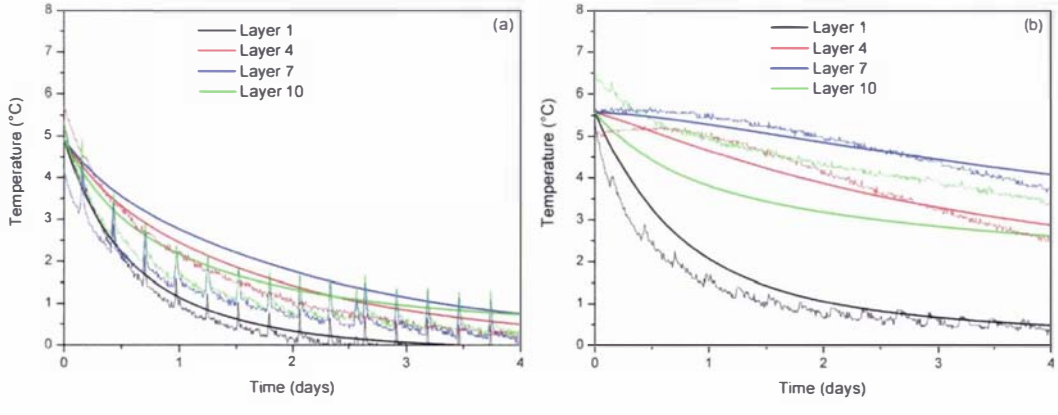

Figure 10-27 - Predicted (smooth lines) and measured (noisy lines) cooling curves for position 3 on four layers within a pallet constructed with prototype cartons (a) near the refrigeration end of the container and (b) near the door end of the container

Again, agreement between predicted and measured cooling rates was good considering the limitations of the experimental data. As flows through the pallet stack were quantified and included in the prototype system model, agreement in position 3 was improved in comparison to the standard packaging system. Again, cooling was slower near the wall. The predicted temperature rise in channels A, B & C surrounding the pallets (Figure 10-20) was approximately 0.1°C, 2.3°C, 1.0°C respectively near the refrigeration end and 0.7°C, 4.5°C, 3.2°C near the door end. The temperature rise in the channels within the pallet stack itself was 0.7°C and 3.4°C for the refrigeration and door ends respectively.

The measured increase of in-package temperatures due to evaporator defrost was greater for the prototype packaging system (Figure 10-25 to Figure 10-27) than for the standard packaging system (Figure 10-22 to Figure 10-24). The difference was due to the greater surface area of the packaging system as a result of the vertical channels; however, some of the difference may also have been due to variable positioning of thermocouples within the cartons.

Figure 10-28 and Figure 10-29 compare the predicted cooling curves for the two packaging systems at both ends of the container. These predictions are presented using fraction unaccomplished temperature change values, calculated using Equation 10-1. Fraction unaccomplished temperature change is a measure of the proportion of cooling achieved and provides a means to present cooling rate information that is less affected by the different initial and final temperatures for the two systems. These results clearly show the improved cooling performance of the prototype cartons throughout the container. The effect of the reduced airflow around the pallets was far outweighed by the increased flow through the pallet stack itself. The improved cooling was most significant in positions central to the stack. The increase in cooling rate was greater in the pallet near the refrigeration end; however the improvement in cooling rate was also substantial near the door end.

$$FUTC = \frac{(T - T_a)}{(T_i - T_a)} \qquad \textit{Equation 10-1}$$

Where:

$FUTC$	=	Fraction unaccomplished temperature change	
T_a	=	Incident air temperature	(°C)
T_i	=	Initial temperature	(°C)
T	=	Temperature	(°C)

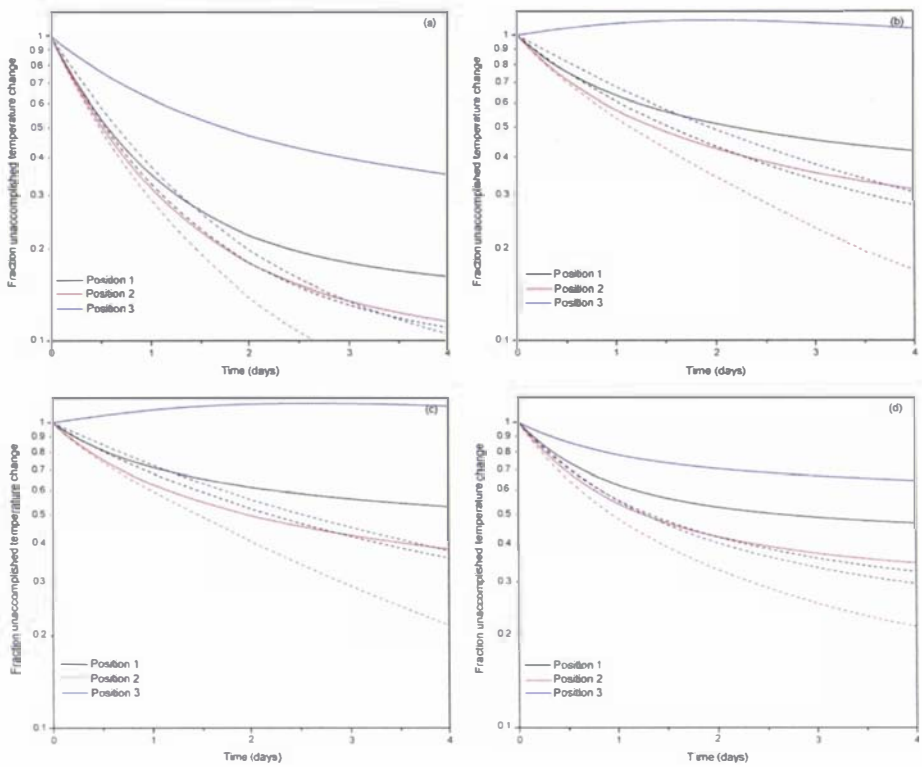

Figure 10-28 - Predicted cooling curves for three positions on (a) layer 1 (b) layer 4 (c) layer 7 and (d) layer 10 of pallets constructed with standard (solid lines) and prototype (broken lines) cartons near the refrigeration end of the container

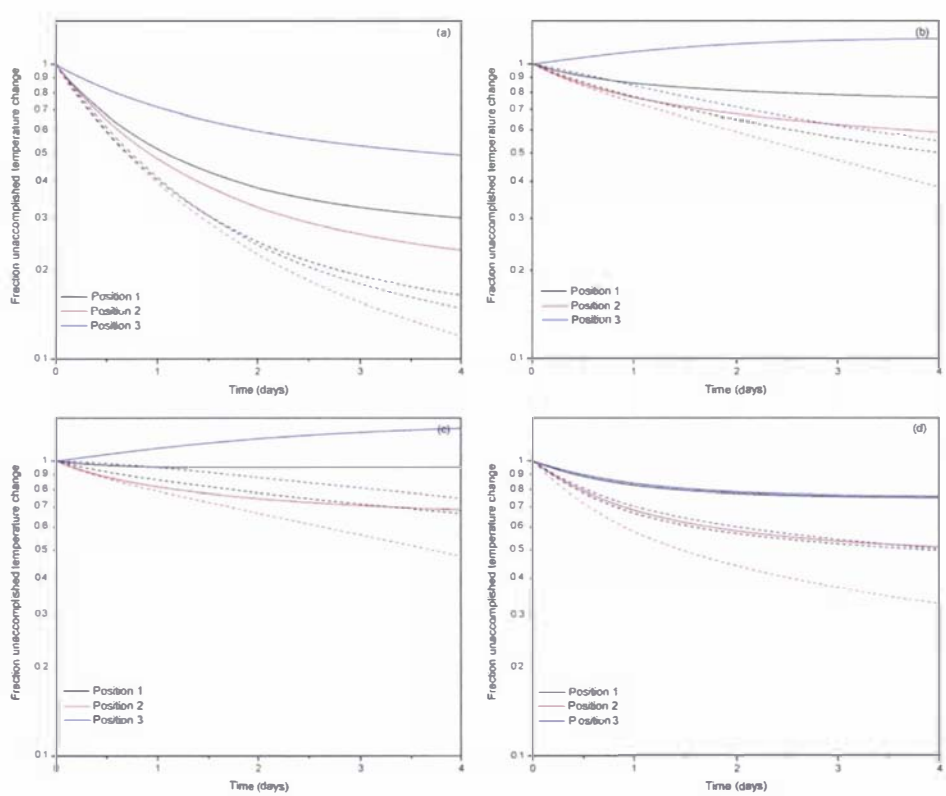

Figure 10-29 - Predicted cooling curves for three positions on (a) layer 1 (b) layer 4 (c) layer 7 and (d) layer 10 of pallets constructed with standard (solid lines) and prototype (broken lines) cartons near the door end of the container

10.5 Scenario testing

The following sections provide an analysis of the influence of several input parameters on the predicted flow distributions. Five scenarios were investigated: an alternative definition of the resistance network, two alternative stowage arrangements, an increased total air circulation rate due to increased fan size or speed and the removal of the T-bar floor gratings (air delivery via pallet bases). The first scenario was designed to assess the effects of minor changes to the network on predicted flows, whilst the other four scenarios were designed to assess possible changes in loading procedures or container design to improve system performance. All scenarios were based on the standard packaging system. For each of the scenarios investigated, predicted airflows and resulting air temperature rises are presented.

10.5.1 Alternative flow resistance network definition

A simulation was performed using an alternative flow resistance network definition to assess the effects of minor changes to the network. In the earlier network definition, there were no horizontal flow channels defined in the transverse gaps between pallets. To assess the effect of neglecting these flow channels, a second network was defined which included these channels. The network was identical to that defined in Section 10.3 in all other respects. The node positions and the horizontal channels connecting them on the three layers above the T-bar layer are depicted in Figure 10-30.

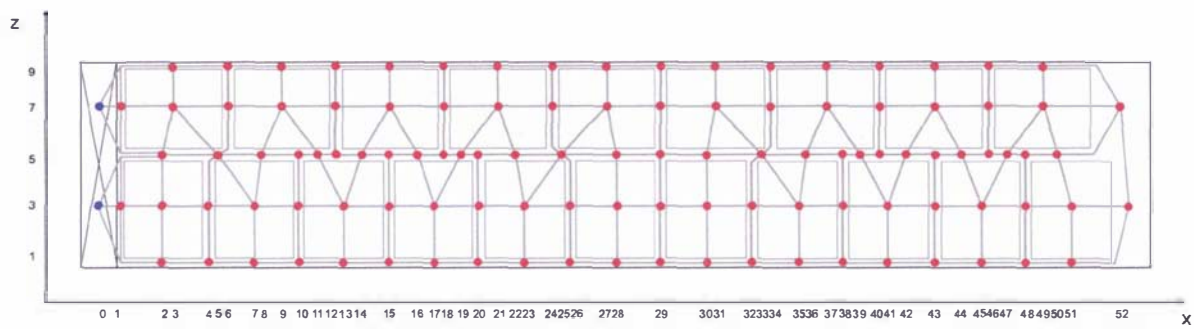

Figure 10-30 - Plan view of the 40' container loaded with 20 pallet showing the alternative flow network defined on the layers above the floor grating layer (Y > 1). Blue circles represent fixed pressure nodes (on Y = 4 layer only), red circles represent unknown pressure nodes, and grey cylinders represent flow channels

The predicted total circulation rate increased 50 $m^3.h^{-1}$ over that predicted with the original network (3% difference). Comparison of the predicted vertical velocities in each of transverse and longitudinal gaps gave a maximum change in velocity between the two simulations of 0.06 $m.s^{-1}$. The predicted flows were therefore not significantly affected by the minor changes in the flow network definition.

10.5.2 Longitudinal gap size

Simulations were performed to assess the influence of the pallet positioning within the container on the predicted fruit temperature profile. The geometry described in Section 10.3 was used; with altered channel widths surrounding the pallets in the positions used for temperature prediction. The channel near the wall was reduced from the standard width of 0.025 m to 0.01 m and the channel in the centre of the container increased to 0.06 m to mimic a pallet placed nearer to the wall. The transverse gaps sizes and the longitudinal gap sizes surrounding other pallets were not altered. Heat transfer simulations as described in Section 10.4.3 were conducted using the predicted air velocities for the standard packaging system for the two pallets marked in Figure 10-3.

Figure 10-31 shows the predicted velocity in each of the vertical channels surrounding the pallets. The velocity in the reduced channels near the wall was lower than those surrounding them due to the increased flow resistance associated with the diminished width. Similarly, the central channels in the same sections

of the container show higher velocities. Figure 10-32 shows the predicted temperature rise in each of the vertical channels. The narrow channels near the walls show large temperature rises due to the reduction in volumetric flow through the channels.

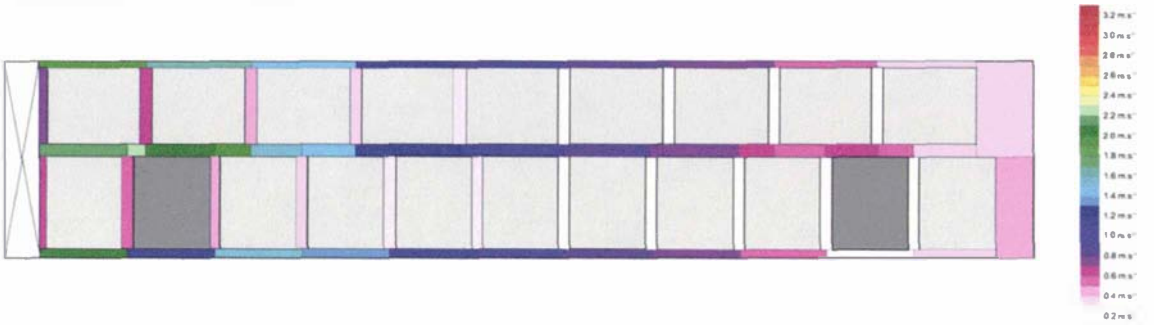

Figure 10-31 - Predicted velocity in each of the vertical flow channels formed by gaps around pallets within the 40' container loaded with kiwifruit packaged in the standard packaging system. Shaded pallets were spaced with a large gap in the centre of the container (0.06 m) and a reduced gap near the wall of the container (0.01 m) (gap dimensions not to scale)

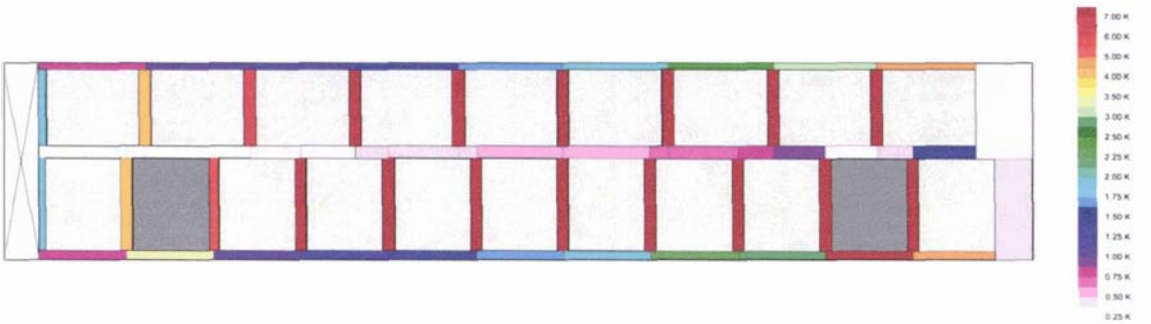

Figure 10-32 - Predicted temperature rise in each of the vertical flow channels formed by gaps around pallets within the 40' container loaded with kiwifruit packaged in the standard packaging system. Shaded pallets were spaced with a large gap in the centre of the container (0.06 m) and a reduced gap near the wall of the container (0.01 m) (gap dimensions not to scale)

Figure 10-33 and Figure 10-34 show the predicted temperature profiles for the two pallets with either 0.025 m or 0.01/0.06 m longitudinal gaps. Temperatures at positions 2 & 3 were not significantly affected while position 1 on layers 4, 7 and 10 was substantially affected by the reduction in the size of the longitudinal gap. Near the door end of the container, the reduced gap size caused the predicted temperatures near the wall to increase substantially. The predicted in-package temperature increase was caused by a large fluid temperature increase due to heat infiltrating the container's structure. Temperatures increases of this magnitude within a container are unlikely for a couple of reasons. Primarily, in the heat transfer model, the air was assumed to flow vertically only; which is unrealistic in practice, where cooler air may enter the channel horizontally, cooling the upper regions of the gap. Secondly, a channel size of just 0.01 m over the entire face of the pallet is unlikely, due to the non-uniform nature of the pallets and the design of the container wall, which often has grooves to ensure a minimum quantity of airflow. Finally, conduction of heat along the metal wall reduces the likelihood of localised hot-spots on the interior of the container wall. Despite these caveats, the predicted temperature increases do indicate that failure to provide substantial airflow pathways along the container wall may cause areas of significantly elevated temperature.

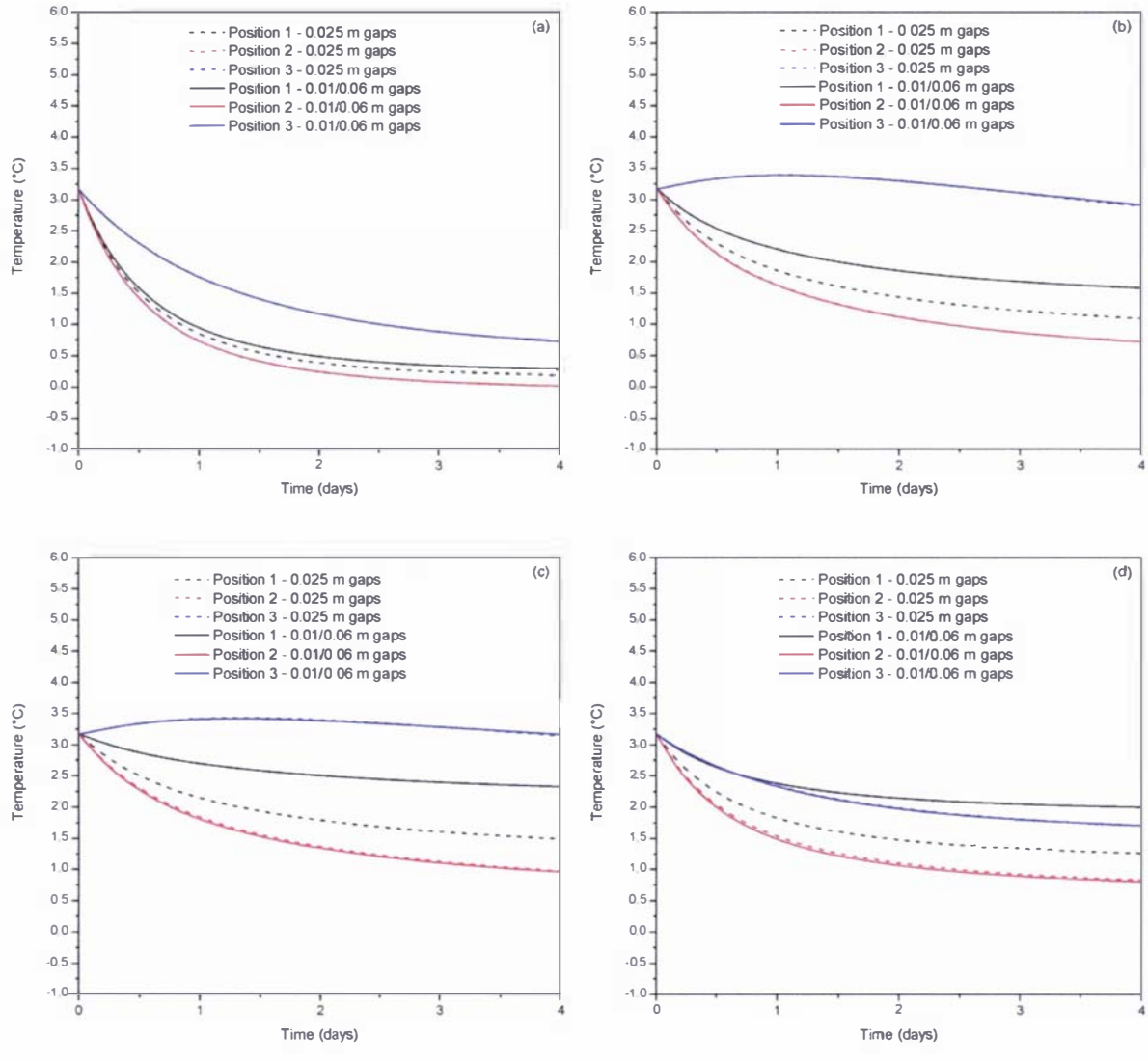

Figure 10-33 - Predicted cooling curves for three positions on (a) layer 1 (b) layer 4 (c) layer 7 and (d) layer 10 of a pallet constructed with standard cartons near the refrigeration end of the container with uniform and variable gap spacing

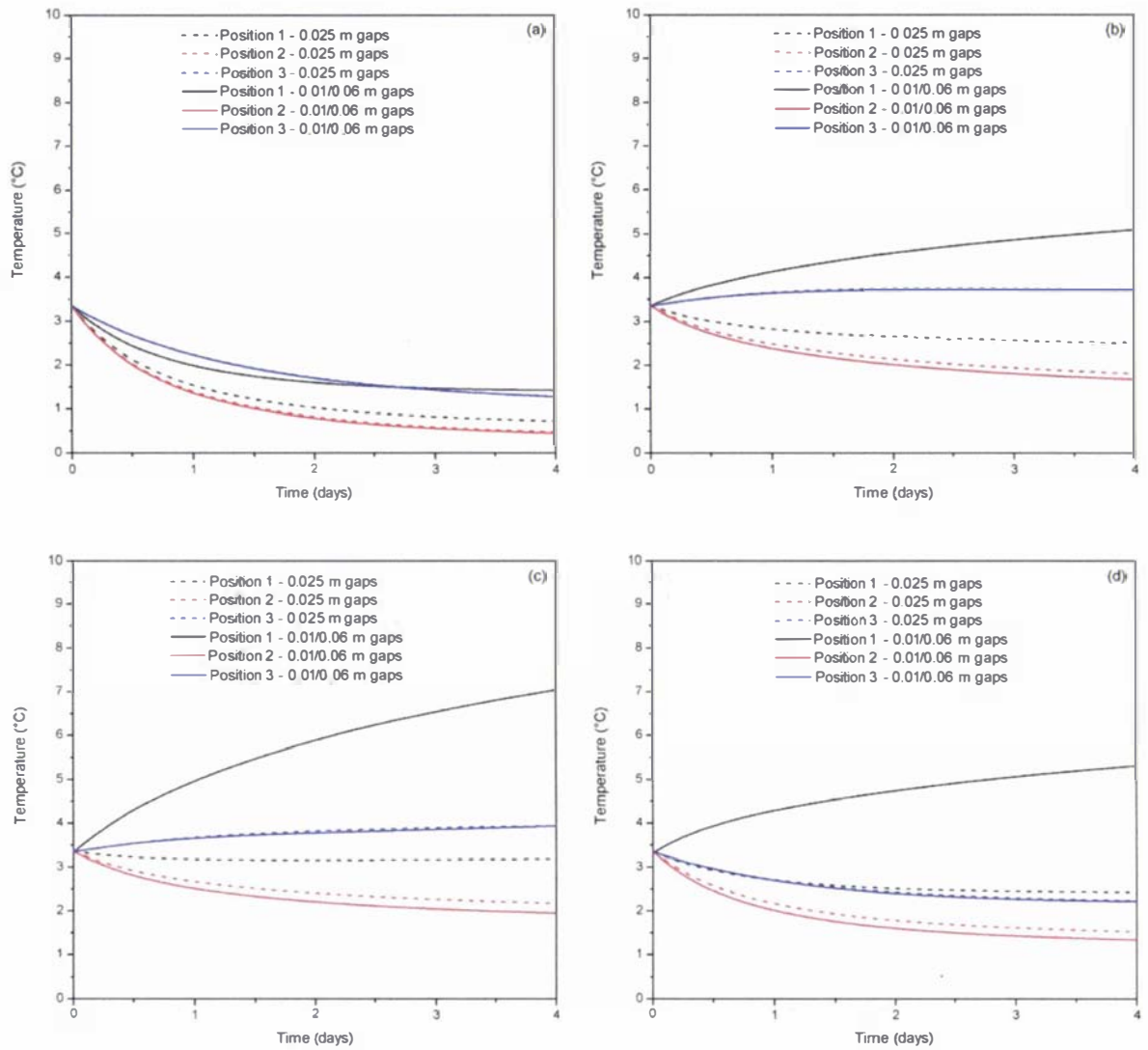

Figure 10-34 - Predicted cooling curves for three positions on (a) layer 1 (b) layer 4 (c) layer 7 and (d) layer 10 of a pallet constructed with standard cartons near the door end of the container with uniform and variable gap spacing

During loading of palletised products into a 40' container, each pallet is generally placed as close as possible to the wall to facilitate the loading of the next pallet. The results of this scenario indicate that reducing channel sizes near the wall may cause greater temperature variability. A minimum spacing between a pallet and the wall is often provided through the use of corner-boards on the pallet (if the corner board is flush with the wall, the majority of the pallet face is held a significant distance from the wall), which provide a simple means to mitigate this cause of temperature variability.

10.5.3 Transverse gap size

In the loading configuration employed to fit 20 pallets within the 40' container, the channels left adjacent to the container doors were large and provided little useful cooling in comparison with the large volume of flow. In contrast, the transverse gaps elsewhere in the container were small and little cooling was being achieved through these faces of the pallets. The possibility of redirecting some air from the door channels through the transverse channels was investigated.

Airflows through the system were predicted using the geometry described in Section 10.3 with the standard packaging system but the transverse gaps were increased in size to reduce the depth of the channels adjacent to the doors to 0.1 m. The width of the transverse gaps became 0.025 m and 0.04 m on the left and right side of the container respectively, as viewed from the door end. Heat transfer simulations were conducted using the predicted air velocities for the two pallets marked in Figure 10-3.and comparison made with the original loading configuration.

Figure 10-35 shows the predicted velocity in each of the vertical channels surrounding the pallets. The greater width of the channels gave a more even velocity distribution across the width of the container. Figure 10-36 shows the predicted temperature rise in each of the vertical channels. The increased volumetric flow in the transverse channels is reflected in reduced temperature rises in the transverse channels between the pallets. The predicted temperature rise in the channels adjacent to the door was increased over the standard arrangement due to its reduced size and volumetric flow rate. Channels near the walls had reduced velocities and increased temperature rises with less air flowing in those channels due to the reduced resistance of the transverse channels. Velocity reductions in these channels ranged from 10% to 40%. Velocity in the large channels near the door did not change substantially, with the volumetric flow diminishing approximately in proportion to the reduction in area.

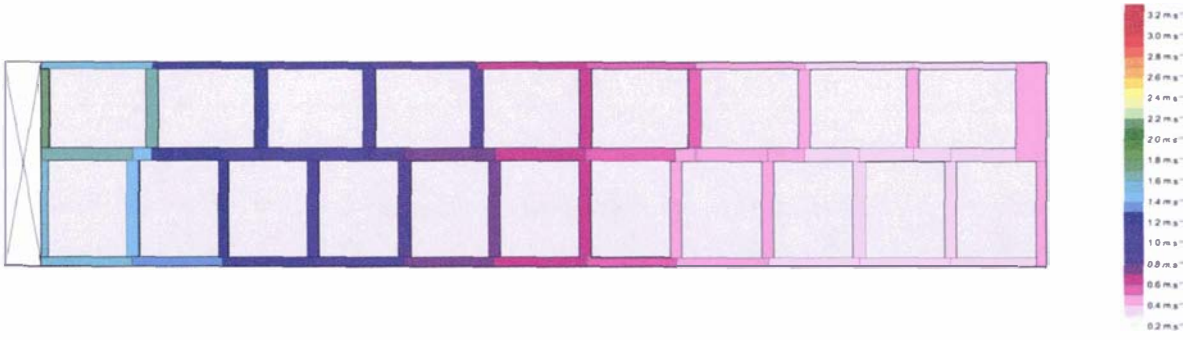

Figure 10-35 - Predicted velocity in each of the vertical flow channels formed by gaps around pallets within the 40' container loaded with kiwifruit packaged in the standard packaging system loaded with altered transverse spacing (gap dimensions not to scale)

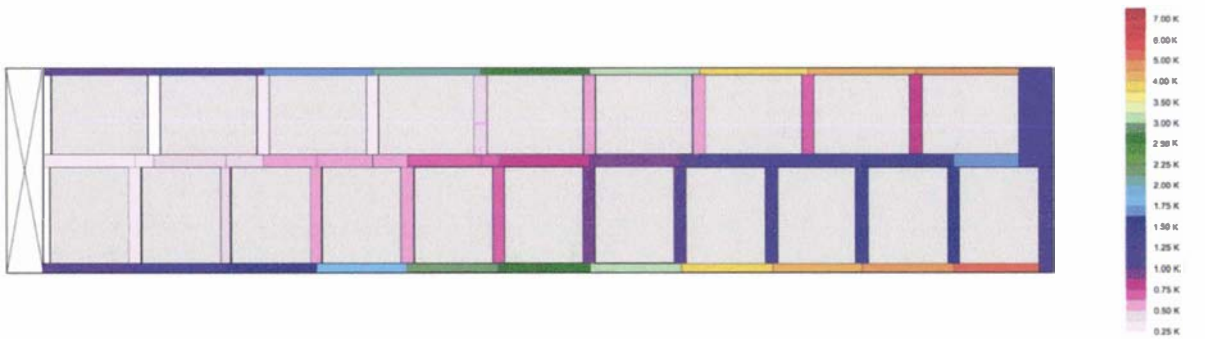

Figure 10-36 - Predicted temperature rise in each of the vertical flow channels formed by gaps around pallets within the 40' container loaded with kiwifruit packaged in the standard packaging system loaded with altered transverse spacing (gap dimensions not to scale)

Figure 10-37 and Figure 10-38 compare the predicted temperature profiles for the two pallets with the increased transverse channel sizes and the original loading arrangement. Positions correspond to those marked on Figure 10-3. Cooling in both pallets was substantially improved by the increase in the width of the transverse gaps.

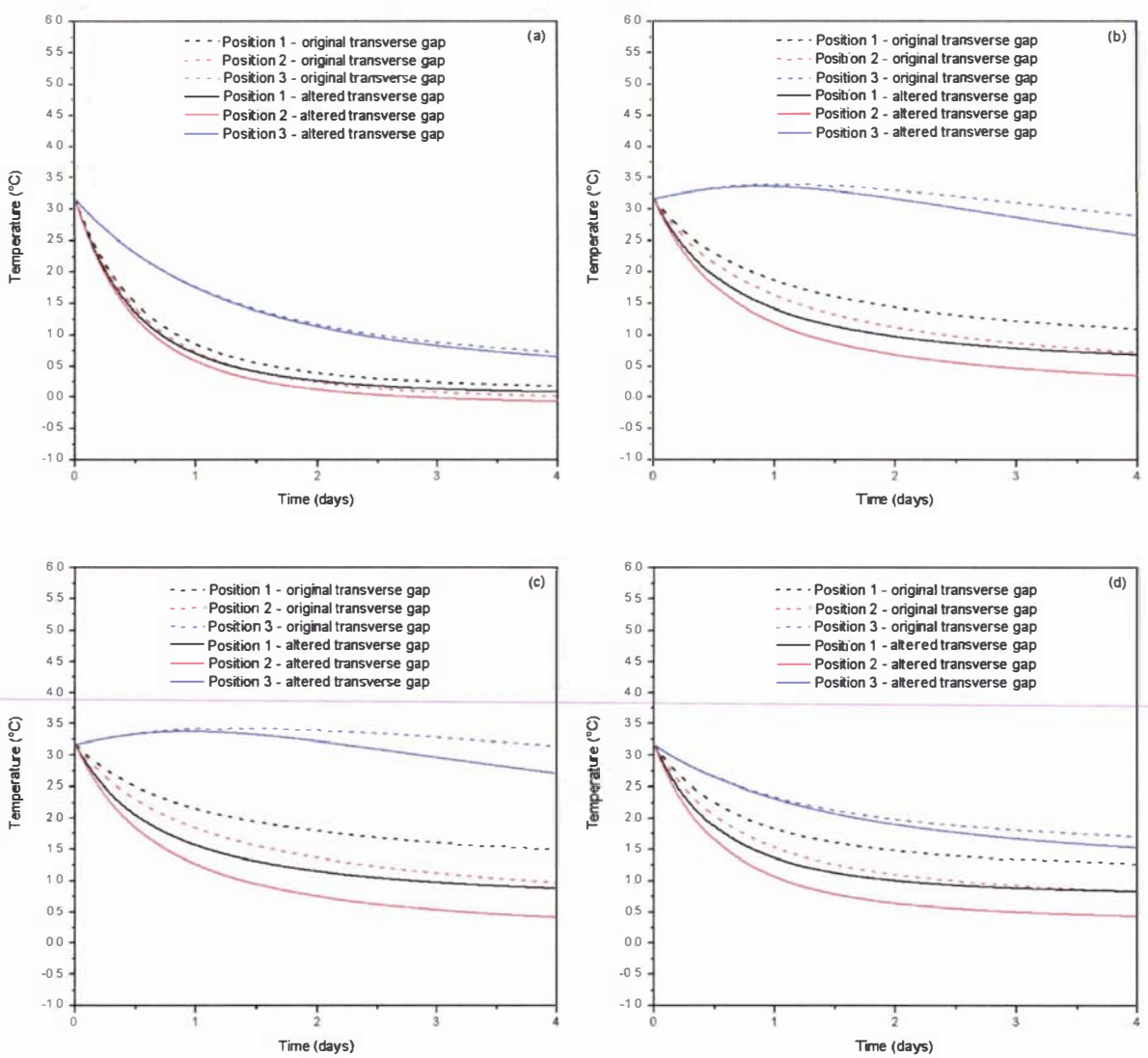

Figure 10-37 - Predicted cooling curves for three positions on (a) layer 1 (b) layer 4 (c) layer 7 and (d) layer 10 of a pallet constructed with standard cartons near the refrigeration end of the container loaded with normal and altered transverse gap spacing

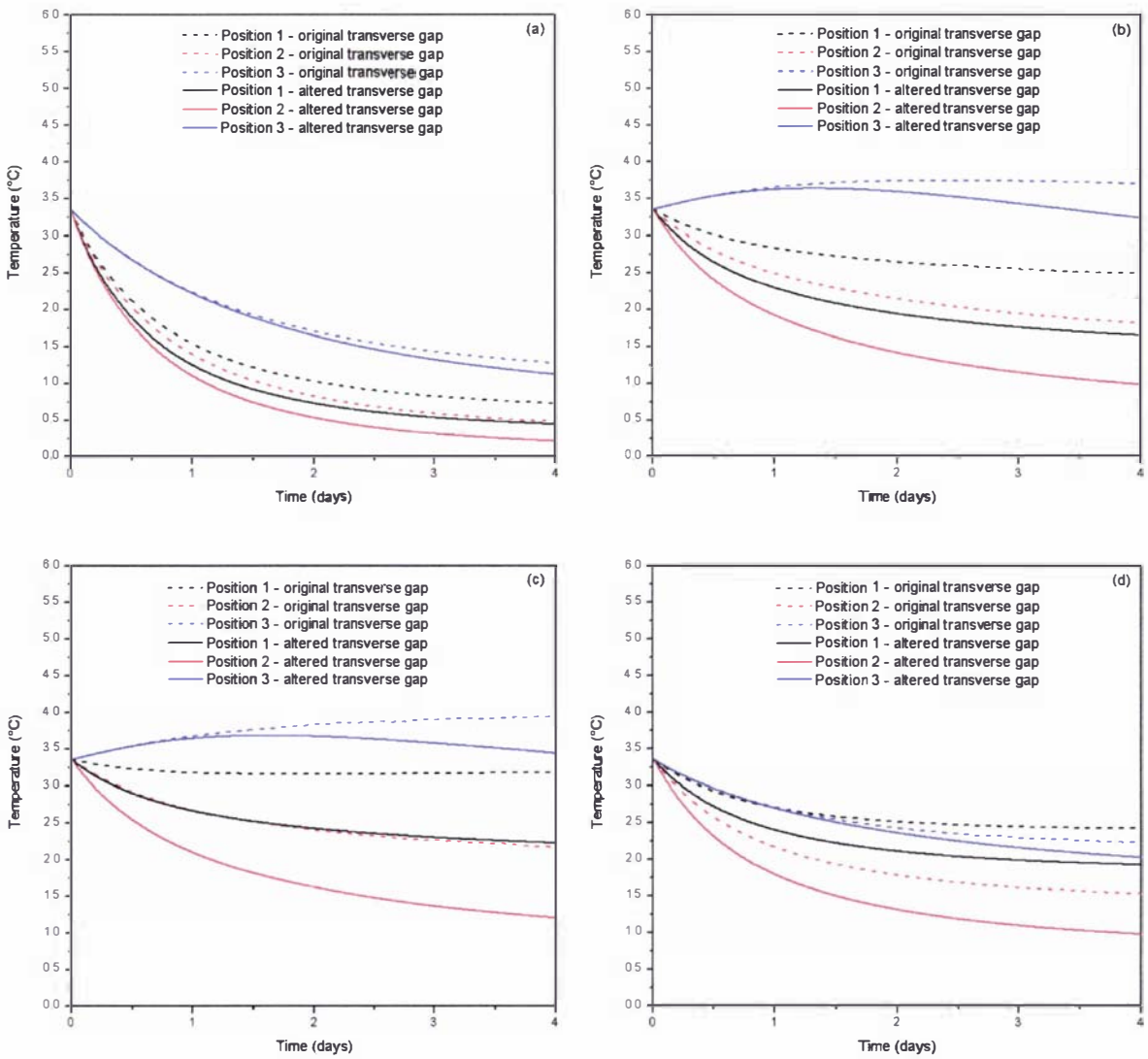

Figure 10-38 - Predicted cooling curves for three positions on (a) layer 1 (b) layer 4 (c) layer 7 and (d) layer 10 of a pallet constructed with standard cartons near the door end of the container loaded with normal and altered transverse gap spacing

The increased cooling was more evident in the pallet near the door end of the container, and on layers 4 and 7. The increased channel sizes allowed significant quantities of air to flow along all four vertical faces of the pallet, effectively increasing the surface area through which heat was removed. Temperatures on layers 1 and 10 had good exposure to the air via the top and bottom faces of the pallet with both loading arrangements, meaning layers 4 and 7 experienced greater benefit. Temperatures in positions near the centre of the pallets on layer 4 and 7 showed less of an improvement than those on the outside of the pallet; however, the improved cooling was still substantial (0.5°C cooler after 4 days cooling).

In practice, significant effort to create transverse channels may not be necessary. Significant transverse channels are likely to be created inadvertently by corner-boards used for pallet stability. These create minimum gap sizes between pallets, with even a small channel sufficient to provide a significant flow of air across the face of the pallet. For packaging systems where pallets may be placed flush and only very narrow gaps are likely, intervention in the form of pallet spacers may be beneficial.

10.5.4 Increased air circulation rate

Simulations were performed to assess the effect of the air circulation rate on the cooling rates throughout the container. The geometry described in Section 10.3 was used and the fixed pressure at the air delivery duct was increased to provide an air circulation rate of approximately 110 changes per hour. Such an increase in the circulation rate could be achieved through increased evaporator fan size and/or speed. Heat transfer simulations were conducted using the predicted air velocities for the standard packaging system as described in Section 10.4.3.

Figure 10-39 shows the predicted velocity in each of the vertical channels surrounding the pallets. The velocity distribution was similar to the distribution predicted with 75 air changes per hour, with flow in most of the channels increasing by approximately 50%. The exceptions to this increase were the transverse channels in the two-thirds nearest the refrigeration end of the container, where flow rates approximately doubled from a low base value. Figure 10-40 shows the predicted temperature rise in each of the vertical channels. The predicted temperature rises were reduced due to the increased rates of flow in all of the channels.

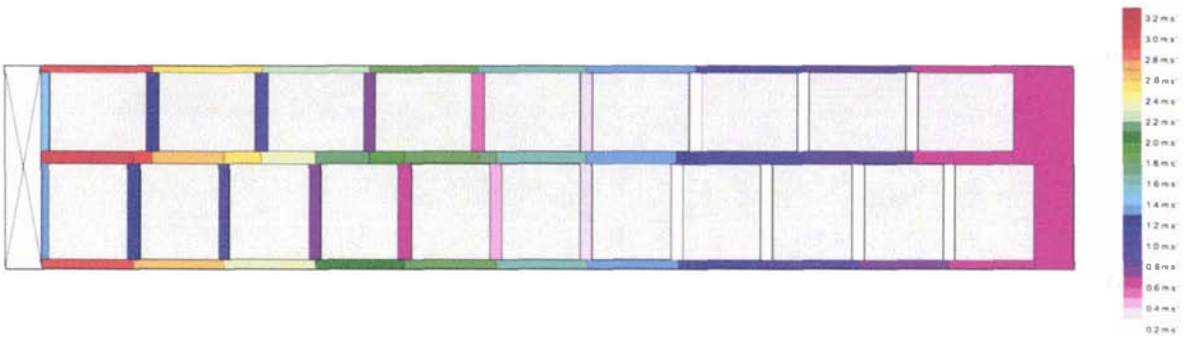

Figure 10-39 - Predicted velocity in each of the vertical flow channels formed by gaps around pallets within the 40' container loaded with kiwifruit packaged in the standard packaging system and an air circulation rate of 110 changes per hour (gap dimensions not to scale)

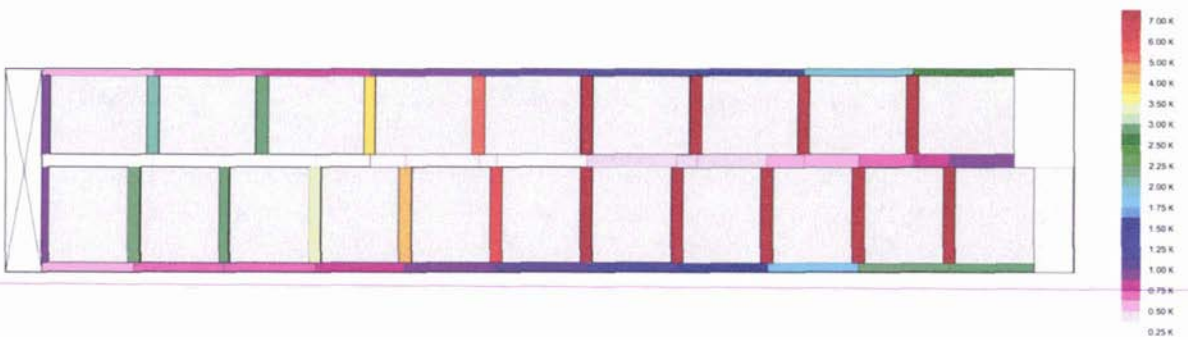

Figure 10-40 - Predicted temperature rise in each of the vertical flow channels formed by gaps around pallets within the 40' container loaded with kiwifruit packaged in the standard packaging system and an air circulation rate of 110 changes per hour (gap dimensions not to scale)

Figure 10-41 and Figure 10-42 show the predicted temperature profiles for the two pallets with air circulation rates of 75 changes per hour and 110 changes per hour. Cooling rates increased with the higher circulation rate in all positions; however, the magnitude of the increase was heavily dependent on the position within the pallet. Cooling rates in positions near the centre of the pallets showed less benefit than those on the outside of the pallet. The pallets at both ends of the container showed a similar increase in cooling rate.

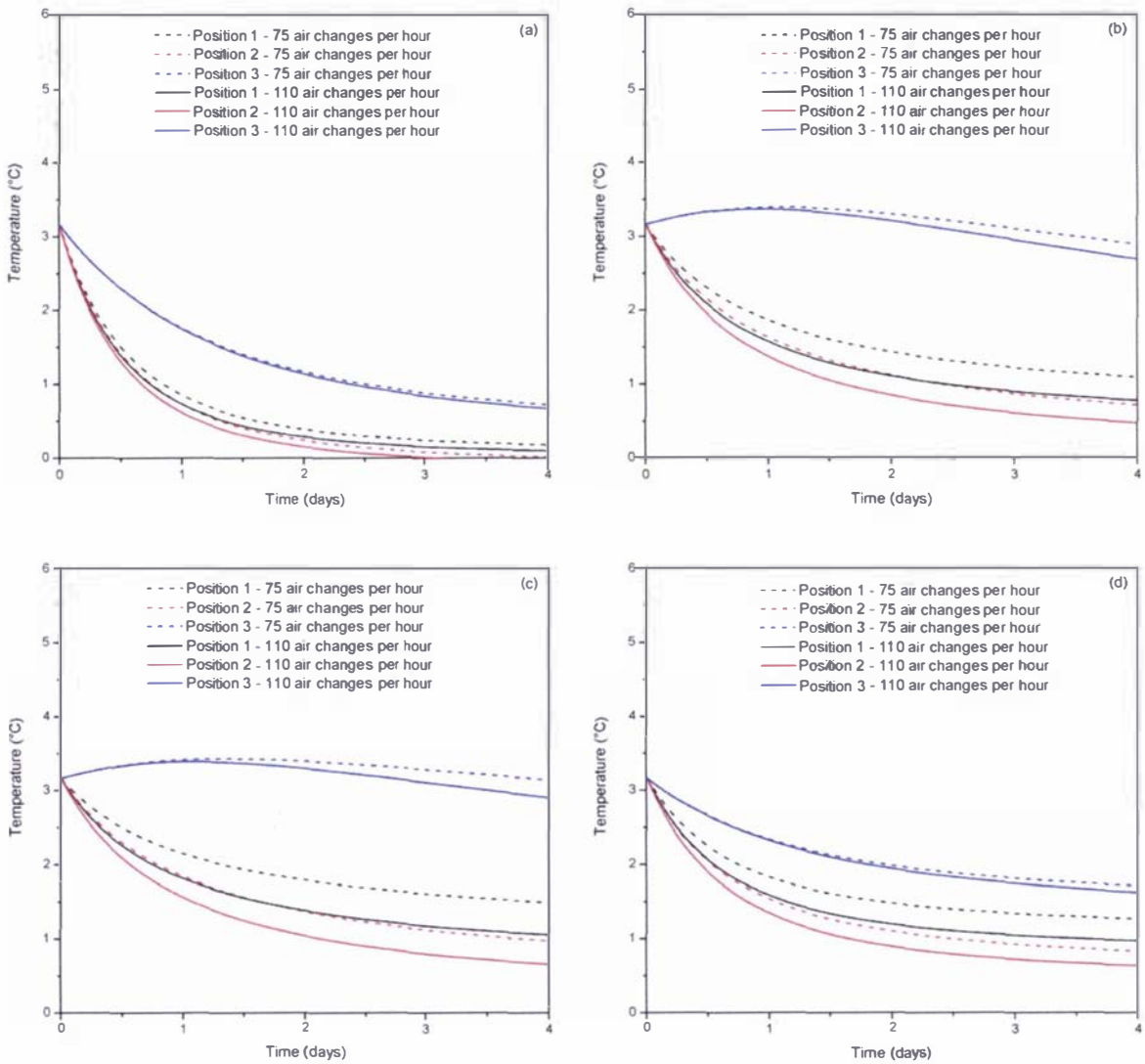

Figure 10-41 - Predicted cooling curves for three positions on (a) layer 1 (b) layer 4 (c) layer 7 and (d) layer 10 of a pallet constructed with standard cartons near the refrigeration end of the container with either 75 or 110 air changes per hour

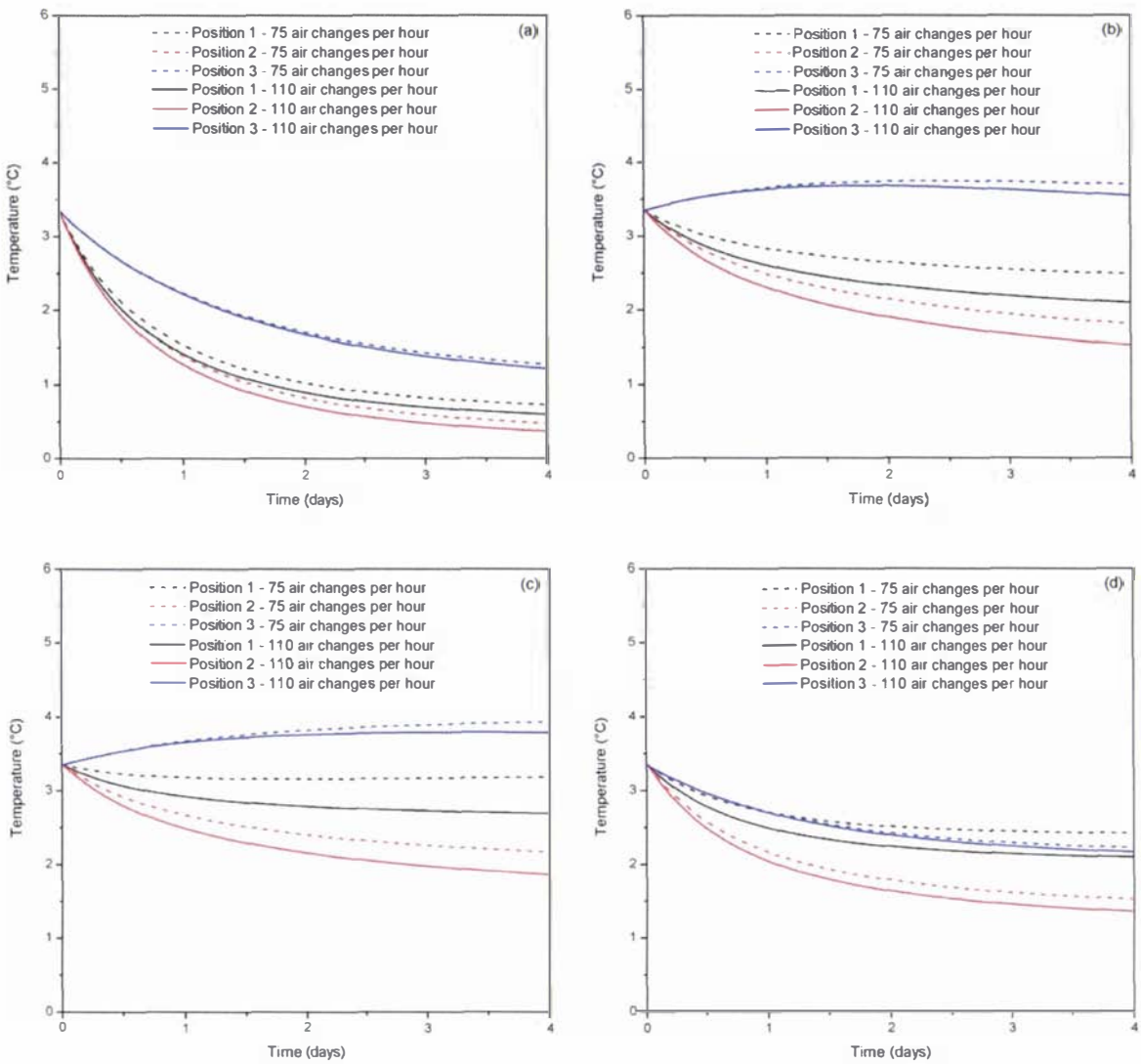

Figure 10-42 - Predicted cooling curves for three positions on (a) layer 1 (b) layer 4 (c) layer 7 and (d) layer 10 of a pallet constructed with standard cartons near the door end of the container with either 75 or 110 air changes per hour

Increasing the circulation rate improved the rates of cooling throughout the container. Maximum temperatures throughout the container were lower; however, the magnitude of the improvement was small given the large increase in flow. After four days of cooling, the temperature reduction caused by the increased fan speed ranged from 0.05°C to 0.5°C. Whilst such an analysis was considered outside the scope of this work, the increased fan power and refrigeration capacity required to achieve the increased circulation rate weighed up against the small improvement in cooling rates would almost certainly render such an increase in circulation rate of little benefit both financially and environmentally.

10.5.5 Container without T-bar floors

The T-bar floors used in refrigerated containers for air distribution provide a plenum for air for both palletised and bulk cargoes. Where the cargo is palletised though, the T-bars may no longer be necessary as the pallet bases themselves could act as an effective plenum. Containers without T-bar floors would be lighter, cheaper to build, easier to load and clean and would have greater useable volume inside the container. The consequences of removing the T-bar floor in terms of air distribution and cargo temperatures were investigated for a palletised cargo.

The airflow through the system was predicted using a network similar to that described in Section 10.3. Flow channels below the level of the T-bar floor were removed and the fixed pressure inlet nodes attached to nodes on the layer of the pallet base (Figure 10-43). The standard packaging system was used. Heat transfer simulations were performed using the predicted air velocities and comparison made with the standard configuration.

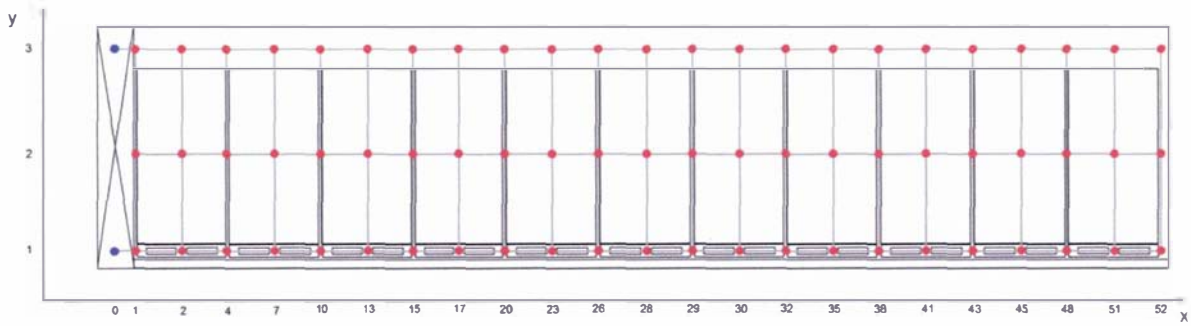

Figure 10-43 - Elevation view of a 40' container without a T-bar floor loaded with 20 pallets showing the defined flow resistance network. Blue circles represent fixed pressure nodes, red circles represent unknown pressure nodes, and grey cylinders represent flow channels

Figure 10-44 shows the predicted velocity in each of the vertical channels surrounding the pallets. The removal of the T-bars increased the flow near the refrigeration end (34% maximum increase) and reduced flows near the door end (25% maximum reduction). Figure 10-45 shows the predicted temperature rise in each of the vertical channels, where the velocity changes were reflected in greater temperature rises at the door end of the container (1.4°C maximum increase).

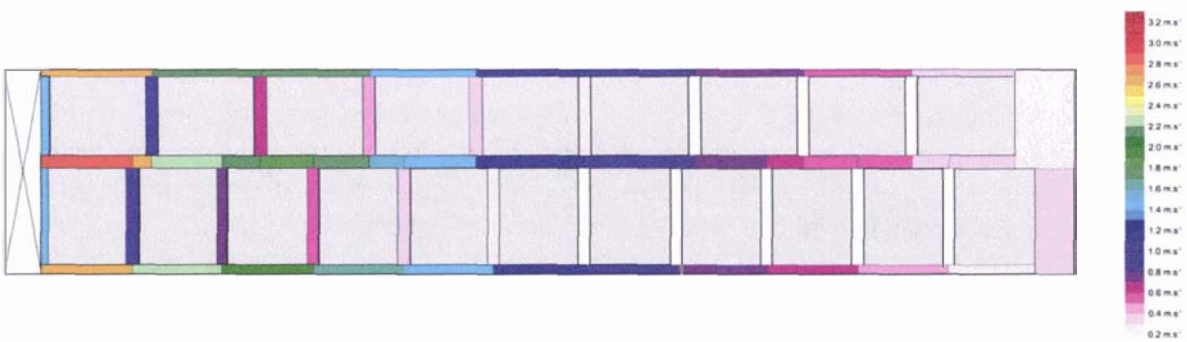

Figure 10-44 - Predicted velocity in each of the vertical channels formed by gaps around pallets within the 40' container without a T-bar floor loaded with kiwifruit packaged in the standard packaging system (gap dimensions not to scale)

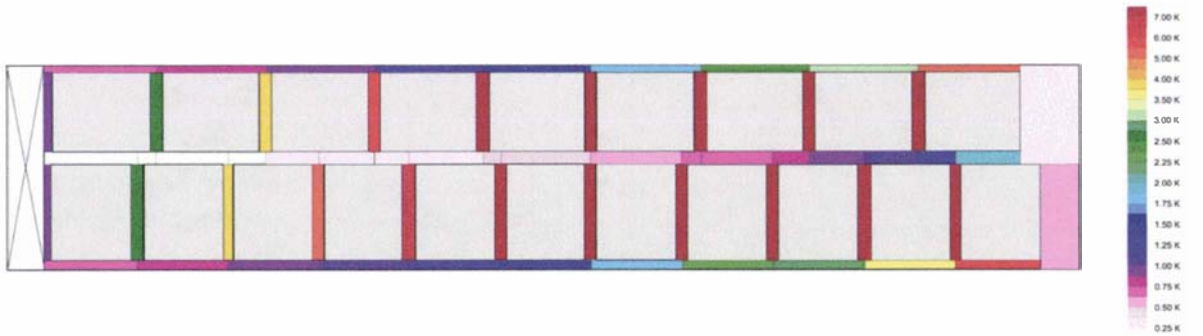

Figure 10-45 - Predicted temperature rise in each of the vertical channels formed by gaps around pallets within the 40' container without a T-bar floor loaded with kiwifruit packaged in the standard packaging system (gap dimensions not to scale)

Figure 10-46 and Figure 10-47 show the predicted temperature profiles for the two pallets with and without the T-bar floor. Positions correspond to those marked on Figure 10-3. Cooling of the pallet near the refrigeration end was improved slightly and cooling of the pallet near the door end was slightly slower. Overall, the effects of the T-bar floor removal were small, with the maximum predicted temperature difference just 0.3°C after four days of cooling.

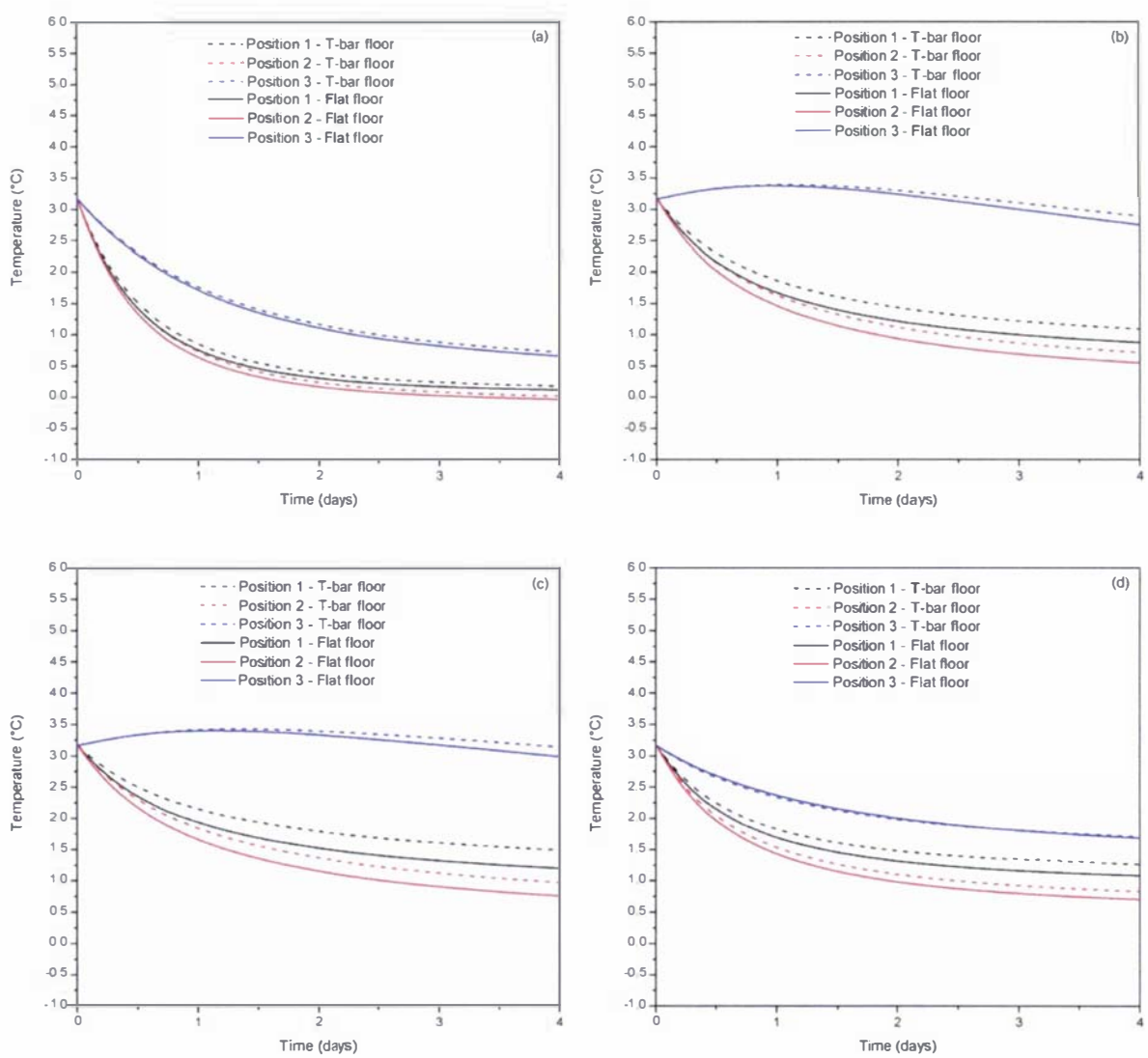

Figure 10-46 - Predicted cooling curves for three positions on (a) layer 1 (b) layer 4 (c) layer 7 and (d) layer 10 of a pallet constructed with standard cartons near the refrigeration end of a container with and without a T-bar floor

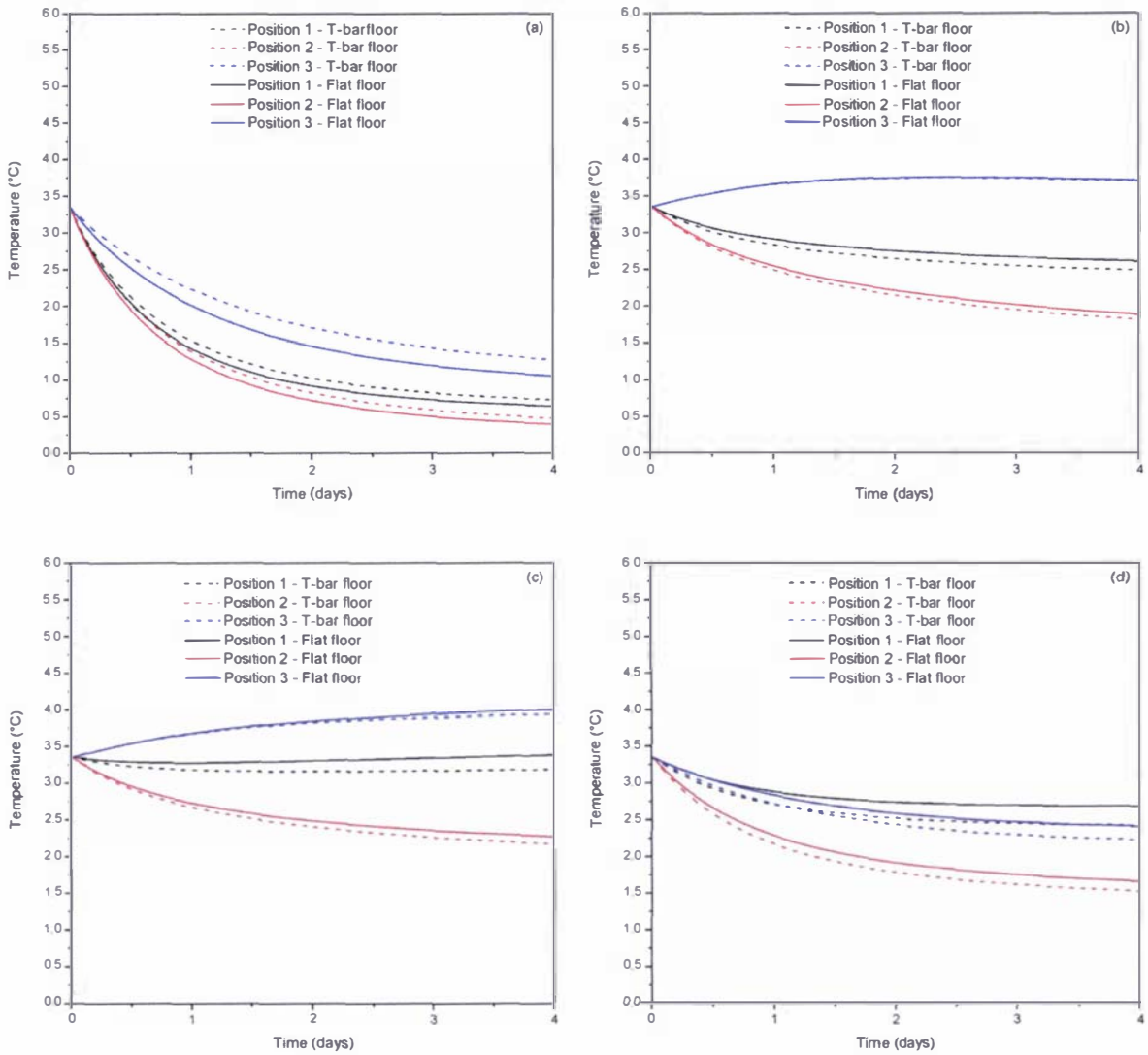

Figure 10-47 - Predicted cooling curves for three positions on (a) layer 1 (b) layer 4 (c) layer 7 and (d) layer 10 of a pallet constructed with standard cartons near the door end of a container with and without a T-bar floor

The small predicted detrimental effect of T-bar floor removal must be weighed up with a number of factors in mind: the pallet base design will impact heavily on their effectiveness as a plenum and non-palletised cargoes would become difficult to cool without the T-bar floor. With the current variety of packaging systems and pallet bases in use, a container without a T-bar floor would be limited to carrying only suitably palletised cargoes; which is likely to present significant logistical difficulties for freight companies.

10.6 Conclusions

Comparison of measured and predicted air velocities in a 40' refrigerated container during simulated shipments of kiwifruit in two packaging systems showed reasonable agreement at different positions down the length of the container, if the measured variation across the width was averaged.

Comparison of in-package temperatures also showed reasonable agreement in most positions; however, cooling near the centre of the standard pallets was under-predicted. The discrepancy was attributed to diffusive flow of air through the pallet stack, which was not included in the model. Agreement of predicted and measured temperatures near the centre of the prototype pallets was good, as the flow

through the pallet was quantified and included in the model. Significant variation in initial fruit temperatures and a small elevation of fruit temperature relative to the container set-point were limitations of the experimental data.

Airflow and heat transfer simulations of containers with altered design or operational factors provided some interesting insights. Reducing the space between pallets and the wall of a container caused significant in-package temperature increases, whilst increasing the size of the gap between pallets stowed on the same side of the container (thereby reducing the size of the channel adjacent to the doors) increased rates of cooling. In both cases, the required size of the gaps was small, such that corner-boards used for pallet stability were likely to inadvertently produce a minimum gap size sufficient to provide benefit. An increased circulation rate improved cooling throughout the container; however, the magnitude of the improvement was relatively small. A container without T-bar floor gratings, making use of the pallet bases as a plenum, was predicted to adversely affect cooling rates at the door end of the container; however, the magnitude of the effect was only moderate. It must also be noted that the magnitude of the effect would be heavily dependent on the design of the pallet bases.

11 Refrigerated Vessel - Spar Deck

11.1 Introduction

Monitoring of temperatures and velocities within a single deck of a refrigerated vessel transporting kiwifruit from New Zealand to Japan was undertaken in conjunction with a commercial monitoring project. Airflow and heat transfer simulations of the refrigerated hold were also conducted and by comparison of predicted and measured velocities and temperatures, the suitability of the airflow model (along with a heat transfer model) for use in a spar deck was tested. The sensitivity of predictions to the flow resistance of the ceiling headspace and the implications of increasing and decreasing the circulation rate were also investigated.

11.2 System information

Monitoring was conducted on a chartered vessel transporting kiwifruit from New Zealand to Japan. The vessel was configured such that the decks were serviced in pairs by a common refrigeration plant and fan system as shown in Figure 11-1. The refrigerated air was delivered in the floor gratings below the lower deck and drawn up through two layers of pallets before returning to the refrigeration plant through the return air grill near the ceiling on the upper of the two decks. The air passed through two decks of pallets before it passed through the evaporator. This configuration is common, and the upper deck often referred to as a 'spar' deck. The spar deck was monitored in this trial.

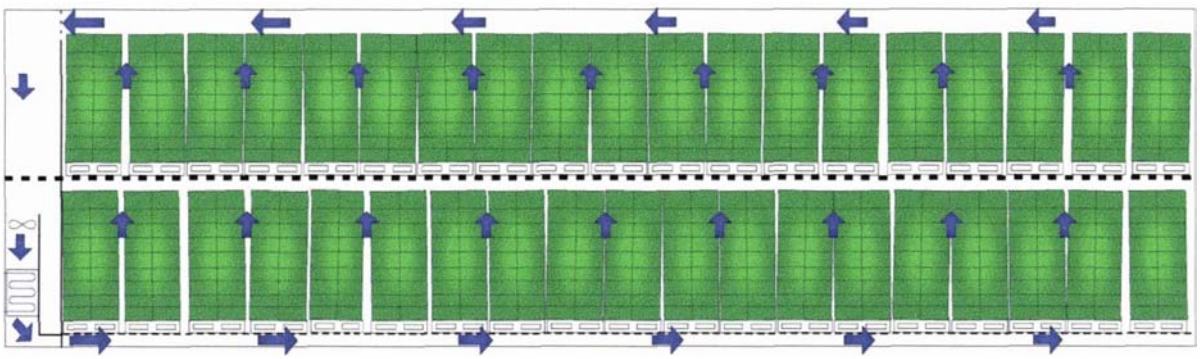

Figure 11-1 - Elevation view of the vessel deck configuration showing simplified airflow pathways between the two decks serviced by a single evaporator/fan system

The deck was approximately 18.4 m wide and 17.4 m long, with the width narrowing with increasing distance from the refrigeration end due to the shape of the hull (Figure 11-2). The kiwifruit was packaged in single layer trays, with a plastic liner. The trays were palletised on wooden bases measuring 1.015 m × 0.885 m. The pallet bases allowed fork access from one direction only. Figure 11-3 shows photographs of a pallet and the packaging system used.

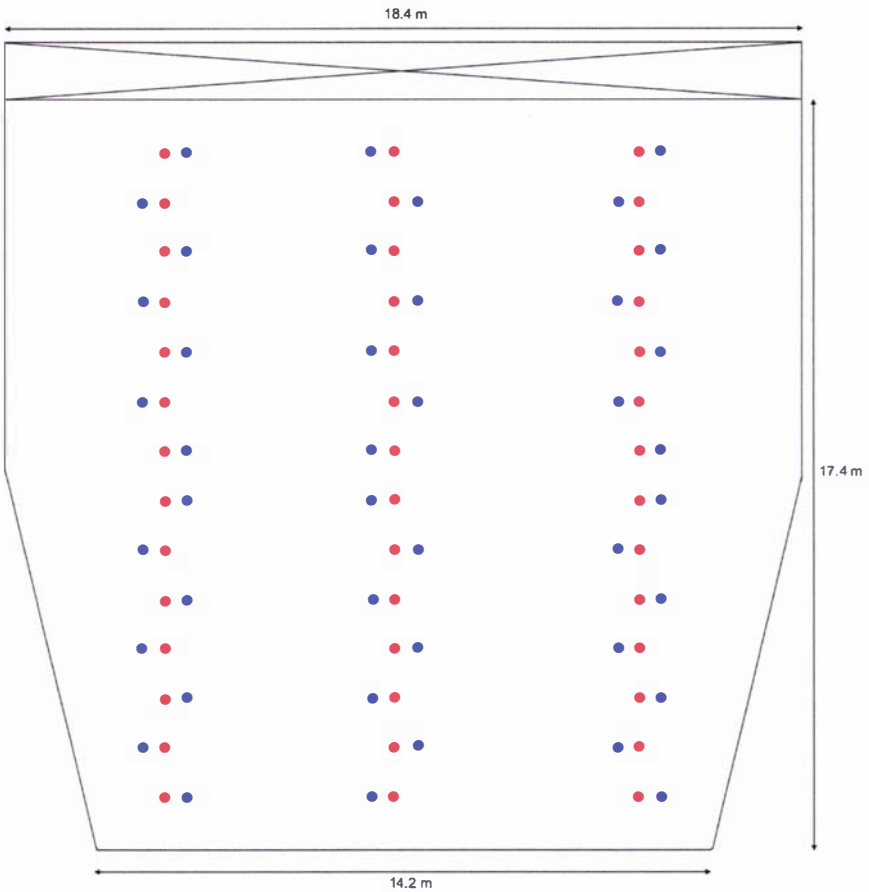

Figure 11-2 - Plan view of the deck monitored during shipment of kiwifruit from New Zealand to Japan showing approximate dimensions and position of thermistor anemometers in the floor (•) and the ceiling (•)

Figure 11-3 - Photographs of a pallet and the packaging system as used during the monitored shipment of kiwifruit from New Zealand to Japan. Placement of thermocouples within the package is shown (right)

All pallets within the deck were instrumented with 7 temperature sensors on a single layer of trays, five down from the top of the pallet. Temperature sensors used were either type-T thermocouples (0.5 mm in diameter) or HOBO temperature loggers (model H08-031-08, Onset Computer Corporation, Massachusetts, USA). Thermocouple outputs were recorded using 32 and 64-channel Eltek Squirrel data-loggers (1000 series, Eltek Ltd. Cambridge, England). Temperature sensors were positioned underneath a fruit, inside the plastic liner of the tray in the pattern shown in Figure 11-4.

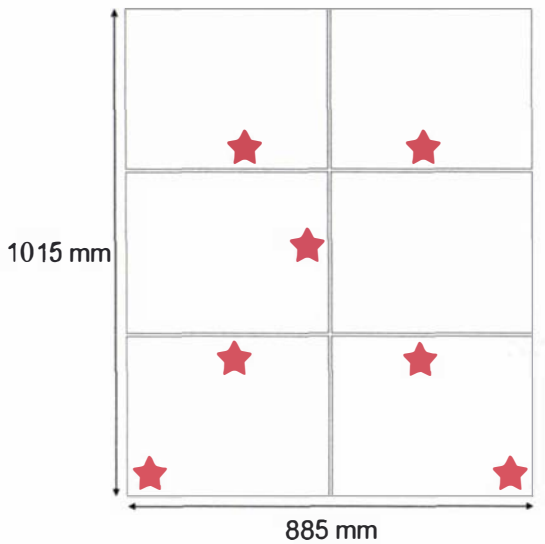

Figure 11-4 - Plan view of a single pallet layer of kiwifruit showing the 7 locations (★) of the type-T thermocouples used to monitor in-package air temperatures

Air delivery and return velocities and temperatures were measured using thermocouples and thermistor anemometers spaced across the width of the deck. Thirty-two type-T thermocouples and 14 thermistor anemometers were placed in the floor gratings on the lower of the two decks, adjacent to the refrigeration end. Thirty-two type-T thermocouples and 14 thermistor anemometers were also placed across the air return grill on the spar deck. Air temperatures and velocities throughout the deck were also measured using thermocouples and thermistor anemometers. Sixty-four thermocouples and 42 thermistors were positioned in both the floor and ceiling headspace of the spar deck. Figure 11-2 shows the approximate positions of the thermistor anemometer sensors. Thermocouples were spaced evenly across the deck in a 8 × 8 grid. Temperatures and voltages were measured using 16 or 32-channel Eltek Squirrel data-loggers (1000 series, Eltek Ltd. Cambridge, England).

Four pressure taps were installed to measure the pressure drop across the upper layer of pallets on either side of the hold. Pressure taps were positioned in the floor approximately 3 m from the refrigeration end, and adjacent to the return air grill. Each set of taps was positioned approximately 6 m from a side wall, and connected to a pressure transducer (Model 2604, Setra Systems Inc., MA, USA) using pressure tubing (6 mm OD). The transducer outputs were logged using a 32-channel Eltek Squirrel data-logger (1000 series, Eltek Ltd. Cambridge, England).

Temperatures, velocities and pressures were recorded at 10-minute intervals throughout the duration of the shipment. The vessel air delivery temperature was set at -0.8 °C.

The spar deck was loaded with 307 pallets to give a free area ratio of approximately 7%. Figure 11-5 shows an estimate of the positioning of the pallets within the deck, made from information collected during loading and photographs of the hatch-square. Due to the hectic nature of the loading process, recording of a complete set of pallet position data was not possible and the diagram may not precisely represent the actual position/orientation for all the pallets.

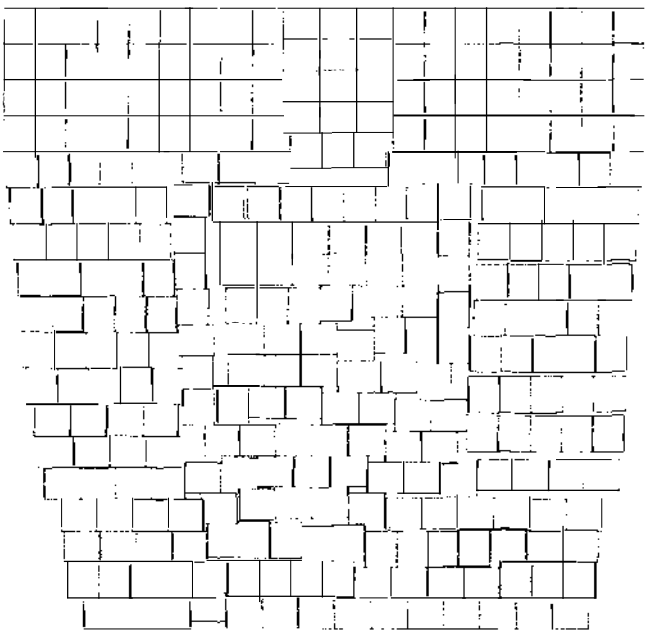

Figure 11-5 - Schematic diagram outlining the positioning of pallets within the monitored shipment of kiwifruit from New Zealand to Japan

11.3 Flow channel definition

Due to the large size of refrigerated holds, collection of data describing the width of gaps between pallets would be a mammoth task. Coupled with this, the nature of an ocean voyage means that the size of the gaps would be likely to change through the duration of the journey due to movement of the pallets and relaxation of the cardboard packaging. As such, specific channels were not modelled in this scenario. Rather, a random distribution of gap sizes was considered adequate to provide a sufficiently accurate description of the actual system. The dimensions of the hold were rounded to simplify channel definition (Figure 11-6).

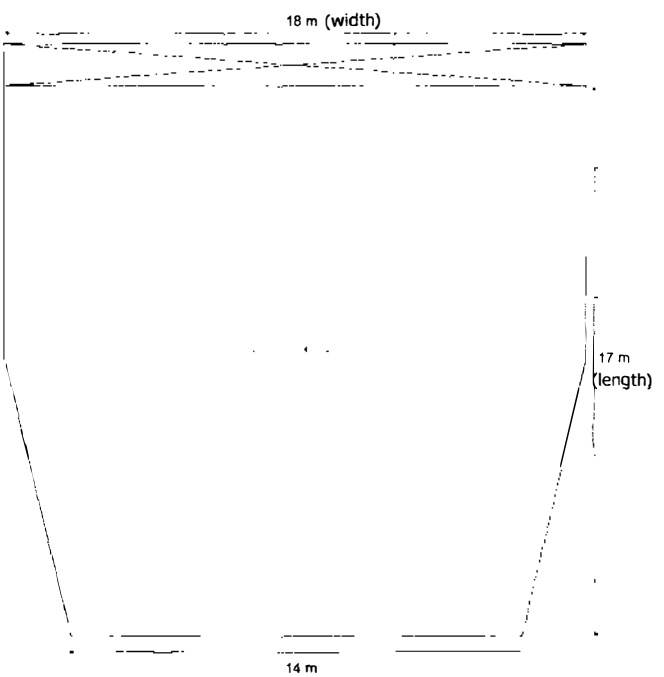

Figure 11-6 - Plan view of the model refrigerated hold

Each of the vertical flow channels within the deck was classified into one of three categories: from the under-floor ducts to the pallet base level, from the pallet base level to the headspace above the pallets through a gap between pallets or between a pallet and the wall, and from the lower deck headspace to the upper deck pallet bases through the spar floor. Flow rates through pallets were assumed to be negligible.

Given that specific channels were not modelled, nodes were positioned across the floor area of the deck in a regular 1 m × 1 m grid as shown in Figure 11-7. Essentially, each square of the grid represents a pallet, and each vertical channel represents a gap between two pallets with a cross-section 1 m long and variable width . The increased size of the modelled pallets (1 m × 1 m) compared with the actual size, reduced the number of pallets from 307 to approximately 289.

There were 5 levels of nodes in the vertical direction corresponding with the level of the lower gratings, in the pallet bases on the lower deck, in the headspace above the pallets in the lower deck, in the pallet bases in the upper deck and in the headspace above the pallets in the upper deck. Figure 11-8 shows the positioning of the vertical planes. Nodes adjacent to the air delivery duct were connected to 18 fixed pressure nodes (inlets) and nodes adjacent to the return air grill were connected to 18 fixed pressure nodes (outlets). Multiple inlet and outlet nodes were used to allow simulation of a non-uniform pressure profile across the width of the refrigeration plant. Figure 11-9 shows a 3-dimensional illustration of the flow resistance network.

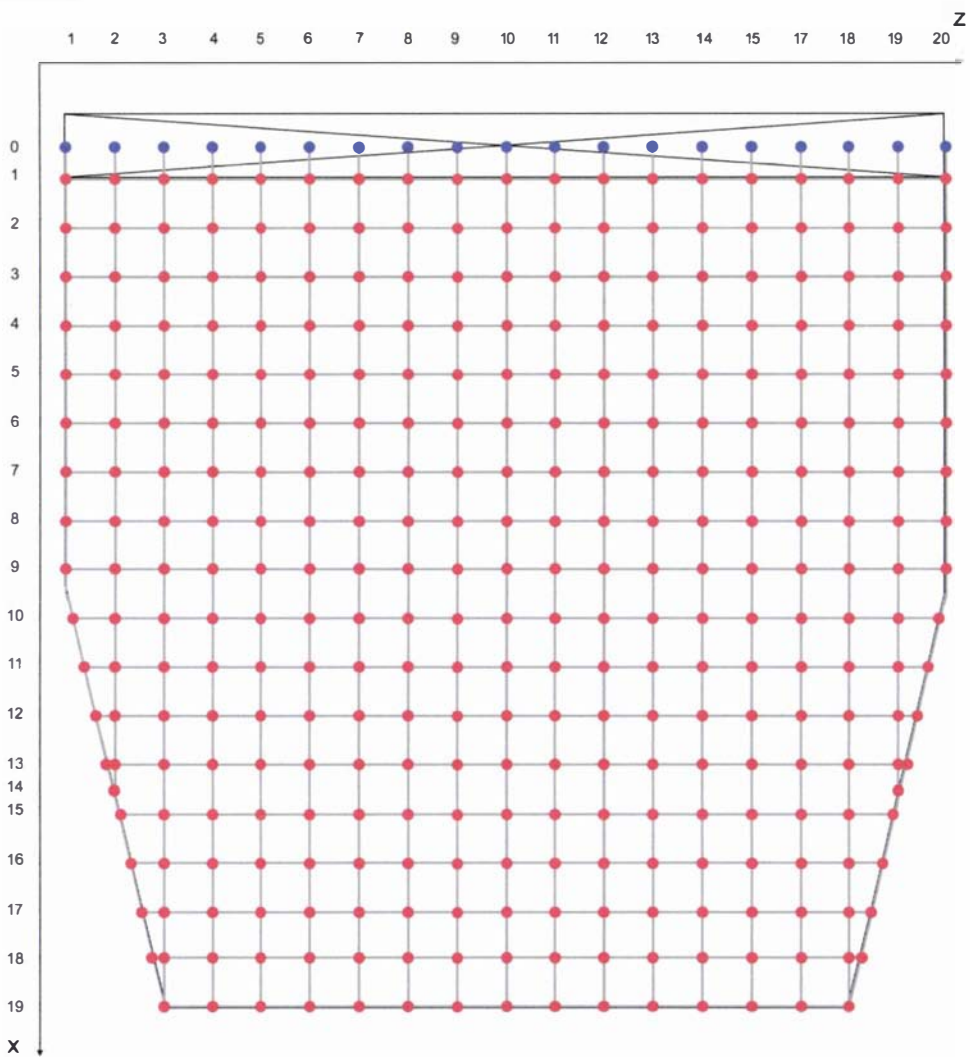

Figure 11-7 - Plan view of the model refrigerated hold showing the defined flow resistance network for the Y = 1 to 5 planes. Blue circles represent fixed pressure nodes, red circles represent unknown pressure nodes, and grey cylinders represent flow channels

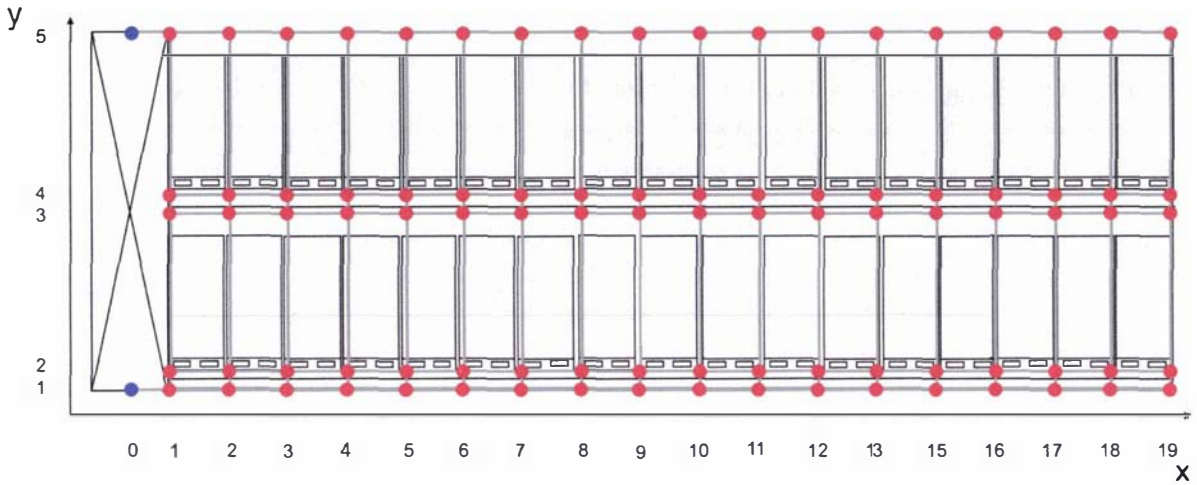

Figure 11-8 - Elevation view of the modelled refrigerated hold showing the defined flow resistance network for the Z = 3 to 18 planes. Blue circles represent fixed pressure nodes, red circles represent unknown pressure nodes, and grey cylinders represent flow channels

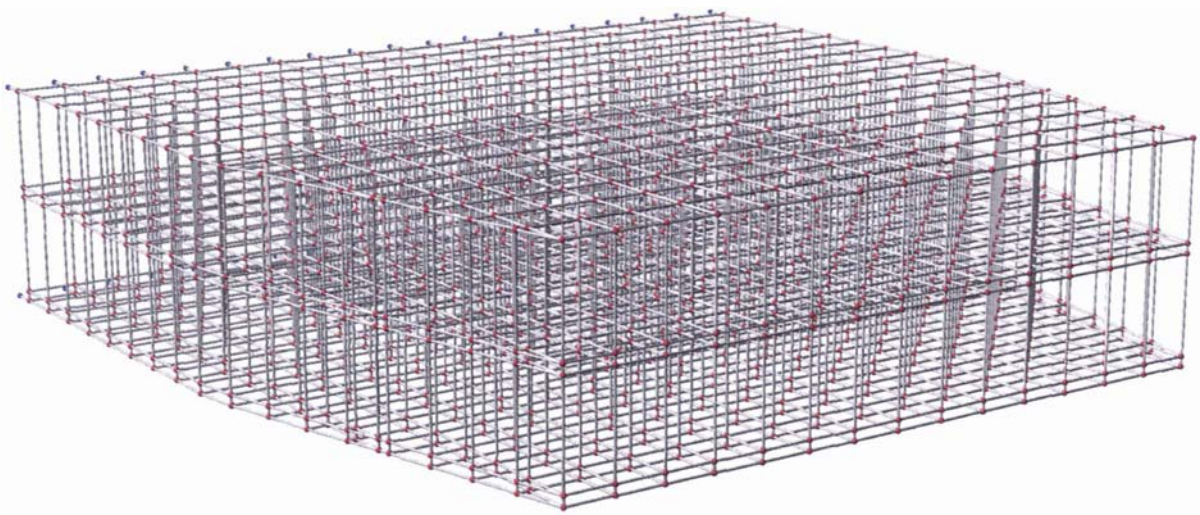

Figure 11-9 - Three-dimensional representation of the flow resistance network approximation of the refrigerated hold loaded with 289 pallets. Blue circles represent fixed pressure nodes, red circles represent unknown pressure nodes, and grey cylinders represent flow channels

The vertical channels connecting the under-floor gratings to the pallet base level on the lower deck were modelled using the perforated plate correlation presented in Section 8.3.4 (Equation 8-12). Perforations in the floor were spaced to give an open area of approximately 2.5%. Flow through the slotted floor of the spar deck (ceiling of the lower deck) was modelled using a correlation for long orifices as reported by Miller (1990). The fraction of the floor area open to flow was 0.25 and the orifice length to width ratio 0.4.

Vertical channels between pallets on the square grid were modelled as Type I channels, with an absolute roughness of 0.0003 m. Channels were not defined at the corner of each pallet, so each vertical channel matched the full dimension of the pallet (1 m). As shown in Figure 11-5, the size of the gaps between the pallets increased towards the area directly underneath the hatch in the centre of the hold (hatch-square). Channels between the pallets and the side walls of the hold were also large in the half of the deck furthest from the refrigeration end due to the irregular shape of the hold. To account for these differences, gap

sizes were generated using a bounded random function, the bounds of which were dependent on the location of the gap within the hold. Along the walls of the hold in the rear half of the hold (opposite the refrigeration end), gap sizes varied randomly between 0.05 and 0.15 m. Between pallets in the hatch-square, half of the gaps were assigned a width of 0.01 m and the remaining gaps varied randomly between 0.05 m and 0.10 m. In the remainder of the hold, half the gaps were assigned a width of 0.01 m and the remaining gaps varied randomly between 0.02 m and 0.04 m. Half of the gaps were assigned a size of 0.01 m to simulate those pallets which were placed flush against adjacent pallets. The minimum spacing of 0.01 m was estimated from the thickness of the corner-boards that effectively stopped a pallet face from being placed flush against an adjacent pallet face. Random gap sizes were generated independently for the lower and upper decks. The resulting free area ratios were 6.7% and 7.1% for the lower and upper decks respectively.

Each of the layers had horizontal flow channels in one of three categories: ducts below the perforated floor, through pallet bases and in the ceiling headspaces. Horizontal flow channels running away from the refrigeration end in the under-floor gratings were modelled as Type I channels, with a height of 0.12 m. Grating supports running along the length of the deck were spaced every 0.5 m with a width of 0.04 m, so flow paths across the width of the deck (transverse channels) in the under-floor gratings were assigned an arbitrarily high resistance. It was assumed there was insignificant horizontal flows in the gaps between pallets, so no such horizontal flow channels were defined.

The design of the pallet bases in use during this shipment, and the arrangement of pallets within the hold, meant that flow through the pallet bases may or may not have been significant depending on the pallet orientation relative to the surrounding pallets. Flow channels between pallet bases were described using the correlation presented in Section 8.3.4 (Equation 8-10) or assigned an arbitrarily high resistance according to the position of the pallet within the hold. The pallet bases were modelled as flush against each other, with channels formed between pallet bases ignored. In regions where pallets were oriented randomly, it was assumed the flow channels were blocked and were assigned arbitrarily high flow resistances. The region near the refrigeration end of the deck, extending along the walls around the hatch-square, was considered the only region where sufficient pallets were aligned in one direction to allow significant flows.

Horizontal flow channels within the ceiling headspace were treated as Type I channels with a constant clearance of 0.4 m. In the actual system, the clearance was variable, with the decks structure reducing the clearance in some areas, whilst the clearance was larger in some areas. To account for contractions and expansions, additional frictional losses in the ceiling headspace channels were estimated (K_{add}= 0.3).

Additional frictional losses were also included in the vertical channels, taken from Perry & Green (1997). Fluid exiting the gaps at the top of the pallet experienced a sudden enlargement (K_{add}= 1) and fluid flow paths entering the vertical channels between pallets were likened to a contraction and a square bend (square 90° bend (1.3) and contraction (0.3); K_{add}= 1.6).

The network as described consisted of 38 fixed pressure nodes, 1660 unknown pressure nodes and 4510 flow channels. A uniform pressure profile was used across the 18 inlet fixed pressure nodes as the observed delivery velocity profile was reasonably uniform. The outlet fixed pressure nodes were assigned zero pressures.

11.4 Simulation results

A circulation rate of 80 air changes per hour was assumed (corresponding to 46000 $m^3.h^{-1}$) and the total pressure at the inlet was set at 100 Pa across the entire width of the deck. Simulation took approximately 135 minutes, with no convergence difficulties.

Contour and wireframe figures in this section were drawn using Surfer v7 (Golden Software Inc., Colorado, USA). Measured data was interpolated using the Kriging method to give a distribution of values for the entire deck area. For some quantities, such as the measured fluid velocity, a limited number of measurements were available and the figures may not represent the level of variation present in the system. It is stressed that figures in this section should be interpreted carefully because of the limited number of measurement points given the large size of the system. Despite this, due to the sizeable quantity of information and its variability both spatially and temporally, these figures served as the most effective means of data visualisation.

Figure 11-10 shows the predicted vertical velocities through the spar floor throughout the deck. The profile did not show any obvious spatial trends across the deck area, other than increased velocities near the walls in the half of the deck furthest from the refrigeration end and in the hatch-square area due to the larger channel sizes in those regions. Figure 11-11 shows the measured velocities through the spar floor interpolated from the 40 measurement points as shown in Figure 11-2. As Figure 11-11 was interpolated from just 40 measurement points, details such as increased velocities near the walls were not expected to be visible. Figure 11-12 is a difference map depicting the inconsistencies between Figure 11-10 and Figure 11-11. Agreement was reasonable, with neither set of data showing substantial differences in velocities across the deck area except near the walls of the deck where the predictions were particularly sensitive to the assumed gap sizes.

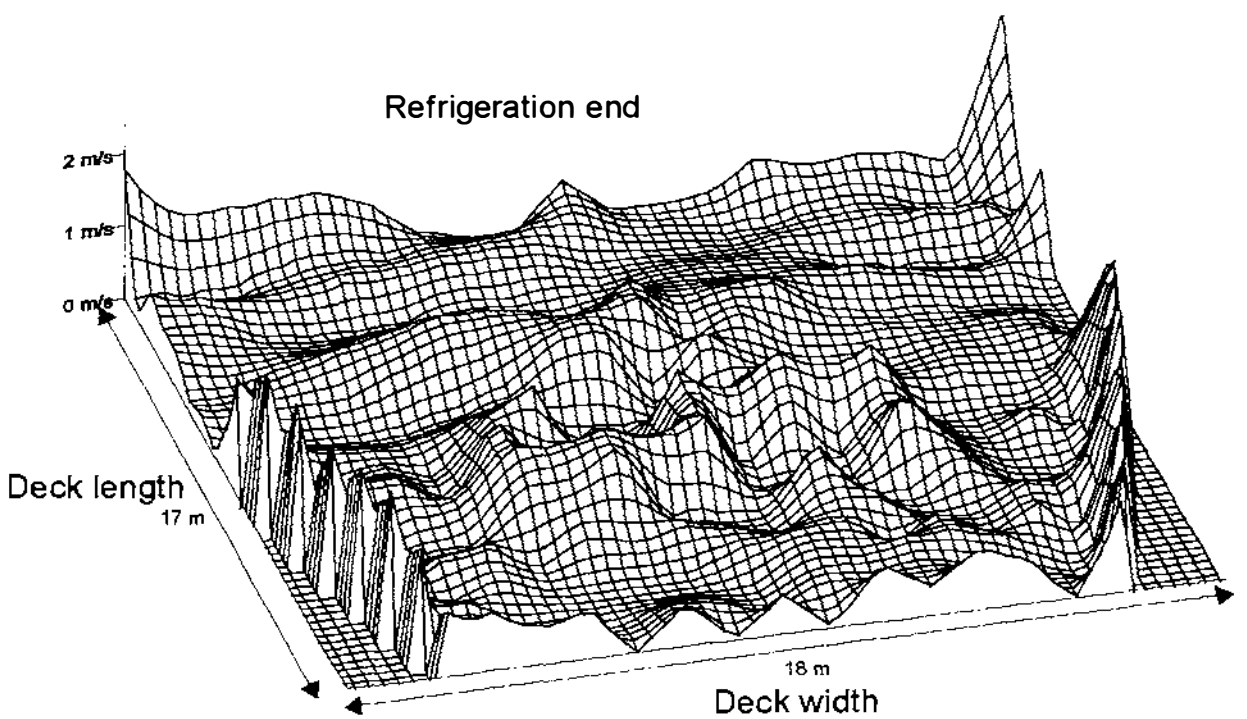

Figure 11-10 - Predicted vertical velocities through the spar floor of the refrigerated deck

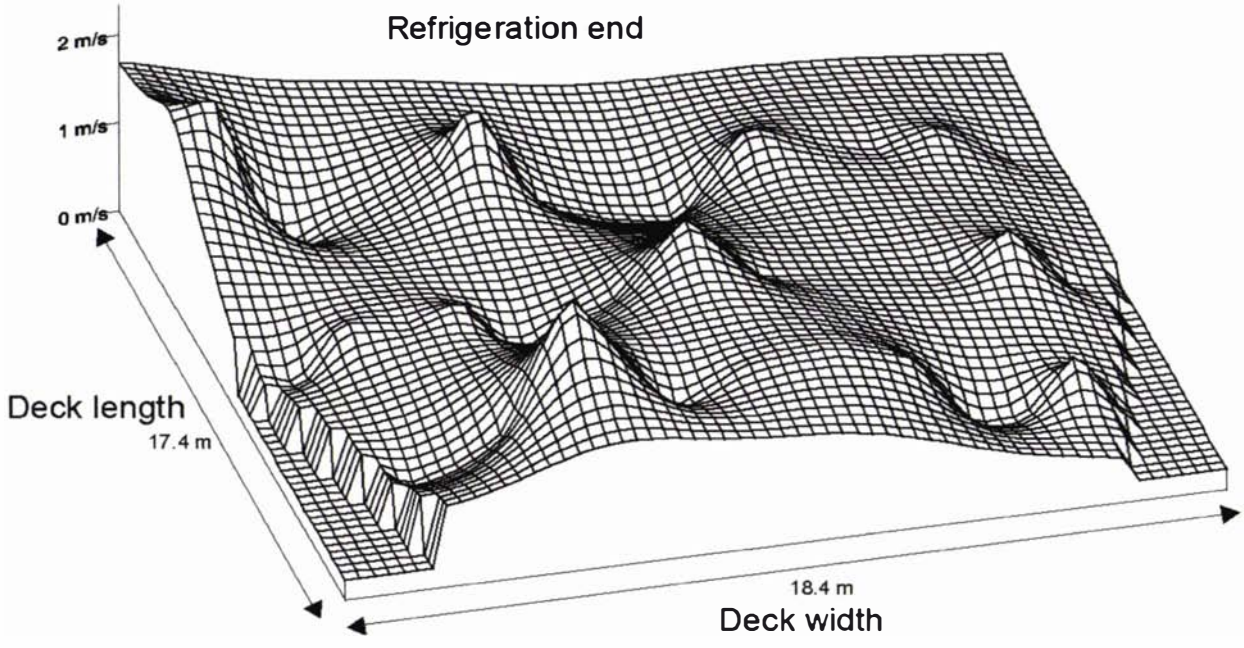

Figure 11-11 – Time-averaged measured velocities through the spar floor of the refrigerated deck

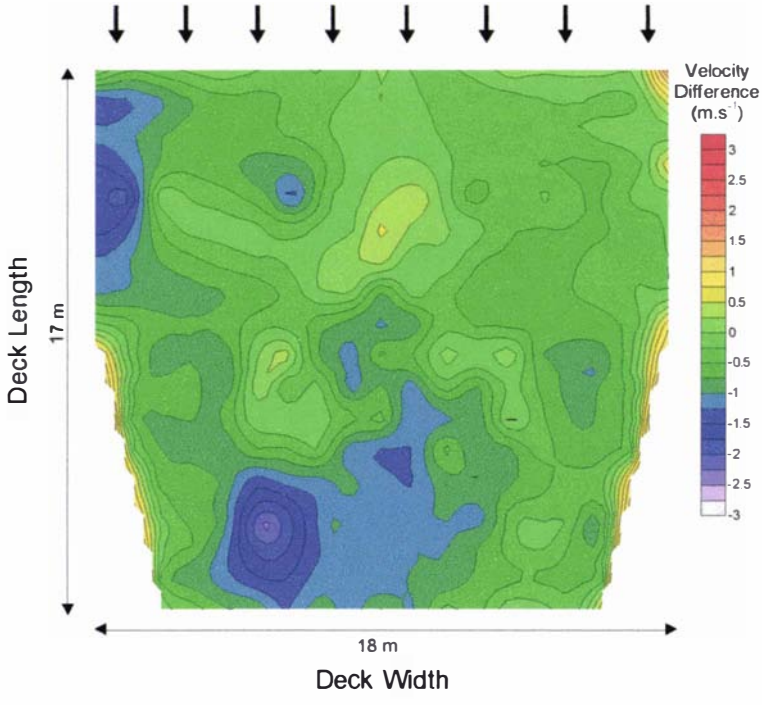

Figure 11-12 –Difference map between measured and predicted velocities through the spar floor of the refrigerated deck (simulated – measured)

Figure 11-13 shows the predicted horizontal velocities in the ceiling headspace above the cargo. Figure 11-14 shows the measured velocities in the ceiling headspace interpolated from the 40 measurement points as shown in Figure 11-2. Headspace velocities were predicted to decrease with increasing distance from the refrigeration end of the deck, with an even profile across the width of the deck. The measured velocities display a similar longitudinal trend; however, the measured values show large variation across the width of the deck, with lower velocities measured on the right-hand side of the deck. Figure 11-15 is

a difference map depicting the inconsistencies between Figure 11-13 and Figure 11-14. Agreement between predicted and measured velocities was reasonable if the variation with width across the deck was averaged (Figure 11-16). The predicted decrease in ceiling velocity with distance from the refrigeration end appeared linear for the two thirds of the deck nearest the refrigeration end. Predicted velocities were 3.7 $m.s^{-1}$ adjacent to the refrigeration end, and 0.8 $m.s^{-1}$ 12 m from the refrigeration end. In the third of the deck furthest from the refrigeration end, the predicted rate of velocity decline slowed. Differences between measured and predicted velocities across the width of the deck may have been caused by the variable height of the headspace.

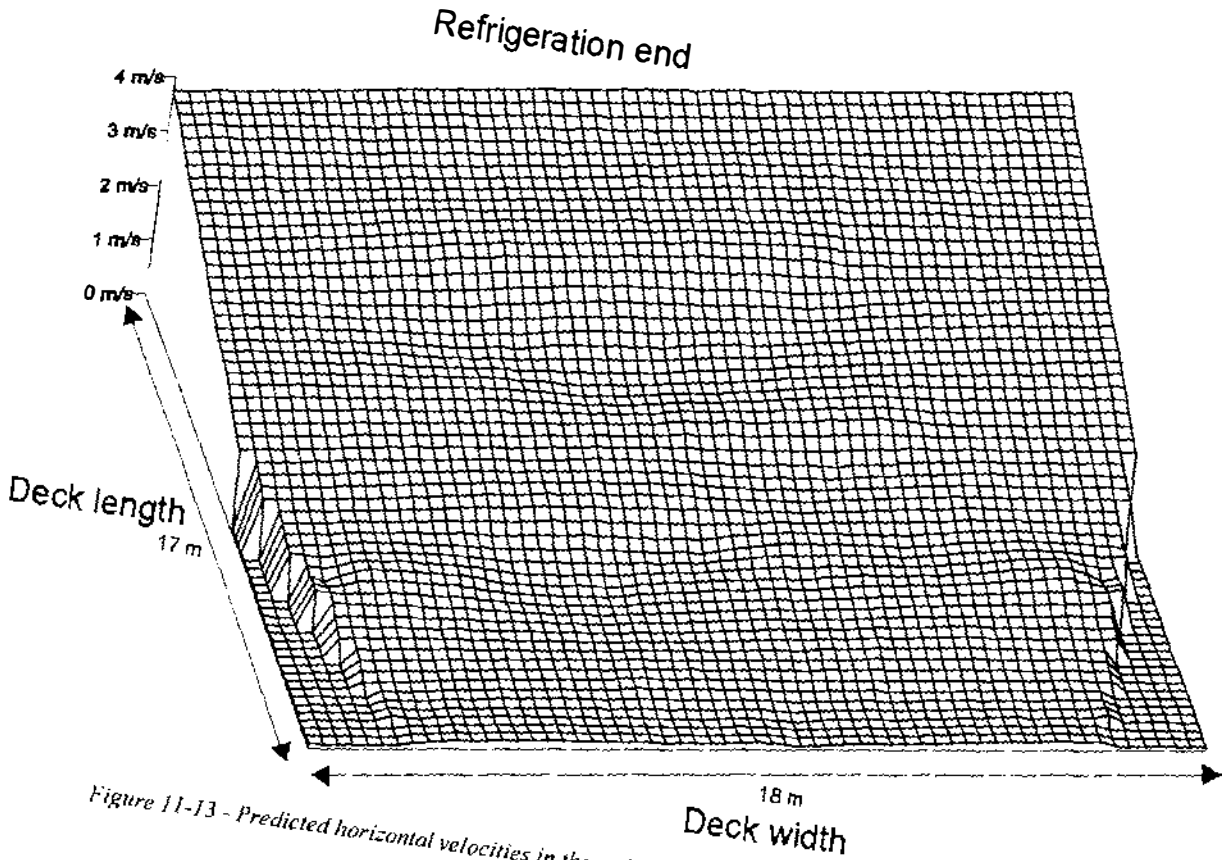

Figure 11-13 - Predicted horizontal velocities in the ceiling headspace throughout the refrigerated deck

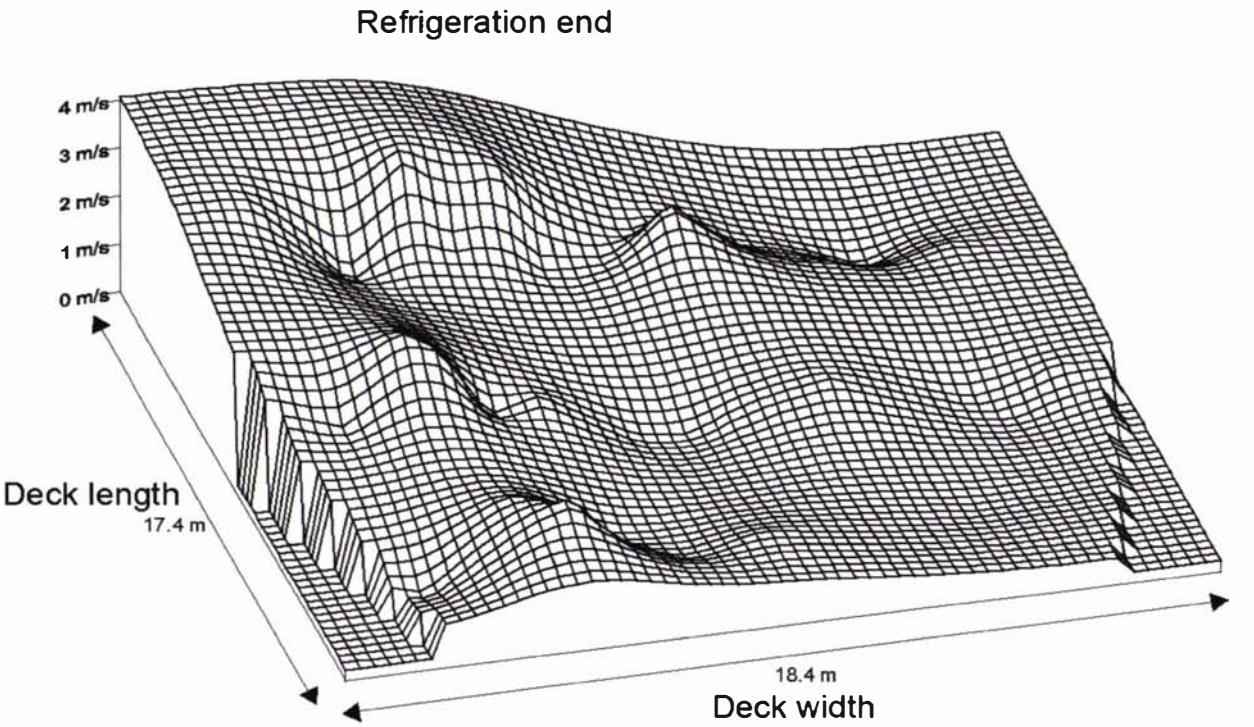

Figure 11-14 – Time-averaged measured horizontal velocities in the ceiling headspace throughout the refrigerated deck

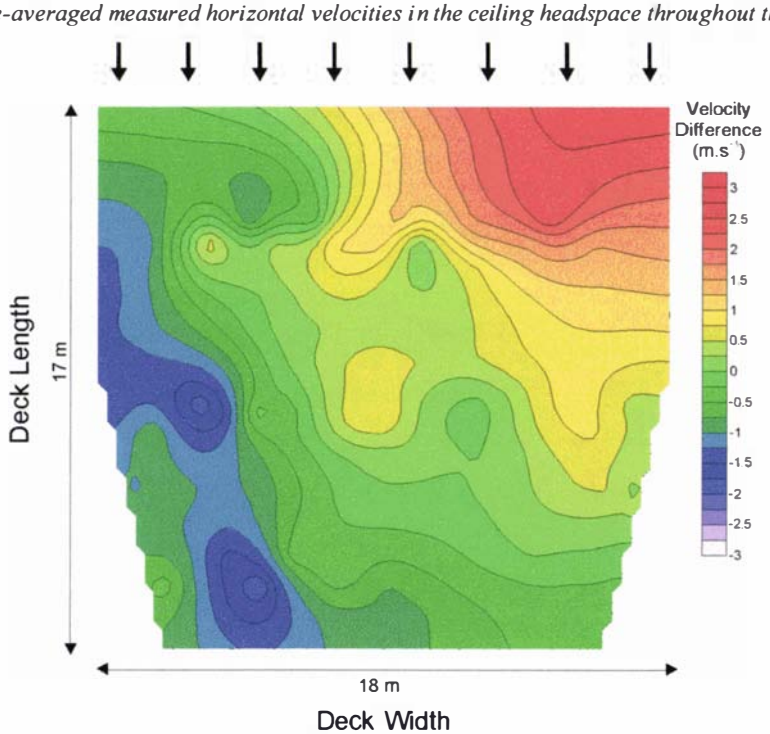

Figure 11-15 –Difference map between measured and predicted horizontal velocities in the ceiling headspace throughout the refrigerated deck (simulated – measured)

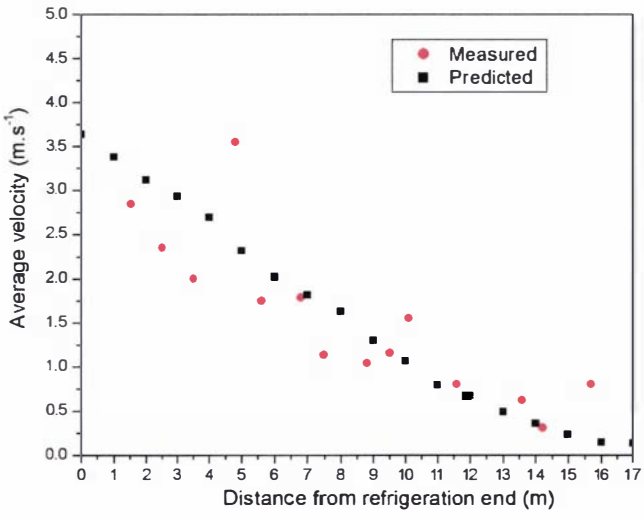

Figure 11-16 – Measured and predicted horizontal velocities in the ceiling headspace averaged across the width of the refrigerated deck

Figure 11-17 shows the predicted vertical velocities in the gaps between pallets throughout the deck. Figure 11-18 shows the corresponding fluid temperature rise predicted as described in Section 9.3.2. A value of 0.3 $W.m^{-2}.K^{-1}$ was used as the insulation 'k-value' of the hold's walls. The predicted fluid temperature rise was low throughout the hold, with maximum values of 1.5°C against the wall and 0.6°C within the hold. There was a trend of decreasing velocity and increasing temperature rise with distance from the refrigeration end. The trend appeared fairly uniform across the width of the deck. Figure 11-19 shows the difference between the measured in-package temperatures and the average air temperature in the spar floor (-0.5°C) 10 days in to the voyage. These values give an indication of the air temperature rise in the channels, and comparison of Figure 11-18 and Figure 11-19 shows good visual agreement. Figure 16-1 to Figure 16-7 of Section 16 show 'snapshots' of the measured in-package temperatures over the duration of the journey, and it can be seen that temperatures were relatively constant by this stage of the voyage, so the in-package temperatures will give an indication of the air temperature rises throughout the hold. Comparison of these figures shows broadly similar spatial trends across the deck area.

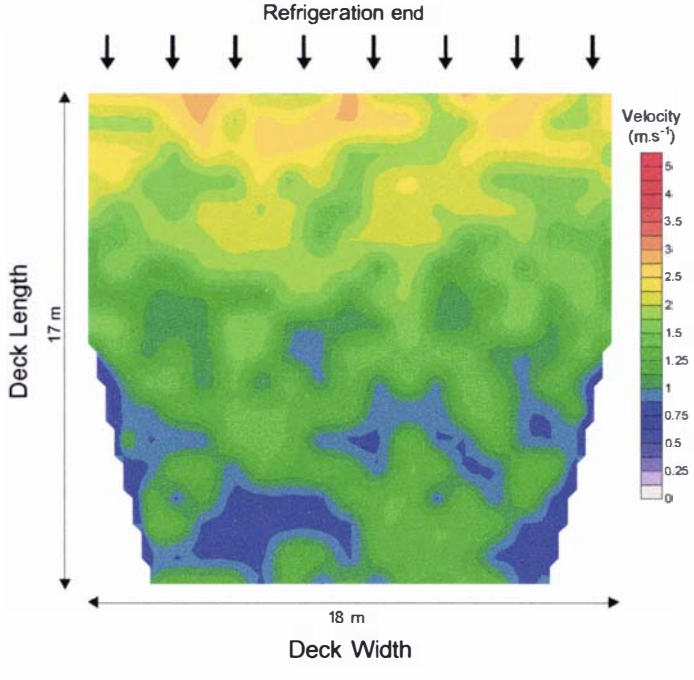

Figure 11-17 - Predicted velocity in the vertical channels formed by gaps around pallets throughout the refrigerated deck

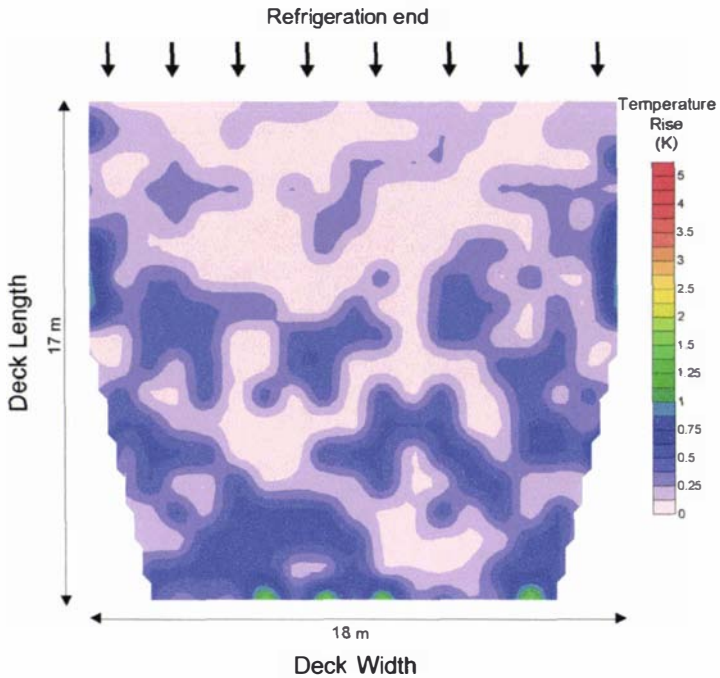

Figure 11-18 - Predicted temperature rise in the vertical channels formed by gaps around pallets within the refrigerated deck

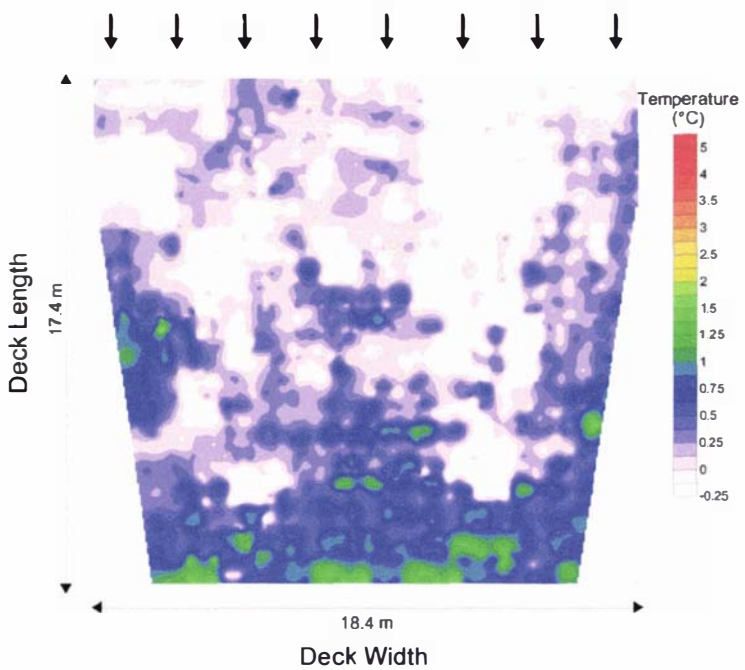

Figure 11-19 – Measured differences between the air temperature in the spar floor and the in-package temperatures 10 days in to the voyage

Figure 11-20 shows the time-averaged measured delivery air temperature and velocity across the width of the deck. Predicted velocities in the air delivery channels are shown in Figure 11-21. Comparison of the predicted and measured flows shows significant disagreement (3 $m.s^{-1}$ measured compared to 14 $m.s^{-1}$ predicted). Given the velocities measured elsewhere in the hold and the level of temperature control achieved, it was considered highly improbable that these measured velocities reflected the actual fluid velocity in the under-floor ducts. The disagreement was attributed to positioning of the anemometer sensors within the under-floor channels. The sensors were placed approximately 0.06 m below the top of the perforated floor, through the perforation nearest the refrigeration end of the hold. Given the low air velocities measured, it is likely that air flowing in to the channel formed a re-circulating zone at the point

of measurement, which led to a significant error in the measurement of the average fluid velocity in the channel.

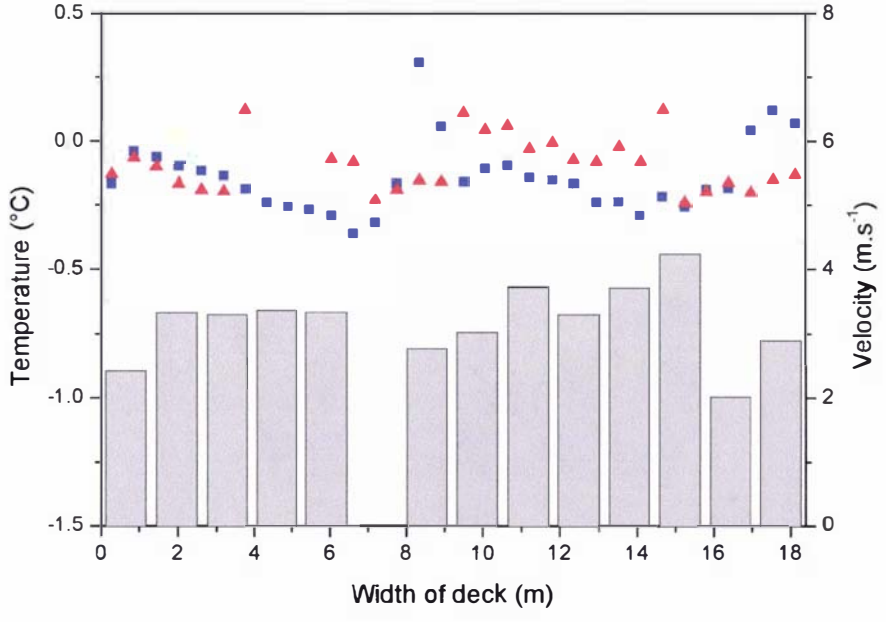

Figure 11-20 – Time-averaged measured air delivery velocities (bars), delivery temperatures (■) and return temperatures (▲) across the width of the deck

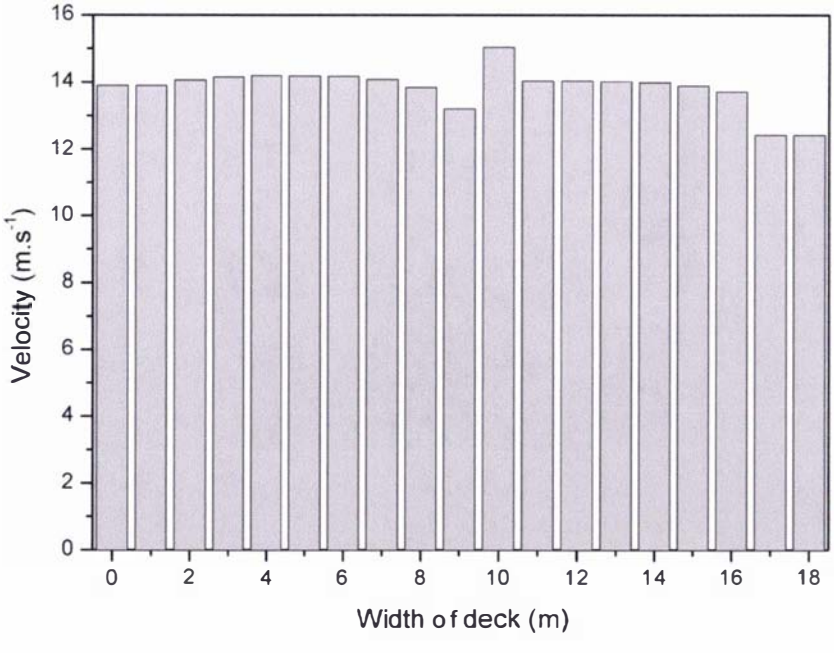

Figure 11-21 - Predicted air delivery velocity across the width of the deck

Figure 11-22 shows the time-averaged measured return air temperatures and velocities across the width of the deck. Predicted velocities in the air return grating are shown in Figure 11-23. Again there was significant disagreement, with predictions being higher than most measured values. In this case, the velocity sensors were placed in the centre of the return air grill prior to loading; however once loaded, the pallets covered approximately half of the return air grill, with the top of the pallets at the same height as the sensors. Therefore, the top of the pallets interfered with the sensors, affecting the validity of the measurements (probably lower velocity than would occur fully above the pallets). The increased return

velocities predicted near the sides of the hold were due to large gaps between pallets near the wall of the deck.

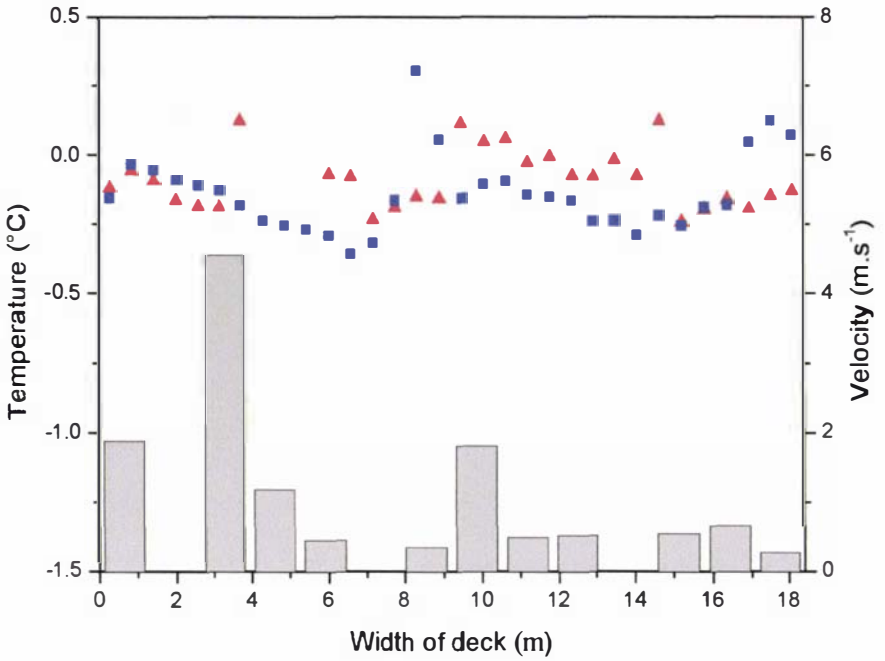

Figure 11-22 – Time-averaged measured air return velocities (bars), delivery temperatures (■) and return temperatures (▲) across the width of the deck

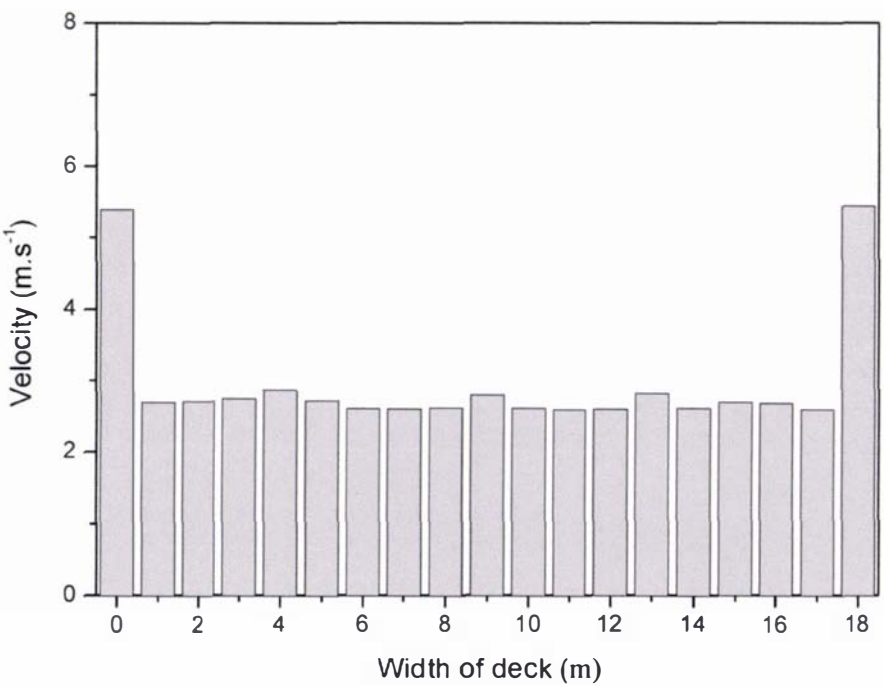

Figure 11-23 - Predicted air return velocity across the width of the deck

Figure 11-24 shows the time-averaged measured temperatures in the spar floor and ceiling headspace. Figure 11-25 shows the calculated differences between the two plots. These figures show air temperatures were consistent throughout the deck area, with a single warm zone in the ceiling temperatures evident in the end furthest from the refrigeration plant. Figure 11-26 shows the difference between the measured floor/ceiling temperature rise (Figure 11-25) and the predicted temperature rise (Figure 11-18) with good agreement shown.

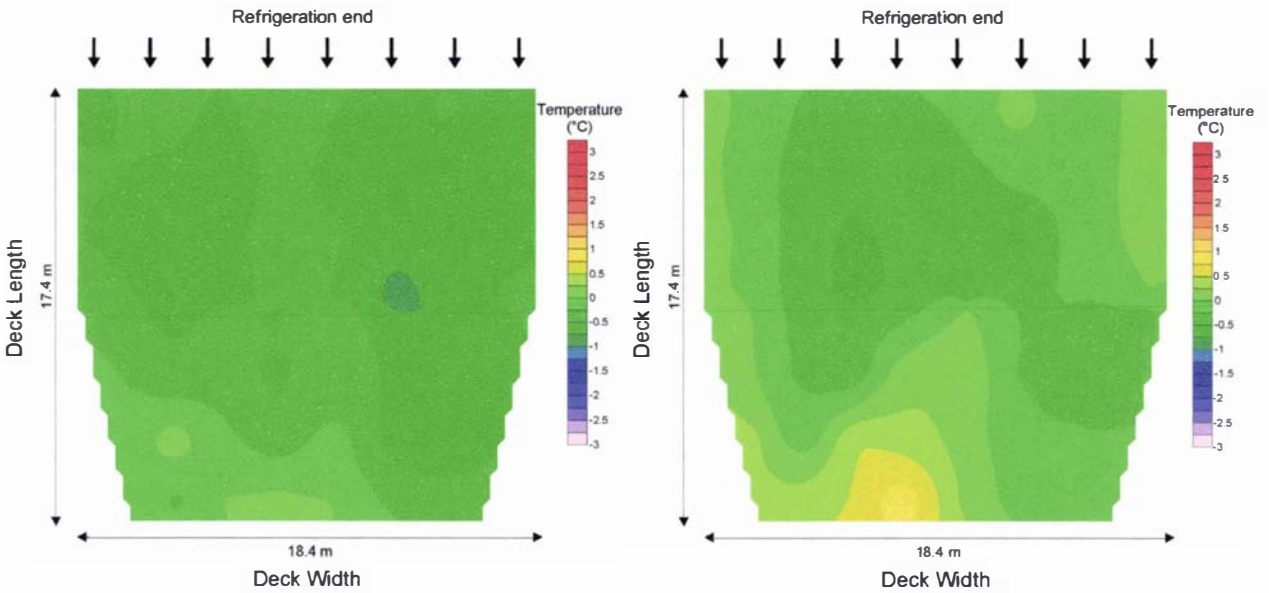

Figure 11-24 – Time-averaged measured air temperature in the spar floor (left) and ceiling headspace (right)

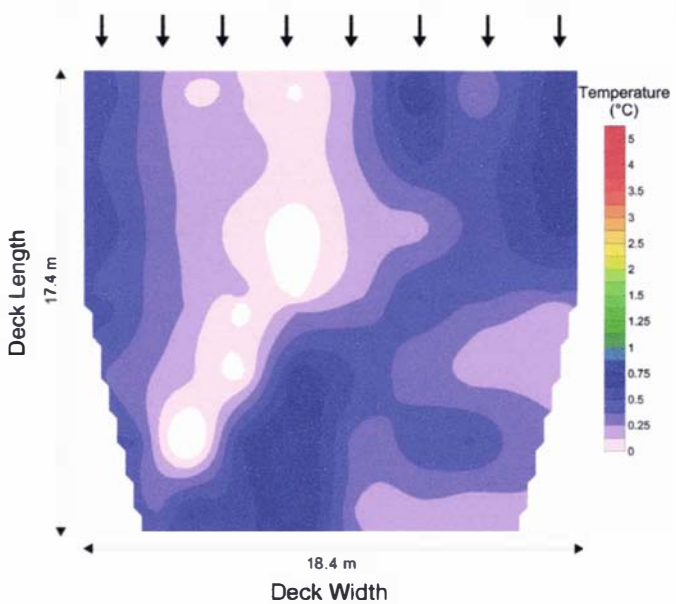

Figure 11-25 – Calculated difference between time-averaged measured temperature in the floor and ceiling headspace

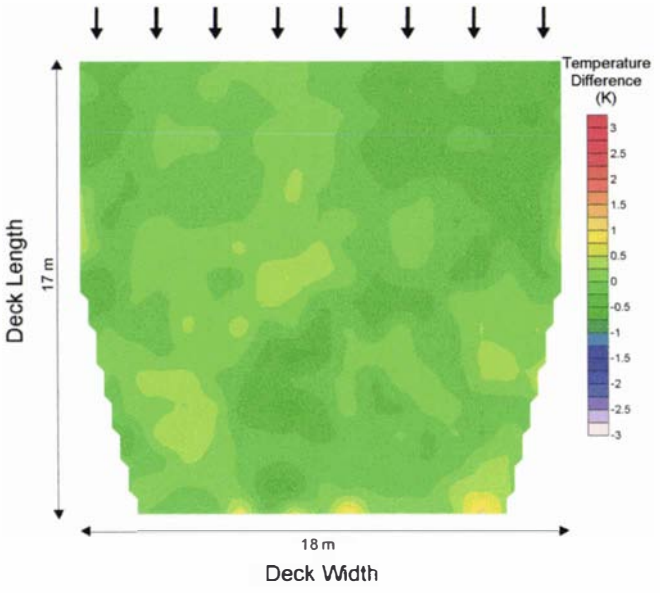

Figure 11-26 – Difference map between measured and predicted temperature rise throughout the refrigerated deck (simulated – measured)

Figure 11-27 and Figure 11-28 show the spatially-averaged measured delivery and return velocities and temperatures throughout the length of the voyage. Velocities were seen to fall rapidly following defrost and in two periods during the voyage, temperatures rose significantly. The first instance followed loading, where delivery air temperatures rose approximately 2°C over a 36-hour period without defrost. The second instance occurred toward the end of the journey over a 48-hour period without defrost. In both cases the temperature rise can be attributed to excessive refrigeration performance deterioration due to evaporator frosting.

Figure 11-29 and Figure 11-30 show the spatially-averaged measured temperatures and velocities in the spar floor and in the ceiling headspace throughout the journey. These figures reflect the same trends as the delivery and return sensors.

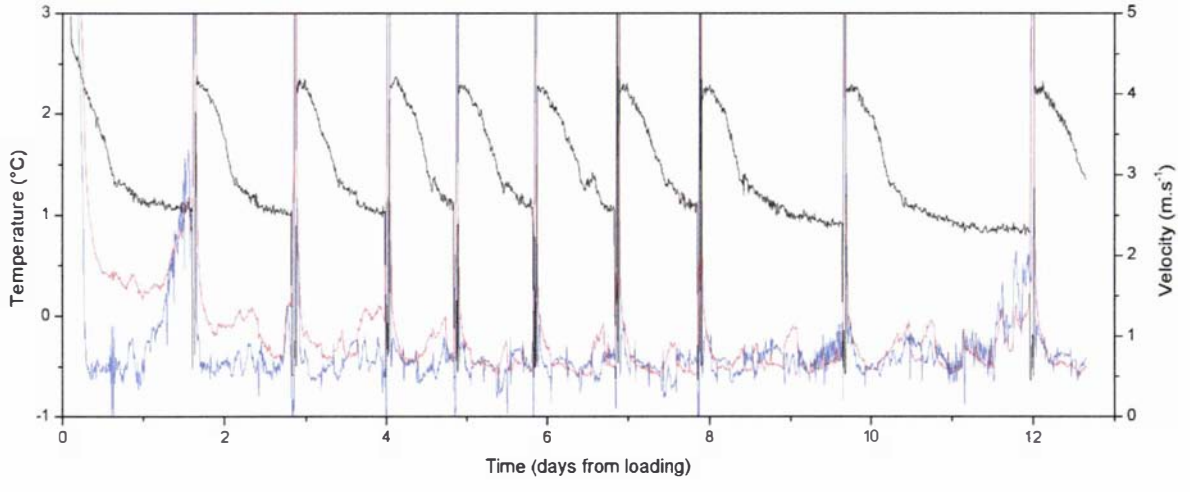

Figure 11-27 – Spatially-averaged measured air delivery velocity (-), temperature (-) and air return temperature (-) across the width of the deck throughout the voyage

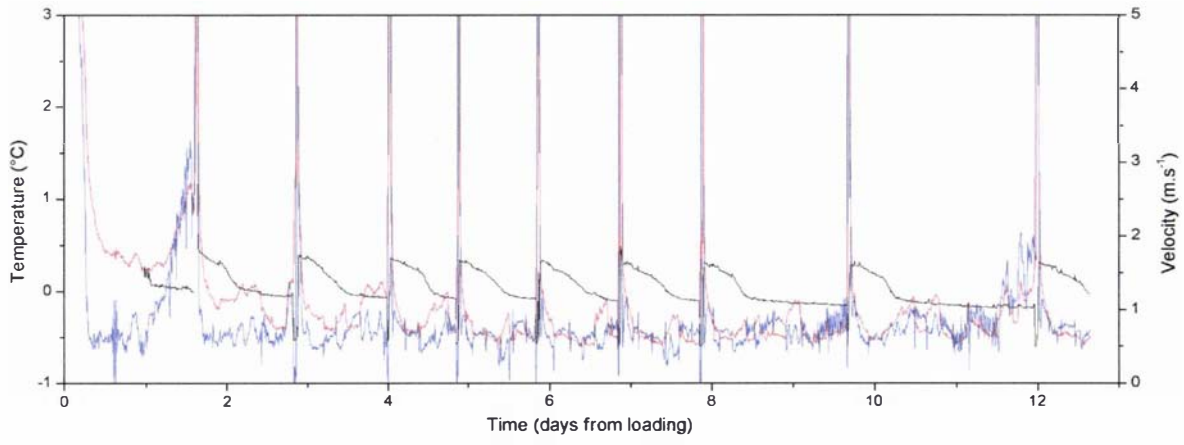

Figure 11-28 - Spatially-averaged measured air return velocity (-), temperature (-) and air delivery temperature (-) across the width of the deck throughout the voyage

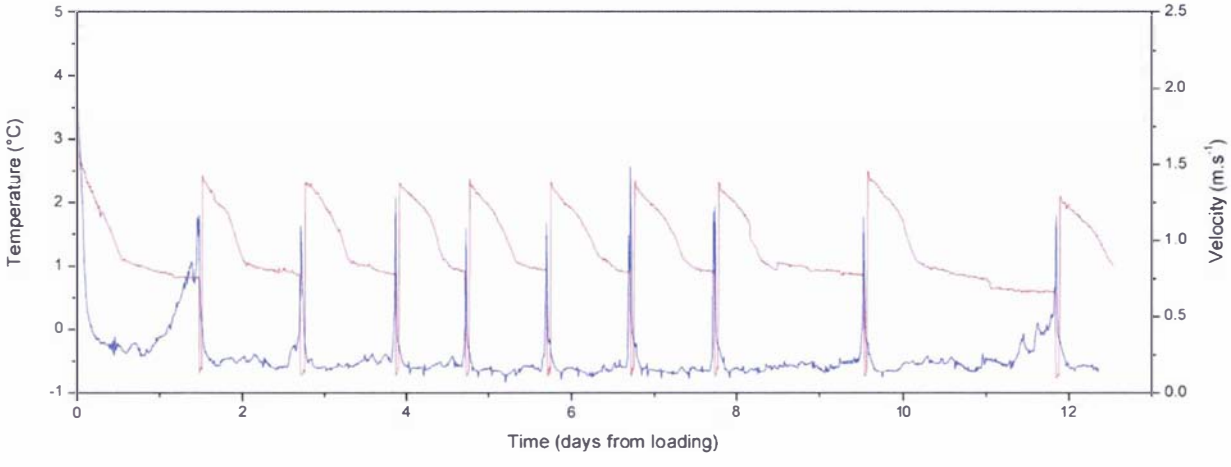

Figure 11-29 - Spatially-averaged measured velocity (-) and temperature (-) through the spar floor throughout the voyage

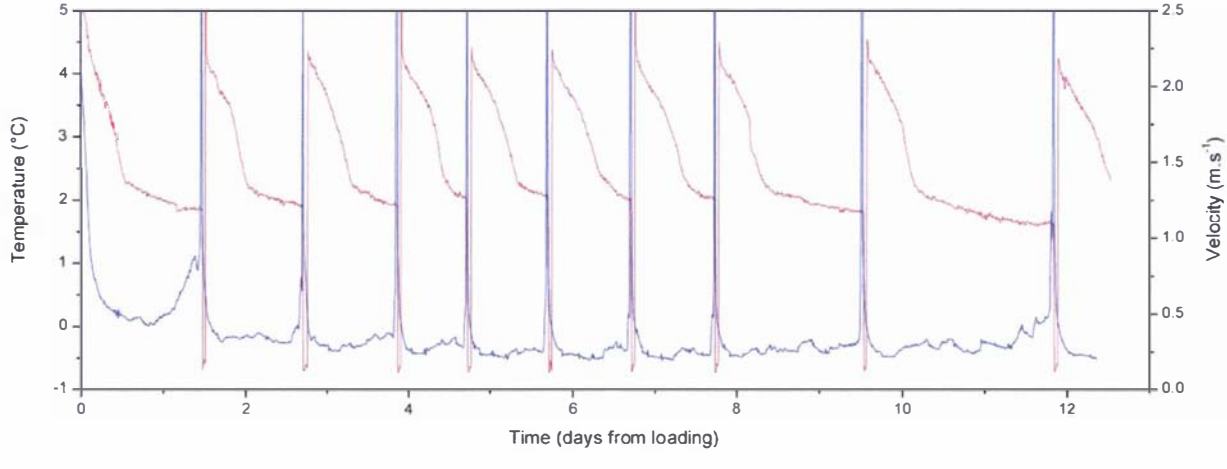

Figure 11-30 - Spatially-averaged measured velocity (-) and temperature (-) in the ceiling headspace throughout the voyage

The temporal trends display a characteristic shape, with a sharp fall in velocity and a relatively stable temperature immediately following defrost, followed by a period with a slower reduction in velocity. Where the stable velocity period was long enough, the temperatures were seen to rise. There was insufficient data to provide a categorical explanation of the temporal trends; however, the following discussion presents one possible scenario leading to the observed effects.

The initial sharp decline in airflow may have been associated with formation of a 'fluffy' frost, which substantially increased the airflow resistance of the evaporator. As the volumetric flow of air and the heat transfer was reducing concurrently in this phase, control of the delivery air temperature was maintained. Over time, this frost layer would consolidate to produce a more solid layer of ice, providing increased insulation of the coil without substantially increasing the airflow resistance. Eventually, loss of control of the delivery air temperature occurs, resulting in the rise in delivery air temperature.

Whilst loss of delivery air temperature control is the primary concern in this scenario, reduction in the circulation rate associated with the first stage of frost formation will also cause greater temperature variability within the hold. Evaporator design parameters, such as fin spacing, should take into account the volumetric flows of air required for temperature maintenance of the entire hold under frosting conditions, rather than just the heat transfer requirements.

In existing systems, defrost management is a key factor in maintaining temperature control within the hold. The ship's engineer is generally responsible for initiating defrost based on his/her judgement and a number of indicators: visual inspection of the evaporators, an increase in return air temperature due to reduced air circulation and/or a reduction in the temperature of the returning refrigerant due to lower capacity utilisation. It is vital to avoid the stage where heat transfer within the deck is significantly impeded, and improved management tools such as velocity sensors may be of use in this regard.

Figure 11-31 shows the measured pressure losses across both sides of the deck. Unfortunately the power supply to the pressure transducers was insufficient, with only 2 and 4 days of sensible data recorded from the two sensors respectively. The trends again mirror the same pattern between defrosts and were sufficient to confirm the observations made using the thermistor anemometers. The predicted pressure loss between the pressure tap locations was approximately 20 Pa, which compares reasonably well with the measured values in the period of relative stability prior to each defrost.

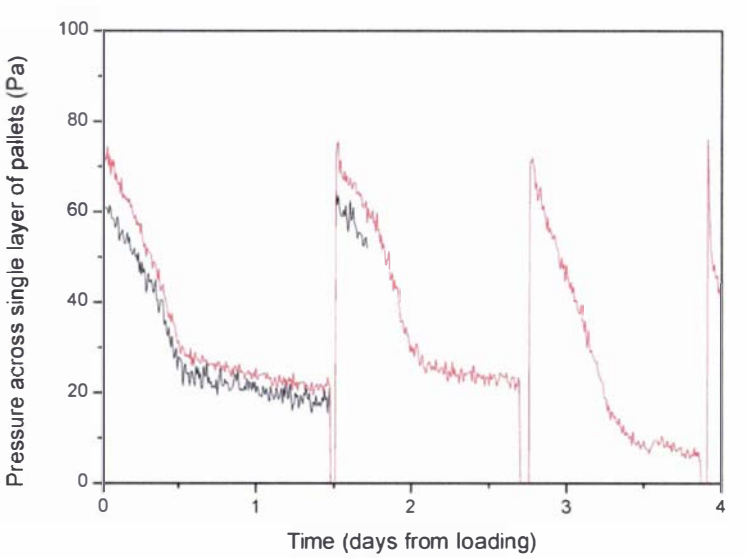

Figure 11-31 - Measured pressure on the left (-) and right (-) sides of the hold throughout the first 4 days of the voyage

11.4.1 In-package temperatures

Heat transfer simulations were performed for pallets positioned both near the refrigeration end and the opposite end of the deck. PackSim was used to predict the cooling rates of pallets surrounded by gaps of variable widths. Simulations were performed with gap widths of 0.04 m, 0.02 m, 0.01 m and 0.005 m. Gaps of the smallest width were not expected to be present in the hold, due to the corner-boards that ensure some spacing between pallets. Simulation of these gaps was performed to illustrate the influence of gap size.

Table 11-1 gives the input data as used in the heat-transfer model and Figure 11-32 shows the zone boundaries for a single layer of cartons. Two lines of symmetry were used to reduce the size of the domain and decrease the simulation time.

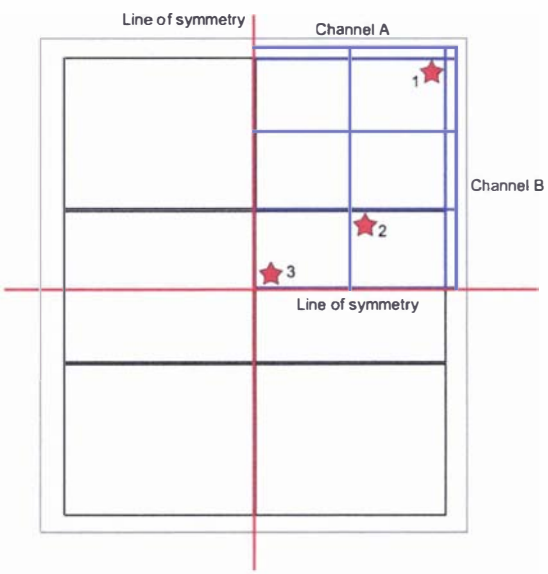

Figure 11-32 - Plan view of a single pallet layer of kiwifruit showing the defined zone boundaries on each layer of cartons and the three locations (★) used for comparison of simulated temperatures

Channels formed by the gaps between the pallet of interest and other pallets were modelled as half their actual thickness with no heat transfer across the external boundary. Essentially this approach assumes the adjacent pallet was at the same temperature as the pallet of interest. The top and bottom faces of the pallet were modelled as external boundaries over which heat transfer may occur. The fluid below and above the pallet was assumed to be of a constant temperature and velocity.

The average measured air temperature in the spar floor over the first 6 days of the voyage was used as the air temperature below the pallet and the air entering the vertical channels (delivery temperature). The average ceiling headspace temperature was used as the external temperature above the pallet (return temperature). Velocities predicted using the FlowSim model were used as the velocity in the channels and above the pallet. The velocity below the pallet was set at 1 $m.s^{-1}$, as the pallet base design restricted airflow through the bases. The system was assumed to be at a uniform initial temperature of 2.5°C as there was insufficient measured temperature data to accurately describe the initial temperature variability. As the air temperatures and velocities were assumed to be constant, the effects of evaporator frosting and defrosting were not included in the model.

Figure 11-33, Figure 11-34 and Figure 11-35 show the measured and predicted temperatures in the three positions depicted in Figure 11-32 for pallets adjacent to the refrigeration end of the hold. Figure 11-36,

Figure 11-37 and Figure 11-38 show the same data for pallets positioned in the end of the hold furthest from the refrigeration end.

Table 11-1 - Data used in the simulation of cooling in a pallet of kiwifruit. Data values were sourced from physical measurement of the cartons and Tanner (1998)

Variable	Value	Units
Physical System Data		
Width of system (x)	0.46	m
Height of system (y)	2.03	m
Length of system (z)	0.53	m
Package properties		
Zones in x - direction	3	
Zones in y – direction	4	
Zones in z – direction	29	
Number of V boundaries	360	
Number of H boundaries	464	
Number of P boundaries	435	
Total internal zones	348	
Total external zones	2	
Number of pack materials	3	
Number of active surfaces	4	
Product data		
Specific heat capacity	3650	$J.kg^{-1}.K^{-1}$
Thermal conductivity	0.427	$W.m^{-1}.K^{-1}$
Total mass of product	143.6	kg
Radius of each product item	0.02	m
Number of products in pack	1436	
Is respiration considered?	Yes	
Respiration coefficient a	8.97×10^{-5}	
Respiration coefficient b	1.74	
Fluid data		
Specific heat capacity	1005	$J.kg^{-1}.K^{-1}$
Thermal conductivity	0.026	$W.m^{-1}.K^{-1}$
Density	1.28	$kg.m^{-3}$
Convection factor	1	
External environment data		
Delivery temperature	-0.5	°C
Return temperature	0	°C
Packaging material data		
Package wall (1, 2, 3 thicknesses)		
Specific heat capacity	1700	$J.kg^{-1}.K^{-1}$
Thermal conductivity	0.065	$W.m^{-1}.K^{-1}$
Density	250	$kg.m^{-3}$
Single thickness	0.004	m

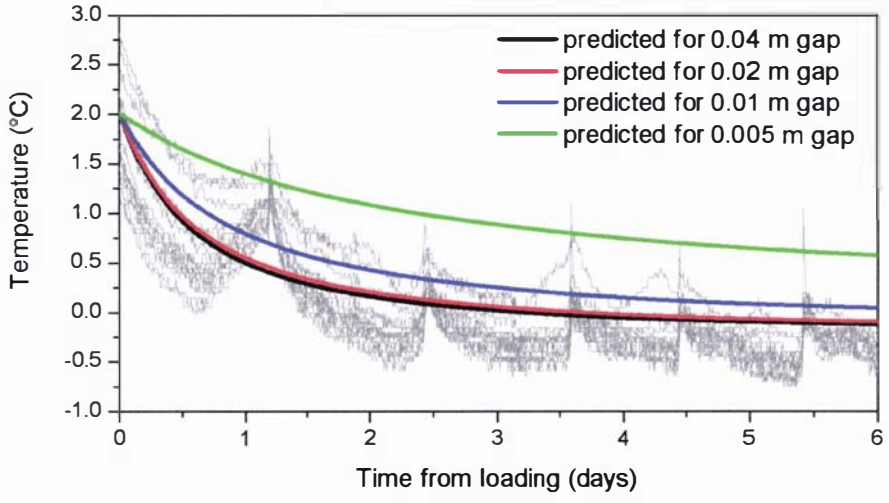

Figure 11-33 - Temperatures in position 1 as depicted in Figure 11-32 predicted for a range of channel sizes and measured in 8 pallets positioned at the end of the hold nearest to the refrigeration end

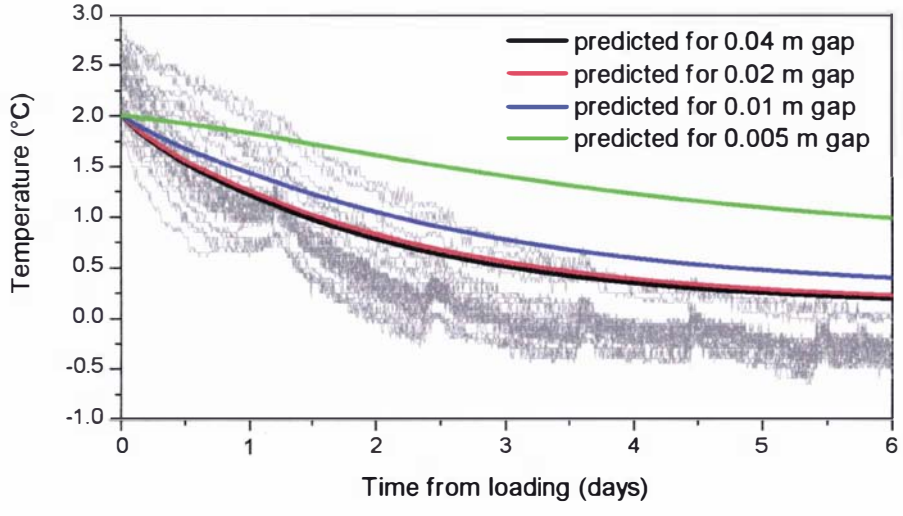

Figure 11-34 - Temperatures in position 2 as depicted in Figure 11-32 predicted for a range of channel sizes and measured in 8 pallets positioned at the end of the hold nearest to the refrigeration end

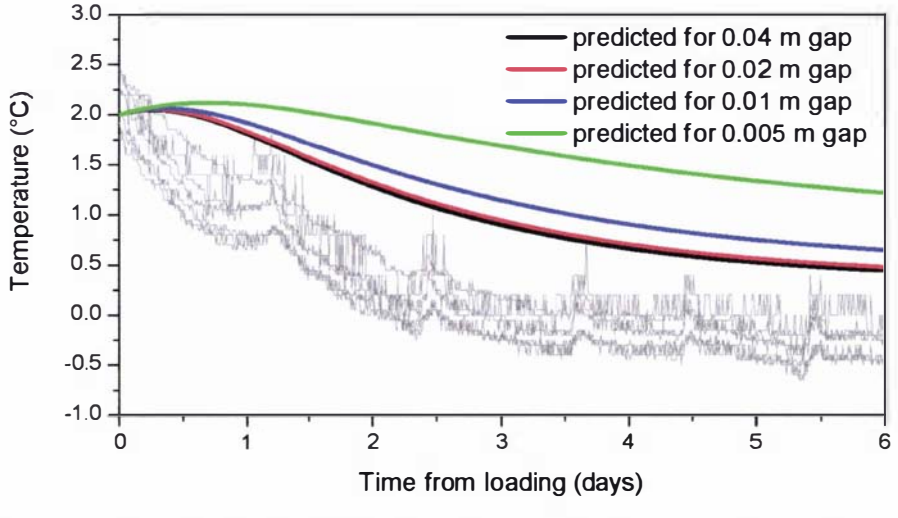

Figure 11-35 - Temperatures in position 3 as depicted in Figure 11-32 predicted for a range of channel sizes and measured in 8 pallets positioned at the end of the hold nearest to the refrigeration end

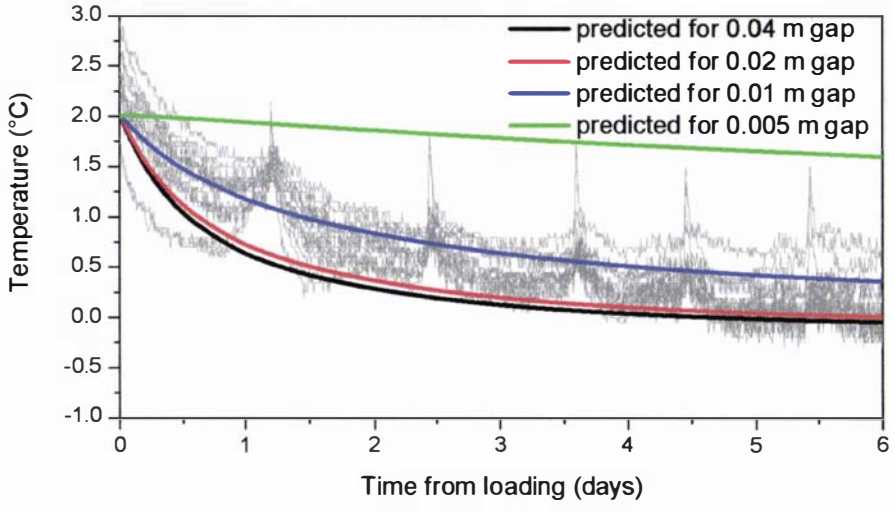

Figure 11-36 - Temperatures in position 1 as depicted in Figure 11-32 predicted for a range of channel sizes and measured in 8 pallets positioned at the end of the hold furthest from the refrigeration end

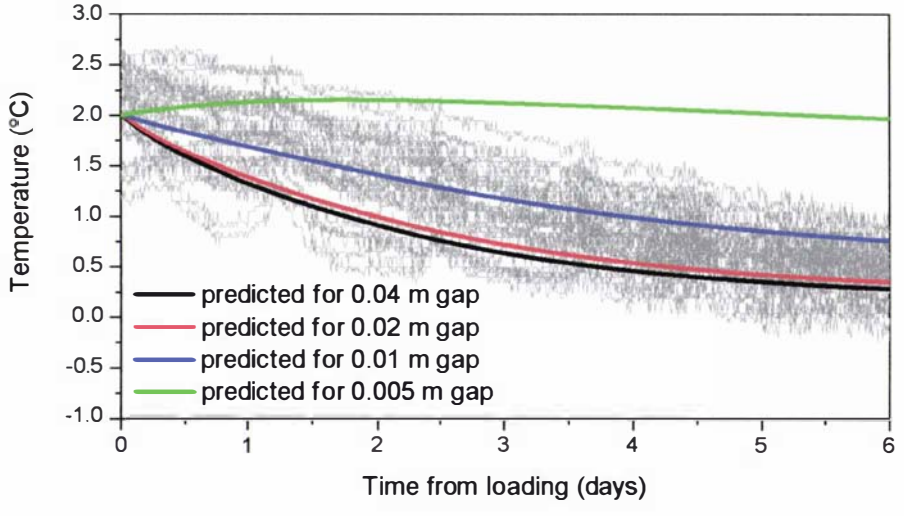

Figure 11-37 - Temperatures in position 2 as depicted in Figure 11-32 predicted for a range of channel sizes and measured in 8 pallets positioned at the end of the hold furthest from the refrigeration end

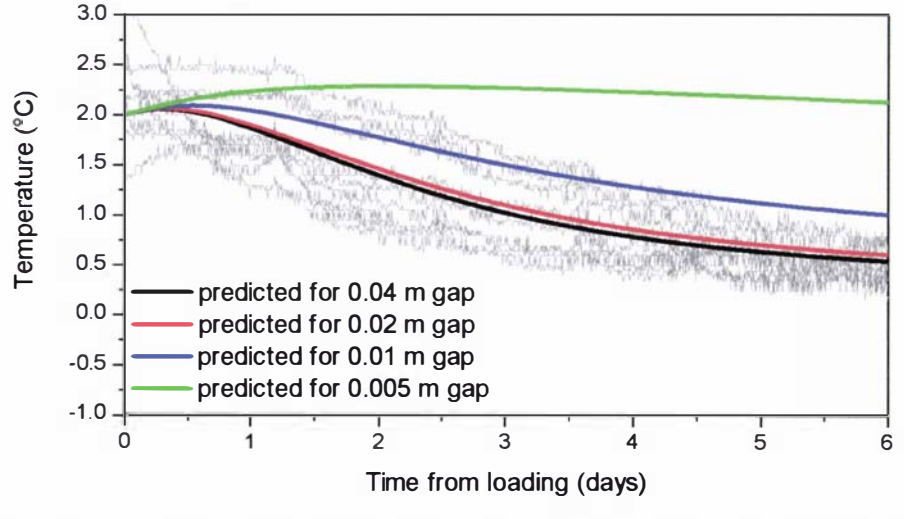

Figure 11-38 - Temperatures in position 3 as depicted in Figure 11-32 predicted for a range of channel sizes and measured in 8 pallets positioned at the end of the hold furthest from the refrigeration end

Measured initial temperatures varied between 1.0°C and 3.0°C. Table 11-2 shows the measured and predicted fractional unaccomplished temperature change after four days in the hold (Equation 10-1) for positions depicted in Figure 11-32.

Table 11-2 - Measured and predicted fraction unaccomplished temperature change (FUTC) after four days in the hold in positions as depicted in Figure 11-32

End of hold	Position	Predicted FUTC (0.04 m, 0.02 m, 0.01 m gap)	Measured FUTC
Refrigeration end	1	0.18,0.19,0.26	0.04 ± 0.06
Refrigeration end	2	0.34,0.36,0.44	0.11 ± 0.12
Refrigeration end	3	0.47,0.48,0.56	0.10 ± 0.12
Opposite refrigeration end	1	0.22,0.24,0.41	0.15 ± 0.10
Opposite refrigeration end	2	0.39,0.42,0.60	0.46 ± 0.31
Opposite refrigeration end	3	0.51,0.54,0.71	0.43 ± 0.37

Predictions agreed well with measured data opposite the refrigeration end of the hold, but under-predicted cooling near the refrigeration end of the hold. The under-prediction of cooling near the refrigeration end of the hold was due to air flow through the pallet stack itself, which was not accounted for in the model. The measured pressure difference across pallets at the front of the hold cycled between approximately 65 and 20 Pa. Whilst the results reported in Section 8.2.2.2 indicate that the quantity of air flowing through the pallet itself was not significant in terms of airflow prediction at these pressures, sufficient flows of air to increase cooling rates near the centre of the pallet may have occurred. Quantification of the small amounts of air flowing between cartons in a pallet stack and inclusion of these flows in the heat transfer model should improve prediction.

Differences in the rate of cooling between channels 0.04 m wide and 0.02 m wide were small. As the channels' size decreased, the impact on the rate of cooling increased dramatically. Channel sizes of 0.005 m gave significantly reduced rates of cooling, which were substantially slower than those measured. As discussed earlier, such small gaps were unlikely to occur in practice.

Overall, prediction of cooling throughout the hold compared reasonably well to the measured data when realistic gap sizes were used. Refinement of the heat transfer model to include the variable delivery temperatures and velocities, and inclusion of the flows through the pallet stack would probably improve prediction accuracy.

11.5 Scenario testing

The following sections present the results of predictions with altered system characteristics. Firstly, the ceiling properties and more specifically the K_{add} values used to describe the effect of the contractions/expansions were investigated. Secondly, the influence of the circulation rate on cooling rates at both ends of the hold was investigated.

11.5.1 Ceiling properties

The properties of the ceiling headspace were not well defined, due to the variable clearance throughout the hold. The ceiling headspace was earlier assigned a K_{add} value of 0.3 due to these expansions and contractions. Flow entering the headspace channel from the vertical channels may also increase resistance. The exact physical configuration of the ceiling headspace was unknown, so the sensitivity of the simulated flows to the K_{add} value used was investigated. Simulations were performed with both an extreme K_{add} value of 0 (zero additional resistance), and an increased K_{add} value of 0.5.

11.5.1.1 Ceiling K_{add} = 0

Figure 11-39 shows the predicted change in velocities through the spar floor with ceiling K_{add} = 0. Differences between the predicted flows in the spar floor were minor despite the altered K_{add} value. Figure 11-40 shows the predicted velocities in the vertical channels around the pallets and Figure 11-41 shows the corresponding temperature rise predictions. The reduced resistance to flow in the ceiling headspace effectively flattened the predicted vertical velocity profile across the deck. Velocities in the vertical channels near the refrigeration plant decreased up to 30%, and velocities at the far end of the deck increased up to 50%. Vertical velocity differences were matched by similar (but opposite) differences in predicted air temperature rises.

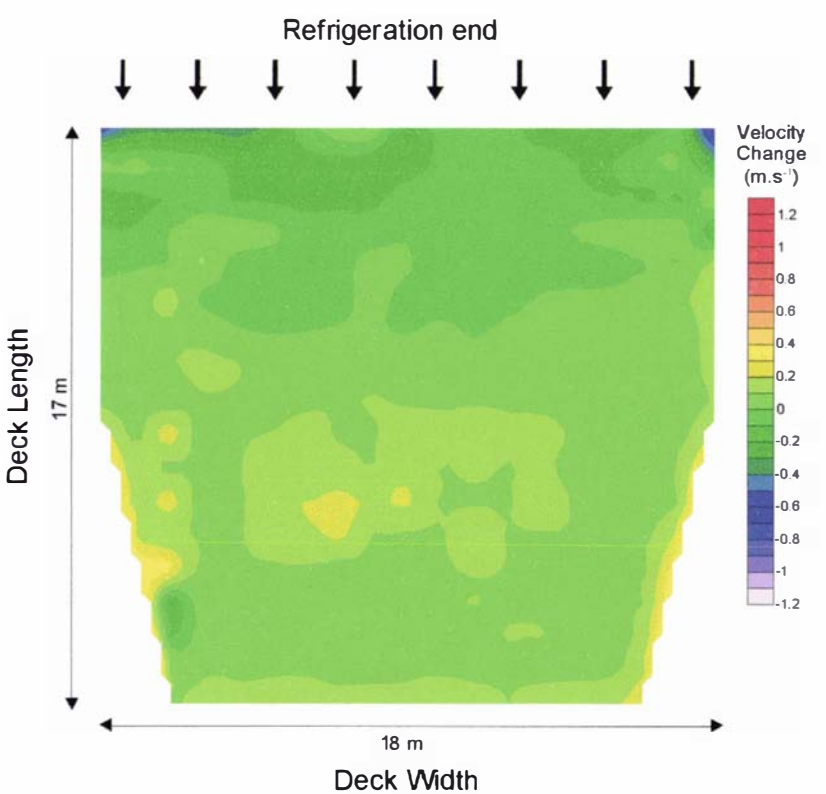

Figure 11-39 – Change in predicted vertical velocities through the spar floor throughout the refrigerated deck with a change in ceiling K_{add} from 0.25 to 0

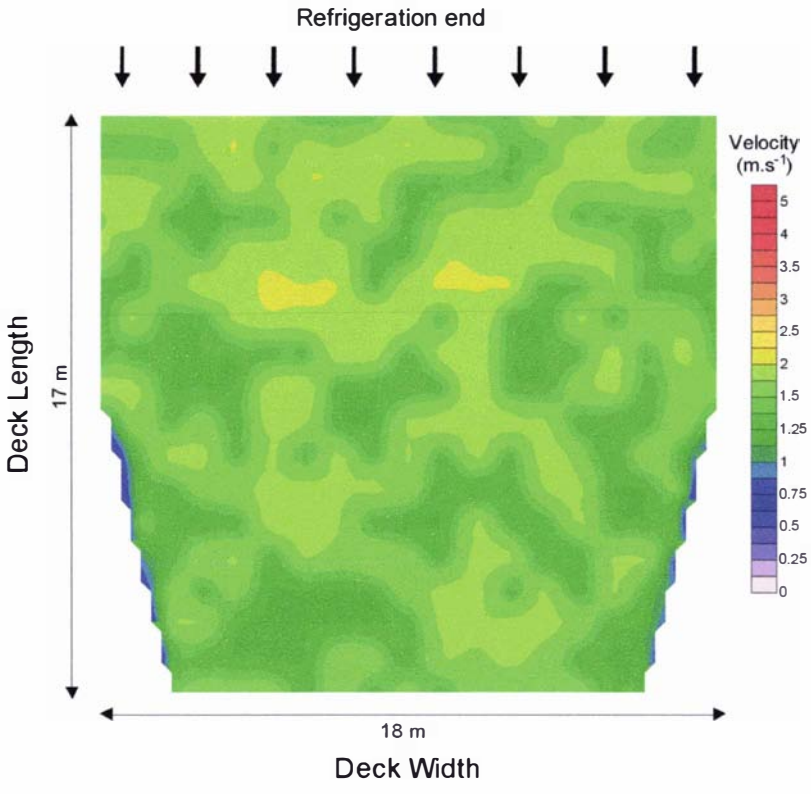

Figure 11-40 - Predicted velocity in the vertical channels formed by gaps around pallets throughout the refrigerated deck with ceiling $K_{add} = 0$

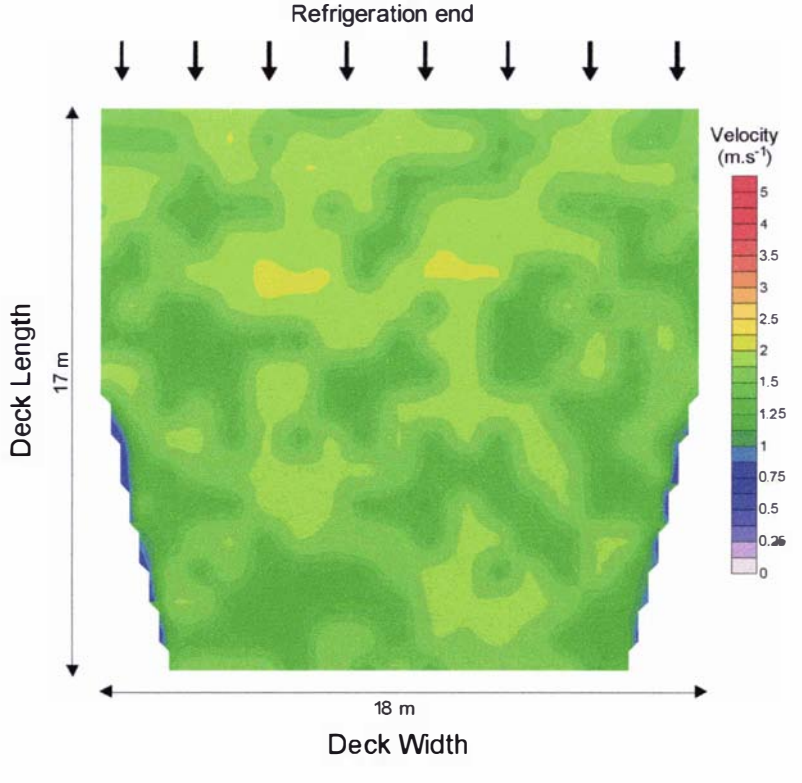

Figure 11-41 - Predicted air temperature rise in the vertical channels formed by gaps around pallets within the refrigerated deck with ceiling $K_{add} = 0$

11.5.1.2 Ceiling K_{add} = 0.5

Figure 11-42 shows the change in predicted velocities through the spar floor with ceiling K_{add} = 0.5. Again, the differences between the predicted flows in the spar floor were minor despite the altered K_{add} value. Figure 11-43 shows the predicted velocities in the vertical channels around the pallets and Figure 11-44 shows the corresponding temperature rise values. The trend of reducing predicted vertical velocity and increasing temperature rise along the length of the deck was slightly exaggerated with the increased K_{add} value. Velocities in the vertical channels near the refrigeration plant increased approximately 10%, and velocities at the far end of the deck were reduced by 12% to 20%.

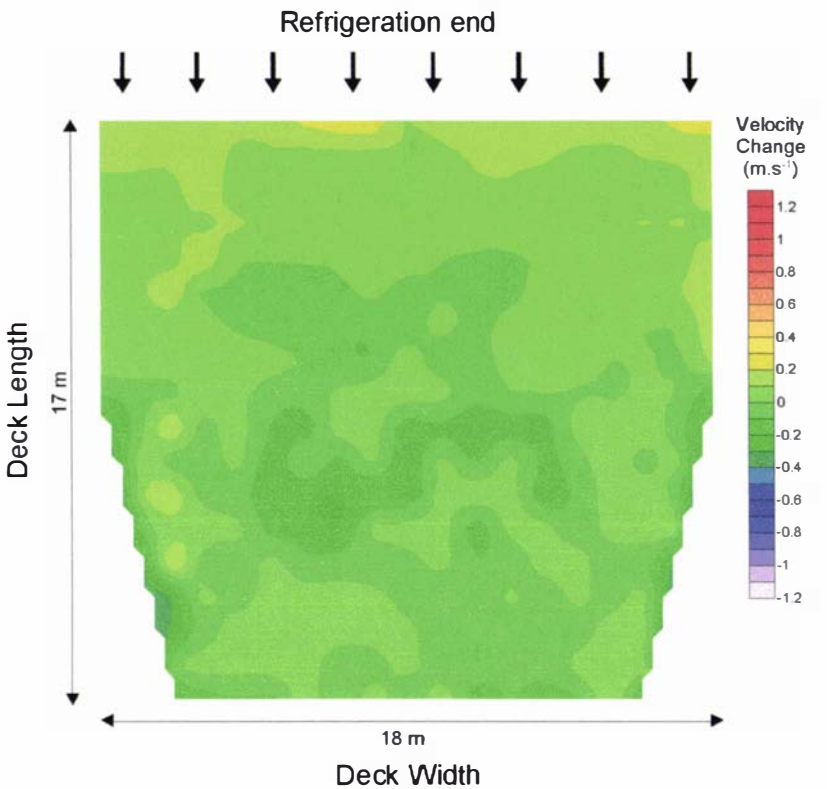

Figure 11-42 - Change in predicted vertical velocities through the spar floor throughout the refrigerated deck with a change in ceiling K_{add} from 0.25 to 0.5

The predictions of the vertical velocity and air temperature rise were sensitive to the K_{add} value assigned to the ceiling headspace, especially where the K_{add} value was reduced. This was considered to reflect both a difficulty in mathematically modelling the refrigerated hold and an opportunity to improve hold design. The sensitivity of the predictions illustrates the importance of sufficient headspace clearance within the hold. Reduction of the flow resistance along the headspace improved the air distribution substantially and could be achieved in practice by increasing the size or smoothness of the headspace.

Accurate estimation of the resistance in the ceiling due to expansions and contractions is likely to remain a problem due to the highly variable nature of the ceiling in refrigerated holds. It is important to note that the problem of accurately describing the ceiling headspace is not specific to resistance-network models, but simply a case of a geometry which is difficult to accurately measure and describe mathematically.

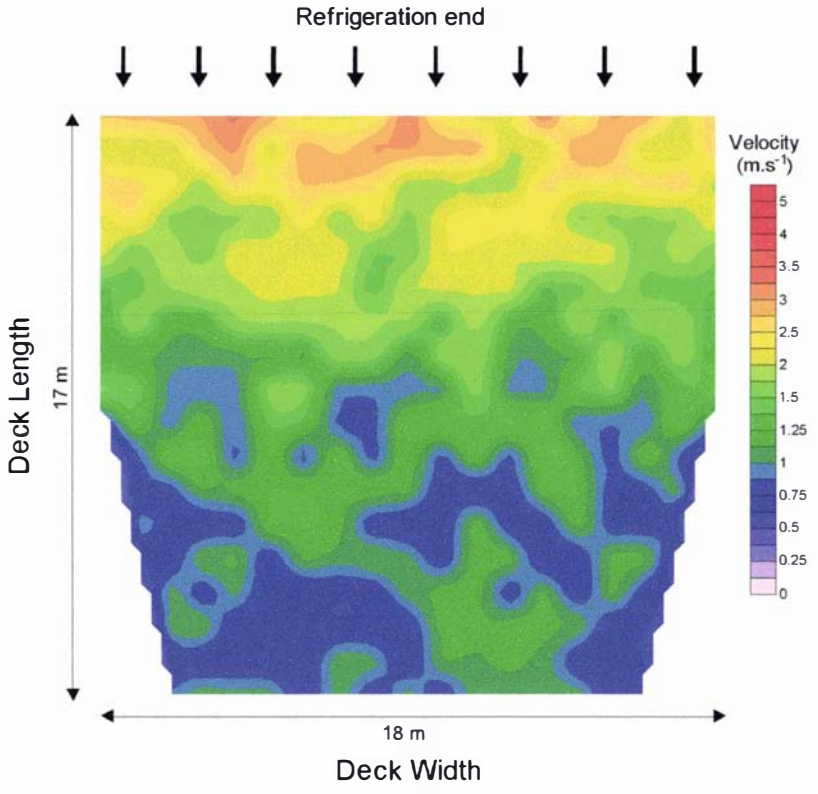

Figure 11-43 - Predicted velocity in the vertical channels formed by gaps around pallets throughout the refrigerated deck with ceiling $K_{add} = 0.5$

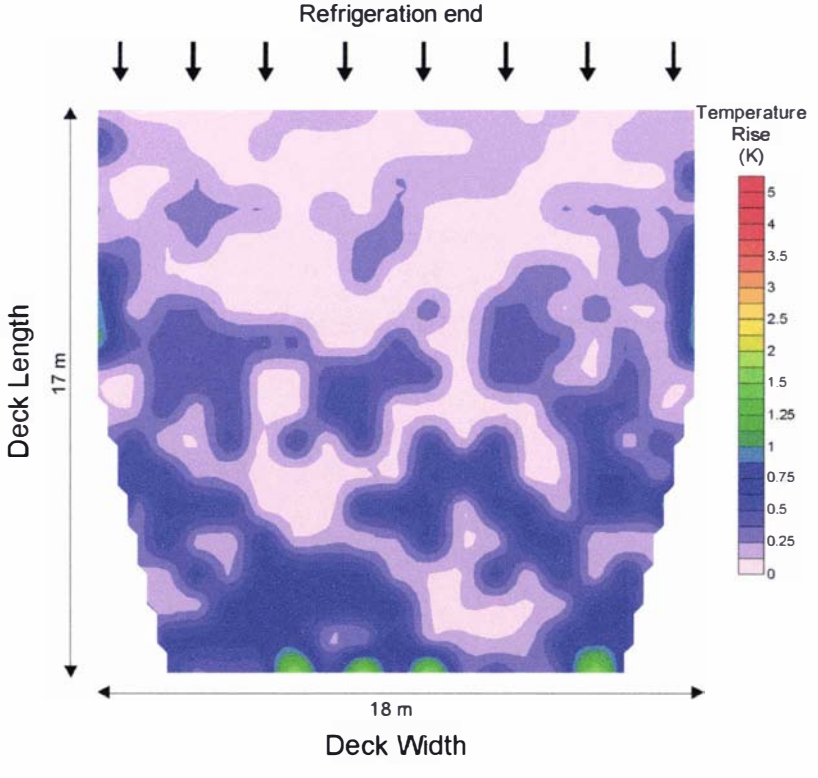

Figure 11-44 - Predicted air temperature rise in the vertical channels formed by gaps around pallets within the refrigerated deck with ceiling $K_{add} = 0.5$

11.5.2 Circulation rate

Industry guidelines for carriage of apples from NZ often stipulate that the air circulation in the hold may be reduced to 45 air changes per hour after carriage temperature is reached to reduce dehydration of the fruit. It is likely that air delivery/return temperature stability and/or a maximum temperature differential determine the time at which the carriage temperature has been deemed to have been reached. Figure 11-27 and Figure 11-28 show the delivery air and return temperatures throughout the monitored voyage, and inspection shows that in this case, it is likely that the carriage temperature would have been deemed to have been reached 2 to 3 days into the voyage. At this stage in this voyage, in-package temperatures remained elevated in the far end of the hold (Figure 16-2) and cooling of these pallets would have been compromised if there were a reduction in circulation rate.

To investigate the concept of reducing the circulation rate, simulations of airflow were performed with a reduced air circulation rate of 45 changes per hour and an increased rate of 100 changes per hour. The implications of the air circulation rate on cooling rates were predicted for pallets positioned near the refrigeration end and the far end of the hold.

Figure 11-45 shows the predicted ratio of velocities through the spar floor for a circulation rate of 100 changes per hour to the same velocities with a circulation rate of 80 changes per hour. Figure 11-46 shows a similar graph for a circulation rate of 45 changes per hour. The velocity pattern was not altered substantially by the change in air circulation rate; with almost all velocities increased or decreased by approximately the same proportion as the overall circulation rate. Positions of particularly low velocity (<0.2 $m.s^{-1}$) were affected more than other regions, showing up to a 50% greater increase or decrease in velocity than regions of greater velocities.

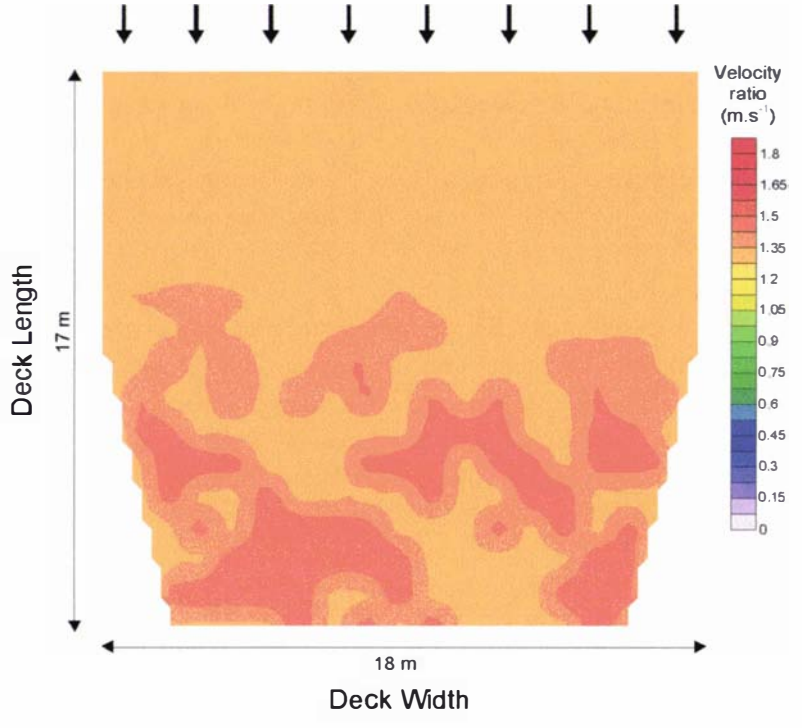

Figure 11-45 – Predicted ratio of vertical velocities for an air circulation rate of 100 changes per hour to 80 air changes per hour through the spar floor throughout the refrigerated deck

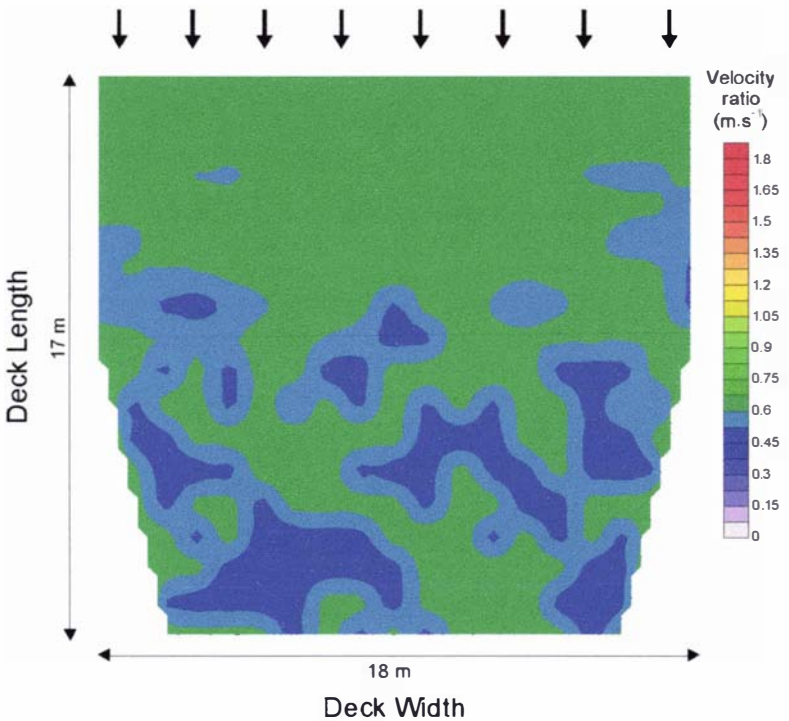

Figure 11-46 - Predicted ratio of vertical velocities for an air circulation rate of 45 changes per hour to 80 air changes per hour through the spar floor throughout the refrigerated deck

Figure 11-47 and Figure 11-48 show the predicted velocities in the vertical channels around the pallets. Figure 11-49 shows a plot of the relationship between the volumetric flow and fraction change in these values from the velocities predicted with an air circulation rate of 80 changes per hour. Figure 11-49 bears a striking resemblance to the friction factor plot Figure 7-18, and provides the explanation for the increased sensitivity of areas with low flow to a change in air circulation rate. Narrow channels with low flows in the laminar regime respond to changes in pressure with proportional changes in velocity, whereas larger channels with turbulent flows respond to pressure changes approximately by a square root law. The change in pressure driving force associated with a change in the circulation rate causes a proportional change in the flows in narrow channels but less than proportional change in the flow in larger channels.

Figure 11-50 and Figure 11-51 show the predicted temperature rises associated with the vertical channel velocities. The increased circulation rate reduces the temperature rise throughout the deck and effectively flattens the profile. The temperature rise values for the 45 changes per hour circulation rate remain low. It should be remembered that the air has already passed through a deck meaning a 1°C temperature rise may result in air being 2°C above the delivery air temperature, assuming there is little mixing of the air between the decks.

Figure 11-52 to Figure 11-57 show the predicted temperature profiles of pallets positioned near the refrigeration end and at the opposite end of the deck under the flow conditions predicted with air circulation rates of 45, 80 and 100 changes per hour. Positions within the pallet refer to those depicted in Figure 11-32.

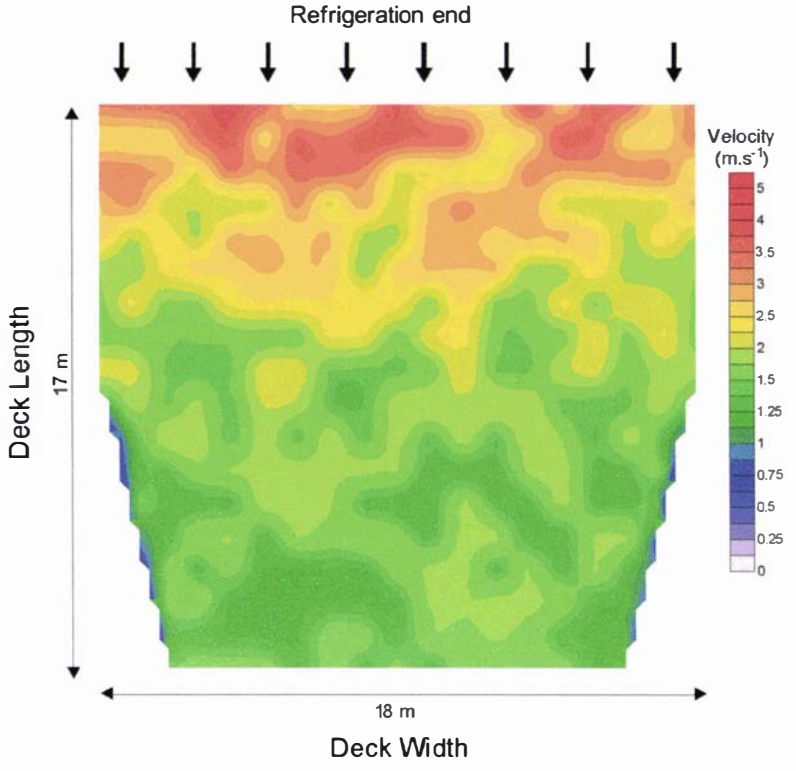

Figure 11-47 - Predicted velocity in the vertical channels formed by gaps around pallets throughout the refrigerated deck with an air circulation rate of 100 changes per hour

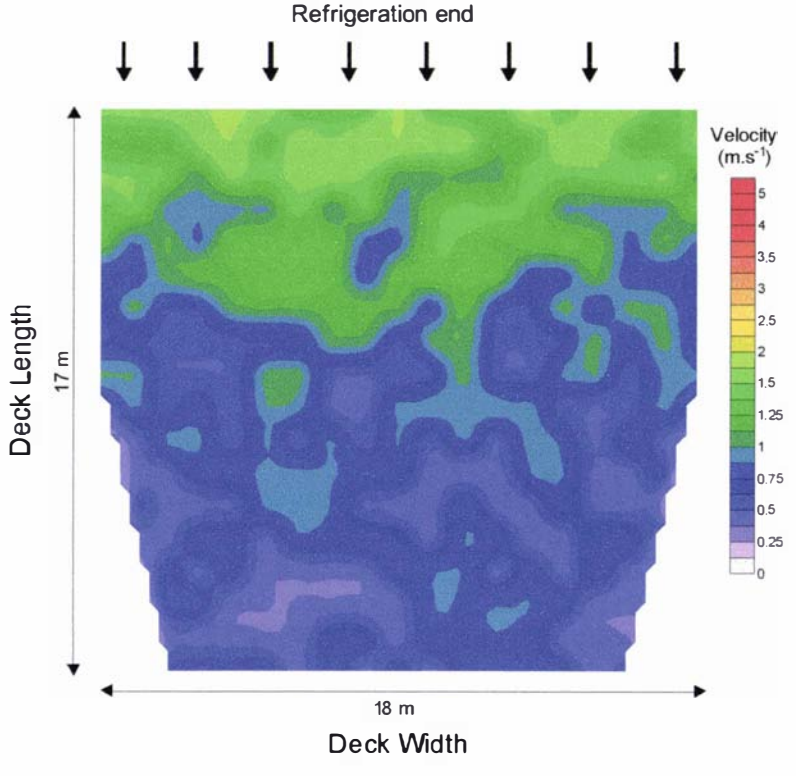

Figure 11-48 - Predicted velocity in the vertical channels formed by gaps around pallets throughout the refrigerated deck with an air circulation rate of 45 changes per hour

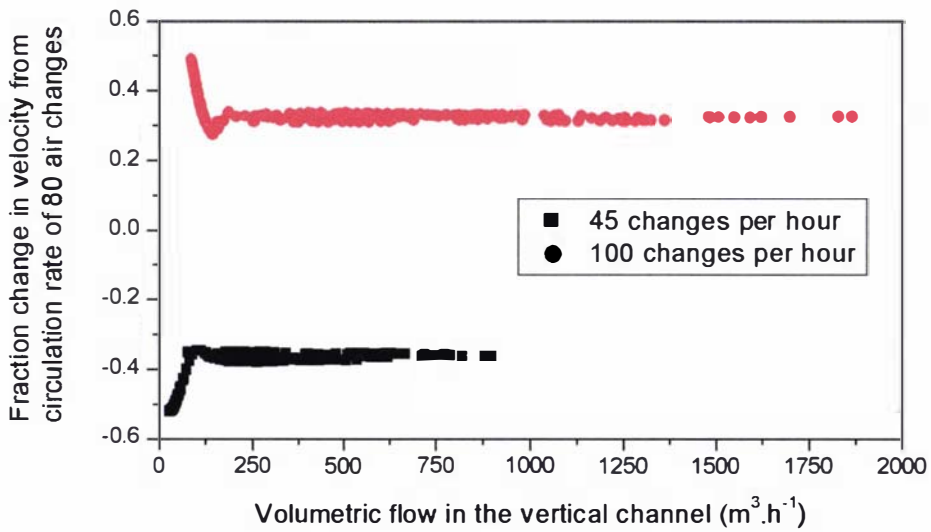

Figure 11-49 - Predicted fractional change in the velocity of each vertical channel formed by gaps around pallets from the value predicted for an air circulation rate of 80 changes per hour

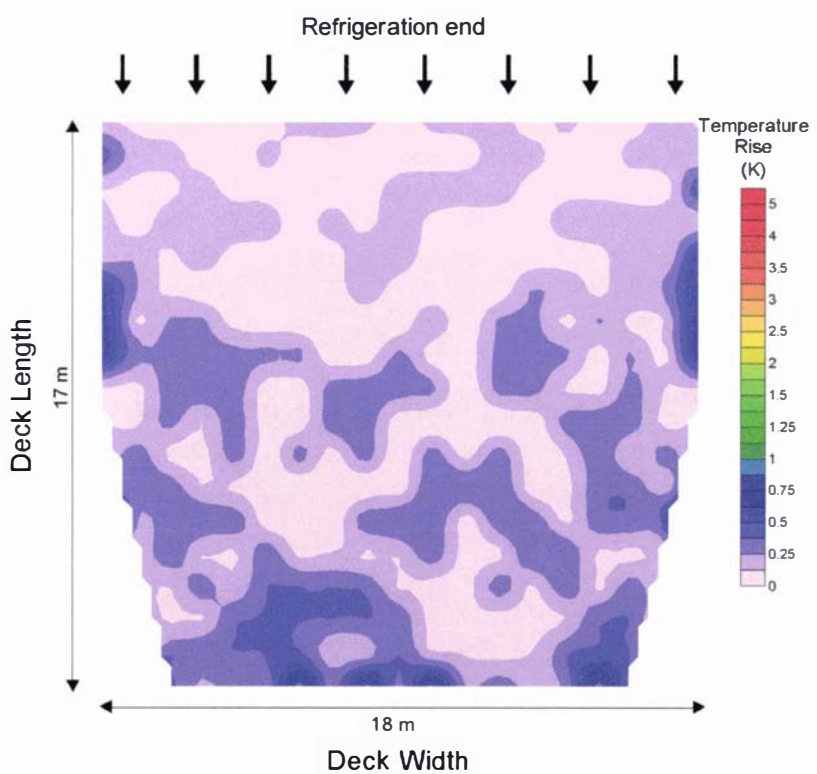

Figure 11-50 - Predicted temperature rise in the vertical channels formed by gaps around pallets within the refrigerated deck with an air circulation rate of 100 changes per hour

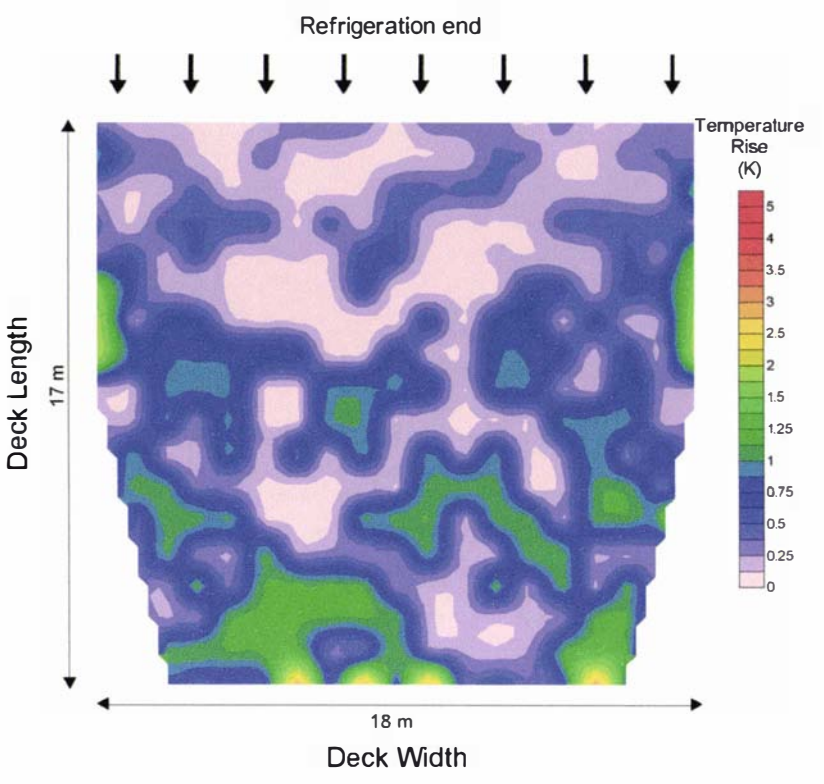

Figure 11-51 - Predicted temperature rise in the vertical channels formed by gaps around pallets within the refrigerated deck with an air circulation rate of 45 changes per hour

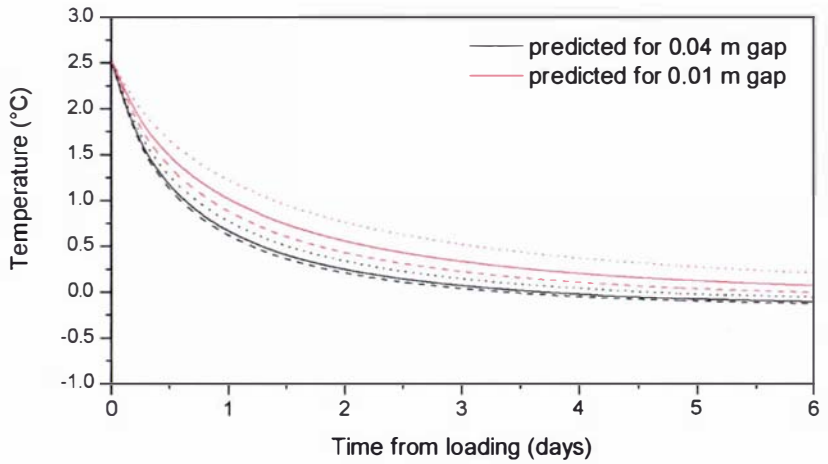

Figure 11-52 - Temperatures in position 1 as depicted in Figure 11-32 predicted for two gap sizes around pallets positioned at the end of the hold adjacent to the refrigeration end with an air circulation rate of 100 (dashed lines), 80 (solid lines) and 45 (dotted lines) changes per hour

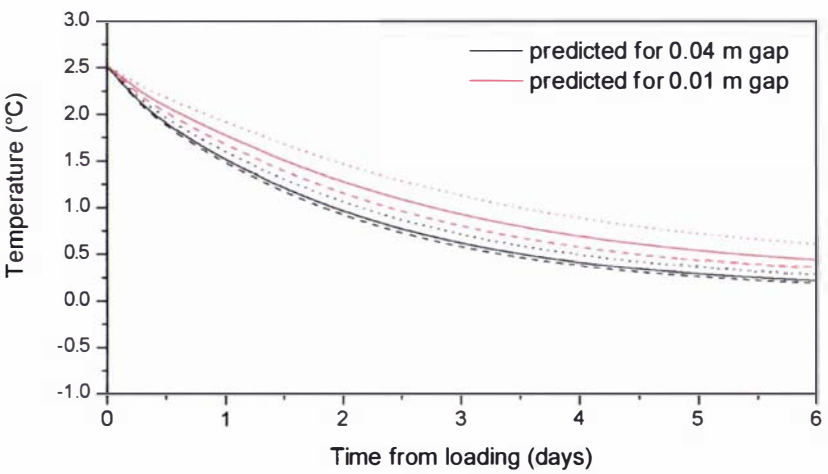

Figure 11-53 - Temperatures in position 2 as depicted in Figure 11-32 predicted for two gap sizes around pallets positioned at the end of the hold adjacent to the refrigeration end with an air circulation rate of 100 (dashed lines), 80 (solid lines) and 45 (dotted lines) changes per hour

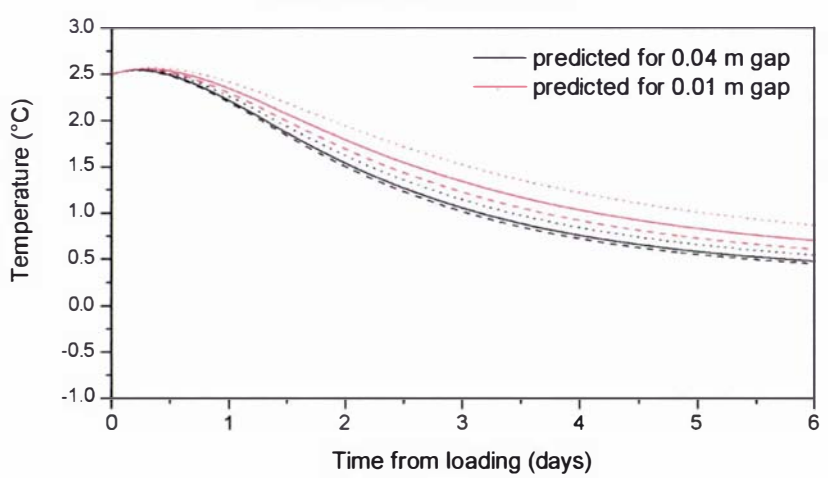

Figure 11-54 - Temperatures in position 3 predicted as depicted in Figure 11-32 for two gap sizes around pallets positioned at the end of the hold adjacent to the refrigeration end with an air circulation rate of 100 (dashed lines), 80 (solid lines) and 45 (dotted lines) changes per hour

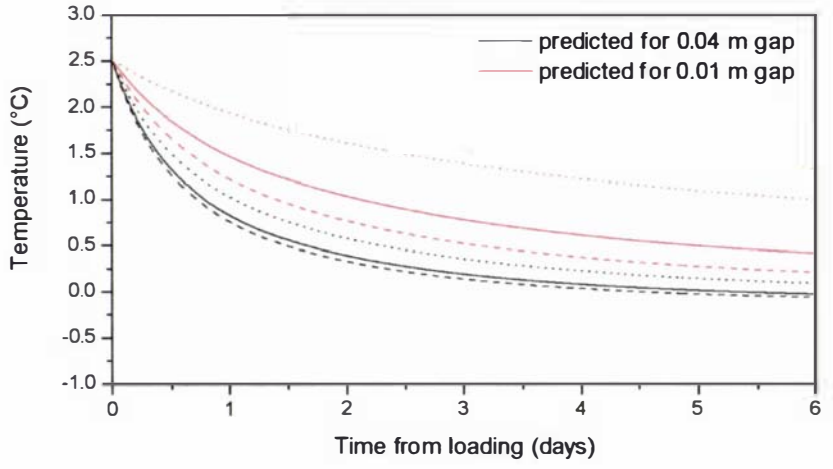

Figure 11-55 - Temperatures in position 1 as depicted in Figure 11-32 predicted for two gap sizes around pallets positioned at the end of the hold opposite the refrigeration end with an air circulation rate of 100 (dashed lines), 80 (solid lines) and 45 (dotted lines) changes per hour

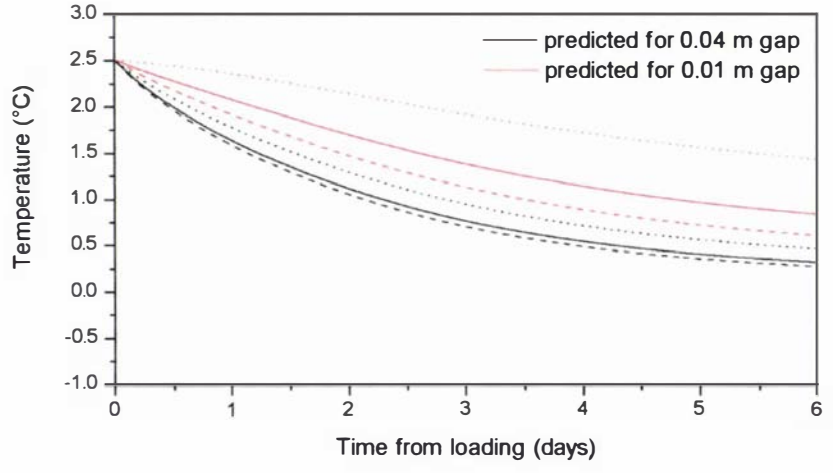

Figure 11-56 - Temperatures in position 2 as depicted in Figure 11-32 predicted for two gap sizes around pallets positioned at the end of the hold opposite the refrigeration end with an air circulation rate of 100 (dashed lines), 80 (solid lines) and 45 (dotted lines) changes per hour

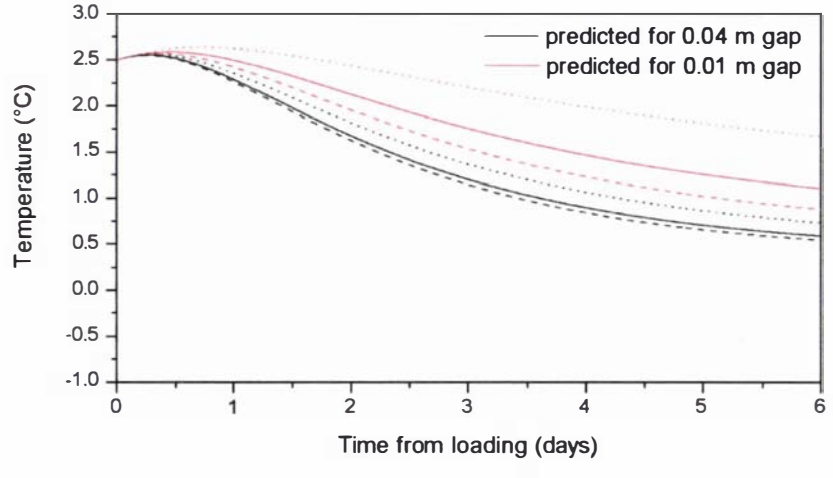

Figure 11-57 - Temperatures in position 3 as depicted in Figure 11-32 predicted for two gap sizes around pallets positioned at the end of the hold opposite the refrigeration end with an air circulation rate of 100 (dashed lines), 80 (solid lines) and 45 (dotted lines) changes per hour

An increased circulation rate provided improved cooling rates in all positions. The magnitude of the increase in cooling of pallets surrounded by larger gaps was very small at both ends of the hold. The cooling rate of a pallet surrounded by smaller gaps was more sensitive to the circulation rate. Pallets at the rear of the hold (opposite the refrigeration end) were also more sensitive to a reduced circulation rate. A pallet surrounded by small channels in the rear of the hold was predicted to be approximately 0.6°C warmer throughout the pallet with a circulation rate of 45 changes compared to a circulation rate of 80 changes per hour.

Variable sized channels within the hold provide variable cooling rates within the hold, and as the slowest cooling positions were those most affected by the change in circulation rate, the circulation rate is an important factor in reducing the spatial variability within the hold. Increases in the circulation rate behave according to the law of diminishing returns; each further increase in circulation rate provides less benefit in terms of reduced temperature variability, at the expense of increased installation and energy costs.

Reducing the air circulation rate in the hold once temperature control has been achieved may cause greater product mass loss than maintaining 100% flow. Reduced circulation rates were shown to reduce cooling rates, especially in the slowest cooling positions. As shown by the measured in-package temperatures in Figure 11-36, the refrigeration system was required to pull down in-package temperatures throughout the voyage due to temperature rises associated with evaporator defrost. Reduction of the circulation rate would have led to elevated in-package temperatures for longer periods and subsequent increased mass loss was likely. Direct comparison of the rates of mass loss under reduced circulation rates with standard circulation rates in different positions within the hold is difficult, and beyond the scope of this work. However, given the relative importance of in-package temperature and air velocity external to the package in determining the rate of mass loss, it is probable that increased rates of mass loss in the slowest cooling positions would outweigh the reduction of the rate of mass loss in the fastest cooling positions due to the reduction in air velocity. It is also possible that the increased steady-state temperature variability caused by a reduction in circulation rate may cause increased rates of mass loss which outweigh the reduction in mass loss due to reduced air velocities. Where air circulation rate reduction is to be implemented, it is important to ensure that the slowest cooling product (opposite the refrigeration end) has fully reached the carriage temperature.

11.6 Conclusions

As was the case in the 40' container, comparison of measured and predicted air velocities in a upper (spar) deck of a hold during a shipment of kiwifruit showed reasonable agreement if the measured variation across the width was averaged. Delivery and return air velocity measurements were problematic, with unrealistically low velocities recorded, probably due to improperly positioned sensors. Comparison of measured and predicted in-package temperatures showed good agreement for pallets positioned opposite the refrigeration end; however, cooling of positions near the centre of pallets adjacent to the refrigeration end was under-predicted. This discrepancy was attributed to diffusive flows of air through the pallets adjacent to the refrigeration end not included in the model, caused by the sizeable pressure differences at that end of the hold.

The importance of reducing the flow resistance of the ceiling headspace was highlighted by the sensitivity of the predicted airflows to this factor. Accurate estimation of this flow resistance was difficult because of the variable geometry of the ceiling in the refrigerated hold. This problem is not specific to resistance network models, as the physical complexity of the ceiling within a hold is not easily described regardless of the framework employed.

An increased circulation rate was predicted to increase cooling rates and decrease temperature variability within the hold. However, the benefit diminished with each subsequent increase in circulation rate. Mass transfer simulations to predict the rate of water loss were not considered within the scope of this work, but from basic principles it is thought that reduced circulation rates (and therefore reduced air velocities) will reduce mass loss in some regions of the hold (due to reduced mass transfer coefficients, rates of air interchange and heat input through the fans), but will increase mass loss in other regions (due to slower cooling of cargo and increased steady-state temperatures). Given the relative significance of fruit temperature and air velocity external to the package in determining the rate of water loss, it is likely that the detrimental temperature effects would outweigh the benefits of reduced velocities for most cargos.

12 Refrigerated Vessel - Single Deck

12.1 Introduction

Air temperatures and velocities within a single deck of a refrigerated vessel were monitored during a shipment of apples from New Zealand to Europe. As the monitoring did not coincide with a commercial program, measurement of product temperatures was not possible. Airflow simulations of the refrigerated hold were conducted and comparison made with measured velocities. Heat transfer simulations were also conducted to aid the interpretation of the airflow information and also to assess the performance of a single layer hold without floor gratings.

12.2 System description

Air temperatures and velocities within a single deck of a refrigerated vessel were monitored during a shipment of apples from New Zealand to Europe. The vessel was configured such that each deck was serviced by a single refrigeration plant and fan system. The refrigerated air was delivered into under-floor channels, flowed through the perforated floor (Figure 12-1) and cargo, and then returned to the refrigeration plant through the return air grill near the ceiling (Figure 12-2).

The deck was of a square shape, approximately 19.7 m wide and 21.45 m long. There was a door positioned on one side of the hold as shown in Figure 12-1 and Figure 12-3. Air delivery and return velocities and temperatures were measured using thermocouples and thermistor anemometers spaced across the width of the deck. Thirty-two type-T thermocouples and 14 thermistor anemometers were placed in the floor gratings, adjacent to the refrigeration end of the deck. Thirty-two type-T thermocouples and 14 thermistor anemometers were also placed across the air return grill. Air temperatures and velocities throughout the deck were also measured using thermocouples and thermistor anemometers. Sixty-four thermocouples and 60 thermistors were positioned in both the floor and ceiling headspace. Figure 12-3 shows the approximate positions of the sensors. Temperatures and voltages were measured using 16 or 32-channel Eltek Squirrel data-loggers (1000 series, Eltek Ltd. Cambridge, England). Temperatures and velocities were recorded at 12-minute intervals throughout the duration of the shipment. No in-package temperature measurements were made and no information on the free area or loading pattern was collected.

Unfortunately, the ridges on the metal perforated floor (Figure 12-1) caused damage to many of the thermocouple and thermistor sensors. Coupled with this, a data-logger failure meant no useful velocity data was successfully collected in the rear half of the hold (opposite the refrigeration end).

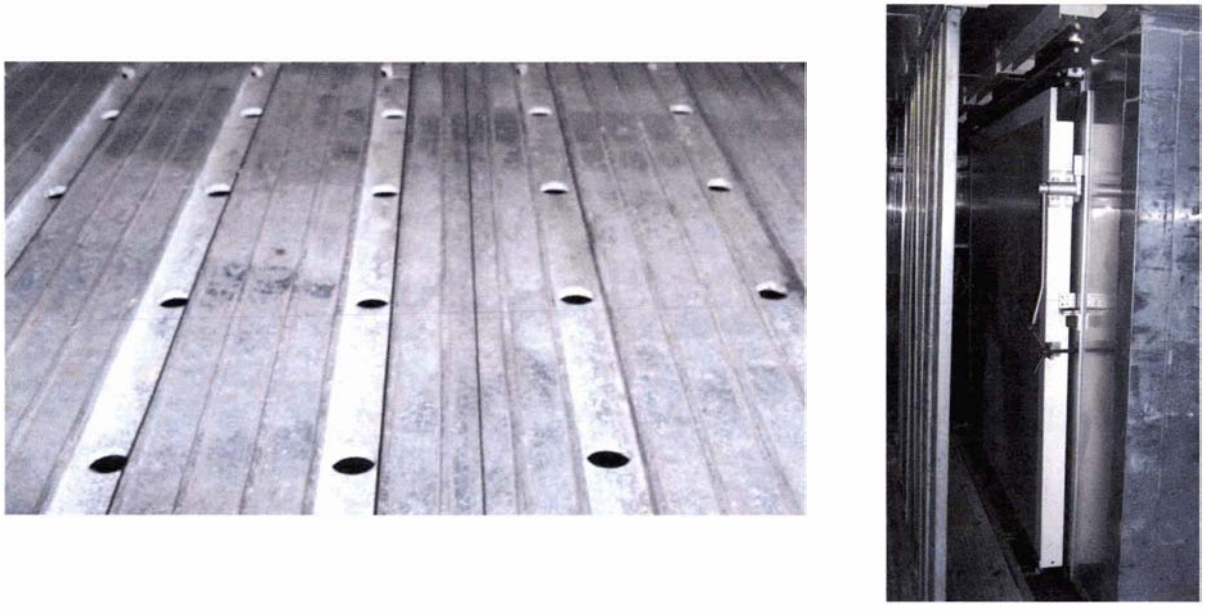

Figure 12-1 - Photographs depicting the perforated floor construction and the door in the side of the hold for the deck monitored during shipment of apples from New Zealand to Europe

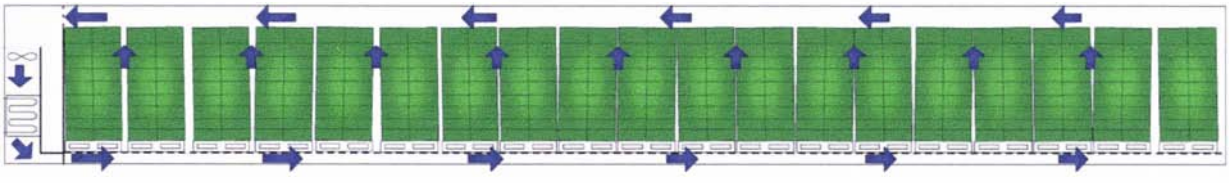

Figure 12-2 - Elevation view of the vessel deck configuration showing simplified airflow pathways

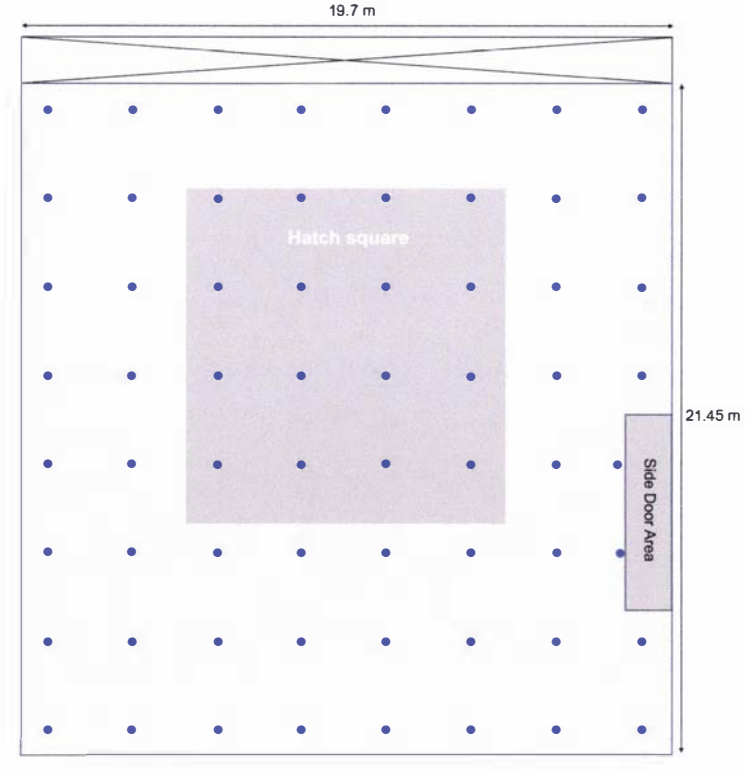

Figure 12-3 - Plan view of the deck monitored during shipment of apples from New Zealand to Europe showing approximate dimensions and position of thermistor anemometers and thermocouples in the floor and ceiling (•)

12.3 Flow channel definition

Flow channels in this vessel were defined in much the same way as for the vessel described in Section 11.3. Specific channels were not modelled. Rather, a random distribution of gap sizes was considered adequate to provide a sufficiently accurate description of the actual system.

Each of the vertical flow channels within the deck was classified into one of two categories: from the under-floor ducts to the pallet base level or from the pallet base level to the headspace above the pallets through a gap between pallets or between a pallet and the wall. Flow rates through the pallets themselves were assumed to be negligible.

As for the vessel in Section 11.3, nodes were positioned across the floor area of the deck in a regular 1 m × 1 m grid as shown in Figure 12-4. Each square of the grid represented a pallet, and the difference between actual and modelled pallet size was not expected to significantly influence predictions. There were 3 levels of nodes in the vertical direction corresponding with the level of the lower gratings, in the pallet bases and in the headspace above the pallets (Figure 12-5). Nodes adjacent to the air delivery duct were connected to 21 fixed pressure nodes (inlets) and nodes adjacent to the return air grill connected to 21 fixed pressure nodes (outlets). Multiple inlet and outlet nodes were used to allow simulation of a non-uniform pressure profile across the width of the refrigeration plant. Figure 12-6 shows a 3-dimensional illustration of the flow network.

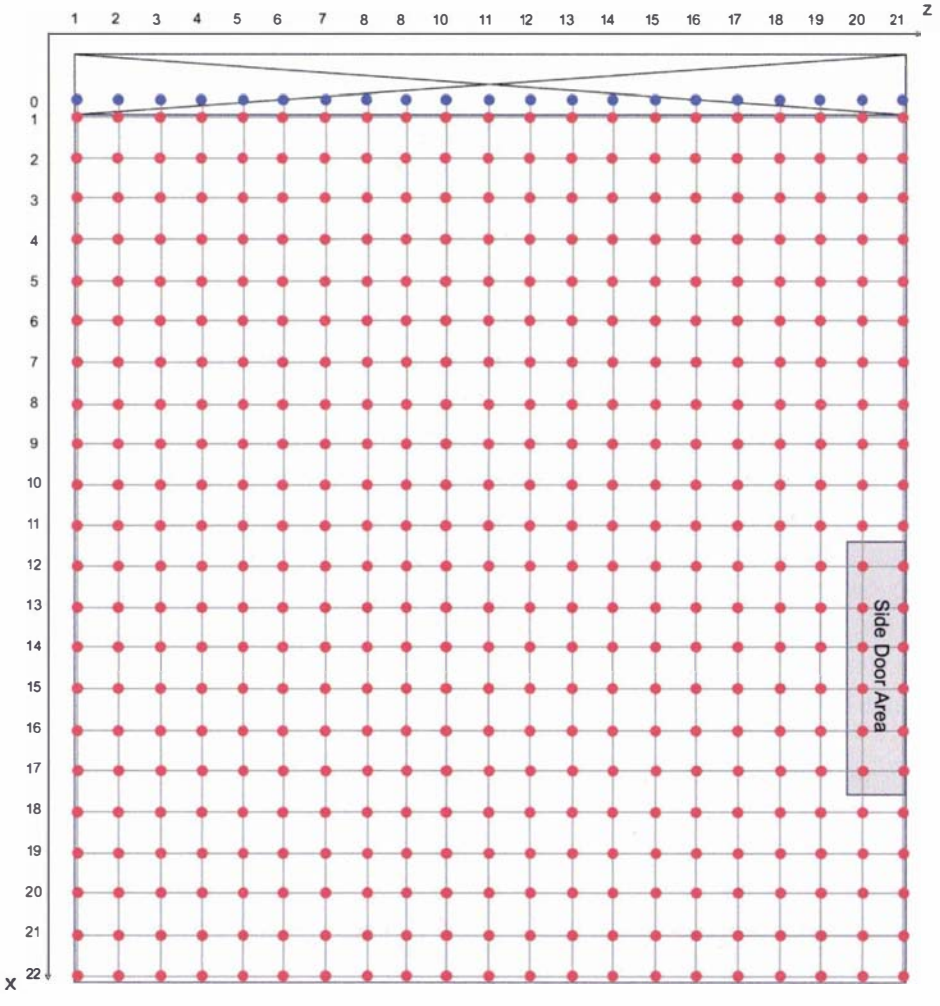

Figure 12-4 - Plan view of the model refrigerated hold showing the defined flow resistance network. Blue circles represent fixed pressure nodes, red circles represent unknown pressure nodes, and grey cylinders represent flow channels

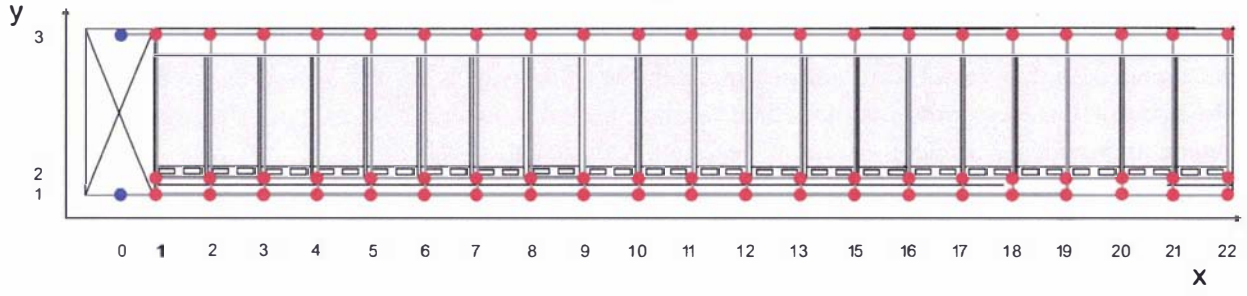

Figure 12-5 - Elevation view of the modelled refrigerated hold showing the defined flow resistance network. Blue circles represent fixed pressure nodes, red circles represent unknown pressure nodes, and grey cylinders represent flow channels

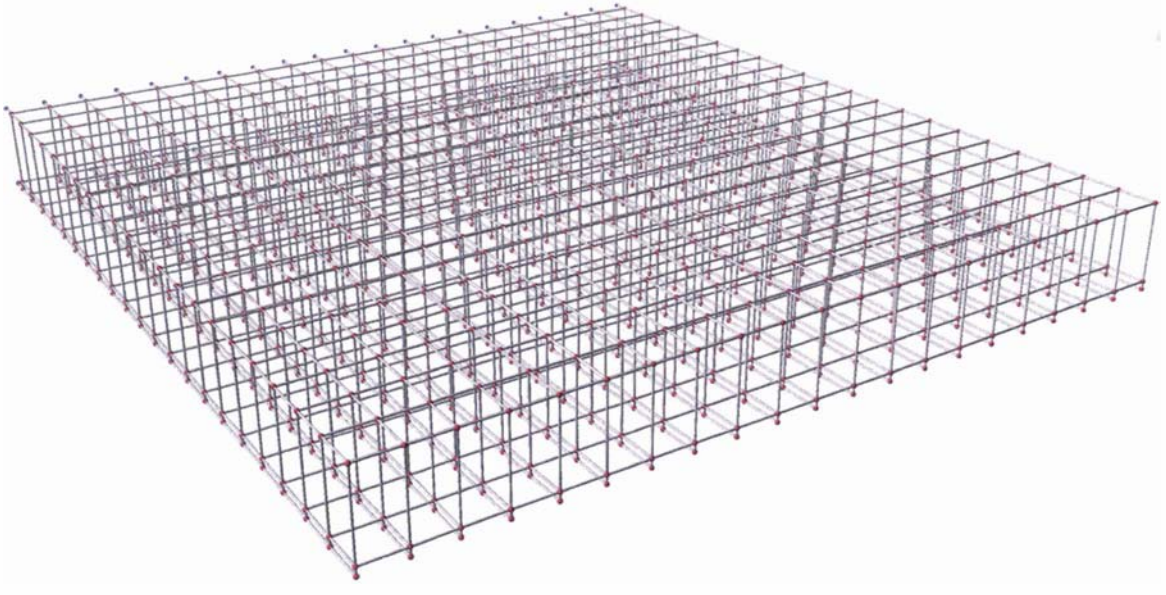

Figure 12-6 - Three-dimensional representation of the flow network approximation of the refrigerated hold. Blue circles represent fixed pressure nodes, red circles represent unknown pressure nodes, and grey cylinders represent flow channels

The channels connecting the under-floor gratings to the pallet base level on the lower deck were modelled using the perforated plate correlation presented in Section 8.3.4, with an open area of 1.8%. Channels between pallets were described as Type I channels, with an absolute roughness of 0.0003 m. The size of the gaps left between pallets and between walls/pallets were considered uniform throughout the deck, except for a large channel formed by the protective reinforcement around the door (Figure 12-1) and the hatch-square region, which were larger due to the difficulty of positioning the final pallets. The channel formed by the protective reinforcing around the door was measured to be approximately 0.4 m wide. The gap sizes in the hatch-square region were generated using a bounded random function with half the channels between pallets assigned a width of 0.01 m and the other half randomly varying between 0.05 m and 0.10 m. In the remainder of the hold, half the gaps were assigned a width of 0.01 m and the remaining gaps varied randomly between 0.02 and 0.04 m. Half of the gaps were assigned a size of 0.01 m to simulate those pallets which were placed flush against adjacent pallets. The minimum spacing of 0.01 m was estimated from the thickness of the corner-boards that effectively stop the pallets from being placed flush against adjacent pallets. The resulting free area ratio was 5.5%.

Horizontal flow channels at different heights within the hold were each classified into one of three categories: ducts below the perforated floor, through the pallet bases or in the ceiling headspace. Longitudinal flow paths in the under-floor gratings were described as Type I channels, with a height of 0.12 m. Grating supports running along the length of the deck were spaced every 0.25 m with a width of

0.01 m, so transverse flow channels in the under-floor gratings were assigned an arbitrarily high resistance (Equation 9-1). It was assumed there was insignificant horizontal flows in the gaps between pallets, so no such horizontal flow channels were defined.

Additional frictional losses to account for the effects of turning flow and the contractions and expansions experienced when fluid flows through the gaps between pallets were estimated using values from Perry & Green (1997). Fluid exiting the gaps at the top of the pallet experienced a sudden enlargement (K_{add} = 1) and fluid flow paths entering the vertical channels between pallets were likened to a contraction and a square bend (square 90° bend (1.3) and contraction (0.3) giving K_{add} = 1.6).

The flow resistance of horizontal flow channels in the pallet base layer were all described using the correlation presented in Section 8.3.4. Horizontal flow paths within the ceiling headspace were treated as Type I channels with a constant clearance of 0.3 m. In the actual system, the clearance was variable with both the decks structure and packaging of varying heights contributing to the variation. To account for contractions and expansions, additional frictional losses were included in the ceiling headspace channels (K_{add} = 0.3).

The network as described consisted of 42 fixed pressure nodes, 1386 unknown pressure nodes and 3169 flow channels. A uniform pressure profile was used across the 21 inlet fixed pressure nodes and outlet fixed pressure nodes were assigned zero pressures.

12.4 Simulation results

A circulation rate of approximately 80 air changes per hour was assumed, so the total pressure at the inlet was set at 35 Pa across the entire width of the deck. This pressure resulted in a predicted circulation rate of 77 air changes per hour (corresponding to 74200 $m^3.h^{-1}$). Simulation took approximately 90 minutes, with no convergence difficulties.

Figure 12-7 shows the predicted horizontal velocities in the under-floor gratings throughout the deck. The velocity diminishes rapidly with distance from the refrigeration end, as air exits the channels. Figure 12-8 shows the measured velocities in the under-floor gratings for the half of the deck nearest the refrigeration end, interpolated from 14 successful measurement points. As mentioned earlier, a data-logger failure meant no velocity data was collected in the half of the deck opposite the refrigeration end (depicted in Figure 12-8 as a minimum velocity). The variability in measured velocities may have been due to sensor positioning within the under-floor channels, where sensors positioned in recirculating zones or in the boundary layers near channel walls may have caused the measurements to be lower than what actually occurred. Sensor movement during cargo loading would have exacerbated this problem. Figure 12-11a shows the average measured and predicted velocities in the floor channels as a function of distance from the refrigeration end. Comparison of the predicted and measured values showed substantial disagreement, with measured velocities lower than those predicted.

Figure 12-9 and Figure 12-10 show similar velocity data for the ceiling headspace, with Figure 12-10 interpolated from 28 velocity measurement points. Headspace velocities were predicted to decrease with increasing distance from the refrigeration end of the deck, with a uniform profile across the width of the deck. Figure 12-11b shows the average measured and predicted velocities in the ceiling as a function of distance from the refrigeration end. Measured values showed the expected trend along the length of the deck, along with considerable variation across the width of the deck. Measured variability across the width was likely to be due to sensor positioning in the headspace, where the variable clearance between the pallets and ceiling of the hold may have affected the measurements. Comparison of these predicted and measured velocities again showed predicted velocities were higher than those measured, although the difference was not as large as that seen in the floor.

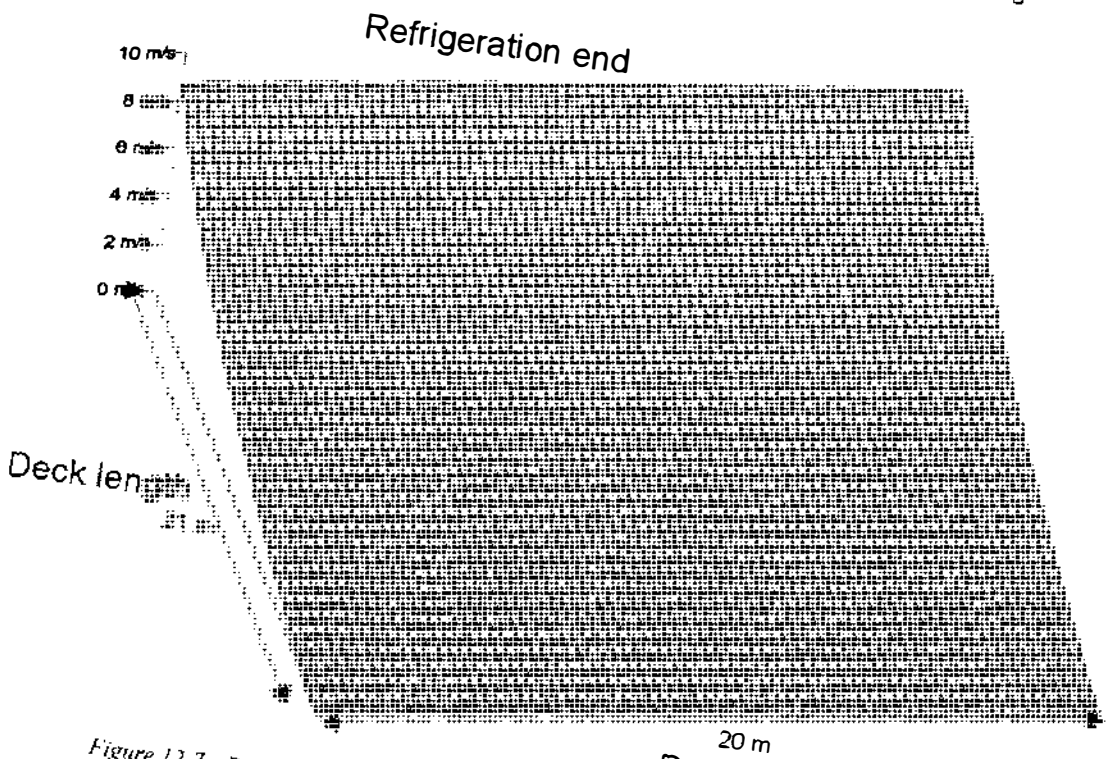

Figure 12-7 - Predicted horizontal velocities in the under-floor gratings throughout the refrigerated deck

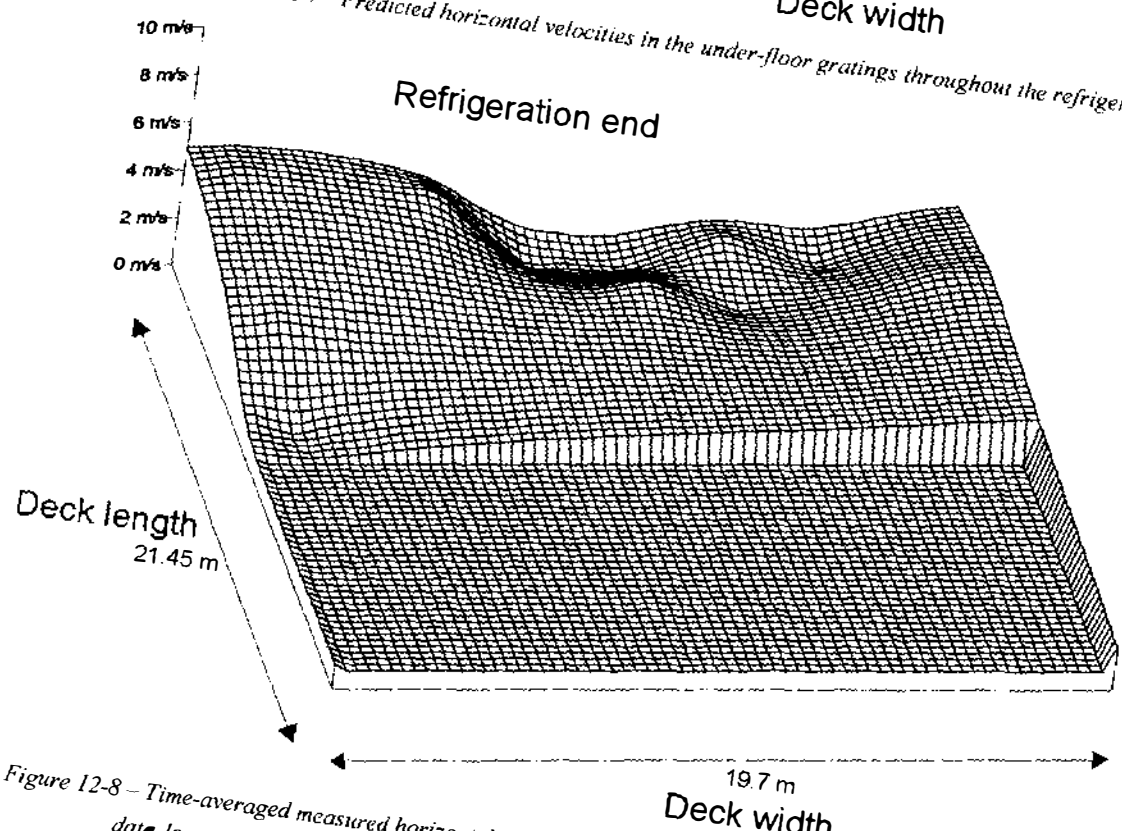

Figure 12-8 – Time-averaged measured horizontal velocities through the floor gratings throughout the refrigerated deck. A data-logger failure meant no data was collected in the half of the deck furthest from the refrigeration

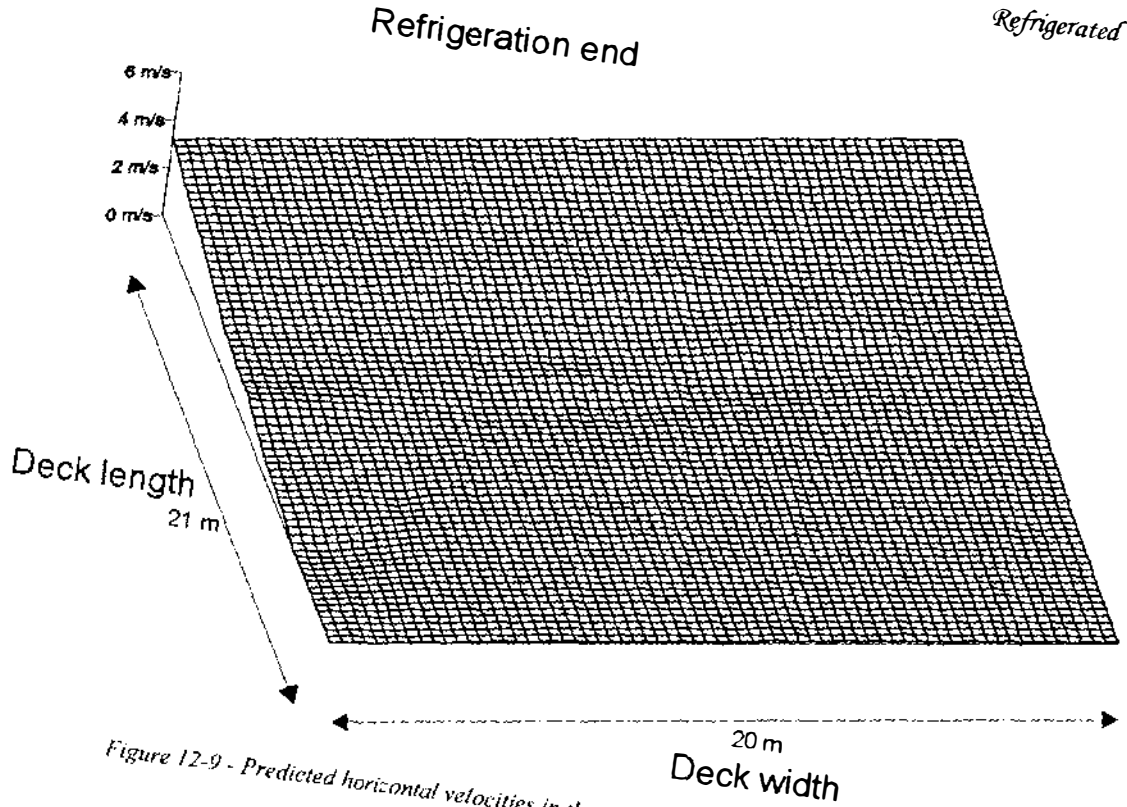

Figure 12-9 - Predicted horizontal velocities in the ceiling headspace throughout the refrigerated deck

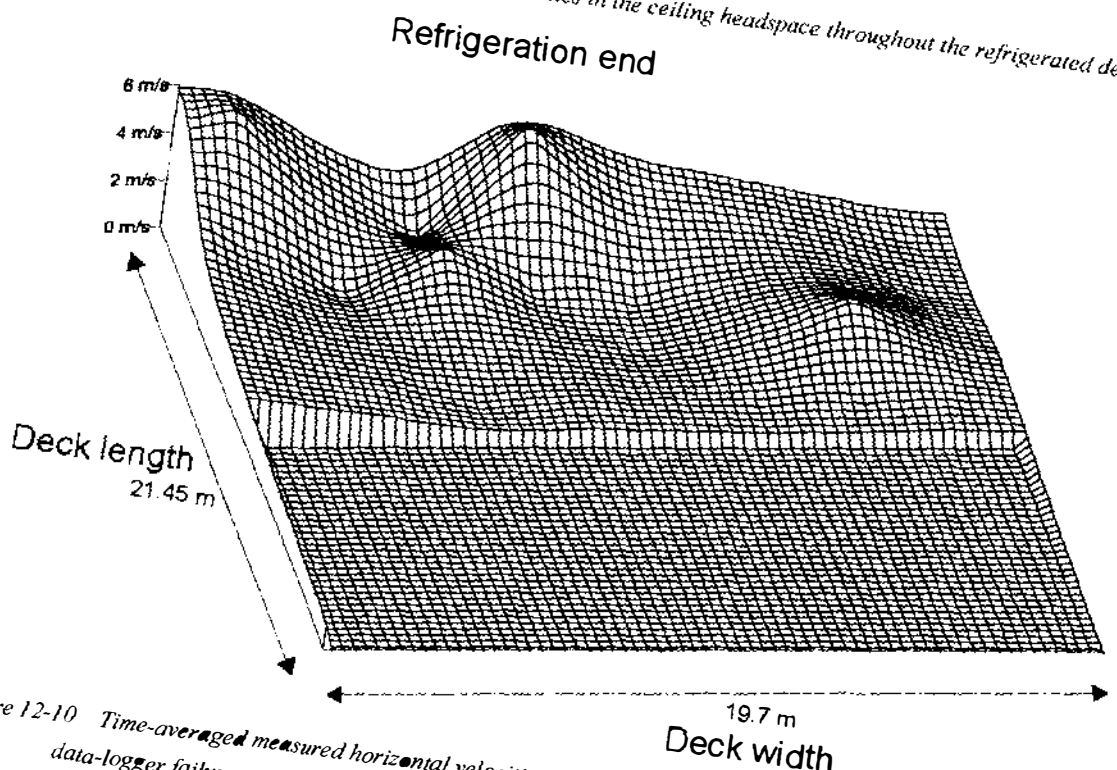

Figure 12-10 Time-averaged measured horizontal velocities in the ceiling headspace throughout the refrigerated deck. A data-logger failure meant no data was collected in the half of the deck furthest from the refrigeration

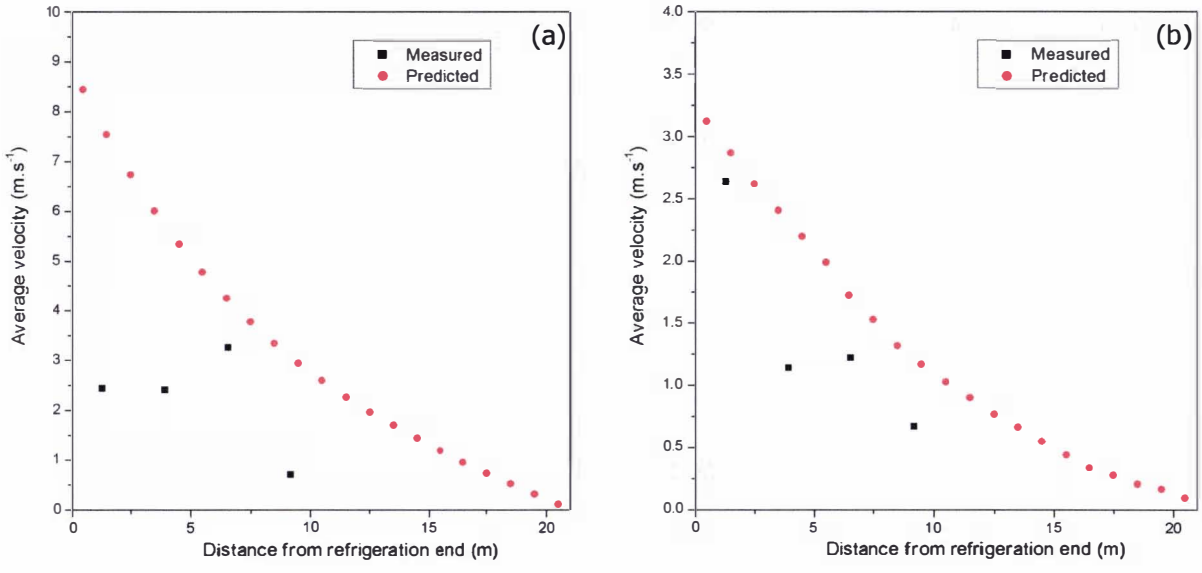

Figure 12-11 – Measured and predicted horizontal velocities in the (a) floor and (b) ceiling headspace averaged across the width of the refrigerated deck

Figure 12-12 shows the predicted vertical velocities in the gaps between pallets throughout the deck. Figure 12-13 shows the corresponding predicted fluid temperature rise using the calculations described in Section 9.3.2. A value of 0.3 $W.m^{-2}.K^{-1}$ was used as the 'k-value' of the hold's walls. The predicted fluid temperature rise was low throughout the majority of the hold, but some positions near the walls gave high results. Maximum values were 9°C against the wall and 1.5°C within the hold. There was a trend of decreasing velocity and increasing temperature rise with distance from the refrigeration end. The area around and behind the position of the door also gave elevated predicted temperature rises.

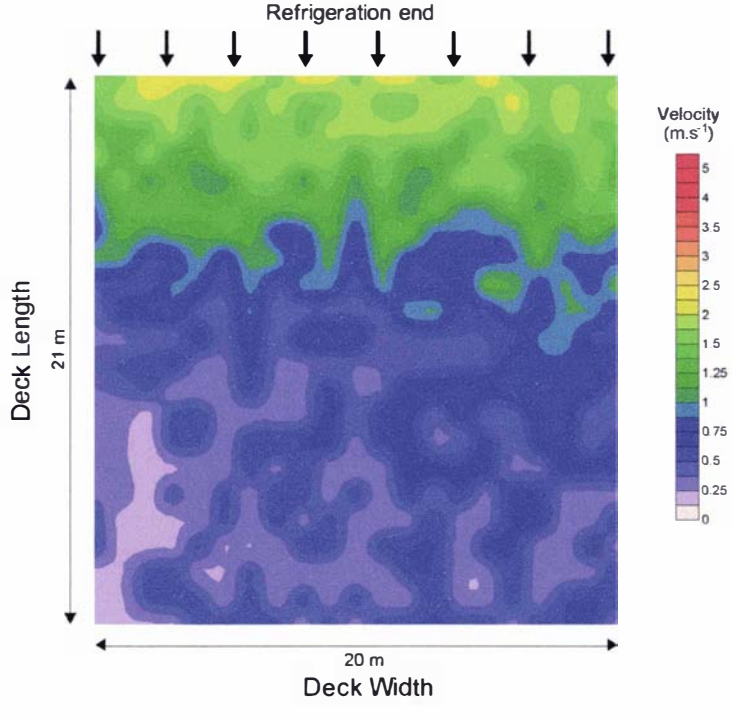

Figure 12-12 - Predicted velocity in the vertical channels formed by gaps around pallets throughout the refrigerated deck

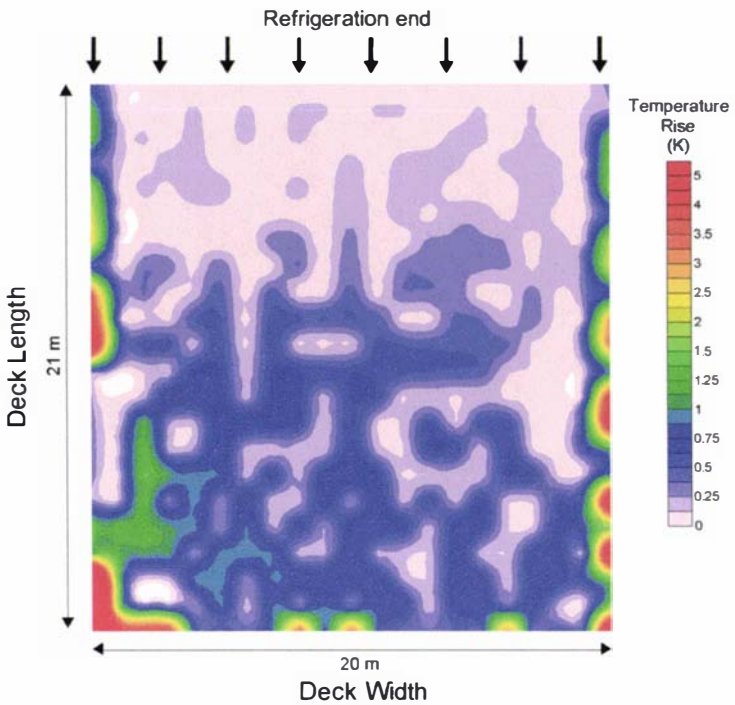

Figure 12-13 - Predicted temperature rise in the vertical channels formed by gaps around pallets throughout the refrigerated deck

Figure 12-14 and Figure 12-15 show the time-averaged measured delivery and return air velocities and temperatures respectively, across the width of the deck. Measured variation across the width of the deck was very high and was thought to be due to sensor positioning as discussed in Section 11.4. Predicted velocities in the air delivery channels and at air return are shown in Figure 12-16. Comparison of the predicted and measured velocities shows significant disagreement, primarily due to the variation across the width.

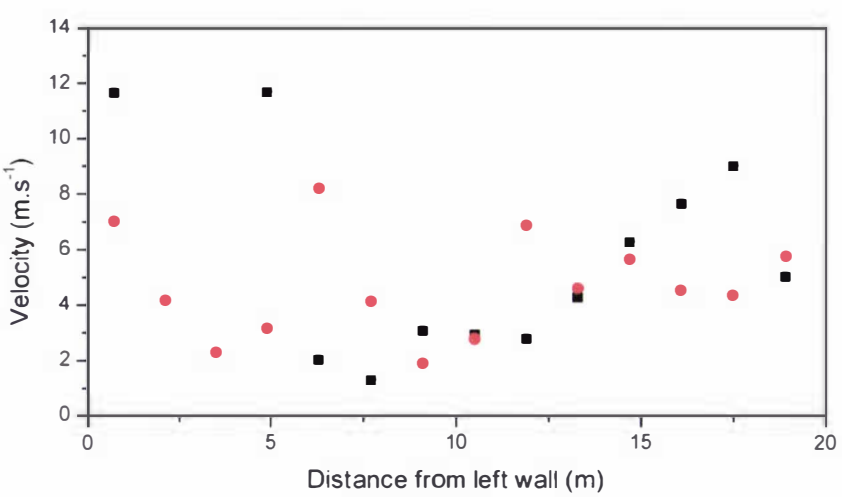

Figure 12-14 – Time-averaged measured air delivery (■) and air return (●) velocities across the width of the deck

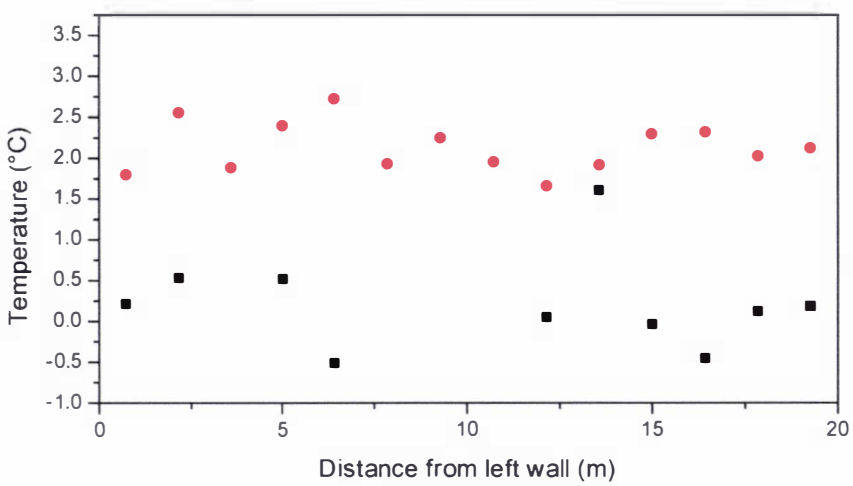

Figure 12-15 - Time-averaged measured air delivery (■) and air return (●) temperatures across the width of the deck

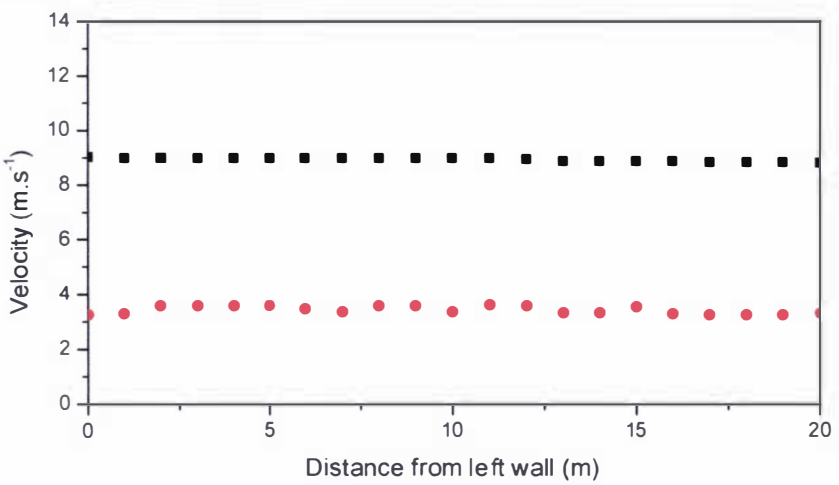

Figure 12-16 - Predicted air delivery (■) and air return (●) velocities across the width of the deck

Figure 12-17 shows the average measured temperatures in the under-floor gratings and ceiling headspace. The under-floor plot was interpolated from 33 successfully measured points and the headspace plot interpolated from 51 points. Figure 12-18 shows the calculated differences between the two plots. The increased temperature rise in the corner behind the door as predicted in Figure 12-13 is evident; however, the temperature differences are significantly higher than the predicted temperature rises shown in Figure 12-13. The increased temperature differences were probably due to removal of sensible heat from the cargo, which was not accounted for in the calculation of the predicted temperature rises. The cause of variability in measured under-floor temperatures was not known.

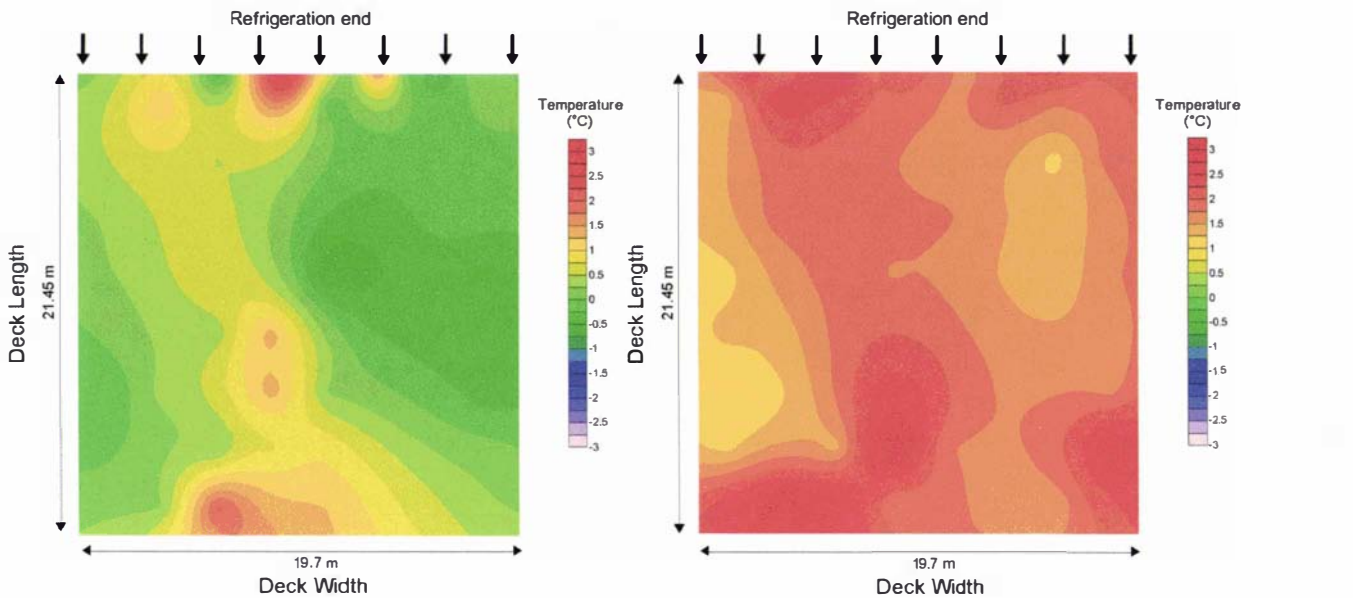

Figure 12-17 - Time-averaged measured air temperature in the floor (left) and ceiling headspace (right)

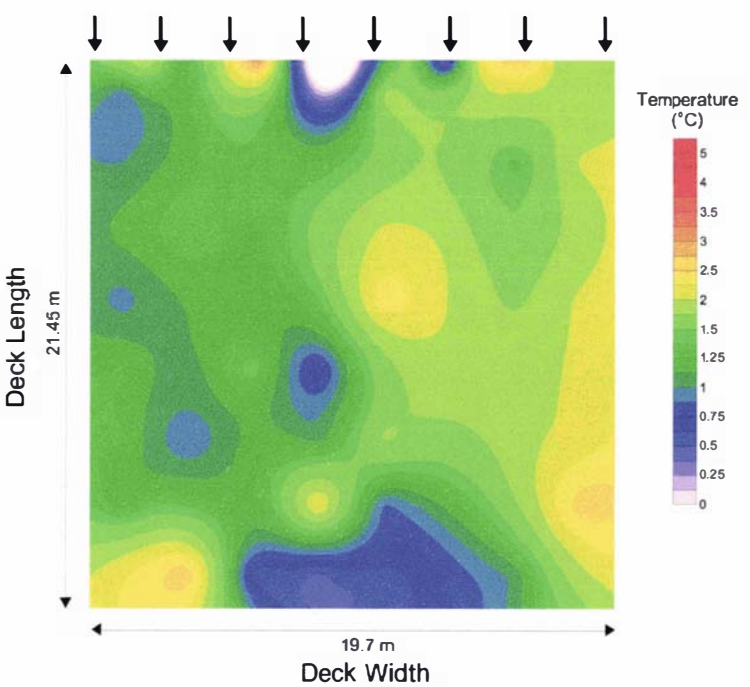

Figure 12-18 – Calculated difference between time-averaged measured temperature in the floor and ceiling headspace

Figure 12-19 and Figure 12-20 show the average measured delivery and return velocities and temperatures during the voyage. Figure 12-21 and Figure 12-22 show the same data measured in the under-floor gratings and the ceiling headspace. The relatively noisy nature of the delivery air data was considered a consequence of water in the under-floor channels near the refrigeration system. Sensors positioned elsewhere in the hold were less noisy and provided results easier to interpret. Trends were similar to those discussed in Section 11.4, with different phases within the refrigeration frosting/defrosting cycle.

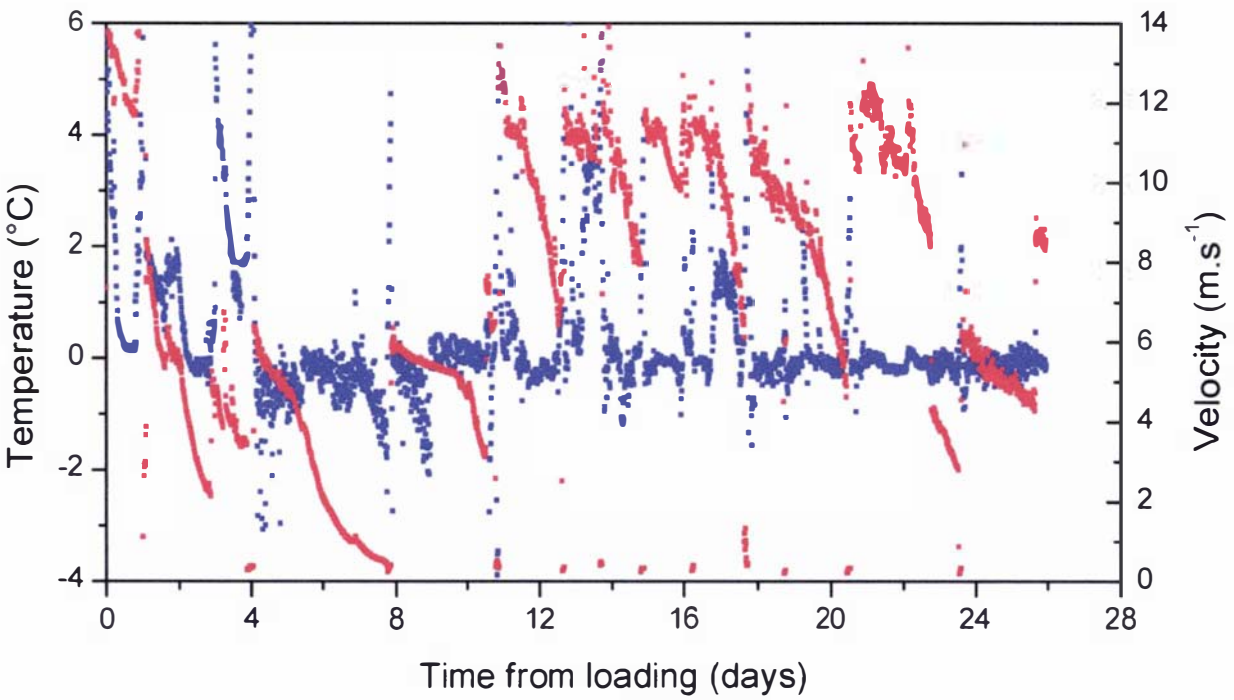

Figure 12-19 – Spatially-averaged measured air delivery velocity (•) and temperature (•) throughout the voyage

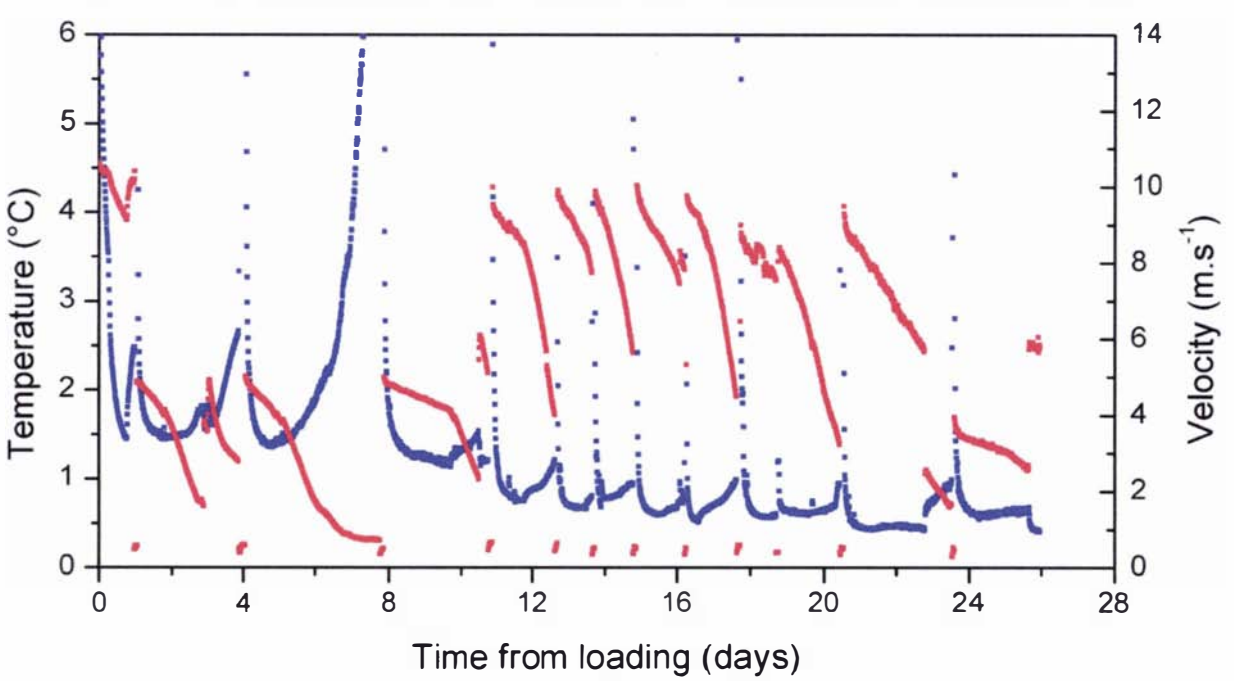

Figure 12-20 - Spatially-averaged measured air return velocity (•) and temperature (•) throughout the voyage

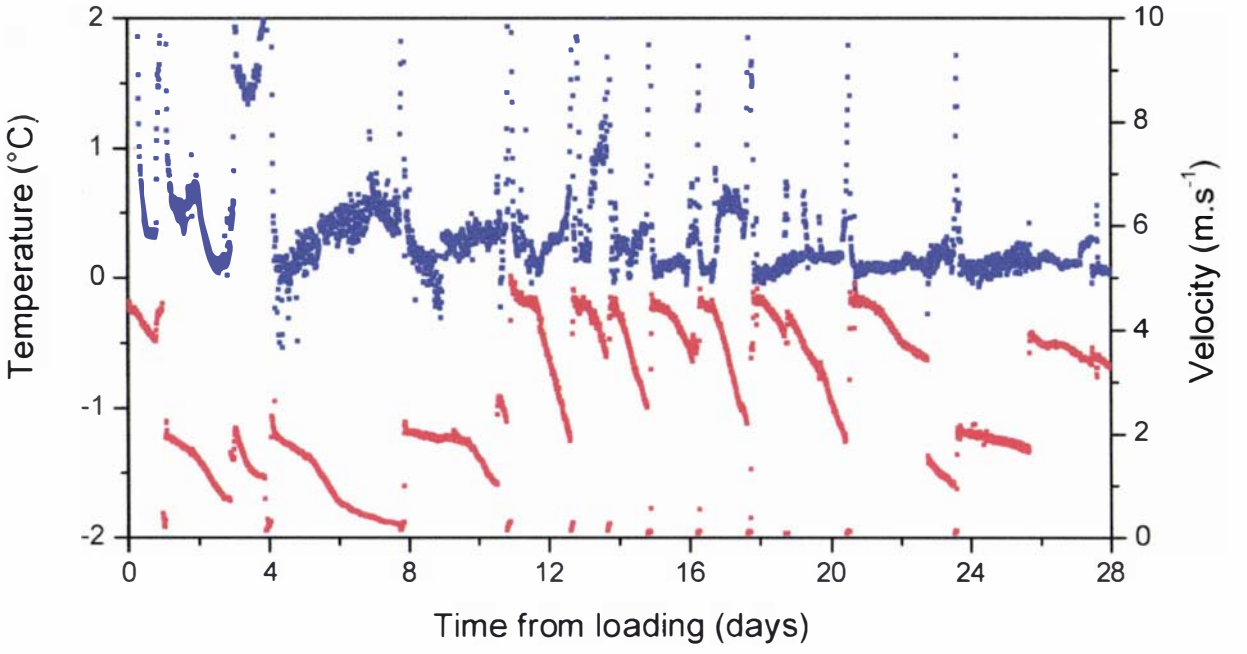

Figure 12-21 - Spatially-averaged measured velocity (•) and temperature (•) in the under-floor gratings throughout the voyage

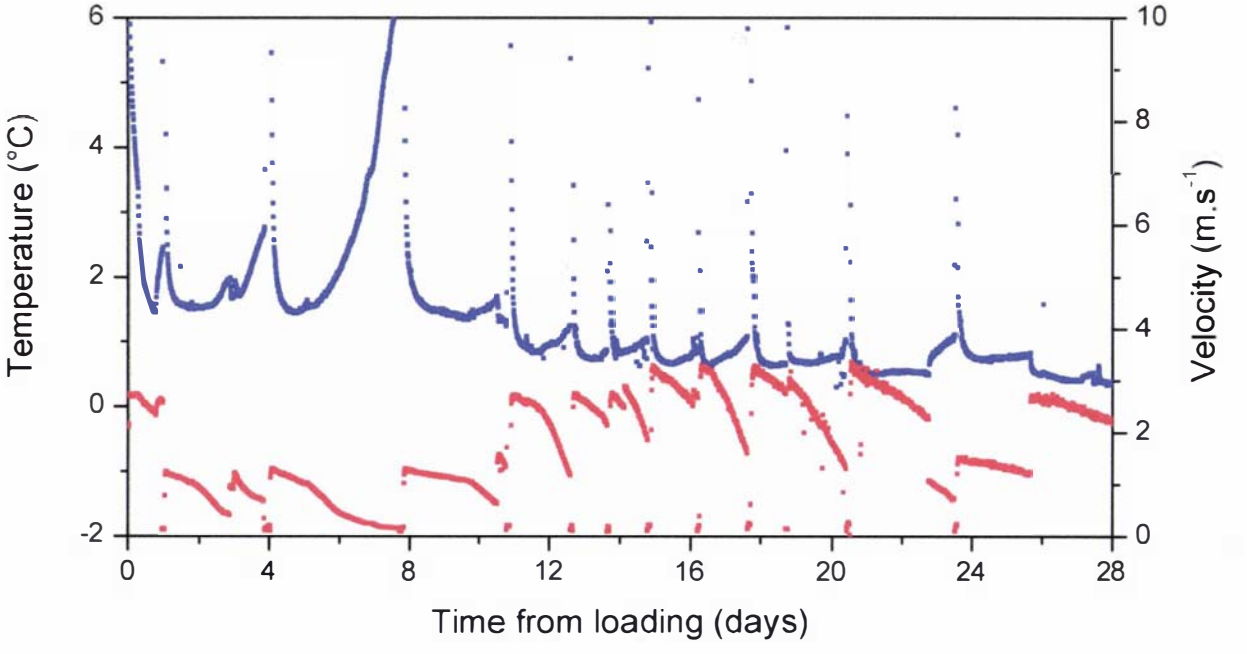

Figure 12-22 - Spatially-averaged measured velocity (•) and temperature (•) in the ceiling headspace throughout the voyage

In this shipment, it appeared 2 fan speeds were used during different portions of the journey. As previously mentioned, carriage conditions for apples often recommend reduction of the circulation rate to 45 changes per hour after temperature control has been achieved. In this case it appeared a low fan speed was used in two periods: from 1 day after loading to 11 days after loading, and briefly from 23 days after loading to 26 days after loading. The high fan speed in the middle stage of the journey was likely to coincide with travel through the tropics. Inspection of the ceiling headspace temperature (Figure 12-22) gives an indication of the temperature of the cargo, which slowly reduced throughout the shipment. The ceiling headspace temperature was falling at least until 16 days after loading after which time the changes in circulation rate make it difficult to determine any trend. Consequently, it was concluded that reduction of the circulation rate was carried out prior to completion of cooling and was therefore likely to be detrimental to fruit quality as discussed in Section 11.5.2.

The temporal trends were similar to that discussed in Section 11.4 in that a repetitive pattern of diminishing velocity was evident between evaporator defrosts. However, the characteristic shape of the velocity decline curve was not similar to that in Section 11.4. In the period immediately following defrost, the velocity fell at a relatively slow rate followed by a period in which the velocity fell more rapidly. In the period between 6 days after loading and 8 days after loading, the velocity trend flattened out after the period of fast decline; however, this may have been due to the system reaching a level of minimum flow as a consequence of flow bypassing the evaporator rather than the changing condition of the evaporator. Whilst delivery air temperature control was not lost at this stage in the journey, the reduced rate of air circulation led to an average air temperature in the ceiling headspace above 6°C.

In the period around 4 days after loading, delivery air temperature control appeared to be lost. The cause of this loss of control was not clear from the measured data.

The two periods with reduced fan speeds, along with the rapid decline in velocities due to evaporator frosting may have contributed to the overestimation of predicted velocities discussed earlier. These regular reductions in the circulation rate were not accounted for in the airflow model, and will have had a substantial impact on the average measured velocities.

There were key differences in the performance of this vessel and the one described in Section 11.4. Firstly, the characteristic shape of the velocity decline curve between evaporator defrosts was different. Secondly, as delivery air temperature control was not lost due to frosting in this vessel, it appeared that heat transfer may not have been affected by frosting as much in this vessel. Sufficient data to determine the cause of these difference was not available, but was probably due to differences in evaporator design.

As discussed in Section 11.4, the management of defrost is of critical importance in shipments of fresh produce. Failure to initiate defrost in this voyage between day 4 and 8 led to average ceiling air temperatures in excess of 6°C. Improved management systems are required to ensure improved temperature control.

12.4.1 In-package temperatures

Although no in-package temperatures were measured in this shipment, heat transfer simulations were performed for pallets positioned both near the refrigeration end and the opposite end of the deck to assess the implications of the air distribution. PackSim was used to predict the cooling rates of pallets surrounded by gaps 0.04 m and 0.01 m in width.

A hypothetical packaging system similar to that used in Section 11.4.1 was modelled, with the height of the carton changed to 0.17 m and a pallet made up of 12 layers. Table 12-1 gives the altered input data, Table 11-1 provides the remaining input data and Figure 11-32 shows the zones used on a single layer of cartons.

Gaps surrounding pallets and the top and bottom faces of the pallet were treated the same as in Section 11.4.1. The average measured under-floor air temperature during the voyage was used as the incident air temperature (delivery air temperature) and the average ceiling headspace temperature used as the external temperature above the pallet (return air temperature). Velocities predicted using the FlowSim model were used as the velocity in the surrounding gaps as well as above and below the pallets. The system was arbitrarily assumed to be at a uniform initial temperature of 6°C.

Figure 12-23, Figure 12-24 and Figure 12-25 show the predicted temperatures in the three positions depicted in Figure 11-32 on the 9th layer (from the bottom) for pallets at both ends of the hold. Differences in the rate of cooling between pallets surrounded by gaps 0.04 m wide and 0.01 m wide were

substantial at both ends of the hold. Differences in the rate of cooling at the two ends of the hold were also substantial. Predicted cooling of the pallet at the far end of the hold surrounded by narrow gaps was slow, with temperatures still hovering around 5°C after 6 days cooling. This rate of cooling could be considered an absolute worst case, with only a small possibility of a pallet having all four faces neatly aligned with surrounding pallets given the non-uniform nature of pallet placement within the deck.

Table 12-1 - Data used in the simulation of cooling in a pallet of a hypothetical pallet of produce. Data values were sourced from physical measurement of the cartons and Tanner (1998)

Variable	Value	Units
Physical System Data		
Width of system (x)	0.46	m
Height of system (y)	2.00	m
Length of system (z)	0.53	m
Package properties		
Zones in x – direction	3	
Zones in y – direction	4	
Zones in z – direction	12	
Number of V boundaries	156	
Number of H boundaries	192	
Number of P boundaries	180	
Total internal zones	144	
Total external zones	2	
Number of pack materials	3	
Number of active surfaces	4	
External environment data		
Delivery temperature	0.0	°C
Return temperature	1.5	°C

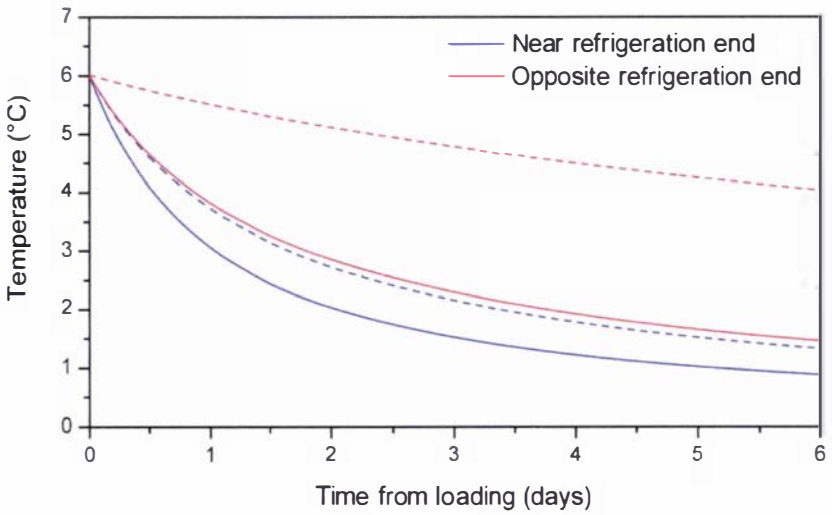

Figure 12-23 - Temperatures in position 1 as depicted in Figure 11-32 predicted for pallets positioned at both ends of the hold surrounded by gaps of 0.01 m (dashed lines) and 0.04 m (solid lines) widths

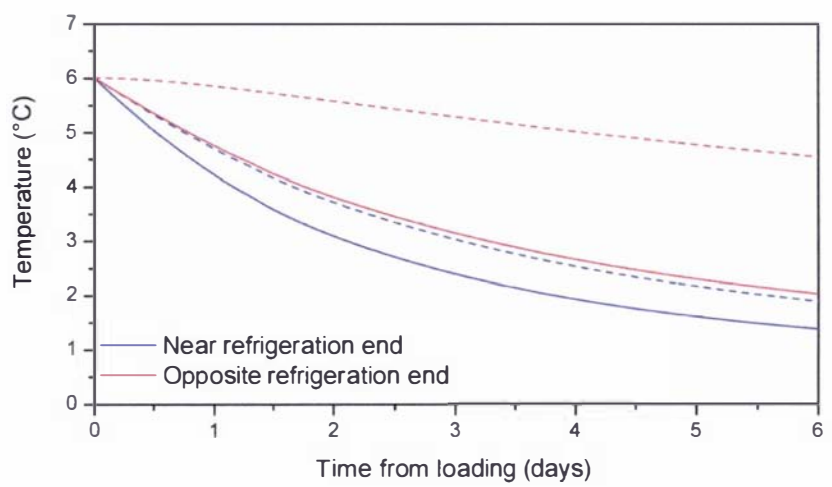

Figure 12-24 - Temperatures in position 2 as depicted in Figure 11-32 predicted for pallets positioned at both ends of the hold surrounded by gaps of 0.01 m (dashed lines) and 0.04 m (solid lines) widths

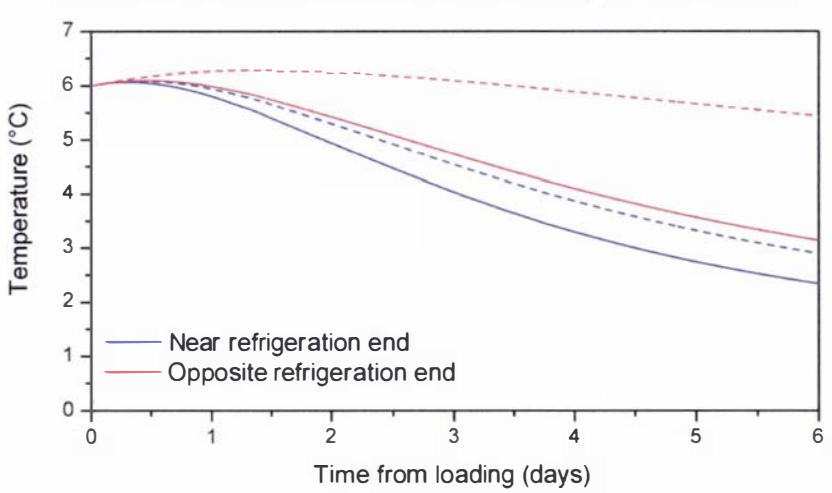

Figure 12-25 - Temperatures in position 3 as depicted in Figure 11-32 predicted for pallets positioned at both ends of the hold surrounded by gaps of 0.01 m (dashed lines) and 0.04 m (solid lines) widths

12.5 Scenario testing

As is the case for containers, removal of gratings from the cargo space in refrigerated holds would yield great benefits in the building and maintenance of refrigerated vessels. Ship building and operational costs would be reduced, and a lower depth of the hull would become possible without reducing capacity, thereby increasing stability (Anon, 2001b). In this section, the possibility of removing the gratings is explored using the FlowSim model. Essentially, the pallet bases become the plenum in which the air is distributed throughout the hold rather than the gratings.

12.5.1 Hold without gratings

Two implementations of a hold without gratings were simulated, one simply removing the gratings without any additional interventions and a second implementation incorporating a 'collar' system around each pallet. The collar system works by increasing the flow resistance of each of the vertical channels between pallets, thereby making the flow more uniform throughout the hold. The method of implementation and logistics of the collar system were not considered; just the value of the concept in terms of velocity and temperature variability.

The geometry described in Section 12.3 was used, with the layer of nodes and channels below the gratings removed. The fixed pressure inlet nodes were attached to the nodes on the pallet base layer adjacent to the refrigeration system. The collars were assumed to be a perforated barrier to flow, which filled the gaps around pallets. This could be achieved by placing a flexible, compressible collar around each of the pallets. The collars were described using the correlation for perforated plates presented in Section 8.3.4, with each vertical channel modelled as incorporating a perforated barrier to flow with 10% open area.

Figure 12-26 shows the predicted horizontal velocity in the pallet bases over the deck area for the three systems simulated. The horizontal velocity fell away rapidly with increasing distance from the refrigeration system; however, collars reduced the rate of this decline. These patterns are mirrored in Figure 12-27, which shows the predicted velocities in the ceiling headspace.

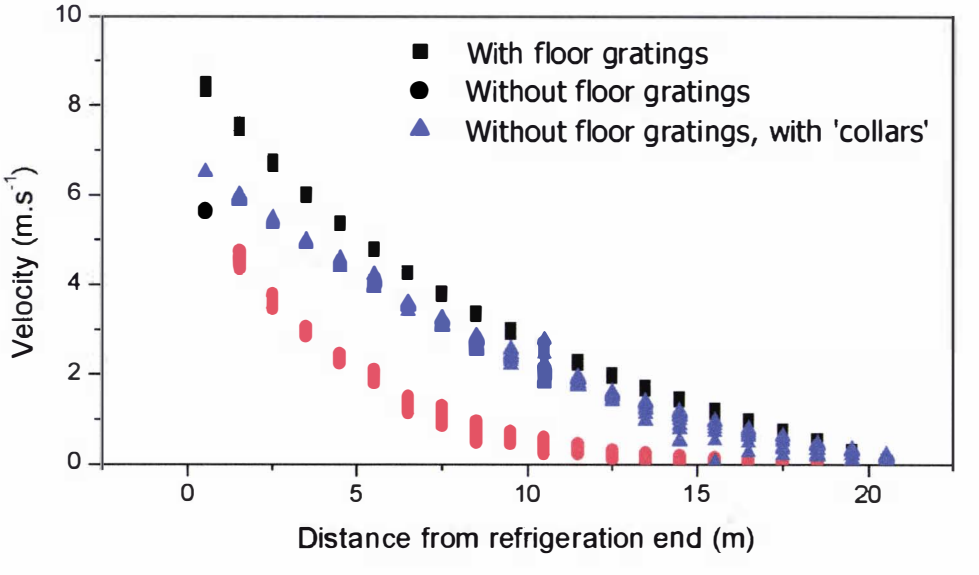

Figure 12-26 - Predicted horizontal velocities in the air delivery duct (with floor gratings) or pallet bases (without floor gratings) throughout the refrigerated deck

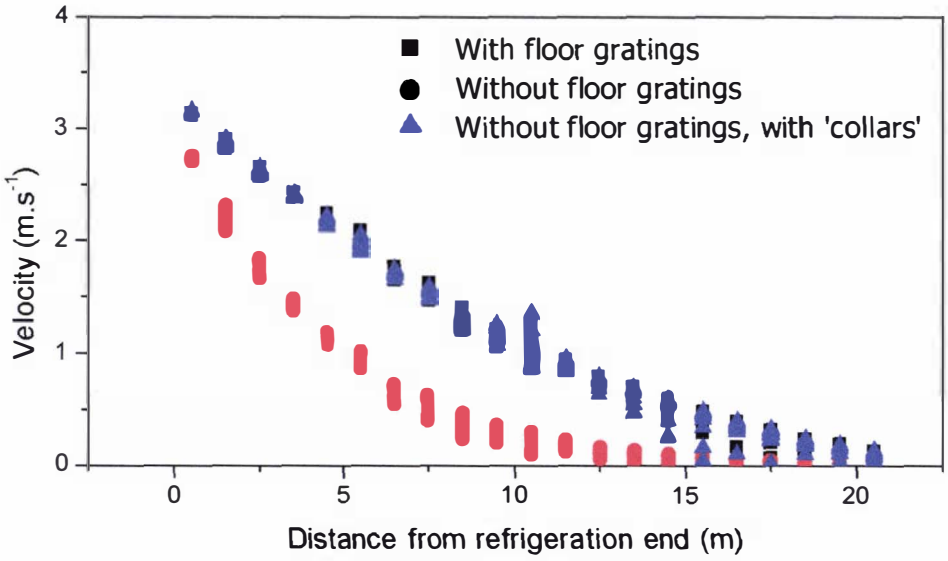

Figure 12-27 - Predicted horizontal velocities in the ceiling headspace throughout the refrigerated deck

Figure 12-28 and Figure 12-29 show the predicted flow in the vertical channels for the system without and with collars respectively. The system without collars showed a sharp decline in vertical velocity with increasing distance from the refrigeration end. The collar system served to reduce the rate of decline and made a substantial improvement to vertical velocity uniformity.

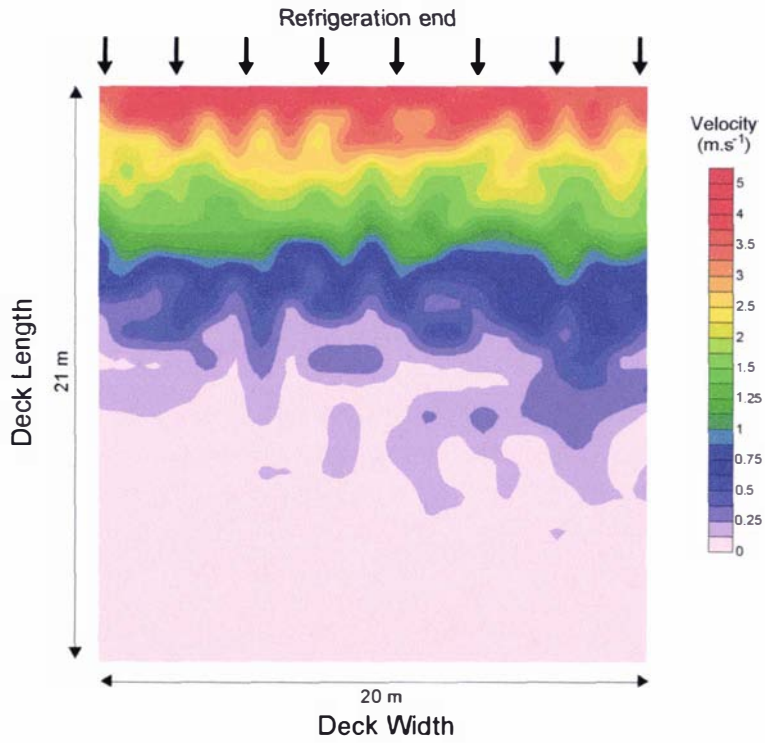

Figure 12-28 - Predicted velocity in the vertical channels formed by gaps around pallets throughout the refrigerated deck without gratings and without 'collars'

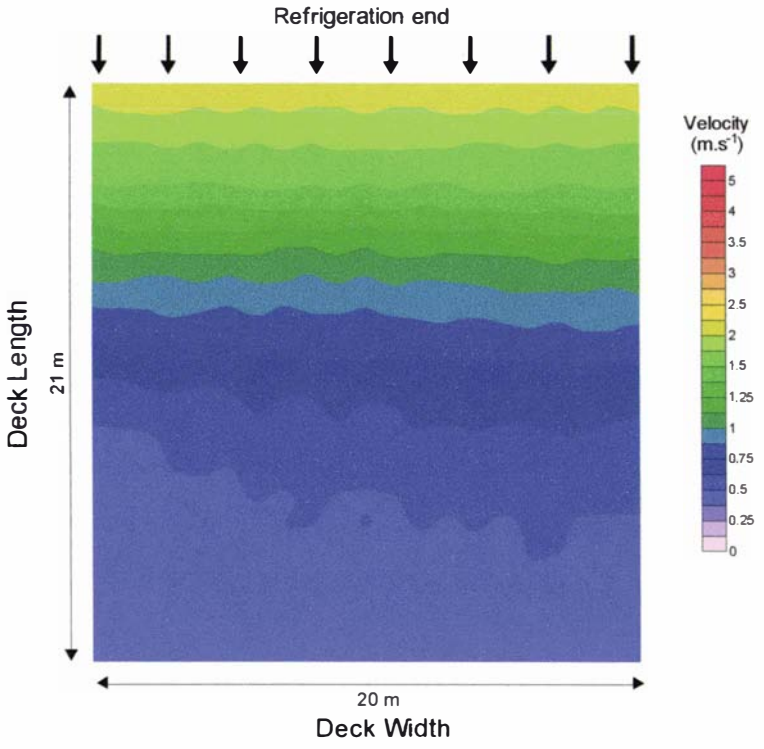

Figure 12-29 - Predicted velocity in the vertical channels formed by gaps around pallets throughout the refrigerated deck without gratings and with 'collars'

Figure 12-30 and Figure 12-31 show the temperature rise associated with the vertical velocities and further illustrates the beneficial effect of the collars. The temperature rises for the system without collars in the half of the deck furthest from the refrigeration system were over 5°C in most cases, whist the collars reduced these to generally under 1°C and were more uniform.

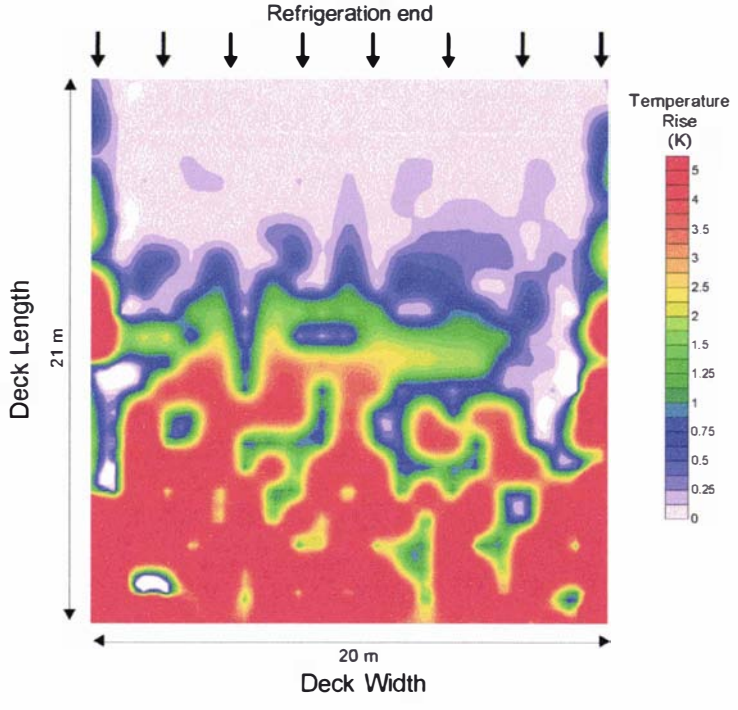

Figure 12-30 - Predicted temperature rise in the vertical channels formed by gaps around pallets throughout the refrigerated deck without gratings

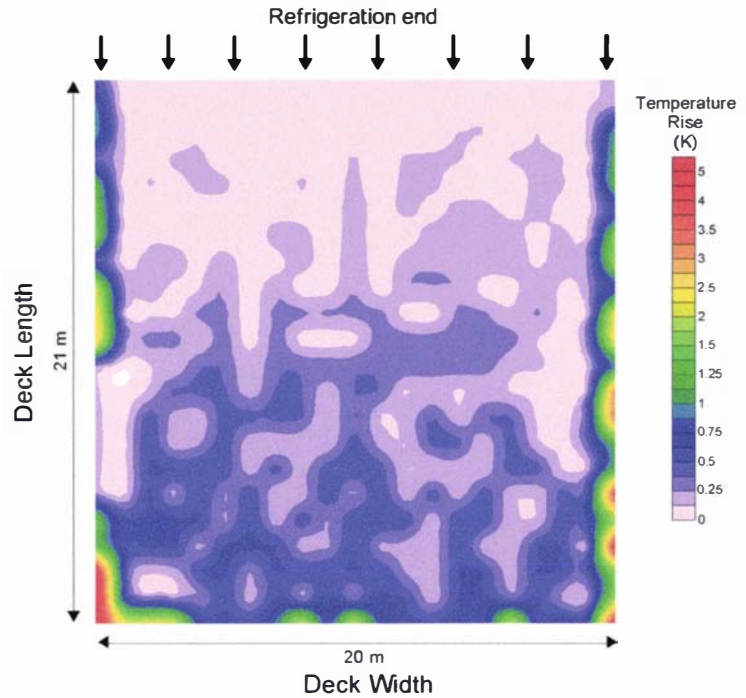

Figure 12-31 - Predicted temperature rise in the vertical channels formed by gaps around pallets throughout the refrigerated deck without gratings and with 'collars'

Heat transfer simulations were conducted using the system described in Section 12.4.1 and the air velocities predicted with and without collars. Figure 12-32 to Figure 12-34 show the predicted temperatures for pallets near the refrigeration end surrounded by gaps of two sizes for the two systems without gratings and the hold with gratings. Temperatures were compared for three positions within the pallet on layer 9 (Figure 11-32). Predicted temperatures for the pallets surrounded by large gaps in the system with gratings and the system with collars were coincident in these figures. Figure 12-35 to Figure 12-37 show the same information for a pallet positioned at the opposite end of the hold.

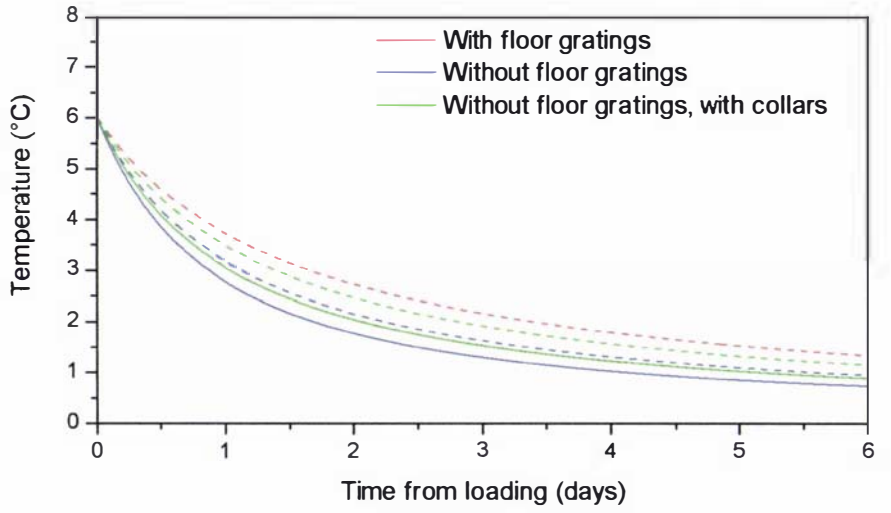

Figure 12-32 - Temperatures in position 1 predicted for pallets positioned at the end of the hold adjacent to the refrigeration end surrounded by 0.01 m wide channels (dashed lines) and 0.04 m wide channels (solid lines)

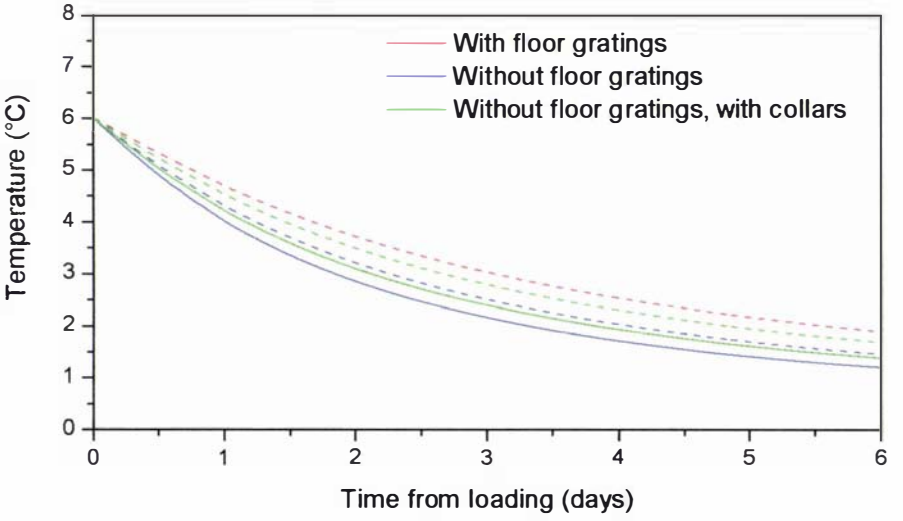

Figure 12-33 - Temperatures in position 2 predicted for pallets positioned at the end of the hold adjacent to the refrigeration end surrounded by 0.01 m wide channels (dashed lines) and 0.04 m wide channels (solid lines)

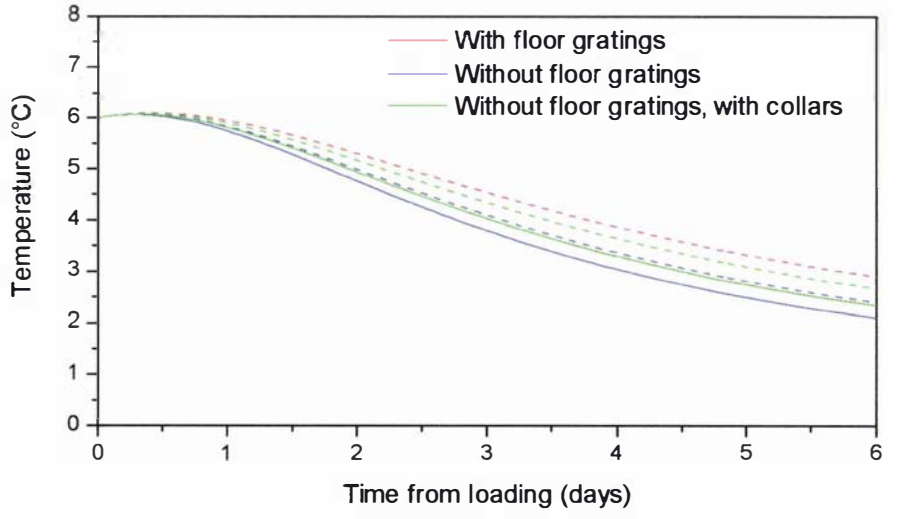

Figure 12-34 - Temperatures in position 3 predicted for pallets positioned at the end of the hold adjacent to the refrigeration end surrounded by 0.01 m wide channels (dashed lines) and 0.04 m wide channels (solid lines)

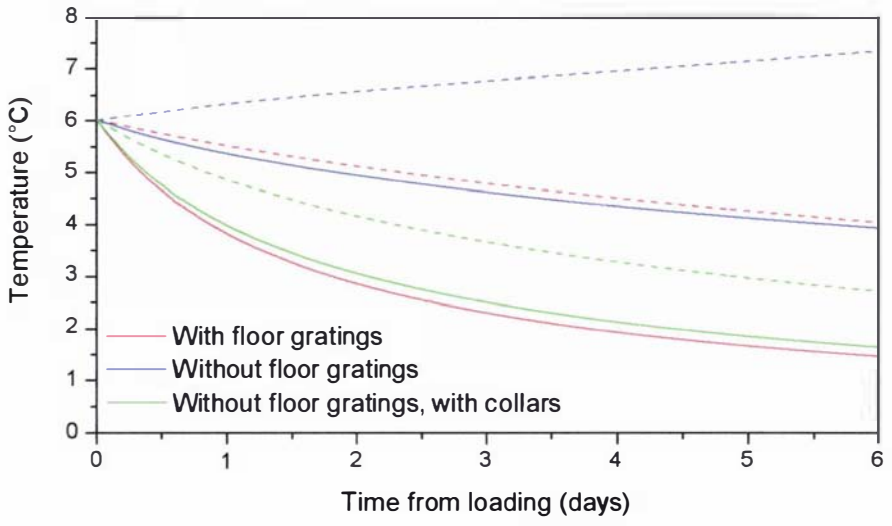

Figure 12-35 - Temperatures in position 1 predicted for pallets positioned at the end of the hold opposite the refrigeration end surrounded by 0.01 m wide channels (dashed lines) and 0.04 m wide channels (solid lines)

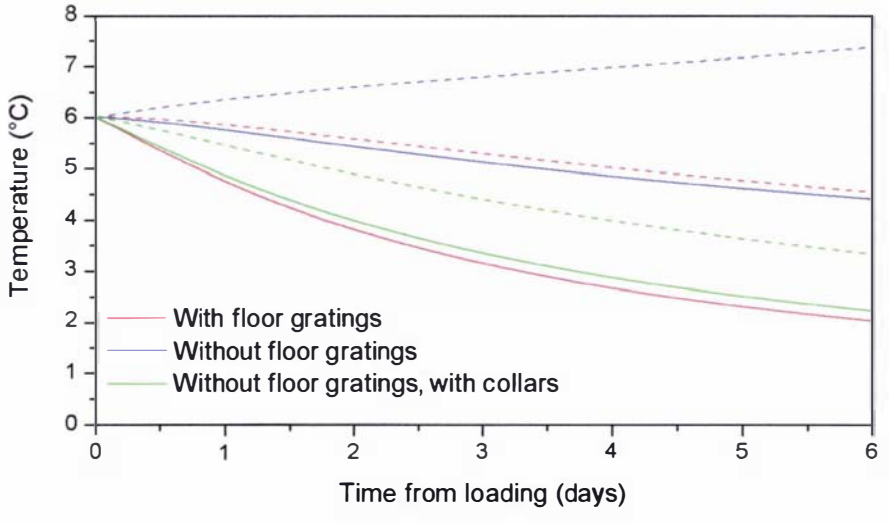

Figure 12-36 - Temperatures in position 2 predicted for pallets positioned at the end of the hold opposite the refrigeration end surrounded by 0.01 m wide channels (dashed lines) and 0.04 m wide channels (solid lines)

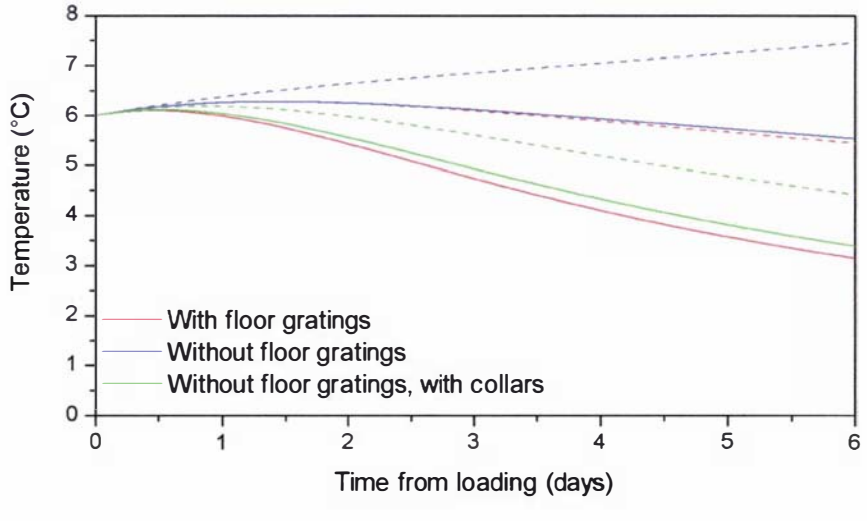

Figure 12-37 - Temperatures in position 3 predicted for pallets positioned at the end of the hold opposite the refrigeration end surrounded by 0.01 m wide channels (dashed lines) and 0.04 m wide channels (solid lines)

For the pallets near the refrigeration end of the hold, the system without gratings or collars cooled the fastest. The system without gratings but with collars performed identically to the system with gratings for large gaps and slightly better than the system with gratings with small gaps. The magnitude of the differences between the three systems at this end of the hold was small. At the opposite end of the hold however, the magnitude of the differences was substantial. A pallet surrounded with small gaps in the system without gratings or collars failed to remove the respiratory heat leading to warming of the pallet. Even if the pallet was surrounded by larger gaps in this system, it cooled relatively slowly. The system with gratings performed much better; however, the system without gratings but with collars performed the best. The collars reduced the variability in cooling rate due to the variable gap size, due to a more uniform air distribution.

The air distribution predicted for the two systems illustrate the need for an intervention of some kind to successfully maintain temperature uniformity within a refrigerated hold without gratings. Without the gratings, minimal quantities of air flowed to the end of the hold furthest from the refrigeration system. The collar system improved the air distribution substantially, even leading to a reduction in temperature variability over that of the standard system incorporating gratings. The logistics of implementing such a system may eventually prove the concept impractical; however, the benefits of successful implementation warrant further investigation.

12.6 Conclusions

Comparison of measured and predicted air velocities in a single layer deck during a shipment of apples showed velocities were generally over-predicted. Measurement difficulties including a data-logger failure, a high level of sensor damage (due to the metal floor) and movement as a consequence of loading meant limited information was successfully gathered and also caused a high level of variability in measured velocities.

From the measured air velocities it appeared that 2 fan speeds were used during different portions of the journey, although the ceiling headspace temperatures indicated that the cargo was cooling for the majority of the voyage. Although a lower fan speed is employed in apple shipments to reduce dehydration, reduction of the fan speed prior to completion of cooling would reduce the rate of cooling, thereby increasing rates of water loss. A repetitive pattern of diminishing velocities between evaporator defrosts was again apparent, with a single instance where failure to initiate a defrost led to an average ceiling headspace temperature of 6°C. The use of the reduced fan speed along with regular velocity reductions due to evaporator frosting may have contributed to the overestimation of velocities by the airflow model.

The possibility of a single layer deck without gratings (using the pallet bases as a plenum) was investigated. Without further interventions, temperature variability within the hold was predicted to be substantially increased. Implementation of a 'collar' system, whereby the gaps between pallets are partially blocked, was predicted to reduce the temperature variability in the system to a level below that of the current design incorporating gratings.

13 Summary of Model Validation and Scenario Testing

Predictions made using FlowSim and PackSim have been tested against static pressure data collected independently in a full-scale model of a section of a refrigerated hold, as well as velocity and temperature data collected in a 40' container and two differently configured refrigerated holds.

Comparisons of predicted static pressures with values measured by Lindqvist (2000) in a model hold showed excellent agreement except for positions under the perforated floor. Predicted pressures and airflows were insensitive to the flow resistance of the perforated floor, with no significant differences in air distribution predicted between systems with floor open areas of 1.2% and 3%. Predictions were also insensitive to the additional loss value attributed to turning geometries; doubling the additional loss values caused only relatively moderate changes in the predicted air distribution (7% maximum change in vertical velocity).

Air velocities and in-package temperatures were recorded during simulated shipments of kiwifruit in two packaging systems in a 40' refrigerated container. Comparison of measured and predicted air velocities showed reasonable agreement at different positions down the length of the container, if the measured variation across the width was averaged. Comparison of in-package temperatures also showed reasonable agreement in most positions; however, cooling near the centre of the standard pallets was under-predicted. The discrepancy was attributed to diffusive flow of air through the pallet stack, which was not included in the model. Agreement of predicted and measured temperatures near the centre of the prototype pallets was good, as the flow through the pallet was quantified and included in the model. Significant variation in initial fruit temperatures and a small elevation of fruit temperature relative to the container set-point were limitations of the experimental data.

Simulations of flow and in-package temperatures were performed for the upper (spar) deck of a hold configured in pairs as well as a single deck. Comparisons were made between predicted and measured flows in both decks, and predicted and measured in-package temperatures in the spar deck. As was the case with the 40' container, agreement was reasonable for velocities throughout the decks if the variability in measured values across the width of the decks was averaged. Delivery and return air velocity measurements were problematic, with unrealistically low velocities recorded, probably due to improperly positioned sensors. Comparison of measured and predicted in-package temperatures showed good agreement for pallets positioned opposite the refrigeration end; however, cooling of positions near the centre of pallets adjacent to the refrigeration end was under-predicted. This discrepancy was again attributed to diffusive flows of air through the pallets adjacent to the refrigeration end not included in the model, caused by the sizeable pressure differences at that end of the hold.

Predictions of air distribution were sensitive to the flow resistance of the ceiling headspace. Accurate estimation of this flow resistance is difficult because of the variable geometry of the ceiling in refrigerated holds; however, it should be noted that characterising this complex geometry is a problem for any airflow model describing these systems regardless of the framework employed. The sensitivity of the model to this flow resistance also illustrates the importance of sufficient ceiling clearance in the hold.

The implications of altered operational or design factors were investigated using the FlowSim and PackSim models. Reducing the space between pallets and the wall of a container caused significant in-package temperature increases. Increasing the size of the gap between pallets stowed on the same side of the container (thereby reducing the size of the channel adjacent to the doors) improved cooling. In both cases, the required size of the gaps was small, such that corner-boards used for pallet stability were

likely to inadvertently produce a minimum gap size sufficient to provide benefit. An increased circulation rate improved cooling throughout the container; however, the magnitude of the improvement was relatively small. Simulations of a 40' container without T-bar floor gratings, making use of the pallet bases as a plenum, predicted only a small detrimental effect on cooling rates at the door end of the container.

Increased circulation rates in a refrigerated hold were predicted to increase cooling rates and decrease temperature variability within a hold. However, improvements obey the law of diminishing returns; that is, each further increase in circulation rate provides less benefit. Reduced circulation rates (and therefore reduced air velocities) will reduce mass loss in some regions of the hold, but will increase mass loss in other regions due to slower cooling of cargo and increased steady-state temperatures. Analysis of the relative size of these effects was not within the scope of this work, but due to the relative importance of fruit temperature and air velocity external to the package, it is likely that the negative temperature effects would outweigh the benefits of reduced velocities for most cargos.

The possibility of a single layer deck without gratings (using the pallet bases as a plenum) was also investigated and was shown to substantially increase temperature variability within the hold. Implementation of a 'collar' system, whereby the gaps between pallets were partially blocked, improved the performance of the system to a level above that of the system incorporating gratings.

Overall, comparison of predicted airflows and temperatures with measured values showed trends were well predicted, although the quantity and reliability of experimental data was a limitation. Cooling rates were under-predicted for the standard packaging system in the 40' container and at the refrigeration end of the spar deck due to diffusive flows through the pallets. Whilst the quantity of diffusive airflow through a non-vented pallet was measured to be small, it was significant in terms of heat transfer. Quantification and inclusion of this diffusive flow in the model would probably improve in-package temperature predictions. The FlowSim and PackSim models provide a useful set of tools for analysis and optimisation of the design and operation of refrigerated marine transport systems.

Part V
Conclusions and References

14 Conclusions

A mathematical model designed to predict airflow in marine transport systems has been developed (FlowSim). The model was based on a resistance network and solved the node equations using a Newton-Raphson algorithm implemented in C++. Flow resistances were adjusted during the calculation process to reflect the predicted flow conditions. The resistance network framework provided an alternative to CFD where the bounds of applicability were relatively well defined. The model relied on defining flow channels to which flow resistances were attributed and thus it relied on the accuracy of the flow resistance relationships used. Simulation times were short in comparison to CFD and boundary conditions were easily defined.

The model was only applicable where the pathways for flow were small and distinct and therefore easily defined. It was not envisaged for use in applications such as coolstores, display cabinets or ovens where the definition of distinct flow channels would be difficult. Therefore, the model did not offer the same level of flexibility offered by CFD.

The model developed was used to predict flows in a full-scale model of a section of a refrigerated hold, a 40' container and two refrigerated holds. Comparison of predicted and measured flows showed good broad agreement, but precision and quantity of measured data was a limitation. The predicted flows were used to predict product temperatures in a 40' container and a refrigerated hold. Comparison with measured temperatures showed good agreement in some areas and under-predicted cooling in others. The under-prediction was due to diffusive flows through the pallet stack, which were found not to substantially affect airflow patterns but did influence rates of cooling. Quantification and inclusion of these diffusive flows in the heat transfer model would improve product temperature prediction.

Correlations for flow resistance for a number of key geometries in marine transport systems were tested or developed. The Darcy-Weisbach, laminar and Colebrook equations were found to be sufficiently accurate for predicting the flow resistance of the channels formed between stacks of horticultural packages. The equations were used to predict the flow resistance of both manufactured channels and a horticultural packaging system incorporating vertical channels. The uncertainty in the measurement of the channel width outweighed other sources of uncertainty.

The relationship between flow resistance and carton vent design was also investigated. The carton vents were found to provide a greater proportion of the flow resistance than the contents of the carton, which is likely to be the case where the vent open area is lower than the porosity of the package. The flow resistance caused by vents on the outside of a stack and those within the stack were significantly different. The nature of the relationship between vent size and flow resistance was also different for the two types of vents. The measured relationships between vent size and flow resistance were significantly different to previously reported relationships.

A novel technique using nitrogen flushing and oxygen sensors was employed to quantify the rate of interchange of in-package air with external air for vented horticultural packages. Calculated rates of air interchange represent a significant contribution to overall heat transfer under conditions typical in marine transport systems and therefore needs to be considered when simulating heat or mass transfer for products in vented cartons. A complex relationship between the vent design and rate of interchange was observed, therefore no quantitative relationships between vent design and interchange rate were developed.

An improved method for determining an in-package flow profile for vented horticultural packages was developed. The method employs optical sensors along with fog as a tracer, and offers several improvements over previous methods employing CO_2 as the tracer. This technique provides a method for

transforming volumetric flow data for a pallet stack provided by the airflow model into the specific in-package velocities required for heat and mass transfer predictions.

Development of a low-cost thermistor anemometry system suitable for use in marine transport conditions has also been achieved. The system operated on the same principle as a hot-wire anemometer. When coupled with an appropriate data-logger and power supply, the system could measure and record velocities throughout the duration of a shipment. The sensors were observed to be insensitive to the direction of flow, and were inexpensive and therefore expendable. The system provided an affordable means to gather flow information in a marine transport environment, where high rates of sensor damage were considered likely.

The anemometry system developed was used to monitor air velocities in four holds of fresh produce shipped from New Zealand along with a simulated container shipment. Whilst problems were encountered with the reliability and accuracy of the collected data due to sensor positioning and damage, much useful data was collected. Substantial reductions in the circulation rate in the period between evaporator defrosts were observed in three of the four shipments. In one shipment, it appeared the circulation rate was reduced prior to completion of cooling, which would have led to unnecessarily elevated cargo temperatures and reduced product quality at delivery. On several occasions in the monitored shipments, temperature control of the cargo was compromised where defrost frequency was insufficient. Improved or automated methods of initiating defrosts in a timely fashion would reduce such incidents and improve the quality of product at out-turn with little capital expense.

The airflow model combined with a heat-transfer model (PackSim) was used to predict the consequences of altered operational and design parameters on product temperatures in both refrigerated containers and holds. Increased circulation rates were found to reduce temperature variability in both types of systems; however, the size of the improvement diminished with increasing rates. Therefore, whilst increasing circulation rates above current levels would reduce temperature variability, it is likely greater benefit could be derived from other interventions at less cost.

Removal of the T-bar floor gratings from a 40' container was predicted to have only a minor negative effect on temperature variability for a palletised cargo; however, the consequences of T-bar removal would depend heavily on the pallet base design. Conversely, removal of the gratings in a refrigerated hold without further intervention was predicted to have a profound negative effect on spatial temperature variability within the hold. Removal of gratings along with a further intervention in the form of a pallet 'collar' system, where channels between pallets are partially blocked, was predicted to reduce temperature variability compared to the current system with gratings. The logistical difficulties of implementing such a system may prove it to be impractical; however, the predicted benefits warrant further consideration of the concept.

The correlations and models developed in this thesis provide useful tools for analysis and optimisation of the design and operation of refrigerated marine transport systems. The airflow model, along with heat and mass transfer models can be used to test the efficacy of proposed changes to design or operational parameters prior to physical implementation.

15 References

1. **Alvarez, G. & Flick, D. (1999)** "Analysis of heterogeneous cooling of agricultural products inside bins - Part I: aerodynamic study". Journal of Food Engineering, 39 p.227-237
2. **Amos, N.D. (1995)** "Mathematical modeling of heat transfer and water vapour transport in apple coolstores". PhD Dissertation, Massey University, Palmerston North, New Zealand
3. **Anon (2001a)** "VFD AFAM/AFAM+ Setting Guide". Thermo King Corporation, Minneapolis, USA
4. **Anon (2001b)** "Reefer revolution". Fresh Info News, published September 16 2001 - Lockwood Press Ltd
5. **ASTM (2000)** "Standard test method for determining air change in a single zone by means of a tracer gas dilution - E741-00". ASTM International, USA
6. **Barber, E.M. & Ogilvie, J.R. (1984)** "Incomplete mixing in ventilated airspaces. Part II: Scale model study". Canadian Agricultural Engineering, 26(2) p.189-196
7. **Bird, R.B., Stewart, W.E. & Lightfoot, E.N. (1960)** "Transport phenomena". John Wiley & Sons Inc., New York, USA
8. **Boldrin, B., Minotto, G., Panozzo, G., Toniolo, B., Lanza, J.W., Florio, G., Jacobini, A. and Sallusti, L. (1993)** "New data about ageing of insulated vehicles in service: a statistical analysis". Refrigeration Science & Technology, 1993-3 p.555-563
9. **Bradshaw, P. (1999)** "The best turbulence models for engineers" in Modeling Complex Turbulent Flows. ed. Salas, M.D., Hefner, J.N. and Sakell, L. Kluwer Academic Publishers, Dordrecht, The Netherlands
10. **British Standards Institute (1980)** "Fans for general purposes, Part 1: Methods of testing performance". British Standards Institute, UK
11. **Chandrasekaran, M., Marcroft, H., Bakalis, S. and Karwe, M.V. (1997)** "Applications of laser Doppler anemometry in understanding food processing operations". Trends in Food Science and Technology, vol 8 p.369-375
12. **Chau, K.V., Gaffney, J.J., Baird, C.D. and Church, G.A. (1985)** "Resistance to air flow of oranges in bulk and in cartons". Transactions of the ASAE, 28 (6) p.2083-2088
13. **Chen, P. , Cleland, D.J., Lovatt, S.J. and Bassett, M.R. (1999)** "Air infiltration into refrigerated stores through rapid-roll doors". Proceedings of 20th International Congress of Refrigeration, Vol. IV, p.925-932
14. **Chen, S. & Doolen, G.D. (1998)** "Lattice Boltzmann method for fluid flows". Annual Review Fluid Mechanics, 30 p.329-364
15. **Cheng, C.-Y., Atkinson, J.F. and Bursik, M.I. (1997)** "Direct measurement of turbulence structures in mixing jar using PIV". Journal of Environmental Engineering, 123(2) p.115-125
16. **Cleland, A.C. (1990)** "Food refrigeration processes - Analysis, design and simulation". Elsevier Science Publishers, London
17. **Cleland, A.C. & Cleland, D.J. (1992)** "Cost Effective Refrigeration ". Dept. of Biotechnology, Massey University, Palmerston North, New Zealand
18. **Corona Integrated Technologies Inc. (2002),** http://www.smokemachines.com, accessed November, 2002
19. **Cross, H. (1936)** "Analysis of Flow in Networks of Conduits or Conductors". University of Illinois Engr. Expr. Station, Bulletin No. 286
20. **Emond, J.P., Mercier, F., Sadfa, S.O., Bourre, M. and Gakwaya, A. (1996)** "Study of parameters affecting cooling rate and temperature distribution in forced-air precooling of strawberry". Transactions of the ASAE, 39(6) p.2185-2191
21. **Falconer, R.M. (1995)** "Experimental forced-air cooling of apple cartons". Report #523 New Zealand Apple and Pear Marketing Board, New Zealand

22. **Frith, J. (1991)** "The Transport of Perishable Foodstuffs". SRCRA, Cambridge, UK
23. **Gaffney, J.J., Baird, C.D. and Chau, K.V. (1985)** "Influence of airflow rate, respiration, evaporative cooling, and other factors affecting weight loss calculations for fruits and vegetables". Trans. ASHRAE , 91(1B) p.690-707
24. **Geankoplis, C.J. (1993)** "Transport processes and unit operations - 3rd edition" Allyn & Bacon, Boston USA.
25. **Grace, J. (1985)** "The measurement of wind speed" in Instrumentation for Environmental Physiology. ed. Marshall, B. & Woodward, F.I. Cambridge University Press, Cambridge UK.
26. **Haas, E. & Felsenstein, G. (1987)** "Factors affecting resistance to air flow through avocados packed in fiberboard crates". Proceedings 17th International Congress of Refrigeration, vol D p.125-130
27. **Haas, E. , Felsenstein, G., Shitzer, A. and Manor, G. (1976)** "Factors affecting resistance to air flow through packed fresh fruit". Trans. ASHRAE. 82 (2) p.548-554
28. **Harral, B.B. & Boon, C.R. (1997)** "Comparison of predicted and measured air flow patterns in a mechanically ventilated livestock building without animals". Journal of Agricultural Engineering Research, 66 p.221-228
29. **Heap, R. (2003)** "International refrigerated transport by sea and air". Proceedings 21st International Congress of Refrigeration, in print
30. **Heap, R.D. (1989)** "Design and performance of insulated and refrigerated ISO intermodal containers". International Journal of Refrigeration, vol. 12 p.137-145
31. **Hefner, J.N. (1999)** "Current and future needs in turbulence modelling" in Modeling Complex Turbulent Flows. ed. Salas, M.D., Hefner, J.N. and Sakell, L. Kluwer Academic Publishers, Dordrecht, The Netherlands
32. **Hoang, M.L., Verboven, P., De Baerdemaeker, J. and Nicolai, B.M. (2000)** "Analysis of the air flow in a cold store by means of computational fluid dynamics". International Journal of Refrigeration, 23 p.127-140
33. **Hoff, S.J. (1995)** "A simplified turbulence model for describing airflow in ceiling slot-ventilated enclosures". Transactions of the ASAE, 38(6) p.1853-1862
34. **Hoff, S.J., Janni, K.A. and Jacobson, L.D. (1992)** "Three-dimensional buoyant turbulent flows in a scaled model, slot-ventilated, livestock confinement facility". Transactions of the ASAE, 35(2) p.671-686
35. **Hu, S.C. , Hu, Y.Z.R., Chao, C.C. and Fan, N.W. (1993)** "Design of flow path for a display case using computational fluid dynamics". Refrigeration Science & Technology, 1993-3 p.332-338
36. **IIF/IIR (1995)** "Guide to Refrigerated Transport". International Institute of Refrigeration, Paris, France
37. **Irving, A.R. (1997)** "Code of practice for handling fresh fruit and vegetables in refrigerated shipping containers". Australian Chamber of Shipping Ltd, Sydney, Australia
38. **Irving, A.R. & Sharp, A.K. (1975)** "The use of a heat dissipation factor in the calibration of a thermistor anemometer". Proceedings of 'IICA 75', Institute Instrumentation and Control, 2.1-2.4
39. **Irving, A.R. & Sharp, A.K. (1976)** "Measurement of air circulation in a refrigerated ISO container". Refrigeration Science & Technology, 1976-1 p.485-492
40. **Irving, A.R. & Sharp, A.K. (1993)** "Refrigerated freight containers of chilled meat: temperature uniformity and temperature rise when left off-power". Refrigeration Science & Technology, 1993-3 p.483-491
41. **Irving, A.R. & Shepherd, I.C. (1982)** "Measurement of air circulation rate in integral refrigerated shipping containers". Refrigeration Science & Technology, 1982-1 p.369-375
42. **ISO (1995)** "ISO 668:1995, Series 1 freight containers - Classification, dimensions and ratings.".

International Organisation for Standardisation, Switzerland

43. **Jolly, P.G., Tso, C.P., Wong, Y.W. and Ng, S.M. (2000)** "Simulation and measurement on the full-load performance of a refrigeration system in a shipping container". International Journal of Refrigeration, vol. 23 p.112-126
44. **Kang, S. (1996)** "Development of a Poisson model to predict recirculating flows in cold storage rooms". PhD dissertation, Cornell University, USA
45. **Kleinstreuer, C. (1997)** "Engineering Fluid Dynamics: A interdisciplinary systems approach". Cambridge University Press, U.K.
46. **Kondjoyan, A. & Boisson, H.C. (1997)** "Comparison of calculated and experimental heat transfer coefficients at the surface of circular cylinders placed in a turbulent cross-flow of air". Journal of Food Engineering, 34(2) p.123-143
47. **Lin, Z., Cleland, A.C., Serralach, G.F. & Cleland, D.J. (1994)** "Practical application of a generally applicable method for chilling time prediction". IRHACE Report, 17p,
48. **Lindqvist, R. (2000)** "Air distribution in reefer holds". PhD Dissertation, Norwegian University of Science & Technology, Norway
49. **Lomax, K.M., Gottfried, S. and Lavelle, H. (1995)** "Airflow indicators for mushroom houses". Journal of Agricultural Engineering, v.60 p.43-48
50. **Lovatt, S.J. (1992)** "A Dynamic Modeling Methodology for the Simulation of Industrial Refrigeration Systems". PhD Dissertation, Massey University, Palmerston North, New Zealand
51. **Lovatt, S.J., Willix, J. and Pham, Q.T. (1993)** "A physical model of airflow in beef chillers". Refrigeration Science & Technology, 1993-3 p.199-206
52. **Maersk Sealand (2003), Maersk Sealand Shipping Containers Worldwide.** http://www.maersksealand.com/, accessed January, 2003
53. **Maguire, K.M. (1998)** "Factors affecting mass loss in apples". PhD Dissertation, Massey University, Palmerston North, New Zealand
54. **Mariotti, M., Rech, G. and Ramagnoni, P. (1995)** "Numerical study of air distribution in a refrigerated room". Proceedings of the International Congress of Refrigeration , vol.2 p.98-105
55. **Mason, P.J. (1998)** "Large-eddy simulation: A critical review of the technique". Quarterly Journal of the Royal Meteorological Society. 120 p.1-26
56. **Meffert, H.F.Th. (1993)** "Temperature conditions in refrigerated vehicles and containers II. Cargo temperature distribution". Refrigeration Science & Technology , 1993-3 p.509-518
57. **Meffert, H.F.Th. (1995)** "Further analysis of the relation air-product temperature on temperature distribution experiments with reefer containers". Proceedings 19th International Congress of Refrigeration, IIR Commission D2/3, 1995, vol 2 p.559-566
58. **Meffert, H.F.Th. (1998)** "Modelling product temperature in refrigerated holds". Refrigeration Science & Technology, 1998-2 p.70-83
59. **Meffert, H.F.Th. & van Beek, G. (1983)** "Basic Elements of a Physical Model for Refrigerated Vehicles - Air Circulation and Distribution". Proceedings 16th International Congress of Refrigeration, IIR Commission D2, 1983, Paris, vol 4 p.465-476
60. **Meffert, H.F.Th. & van Beek, G. (1988)** "Basic Elements of a Physical Model for Refrigerated Vehicles II - Temperature Distribution". Refrigeration Science & Technology, 1988-1 p.221-229
61. **Miller, D.S. (1990)** "Internal Flow Systems 2nd Ed.". BHRA (information services), Cranfield UK
62. **Mirade, P.S. & Daudin, J.D. (1998)** "A new experimental method for measuring and visualising air flow in large food plants". Journal of Food Engineering, 36 (1) p.31-49
63. **Moureh, J., Menia, N. and Flick, D. (2002)** "Numerical and experimental study of airflow in a typical refrigerated truck loaded with pallets". Computers and Electronics in Agriculture,

vol. 34 p.25-42

64. **Nobel, P.S. (1991)** "Cells and diffusion" in Physicochemical and environmental plant physiology. ed. Academic Press Inc, San Diego, USA
65. **Ower, E. & Pankhurst, R.C. (1966)** "The Measurement of Air Flow 4th Edition". Oxford Pergamon, New York, USA
66. **Perry, R.H. & Green, D. (1997)** "Perry's Chemical Engineers' Handbook 7th Ed.". McGraw-Hill Book Company, New York, USA
67. **Press, W.H., Teukolsky, S.A., Vetterling, W.T. & Flannery, B.P. (1992)** "Numerical Recipes in C - 2nd Edition". Cambridge University Press, New York, USA
68. **Rizzi, A. (2003)** "Development of a numerical model for the fluid dynamic simulation of an ascending flow ripening chamber". Journal of Food Engineering, 58 p.151-171
69. **RS Components (1999)** "Thermistors". RS Data sheet, Data Sheet # 232-538, Issued March 1999
70. **Santanam, C.B. & Tietbohl, G.L. (1983)** "Complex flow visualisation by a unique method". Flow Visualisation III : Proceedings of the Third International Symposium on Flow Visualisation, p.1-6
71. **Scott, G. & Richardson, P. (1997)** "Applications of computational fluid dynamics in the food industry". Trends in Food Science & Technology, 8(4) p.119-124
72. **Seatrade Reefer Chartering (2001), Seatrade.** www.seatradereefer.com, accessed October 2001
73. **Sharp, A.K. (1982a)** "Measurement of gas tightness with an automatic pressure-decay timer". Refrigeration Science & Technology, 1982-1 p.361-367
74. **Sharp, A.K. (1982b)** "Determination of gas-tightness of containers using a pressure-decay timer". International Journal of Refrigeration, vol 6 no 5 p.348-350
75. **Sharp, A.K., Banks, H.J. and Irving, A.R. (1986)** "The effect of age on the gastightness of ISO freight containers". Journal of Food Process Engineering, 8 p.65-80
76. **Sharp, A.K., Irving, A.R. and Banks, H.J. (1976)** "Leakage of air into ISO containers". Refrigeration Science & Technology, 1976-1 p.501-508
77. **Sharp Corp. (2003)** "Datasheet - PT480/PT481 Narrow Acceptance Phototransistor".
78. **Siemens (1986)** "NTC Thermistors - Data Book". Siemens AG, Munich, Germany
79. **Smale, N.J., Amos, N.D., Tanner, D.J. and Cleland, D.J. (2003b)** "Airflow Characteristics of Vented Horticultural Packaging". Proceedings 21st International Congress of Refrigeration, paper #244
80. **Smale, N.J., Tanner, D.J., Amos, N.D. and Legg, A. (2003a)** "Container leakage and air exchange rates: a simple measurement method and survey results". Proceedings 21st International Congress of Refrigeration, paper #245
81. **Statistics NZ (2003), Statistics New Zealand.** http://www.stats.govt.nz/, accessed 20 March 2003
82. **Stera, A.C. (1993)** "Developments in transportation of chilled produce by sea and air". Refrigeration Science & Technology, 1993-3 p.46-67
83. **Stera, A.C. (1999)** "Long distance refrigerated transport into the third millenium". Proceedings 20th International Congress of Refrigeration, Vol 4, Paper 736, 18p
84. **Talbot, M.T. (1988)** "An approach to better design of pressure cooled produce containers". Proceedings Florida State Horticultural Society, 101 p.165-175
85. **Tanner, D.J. (1998)** "Mathematical modelling for design of horticultural packaging". PhD Dissertation, Massey University, Palmerston North, New Zealand
86. **Tanner, D.J. & Amos, N.D. (2003)** "Temperature variability during shipment of fresh produce". Acta Horticulturae, 599 p.193-203
87. **Tanner, D.J., Cleland, A.C., Robertson, T.R. and Opara, L.U. (2000)** "Use of carbon dioxide as a tracer gas for determining in-package airflow distribution". Journal of Agricultural Engineering Research, 77(4) p.409-417

88. **Tassou, S.A. & Xiang, W. (1998)** "Modelling the environment within a wet air cooled vegetable store". Journal of Food Engineering , 38(2) p.169-187
89. **Thermometrics Inc. (2002),** **NTC Thermistors.** http://www.thermometrics.com/assets/images/ntcnotes.pdf, accessed 15 May 2002
90. **Tumambing, J., Amos, N. & Eggleston, V. (2001)** "Application of carbon monoxide detection technique to airflow distribution in an apple coolstore". Refrigeration , Storage and Transport Report #73, Food Science Australia, North Ryde, Australia
91. **U.S. Department of Health and Human Services (1997)** "Toxicological profile for ethylene glycol and propylene glycol". U.S. Department of Health and Human Services, Washington, USA
92. **van der Ree, H., Basting, W.J. and Nievergold, P.G.M. (1974)** "Prediction of temperature distributions in cargoes with the aid of a computer program using the method of finite elements". Refrigeration Science & Technology, 1974-2 p.195-220
93. **van der Sman, R.G.M. (1999)** "Lattice Boltzmann schemes for convection-diffusion phenomena; application to packages of agricultural products". PhD thesis, Wageningen, The Netherlands
94. **van der Sman, R.G.M. (2002)** "Prediction of airflow through a vented box by the Darcy-Forcheimer equation". Journal of Food Engineering, 55 p.49-57
95. **van Gerwen, R.J.M., van der Sluis, S.M. and van Oort, H. (1991)** "Computer modelling of carcass chilling processes". Proc. of the 18th Int'l Congress of Refrigeration , vol 4 p.1893-1897
96. **van Gerwen, R.J.M. & van Oort, H. (1989)** "The use of fluid dynamics simulation models in cold store design". Refrigeration Science & Technology, 1989-1 p.233-239
97. **Van Nieuwenhuizen, G.H. (1974)** "Air distribution by T-floor profiles". Refrigeration Science & Technology, 1974-2 p.81-87
98. **Van Pee, M., Berckmans, D., De Moor, M. and Van de Weyer, K. (1994)** "Visualisation and quantification of the air flow pattern in ventilated spaces using image analysis". Refrigeration Science & Technology, 1994-5 p.433-440
99. **Verboven, P., Hoang, M., De Baerdemaeker, J. and Nicolai, B.M. (1998)** "Numerical analysis of the air flow in a cool store by means of computational fluid dynamics". Acta Horticulturae, 476 p.121-128
100. **Verboven, P., Nicolai, B.M., Scheerlinck, N. and de Baerdemaeker, J. (1997)** "The local surface heat transfer coefficient in thermal food process calculations: a CFD approach". Journal of Food Engineering, 33(1/2) p.15-35
101. **Wang, H. (1990)** "Modeling of a refrigerating system coupled with a refrigerated room". PhD dissertation, Delft University of Technology, Delft, The Netherlands
102. **Wang, H. & Touber, S. (1988)** "Simple non-steady state modelling of a refrigerated room accounting for air flow and temperature distribution". Refrigeration Science & Technology, 1988-1 p.211-219
103. **Wang, S., Yernaux, M. and Deltour, J. (1999)** "A networked two-dimensional sonic anemometer system for the measurement of air velocity in greenhouses". Journal of Agricultural Engineering, 73 p.189-197
104. **Whale, J., Papadopoulos, K.H., Anderson, C.G., Helmis, C.G. and Skyner, D.J. (1996)** "A study of the near wake structure of a wind turbine comparing measurements from laboratory and full-scale experiments". Solar Energy, 56(6) p.621-633
105. **Wood, D.J. & Rayes, A.G. (1981)** "Reliability of Algorithms for Pipe Network Analysis". Journal of the Hydraulic Division ASCE, Vol.107 No. HY10
106. **Worley, M.S. & Manbeck, H.B. (1995)** "Modeling particle transport and air flow in ceiling inlet ventilation systems". Transactions of the ASAE, 38(1) p.231-239
107. **Yekutieli, O. (1974)** "A transport experiment with paprika in a stationary clip-on reefer container". Refrigeration Science & Technology, 1974-2 p.179-187

108. **Yongfu-Xu & Burfoot, D. (1999)** "Simulating the bulk storage of foodstuffs". Journal of Food Engineering, 39(1) p.23-29
109. **Yu, H. & Hoff, S.J. (1999)** "Airflow pattern similarity criteria for ceiling slot ventilated agricultural enclosures under isothermal conditions". Transactions of the ASAE, 42(2) p.459-469
110. **Zertal-Menia, N., Moureh, J. and Flick, D. (2002)** "Modelisation simplifee des coulements d'air dans un vehicule frigorifique". International Journal of Refrigeration, 25 p.660-672
111. **Zhang, G., Morsing, S., Bjerg, B., Svidt, K. and Strom, J.S. (2000)** "Test room for validation of airflow patterns estimated by computational fluid dynamics". Journal of Agricultural Engineering Research, v.76 p.141-148
112. **Zou, Q. (1998)** "CFD modelling of air flow and heat transfer in a ventilated carton". Masters Dissertation, Massey University, Palmerston North, New Zealand

16 Appendix 1

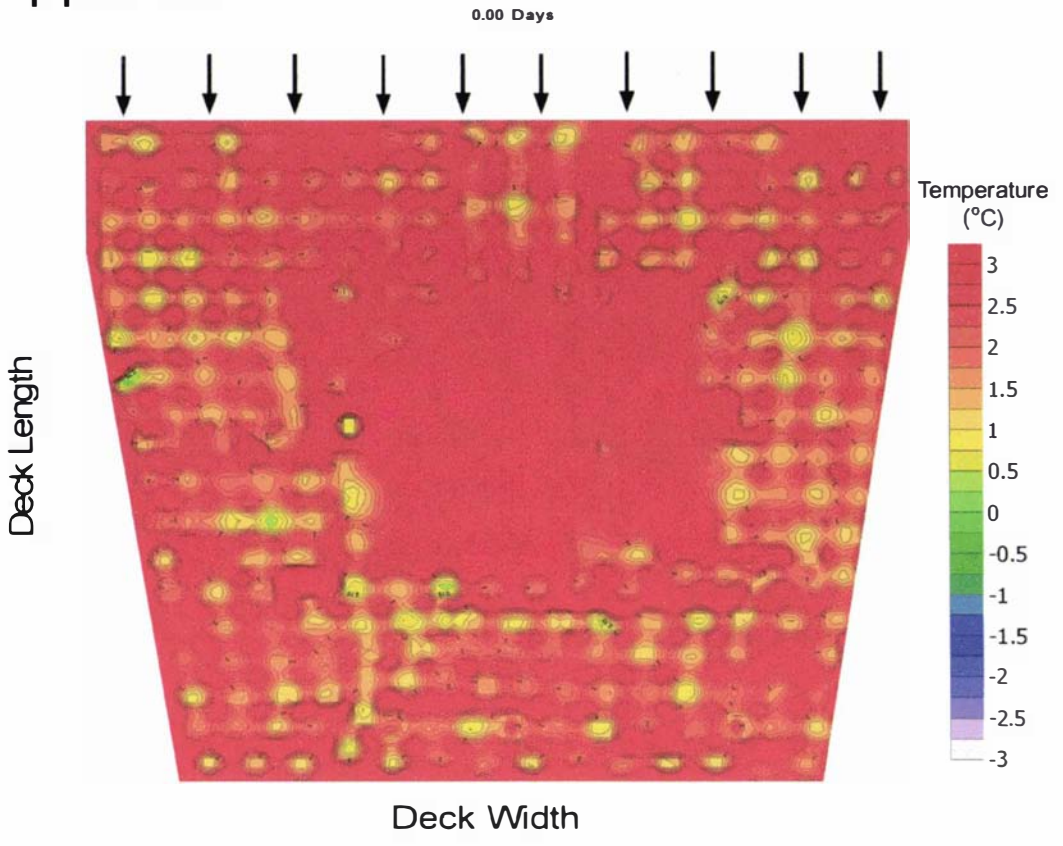

Figure 16-1 - Plan view of the refrigerated hold loaded with 307 pallets of kiwifruit showing the measured in-package air temperatures throughout the hold upon completion of loading

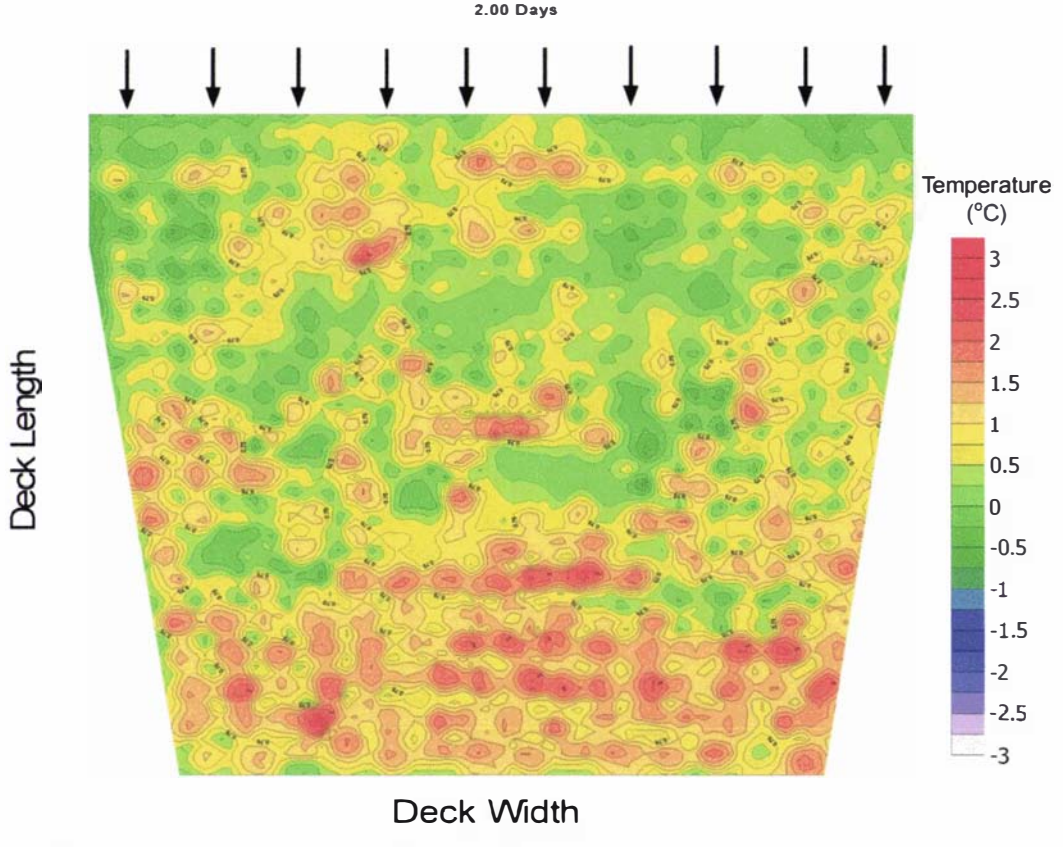

Figure 16-2 - Plan view of the refrigerated hold loaded with 307 pallets of kiwifruit showing the measured in-package air temperatures throughout the hold 2 days after loading

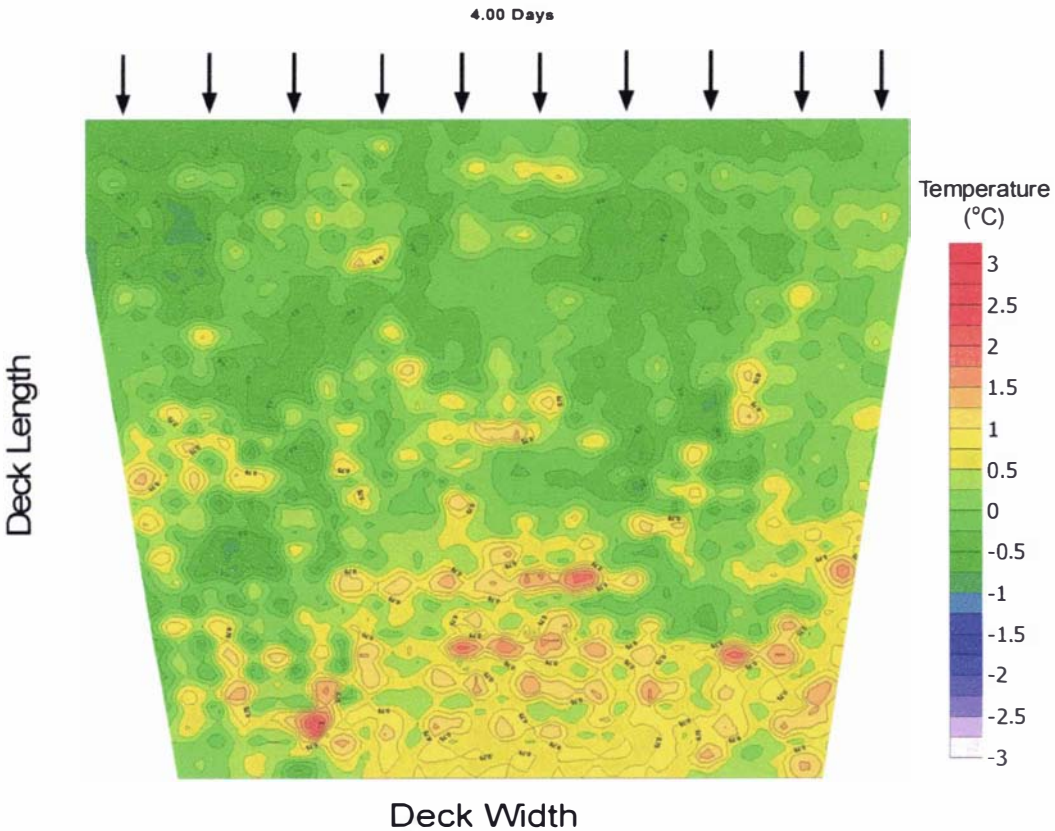

Figure 16-3 - Plan view of the refrigerated hold loaded with 307 pallets of kiwifruit showing the measured in-package air temperatures throughout the hold 4 days after loading

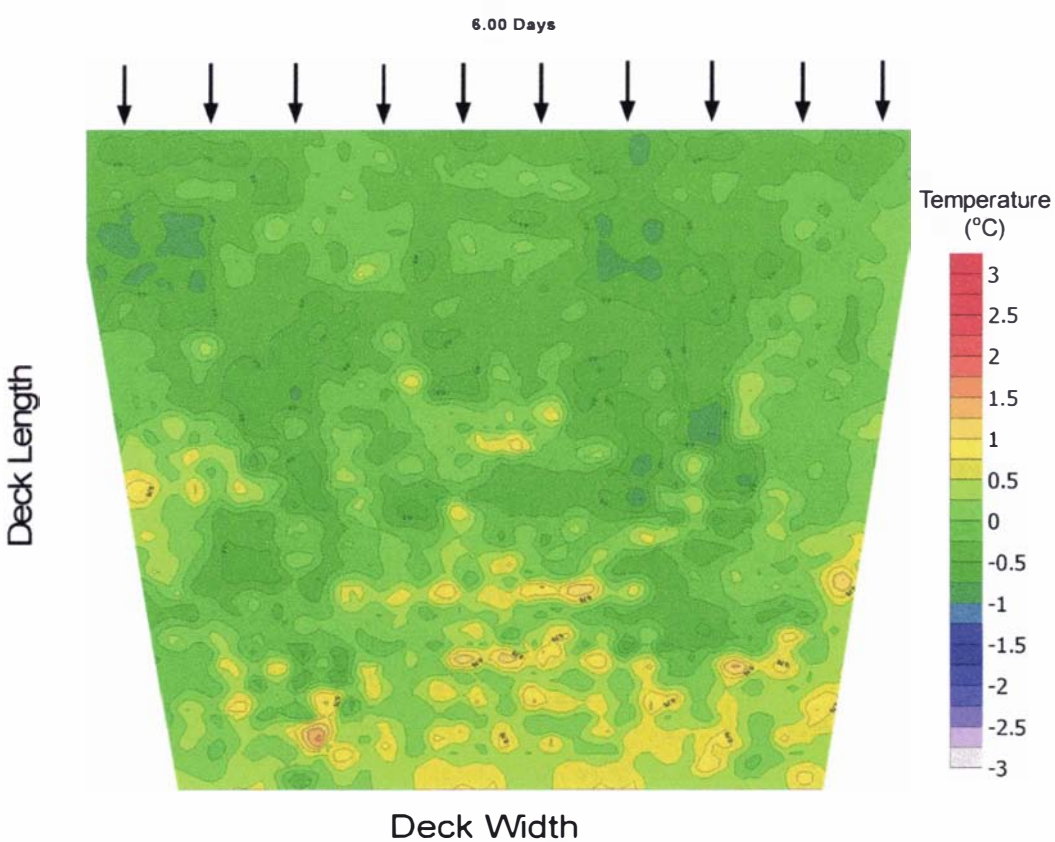

Figure 16-4 - Plan view of the refrigerated hold loaded with 307 pallets of kiwifruit showing the measured in-package air temperatures throughout the hold 6 days after loading

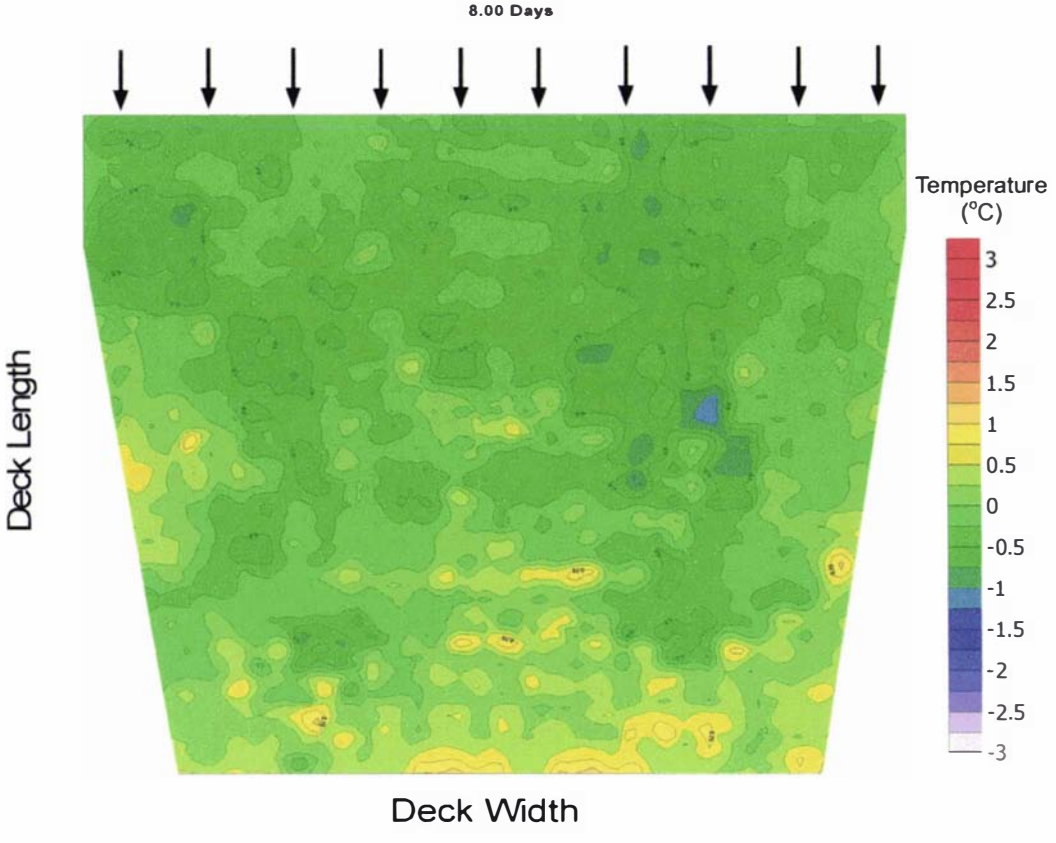

Figure 16-5 - Plan view of the refrigerated hold loaded with 307 pallets of kiwifruit showing the measured in-package air temperatures throughout the hold 8 days after loading

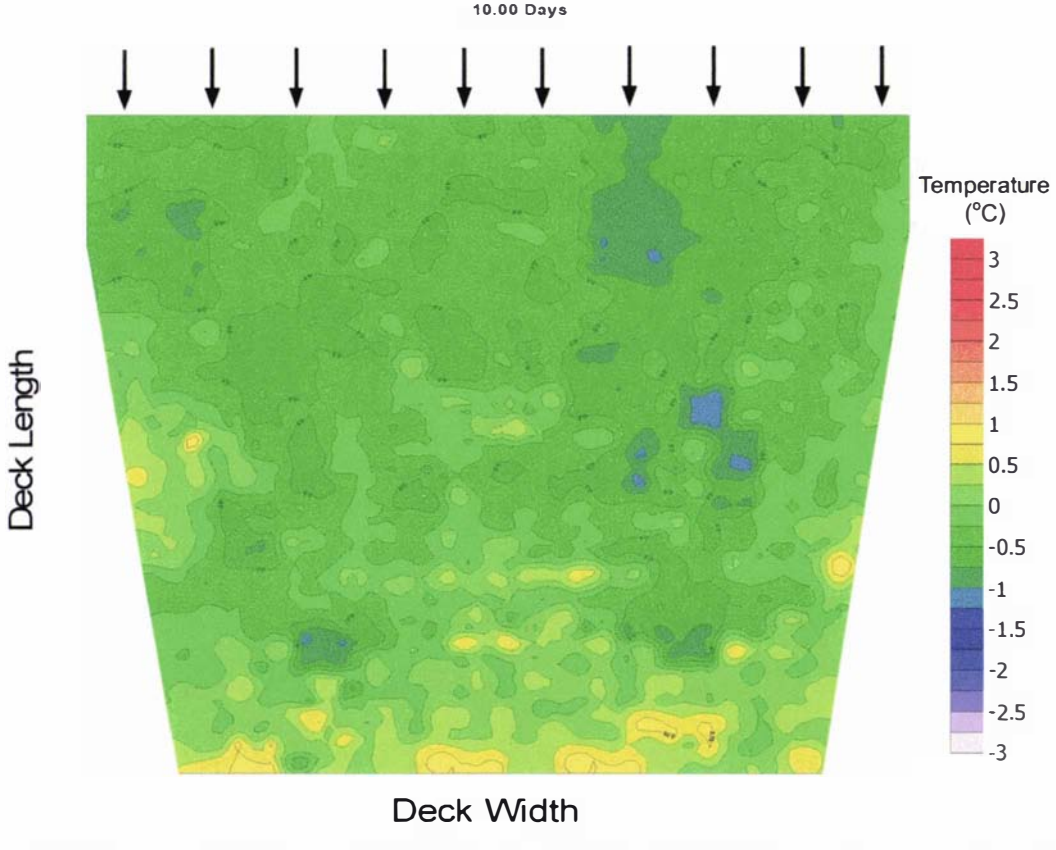

Figure 16-6 - Plan view of the refrigerated hold loaded with 307 pallets of kiwifruit showing the measured in-package air temperatures throughout the hold 10 days after loading

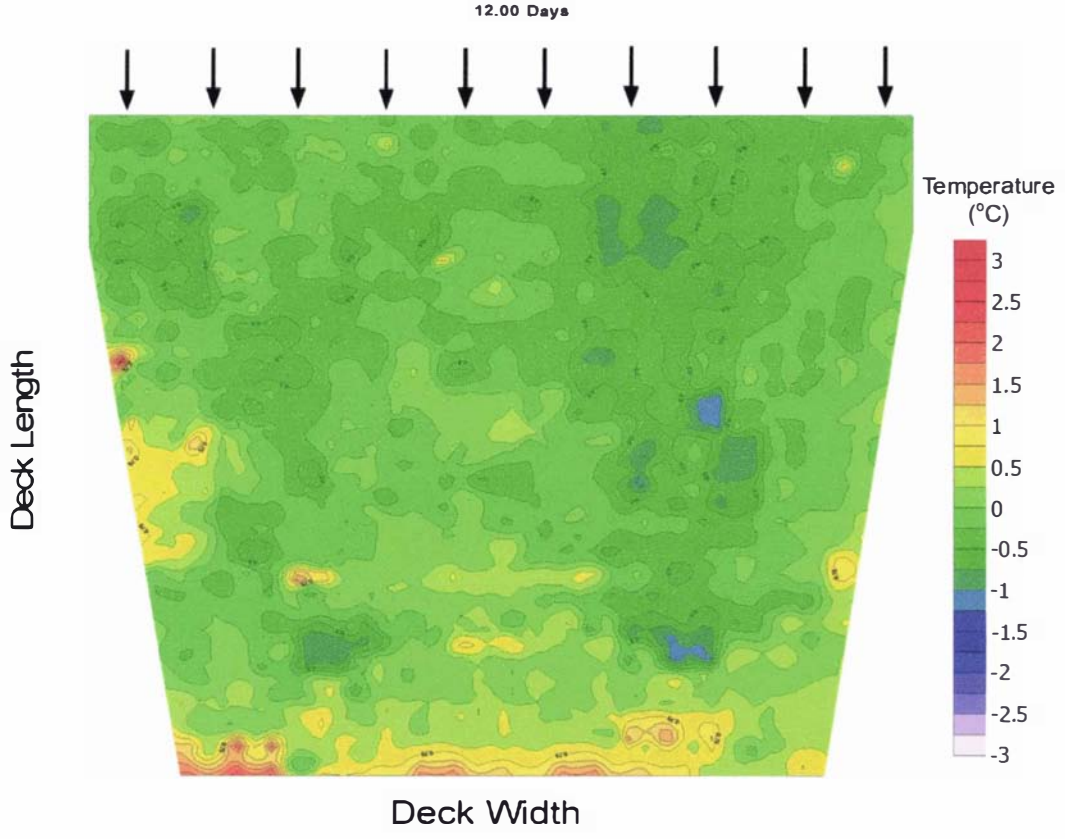

Figure 16-7 - Plan view of the refrigerated hold loaded with 307 pallets of kiwifruit showing the measured in-package air temperatures throughout the hold 12 days after loading

17 Appendix 2

Paper presented at the international conference Postharvest Unlimited, 12-14 June 2002, Leuven Belgium.

Smale, N.J., Tanner, D.J., Amos, N.D. and Cleland, D.J. (2003) "Airflow properties of packaged horticultural produce - a practical study". Acta Horticulturae, 599 p.443-450

Massey University

August 26, 2004

TO WHOM IT MAY CONCERN

This is to state that the research carried out for the Doctoral thesis entitled "*Mathematical Modelling of Airflow in Shipping Systems: Model Development and Testing*" was done by *Nicholas John Smale* in the *Institute of Food, Nutrition and Human Health*, Massey University, *Palmerston North Campus*, New Zealand in accordance with the University's Doctoral regulations.

Supervisor:

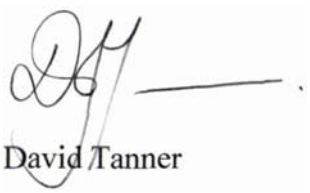

Dr David Tanner

Date: August 26, 2004

Massey University

August 26, 2004

TO WHOM IT MAY CONCERN

This is to state that the research carried out for the Doctoral thesis entitled "*Mathematical Modelling of Airflow in Shipping Systems: Model Development and Testing*" was done by *Nicholas John Smale* under the supervision of David Tanner, Nevin Amos and Don Cleland, along with the assistance of the technical and scientific staff of the *Institute of Food, Nutrition and Human Health*, Massey University, *Palmerston North Campus*, New Zealand and the *Supply Chain Innovation section*, Food Science Australia, *North Ryde*, Australia. This thesis material has not been used for any other degree.

Candidate:

Nicholas Smale

Date: August 26, 2004

Massey University

August 26, 2004

TO WHOM IT MAY CONCERN

This is to state with respect to the Doctoral thesis entitled "*Mathematical Modelling of Airflow in Shipping Systems: Model Development and Testing*":

- References to work other than that of the candidate has been appropriately acknowledged
- Research practice, ethical and genetic technology policies have been complied with
- The thesis does not exceed 100,000 words

Supervisor:

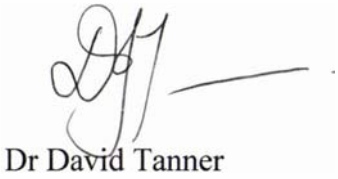

Dr David Tanner

Candidate:

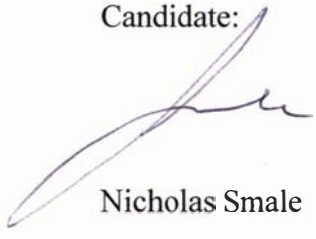

Nicholas Smale

Date: August 26, 2004